Spring 5-11-2019

Development of Bismuth Oxyhalide Photocatalysts for Environmental and Industrial Applications

Robert Arthur

University of Maine, robert.arthur@maine.edu

Follow this and additional works at: https://digitalcommons.library.umaine.edu/etd

Part of the <u>Analytical Chemistry Commons</u>, <u>Environmental Chemistry Commons</u>, and the <u>Inorganic Chemistry Commons</u>

DEVELOPMENT OF BISMUTH OXYHALIDE

PHOTOCATALYSTS FOR ENVIRONMENTAL AND INDUSTRIAL APPLICATIONS

By

Robert Brent Arthur

B.Sc., College of Charleston, 2013

A DISSERTATION

Submitted in Partial Fulfillment of the

Requirements for the Degree of

Doctor of Philosophy

(in Chemistry)

The Graduate School

The University of Maine

May 2019

Advisory Committee:

Dr. Howard Patterson, Professor of Chemistry, Co-advisor

Dr. Elizabeth Stemmler, Professor of Chemistry, Bowdoin College, Co-advisor

Dr. Scott Collins, Professor of Chemistry, Co-advisor

Dr. Alice Bruce, Professor of Chemistry

Dr. Matthew Brichacek, Assistant Professor of Chemistry

Dr. Carl Tripp, Professor of Chemistry

DEVELOPMENT OF BISMUTH OXYHALIDE

PHOTOCATALYSTS FOR ENVIRONMENTAL AND INDUSTRIAL APPLICATIONS

By Robert B. Arthur

Co-advisors: Dr. Howard H. Patterson, Dr. Elizabeth A. Stemmler, and Dr. Scott D. Collins

An Abstract of the Dissertation Presented
in Partial Fulfillment of the Requirements for the
Degree of Doctor of Philosophy
(in Chemistry)

May 2019

Heterogeneous semiconductor photocatalysis, of interest for water splitting and environmental remediation applications, uses light to drive reactions. Metal oxide and sulfide semiconductors have been previously studied but have limitations that include large band gap energies and high rates of recombination. Bismuth oxyhalides (BiOX) are an emerging class of photocatalysts with tunable band gaps and low rates of recombination due to their unique crystal structures. Studies of BiOX photocatalytic activity have largely focused on removal of azo dyes from aqueous solutions, with little attention paid to degradation byproducts. Furthermore, these catalysts have not been explored as a means to conduct organic transformations including C-C bond formation. In this work, BiOX solids were evaluated for the photocatalytic degradation of the persistent organic pollutants atrazine and ibuprofen. Work with atrazine, degraded with BiOCl and Cu-BiOCl under 254 nm light conditions was explored for $^{\bullet}OH$ radical, $O_2^{\bullet-}$ and electron hole contributions to the reaction pathway. The reaction rates and products generated by the photocatalytic degradation of ibuprofen using BiOCl were characterized and a degradation mechanism was proposed. The photocatalytic degradation studies suggest the high reactivity of electron holes in the valence band of BiOCl play an important role in the observed degradation efficiency. Finally, BiOI photocatalysts were evaluated for their potential to drive coupling reactions under visible light irradiation. It was found that coupling products of cyclohexyl halides and toluene are achieved in high yield, but cyclohexane dehydrodimerization reactions proceeded with low yields.

DEDICATION

Dedicated to

My parents, John and Cathy Arthur

For their love, support and encouragement.

ACKNOWLEDGEMENTS

TABLE OF CONTENTS

LIST OF TABLES

LIST OF FIGURES

CHAPTER 1

INTRODUCTION

1.1 Motivation

1.1.1 Environmental

Public health related environmental concerns and a growing demand for pharmaceuticals and other complex organic chemicals represent two issues facing our rapidly increasing population. Countries undergoing widespread industrialization, which encourages minimal regulation to maximize economic benefit, has led to potentially harmful contamination of the environment, including local water sources [1]. Even in countries where environmental inputs are regulated, contamination occurs. One area of concern is the growing global use of pharmaceuticals.

As a result of modern industrial development, nearly 9000 compounds are currently in use worldwide for pharmaceutical applications [2]. Pharmaceuticals and personal care products (PPCPs) form a group of biologically active chemicals that have well-established routes of entry to water supplies and can cause long-term contamination [3–7]. Since these molecules do not interact appreciably with water, their rate of hydrolysis and subsequent removal proceeds very slowly, meaning that these compounds have long half-lives and will slowly build up in water supplies [8,9].

Current wastewater treatment processes have been shown to be insufficient in removing PPCPs from drinking water [3]. Additionally, traditional techniques such as chlorination, while efficient at removing bacteria, have shown the potential to chemically generate more toxic disinfection byproducts [10]. Alternative options to traditional methods must be explored to combat this emerging issue.

1.1.2 Industrial

Transportation fuels including gasoline, diesel, and jet fuel are an integral part of modern life. Currently these fuels are obtained from the refinement of crude oil extracted from limited deposits located in the Earth's crust. Only about half of crude oil can be refined into molecules that provide sufficient energy to operate the machines and vehicles that support industrial efforts [11]. The remaining half of crude oil consists of methane, ethane and propane [11]. While these low molecular weight hydrocarbons can be used for heating or in the production of plastics, they provide insufficient energy density to be efficiently used as transportation fuel.

Recently, advanced drilling techniques have enabled producers of petroleum to access large quantities of natural gas. After drying, natural gas consists of 97% methane [12]. Methane becomes more valuable to producers after it has been converted to higher molecular weight hydrocarbons for use in high energy density transportation fuels. This is very desirable for producers, but few companies currently operate gas-to-liquid plants due to the high capital investment and operating costs associated with the current process. The state-of-the-art Fischer-Tropsch process requires multiple steps to generate higher order hydrocarbons from natural gas [13].

C-H activation to form hydrocarbons has been a major goal of the petroleum industry in order to increase the value obtained from natural gas. Converting these gases into liquid fuels would enable their direct use in current automobile engines, as well as making them easier to store and transport to the consumer. This advantage has driven researchers to seek methods that activate C-H bonds in saturated hydrocarbons to induce formation of C-C bonds [14]. In general, C-C coupling reactions are a widely utilized synthesis strategy throughout the chemical industry

[15,16]. However, these reactions require the use of expensive reagents leading researchers to seek alternative approaches [16].

1.2 Introduction to Photocatalysis

Energy demands of modern industry will continue to increase as world population grows. Utilization of solar energy presents an alternative to traditional forms of energy generation due to the large and consistent amount of radiation that reaches the earth daily. The photovoltaic industry is already beginning to mature and carve out its place in the global economy, however other direct applications of solar energy usage are also being explored [17]. Photochemical reactions have been studied since the early 20th century and proved that solar irradiation could potentially be used directly in chemical processes [18]. Photocatalysis is a process that proceeds at room temperature using light to overcome energy barriers and drive reactions. Photocatalysis was first demonstrated by Fujishima and Honda in 1972 where they showed that irradiating single crystal rutile titanium dioxide (TiO_2) with ultraviolet light enabled the production of H_2 and O_2 via water splitting (see Figure 1.1) [19]. Since these initial reports, photocatalysis has become a widely researched field for applications including solar energy production [20], air and water purification [21], self-cleaning surfaces [22], and chemical synthesis [23].
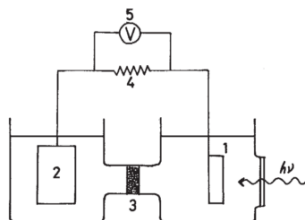
Figure 1.1. Electrochemical cell used by Fujishima and Honda in the initial demonstration of photocatalysis [19].

3

1.3 Heterogeneous Semiconductor Photocatalysis

Heterogeneous semiconductor photocatalysts are solid particles of semiconductors such as TiO_2, ZnO, Fe_2O_3, and CdS that can be used to drive reactions using light. They work by absorbing light of an appropriate wavelength to promote electrons from the valence band to the conduction band. The energy of photons necessary to promote electrons is called the band gap. This process generates excited electrons in the conduction band and effective "electron holes" (h^+) in the valence band. The electron-hole pairs are then able to move to the surface of the semiconductor, where reactions can occur, or thermally recombine. Recombination is detrimental to the overall activity of a catalytic system since recombined electron-hole pairs are not able to participate in the intended reaction. The surface reactions that take place in semiconductor photocatalysis consist of either oxidation by electron holes in the valence band, or reduction by excited electrons in the conduction band. An overall scheme for photocatalysis is represented in Figure 1.2. The properties of an ideal photocatalyst are high photoactivity, broadband light absorption in the UV-Vis range, chemically inert behavior with respect to catalyst decomposition, and resistance to photocorrosion.
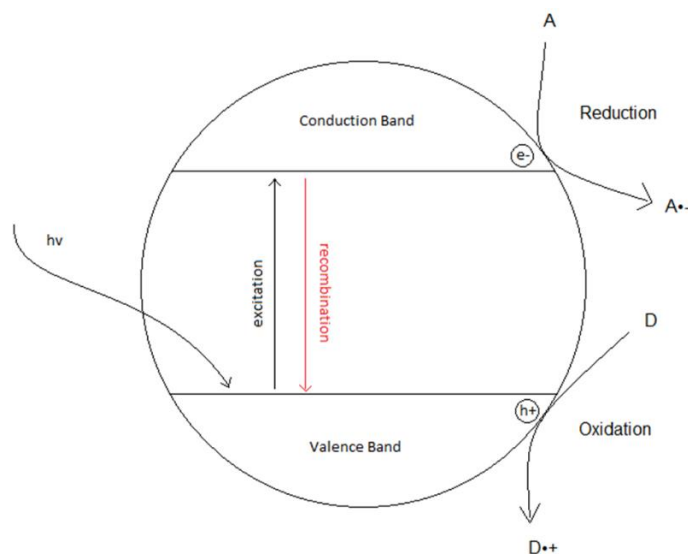
Figure 1.2. General photocatalytic reaction scheme.

1.3.1 Application in Environmental Remediation

In 1976 Carey et al. showed that UV irradiation of aqueous suspensions of TiO_2 in the presence of polychlorobiphenyls (PCBs) resulted in dechlorination of the PCBs [24]. This study sparked intense interest in the development of photocatalysts for environmental remediation applications. It is commonly accepted that UV irradiation of TiO_2 in aqueous solutions produces hydroxyl radicals (•OH) via the reaction of h^+ with either OH^- or H_2O [25,26]. This is considered to be the source of the high activity of TiO_2 for photocatalytic degradation of organic pollutants. This phenomenon of hydroxyl and superoxide radical production has been exploited by a large number of researchers who have demonstrated photocatalytic degradation of organic pollutants using the UV/TiO_2 system [27–40].

Other oxide and sulfide semiconductors with advantageous band gaps have been evaluated as potential photocatalysts for environmental remediation. However, the iron oxide polymorphs as well as the sulfides tested to date are all susceptible to photocorrosion and break down during the degradation process [41]. CdS has been shown to be an effective visible light photocatalyst, however cadmium is generally known to be a carcinogen, and the CdS nanoparticles are toxic to aquatic life [42]. ZnO in particular is an alternative semiconductor that has been researched instensely, since it has a wider band gap than TiO_2 (3.37 eV) and presents high photocatalytic activity [43,44]. ZnO has also been shown to proceed through a similar photocatalytic mechanism as TiO_2 based on the production of hydroxyl radicals [44]. It was also found that superoxide radical formation is also found to be prominent in ZnO-based photocatalytic processes [44]. However, ZnO has been found to be an ineffective semiconductor photocatalytic system due to a slow dissolution process in water that converts ZnO to $Zn(OH)_2$ on the particle surface, thus deactivating the catalyst and reducing reusability [45]. The need to develop new and more effective

photocatalysts for environmental remediation provides one motivation for the work described in this thesis.

1.3.2 Application in C-C Coupling Reactions

Photocatalysts also hold promise for industrial applications, including C-C coupling reactions. Catalytic processes have been reported over Rh and W/HZSM-5 for conversion of methane to hydrocarbons; however, these methods require high temperatures that lead to deactivation of the catalyst via coking [46,47]. A reaction that proceeds at room temperature using a photocatalyst to overcome the activation energy could achieve the goal of C-C bond formation from methane in an energy efficient process [48–50]. Several recent literature reports provide details on attempts to convert small hydrocarbons to larger coupled molecules using traditional heterogeneous catalysis methods [51,52].

Photocatalytic coupling and dehydrodimerization reactions have been studied previously by H. Kisch et al. [53–55]. This group has authored several reports concerning the mechanisms of selective photocatalytic transformations and has developed a classification system for types of organic photocatalytic reactions. The "Type A" reactions reported by Kisch et al. involve the reduction/oxidation of two or more substrates. This reaction type includes C-C coupling through dehydrodimerization, where two molecules of the same structure are coupled oxidatively while simultaneously generated hydrogen ions are reduced to molecular hydrogen. This process was demonstrated through UV and visible-light irradiation of solutions of 2,5-dihydrofuran in D_2O with suspended ZnS and Pt/CdS (see Figure 1.3) [54]. The authors report yields of 60%, demonstrating the potential of photocatalytic systems for efficient dehydrodimerization.

6
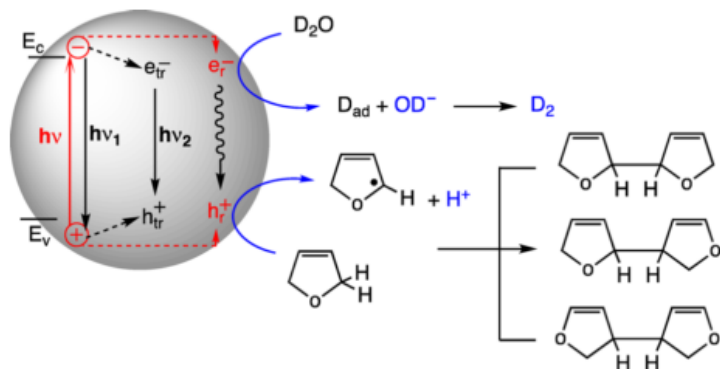
Figure 1.3. Anaerobic dehydrodimerization of 2,5-dihydrofuran in D_2O [54].

Non-oxidative coupling of methane (NOCM) achieved via photocatalysis is a process that aims to reduce the capital and operating costs of gas-to-liquids upgrading and unlock the value stored in natural gas. Yoshida et al. have studied the non-oxidative coupling of methane (NOCM) utilizing a variety of strategies to overcome the energy of activation of the C-H bond [56–59]. One report demonstrated the activity of Al_2O_3 photocatalysts highly dispersed in SiO_2 [59]. The authors reported that this is an effective strategy of photocatalyst design for NOCM due to the insulating nature of the silica. This design is advantageous because the silica support material is resistant to photoreduction by methane or hydrogen gas. The resistance to photoreduction of the catalyst helped prevent the catalyst from losing active sites and becoming unreactive. Yoshida et al. have also reported on NOCM using a β-Ga_2O_3 photocatalyst showing a yield of roughly 0.5% for total hydrocarbons [57]. Interestingly, no significant difference was seen in hydrocarbon yield when CO_2 was added as a reactant; however, CO was then detected as a product.

More recent studies from the Yoshida group have focused on dehydrodimerization reactions of organic molecules with an emphasis on C-C bond formation. For example, metal-doped TiO_2 was investigated for the photocatalytic cross-dimerization of THF with cyclohexane in 2017 [14]. The authors found that Pt-doped TiO_2 showed a significant increase in photocatalytic

dehydrodimerization activity compared with TiO_2 alone or Pd-, Au-, or Rh-doped TiO_2. Although these results have shown low hydrocarbon yields, they demonstrate the viability of this method of hydrocarbon upgrading and suggest that yields could be improved by altering the composition of the catalyst.

1.4 Bismuth Oxyhalides

TiO_2 has received the most attention in photocatalysis research as it was the first photocatalyst discovered and is still one of the most widely-utilized materials [19]. TiO_2 has been applied to diverse applications ranging from self-cleaning surfaces and dye-sensitized solar cells [60]. However, TiO_2 has the drawback of possessing a large band gap of 3.2 eV, which prevents it from being applied in solar photocatalytic applications. Using ambient solar light in an outdoor treatment facility can reduce the cost of photocatalysis-based water treatment vs. using lamps over tanks at a typical indoor water treatment plant. Various strategies have been employed to develop robust photocatalysts capable of functioning under ambient solar light. Investigators have tried to imbue visible-light activity to TiO_2 by including metal and non-metal doping and employing nanoparticles and heterojunction formation [61–63]. However, these systems are inherently more complicated to synthesize and more expensive to produce [61–63].

Traditional photocatalytic reaction systems also exhibit high rates of electron-hole recombination. This occurs when excited state electrons and electron holes collide in either the photocatalyst bulk or on the photocatalyst surface. This results in the loss of photocatalytic activity since the active species are prevented from further reacting with the target molecules. Although

8

doping strategies have been previously attempted, this issue may be better addressed by using a material with a different crystal structure to promote charge separation.

Compounds of the bismuth oxyhalide (BiOX) series exhibit interesting optical and semiconducting properties. The crystal structure of BiOX was first elucidated by Bannister in 1935 and found to possess tetragonal geometry consisting of covalently bonded layers of [X-Bi-O-Bi-X] [64]. This structure results in the presence of an internal electric field that facilitates the separation of holes and electrons, thus increasing the photocatalytic activity [65]. The general crystal structure for BiOX is given in Figure 1.4.
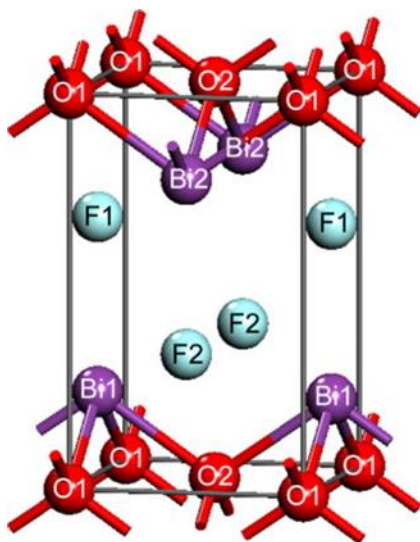
Figure 1.4. Computer-generated model of BiOX structure [66].

Bismuth oxychloride (BiOCl) was the first BiOX compound to be tested for photocatalytic properties by Zhang et al. in 2006 [67]. After this initial study, many other reports have followed further establishing the capabilities and potential of BiOX compounds as photocatalysts. Many researchers have undertaken attempts to improve the photocatalytic activity of BiOX compounds

in order to enable their use in industrial applications. Two primary approaches have been undertaken toward this goal: (1) the development of synthetic methods directed at novel BiOX structures, and (2) the modulation of BiOX using various dopants. Since the properties of a material are derived from structure, synthetic methods such as crystal facet engineering [68–81], production of ultrathin nanosheets [82–84], synthesizing hollow and porous nanostructures [85–90] and nanospheres [91,92] have been developed to access novel morphologies. Doping strategies include metal-doping [93–98], nonmetal-doping [99,100], introduction of structural defects [74,75,80,101–104], use of dye-sensitizers [105,106], and inclusion in heterojunctions with other semiconductors [97,98,104,107–116]. For in-depth discussion of the diverse approaches to BiOX synthesis see reviews by Di et al. [117] and Yang et al. [118].

While bismuth oxyhalide compounds are not as widely used in industry as TiO_2, they hold potential to become the preferred option for photocatalytic degradation of water-borne organic contaminants. Numerous groups have shown that BiOX catalysts present high photocatalytic activity under visible light irradiation [119,120,65,121]. This is a tremendous advantage of using BiOX catalysts since water can be treated in outdoor facilities vs. storing it in tanks or channels at a wastewater treatment facility with continuously running UV lights. Being able to treat water with ambient sunlight reduces logistical difficulties with treating the water and saves the cost of additional wastewater treatment plant space and electricity for operating UV lamps.

BiOX photocatalysts have been previously used in applications including water splitting [112,115,122], solar cells [123], photoreduction of CO_2 [70,80,124], N_2 fixation [125,126], bacterial disinfection [127], removal of air contaminants [128–132], oxidation of heavy metal pollutants [133–138], and photodynamic therapy [94]. They hold promise for many applications that include remediation of environmental pollutants and industrial C-C coupling reactions.

1.4.1 Applications of BiOX Photocatalysts

This dissertation is focused on the development of bismuth oxyhalide photocatalysts for environmental and industrial applications. Photocatalytic degradation of aqueous pollutants by BiOX for water purification has been previously explored. On the other hand, industrial applications have been investigated only minimally. Background on BiOX photocatalysis in these areas is summarized below.

1.4.1.1 Environmental Applications of BiOX Photocatalysts

Previous studies on application of BiOX to the degradation of organic pollutants have focused on pollutants such as dyes, pharmaceuticals, and industrial effluents [97,103,108,139–145]. The primary active species responsible for the high photocatalytic degradation properties of BiOX have been identified to be electron holes and superoxide radicals [97,143,144].

The application of BiOX photocatalysts for environmental remediation was first reported by Zhang et al. who demonstrated that BiOCl outperformed Degussa P25 TiO_2 under 365 nm irradiation for the photocatalytic degradation of aqueous methyl orange dye [67]. Electronic structure calculations were conducted as a part of this study and showed that the highest occupied molecular orbitals for BiOCl originate from Cl 3p orbitals, while the lowest unoccupied molecular orbitals originate from Bi 6p orbitals [67]. Lei et al. later reported on photocatalytic degradation of dyes, including methyl orange, rhodamine B, methylene blue, and ethylene violet, with BiOCl. The activity of the catalyst was dependent on catalyst morphology, with flower-like microspheres presenting the highest rate of degradation under 254 nm irradiation [146]. BiOCl and BiOBr microspheres were both tested for photocatalytic degradation of ibuprofen under visible light irradiation, and the authors found that adsorption was the main contributor to ibuprofen removal

[147,148]. A novel $BiOCl_{0.875}Br_{0.125}$ photocatalyst was synthesized and found to degrade pharmaceuticals, including carbamazepine, ibuprofen, bezafibrate, and propranolol, under simulated solar irradiation [149].

BiOI has been explored as a visible light active photocatalyst for environmental remediation and water treatment. BiOI nanoplates were synthesized and evaluated for photocatalytic degradation of methyl orange and phenol [150]. Radical scavenging experiments showed that electron holes and superoxide radicals were primarily responsible for the observed photocatalytic activity [150]. Ionic liquid-modified BiOI was demonstrated to effectively degrade methyl orange under visible light photocatalytic conditions [151]. Using radical scavenging experiments, the authors found that the ionic liquid modification acted as an electron trap, and that electron holes were the primary species responsible for the photocatalytic activity (see Figure 1.5) [151]. A series of BiOI compounds were synthesized with varying ratios of Bi:O:I by changing the temperature of the hydrothermal synthesis conditions. The variation in stoichiometry was found to result in a range of band gap energies (1.86-3.32 eV), with higher iodine content producing smaller band gaps. After performing photocatalytic degradation and radical scavenging experiments with the synthesized catalysts and crystal violet dye, the researchers found that superoxide radicals were the dominant species during the degradation process [101]. Hao et al. showed that BiOI, synthesized using polyvinylpyrrolidone (PVP) as a directing agent toward microsphere structure, was effective at photocatalytic degradation of tetracycline under visible light irradiation, demonstrating the potential for BiOI to degrade persistent organic pollutants [142].
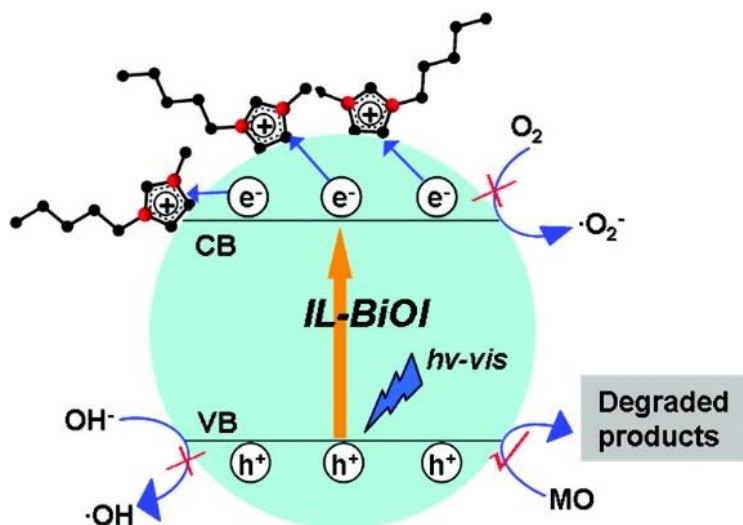
Figure 1.5. Photocatalytic degradation scheme for ionic liquid modified BiOI with methyl orange [151].

1.4.1.2 Industrial Applications of BiOX Photocatalysts

Up to this point, the use of BiOX compounds for industrial applications has been extremely limited. Henriquez et al. demonstrated the first application of BiOX and TiO_2 compounds for selective oxofunctionalization of cyclohexane in water with O_2 [152]. For both photocatalysts the observed products are cyclohexanol and cyclohexanone. The proposed reaction mechanism (see Figure 1.6) suggests that oxidation of cyclohexane by an electron hole in the valence band of the photocatalyst initiates the reaction. This results in the formation of a cyclohexyl radical on the surface of the photocatalyst that reacts with oxygen species to form the final oxidized products.
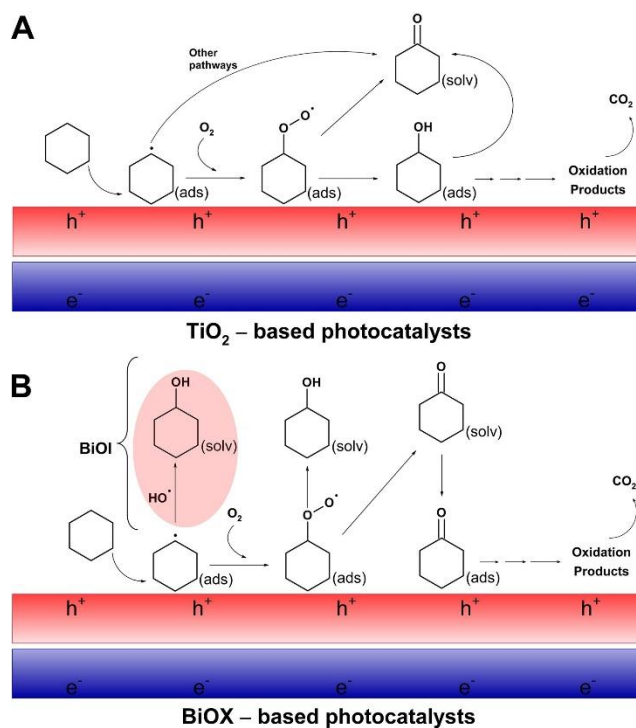
Figure 1.6. Proposed pathways for cyclohexane oxidation over (A) TiO$_2$ and (B) BiOX photocatalysts [152].

1.5 Thesis Objectives and Organization

Photocatalysis holds promise as an energy-efficient approach for environmental remediation and industrial synthesis; however, the current preferred heterogeneous semiconductor photocatalyst, TiO$_2$, is limited by a large band gap, high rate of electron-hole recombination, and lack of direct reaction with target substrates. This work aims to determine whether BiOX photocatalysis is capable of addressing challenges in environmental and industrial applications by exploring photocatalytic degradation of model environmental pollutants and photocatalytic C-C coupling reactions.

14

The work addressing these goals has been organized into the following sections. Chapter 2 presents the synthesis, characterization, and application of Cu-BiOCl to the photcatalytic degradation of atrazine. Cu-BiOCl was synthesized utilizing an ionic liquid method and characterized by X-Ray diffraction, diffuse reflectance spectroscopy, photoluminescence spectroscopy, and infrared spectroscopy. Both Cu-BiOCl and BiOCl were evaluated for dark adsorption and photocatalytic degradation of atrazine, one of the most widely used pesticides in the United States. Radical scavenging experiments were performed to determine the influence of electron holes, hydroxyl radicals, and superoxide radicals on the photocatalytic degradation process. For both photocatalysts, electron holes were found to exhibit the largest effect on the photocatalytic degradation process. This information was used to formulate a mechanism for photocatalytic degradation of atrazine by Cu-BiOCl.

Chapter 3 focuses on the identification of ibuprofen degradation intermediates generated by BiOCl photocatalysis. Previous work on photocatalytic degradation of ibuprofen with BiOX compounds suggested that adsorption was the main route of ibuprofen removal from solution. [147,148] However, in our work we identified a total of thirteen degradation products using HPLC-DAD and LC-MS/MS. Of these photoproducts, two were attributed to the relatively fast decarboxylation of ibuprofen and were considered "primary" photoproducts. Kinetic models were used to describe production and reactions of both primary photoproducts. Secondary degradation products were attributed to one of the primary photoproducts. A mechanism for ibuprofen degradation by BiOCl photocatalysis was proposed based on the identified intermediates.

Chapter 4 consists of three projects directed at the application of BiOX photocatalysis to reactions that are either currently used or would be useful in chemical industry. The first project focused on the application of BiOX photocatalysts to natural gas condensation with the goal of

demonstrating that photocatalytic methods could be applied to convert natural gas to higher molecular weight liquid hydrocarbons under mild conditions. Using cyclohexane, only limited dehydrodimerization was observed. The second project explored the effect of visible light irradiation on the addition of iodine to cyclohexane with the goal of using BiOX photocatalysts to generate iodocyclohexane *in situ* for coupling reactions with aryl compounds. Coupling reactions were then explored using cyclohexyl halides and aryl substrates to mimic coupling reactions commonly used in synthesis of complex organic molecules.

The appendices collect some other work published during the completion of this work, but are not directly related to the overarching theme of the dissertation. Appendix B is comprised of a manuscript published in *Inorganic Chemistry* on the photophysical characterization of copper halide complexes. Appendix D consists of a publication in *Gold Bulletin* discussing the photoluminescence properties of samarium-gold coordination polymers. Appendix E is a review of TiO$_2$-based photocatalytic degradation of pesticide compounds that has just been accepted in *Catalysis Reviews*. Appendix G is a manuscript recently submitted to *Dalton Transactions* that discusses the synthesis and photophysical characterization of a gold-viologen complex.

1.6 References

1.   Ebenstein, A. The Consequences of Industrialization: Evidence from Water Pollution and Digestive Cancers in China. *Rev. Econ. Stat.* **2019**, *94*, 186–201.

2.   Offermanns, S.; Rosenthal, W. . *Encyclopedic Reference of Molecular Pharmacology*; 1st ed.; Springer Verlag: Berlin, 2004;

3.   Jones, O. A.; Lester, J. N.; Voulvoulis, N. Pharmaceuticals: a threat to drinking water? *Trends Biotechnol.* **2005**, *23*, 163–167, doi:10.1016/j.tibtech.2005.02.001.

4.   Jux, U.; Baginski, R. M.; Arnold, H.-G.; Krönke, M.; Seng, P. N. Detection of pharmaceutical contaminations of river, pond, and tap water from Cologne (Germany) and surroundings. *Int. J. Hyg. Environ. Health* **2002**, *205*, 393–398, doi:10.1078/1438-4639-00166.

5.   Kümmerer, K. Drugs in the environment: emission of drugs, diagnostic aids and disinfectants into wastewater by hospitals in relation to other sources – a review. *Chemosphere* **2001**, *45*, 957–969, doi:10.1016/S0045-6535(01)00144-8.

6.   Jones, J. G. Pollution from Fish Farms. *Water Environ. J.* **1990**, *4*, 14–18, doi:10.1111/j.1747-6593.1990.tb01552.x.

7.   Boxall, A. B. A.; Rudd, M. A.; Brooks, B. W.; Caldwell, D. J.; Choi, K.; Hickmann, S. Pharmaceuticals and personal care products in the environment: what are the big questions? Alistair B.A. Boxall, Murray A. Rudd, Bryan W. Brooks, Daniel J. Caldwell, Kyungho Choi and Silke Hickmann. *Environ. Health Perspect.* **2012**, *9*, 1221.

8.   Richardson, M. L.; Bowron, J. M. The fate of pharmaceutical chemicals in the aquatic environment. *J. Pharm. Pharmacol.* **1985**, *37*, 1–12, doi:10.1111/j.2042-7158.1985.tb04922.x.

9.   Vione, D.; Maddigapu, P. R.; De Laurentiis, E.; Minella, M.; Pazzi, M.; Maurino, V.; Minero, C.; Kouras, S.; Richard, C. Modelling the photochemical fate of ibuprofen in surface waters. *Water Res.* **2011**, *45*, 6725–6736, doi:10.1016/j.watres.2011.10.014.

10.   Krasner, S. W.; Weinberg, H. S.; Richardson, S. D.; Pastor, S. J.; Chinn, R.; Sclimenti, M. J.; Onstad, G. D.; Thruston, A. D. Occurrence of a new generation of disinfection byproducts. *Environ. Sci. Technol.* **2006**, *40*, 7175–7185, doi:10.1021/es060353j.

11. IHDRC Crude Oil and Natural Gas: From Source to Final Products Available online: https://www.ihrdc.com/els/po-demo/module01/mod_001_02.htm.

12. Wood, D. A.; Nwaoha, C.; Towler, B. F. Journal of Natural Gas Science and Engineering Gas-to-liquids (GTL): A review of an industry offering several routes for monetizing natural gas. *J. Nat. Gas Sci. Eng.* **2012**, *9*, 196–208.

13. Lutz, B. New Age Gas-to-Liquid Processing. *Hydrocarb. Eng.* **2001**, *6*, 63–67.

14. Tyagi, A.; Yamamoto, A.; Kato, T.; Yoshida, H. Bifunctional property of Pt nanoparticles deoposited on TiO2 for the photocatalytic sp3C-sp3C cross-coupling reactions between THF and alkanes. *Catal. Sci. Technol.* **2017**, *7*, 2616–2623, doi:10.1039/c7cy00535k.

15. Torborg, C.; Beller, M. Recent Applications of Palladium-Catalyzed Coupling Reactions in the Pharmaceutical, Agrochemical, and Fine Chemical Industries. *Adv. Synth. Catal.* **2009**, *351*, 3027–3043, doi:10.1002/adsc.200900587.

16. Jagtap, S. Heck Reaction—State of the Art. *Catalysts* **2017**, *7*, 267, doi:10.3390/catal7090267.

17. Gul, M.; Kotak, Y.; Muneer, T. Review on recent trend of solar photovoltaic technology. *Energy Explor. Exploit.* **2016**, *34*, 485–526, doi:10.1177/0144598716650552.

18. Albini, A.; Fagnoni, M. 1908 : Giacomo Ciamician and the Concept of Green Chemistry. *ChemSusChem* **2008**, *1*, 63–66, doi:10.1002/cssc.200700015.

19. Fujishima, A. and Honda, K.; Fujishima, A.; Honda, K. Electrochemical Photolysis of Water at a Semiconductor Electrode. *Nature* **1972**, *238*, 37, doi:10.1038/239137a0.

20.   Ahmad, H.; Kamarudin, S. K.; Minggu, L. J.; Kassim, M. Hydrogen from photo-catalytic water splitting process: A review. *Renew. Sustain. Energy Rev.* **2015**, *43*, 599–610.

21.   Ollis, D. F. Photocatalytic purification and remediation of contaminated air and water. *Surf. Chem. Catal.* **2000**, *3*, 405–411.

22.   Banerjee, S.; Dionysiou, D. D.; Pillai, S. C. Environmental Self-cleaning applications of TiO2 by photo-induced hydrophilicity and photocatalysis. *Appl. Catal. B Environ.* **2015**, *177*, 396–428.

23.   Friedmann, D.; Hakki, A.; Kim, H.; Choi, W.; Bahnemann, D. Heterogeneous photocatalytic organic synthesis : state-of-the-art and future perspectives. *Green Chem.* **2016**, *18*, 5391–5411, doi:10.1039/c6gc01582d.

24.   Carey, J. H.; Lawrence, J.; Tosine, H. M. Photodechlorination of PCB's in the Presence of Titanium Dioxide in Aqueous Suspensions. *Bull. Environ. Contam. Toxicol.* **1976**, *16*, 697–701.

25.   Baird, N. C. Free Radical Reactions in Aqueous Solutions : Examples from Advanced Oxidation Processes for Wastewater and from the Chemistry in Airborne Water Droplets. *J. Chem. Educ.* **1997**, *74*, 817–819.

26.   Schwarz, P. F.; Turro, N. J.; Bossmann, S. H.; Braun, A. M.; Wahab, A. A. A. A New Method To Determine the Generation of Hydroxyl Radicals in Illuminated TiO2 Suspensions. *J. Phys. Chem. B* **1997**, *5647*, 7127–7134.

27. Miranda-García, N.; Suárez, S.; Sánchez, B.; Coronado, J. M.; Malato, S.; Maldonado, M. I. Photocatalytic degradation of emerging contaminants in municipal wastewater treatment plant effluents using immobilized TiO2 in a solar pilot plant. *Appl. Catal. B Environ.* **2011**, *103*, 294–301, doi:10.1016/j.apcatb.2011.01.030.

28. Friedmann, D.; Mendive, C.; Bahnemann, D. TiO2for water treatment: Parameters affecting the kinetics and mechanisms of photocatalysis. *Appl. Catal. B Environ.* **2010**, *99*, 398–406, doi:10.1016/j.apcatb.2010.05.014.

29. Libanori, R.; Giraldi, T. R.; Longo, E.; Leite, E. R.; Ribeiro, C. Effect of TiO2 surface modification in Rhodamine B photodegradation. *J. Sol-Gel Sci. Technol.* **2009**, *49*, 95–100, doi:10.1007/s10971-008-1821-1.

30. Bilgin Simsek, E. Solvothermal synthesized boron doped TiO2 catalysts: Photocatalytic degradation of endocrine disrupting compounds and pharmaceuticals under visible light irradiation. *Appl. Catal. B Environ.* **2017**, *200*, 309–322, doi:10.1016/j.apcatb.2016.07.016.

31. Zhuang, J.; Dai, W.; Tian, Q.; Li, Z.; Xie, L.; Wang, J.; Liu, P.; Shi, X.; Wang, D. Photocatalytic degradation of RhB over TiO2 bilayer films: Effect of defects and their location. *Langmuir* **2010**, *26*, 9686–9694, doi:10.1021/la100302m.

32. Santacruz-Chávez, J. A.; Oros-Ruiz, S.; Prado, B.; Zanella, R. Photocatalytic degradation of atrazine using TiO2 superficially modified with metallic nanoparticles. *J. Environ. Chem. Eng.* **2015**, *3*, 3055–3061, doi:10.1016/j.jece.2015.04.025.

33. Ong, W. J.; Tan, L. L.; Chai, S. P.; Yong, S. T.; Mohamed, A. R. Facet-dependent photocatalytic properties of TiO2-based composites for energy conversion and environmental remediation. *ChemSusChem* **2014**, *7*, 690–719, doi:10.1002/cssc.201300924.

34. Braz, F. S.; Silva, M. R. A.; Silva, F. S.; Andrade, S. J.; Fonseca, A. L.; Kondo, M. M. Photocatalytic Degradation of Ibuprofen Using TiO2 and Ecotoxicological Assessment of Degradation Intermediates against Daphnia similis. *J. Environ. Prot. (Irvine,. Calif).* **2014**, *5*, 620–626, doi:10.4236/jep.2014.57063.

35. Konstantinou, I. K.; Albanis, T. A. TiO2-assisted photocatalytic degradation of azo dyes in aqueous solution: kinetic and mechanistic investigations. *Appl. Catal. B Environ.* **2004**, *49*, 1–14, doi:10.1016/j.apcatb.2003.11.010.

36. Shavisi, Y.; Sharifnia, S.; Zendehzaban, M.; Mirghavami, M. L.; Kakehazar, S. Application of solar light for degradation of ammonia in petrochemical wastewater by a floating TiO2/LECA photocatalyst. *J. Ind. Eng. Chem.* **2014**, *20*, 2806–2813, doi:10.1016/j.jiec.2013.11.011.

37. Yaparatne, S.; Tripp, C. P.; Amirbahman, A. Photodegradation of taste and odor compounds in water in the presence of immobilized TiO2-SiO2 photocatalysts. *J. Hazard. Mater.* **2018**, *346*, 208–217, doi:10.1016/j.jhazmat.2017.12.029.

38. Achilleos, A.; Hapeshi, E.; Xekoukoulotakis, N. P.; Mantzavinos, D.; Fatta-Kassinos, D. UV-A and solar photodegradation of ibuprofen and carbamazepine catalyzed by TiO2. *Sep. Sci. Technol.* **2010**, *45*, 1564–1570, doi:10.1080/01496395.2010.487463.

39. Pan, Z.; Stemmler, E. A.; Cho, H. J.; Fan, W.; LeBlanc, L. A.; Patterson, H. H.; Amirbahman, A. Photocatalytic degradation of 17α-ethinylestradiol (EE2) in the presence of TiO2-doped zeolite. *J. Hazard. Mater.* **2014**, *279*, 17–25, doi:10.1016/j.jhazmat.2014.06.040.

40. Pathirana, H. M. K. K.; Maithreepala, R. A. Photodegradation of 3,4-dichloropropionamide in aqueous TiO2 suspensions. *J. Photochem. Photobiol. A Chem.* **1997**, *102*, 273–277, doi:10.1016/S1010-6030(96)04455-3.

41. Hoffmann, M. R.; Martin, S. T.; Choi, W.; Bahnemann, D. W. Environmental Applications of Semiconductor Photocatalysis. *Chem. Rev.* **1995**, *95*, 69–96.

42. Katsumiti, A.; Gilliland, D.; Arostegui, I.; Cajaraville, M. P. Cytotoxicity and cellular mechanisms involved in the toxicity of CdS quantum dots in hemocytes and gill cells of the mussel Mytilus galloprovincialis. *Aquat. Toxicol.* **2014**, *153*, 39–52.

43. Choi, K.; Kang, T.; Oh, S. Preparation of disk shaped ZnO particles using surfactant and their PL properties. *Mater. Lett.* **2012**, *75*, 240–243, doi:10.1016/j.matlet.2012.02.031.

44. Rajamanickam, D.; Shanthi, M. Photocatalytic degradation of an organic pollutant by zinc oxide – solar process. *Arab. J. Chem.* **2016**, *9*, 1858–1868.

45. Carraway, E. R.; Hoffman, A. J.; Hoffmann, M. R. Photocatalytic Oxidation of Organic Acids Colloids Quantum-Sized Semiconductor. *Environ. Sci. Technol.* **1994**, *28*, 786–793.

46. Zeng, J.; Xiong, Z.; Zhang, H.; Lin, G.; Tsai, K. Nonoxidative dehydrogenation and aromatization of methane over W/HZSM-5-based catalysts. *Catal. Letters* **1998**, *53*, 119–124.

47. Belgued, M.; Amariglio, H.; Pareja, P.; Amariglio, A.; Saint-Just, J. Low Temperature Catalytic Homologation of Methane on Platinum, Ruthenium and Cobalt. *Catal. Today* **1992**, *13*, 437–445, doi:https://doi.org/10.1016/0920-5861(92)80169-N.

48. Zhao, Y.; Zhao, B.; Liu, J.; Chen, G.; Gao, R.; Yao, S.; Li, M.; Zhang, Q.; Gu, L.; Xie, J.; Wen, X.; Wu, L.; Tung, C.; Ma, D.; Zhang, T. Oxide-Modified Nickel Photocatalysts for the Production of Hydrocarbons in Visible Light. *Angew. Chemie Int. Ed.* **2016**, *55*, 4215–4219, doi:10.1002/anie.201511334.

49. Li, L.; Cai, Y.; Li, G.; Mu, X.; Wang, K.; Chen, J. Synergistic Effect on the Photoactivation of the Methane C-H Bond over Ga(3+)-Modified ETS-10. *Angew. Chemie Int. Ed.* **2012**, *51*, 4702–4706, doi:10.1002/anie.201200045.

50. Li, L.; Li, G.; Yan, C.; Mu, X.; Pan, X.; Zou, X.; Wang, X.; Chen, J. Efficient Sunlight-Driven Dehydrogenative Coupling of Methane to Ethane over a Zn(+)-Modified Zeolite. *Angew. Chemie Int. Ed.* **2011**, *50*, 8299–8303, doi:10.1002/anie.201102320.

51. Trinh, Q. T.; Banerjee, A.; Yang, Y.; Mushrif, S. H. Sub-Surface Boron-Doped Copper for Methane Activation and Coupling: First-Principles Investigation of the Structure, Activity, and Selectivity of the Catalyst. *J. Phys. Chem. C* **2017**, *121*, 1099–1112, doi:10.1021/acs.jpcc.6b09236.

52. Xie, S.; Shen, Z.; Zhang, H.; Cheng, J. Photocatalytic coupling of formaldehyde to ethylene glycol and glycolaldehyde over bismuth vanadate with controllable facets and cocatalysts. *Catal. Sci. Technol.* **2017**, *7*, 923–933, doi:10.1039/c6cy02510b.

53. Hörner, G.; Johne, P.; Künneth, R.; Twardzik, G.; Roth, H.; Clark, T.; Kisch, H. Semiconductor Type A Photocatalysis: Role of Substrate Adsorption and the Nature of Photoreactive Surface Sites in Zinc Sulfide Catalyzed C-C Coupling Reactions. *Chem. - A Eur. J.* **1999**, *5*, 208–217.

54. Kisch, H. Semiconductor Photocatalysis for Chemoselective Radical Coupling Reactions. *Acc. Chem. Res.* **2017**, *50*, 1002–1010, doi:10.1021/acs.accounts.7b00023.

55. Künneth, R.; Twardzik, G.; Emig, G.; Kisch, H. Heterogeneous photocatalysis XI . Zinc sulphide catalysed dehydrodimerization of dihydropyrans and cyclohexene. *J. Photochem. Photobiol. A Chem.* **1993**, *76*, 209–215.

56. Shimura, K.; Yoshida, H. Semiconductor Photocatalysts for Non-oxidative Coupling, Dry Reforming and Steam Reforming of Methane. *Catal. Surv. Asia* **2014**, *18*, 24–33, doi:10.1007/s10563-014-9165-z.

57. Yuliati, L.; Itoh, H.; Yoshida, H. Photocatalytic conversion of methane and carbon dioxide over gallium oxide. *Chem. Phys. Lett.* **2008**, *452*, 178–182, doi:10.1016/j.cplett.2007.12.051.

58. Yuliati, L.; Yoshida, H. Photocatalytic conversion of methane. *Chem. Soc. Rev.* **2008**, *37*, 1592–1602, doi:10.1039/b710575b.

59. Kato, Y.; Yoshida, H.; Hattori, T. Photoinduced non-oxidative coupling of methane over silica-alumina and alumina around room temperature. *Chem. Commun.* **1998**, 2389–2390.

60. Mitzi, D.B., Feild, C.A., Harrison, W. T. A., Guloy, A. M. A low-cost, high-efficiency solar cell based on dye-sensitized colloidal TiO2 films. *Nature* **1994**, *367*, 532–8, doi:10.1038/350055a0.

61. Ali, I.; Kim, J. Visible-light-assisted photocatalytic activity of bismuth-TiO 2 nanotube composites for chromium reduction and dye degradation. *Chemosphere* **2018**, *207*, 285–292, doi:10.1016/j.chemosphere.2018.05.075.

62. Chen, S. M.; Lu, N.; Chen, J. Y.; Yang, C. Y.; Yeh, Y. P.; Feng, T. Y.; Shih, Y. H.; Kokulnathan, T.; Chen, D. Enhanced photocatalytic degradation of atrazine by platinized titanium dioxide under 352 nm irradiation. *Water Sci. Technol.* **2017**, *75*, 1128–1137, doi:10.2166/wst.2016.593.

63. Cao, J.; Xu, B.; Luo, B.; Lin, H.; Chen, S. Preparation, characterization and visible-light photocatalytic activity of AgI/AgCl/TiO2. *Appl. Surf. Sci.* **2011**, *257*, 7083–7089, doi:10.1016/j.apsusc.2011.03.046.

64. Bannister, F. A. The crystal structure of the bismuth oxyhalides. *J. Mineral. Soc.* **1935**, *24*, 49–58.

65. Liu, Y.; Xu, J.; Wang, L.; Zhang, H.; Xu, P.; Duan, X.; Sun, H.; Wang, S. Three-Dimensional BiOI/BiOX (X = Cl or Br) Nanohybrids for Enhanced Visible-Light Photocatalytic Activity. *Nanomater.* **2017**, *7*, 64, doi:10.3390/nano7030064.

66. Wen Lai, H.; Qingshan, Z. Electronic structures of relaxed BiOX (X=F, Cl, Br, I) photocatalysts. *Comput. Mater. Sci.* **2008**, *43*, 1101–1108, doi:10.1016/j.commatsci.2008.03.005.

67. ZHANG, K.; LIU, C.; HUANG, F.; ZHENG, C.; WANG, W. Study of the electronic structure and photocatalytic activity of the BiOCl photocatalyst. *Appl. Catal. B Environ.* **2006**, *68*, 125–129, doi:10.1016/j.apcatb.2006.08.002.

68. Wang, H.; Xu, H.; Zeng, C.; Shen, Y.; Lin, Y. H.; Nan, C. W. Visible Light Photocatalytic Activity of Bismuth Ferrites Tuned by Bi/Fe Ratio. *J. Am. Ceram. Soc.* **2016**, *99*, 1133–1136, doi:10.1111/jace.14113.

69. Rawashdeh-omary, M. A.; Omary, M. A.; Patterson, H. H.; May, R. V Oligomerization of Au (CN) 2 - and Ag (CN) 2 - Ions in Solution via Ground-State Aurophilic and Argentophilic Bonding. *J. Am. Chem. Soc.* **2000**, *122*, 10371–10380.

70. Wu, D.; Ye, L.; Yip, H. Y.; Wong, P. K. Organic-free synthesis of {001} facet dominated BiOBr nanosheets for selective photoreduction of CO 2 to CO. *Catal. Sci. Technol.* **2017**, *7*, 265–271, doi:10.1039/C6CY02040B.

71. Peng, Y.; Wang, D.; Zhou, H.-Y.; Xu, A.-W. Controlled synthesis of thin BiOCl nanosheets with exposed {001} facets and enhanced photocatalytic activities. *CrystEngComm* **2015**, *17*, 3845–3851, doi:10.1039/C5CE00289C.

72. Wang, D.-H.; Gao, G.-Q.; Zhang, Y.-W.; Zhou, L.-S.; Xu, A.-W.; Chen, W. Nanosheet-constructed porous BiOCl with dominant {001} facets for superior photosensitized degradation. *Nanoscale* **2012**, *4*, 7780, doi:10.1039/c2nr32533k.

73. Duan, F.; Wang, X.; Tan, T.; Chen, M. Highly exposed surface area of {001} facets dominated BiOBr nanosheets with enhanced visible light photocatalytic activity. *Phys. Chem. Chem. Phys.* **2016**, *18*, 6113–6121, doi:10.1039/C5CP06711A.

74. Haider, Z.; Zheng, J. Y.; Kang, Y. S. Surfactant free fabrication and improved charge carrier separation induced enhanced photocatalytic activity of {001} facet exposed unique octagonal BiOCl nanosheets. *Phys. Chem. Chem. Phys.* **2016**, *18*, 19595–19604, doi:10.1039/C6CP01740A.

75. Xu, Y.; Xu, S.; Wang, S.; Zhang, Y.; Li, G. Citric acid modulated electrochemical synthesis and photocatalytic behavior of BiOCl nanoplates with exposed {001} facets. *Dalt. Trans.* **2014**, *43*, 479–485, doi:10.1039/C3DT52004H.

76. Li, H.; Zhang, L. Oxygen vacancy induced selective silver deposition on the {001} facets of BiOCl single-crystalline nanosheets for enhanced Cr(VI) and sodium pentachlorophenate removal under visible light. *Nanoscale* **2014**, *6*, 7805–7810, doi:10.1039/C4NR01315H.

77. Kong, T.; Wei, X.; Zhu, G.; Huang, Y. First-principles studies on facet-dependent photocatalytic properties of BiOI {001} surface. *J. Mater. Sci.* **2017**, *52*, 5686–5695, doi:10.1007/s10853-017-0803-5.

78. Li, H.; Shi, J.; Zhao, K.; Zhang, L. Sustainable molecular oxygen activation with oxygen vacancies on the {001} facets of BiOCl nanosheets under solar light. *Nanoscale* **2014**, *6*, 14168–14173, doi:10.1039/C4NR04810E.

79. Xiong, X.; Ding, L.; Wang, Q.; Li, Y.; Jiang, Q.; Hu, J. Synthesis and photocatalytic activity of BiOBr nanosheets with tunable exposed (0 1 0) facets. *Appl. Catal. B Environ.* **2016**, *188*, 283–291, doi:10.1016/j.apcatb.2016.02.018.

80. Song, G.; Wu, X.; Xin, F.; Yin, X. ZnFe2O4deposited on BiOCl with exposed (001) and (010) facets for photocatalytic reduction of CO2in cyclohexanol. *Front. Chem. Sci. Eng.* **2017**, *11*, 197–204, doi:10.1007/s11705-016-1606-y.

81. Tan, C.; Zhu, G.; Hojamberdiev, M.; Okada, K.; Liang, J.; Luo, X.; Liu, P.; Liu, Y. Co3O4 nanoparticles-loaded BiOCl nanoplates with the dominant {001} facets: efficient photodegradation of organic dyes under visible light. *Appl. Catal. B Environ.* **2014**, *152–153*, 425–436, doi:10.1016/j.apcatb.2014.01.044.

82. Ye, L.; Chen, J.; Tian, L.; Liu, J.; Peng, T.; Deng, K.; Zan, L. BiOI thin film via chemical vapor transport: Photocatalytic activity, durability, selectivity and mechanism. *Appl. Catal. B Environ.* **2013**, *130–131*, 1–7, doi:10.1016/j.apcatb.2012.10.011.

83. Wu, Y.; Yuan, B.; Li, M.; Zhang, W. H.; Liu, Y.; Li, C. Well-defined BiOCl colloidal ultrathin nanosheets: Synthesis, characterization, and application in photocatalytic aerobic oxidation of secondary amines. *Chem. Sci.* **2015**, *6*, 1873–1878, doi:10.1039/c4sc03229b.

84. Li, J.; Zhang, L.; Li, Y.; Yu, Y. Synthesis and internal electric field dependent photoreactivity of Bi3O4Cl single-crystalline nanosheets with high {001} facet exposure percentages. *Nanoscale* **2014**, *6*, 167–171, doi:10.1039/c3nr05246j.

85. da Silva, J. C. C.; Teodoro, J. A. R.; Afonso, R. J. D. C. F.; Aquino, S. F.; Augusti, R. Photolysis and photocatalysis of ibuprofen in aqueous medium: characterization of by-products via liquid chromatography coupled to high-resolution mass spectrometry and assessment of their toxicities against Artemia Salina. *J. Mass Spectrom.* **2014**, *49*, 145–153, doi:10.1002/jms.3320.

86.   Mendez-Arriaga, F.; Torres-Palma, R. A.; Petrier, C.; Esplugas, S.; Gimenez, J.; Pulgarin, C. Ultrasonic treatment of water contaminated with ibuprofen. *Water Res.* **2008**, *42*, 4243–4248, doi:10.1016/j.watres.2008.05.033.

87.   Cunha-Silva, L.; Lima, S.; Ananias, D.; Silva, P.; Mafra, L.; Carlos, L. D.; Pillinger, M.; Valente, A. a.; Almeida Paz, F. a.; Rocha, J. Multi-functional rare-earth hybrid layered networks: photoluminescence and catalysis studies. *J. Mater. Chem.* **2009**, *19*, 2618, doi:10.1039/b817381h.

88.   Kaldas, S. J.; Cannillo, A.; Mccallum, T.; Barriault, L. Indole Functionalization via Photoredox Gold Catalysis. *Org. Lett.* **2015**, *17*, 2864–2866, doi:10.1021/acs.orglett.5b01260.

89.   Benisvy, L.; Gamez, P.; Fu, T.; Kooijman, H.; Spek, A. L.; Reedijk, J. Efficient near-UV photosensitization of the Tb (III) green luminescence by use of 2-hydroxyisophthalate ligands †. *Dalt. Trans.* **2008**, *3296*, 3147–3149, doi:10.1039/b805507f.

90.   Zhang, X.; Ai, Z.; Jia, F.; Zhang, L. Generalized One-Pot Synthesis , Characterization , and Photocatalytic Activity of Hierarchical BiOX (X) Cl , Br , I) Nanoplate Microspheres. **2008**, 747–753.

91.   Xia, J.; Zhang, J.; Yin, S.; Li, H.; Xu, H.; Xu, L.; Zhang, Q. Advanced visible light photocatalytic properties of BiOCl micro/nanospheres synthesized via reactable ionic liquids. *J. Phys. Chem. Solids* **2013**, *74*, 298–304, doi:10.1016/j.jpcs.2012.10.002.

92.   Xiong, J.; Jiao, Z.; Lu, G.; Ren, W.; Ye, J.; Bi, Y. Facile and rapid oxidation fabrication of BiOCl hierarchical nanostructures with enhanced photocatalytic properties. *Chem. - A Eur. J.* **2013**, *19*, 9472–9475, doi:10.1002/chem.201300384.

93. Lin, H.; Ding, L.; Pei, Z.; Zhou, Y.; Long, J.; Deng, W.; Wang, X. Au deposited BiOCl with different facets: On determination of the facet-induced transfer preference of charge carriers and the different plasmonic activity. *Appl. Catal. B Environ.* **2014**, *160–161*, 98–105, doi:10.1016/j.apcatb.2014.05.018.

94. Xu, L.; He, F.; Wang, C.; Gai, S.; Gulzar, A.; Yang, D.; Zhong, C.; Yang, P. Lanthanide-doped bismuth oxobromide nanosheets for self-activated photodynamic therapy. *J. Mater. Chem. B* **2017**, *5*, 7939–7948, doi:10.1039/C7TB01983A.

95. Zhang, H.; Liu, L.; Zhou, Z. Towards better photocatalysts: first-principles studies of the alloying effects on the photocatalytic activities of bismuth oxyhalides under visible light. *Phys. Chem. Chem. Phys.* **2012**, *14*, 1286–1292, doi:10.1039/C1CP23516H.

96. Xia, J.; Xu, L.; Zhang, J.; Yin, S.; Li, H.; Xu, H.; Di, J. Improved visible light photocatalytic properties of Fe/BiOCl microspheres synthesized via self-doped reactable ionic liquids. *CrystEngComm* **2013**, *15*, 10132, doi:10.1039/c3ce41555d.

97. Yu, Y.; Cao, C.; Liu, H.; Li, P.; Wei, F.; Jiang, Y.; Song, W. A Bi/BiOCl heterojunction photocatalyst with enhanced electron–hole separation and excellent visible light photodegrading activity. *J. Mater. Chem. A* **2014**, *2*, 1677–1681, doi:10.1039/C3TA14494A.

98. Ye, L.; Liu, J.; Gong, C.; Tian, L.; Peng, T.; Zan, L. Two Different Roles of Metallic Ag on Ag/AgX/BiOX (X = Cl, Br) Visible Light Photocatalysts: Surface Plasmon Resonance and Z-Scheme Bridge. *ACS Catal.* **2012**, *2*, 1677–1683, doi:10.1021/cs300213m.

99. Lin, H.; Li, X.; Cao, J.; Chen, S.; Chen, Y. Novel I−-doped BiOBr composites: Modulated valence bands and largely enhanced visible light phtotocatalytic activities. *Catal. Commun.* **2014**, *49*, 87–91, doi:10.1016/j.catcom.2014.02.010.

100. Liu, Z.; Liu, J.; Wang, H.; Cao, G.; Niu, J. Boron-doped bismuth oxybromide microspheres with enhanced surface hydroxyl groups: Synthesis, characterization and dramatic photocatalytic activity. *J. Colloid Interface Sci.* **2016**, *463*, 324–331, doi:10.1016/j.jcis.2015.10.028.

101. Lee, W.; Lu, C.-S.; Chuang, C.-W.; Chen, Y.-J.; Fu, J.-Y.; Siao, C.-W.; Chen, C.-C. Synthesis of bismuth oxyiodides and their composites: characterization, photocatalytic activity, and degradation mechanisms. *RSC Adv.* **2015**, *5*, 23450–23463, doi:10.1039/C4RA15072D.

102. Li, Q.; Zhao, X.; Yang, J.; Jia, C.-J.; Jin, Z.; Fan, W. Exploring the effects of nanocrystal facet orientations in g-C3N4/BiOCl heterostructures on photocatalytic performance. *Nanoscale* **2015**, *7*, 18971–18983, doi:10.1039/c5nr05154a.

103. Cheng, H.; Huang, B.; Dai, Y. Engineering BiOX (X = Cl, Br, I) nanostructures for highly efficient photocatalytic applications. *Nanoscale* **2014**, *6*, 2009–2026, doi:10.1039/c3nr05529a.

104. Sun, M.; Zhao, Q.; Du, C.; Liu, Z. Enhanced visible light photocatalytic activity in BiOCl/SnO 2 : heterojunction of two wide band-gap semiconductors. *RSC Adv.* **2015**, *5*, 22740–22752, doi:10.1039/C4RA14187C.

105. Liu, R.; Wu, Z.; Tian, J.; Yu, C.; Li, S.; Yang, K.; Liu, X.; Liu, M. The excellent dye-photosensitized degradation performance over hierarchical BiOCl nanostructures fabricated via a facile microwave-hydrothermal process. *New J. Chem.* **2018**, *42*, 137–149, doi:10.1039/C7NJ02990J.

106. Li, G.; Jiang, B.; Xiao, S.; Lian, Z.; Zhang, D.; Yu, J. C.; Li, H. An efficient dye-sensitized BiOCl photocatalyst for air and water purification under visible light irradiation. *Environ. Sci. Process. Impacts* **2014**, *16*, 1975–1980, doi:10.1039/C4EM00196F.

107. Zhang, X.; Wang, C.-Y.; Wang, L.-W.; Huang, G.-X.; Wang, W.-K.; Yu, H.-Q. Fabrication of BiOBrxI1−x photocatalysts with tunable visible light catalytic activity by modulating band structures. *Sci. Rep.* **2016**, *6*, 22800, doi:10.1038/srep22800.

108. Jia, X.; Cao, J.; Lin, H.; Zhang, M.; Guo, X.; Chen, S. Transforming type-I to type-II heterostructure photocatalyst via energy band engineering: A case study of I-BiOCl/I-BiOBr. *Appl. Catal. B Environ.* **2017**, *204*, 505–514, doi:10.1016/j.apcatb.2016.11.061.

109. Sánchez-Rodríguez, D.; Méndez Medrano, M. G.; Remita, H.; Escobar-Barrios, V. Photocatalytic properties of BiOCl-TiO2 composites for phenol photodegradation. *J. Environ. Chem. Eng.* **2018**, *6*, 1601–1612, doi:10.1016/j.jece.2018.01.061.

110. Zhang, Y.; Park, M.; Kim, H.; Park, S. In-situ synthesis of graphene oxide/BiOCl heterostructured nanofibers for visible-light photocatalytic investigation. *J. Alloys Compd.* **2016**, *686*, 106–114, doi:10.1016/j.jallcom.2016.06.004.

111. Zhang, J.; Zhang, L.; Shen, X.; Xu, P.; Liu, J. Synthesis of BiOBr/WO 3 p–n heterojunctions with enhanced visible light photocatalytic activity. *CrystEngComm* **2016**, *18*, 3856–3865, doi:10.1039/C6CE00824K.

112. Feng, Y.; Liu, C.; Chen, J.; Che, H.; Xiao, L.; Gu, W.; Shi, W. Facile synthesis of BiOI/CdWO 4 p–n junctions: enhanced photocatalytic activities and photoelectrochemistry. *RSC Adv.* **2016**, *6*, 38290–38299, doi:10.1039/C5RA23383F.

113. Lei, L.; Jin, H.; Zhang, Q.; Xu, J.; Gao, D.; Fu, Z. A novel enhanced visible-light-driven photocatalyst via hybridization of nanosized BiOCl and graphitic C 3 N 4. *Dalt. Trans.* **2015**, *44*, 795–803, doi:10.1039/C4DT02082K.

114. Ye, L.; Liu, X.; Zhao, Q.; Xie, H.; Zan, L. Dramatic visible light photocatalytic activity of MnOx–BiOI heterogeneous photocatalysts and the selectivity of the cocatalyst. *J. Mater. Chem. A* **2013**, *1*, 8978, doi:10.1039/c3ta11441d.

115. Fan, W.-Q.; Yu, X.-Q.; Song, S.-Y.; Bai, H.-Y.; Zhang, C.; Yan, D.; Liu, C.-B.; Wang, Q.; Shi, W.-D. Fabrication of TiO 2 –BiOCl double-layer nanostructure arrays for photoelectrochemical water splitting. *CrystEngComm* **2014**, *16*, 820–825, doi:10.1039/C3CE42001A.

116. Ferreira, V. C.; Neves, M. C.; Hillman, A. R.; Monteiro, O. C. Novel one-pot synthesis and sensitisation of new BiOCl–Bi 2 S 3 nanostructures from DES medium displaying high photocatalytic activity. *RSC Adv.* **2016**, *6*, 77329–77339, doi:10.1039/C6RA14474H.

117. Di, J.; Xia, J.; Li, H.; Guo, S.; Dai, S. Bismuth oxyhalide layered materials for energy and environmental applications. *Nano Energy* **2017**, *41*, 172–192, doi:10.1016/j.nanoen.2017.09.008.

118. Yang, Y.; Zhang, C.; Lai, C.; Zeng, G.; Huang, D.; Cheng, M.; Wang, J.; Chen, F.; Zhou, C.; Xiong, W. BiOX (X = Cl , Br , I) photocatalytic nanomaterials : Applications for fuels and environmental management. *Adv. Colloid Interface Sci.* **2018**, *254*, 76–93, doi:10.1016/j.cis.2018.03.004.

119. Wang, G.; Luo, X.; Huang, Y.; Kuang, A.; Yuan, H.; Chen, H. BiOX/BiOY (X, y = F, Cl, Br, I) superlattices for visible light photocatalysis applications. *RSC Adv.* **2016**, *6*, 91508–91516, doi:10.1039/c6ra14915d.

120. Song, J.; Wang, B.; Guo, X.; Wang, R.; Dong, Z. Hierarchical nanostructured 3D flowerlike BiOX particles with excellent visible-light photocatalytic activity. *J. Nanoparticle Res.* **2016**, *18*, 1–11, doi:10.1007/s11051-016-3556-1.

121. Cui, P.; Wang, J.; Wang, Z.; Chen, J.; Xing, X.; Wang, L.; Yu, R. Bismuth oxychloride hollow microspheres with high visible light photocatalytic activity. *Nano Res.* **2016**, *9*, 593–601, doi:10.1007/s12274-015-0939-z.

122. Zhang, L.; Wang, W.; Sun, S.; Jiang, D.; Gao, E. Selective transport of electron and hole among {0 0 1} and {1 1 0} facets of BiOCl for pure water splitting. *Appl. Catal. B Environ.* **2015**, *162*, 470–474, doi:10.1016/j.apcatb.2014.07.024.

123. Sfaelou, S.; Raptis, D.; Dracopoulos, V.; Lianos, P. BiOI solar cells. *RSC Adv.* **2015**, *5*, 95813–95816, doi:10.1039/C5RA19835F.

124. Jin, J.; Wang, Y.; He, T. Preparation of thickness-tunable BiOCl nanosheets with high photocatalytic activity for photoreduction of CO 2. *RSC Adv.* **2015**, *5*, 100244–100250, doi:10.1039/C5RA21888H.

125. Li, H.; Shang, J.; Shi, J.; Zhao, K.; Zhang, L. Facet-dependent solar ammonia synthesis of BiOCl nanosheets via a proton-assisted electron transfer pathway. *Nanoscale* **2016**, *8*, 1986–1993, doi:10.1039/c5nr07380d.

126. Li, H.; Shang, J.; Ai, Z.; Zhang, L. Efficient visible light nitrogen fixation with BiOBr nanosheets of oxygen vacancies on the exposed {001} Facets. *J. Am. Chem. Soc.* **2015**, *137*, 6393–6399, doi:10.1021/jacs.5b03105.

127. Cheng, H.; Huang, B.; Wang, P.; Wang, Z.; Lou, Z.; Wang, J.; Qin, X.; Zhang, X.; Dai, Y. In situ ion exchange synthesis of the novel Ag/AgBr/BiOBr hybrid with highly efficient decontamination of pollutants. *Chem. Commun.* **2011**, *47*, 7054–7056, doi:10.1039/c1cc11525a.

128. Dong, F.; Xiong, T.; Yan, S.; Wang, H.; Sun, Y.; Zhang, Y.; Huang, H.; Wu, Z. Facets and defects cooperatively promote visible light plasmonic photocatalysis with Bi nanowires@BiOCl nanosheets. *J. Catal.* **2016**, *344*, 401–410, doi:10.1016/j.jcat.2016.10.005.

129. Ai, Z.; Ho, W.; Lee, S.; Zhang, L. Efficient photocatalytic removal of NO in indoor air with hierarchical bismuth oxybromide nanoplate microspheres under visible light. *Environ. Sci. Technol.* **2009**, *43*, 4143–4150, doi:10.1021/es9004366.

130. Huang, C.; Hu, J.; Cong, S.; Zhao, Z.; Qiu, X. Hierarchical BiOCl microflowers with improved visible-light-driven photocatalytic activity by Fe(III) modification. *Appl. Catal. B Environ.* **2015**, *174–175*, 105–112, doi:10.1016/j.apcatb.2015.03.001.

131. Dong, G.; Ho, W.; Zhang, L. Photocatalytic NO removal on BiOI surface: The change from nonselective oxidation to selective oxidation. *Appl. Catal. B Environ.* **2015**, *168–169*, 490–496, doi:10.1016/j.apcatb.2015.01.014.

132. Dawody, J.; Skoglundh, M.; Fridell, E. The effect of metal oxide additives (WO3, MoO3, V2O5, Ga2O3) on the oxidation of NO and SO2 over Pt/Al2O3 and Pt/BaO/Al2O3 catalysts. *J. Mol. Catal. A Chem.* **2004**, *209*, 215–225, doi:10.1016/j.molcata.2003.08.025.

133. Qamar, M.; Yamani, Z. H. Bismuth oxychloride-mediated and laser-induced efficient reduction of Cr(VI) in aqueous suspensions. *Appl. Catal. A Gen.* **2012**, *439–440*, 187–191, doi:10.1016/j.apcata.2012.07.004.

134. Xu, H.; Wu, Z.; Ding, M.; Gao, X. Microwave-assisted synthesis of flower-like BN/BiOCl composites for photocatalytic Cr(VI) reduction upon visible-light irradiation. *Mater. Des.* **2017**, *114*, 129–138, doi:10.1016/j.matdes.2016.10.057.

135. Li, G.; Qin, F.; Yang, H.; Lu, Z.; Sun, H.; Chen, R. Facile microwave synthesis of 3D flowerlike BiOBr nanostructures and their excellent CrVIremoval capacity. *Eur. J. Inorg. Chem.* **2012**, 2508–2513, doi:10.1002/ejic.201101427.

136. Li, G.; Qin, F.; Wang, R.; Xiao, S.; Sun, H.; Chen, R. Journal of Colloid and Interface Science BiOX (X = Cl , Br , I) nanostructures : Mannitol-mediated microwave synthesis , visible light photocatalytic performance , and Cr (VI) removal capacity. *J. Colloid Interface Sci.* **2013**, *409*, 43–51, doi:10.1016/j.jcis.2013.07.068.

137. Shang, J.; Hao, W.; Lv, X.; Wang, T.; Wang, X.; Du, Y.; Dou, S.; Xie, T.; Wang, D.; Wang, J. Bismuth oxybromide with reasonable photocatalytic reduction activity under visible light. *ACS Catal.* **2014**, *4*, 954–961, doi:10.1021/cs401025u.

36

138. Bai, Y.; Ye, L.; Chen, T.; Wang, P.; Wang, L.; Shi, X.; Wong, P. K. Synthesis of hierarchical bismuth-rich Bi 4 O 5 Br x I 2-x solid solutions for enhanced photocatalytic activities of CO 2 conversion and Cr(VI) reduction under visible light. *Appl. Catal. B Environ.* **2017**, *203*, 633–640, doi:10.1016/j.apcatb.2016.10.066.

139. Ye, L.; Su, Y.; Jin, X.; Xie, H.; Zhang, C. Recent advances in BiOX (X = Cl, Br and I) photocatalysts: synthesis, modification, facet effects and mechanisms. *Environ. Sci. Nano* **2014**, *1*, 90–112, doi:10.1039/c3en00098b.

140. Di, J.; Xia, J.; Ji, M.; Yin, S.; Li, H.; Xu, H.; Zhang, Q.; Li, H. Controllable synthesis of Bi4O5Br2ultrathin nanosheets for photocatalytic removal of ciprofloxacin and mechanism insight. *J. Mater. Chem. A* **2015**, *3*, 15108–15118, doi:10.1039/c5ta02388b.

141. Di, J.; Xia, J.; Yin, S.; Xu, H.; Xu, L.; Xu, Y.; He, M.; Li, H. Preparation of sphere-like g-C3N4/BiOI photocatalysts via a reactable ionic liquid for visible-light-driven photocatalytic degradation of pollutants. *J. Mater. Chem. A* **2014**, *2*, 5340–5351, doi:10.1039/c3ta14617k.

142. Hao, R.; Xiao, X.; Zuo, X.; Nan, J.; Zhang, W. Efficient adsorption and visible-light photocatalytic degradation of tetracycline hydrochloride using mesoporous BiOI microspheres. *J. Hazard. Mater.* **2012**, *209–210*, 137–145, doi:10.1016/j.jhazmat.2012.01.006.

143. Di, J.; Xia, J.; Ji, M.; Wang, B.; Yin, S.; Zhang, Q.; Chen, Z.; Li, H. Advanced photocatalytic performance of graphene-like BN modified BiOBr flower-like materials for the removal of pollutants and mechanism insight. *Appl. Catal. B Environ.* **2016**, *183*, 254–262, doi:10.1016/j.apcatb.2015.10.036.

144. Chen, F.; Yang, Q.; Sun, J.; Yao, F.; Wang, S.; Wang, Y.; Wang, X.; Li, X.; Niu, C.; Wang, D.; Zeng, G. Enhanced Photocatalytic Degradation of Tetracycline by AgI/BiVO4Heterojunction under Visible-Light Irradiation: Mineralization Efficiency and Mechanism. *ACS Appl. Mater. Interfaces* **2016**, *8*, 32887–32900, doi:10.1021/acsami.6b12278.

145. Gao, S.; Guo, C.; Lv, J.; Wang, Q.; Zhang, Y.; Hou, S.; Gao, J.; Xu, J. A novel 3D hollow magnetic Fe3O4/BiOI heterojunction with enhanced photocatalytic performance for bisphenol A degradation. *Chem. Eng. J.* **2017**, *307*, 1055–1065, doi:10.1016/j.cej.2016.09.032.

146. Lei, Y.; Wang, G.; Song, S.; Fan, W.; Zhang, H. Synthesis, characterization and assembly of BiOCl nanostructure and their photocatalytic properties. *CrystEngComm* **2009**, *11*, 1857, doi:10.1039/b909013b.

147. Li, J.; Sun, S.; Chen, R.; Zhang, T.; Ren, B.; Dionysiou, D. D.; Wu, Z.; Liu, X.; Ye, M. Adsorption behavior and mechanism of ibuprofen onto BiOCl microspheres with exposed {001} facets. *Environ. Sci. Pollut. Res.* **2017**, *24*, 9556–9565, doi:10.1007/s11356-017-8564-x.

148. Li, J.; Sun, S.; Qian, C.; He, L.; Chen, K. K.; Zhang, T.; Chen, Z.; Ye, M. The role of adsorption in photocatalytic degradation of ibuprofen under visible light irradiation by BiOBr microspheres. *Chem. Eng. J.* **2016**, *297*, 139–147, doi:10.1016/j.cej.2016.03.145.

149. Lester, Y.; Avisar, D.; Gnayem, H.; Sasson, Y.; Shavit, M.; Mamane, H. Demonstrating a New BiOCl0.875Br0.125 Photocatalyst to Degrade Pharmaceuticals Under Solar Irradiation. *Water, Air, Soil Pollut.* **2014**, *225*, 2132, doi:10.1007/s11270-014-2132-5.

150. Li, Y.; Wang, J.; Yao, H.; Dang, L.; Li, Z. Efficient decomposition of organic compounds and reaction mechanism with BiOI photocatalyst under visible light irradiation. *J. Mol. Catal. A Chem.* **2011**, *334*, 116–122, doi:10.1016/j.molcata.2010.11.005.

151. Wang, Y.; Deng, K.; Zhang, L. Visible Light Photocatalysis of BiOI and Its Photocatalytic Activity Enhancement by in Situ Ionic Liquid Modification. *J. Phys. Chem. C* **2011**, *115*, 14300–14308.

152. Henríquez, A.; Mansilla, H. D.; Martínez, A.; Cruz, M.; Freer, J.; Contreras, D. Selective oxofunctionalization of cyclohexane over titanium dioxide – based and bismuth oxyhalide (BiOX, X = Cl, Br, I) photocatalysts by visible light irradiation. *Appl. Catal. B Environ.* **2017**, *206*, 252–262.

CHAPTER 2

THE ROLE OF COPPER (II) IONS IN Cu-BiOCl FOR USE IN THE PHOTOCATALYTIC DEGRADATION OF ATRAZINE

2.1 Introduction

Organic pollutants are the most common form of environmental contaminants detected within the United States [1]. These types of compounds include herbicides and pharmaceuticals, which increases the likelihood of human exposure as commercial consumption increases annually [1,2]. These compounds exist in media such as aqueous and gaseous solutions, which are introduced into the environment through practices in the agricultural and commercial landscaping industries. Atrazine is an environmentally persistent compound that is known to resist natural degradation [3,4]. Reports on accumulation of atrazine in soil indicates increases in the bacterial populations in areas that have continuous applications [3]. The molecular structure of atrazine (see Figure 2.1) and other molecules allows increased resistance to current drinking water treatments, enabling possible accumulation in biological systems. This exposure propagates several negative health effects including cancer, birth defects, and endocrine system disruption [5].

Traditional ultraviolet irradiation has shown promise in rapid removal but is limited in the overall mineralization of pollutants [6]. Photocatalysts have become a new alternative for drinking water treatment due to their unique reactivity with ultraviolet radiation, producing increased degradation and overall detoxification [6,7]. Photocatalysts provide an alternative in drinking water treatment due to their ability to degrade hazardous pollutants in a variety of mediums,

including water [8]. These compounds are semiconductors composed of inorganic compounds that accelerate chemical reactions using ultraviolet radiation present in the atmosphere.

Degradation of harmful pollutants into nontoxic byproducts is a result of this process and can be used in the removal of herbicides, such as atrazine, from drinking water [8,9]. Traditional treatment methods focus on the addition of chemical species such as chlorine for contaminant removal, yet this technique has the potential for increased toxicity due to compound transformations [10]. As these photocatalysts adsorb pollutants such as atrazine, photochemical oxidation-reduction reactions create reactive chemical species that cleave the molecule into smaller compounds. A previous study conducted by the Patterson research group indicated superior degradation of pharmaceuticals using bismuth photocatalysts versus titanium dioxide [7]. The results of Ahern et al. indicated bismuth oxyhalide has a smaller surface area compared to titanium dioxide, yet it exhibited increased degradation rates [7,11].

Enhancement of photocatalytic compounds can be achieved through targeting the addition of metallic ions into the chemical arrangement of a known photocatalyst to act as an electron trap to prevent recombination of excited-state electrons and electron holes [12,13]. Previous studies using metal-doped compounds have reported increased photodegradation behavior from this addition. Reports on the enhancement by addition of copper, specifically Cu(II), have indicated the most successful degradation rates when comparing the addition to other ions, such as iron [14]. The addition of metallic impurities facilitates the transfer of excited state electrons from the conduction band of the photocatalyst [15]. The transfer of electrons from the conduction band of bismuth oxyhalide to the copper ions facilitates extended lifetimes of these excited state electrons [16]. Previous studies using transition elements such as nickel, copper, and gold have indicated these compounds are sufficient additives to facilitate increased degradation of pollutants [17].

In this study, we present the application of Cu-BiOCl to photocatalytic degradation of atrazine. We demonstrate the reproducibility of the earlier reported Cu-BiOCl ionic liquid synthetic method through characterization via XRD, DRS, SEM-EDS, and photoluminescence [18]. The properties of the copper-modified material are characterized by DRS, FTIR, and photoluminescence measurements. The photocatalytic activity for Cu-BiOCl is measured in the absence of hydrogen peroxide and uses atrazine as a target model organic pollutant. Active species trapping experiments are used to assist in proposing a mechanism of Cu-BiOCl photocatalytic activity.
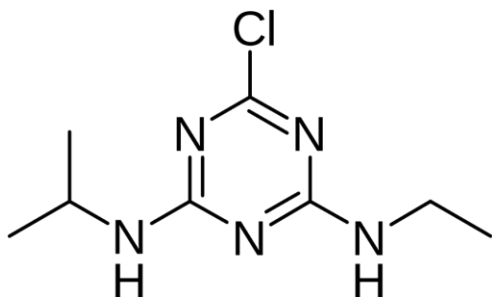
Figure 2.1. Molecular structure of atrazine.

2.2 Experimental

2.2.1 Materials and Sample Preparation

Synthesis of 5:1 Cu(II):BiOCl photocatalysts was first demonstrated by Jun Di et al [18]. The synthesis presented in this study was achieved by mixing a 1 mmol (0.485 g) solution of Bi(NO$_3$)$_3 \cdot$5 H$_2$O in a 20 mL solution of ethylene glycol. The source of copper ions was an ionic fluid consisting of 5 mmol 1-methyl-3-octylimidazolium (Omim) chloride mixed with 5 mmol copper(II) chloride to yield ([Omim]CuCl$_3$), and this solution was added to the ethylene glycol

solution and stirred for 30 minutes. The resulting solution was then transferred to a Teflon-lined autoclave system where it was left to bake overnight at 140°C. The remaining mixture separated into two distinct layers, with the solid product found in the aqueous teal layer. Upon separation the particles were washed twice with a 1:1 ethanol to water solution. The remaining sample was transferred to a watch glass and left to dry overnight at 50°C and collected for further characterization. Pure BiOCl (99.8%; Alfa Aesar) was used as a reference photocatalyst for both characterization and photodegradation experiments.

2.2.2   Catalyst Characterization

To characterize the surface morphology and elemental composition of the catalysts, Scanning Electron Microscopy with Energy Dispersive X-Ray Spectroscopy (SEM-EDS) was used. SEM-EDS scans were performed using a Zeiss SII Nvision 40 SEM with Ametek EDAX Genesis EDS mounted on it. The SEM image was done at a working distance of 4.2 mm and an EHT value of 2.00 kV. The EDS was run at 10.0 kV. The results of the EDS analysis were used to determine the elemental composition of the catalyst crystal structures. X-ray diffraction (XRD) scans on the catalysts were used to verify the compositional purity and crystallinity of the compounds. XRD patterns were obtained using a PANalytical X'Pert Pro diffractometer operated with Cu Kα radiation (45 keV and 40 mA). The samples were prepared for XRD analysis by depositing a MeOH/catalyst slurry onto a pre-cleaned glass slide and allowing the methanol to evaporate under reduced pressure. Diffuse Reflectance Spectroscopy (DRS) experiments were used to determine the optical band gap energy of both pure BiOCl and BiOCl with copper impurities present. The light source was a Mikropack DH-2000 deuterium and halogen light source coupled with an Ocean Optics USB4000 detector. A fiber optic cable was used to gather collected

light. Spectra was referenced with PTFE and potassium chloride. Data was processed using SpectraSuite software model 1.4.2_09.

Steady-state luminescence scans were run on the BiOCl and Cu-BiOCl at 78 K. Spectra were collected with a Model Quantamaster-1046 photoluminescence spectrometer from Photon Technology International. The device utilizes a 75 W xenon arc lamp coupled with two excitation monochromators and one emission monochromator to adjust the bandwidth of light hitting the sample and detector, respectively. Light intensity was measured using a photomultiplier tube. The samples were mounted on a copper plate using a non-emitting copper-dust-high vacuum grease. Low-temperature scans were run on the same system coupled with a Janis ST-100 optical cryostat and used liquid nitrogen as a cooling agent.

2.2.3 Dark Adsorption and Photocatalytic Activity

Atrazine samples (100 ppm) were prepared by dissolving 10 mg of atrazine in 10 mL methanol and bringing the solution up to 100 mL with deionized water. For photocatalytic activity trials, a 10-ppm solution of atrazine was prepared by adding 10 mL of stock solution to 100 mL of deionized water. Irradiation trials took place in a 250 mL round bottom flask with 25 mg of catalyst added in each trial. Catalysts were loaded into the solution and stirred for 15 minutes to achieve adsorption-desorption equilibrium. The light source used in experiments was a Steripen Mercury UV lamp with emission wavelength of 254 nm. The solution was sampled at five-min intervals for a period of 30 min to obtain degradative information on the reaction. Each photocatalytic trial was repeated at least three different times with the averages of each trial compiling each figure.

Radical scavenging experiments were performed using the same setup as detailed above except with an added component acting as a radical scavenger. The radical scavenging compounds

44

used in these trials included KI (for electron holes), IPA (for $^{\bullet}$OH), and BQ (for $O_2^{\bullet-}$). Throughout these irradiations, the atrazine concentration was determined by referencing the characteristic 260 nm absorption peak of atrazine to an external calibration curve. Trials measuring adsorption were run in a similar fashion yet in the absence of ultraviolet irradiation. The samples were collected and filtered through a chromatography syringe filter (PTFE, 25 mm diameter, pore size = 0.25 µm) to remove catalysts prior to analysis. UV-Vis spectra were collected using a Vernier UV-vis spectrophotometer with the corresponding Logger-Lite spectroscopy software.

2.2.4   Fourier-Transform Infrared Spectroscopy

Fourier Transform-Infrared Spectroscopy (FT-IR) was used to characterize the structure of the synthesized photocatalysts before and after irradiation. Spectra were collected on solid samples at 298 K using a Perkin Elmer FT-IR Spectrum Two equipped with a Universal Attenuated Total Reflectance (UATR) accessory. The UATR consists of a diamond crystal with a 2-micron pathlength. The detector is a $LiTaO_3$ MIR detector with a range of 8,300 cm^{-1} to 350 cm^{-1}. Spectra were collected using resolution of 2 cm^{-1}.

2.3 Results and Discussion

2.3.1   Catalyst Characterization

2.3.1.1 X-Ray Diffraction

X-Ray Diffraction scans were acquired for both pure BiOCl and Cu-BiOCl samples to characterize the structure and purity of the photocatalysts. The diffraction patterns for BiOCl and Cu-BiOCl are displayed in Figure 2.2. The diffraction pattern observed for BiOCl was found to match that of tetragonal (P4/nmm) BiOCl (JCPDS 1-073-2060). The pattern obtained for Cu-

BiOCl matches that reported by Di et al. [18] (JCPDS 06-0249). Consistent with their report, we do not note any characteristic patterns of copper species. Di et al. suggest that this result could be due to the chemical deposition of copper ions onto the surface of BiOCl. The diffraction pattern obtained for Cu-BiOCl is qualitatively less resolved than that obtained by Di et al., this may indicate that the size of our synthesized Cu-BiOCl microspheres are smaller. Both photocatalyst samples were determined to be of high purity based on the absence of contaminant peaks in either diffraction pattern.
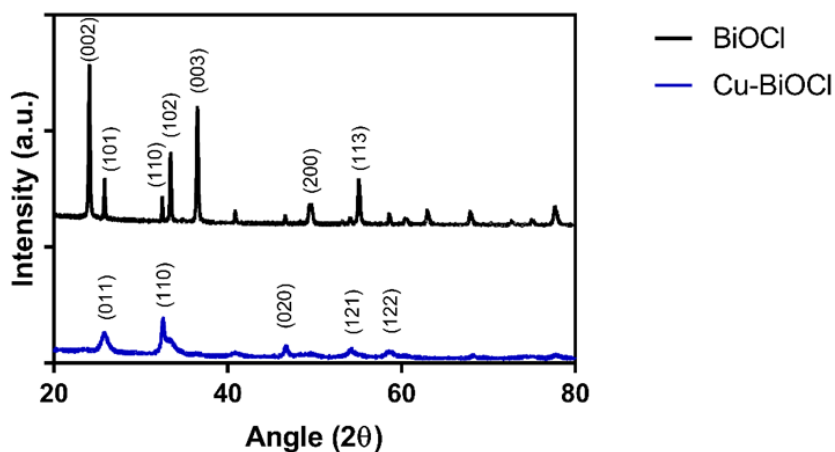
Figure 2.2. X-ray diffraction patterns obtained for BiOCl and Cu-BiOCl.

2.3.1.2 Scanning Electron Microscopy-Electron Dispersive Spectroscopy

Scanning electron microscopy coupled with energy dispersive X-ray spectroscopy (SEM-EDS) was utilized to investigate the structural morphology and elemental composition of Cu-BiOCl. The commercial BiOCl samples imaged confirm the morphology of BiOCl as stacked 2D nanosheets (Figure 2.3). The nanosheets range from 2 to 10-µm in diameter and are ~100-nm thick. SEM images obtained (Figure 2.3) indicate that the Cu-BiOCl samples synthesized in this report

are spherical formations of aggregated nanoplates, corresponding with the catalysts synthesized by Jun Di et al. [18]. From the SEM images, we determine that the diameter of the synthesized Cu-BiOCl spheres is ~0.3 μm. This diameter is smaller than that observed in previous reports [18].

Figure 2.4 shows the same region of Cu-BiOCl visualized as in Figure 2.3, however this image was generated using a backscatter detector instead of the secondary electron detector. This image appears uniformly bright, indicating that the surface of the synthesized Cu-BiOCl does not vary significantly in composition. This result suggests that the Cu(II) ions are evenly distributed throughout the BiOCl structure during the synthesis process and are not localized in any one area.

Figure 2.5 shows the total area averaged EDS results obtained for the synthesized Cu-BiOCl. Characteristic X-ray peaks associated with Cu, Bi, O, and Cl are all identified and labeled in Figure 2.5. The weight percent of each element was determined to be 13.1% oxygen, 14.3% bismuth, 11.1% chlorine, and 56.9% copper. These estimations are roughly consistent with the 1:1:1 (bismuth:oxygen:chlorine) ratio expected, and correspond to a 5x loading of copper. The remaining weight percent is accounted for by the large bromine peak visible in the EDS spectrum. We attribute this bromine present to be an impurity potentially acquired during the synthesis process.
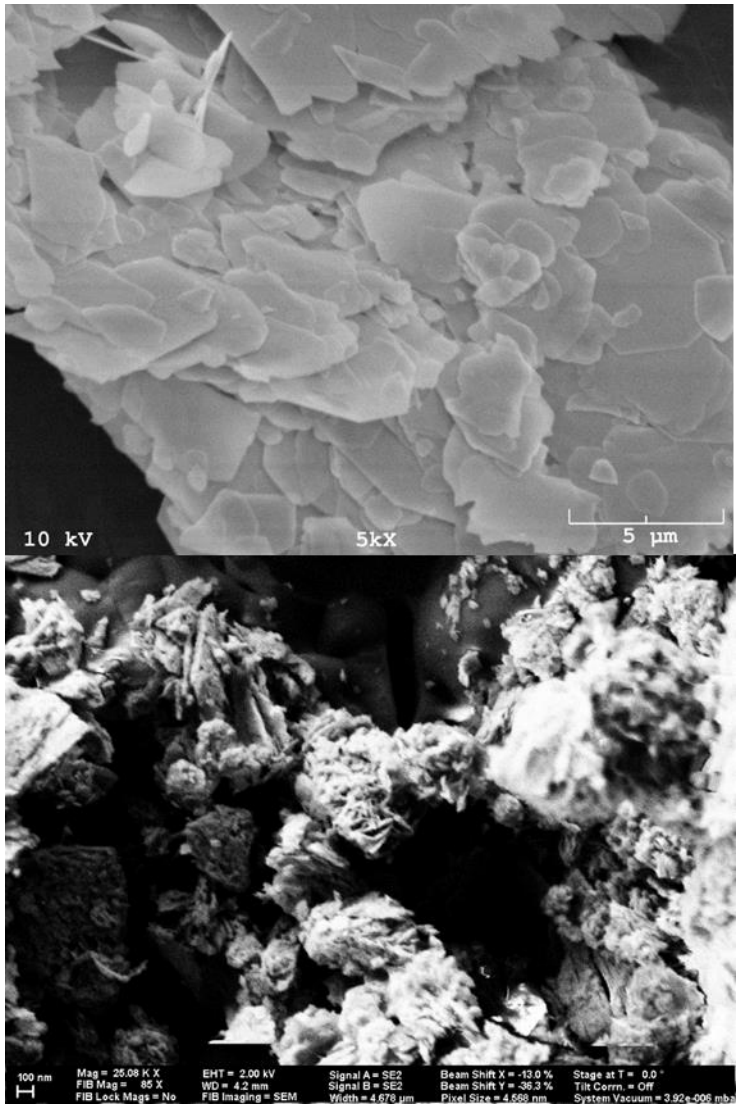
Figure 2.3. SEM images of BiOCl at 5kX magnification (top), and Cu-BiOCl at 25kX magnification (bottom).
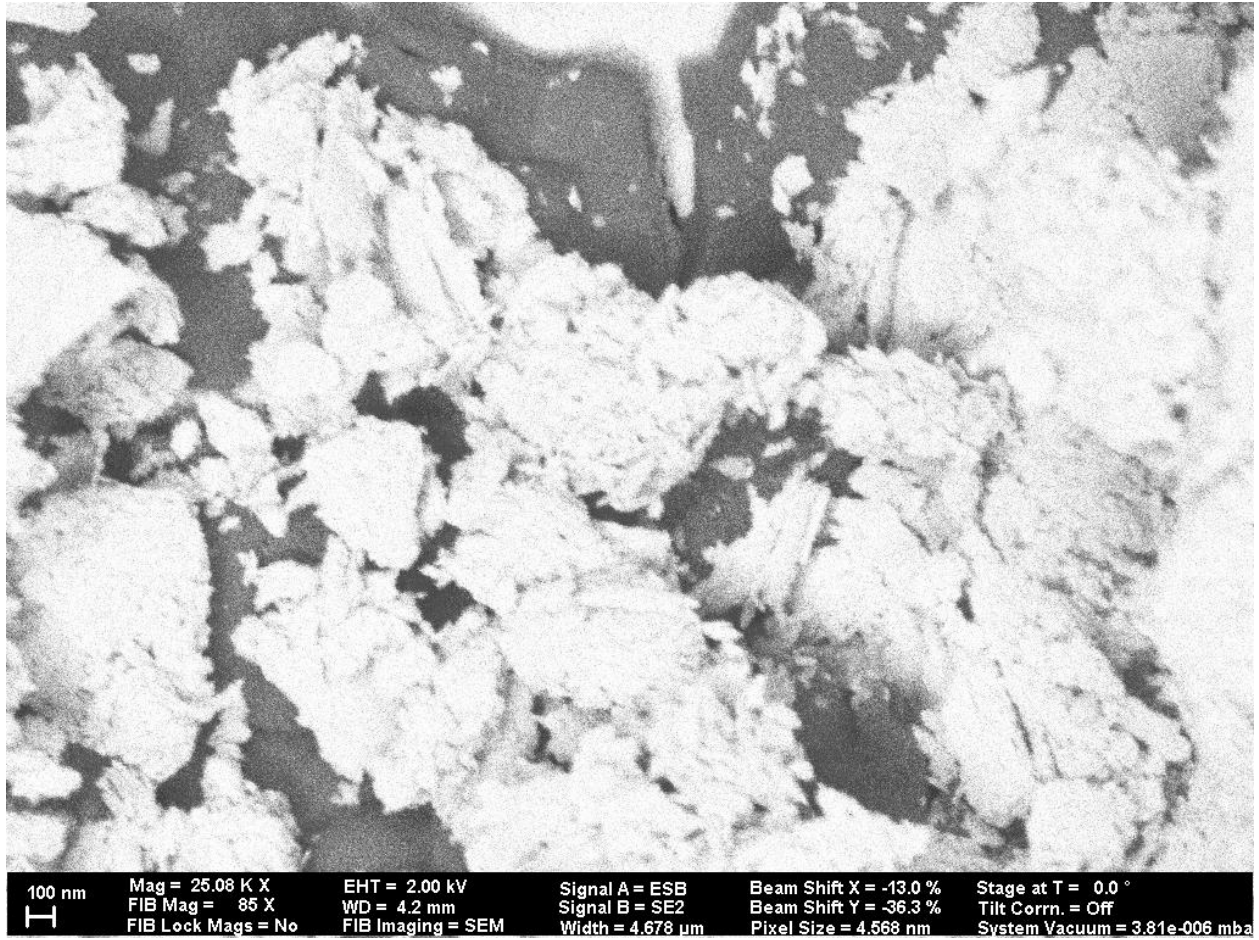
Figure 2.4. SEM image of Cu-BiOCl at 25kX magnification using the backscatter detector.
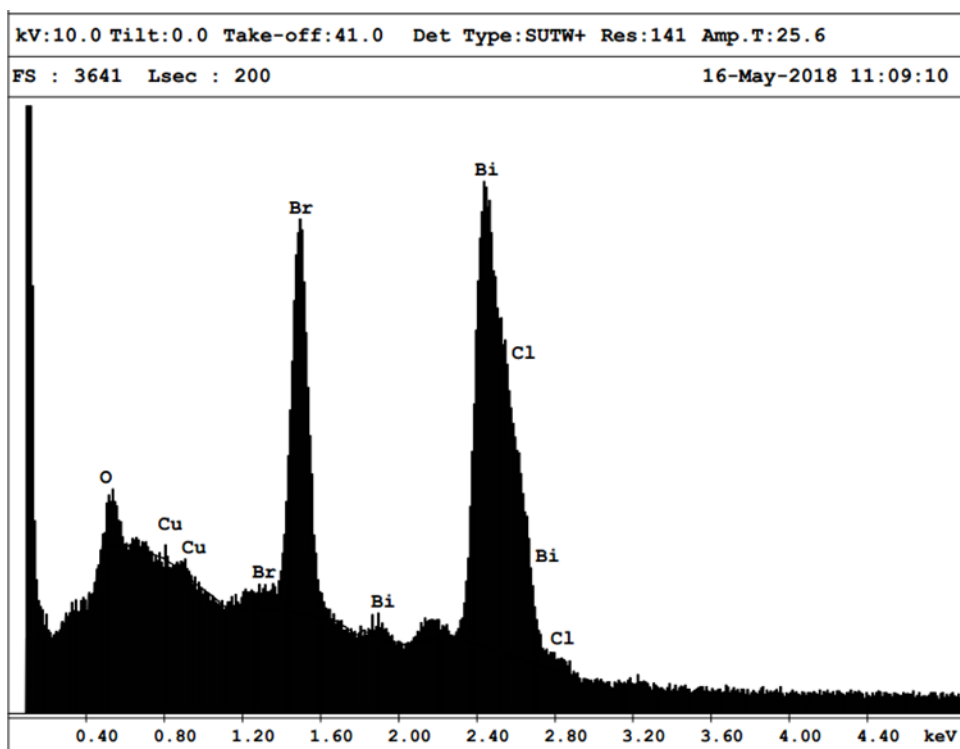
Figure 2.5. EDAX spectrum acquired for the synthesized Cu-BiOCl sample.

2.3.1.3 UV-Vis Diffuse Reflectance Spectroscopy

The determination of optical band gap energy was achieved using UV-Vis Diffuse Reflectance Spectroscopy (DRS). Determination of absorbance is achieved through the SpectraSuite analysis software using the equation:

$$f(R) = [1 - R]^{2}/2R \tag{1}$$

where R is equal to reflectance. Figure 2.6 shows the absorption spectra acquired for both BiOCl and Cu-BiOCl from 300-800 nm. Both spectra show a distinct absorption edge at 360 nm, while the Cu-BiOCl spectra also shows a band at 550 nm, consistent with previous reports. The Kubelka-Munk method was used to determine the optical band gap value for both photocatalysts based on

the absorption spectra. BiOCl is determined to have an optical band gap of 3.2 eV, while Cu-BiOCl was found to have an optical band gap of 3.0 eV.
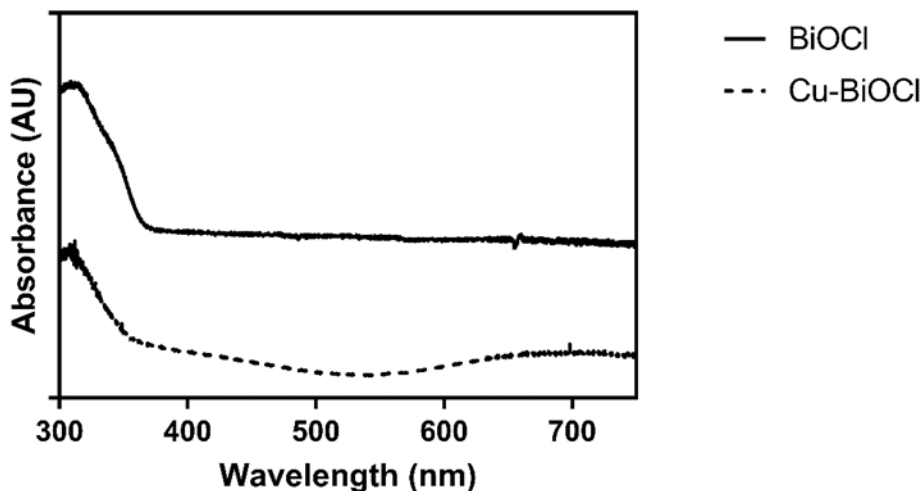
Figure 2.6. UV-Vis spectra acquired for BiOCl (top) and Cu-BiOCl (bottom).

2.3.1.4 Photoluminescence Spectroscopy

Photoluminescence spectroscopy was used to further characterize the synthesized Cu-BiOCl. The luminescence spectra are shown in Figure 2.7. The excitation wavelength used to acquire the spectrum was 265 nm and measurements were recorded at 78 K. Evidence of Cu(I) emission at 450 nm can be seen here, indicating that excited electrons are transferred from the conduction band of BiOCl to the deposited Cu(II) species, reducing it to Cu(I) and resulting in the observed photoluminescence. Cu(I) is a d^{10} photoluminescent species, which our group has previously investigated and reported on [19]. The photoluminescence spectra exhibit vibrational fine structure. We attribute the presence of this stretch to interaction with the Bi-O Raman mode, further indicating the close interaction of Cu(II) and BiOCl.
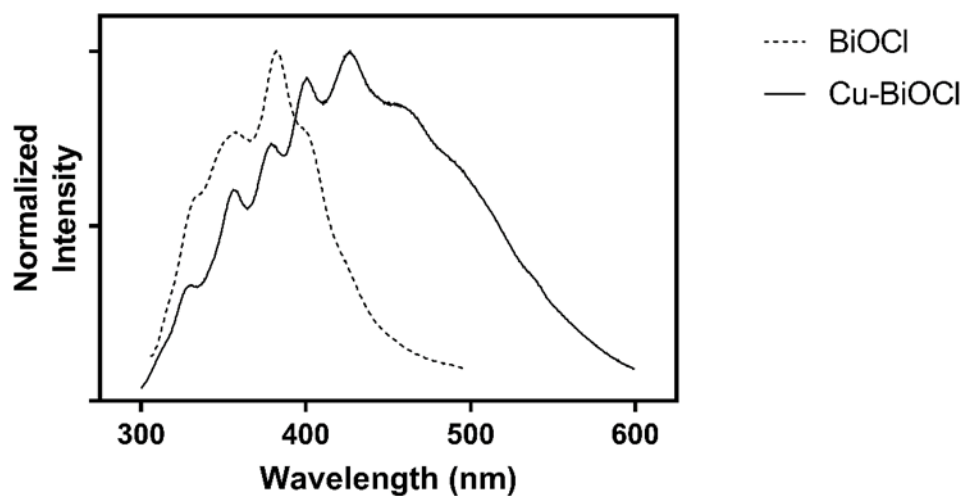
Figure 2.7. Photoluminescence emission spectrum of BiOCl and Cu-BiOCl measured at 78 K with excitation at 265 nm.

2.3.2 Adsorption and Photocatalytic Activity

Catalyst evaluation trials were conducted under dark and ultraviolet light irradiation conditions to investigate atrazine removal from aqueous solutions by adsorption or photocatalysis. The results of dark trials (Figure 2.8) indicate that neither BiOCl nor Cu-BiOCl show significant adsorption of atrazine onto the surface of the catalysts. This result confirms that photocatalytic removal of atrazine from aqueous solutions is not due solely to adsorption and suggests reactive chemical species play a significant role in the degradation of atrazine.

Removal of atrazine was observed in photocatalytic degradation trials in the presence of Cu-BiOCl (Figure 2.8). Photodegradation trials indicated that 35% of atrazine was removed during pure BiOCl photocatalysis, whereas 29% of atrazine was removed during Cu-BiOCl photocatalysis. The rate of BiOCl photodegradation is qualitatively similar when compared to the

degradation rate exhibited by Cu-BiOCl. These results suggest that the addition of Cu(II) ions to this system do not provide a significant benefit for the photocatalytic degradation of organics without the aid of a sacrificial donor. To better investigate radical and electron transition activity, photocatalytic trials in the presence of radical scavenging compounds were used.
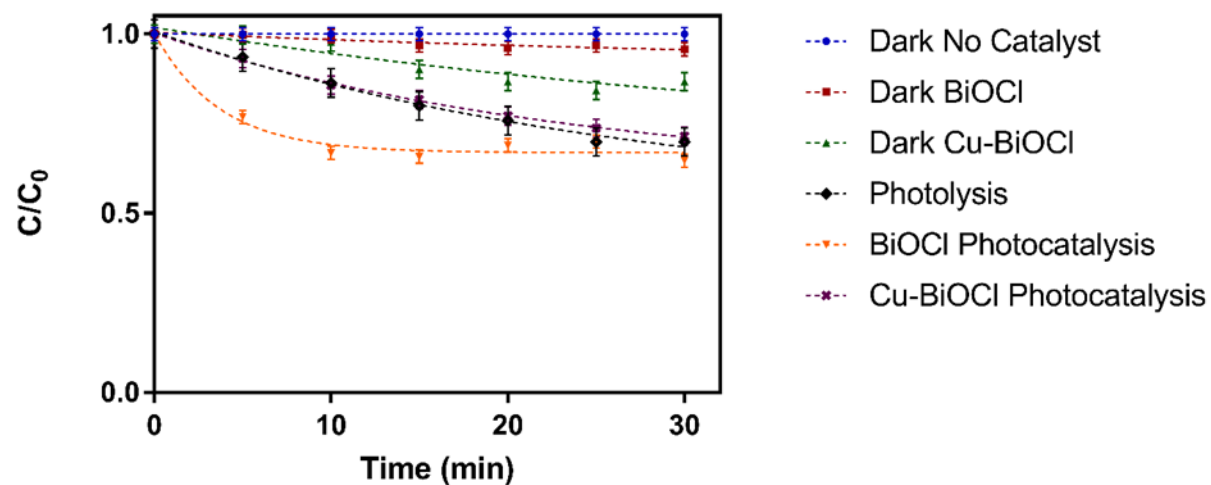
Figure 2.8. Atrazine removal rates for dark and photocatalytic degradation conditions as monitored by UV-Vis spectroscopy.

2.3.3   Radical Scavenging Experiments

Radical scavenging experiments were performed to determine the active species generated by both pure and modified BiOCl that are responsible for atrazine degradation. These investigations are used to assist in constructing a proposed mechanism that details the flow of photo-generated electrons in BiOCl in the presence of Cu(II). The results for pure BiOCl and copper-modified BiOCl scavenging experiments are shown in Figure 2.9 and Figure 2.10,

respectively. For BiOCl, the addition of potassium iodide (KI) resulted in no observable degradation of atrazine. When isopropanol (IPA) is added as a radical scavenger, a moderate amount of degradation is observed, with a percentage of atrazine removed to be around 23%. Addition of benzoquinone (BQ) resulted in no reduction in removal activity, indicating superoxide radicals may not be a dominant reactive species in aqueous photocatalytic degradation. The results displayed in Figure 2.9 indicate that electron holes and hydroxyl radicals play a substantial role in atrazine degradation using BiOCl, while superoxide radicals do not participate in the photocatalytic degradation process.

The addition of Cu(II) allows for sustained photo-induced separations that generate these electron vacancies as well as the excited state radical species. A similar degradation trend is observed using Cu-BiOCl, with KI completely shutting down atrazine removal while normal degradation was still observed after the addition of either IPA or BQ, as shown in Figure 2.10. The percentage of atrazine removed remained more pronounced for Cu-BiOCl in the presence of IPA than for BiOCl, indicating a lack of hydroxyl radical activity in the copper-modified systems. These results suggest that hydroxyl radicals play a more integral role in atrazine degradation for BiOCl than for Cu-BiOCl in aqueous solutions.
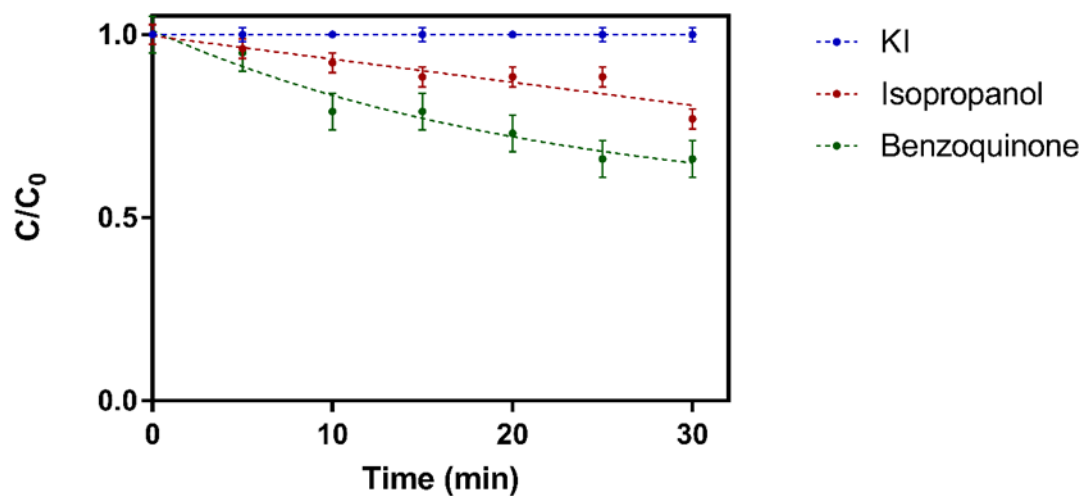
Figure 2.9. Atrazine removal rates via BiOCl photocatalysis in the presence of KI (hole scavenger), isopropanol (hydroxyl radical scavenger), and benzoquinone (superoxide scavenger).
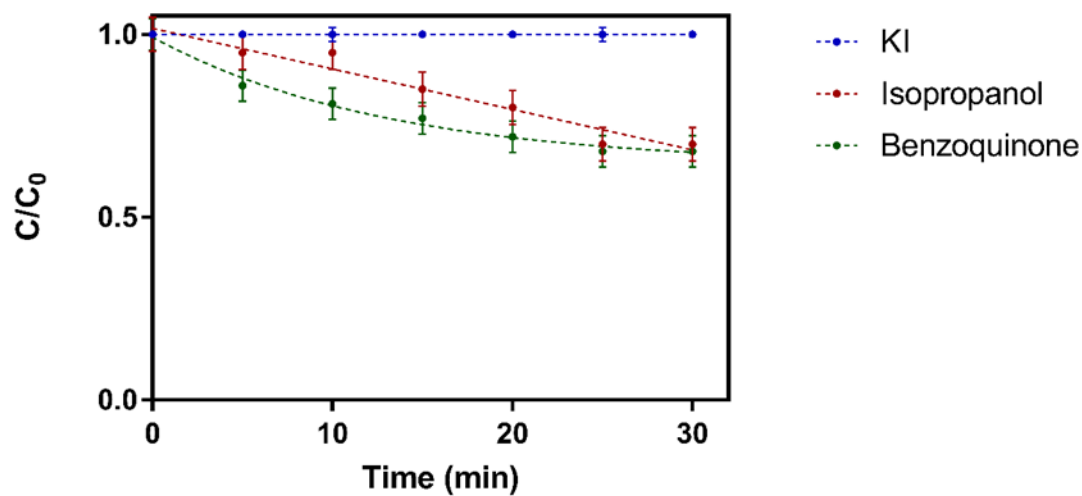
Figure 2.10. Atrazine removal rates via Cu-BiOCl photocatalysis in the presence of KI (hole scavenger), isopropanol (hydroxyl radical scavenger), and benzoquinone (superoxide scavenger).

2.3.4   Proposed Mechanism

The results from photocatalytic and radical scavenging trials indicated that electron holes play a substantial role in the degradation process of BiOCl and Cu-BiOCl. Scavenging of superoxide radicals did not effect either BiOCl or Cu-BiOCl photocatalytic degradation processes. The results displayed in Figure 2.9 suggest hydroxyl radicals are not a primary active species during photocatalytic degradation of atrazine with BiOCl. Dependence on the hydroxyl radical during degradation is less prominent in the copper-modified systems based on Figure 2.10, which indicates only a minor reduction in atrazine removal during radical scavenging trials. The proposed electron transition mechanism for Cu-BiOCl is shown below.

Irradiation of the BiOCl catalyst by light of sufficient energy (represented by hv) excites an electron from the valence band to the conduction band of BiOCl (Equation 2), generating both an excited electron (e^-) and an electron hole (h^+). As shown in part (3) and (4) of the proposed mechanism, irradiation of Cu-BiOCl creates photo-induced separations that reduces the surface-deposited Cu(II) species to Cu(I) via transfer of electrons originating from the conduction band of BiOCl (Equation 3). As Cu(I) oxidizes to regain charge balance, remaining electrons participate in oxidation-reduction reactions that facilitate increased radical species formation.

$$BiOCl + hv \; \rightarrow \; e^- + h^+ \tag{2}$$

$$Cu^{2+} + e^- \rightarrow Cu^+ \tag{3}$$

$$Cu^+ + O_2 \; \rightarrow Cu^{2+} + O_2^- \tag{4}$$
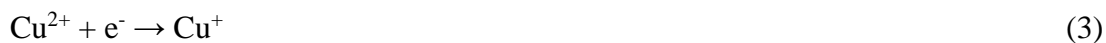
This electronic transition is facilitated through interactions between the Cu(II) ion and the crystal structure of the BiOCl system, which is thought to exist in a terminal $Cu(OH)_2$ complex as proposed in studies using bismuth oxide complexes by Sudrajat and coworkers [20]. This

configuration and catalytic stability is further suggested by the lack of degradation using hydroxyl radicals, which is also indicated in Figure 2.9. The interactions between the copper complex and the bismuth center of the catalyst allow for increased transition of electrons that allow for the increased formation of reactive chemical species, which equate to increased degradation of atrazine.

$$O_2^- + ATZ \quad \rightarrow \quad \text{Degradation Products} \tag{5}$$

$$ATZ + h^+ \quad \rightarrow \quad ATZ^+ \tag{6}$$

$$ATZ^+ \quad \rightarrow \quad \text{Degradation Products} \tag{7}$$

This radical species generation pathway may be de-emphasized in the copper-modified system, since the radical scavenging experiments showed that superoxide does not play a large role in photocatalytic degradation of atrazine. However, any superoxide radicals generated during the irradiation process will react with atrazine to form degradation products (Equation 5). The direct interaction of electron holes with the pollutant was found to be the major pathway associated with photocatalytic degradation of atrazine. We propose that this reaction may take place through an electron transfer from atrazine to the electron hole in the valence band of BiOCl to generate ATZ^+ (Equation 6). ATZ^+ is an electron deficient and unstable species and will then react to form degradation products (Equation 7). The proposed mechanism of atrazine degradation by Cu-BiOCl is summarized in Figure 2.11.
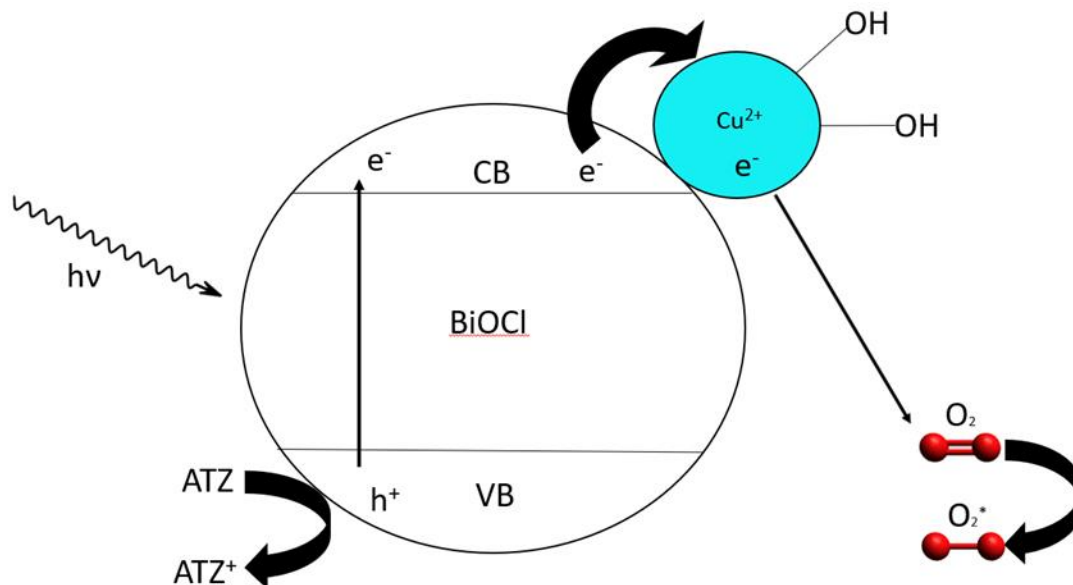
Figure 2.11. Graphical representation of the photocatalytic mechanism proposed for removal of atrazine by Cu-BiOCl.

2.3.5 Fourier-Transform Infrared Spectroscopy

The stability of the modified bismuth oxyhalide photocatalysts were investigated using Fourier-Transformed infrared spectra. Initial scans of Cu-BiOCl indicated bismuth-oxygen stretch in the fingerprint region (0-500 cm^{-1}), which is indicated in Figure 2.12. This stretch was determined to be the Bi-O chemical signature based on previous literature and was observed at a wavelength of 521 cm^{-1}. Di et al. indicated the presence of a Bi-O stretch at 528 cm^{-1} for pure and the copper-modified BiOCl [19]. Upon one hour of irradiation, no shifts in the 521 cm^{-1} peaks were observed, suggesting the Bi-O stretch remained upon exposure to UV irradiation. The results displayed in Figure 2.11 suggest the synthesized catalyst resists photo-corrosion and other detrimental processes that can disrupt catalytic capabilities.
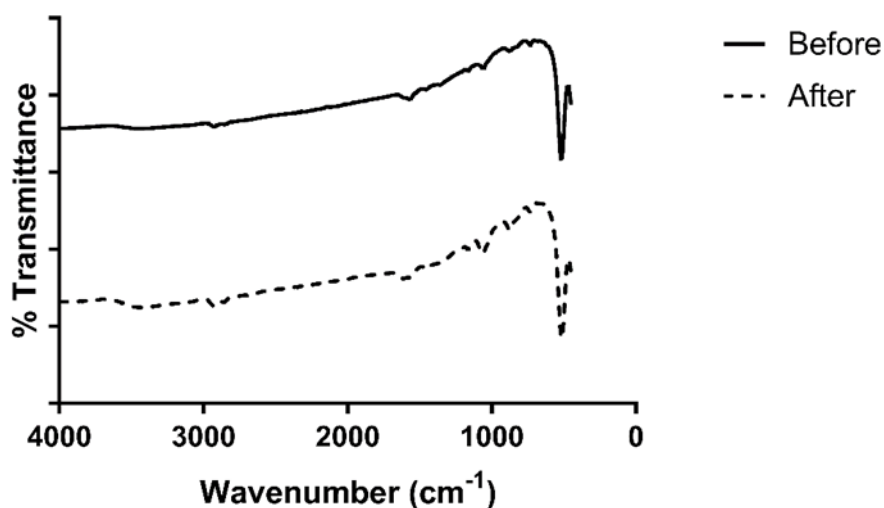
Figure 2.12. FT-IR spectra of Cu-BiOCl collected before and after 1 hour of UV radiation exposure.

2.4 Conclusion

Characterization results indicated successful synthesis of copper-modified BiOCl in agreement with results reported by Di. et al. [19]. The results of the photocatalytic investigations suggest a decrease in photocatalytic activity for atrazine degradation in the copper modified photocatalysts compared to the pure BiOCl counterparts. This change in photocatalytic activity is thought to arise from electronic transitions between the BiOCl framework and copper (II) ions present, which facilitate increased electron transitions and radical formation. The reduction of surface deposited Cu(II) to Cu(I) promote increased electron flow from the conduction band of the BiOCl catalyst, thereby increasing photo-induced charge separations which assist in the degradation of atrazine. Enhancement of photocatalytic complexes using metallic ions such as copper have been suggested as a possible method to decrease recombination of excited state electrons and allow for increased degradation of pollutants. Interestingly, the results presented here

suggest that the presence of Cu-dopants may prevent some of the photocatalytic activity of pure BiOCl that originates from hydroxyl radical generation. This observation may be exploited in future work to access only the photocatalytic activity originating from electron holes, increasing the selectivity of the photocatalytic reaction system.

2.5 References

1.   Jablonowski, N. D.; Schäffer, A.; Burauel, P. Still present after all these years: Persistence plus potential toxicity raise questions about the use of atrazine. Environ. Sci. Pollut. Res. 2011, 18, 328–331, doi:10.1007/s11356-010-0431-y.

2.   Jackson, H. Maine Board of Pesticides Control Pesticides and ground water monitoring program. 2006, 28.

3.   Fang, H.; Lian, J.; Wang, H.; Cai, L.; Yu, Y. Exploring bacterial community structure and function associated with atrazine biodegradation in repeatedly treated soils. J. Hazard. Mater. 2015, 286, 457–465, doi:10.1016/j.jhazmat.2015.01.006.

4.   Gammon, D. W.; Silva, M.; Aldous, C.; Sanborn, J. R.; Carr, W. C.; Pfeifer, K.; Schreider, J. P. Atrazine: Risk characterization document. Med. Toxicol. Branch, Calif. Dep. Pestic. Regul. Calif. Environ. Prot. Agency 2001.

5.   Rowe, A. M.; Brundage, K. M.; Barnett, J. B. Developmental immunotoxicity of atrazine in rodents. Basic Clin. Pharmacol. Toxicol. 2008, 102, 139–145, doi:10.1111/j.1742-7843.2007.00175.x.

6. Chen, C.; Yang, S.; Guo, Y.; Sun, C.; Gu, C.; Xu, B. Photolytic destruction of endocrine disruptor atrazine in aqueous solution under UV irradiation: Products and pathways. J. Hazard. Mater. 2009, 172, 675–684, doi:10.1016/j.jhazmat.2009.07.050.

7. Ahern, J. C.; Fairchild, R.; Thomas, J. S.; Carr, J.; Patterson, H. H. Characterization of BiOX compounds as photocatalysts for the degradation of pharmaceuticals in water. Appl. Catal. B Environ. 2015, 179, 229–238, doi:10.1016/j.apcatb.2015.04.025.

8. Zhao, H.; Tian, F.; Wang, R.; Chen, R. A Review on Bismuth-Related Nanomaterials for Photocatalysis. Rev. Adv. Sci. Eng. 2014, 3, 3–27, doi:10.1166/rase.2014.1050.

9. Shamsedini, N.; Dehghani, M.; Nasseri, S.; Baghapour, M. A. Photocatalytic degradation of atrazine herbicide with Illuminated Fe^{+3}-TiO_2 Nanoparticles. J. Environ. Heal. Sci. Eng. 2017, 15, 7, doi:10.1186/s40201-017-0270-6.

10. Pantelaki, I.; Voutsa, D. Formation of iodinated THMs during chlorination of water and wastewater in the presence of different iodine sources. Sci. Total Environ. 2018, 613–614, 389–397, doi:10.1016/j.scitotenv.2017.09.072.

11. Pan, Z.; Stemmler, E. A.; Cho, H. J.; Fan, W.; LeBlanc, L. A.; Patterson, H. H.; Amirbahman, A. Photocatalytic degradation of 17α-ethinylestradiol (EE2) in the presence of TiO_2-doped zeolite. J. Hazard. Mater. 2014, 279, 17–25, doi:10.1016/j.jhazmat.2014.06.040.

12. Chen, S. M.; Lu, N.; Chen, J. Y.; Yang, C. Y.; Yeh, Y. P.; Feng, T. Y.; Shih, Y. H.; Kokulnathan, T.; Chen, D. Enhanced photocatalytic degradation of atrazine by platinized titanium dioxide under 352 nm irradiation. Water Sci. Technol. 2017, 75, 1128–1137, doi:10.2166/wst.2016.593.

13.   Granados-Oliveros, G.; Páez-Mozo, E. A.; Ortega, F. M.; Ferronato, C.; Chovelon, J. M. Degradation of atrazine using metalloporphyrins supported on TiO_2 under visible light irradiation. Appl. Catal. B Environ. 2009, 89, 448–454, doi:10.1016/j.apcatb.2009.01.001.

14.   Libanori, R.; Giraldi, T. R.; Longo, E.; Leite, E. R.; Ribeiro, C. Effect of TiO_2 surface modification in Rhodamine B photodegradation. J. Sol-Gel Sci. Technol. 2009, 49, 95–100, doi:10.1007/s10971-008-1821-1.

15.   Liu, Z.; Liu, J.; Wang, H.; Cao, G.; Niu, J. Boron-doped bismuth oxybromide microspheres with enhanced surface hydroxyl groups: Synthesis, characterization and dramatic photocatalytic activity. J. Colloid Interface Sci. 2016, 463, 324–331, doi:10.1016/j.jcis.2015.10.028.

16.   Wen, X. J.; Niu, C. G.; Guo, H.; Zhang, L.; Liang, C.; Zeng, G. M. Photocatalytic degradation of levofloxacin by ternary $Ag_2CO_3/CeO_2/AgBr$ photocatalyst under visible-light irradiation: Degradation pathways, mineralization ability, and an accelerated interfacial charge transfer process study. J. Catal. 2018, 358, 211–223, doi:10.1016/j.jcat.2017.12.005.

17.   Santacruz-Chávez, J. A.; Oros-Ruiz, S.; Prado, B.; Zanella, R. Photocatalytic degradation of atrazine using TiO_2 superficially modified with metallic nanoparticles. J. Environ. Chem. Eng. 2015, 3, 3055–3061, doi:10.1016/j.jece.2015.04.025.

18.   Di, J.; Xia, J.; Yin, S.; Xu, H.; Xu, L.; Xu, Y.; He, M.; Li, H. One-pot solvothermal synthesis of Cu-modified BiOCl via a Cu-containing ionic liquid and its visible-light photocatalytic properties. RSC Adv. 2014, 4, 14281–14290, doi:10.1039/c3ra45670f.

19.   Ahern, J. C.; Kanan, S.; Patterson, H. H. Heterogeneous Photocatalysis with Nanoclusters of D^{10} Metal Ions Doped in Zeolites. Comments Inorg. Chem. 2015, 35, 59–81, doi:10.1080/02603594.2014.973106.

20.	Sudrajat, H.; Sujaridworakun, P. Insights into structural properties of Cu species loaded on Bi$_2$O$_3$ hierarchical structures for highly enhanced photocatalysis. J. Catal. 2017, 352, 394–400, doi:10.1016/j.jcat.2017.05.027.

CHAPTER 3

PHOTOCATALYTIC DEGRADATION OF IBUPROFEN OVER BiOCl NANOSHEETS WITH IDENTIFICATION OF INTERMEDIATES

3.1 Introduction

Almost 9000 chemical compounds are currently approved for use in pharmaceutical applications worldwide [1]. These compounds necessarily comprise a diverse array of chemical structures in order to obtain the desired range of biological activities. For many pharmaceuticals, the active form is excreted as an unaltered form of the drug; for others, some percentage is altered when metabolized [2]. Increasing use of pharmaceuticals has led to growing concerns about pharmaceutical-related pollution. Extended use of pharmaceuticals has resulted in their accumulation in ground and surface water [3–6], presenting risks to humans and environmental systems. Additionally, a variety of pharmaceuticals and personal care products (PPCPs) are detected in the influent and effluent wastewater treatment plants [7,8], demonstrating that current systems are not adequately removing compounds prior to discharge to the environment. Developing approaches to PPCP removal is critical to mitigating the risks associated with environmental contamination by these products.

Photocatalysis is a promising approach for the abatement of pharmaceutical pollution [9,10]. Photocatalysts are semiconductor materials that can absorb light of energy greater than or equal to the band gap energy to promote an electron from its valence band to the conduction band. This absorption produces an excited-state electron in the conduction band and a complementary electron hole (h^+) in the valence band of the semiconductor material. The holes and electrons can

64

react and break down pollutants either through the generation of ROS (hydroxyl radicals, for example) or through a direct redox interaction with the pollutant [11,12].

Non-Steroidal Anti-Inflammatory Drugs (NSAIDs) are a popular class of drugs that exhibit analgesic, antipyretic, and anti-inflammatory effects [13]. Excretion of NSAIDs and their metabolites have been found to be a major source of aquatic pollution [14,15]. The removal of low concentrations of these hazardous pollutants is a challenge that must be addressed to prevent public health problems. Ibuprofen (IBP; (RS)-2-(4-(2-methylpropyl)phenyl)propanoic acid)) is one of the most widely used NSAIDs. Both IBP and its metabolites, which are both found in surface waters and sewage at µg/L levels [16], exhibit toxic effects even at ng/L concentrations [17,18].

The photolytic and photocatalytic degradation of IBP has been studied extensively. Early work [19] established that IBP was susceptible to photodegradation by UV light and provided support for the important role of photodecarboxylation in the photodegradation of this 2-arylacetic acid. Additionally, this early study demonstrated that two photoproducts, 1-(4-isobutylphenyl)ethanol (IBPE) and 4-isobutylacetophenone (IBAP), exhibited toxic effects towards cultured fibroblasts. Subsequent investigations have examined the photolysis of IBP in natural waters [20–26], with some studies concluding that the photolysis of IBP results in the production of degradation products that were more stable [20,25] and exhibited enhanced toxicity [23,24] relative to IBP. Studies have also been directed at the photocatalytic degradation of IBP, most commonly using TiO_2 as the photocatalyst [5,20,27–29]. While all studies showed that UV photocatalytic degradation with TiO_2 was effective with respect to IBP removal, less than total mineralization was reported [20] and degradation products were found to have toxicities that were similar to or exceeded that of IBP [5,21,24]. This data highlights the need to identify photocatalysts that more effectively degrade both IBP and its photodegradation products.

Another photocatalyst that holds promise for the photodegradation of pharmaceuticals is bismuth oxychloride (BiOCl). BiOCl was initially discovered to possess UV photocatalytic activity for methyl orange degradation, with the excellent activity attributed to the open crystal structure and indirect optical transitions [30]. The crystal structure of BiOCl is known to be a tetragonal matlockite structure consisting of layers of $[Bi_2O_2]^{2+}$ slabs interwoven with a Cl^- double layer. The structure of BiOCl contributes to the presence of strong internal electric fields perpendicular to the Cl^- layer that assist in preventing recombination of photoinduced electron-hole pairs [31]. Further research with BiOCl confirmed the photocatalytic activity with rhodamine B [32], and neutral Red [33]. While early work focused on BiOCl nanosheets, it was also found that the nanosheets could easily aggregate into 3D hierarchical structures [34]. The potential practical application of BiOCl has led researchers to probe synthetic strategies and their photocatalytic activity for degradation of pharmaceuticals including carbamazepine [35] and estradiol [36]. Lester et al. synthesized $BiOCl_{0.875}Br_{0.125}$ and showed that this catalyst exhibits visible light activity for the degradation of IBP [37].

In a recent study, BiOCl formulated in nanosheets was shown to efficiently degrade perfluorooctanoic acid [38], with the photocatalytic efficacy attributed to direct hole oxidation. Decarboxylation of perfluorooctanoic acid via interactions between BiOCl and the carboxylate anion was proposed as a key initiating step in the photodegradation process. In this work, the photocatalytic activity via h^+ oxidation was related to oxygen vacancies in the photocatalyst [38]. In contrast with the photodegradation efficiency observed for perfluorooctanoic acid, IBP, another analyte with a carboxylic acid group, was found to be lost from solution due to surface adsorption, not photodegradation, when IBP was subjected to photocatalytic degradation using BiOCl or BiOBr formulated as microspheres [39,40].

In this study, we have addressed a deficiency in the current literature. We evaluated the photocatalytic degradation of IBP using BiOCl nanosheets, assessing IBP removal by both photodegradation and adsorption, quantifying the yields of two primary photoproducts, and creating an inventory of products detected by HPLC-DAD and (+)ESI-LC-MS/MS to determine if the demonstrated photoactivity towards perfluorooctanoic acid extends to the photodecomposition of IBP. This study presents data that increases our understanding of processes that impact the photodegradation and mineralization of both IBP and its photoproducts by BiOCl.

3.2 Experimental

3.2.1 Materials and Sample Preparation

BiOCl (99.8%; Alfa Aesar) was used as a photocatalyst. Experimental solutions were prepared by dissolving 10-mg of ibuprofen (IBP (1); >98%; Ark Pharma), 1-(4-isobutylphenyl)ethanol (IBPE (2); Sigma-Aldrich), or 4-isobutylacetophenone (IBAP (3); Sigma-Aldrich) in 5-mL of HPLC grade methanol (MeOH, 99.99%; Sigma-Aldrich) and then diluting the solution to 100-mL in deionized water to prepare a 100 mg/L stock solution. The stock solution was then diluted to 10 mg/L in deionized water for each photocatalyst evaluation. All reagents were used without further purification.

3.2.2 Catalyst Characterization

X-ray diffraction (XRD) scans on the catalysts were used to verify the compositional purity and crystallinity of the compounds. XRD patterns were obtained using a PANalytical X'Pert Pro diffractometer operated using Cu Kα radiation (45 keV and 40 mA). The samples were prepared for XRD analysis by depositing a MeOH/catalyst slurry onto a pre-cleaned glass slide and allowing

the MeOH to evaporate under reduced pressure. Scanning electron microscopy (SEM) was used to characterize the morphology and size of the photocatalysts. SEM scans were conducted using an AMRay 1820 operating at 10 kV. The photocatalysts were mounted on stainless steel sample mounts and imaged at 5kX magnification. Brunauer-Emmett-Teller analysis (BET) was used to determine the specific surface area of the catalysts. The nitrogen adsorption-desorption isotherms were measured on a Quantachrome Autosorb iQ Station 2 gas sorption analyzer at 77K. UV-Vis Diffuse reflectance spectra (DRS) were collected on solid samples at 298 K. The broadband light source operating from 178-800 nm was a Mikropack DH-2000 deuterium and halogen light source which was coupled with an Ocean Optics USB4000 detector. Reflected light from the sample was collected with a fiber optic cable. Spectra was referenced with polytetrafluoroethylene (PTFE) considered as a completely reflective surface. Data was processed using SpectraSuite 1.4.2_09.

3.2.3   Photocatalytic Degradation of IBP and IBAP

Photocatalytic batch experiments were undertaken to compare the kinetic properties of each photocatalyst. A 10 mg/L stock solution (100-mL) of IBP or IBAP in deionized water was placed in a quartz flask along with 25-mg of catalyst. The 10 mg/L starting concentration was chosen to ensure enough material was available for observation and characterization of reaction intermediates. The pH of the IBP solutions were monitored using a pH meter (Orion Star A111; ThermoFisher Scientific) throughout the course of the experiments. The initial solution pH was 4.5 and decreased slightly throughout the course of the experiment with maximum variation of 1 pH unit. The solutions were stirred in the dark for 15-min to achieve adsorption/desorption equilibrium before placing them in a Rayonet-RPR 100 UV Photoreactor equipped with four 254-nm 128 W/m two-prong bulbs. The solutions were irradiated for up to 30- or 120-min while stirring, with aliquots removed at specified intervals for analysis.

In early work, samples were analyzed using fluorescence. Subsequent HPLC-DAD analyses showed that the fluorescence measurements were subject to interference. For dark experiments, quenching effects attenuated the IBP signal; however, signal reduction was not observed from measurements made by HPLC-DAD or UV-Vis absorption. For photodegradation experiments monitored using fluorescence one photodegradation product, IBPE, interfered with IBP because both exhibited identical excitation and emission spectra. In this work, a Vernier UV-Vis Spectrophotometer was used to monitor IBP absorption at 220-nm. For photodegradation studies, samples were analyzed by HPLC-DAD and LC-MS/MS.

3.2.4 HPLC Analysis

An Agilent 1100 series HPLC with a diode array detector (DAD) was used for sample analysis. A reversed-phase, Luna C18 (3-μm, 100- x 4.6-mm; Phenomenex) column was used to conduct gradient separations, using 0.1% formic acid in water (mobile phase A) and acetonitrile (mobile phase B). The gradient began with 85% (A) with a linear change to 20% (A) at 30-min. The injection volume for reaction samples was 100-μL; smaller volumes (10- or 20-μL) were used to analyze standards. DAD chromatograms were monitored at four different absorbance wavelengths (210-, 223-, 254-, 310-nm).

3.2.5 LC-MS/MS Analysis

A 6530 series chip-based quadrupole time-of-flight mass spectrometer (LC-MS/MS; Agilent Technologies, Santa Clara, CA) was used to analyze all samples. Liquid chromatography separations and nano-electrospray ionization (nanoESI) were conducted using a 1260 Chip Cube system (Agilent Technologies) with a reversed-phase ProtID II chip (Agilent technologies; C18 stationary phase, 5-μm, 150- x 0.075-mm). Mobile phase A was 5-mM ammonium formate

(Agilent) in water or 0.1% formic acid in water (LCMS grade; Fisher); mobile phase B was 0.1% formic acid (LCMS grade; Fisher) and 2% water in acetonitrile (LCMS grade; Fisher). Samples (8-µL) were injected onto an enrichment column and were analyzed using a gradient that started with 99% (A) and changed linearly to 40% (A) at 30-min; 20% (A) at 35-min; and 0% (A) at 42-min.

Mass spectra (MS and MS/MS) were collected in positive ion mode with ESI source potentials ranging from 1850 to 1950 V and an ion source temperature held at 350°C. Spectra were internally calibrated using a solvent dimer ($[CH_3CN+H2O+H]^+$: m/z = 60.0444) and the reference compound hexakis (1H, 1H, 4H-hexafluorobutyloxy)phosphazine (HP-1221; $C_{24}H_{18}O_6N_3P_3F_{36}$; m/z = 1221.9906). MS/MS spectra were collected using collision energies of 15-eV using nitrogen as the collision gas.

3.3 Results and Discussion

3.3.1 Catalyst Characterization

Using XRD, we determined the crystal structure and particle size for BiOCl. The diffraction pattern of the BiOCl sample (Appendix A, Figure A.1) matched that of tetragonal (P4/nmm) BiOCl (JCPDS 1-073-2060). SEM images of the photocatalyst were collected to provide insight into its morphology. SEM images confirm the morphology of BiOCl as stacked 2D nanosheets (Appendix A, Figure A.2). The nanosheets range from 2 to 10-µm in diameter and are ~100-nm thick. Surface area analysis was conducted using the Brunauer-Emmett-Teller method and the adsorption-desorption isotherm is shown in Appendix A, Figure A.3. The surface area results show that BiOCl has a surface area of 2.53 m^2/g.

DRS was used to measure reflectance spectra of the powdered semiconductor photocatalysts (Appendix A, Figure A.4) to determine their absorption band edge and optical band gap using the Kubelka-Munk method. The absorption band edge can be observed as the linear portion of the spectrum where absorption begins. A line of best fit was determined for this region with the x-intercept of the best fit line used to calculate the energy of the material's band gap. The band gap for BiOCl was determined to be 3.28 eV. These values are in good agreement with optical band gaps of these materials previously determined [27]. The absorption spectrum for BiOCl indicates that ultraviolet light will be necessary for electronic excitation and activation. Furthermore, the spectra indicate that the 254-nm light source chosen for photocatalyst evaluation will activate BiOCl.

3.3.2   Dark Adsorption of IBP to BiOCl

In previous work with BiOBr and BiOCl microspheres [39,40], surface adsorption, not photocatalytic oxidation, was found to be the most significant IBP (1) removal process. To determine if surface adsorption was a significant loss mechanism when IBP (1) was exposed to the BiOCl nanosheets used in this study, dark adsorption trials were conducted to test for IBP (1) removal in the absence of light. After 30-min of stirring under dark conditions with 0.25-g/L catalyst loading, we observed that less than 6% of IBP (1) was removed by BiOCl (Figure 3.1). These measurements provide evidence to support the conclusion that adsorption does not play a significant role in IBP (1) removal for the BiOCl nanosheets under the conditions used in this study. This finding differs significantly from that reported for IBP loss to BiOCl microspheres by Li et al. [40]. The difference may result from the lower surface area of our nanosheets (2.53 m^2/g) compared with the microspheres (16.31 m^2/g); furthermore, the different morphologies

(nanosheets vs microspheres) may also play a role. Cumulatively, the nanosheets may present fewer sites for IBP loss by surface adsorption.
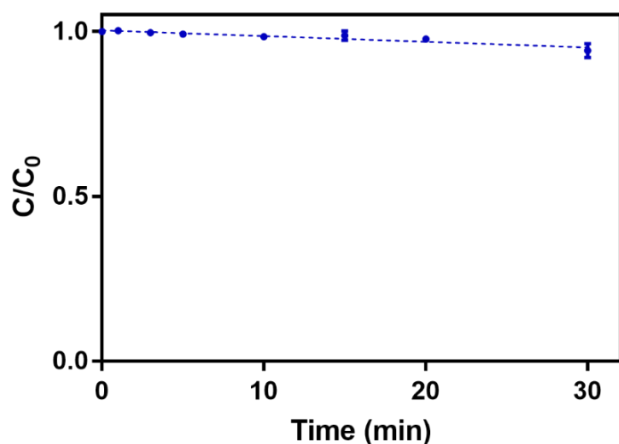
Figure 3.1. IBP adsorption of BiOCl under dark conditions, as monitored by UV-Vis spectroscopy

3.3.3 IBPE and IBAP are the Primary IBP Photocatalytic Degradation Products for BiOCl

To provide the most comprehensive analysis of IBP and its photodegradation products, IBP (**1**) was subjected to photocatalytic degradation for 120-min and sample aliquots were analyzed by HPLC-DAD. Signals were monitored at 210-, 254-, and 310-nm (Figure 3.2 and Appendix A, Figures A.5-A.7). The chromatograms generated using 210-nm were most useful for monitoring both the degradation of IBP (**1**) and formation of primary degradation products **2** and **3** (Figure 3.2A-D); chromatograms monitored at 254- and 310-nm were useful for monitoring formation of secondary degradation products **4-14** (Figure 3.2E-L).

Using analytical standards, we established that 1-(4-isobutylphenyl)ethanol (IBPE; **2;** eluting at 18.0-min) and 4-isobutylacetophenone (IBAP; **3**; eluting at 21.9-min) are the primary photocatalytic degradation products for IBP (**1;** eluting at 19.3-min) (see Figure 3.2). Early work [19] identified IBPE (**2**) and IBAP (**3**) as products from the photolytic degradation of IBP (**1**) in methanol, and these products have been identified in other photolytic and photocatalytic degradation studies [19,22]. A proposed mechanism for the formation of these two products is shown in Figure 3.3, where deprotonated IBP (**1**) is oxidized by either direct excitation with light (photolytic mechanism) or by interaction with a hole (h$^+$) created by photoexcitation of BiOCl. Subsequent loss of CO_2 generates a benzyl radical, which is converted to IBPE (**2**) and IBAP (**3**) via reactions with water and oxygen. This mechanism aligns with the proposed initiating step in the photocatalytic degradation of perfluorooctanoic acid with BiOCl nanosheets [38].
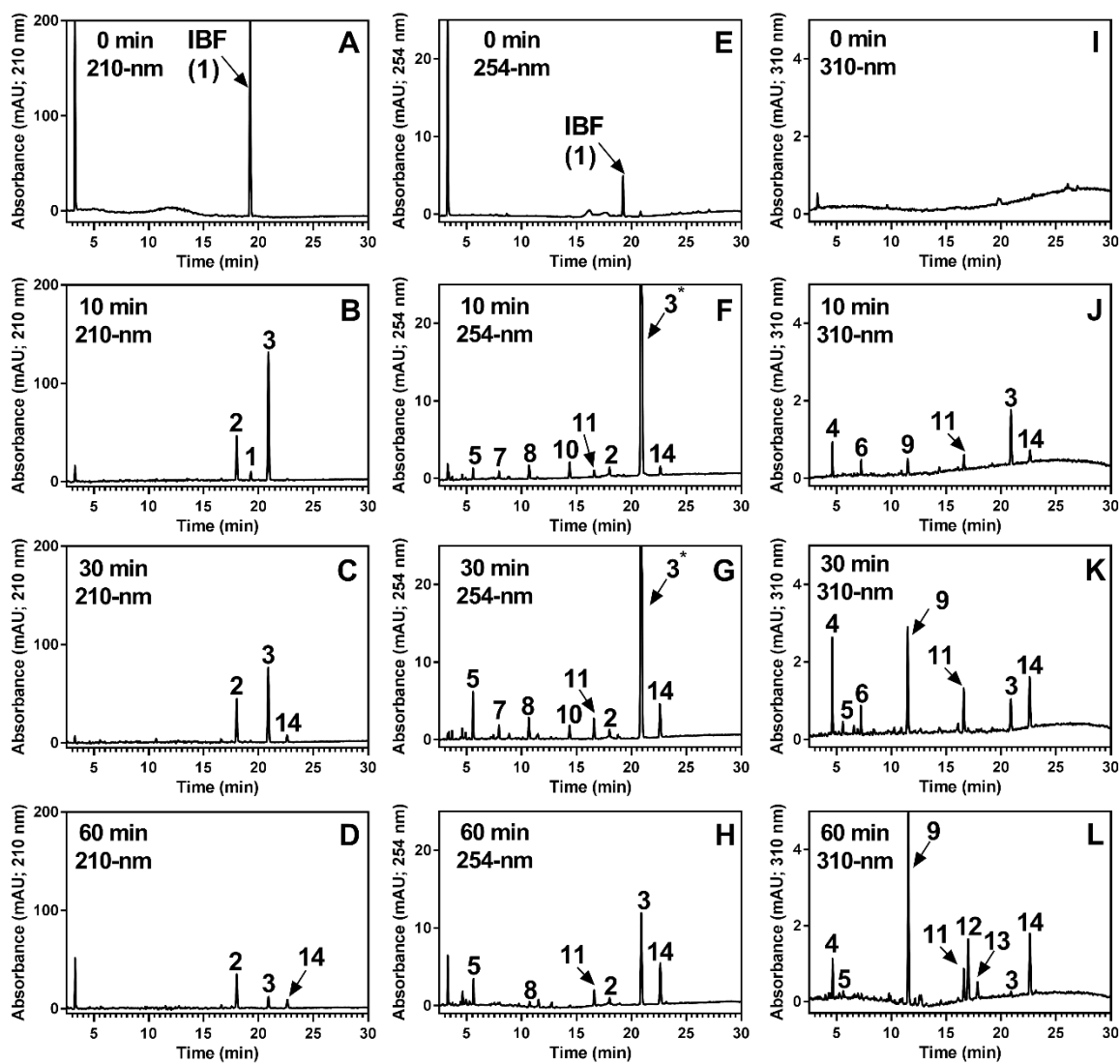
Figure 3.2. HPLC-DAD chromatograms for ibuprofen (1) photocatalytically degraded with BiOCl

for 0-, 10-, 30-, and 60-min. (A)-(D) absorbance (mAU) detected at 210-nm, (E)-(H) absorbance

(mAU) detected at 254-nm; (I)-(L) absorbance (mAU) detected at 310-nm. Compounds are

identified in Table 2; peaks with an asterisk are off scale.
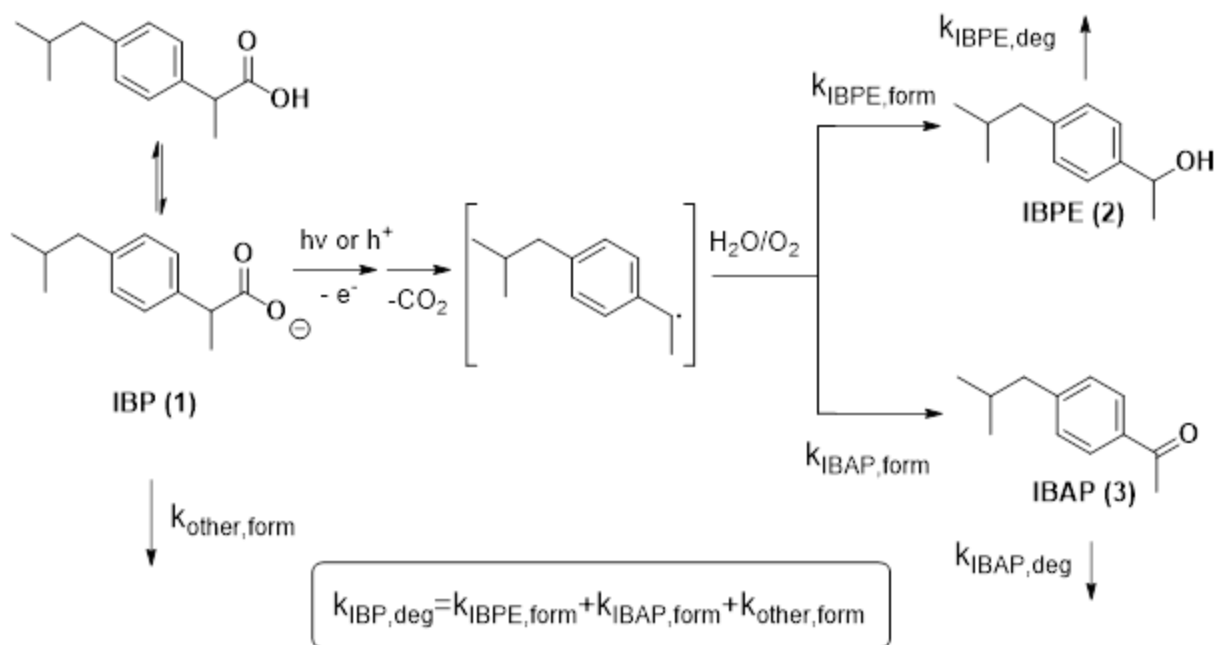
Figure 3.3. Production of IBAP (3) and IBPE (2) from the photodegradation of IBP (1)

Kinetic analysis of this data (Figure 3.4A) shows that IBP (**1**) decays quickly and is no longer observed after 15-min, while IBPE (**2**) and IBAP (**3**), once formed, are degraded more slowly, with IBPE (**2**) still present after 120-min of photocatalytic degradation. In an attempt to assess our kinetic data to determine if formation of IBPE (**2**) and IBAP (**3**) are the principle degradation pathways for IBP (**1**), we analyzed the data by applying a kinetic model where we assumed pseudo-first order kinetics for IBP (**1**) photodegradation (equation 1), and where the rate constant for degradation, $k_{IBP,deg}$, is assumed to be equal to the sum of the rate constants for formation of IBPE (**2**) ($k_{IBPE,form}$), IBAP (**3**) ($k_{IBAP,form}$), and other products ($k_{other,form}$), as described in equation 2.

$$(1) \quad [IBP] = [IBP]_0 e^{-k_{IBP,deg}t}$$

$$(2) \quad k_{IBP,deg} = k_{IBPE,form} + k_{IBAP,form} + k_{other,form}$$

We modeled the formation of IBPE (**2**) and IBAP (**3**) using the rate equation for a consecutive, pseudo-first order reaction. For IBPE (**2**), we used equations 3 and 4, where we assumed that $[IBP]_{0,IBPE}$ represented the fraction of $[IBP]_0$ that was converted to IBPE (**2**), $k_{IBPE,form}$ was the rate constant for formation of IBPE (**2**), and $k_{IBPE,deg}$ was the rate constant for IBPE degradation.

$$(3) \quad [IBP]_{IBPE} = [IBP]_{0,IBPE}\left(e^{-k_{IBPE,form}}\right)$$

$$(4) \quad [IBPE] = \frac{k_{IBPE,form}[IBP]_{0,IBPE}}{k_{IBPE,deg}-k_{IBPE,form}}\left(e^{-k_{IBPE,form}t}-e^{-k_{IBPE,deg}t}\right)$$

For IBAP (**3**), we used equations 5 and 6, where we assumed that $[IBP]_{0,IBAP}$ represented the fraction of $[IBP]_0$ that was converted to IBAP (**3**), $k_{IBAP,form}$ was the rate constant for formation of IBAP (**2**), and $k_{IBAP,deg}$ was the rate constant for IBAP degradation.

$$(5) \quad [IBP]_{IBAP} = [IBP]_{0,IBAP}\left(e^{-k_{IBAP,form}}\right)$$

$$(6) \quad [IBAP] = \frac{k_{IBAP,form}[IBP]_{0,IBAP}}{k_{IBAP,deg}-k_{IBAP,form}}\left(e^{-k_{IBAP,form}t}-e^{-k_{IBAP,deg}t}\right)$$

With this treatment, we assumed that the initial concentration of IBP is accounted for by the sum of $[IBP]_{0,IBPE}$ and $[IBP]_{0,IBPE}$ (calculated by the model) and $[IBP]_{0,other\ products}$, as summarized in equation 7.

$$(7) \quad [IBP]_0 = [IBP]_{0,IBPE} + [IBP]_{0,IBAP} + [IBP]_{0,other\ products}$$
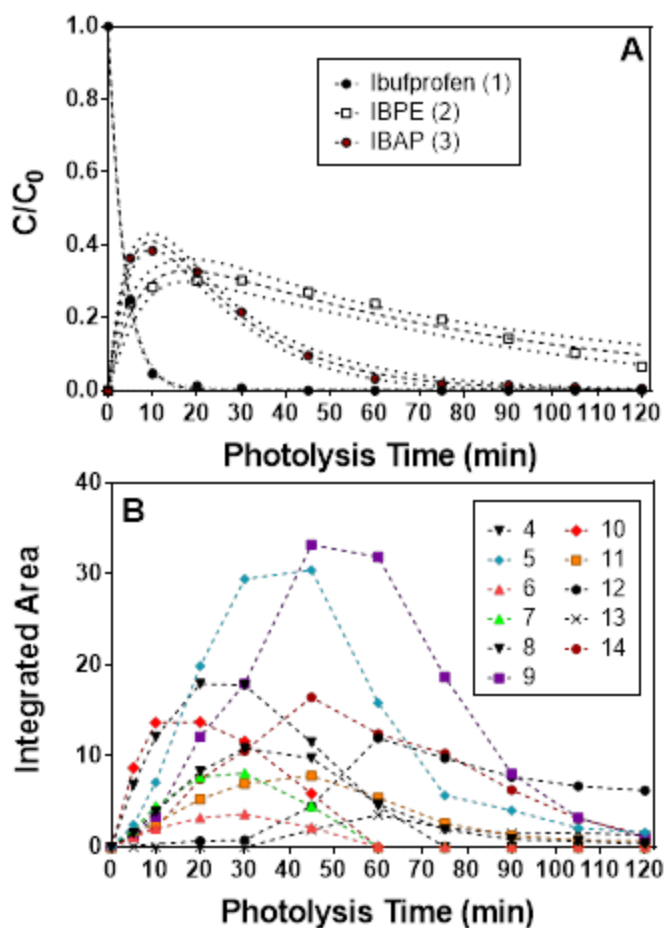
Figure 3.4. Plots of signal intensities as a function of reaction time for samples from the photocatalytic degradation of IBP (1) with BiOCl. (A) C/C_0 for IBP (1), IBPE (2), and IBAP (3) as quantified by HPLC-DAD at 210-nm, with C_0 equal to the initial concentration of IBP (1); curve fits with 95% confidence intervals using equation 1 for IBP (1), equation 4 for IBPE (2), and equation 6 for IBAP (3); (B) Integrated areas for peaks detected at either 254- or 310-nm. Compounds are identified in Table 3.2.

This approach was used to successfully model the experimental data, as shown by the 95% confidence intervals displayed in Figure 3.4A. The kinetic parameters extracted from the data (Table 3.1) showed a pseudo-first order rate constant for IBP (**1**) degradation equal to 0.28 ± 0.01 min^{-1} ($t_{1./2} = 2.4$ min). The rate constants for formation of IBPE (**2**) and IBAP (**3**) were of similar magnitudes ($k_{IBPE,form} = 0.15\pm0.03$ min^{-1}; $k_{IBAP,form} = 0.18\pm0.03$ min^{-1}) and IBAP (**3**) was found to have a degradation rate that is approximately four times faster than IBPE (**2**) ($k_{IBPE,deg} = 0.049\pm0.005$ min^{-1}; $k_{IBAP,form} = 0.013\pm0.002$ min^{-1}). The modeling results provide additional support for the conclusion that other pathways for IBP (**1**) degradation or loss, such as adsorption to the catalyst or additions of hydroxyl radicals, are not playing a significant role in IBP photodegradation with BiOCl. This is based on the fact that the IBP degradation rate constant of (0.28 ± 0.01 min^{-1}) is slightly lower, but not significantly different than, the sum of the rate constants for IBPE (**2**) and IBAP (**3**) formation ($k_{IBPE,form} + k_{IBAP,form} = 0.34\pm0.04$ min^{-1}) and that the initial concentration of IBP (**1**), which was normalized to 1, showed good agreement between the value predicted from the modelling ($[IBP]_0 = 1.00\pm0.01$) and the values accounted for by $[IBP]_{0,IBPE} + [IBP]_{0,IBAP} = 1.07\pm0.06$. In summary, our data supports the formation of two primary products, IBPE (**2**) and IBAP (**3**), from the BiOCl photocatalytic decomposition of IBP (**1**).

Table 3.1. Kinetic parameters[a] for the photocatalytic degradation of IBP and the formation and degradation of IBPE and IBAP.

	Degradation of IBP (1)	Formation and Degradation of IBPE (2)		Formation and Degradation of IBAP (3)	
Rate constant (min^{-1})	$k_{IBP, deg} =$ 0.28 ($\pm$0.01)	$k_{IBPE, form} =$ 0.15 ($\pm$0.03)	$k_{IBPE, deg} =$ 0.013 ($\pm$0.002)	$k_{IBAP, form} =$ 0.18 ($\pm$0.03)	$k_{IBAP, deg} =$ 0.049 ($\pm$0.005)
t$_{1/2}$ (min)	2.4				
R^2	0.9996	0.9594		0.9940	
Initial Concentration[b]	[IBP]$_0$= 1.00 ($\pm$0.01)	[IBP]$_{0,IBPE} =$ 0.41 ($\pm$0.03)		[IBP]$_{0,IBAP} =$ 0.66 ($\pm$0.05)	

[a]Values obtained from fitting data to equations (1), (4), and (6); [b]Concentrations (μM) were normalized to the initial concentration of IBP (**1**).

3.3.4 Photocatalytic Degradation of IBAP is an Important Pathway for the Formation of Secondary Products for BiOCl

Photocatalytic degradation of IBP (1) also yielded a large number of less abundant secondary degradation products. These products were best detected by HPLC-DAD when monitoring at 254- and 310-nm (Figure 3.2 and Appendix A, Figures A.6 and A.7). This collection of photoproducts was also detected when IBAP (3) was subjected to photocatalytic degradation with BiOCl (see Figure 3.5A-C). Notably, the chromatograms at 254- and 310-nm following 30-min of photocatalysis (Figures 3.5B and C) show peaks for all 11 secondary photocatalytic degradation products observed for the photocatalyzed degradation of IBP (1). These results also demonstrate that IBPE (2) is not produced from IBAP (3) via photocatalysis and provides support for the initial production and subsequent photocatalytic degradation of IBAP (3) as the primary source of photocatalytic products from IBP (1).
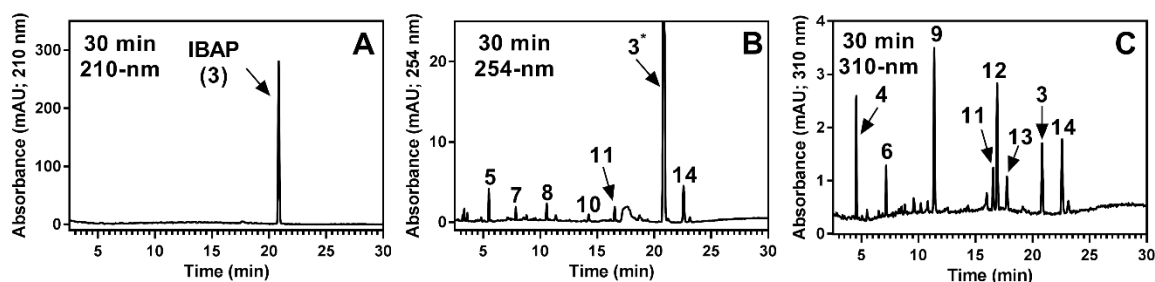
Figure 3.5. HPLC-DAD chromatograms for IBAP (3) photocatalytically degraded with BiOCl for 30-min. (A) absorbance (mAU) detected at 210-nm, (B) absorbance (mAU) detected at 254-nm; (C) absorbance (mAU) detected at 310-nm. Compounds are identified in Table 3.2; peaks with an asterisk are off scale.

We focused on 11 secondary photoproducts, 4-14 (Table 3.2) that were detected in the chromatograms. UV-Vis spectra were obtained for each photoproduct (Appendix A, Figure A.8). Kinetic analysis of this data showed the rapid formation and degradation of photoproducts 6-8 and 10; with slower formation of photoproducts 4, 5, 9, 11, and 14, and delayed production and degradation of 12 and 13 (see Figure 3.4B).

Table 3.2. Summary of compounds detected by HPLC-DAD and LC-MS/MS with retention times, molecular formulas, and characteristic ions detected by (+)nanoESI-MS and MS/MS

Compound Number[a]	Retention Time (HPLC; min)	Retention Time (LCMS; min)	Wavelength Max (nm)[c]	Molecular Formula	Exact Mass (Predicted)[d]	Ions Detected, MS	Product Ions Detected, MS/MS[i]
1 (IBP)	19.29	25.87	220, 264	$C_{13}H_{18}O_2$	206.131	224.165[f]; 207.138[e]	<u>224.16</u>; **161.13** (-CO_2H); 119.08 (-C_3H_6); 105.07 ($C_8H_9^+$); 91.05 ($C_7H_7^+$); 57.07 ($C_4H_9^+$); 43.06 ($C_3H_7^+$); 41.04 ($C_3H_5^+$)
2 (IBPE)	18.01	24.43	220, 264	$C_{12}H_{18}O$	178.136	161.132[g]	<u>161.13</u>; **119.08** (-C_3H_6); 117.07 (-C_3H_8); 105.07 ($C_8H_9^+$); 91.05 ($C_7H_7^+$); 57.07 ($C_4H_9^+$); 43.06 ($C_3H_7^+$); 41.04 ($C_3H_5^+$)
3 (IBAP)	20.93	26.97	255	$C_{12}H_{16}O$	176.120	177.127[e]	<u>177.12</u>; 121.06 (-C_4H_8); 57.07 ($C_4H_9^+$); **43.02 (CH_3CO^+)**
4	4.64	11.06	310	$C_{12}H_{18}O_3$	210.126	193.123[g], 233.116[h]	---[j]
5	5.58	---[b]	254, 300 (w)	---[b]	---[b]	---[b]	---[b]
6	7.25	---[b]	320	---[b]	---[b]	---[b]	---[b]
7	7.97	14.40	258	$C_{12}H_{18}O_3$	210.126	193.123[g], 233.116[h]	<u>193.123</u>; 175.10 (-H_2O); 137.06 (-C_4H_8); 57.07 ($C_4H_9^+$); **43.02 (CH_3CO^+)**
8	10.68	17.31	254	$C_{12}H_{16}O_2$	192.115	193.119[e]	
9	11.54	17.83	296	$C_{12}H_{16}O_3$	208.1099	209.117[c]	<u>209.12</u>; 191.09 (-H_2O); **125.06 (-C_6H_8O)**; 85.07 ($C_5H_9O^+$); 57.07 ($C_4H_9^+$); 43.02 (CH_3CO^+)
10	14.37	---[b]	260, 300 (w)	---[b]	---[b]	---[b]	---[b]
11	16.61	23.22	220, 264, 315	$C_{12}H_{16}O_2$	192.115	193.119[e]	<u>193.12</u>; 57.07 ($C_4H_9^+$); **43.02 (CH_3CO^+)**
12	17.00	23.42	312	$C_{11}H_{16}O$	164.120	165.127[e]	<u>165.13</u>; 147.12 (-H_2O); **43.02 (CH_3CO^+)**
13	17.85	24.18	305	$C_{11}H_{16}O$	164.120	165.127[e]	---[j]
14	22.63	28.49	215, 263, 327	$C_{12}H_{16}O_2$	192.115	193.122[e]	<u>193.12</u>; 175.11 (-H_2O); 137.07 (-C_4H_8); 57.07 ($C_4H_9^+$); **43.02 (CH_3CO^+)**

[a]IBP=ibuprofen; IBPE=1-(4-isobutylphenyl)ethanol; IBAP=4-Isopropylacetophenone (IBAP); [b]No peak detected by (+)nanoESI-LCMS to correlate with HPLC data; [c]Full UV/Vis DAD spectra in Figure S7, Supplemental Materials; solvent varied based upon gradient composition for peak elution; (w) signifies a weak absorption band; [d]monoisotopic mass; [e][M+H]$^+$; [f][M+NH$_4$]$^+$; [g][MH-H$_2$O]$^+$; [h][M+Na]$^+$; [i]precursor ion is underlined; base peak in spectrum appears in bold; collision energy = 15 eV; [j]no MS/MS data collected.

Aliquots from the photocatalytic degradation of IBP (1) with BiOCl were subjected to high resolution LC-MS/MS analysis using a chip-based reversed-phase chromatographic separation [42] and positive-ion nanoelectrospray ionization ((+)nanoESI). Most previous work has used (-)ESI, which is useful for the detection of deprotonated analytes. Both positive and negative forms of ESI will discriminate against the detection of analytes that are not easily ionized by ESI; however, we were able to obtain easily-detected signals for IBP (1), IBPE (2), and IBAP (3) without subjecting the samples to preconcentration. We do not expect to detect non-oxygenated degradation products and were unable to correlate all HPLC-DAD signals with data generated by LC-MS.

The results of our analysis, summarized in Table 3.2, provided molecular formulas for the more abundant degradation products detected by HPLC. For some degradation products, including IBPE (2), 4, and 7, the base peak in the (+)-nanoESI mass spectrum was the $[MH-H_2O]^+$ ion, resulting from facile water loss upon ionization. IBP (1) yielded an abundant $[M+NH4]^+$ signal that was most prominent for compounds containing carboxylic acid groups. Other ions, including $[M+Na]^+$, provided evidence to support the assigned molecular mass and formula. For more abundant degradation products, where signal intensities permitted, collision-induced dissociation (CID) experiments were conducted to generate MS/MS spectra, providing additional insights regarding molecular structures. Product ions detected in those experiments are summarized in Table 3.2. The mass spectral data was correlated with results from HPLC using comparisons of retention times and the kinetic profiles for products detected by both techniques (see Appendix A, Figure A.9 for LC-MS data). MS and MS/MS spectra appear in Appendix A, Figures A.10-A.15.

3.3.5 Summary of Products and Mechanistic Insights for the Photodegradation of IBP and IBAP with BiOCl

The following mechanism and inventory of products (Figure 3.6) is proposed for IBP (1) photodegradation by BiOCl based on the observed kinetic profiles for photodegradation products generated from both IBP (1) and IBAP (3), as well as the molecular formulas and MS/MS spectra from (+)-nanoESI LC-MS/MS analysis (Table 3.2), and the absorption spectra of the detected products (Table 3.2 and Appendix A, Figure A.8).

Previous studies have reported the formation of isomeric hydroxylated IBPs (pathway a, Figure 3.6) when IBP was subjected to direct photolysis [22], pulse radiolysis [43], (sono)photocatalysis [44], and TiO2 photocatalysis [5,20]. In our work with the photodegradation of IBP (1) with BiOCl, only very low intensity signals for isomeric forms of hydroxylated IBPs (pathway a, Figure 3.6) were detected at early points in the BiOCl photodegradation process, although we found strong evidence to support the production of these compounds when TiO_2 or direct photolysis was employed for photodegradation (data not shown) and are confident in our ability to detect these photoproducts. Thus, pathway a (Figure 3.6) is not an important mechanism for the photocatalytic degradation of IBP (1) with BiOCl, which may be a consequence of the rapid decarboxylation reaction for IBP (1), coupled with the lower hydroxyl radical production rates that have been observed for BiOCl [38,45].

The predominant pathway for photodegradation of IBP (1) with BiOCl is most consistent with decarboxylation initiated by h^+ oxidation to form a benzyl radical (pathway b, Figure 3.6), which is converted to IBPE (2) (pathway c, Figure 3.6) and IBAP (3) (pathway d, Figure 3.6). Only IBAP (3) is subject to significant subsequent photodegradation, yielding at least 11 photodegradation products. Most products detected by HPLC yielded absorption spectra showing

shifts to longer wavelengths, which would be most consistent with hydroxyl additions to the aromatic ring or ring-opening oxidation processes that increase conjugation. Many products detected by mass spectrometry yielded MS/MS product ions, including m/z 43.02 (CH_3CO^+) and m/z 57.07 ($C_4H_9^+$), that provided evidence that IBAP's acetyl and isobutyl groups have not been structurally altered by photocatalytic degradation. We propose photodegradation of IBAP (3) initiated by hydroxyl radical attack on the aromatic ring of IBAP (3) via pathways d-f (Figure 3.6), resulting in formation of hydroxyl-substituted forms of IBAP (3). We hypothesize that photodegradation products 11 and 14, with molecular masses consistent with the net addition of one oxygen atom to IBAP (3), absorption spectra consistent with that of a substituted acetophenone, and MS/MS spectra consistent with water loss from an aromatic ring with and support for acetyl and isobutyl substituents, are most consistent with isomeric forms of ring-hydroxylated IBAP (3) depicted in Figure 3.6. Mass spectral data for photodegradation product 9 has a molecular formula indicating the net addition of two oxygen atoms to IBAP (3). While this product could correspond to a dihydroxy-substituted IBAP (see pathway 3, Figure 3.6), this structure is not supported by the MS/MS spectrum, which shows abundant and complementary fragments at m/z 125.06 and m/z 85.06 (see Appendix A, Figure A.14). The MS/MS data and the measured absorption spectrum suggest that the aromatic ring has been opened by oxidation. A possible structure can be found in Figure A.14. Other products for which mass spectral data was obtained included two additional hydroxylated products, which also may have ring-opened structures (pathway f, Figure 3.6). At a later time point, we observed products 12 and 13, which may result from decarboxylation of product 9. Overall, our results support the initial formation and subsequent degradation of IBAP (3), with the formation of products characterized by oxidation directed at the aromatic ring of IBAP (3).
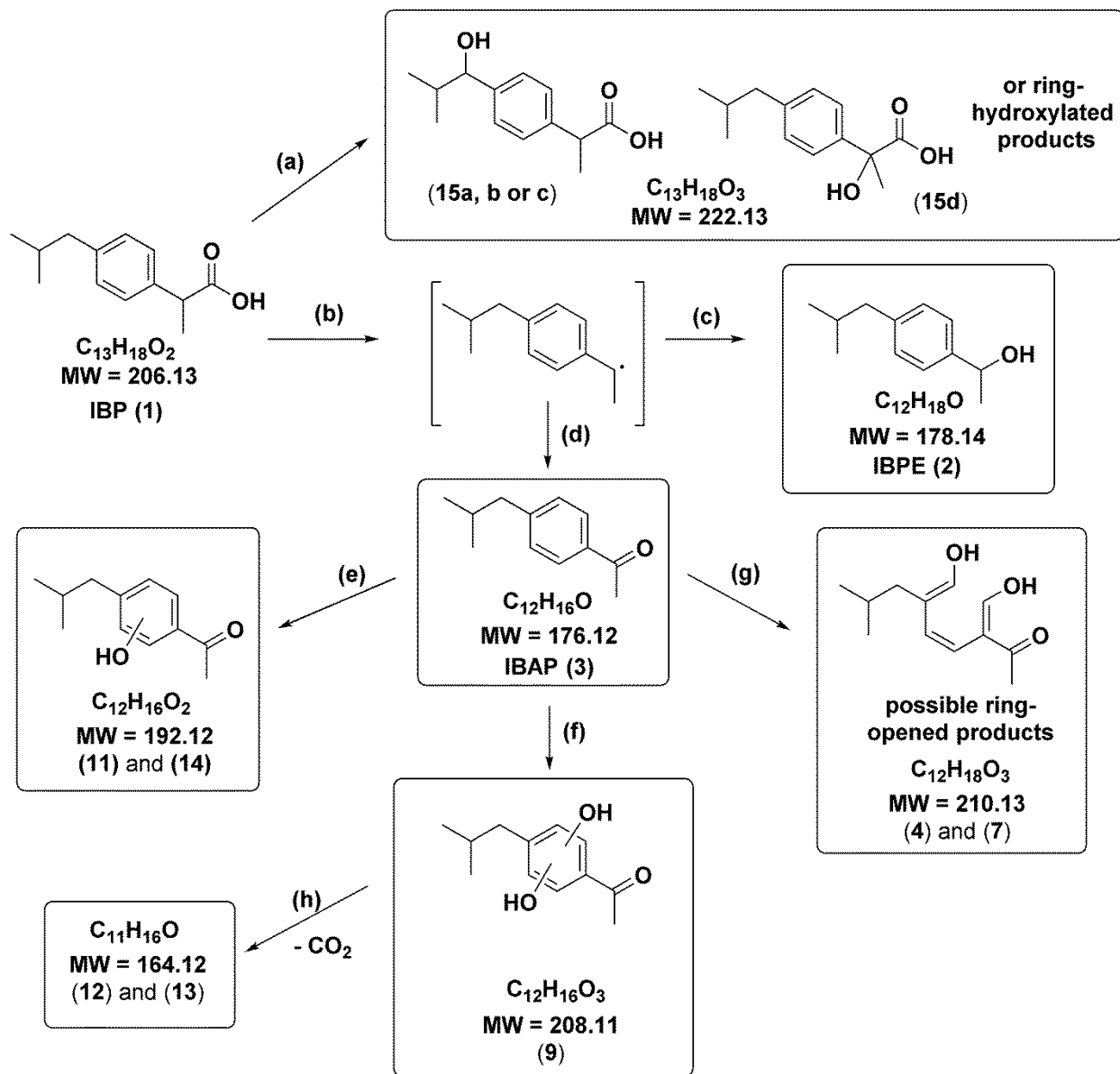
Figure 3.6. Proposed secondary products from the photolysis of IBP (**1**) and IBAP (**3**)

3.4 Conclusion

We have shown for the first time the high photocatalytic activity for BiOCl photocatalysis for the removal of IBP (1) from water, and provide evidence to show that photocatalytic degradation, not adsorption, is the primary removal mechanism for the BiOCl nanosheets used in this study. The high photocatalytic activity is best explained by h^+ oxidation and decarboxylation of the carboxylate group, and suggests that BiOCl may play a role is the activation of other structurally similar pharmaceuticals, such as ketoprofen, naproxen, and benoxaprofen. This work highlights how structural alterations to contaminants that occur upon photocatalytic degradation can impact the rates associated with subsequent photodegradation processes. While BiOCl exhibits rapid conversion of IBP (1) to IBPE (2) and IBAP (3), these secondary products, which have demonstrated toxicities, showed greater recalcitrance toward photodegradation. This may be a consequence of the lower hydroxyl radical production rate or a reduced ability to react with IBPE (2) or IBAP (3) by h^+ oxidation for BiOCl. Clearly, characterizing photodegradation products and their degradation rates can provide important insights into photocatalytic degradation mechanisms, which can then inform catalyst development. This work suggests the need to develop catalysts that have parallel pathways of reactivity towards substrates with different chemical properties.

3.5 References

1.   Huang, R.; Southall, N.; Wang, Y.; Yasgar, A.; Shinn, P.; Jadhav, A.; Nguyen, D. T.; Austin, C. P. The NCGC pharmaceutical collection: A comprehensive resource of clinically approved drugs enabling repurposing and chemical genomics. Sci. Transl. Med. 2011, 3.

2.   Ternes, T. A. Analytical methods for the determination of pharmaceuticals in aqueous environmental samples. TrAC - Trends Anal. Chem. 2001, 20, 419–434, doi:10.1016/S0165-9936(01)00078-4.

3.   Kolpin, D. W.; Furlong, E. T.; Meyer, M. T.; Thurman, E. M.; Zaugg, S. D.; Barber, L. B.; Buxton, H. T. Pharmaceuticals, Hormones, and Other Organic Wastewater Contaminants in U.S. Streams, 1999−2000: A National Reconnaissance. Environ. Sci. Technol. 2002, 36, 1202–1211, doi:10.1021/es011055j.

4.   Jones, O. A.; Lester, J. N.; Voulvoulis, N. Pharmaceuticals: a threat to drinking water? Trends Biotechnol. 2005, 23, 163–167, doi:10.1016/j.tibtech.2005.02.001.

5.   Mendez-Arriaga, F.; Torres-Palma, R. A.; Petrier, C.; Esplugas, S.; Gimenez, J.; Pulgarin, C. Ultrasonic treatment of water contaminated with ibuprofen. Water Res. 2008, 42, 4243–4248, doi:10.1016/j.watres.2008.05.033.

6.   Jux, U.; Baginski, R. M.; Arnold, H.-G.; Krönke, M.; Seng, P. N. Detection of pharmaceutical contaminations of river, pond, and tap water from Cologne (Germany) and surroundings. Int. J. Hyg. Environ. Health 2002, 205, 393–398, doi:10.1078/1438-4639-00166.

7.   Lindholm-Lehto, P. C.; Ahkola, H. S. J.; Knuutinen, J. S.; Herve, S. H. Widespread occurrence and seasonal variation of pharmaceuticals in surface waters and municipal wastewater treatment plants in central Finland. Environ. Sci. Pollut. Res. 2016, 23, 7985–7997, doi:10.1007/s11356-015-5997-y.

8.   Heberer, T. Occurrence, fate, and removal of pharmaceutical residues in the aquatic environment: a review of recent research data. Toxicol. Lett. 2002, 131, 5–17, doi:10.1016/S0378-4274(02)00041-3.

9.   Bhatkhande, D. S.; Pangarkar, V. G.; Beenackers, A. A. Photocatalytic degradation for environmental applications - a review. J. Chem. Technol. Biotechnol. 2002, 77, 102–116, doi:10.1002/jctb.532.

10.   Ameta, R.; Benjamin, S.; Ameta, A.; Ameta, S. C. Photocatalytic Degradation of Organic Pollutants: A Review. Mater. Sci. Forum 2012, 734, 247–272, doi:10.4028/www.scientific.net/MSF.734.247.

11.   Chen, F.; Yang, Q.; Yao, F.; Wang, S.; Sun, J.; An, H.; Yi, K.; Wang, Y.; Zhou, Y.; Wang, L.; Li, X.; Wang, D.; Zeng, G. Visible-light photocatalytic degradation of multiple antibiotics by AgI nanoparticle-sensitized Bi_5O_7I microspheres: Enhanced interfacial charge transfer based on Z-scheme heterojunctions. J. Catal. 2017, 352, 160–170, doi:10.1016/j.jcat.2017.04.032.

12.   Wang, D.; Jia, F.; Wang, H.; Chen, F.; Fang, Y.; Dong, W.; Zeng, G.; Li, X.; Yang, Q.; Yuan, X. Simultaneously efficient adsorption and photocatalytic degradation of tetracycline by Fe-based MOFs. J. Colloid Interface Sci. 2018, 519, 273–284, doi:10.1016/j.jcis.2018.02.067.

13.   Offermanns, S.; Rosenthal, W. . Encyclopedic Reference of Molecular Pharmacology; 1st ed.; Springer Verlag: Berlin, 2004;

14.   Jones, J. G. Pollution from Fish Farms. Water Environ. J. 1990, 4, 14–18, doi:10.1111/j.1747-6593.1990.tb01552.x.

15.   Rigos, G.; Nengas, I.; Alexis, M.; Troisi, G. M. Potential drug (oxytetracycline and oxolinic acid) pollution from Mediterranean sparid fish farms. Aquat. Toxicol. 2004, 69, 281–288, doi:10.1016/j.aquatox.2004.05.009.

16.   Gamarra, J. S.; Godoi, A. F. L.; de Vasconcelos, E. C.; de Souza, K. M. T.; Ribas de Oliveira, C. M. Environmental Risk Assessment (ERA) of diclofenac and ibuprofen: A public health perspective. Chemosphere 2015, 120, 462–469, doi:10.1016/j.chemosphere.2014.08.020.

17.   Murdoch, R. W.; Hay, A. G. Genetic and chemical characterization of ibuprofen degradation by Sphingomonas Ibu-2. Microbiology 2013, 159, 621–632, doi:10.1099/mic.0.062273-0.

18.   Pomati, F.; Netting, A. G.; Calamari, D.; Neilan, B. A. Effects of erythromycin, tetracycline and ibuprofen on the growth of Synechocystis sp. and Lemna minor. Aquat. Toxicol. 2004, 67, 387–396, doi:10.1016/j.aquatox.2004.02.001.

19.   Castell, J. V.; Gomez-L., M. J.; Miranda, M. A.; Morera, I. M. Photolytic Degradation of Ibuprofen. Toxicity of the Isolated Photoproducts on Fibroblasts and Erythrocytes. Photochem. Photobiol. 1987, 46, 991–996, doi:10.1111/j.1751-1097.1987.tb04882.x.

20.   da Silva, J. C. C.; Teodoro, J. A. R.; Afonso, R. J. D. C. F.; Aquino, S. F.; Augusti, R. Photolysis and photocatalysis of ibuprofen in aqueous medium: characterization of by-products via liquid chromatography coupled to high-resolution mass spectrometry and assessment of their toxicities against Artemia Salina. J. Mass Spectrom. 2014, 49, 145–153, doi:10.1002/jms.3320.

21.   Jacobs, L. E.; Fimmen, R. L.; Chin, Y.-P.; Mash, H. E.; Weavers, L. K. Fulvic acid mediated photolysis of ibuprofen in water. Water Res. 2011, 45, 4449–4458, doi:10.1016/j.watres.2011.05.041.

22.   Jakimska, A.; Śliwka-Kaszyńska, M.; Reszczyńska, J.; Namieśnik, J.; Kot-Wasik, A. Elucidation of transformation pathway of ketoprofen, ibuprofen, and furosemide in surface water and their occurrence in the aqueous environment using UHPLC-QTOF-MS. Anal. Bioanal. Chem. 2014, 406, 3667–3680, doi:10.1007/s00216-014-7614-1.

23.   Li, F. H.; Yao, K.; Lv, W. Y.; Liu, G. G.; Chen, P.; Huang, H. P.; Kang, Y. P. Photodegradation of Ibuprofen Under UV–Vis Irradiation: Mechanism and Toxicity of Photolysis Products. Bull. Environ. Contam. Toxicol. 2015, 94, 479–483, doi:10.1007/s00128-015-1494-8.

24.   Ruggeri, G.; Ghigo, G.; Maurino, V.; Minero, C.; Vione, D. Photochemical transformation of ibuprofen into harmful 4-isobutylacetophenone: Pathways, kinetics, and significance for surface waters. Water Res. 2013, 47, 6109–6121, doi:10.1016/j.watres.2013.07.031.

25.   Szabó, R. K.; Megyeri, C.; Illés, E.; Gajda-Schrantz, K.; Mazellier, P.; Dombi, A. Phototransformation of ibuprofen and ketoprofen in aqueous solutions. Chemosphere 2011, 84, 1658–1663, doi:10.1016/j.chemosphere.2011.05.012.

26.   Vione, D.; Maddigapu, P. R.; De Laurentiis, E.; Minella, M.; Pazzi, M.; Maurino, V.; Minero, C.; Kouras, S.; Richard, C. Modelling the photochemical fate of ibuprofen in surface waters. Water Res. 2011, 45, 6725–6736, doi:10.1016/j.watres.2011.10.014.

27.   Achilleos, a.; Hapeshi, E.; Xekoukoulotakis, N. P.; Mantzavinos, D.; Fatta-Kassinos, D. UV-A and Solar Photodegradation of Ibuprofen and Carbamazepine Catalyzed by TiO_2. Sep. Sci. Technol. 2010, 45, 1564–1570, doi:10.1080/01496395.2010.487463.

28.   Braz, F. S.; Silva, M. R. A.; Silva, F. S.; Andrade, S. J.; Fonseca, A. L.; Kondo, M. M. Photocatalytic Degradation of Ibuprofen Using TiO_2 and Ecotoxicological Assessment of Degradation Intermediates against Daphnia similis. J. Environ. Prot. (Irvine,. Calif). 2014, 5, 620–626, doi:10.4236/jep.2014.57063.

29.   Choina, J.; Kosslick, H.; Fischer, C.; Flechsig, G.-U.; Frunza, L.; Schulz, A. Photocatalytic decomposition of pharmaceutical ibuprofen pollutions in water over titania catalyst. Appl. Catal. B Environ. 2013, 129, 589–598, doi:10.1016/j.apcatb.2012.09.053.

30.   Zhang, K.; Liu, C.; Huang, F.; Zheng, C.; Wang, W. Study of the electronic structure and photocatalytic activity of the BiOCl photocatalyst. Appl. Catal. B Environ. 2006, 68, 125–129, doi:10.1016/j.apcatb.2006.08.002.

31.   Lin, X.; Huang, T.; Huang, F.; Wang, W.; Shi, J. Photocatalytic Activity of a Bi-Based Oxychloride Bi_3O_4Cl. J. Phys. Chem. B 2006, 110, 24629–24634, doi:10.1021/jp065373m.

32.   Mao, X.; Li, X.; Wang, Y.; Fan, C.; Zhang, H. KI/H_2O_2 assisted synthesis and the changed properties of BiOCl photocatalysts. Chem. Eng. J. 2014, 247, 241–249, doi:10.1016/j.cej.2014.02.020.

33.   Sarwan, B.; Pare, B.; Acharya, A. D.; Jonnalagadda, S. B. Mineralization and toxicity reduction of textile dye neutral red in aqueous phase using BiOCl photocatalysis. J. Photochem. Photobiol. B Biol. 2012, 116, 48–55, doi:10.1016/j.jphotobiol.2012.07.006.

34.   Lei, Y.; Wang, G.; Song, S.; Fan, W.; Zhang, H. Synthesis, characterization and assembly of BiOCl nanostructure and their photocatalytic properties. CrystEngComm 2009, 11, 1857, doi:10.1039/b909013b.

35.   Gao, X.; Zhang, X.; Wang, Y.; Peng, S.; Yue, B.; Fan, C. Rapid synthesis of hierarchical BiOCl microspheres for efficient photocatalytic degradation of carbamazepine under simulated solar irradiation. Chem. Eng. J. 2015, 263, 419–426, doi:10.1016/j.cej.2014.10.110.

36.   Ahern, J. C.; Fairchild, R.; Thomas, J. S.; Carr, J.; Patterson, H. H. Characterization of BiOX compounds as photocatalysts for the degradation of pharmaceuticals in water. Appl. Catal. B Environ. 2015, 179, 229–238, doi:10.1016/j.apcatb.2015.04.025.

37.   Lester, Y.; Avisar, D.; Gnayem, H.; Sasson, Y.; Shavit, M.; Mamane, H. Demonstrating a New BiOCl$_{0.875}$Br$_{0.125}$ Photocatalyst to Degrade Pharmaceuticals Under Solar Irradiation. Water, Air, Soil Pollut. 2014, 225, 2132, doi:10.1007/s11270-014-2132-5.

38.   Song, Z.; Dong, X.; Wang, N.; Zhu, L.; Luo, Z.; Fang, J.; Xiong, C. Efficient photocatalytic defluorination of perfluorooctanoic acid over BiOCl nanosheets via a hole direct oxidation mechanism. Chem. Eng. J. 2017, 317, 925–934, doi:10.1016/j.cej.2017.02.126.

39.   Li, J.; Sun, S.; Qian, C.; He, L.; Chen, K. K.; Zhang, T.; Chen, Z.; Ye, M. The role of adsorption in photocatalytic degradation of ibuprofen under visible light irradiation by BiOBr microspheres. Chem. Eng. J. 2016, 297, 139–147, doi:10.1016/j.cej.2016.03.145.

40.   Li, J.; Sun, S.; Chen, R.; Zhang, T.; Ren, B.; Dionysiou, D. D.; Wu, Z.; Liu, X.; Ye, M. Adsorption behavior and mechanism of ibuprofen onto BiOCl microspheres with exposed {001} facets. Environ. Sci. Pollut. Res. 2017, 24, 9556–9565, doi:10.1007/s11356-017-8564-x.

41.   Tang, H.; Berger, H.; Schmid, P. E.; Lévy, F.; Burri, G. Photoluminescence in TiO$_2$ anatase single crystals. Solid State Commun. 1993, 87, 847–850, doi:10.1016/0038-1098(93)90427-O.

42.   Yin, H.; Killeen, K. The fundamental aspects and applications of Agilent HPLC-Chip. J. Sep. Sci. 2007, 30, 1427–1434, doi:10.1002/jssc.200600454.

43.   Illés, E.; Takács, E.; Dombi, A.; Gajda-Schrantz, K.; Rácz, G.; Gonter, K.; Wojnárovits, L. Hydroxyl radical induced degradation of ibuprofen. Sci. Total Environ. 2013, 447, 286–292, doi:10.1016/j.scitotenv.2013.01.007.

44.   Michael, I.; Achilleos, A.; Lambropoulou, D.; Torrens, V. O.; Pérez, S.; Petrović, M.; Barceló, D.; Fatta-Kassinos, D. Proposed transformation pathway and evolution profile of diclofenac and ibuprofen transformation products during (sono)photocatalysis. Appl. Catal. B Environ. 2014, 147, 1015–1027, doi:10.1016/j.apcatb.2013.10.035.

45.   Tobergte, D. R.; Curtis, S. Environmentally Benign Photocatalysts Applications of Titanium Oxide-based Materials; Vol. 53; ISBN 9788578110796.

CHAPTER 4

DEVELOPMENT OF BiOX PHOTOCATALYSTS FOR INDUSTRIAL APPLICATIONS

4.1.Introduction

Recently, advanced drilling techniques have enabled producers of petroleum access to large quantities of natural gas [1]. Natural gas can be directly used as a transportation fuel but its value can be increased through conversion into liquid hydrocarbons through C-C bond formation in a process known as gas-to-liquid (GTL). However, current GTL operations are based on the Fischer-Tropsch process, which has large energy requirements, proceeds through multiple steps, and has large capital costs constraining plant startup [2]. A GTL process based on photocatalysis, with the coupling of natural gas molecules initiated by activating a catalyst material with light, has great potential to reduce operating costs of GTL plants and enable maximum utilization of natural gas. Photocatalytic activation of methane has been previously studied by Li et al. who showed that metal doped zeolite frameworks promote dehydrogenative coupling under UV irradiation [3,4].

In addition to photocatalytic GTL conversion, other photocatalytic methodologies hold potential for industrial application. One interesting possibility is the use of photocatalysis to produce complex organic molecules for the specialty chemicals and pharmaceuticals industries. The processes employed in these industries often require carbon-carbon bond formation as large molecules are synthesized to fulfill niche applications [5]. One of the reactions commonly used for this purpose is the Heck reaction, which forms a carbon-carbon bond between an alkyl halide and an alkene [6]. However, this reaction requires the use of a base to drive the removal of -HX, which is harsh, expensive and requires additional downstream processing to purify the product. If

94

a photocatalyst is able to both drive the reaction and act as a base, both reagent and energy costs will be reduced, increasing the value of these processes.

Photocatalytic processes have been previously applied to coupling reactions. Tyagi et. al demonstrated the coupling of tetrahydrofuran (THF) with alkanes and alkenes using Pt/TiO$_2$ as the photocatalyst [7,8]. The Kisch group has demonstrated the ability of ZnS photocatalysts to drive the dehydrodimerization of 2,5-dihydrofuran and cyclohexene [9,10]. Suzuki coupling reactions, where an organoboron species is coupled with an aryl halide, have been reported using visible-light irradiation and Pd/SiC photocatalysts by Jiao et. al [11]. Coupling reactions of diazo salts with arene substrates have been conducted over both TiO$_2$ [12] and Bi$_2$O$_3$ [13]. Visible light activity in photocatalysis is an important step towards industrial relevance due to the energy cost savings to be realized by utilizing freely available solar energy instead of operating high-powered lamps. Our previous research on bismuth oxyhalides suggested the presence of highly reactive electron holes in the valence band generated under photoirradiation [14,15]. This high activity coupled with the visible light absorption properties of BiOI has the potential to be highly useful in industrial settings.

This chapter consists of three projects all directed at the application of BiOI photocatalysis to reactions that are either currently used or would be useful in the chemical industry. The first project focused on the application of BiOI photocatalysts to natural gas condensation, with the goal of demonstrating that BiOI photocatalytic methods could be used to convert natural gas, which after drying is composed of primarily methane gas, to higher molecular weight liquid hydrocarbons under mild conditions. Cyclohexane was selected as a model compound to demonstrate proof of principle, because it was easier to handle and because all the potential reaction sites are chemically identical. The second project investigated the effect of visible light

irradiation on the addition of iodine to cyclohexane and toluene. This was done to explore the possibility of generating iodocyclohexane *in situ* for coupling reactions with aryl compounds. These conditions were then later tested using cyclohexyl halides and aryl substrates to mimic coupling reactions commonly used in synthesis of complex organic molecules.

4.2. Materials and Methods

Cyclohexane (HPLC grade), chlorocyclohexane, bromocyclohexane, iodocyclohexane, toluene, furan, fluorene, iodine, iodine monochloride, bismuth nitrate pentahydrate and potassium iodide were all purchased from Sigma-Aldrich and used as received. Zeolite samples CBV300 (zeolite Y) and CBV21A (mordenite) were purchased from Zeolyst International and stored in a desiccator to prevent absorption of moisture by the samples.

4.2.1. Synthesis of Catalysts

4.2.1.1. BiOI

The bismuth oxyiodide photocatalysts used in these experiments were synthesized using hydrothermal autoclave synthesis methods. Hydrothermal autoclaves are stainless steel "bomb" autoclaves that allow a system to be safely exposed to high pressures for synthesis purposes. The photocatalyst was synthesized by slowly adding 20 mL of 50 mM KI to 20 mL of 50 mM $Bi(NO_3)_3$ • $5H_2O$ to form an orange precipitate. This solution was then stirred in air for 30 min before transferring the solution to a 50 mL stainless steel hydrothermal autoclave. The bomb was sealed and placed in an electric oven at 160°C for 16 h. The products were recovered by gravity filtration and washed thoroughly with deionized water and ethanol and dried at 50°C overnight. The synthesis scheme is shown in Figure 4.1.

Bi(NO₃)₃•5H₂O + KI
1 mmol   1 mmol

Hydrothermal Autoclave
160°C
16 hr
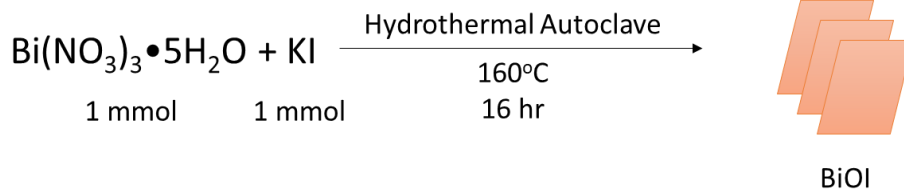
BiOI

Figure 4.1. Synthetic scheme for BiOI photocatalyst.

4.2.1.2. Metal Doping

Metal doping of the synthesized photocatalysts was used to study the effect, if any, on the overall photocatalytic activity for C-H activation in cyclohexane. The doping was achieved using a photodeposition method modified from Yoshida et al. [8]. Briefly, 4 g of the powdered photocatalyst was dispersed in 300 mL of deionized water and stirred for 30 min under photoirradiation from a mercury lamp (Steripen, $\lambda > 254$ nm). Then 100 mL methanol and an aqueous solution of the appropriate metal precursor ($PdCl_2$, $Ni(NO_3)_2$, $CuCl_2$) were added and stirred for 15 min in the dark and then 1 h under photoirradiation. The solids resulting from this process were separated from the suspension via vacuum filtration and washed thoroughly with deionized water. Following this the samples were dried overnight in an electric oven at 50°C. The resulting samples were called M-BiOX, where M refers to the identity of the doped metal ion.

4.2.1.3. Insertion of BiOI into Zeolite Support

Zeolite supports were used to increase the stability as well as selectivity of the BiOX photocatalysts. The combination of synthesized BiOI samples with zeolite Y and mordenite was accomplished using a facile room temperature method [16]. First, 500 mg of the designated zeolite sample was added to 30 mL of deionized water and sonicated for 15 min. Then, 25 mg of BiOI

powder sample was slowly added to the zeolite/water solution. The resulting solution was stirred vigorously in a fume hood for 24 h. The solid samples produced were collected, dried at 80°C, and then calcined at 250°C for 3 h. This synthesis scheme is shown in Figure 4.2.
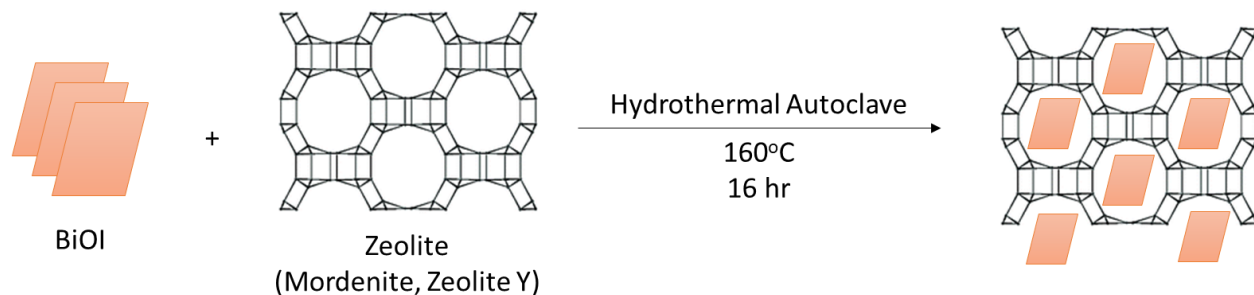
Figure 4.2. Synthetic scheme for BiOI/Zeolite samples

4.2.2. Characterization of Catalysts

Characterization is a critical aspect of catalyst evaluation, both to ensure that the synthesized catalyst is the expected compound as well as to determine relationships between properties and reactivity. For these studies Fourier transform infrared spectroscopy (FTIR) was employed to study the structure of the synthesized catalysts, while diffuse reflectance spectroscopy (DRS) was used to evaluate the light absorption properties.

4.2.2.1. Infrared Spectroscopy

FTIR was used to characterize the structure of the synthesized photocatalysts. FTIR spectra were collected over the range of 4000-450 cm^{-1} using a Perkin Elmer FTIR Spectrum Two equipped with a Universal Attenuated Total Reflectance (UATR) accessory. The UATR consists of a diamond crystal with a 2-micron pathlength. The detector is a LiTaO$_3$ MIR detector with a total effective range of 8,300 cm^{-1} to 350 cm^{-1}. Spectra were collected with a resolution of 2 cm^{-1}.

To collect FTIR spectra, the UATR detector was gently cleaned using reagent grade ethanol and a KimWipe and a background spectrum was collected. Then a small sample of the synthesized photocatalyst powder was carefully placed on the detector using a spatula. The Perkin Elmer FTIR Spectrum Two UATR is equipped with an arm that presses the sample into the detector window to achieve optimal contact and infrared irradiation conditions. The position of the pressure arm was adjusted while continuously collecting spectra to maximize the signal from the sample, and the final spectrum was created from a total of 10 averaged spectra. The resulting spectrum was exported to .csv format and processed using Microsoft Excel.

4.2.2.2.   Diffuse Reflectance Spectroscopy

Diffuse reflectance is the property of a material to reflect incident light at many different angles as opposed to specular reflection that reflects light at just one angle. DRS is a spectrophotometric technique that measures UV-Vis light diffusely reflected by a material to determine its absorption properties. The absorption spectrum generated can be used to determine the optical band gap of a semiconductor material by applying the Kubelka-Munk theory of reflectance. Determination of the band gap by this technique provides information on the potential activity of each catalyst for the selected light wavelength. DRS experiments were used to determine the optical band gap energy of all synthesized photocatalysts. The light source used in DRS experiments was a DH-2000 deuterium and halogen light source (Mikropack) coupled with an USB4000 spectrometer (Ocean Optics). A fiber optic cable was used to gather collected light. Spectra were referenced to polytetrafluoroethylene (PTFE) and potassium chloride. Data was processed using SpectraSuite software model 1.4.2_09 (Ocean Optics).

4.2.3. General Reaction Setup

4.2.3.1. Photocatalytic Dehydrodimerization of Cyclohexane

The activity of each prepared catalyst was evaluated for C-C coupling in cyclohexane via dehydrodimerization in a batch process using a photocatalytic reaction system. Reactions were conducted inside a closed system to prevent side reactions with oxygen. Initially, 50 mg of the catalyst to be tested was deposited inside of the reaction vessel and sealed. The vessel was then pre-irradiated with a visible-light lamp (100W D-LED, Sylvania, $\lambda > 420$ nm, see Figure 4.3 for lamp emission spectrum) for 1 h. Following pre-irradiation, the reaction chamber was purged with argon gas for 10 min to remove air from the reactor system. Continuing to purge the system with argon, 2 mL of cyclohexane was injected into the system through a septum. The semiconductor photocatalyst was suspended in cyclohexane via magnetic stirring and irradiated using the D-LED lamp for the specified reaction time. Samples were removed from the reaction mixture and were prepared for GCMS analysis by filtering through a syringe equipped with a 0.2 µm PTFE chromatography filter (25 mm, Fisher Scientific).
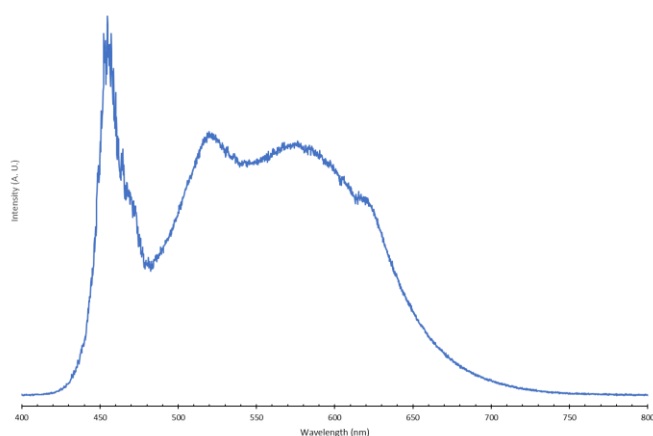
Figure 4.3. Emission spectrum for the D-LED lamp used in the visible light irradiation experiments.

4.2.3.2. Visible-light Photoinitiated Iodination of Cyclohexane

Iodine addition experiments were conducted to evaluate the ability of visible light to iodinate cyclohexane. For the iodine addition experiments, 2 mmol of the iodinating agent (either I_2 or ICl) was placed in a 14 mL vial, which was sealed and degassed for 15 min with N_2. Then, 10 mL of HPLC grade cyclohexane (Sigma-Aldrich) was added to the vial using a syringe. The solution was stirred and irradiated using a visible-light lamp (100W, D-LED, $\lambda > 420$ nm) for 16 h. After irradiation, the solution was removed from the vial using a syringe and filtered through a 0.2 µm PTFE filter into a GC vial for GCMS analysis.

4.2.3.3. Photocatalytic Coupling Reactions with Cyclohexyl Halides

Coupling reactions of cyclohexyl halides with aryl and heteroaryl substrates were examined as analogs to Heck-type carbon-carbon bond formation methodologies. To conduct these experiments, 10 mL of the aromatic substrate (toluene or furan) and 50 µL of the cyclohexyl halide (chlorocyclohexane, bromocyclohexane, or iodocyclohexane) was added to a 14 mL vial. The selected photocatalyst (100 mg) was then added to the reaction mixture, and the solution was stirred in the dark for 30 min. After taking a dark sample from the vial, the solution was irradiated using the D-LED lamp for 16 h. A sample was then removed from the solution, filtered through a 0.2 µm PTFE filter into a GC vial, and analyzed by GCMS.

4.2.4. Analysis of Reaction Products

The GCMS system was an Agilent Technologies 6890 Gas Chromatograph operated in the splitless injection mode equipped with an Agilent HP-5MS (Agilent Technologies, 30 m x 0.25 mm, 0.25 µm) column interfaced to a 5973N Mass Selective Detector (Agilent Technologies). The temperature program consisted of a 5 min hold at 50°C, followed by a 5°C/min ramp to 200°C with

a final time of 1 min. The carrier gas was helium flowing at 1 mL/min. The electron ionization source temperature was set at 280°C and the source inlet temperature was 250°C. The mass spectra obtained for species eluting from the GC column were identified using the NIST 2013 database for best-match identification. Fluorene was used as an internal standard for all measurements and relative response factors were determined for each target analyte.

For quantification purposes the response factor for the internal standard (IS) was calculated through analysis of a sample containing both the analyte standard (bicyclohexane, chlorocyclohexane, bromocyclohexane, iodocyclohexane, or cyclohexyl toluene) and the IS (all standards obtained from Sigma-Aldrich). The response factor is the ratio of the instrument response to known amounts of the analyte and an IS. A sample containing known amounts of both the analyte standard and the internal standard is injected and analyzed. After integrating both peaks to determine the peak area, a ratio (the relative response factor) can be determined to relate the instrument response of the analyte to the instrument response to the internal standard. After determining the appropriate response factors, a known mass of the internal standard was added to each sample after filtering and preparation. This mass was determined based on the potential range of product masses in the sample. The mass of analyte in the original sample was then determined using the rearranged response factor equation.

$$F = \frac{A_{Analyte}/m_{Analyte}}{A_{IS}/m_{IS}} \tag{1}$$

Where F = relative response factor, $A_{Analyte}$ = the integrated area of the analyte peak, $m_{Analyte}$ = the mass of analyte in the sample, A_{IS} = the integrated area of the analyte peak, and m_{IS} = the mass of internal standard added to the sample solution. This process was repeated for each product identified in this study.

4.3.Results and Discussion

4.3.1. Photocatalyst Selection

With the goal of exploring BiOX photocatalysts for C-C bond formation and other synthetic transformations, we focused on the use of BiOI. BiOI was selected due to its visible light absorption properties. In addition to studying BiOI powders, we also synthesized BiOI incorporated into two zeolites, mordenite and zeolite Y. By restricting the area available for coupling reactions via inserting the photocatalyst into a zeolite framework, we believed that the formation of dimers would be encouraged over formation of more complex products. We also synthesized BiOI doped with metals (M = Ni, Pd, Cu) because the introduction of metals to BiOX photocatalysts has previously been shown to increase reactivity [17,18].

4.3.2. Characterization of Synthesized Photocatalysts

4.3.2.1.Vibrational Spectroscopy

All of the synthesized photocatalysts were characterized using Fourier Transform Infrared Spectroscopy (FTIR). This technique was used to verify the expected structure of the photocatalysts as well as the catalyst supports. The collected FTIR spectra are shown in Figure 4.4. Based on the IR spectra collected, it is clear that the synthesized BiOI/Zeolite samples consist of simple combinations of the two compounds. The separate structures of BiOI and zeolite are not affected by the synthesis process. The spectra of the metal-doped BiOI samples (data not shown) appeared identical to neat BiOI samples since the IR absorption of metal species is not expected to be observed within the collection window for the experimental conditions.
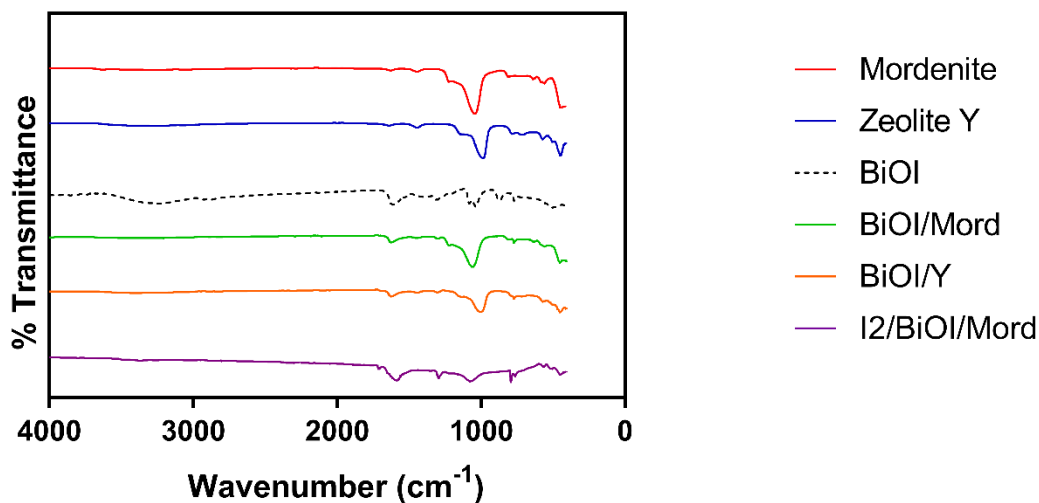
Figure 4.4. FTIR spectra for the synthesized photocatalysts.

4.3.2.2. Diffuse Reflectance Spectroscopy

In order for a photocatalyst to work, it must be able to absorb the incident irradiation provided by the lamp used in the system. For this reason each photocatalyst synthesized as a part of this study was studied by UV-Vis Diffuse Reflectance Spectroscopy (DRS). Since DRS only measures the light reflected by the sample, it is necessary to convert reflectance into absorption using the Kubelka-Munk Transformation. DRS spectra for each of the synthesized photocatalysts are shown in Figure 4.5.
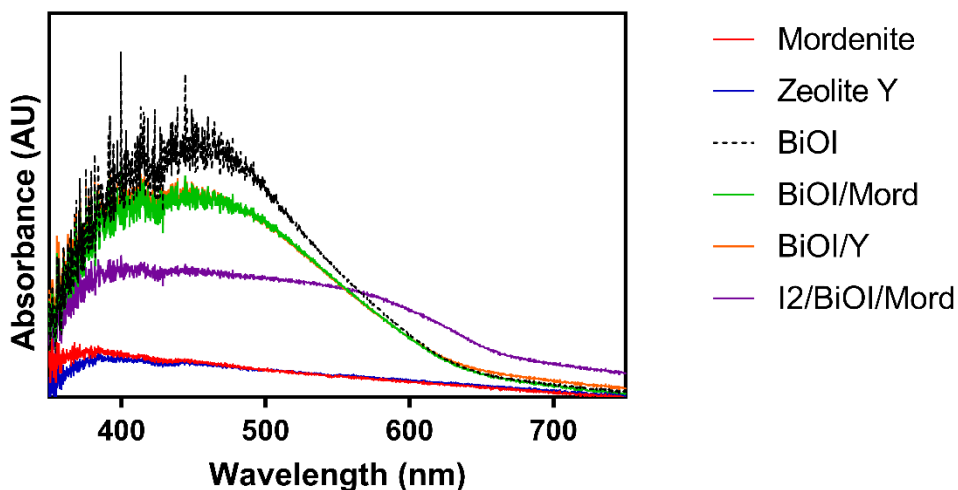
Figure 4.5. DRS spectra for the synthesized photocatalysts.

It can be seen that neither zeolite sample absorbs light in the visible region. BiOI shows an absorption maximum at 450 nm. The position of the absorption maximum does not change after the synthesis of BiOI/Zeolite samples. This indicates that the simple combination of the two materials has not chemically changed the structures. For one sample, I_2/BiOI/Mordenite, the absorption band edge redshifts significantly, suggesting an even smaller bandgap. This material was calcined at a higher temperature (450^oC) than other BiOI/Zeolite samples. These considerations led us to conclude that some BiOI was converted to Bi_2O_3 as iodine was removed from the crystal structure resulting in deposition of molecular I_2 on the surface of the catalyst. This is further supported by previous reports on the temperature dependence of BiOI synthesis [19].

4.3.3. Photocatalytic Dehydrodimerization of Cyclohexane

A wide range of synthesized photocatalysts were tested for dehydrodimerization reactions with cyclohexane. This reaction was used to represent a potential natural gas upgrading process, where C-C bond formation under mild conditions would increase the value of natural gas as well as enable easier storage in a liquid form.

4.3.3.1. Proposed Mechanism

Our previous work on bismuth oxyhalides suggests that highly reactive electron holes are generated within the valence band upon photoirradiation. Based on this, we hypothesized that cyclohexane could dehydrodimerize non-oxidatively via the following mechanism. First, the electron hole present in the valence band of the photocatalyst initiates hydrogen abstraction to the photocatalyst surface. This process results in the formation of a cyclohexyl radical also on the surface of the photocatalyst. This radical is then expected to attack a cyclohexane molecule at the solid-liquid interface resulting in the loss of an additional hydrogen atom. The proposed reaction could be further thermodynamically driven by the release of hydrogen gas, which is proposed to be formed by the combination of two hydrogens on the surface of the photocatalyst. The hypothesized mechanistic scheme is shown below.

$$\text{BiOI} + h\nu \ (>450 \text{ nm}) \rightarrow h^+ + e^-$$

$$2\text{R-H} + 2h^+ \rightarrow 2\text{R}\bullet + 2\text{H}^+$$

$$2\text{R}\bullet \rightarrow \text{R-R}$$

$$2\text{H}^+ + 2e^- \rightarrow \text{H}_2$$
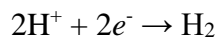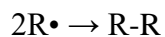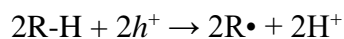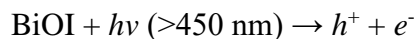
4.3.3.2. Photocatalysis and product analysis by GCMS

Dehydrodimerization reactions of cyclohexane using BiOI and visible light (Figure 4.6) were attempted to determine if the expected reaction product, bicyclohexane, was formed. After irradiating the dry, deoxygenated solution overnight, the catalyst was removed from the reaction mixture via a 0.2 µm syringe filter and the cyclohexane solutions were analyzed by GCMS. As a control, we analyze a sample of cyclohexane with BiOI without visible light irradiation. A representative total ion chromatogram (TIC) for this reaction is shown in Figure 4.7. The peak at 16.5 min was identified as bicyclohexane based upon the mass spectrum (Figure 4.8) which showed a molecular ion (m/z = 166) and fragment ions that agreed with the reference spectrum.
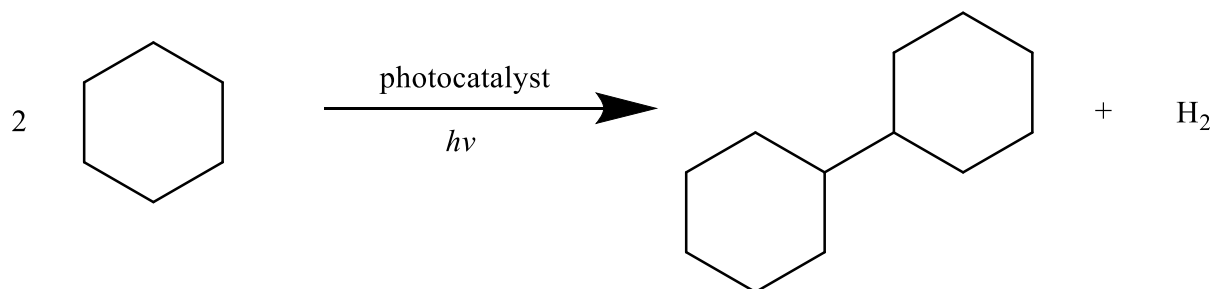
Figure 4.6. Scheme for photocatalytic dehydrodimerization of cyclohexane to bicyclohexane.
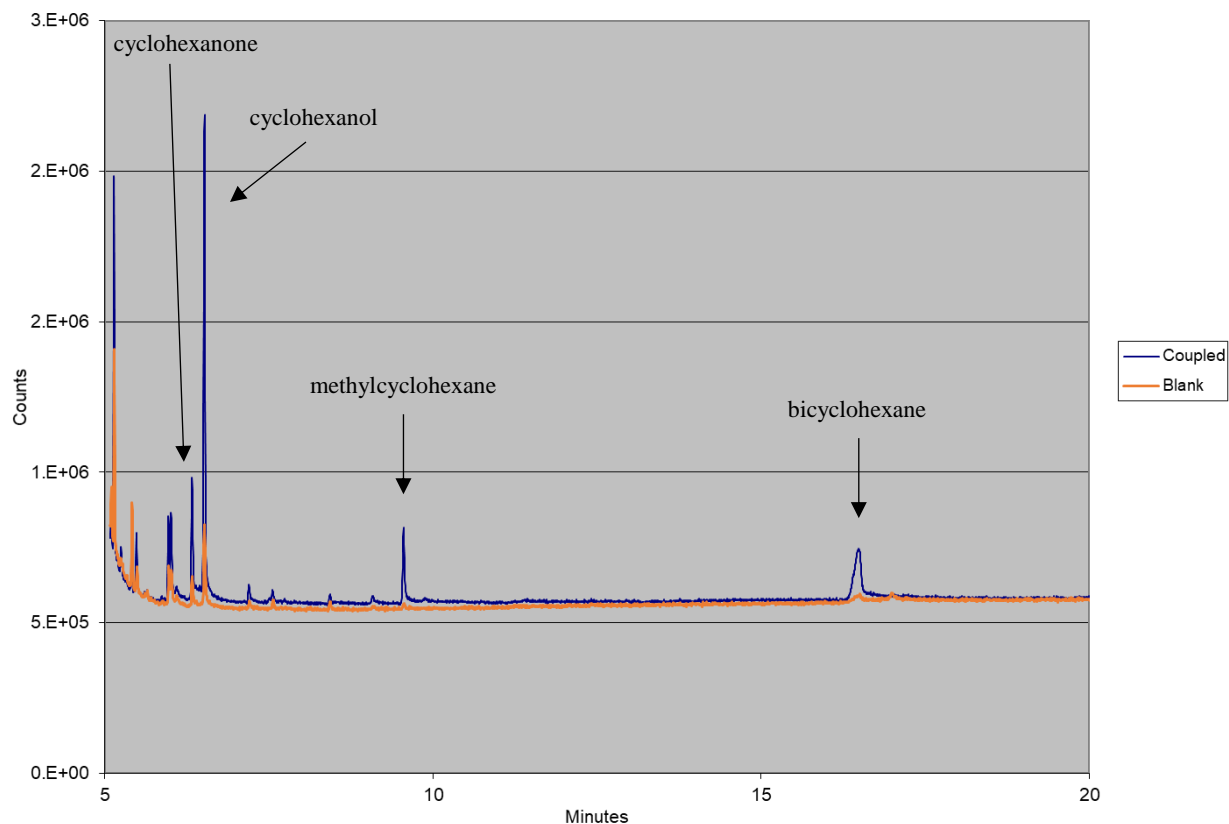
Figure 4.7. TIC for cyclohexane direct coupling to bicyclohexane with BiOI and visible light.

The peaks detected in the range of 6-7 min correspond to cyclohexanol and cyclohexanone, agreeing with previously published reports of cyclohexane oxidation by photocatalysis. These compounds were also present in the blank in lower amounts, suggesting that adventitious oxygen was adding to the cyclohexyl radical, and also suggesting that oxidized cyclohexanes could participate in the coupling process. The peak at 9 min was identified as methylcyclohexane, indicating that some degradation of cyclohexane is likely occurring concurrently with cyclohexane coupling. With the chromatographic conditions optimized and major products identified, we moved forward with evaluating reaction conditions to maximize production of bicyclohexane.
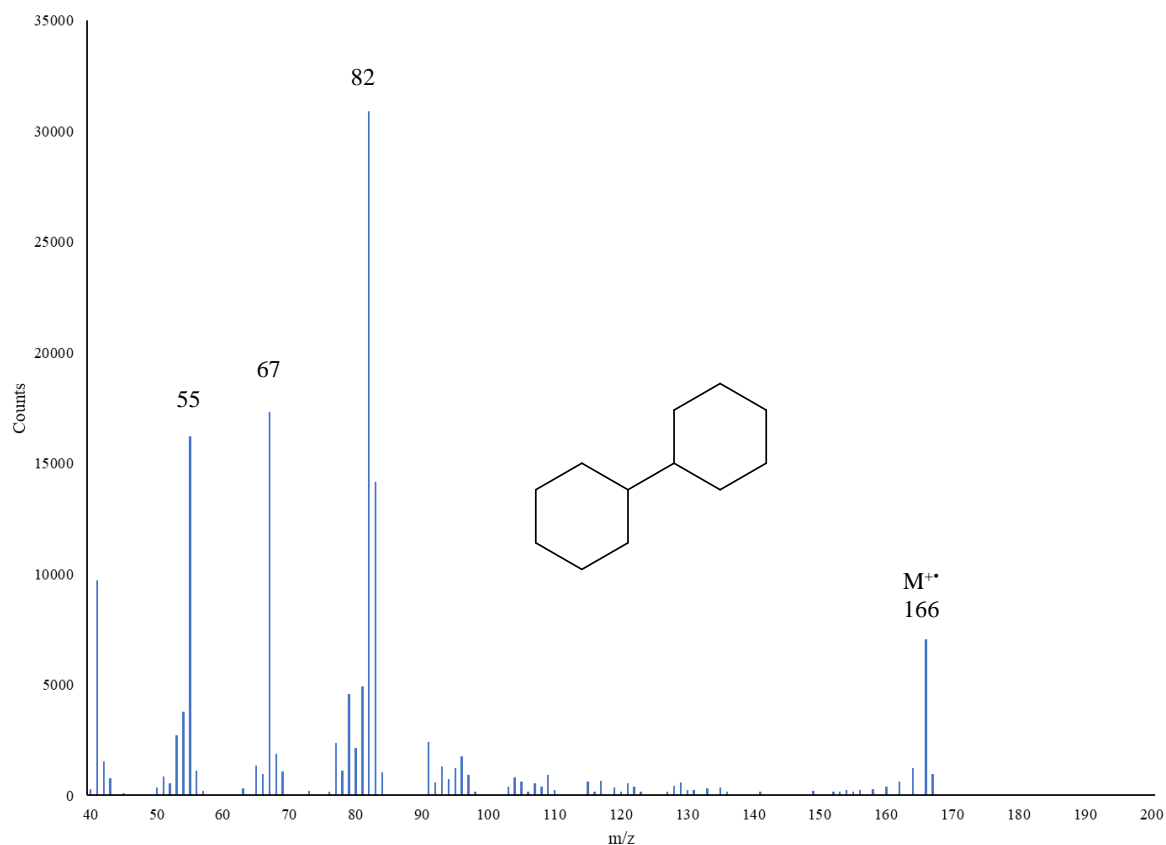
Figure 4.8. Mass spectrum of the compound eluting at 16.5 min, identified as bicyclohexane.

4.3.3.3.   Optimization of Reaction Conditions

An important consideration for photocatalytic reactions is the ability of light to fully irradiate the solution. This is an important difference when compared with thermal heterogeneous catalysis where heat can be conducted evenly throughout the solution. For photocatalytic systems, increasing the catalyst loading will also increase the turbidity of the solution, which decreases the light penetration depth and the photocatalytic efficiency. After the expected reaction product, bicyclohexane was confirmed by GCMS, the catalyst loading and irradiation time parameters were varied in order to maximize the efficiency of the reaction. The catalyst loading was varied from

100 mg/L to 100 g/L by keeping the volume of cyclohexane constant and changing the mass of catalyst added to the container. The bicyclohexane product yields were quantified using fluorene as an internal standard until no further product formation was observable by GCMS. All reaction optimization conditions are listed along with observed yield in Table 4.1. As can be seen from the table, the catalyst loading of 25 mg/L produces the optimal yield of bicyclohexane. The optimized conditions were then used throughout the remaining experiments.

Table 4.1. Results for reaction condition optimization trials for photocatalytic dehydrodimerization of neat cyclohexane with BiOI ($hv > 450$ nm, 16 h).

Trial	Catalyst Loading	Yield (µmol)
1	100 mg/L	0.006± 0.0004
2	500 mg/L	0.014± 0.0008
3	5 g/L	0.020± 0.0011
4	25 g/L	0.024± 0.0012
5	100 g/L	0.018± 0.0011

4.3.3.4.   Catalyst Variation

After determining the optimum conditions for cyclohexane coupling via BiOI photocatalysis, the reaction was further investigated by comparing BiOI with Ni-BiOI, Pd-BiOI, Cu-BiOI, BiOI/Mordenite, BiOI/Zeolite Y and I_2/BiOI/Mordenite as the employed photocatalyst. The results from the catalyst variation trials are shown below in Table 4.2.

Table 4.2. Results of catalyst variation trials for photocatalytic dehydrodimerization of neat cyclohexane with BiOI ($hv > 450$ nm, 16 hr).

Catalyst	Bicyclohexane Yield (μmol)
BiOI	0.024 ± 0.0012
Ni-BiOI	0.020 ± 0.0011
Pd-BiOI	0.025 ± 0.0013
Cu-BiOI	0.023 ± 0.0012
BiOI/Mordenite	0.056 ± 0.0028
BiOI/Zeolite Y	0.034 ± 0.0020
I_2/BiOI/Mordenite	0.027 ± 0.0015

Overall, the yield of coupling of neat cyclohexane using BiOI as the photocatalyst with visible light irradiation is similar to previous reports [7]. Metal doping did not produce a large effect on the yield. This may be due to the choices of metals used as dopants, or this may be due to the metal doping procedure utilized in this study. Metal dopants can act to trap electrons through the generation of additional states that allow for oxidation of the conduction band. However, if the state does not exist at a favorable energy level the oxidation process will not be favorable. Metal doping should continue to be explored for BiOX compounds in various applications. Theoretical modelling of the states created by the metal dopant may prove useful for designing future studies.

4.3.3.5.   Conclusions and Directions for Future Work

The use of zeolite supports also provided interesting results for cyclohexane coupling. Overall, it was found that BiOI/Mordenite produced the largest yield of bicyclohexane under the present reaction conditions. This increase in product yield is attributed to the deposition of BiOI on the surface of the zeolite structures, where the number of reactive sites available may be increased. It is also possible that the reactants prefer to adsorb to the surface of the zeolite, facilitating the reactions between radical species generated at the photocatalyst. Future work should validate the non-oxidative nature of this reaction through detection of H_2 in the reaction headspace using GC/TCD analysis. BiOI/Mordenite was then selected as the catalyst that would be used in future coupling reactions due to its reactivity with neat cyclohexane.

4.3.4. Visible-light Photocatalytic Iodination of Cyclohexane

Although the results from direct coupling of cyclohexane via photocatalytic dehydrodimerization demonstrated a potential route to natural gas upgrading, we wanted to find alternative options with greater coupling yields. One way to achieve greater reactivity is through first functionalizing the substrate intended to be coupled. Since we are using bismuth oxyhalide materials as photocatalysts, an interesting possibility is to functionalize cyclohexane with halide atoms to create regions of differing electron density on the cyclohexane ring. This section will detail the efforts directed at adding iodine atoms to cyclohexane in order to increase coupling yields.

4.3.4.1. Study of the Iodinating Agent

The iodinating agents studied in this project were molecular iodine and iodine monochloride. These reagents were evaluated for iodine addition to cyclohexane. We found that this reaction does not proceed under dark or irradiation conditions when no catalyst is present. However, when BiOI/Mordenite is added as a photocatalyst, product formation is observed. In trials with cyclohexane using I_2 as the iodinating agent, the only product observed by GCMS was iodocyclohexane. The mass spectrum for this compound is shown in Figure 4.9. The molecular ion can be observed ($m/z = 210$) as well as the $[M-I]^+$ fragment at $m/z = 127$.
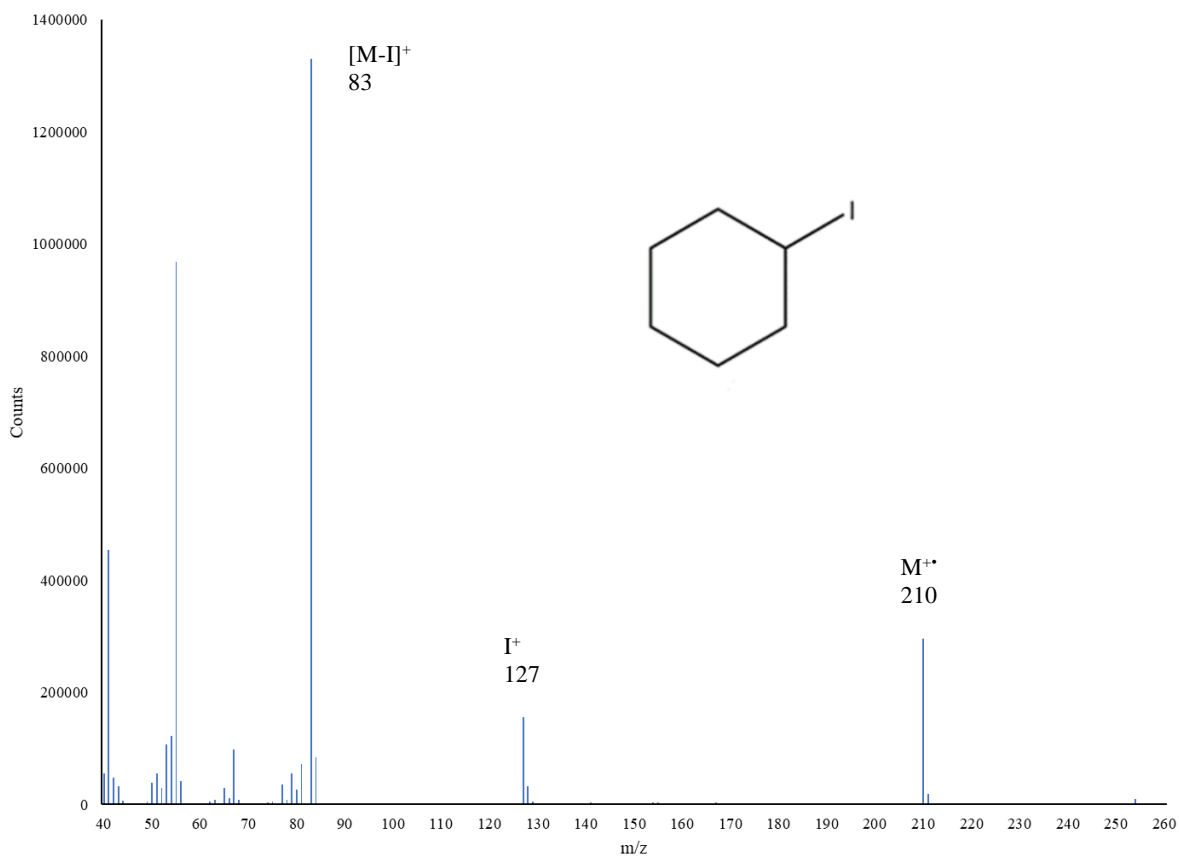
Figure 4.9. Mass spectrum of iodocyclohexane.

The reaction for iodination of cyclohexane using iodine monochloride is shown in Figure 4.10. The observed color of the reaction solutions provided additional information on the progress of the reaction. Iodine monochloride appeared red when dissolved in cyclohexane and during the course of the reaction the color of the solution changed from red to purple. This provided a qualitative method of following the progress of the reaction because the color reflected the amount of iodine monochloride that remained in the reaction solution. The GCMS analysis of the reaction of ICl with cyclohexane showed iodocyclohexane as the major product (R_t = 6.2 min, Figure 4.11).The reaction of cyclohexane with ICl also produced iodochlorocyclohexane isomers as minor products (R_t = 9.4 min, 10.5 min, 11.9 min). Iodochlorocyclohexane was identified using the mass spectrum collected for this compound (m/z = 244) and is shown in Figure 4.12.
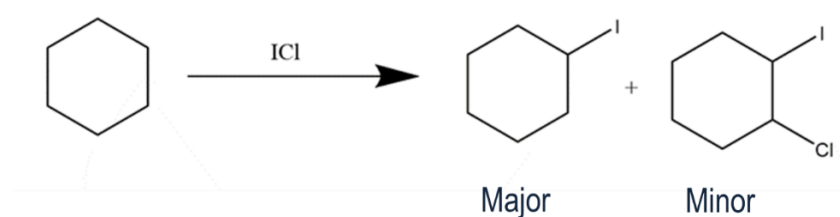
Figure 4.10. Scheme for photocatalytic iodination of cyclohexane with iodine monochloride.
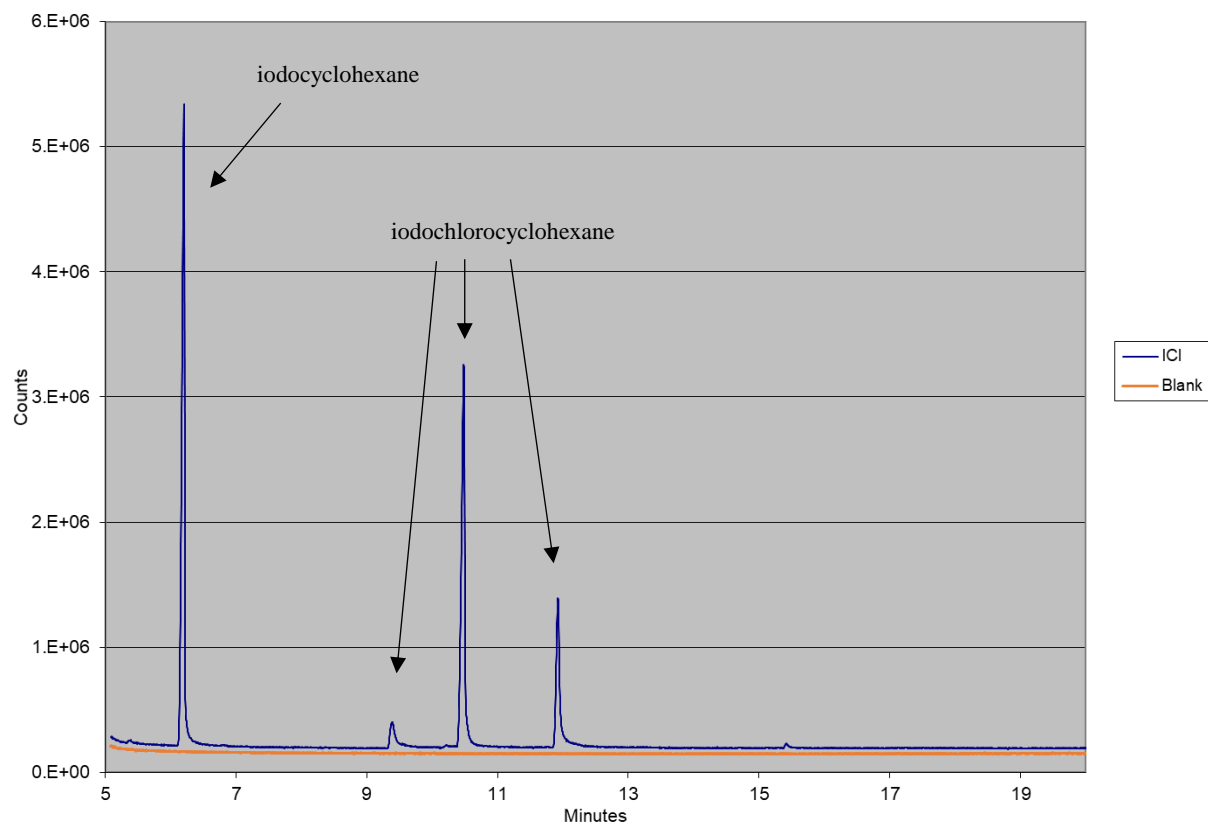
Figure 4.11. TIC for addition of iodine to cyclohexane using ICl as the reagent with BiOI/Mordenite catalyst and irradiation for 16 h with >450 nm light.
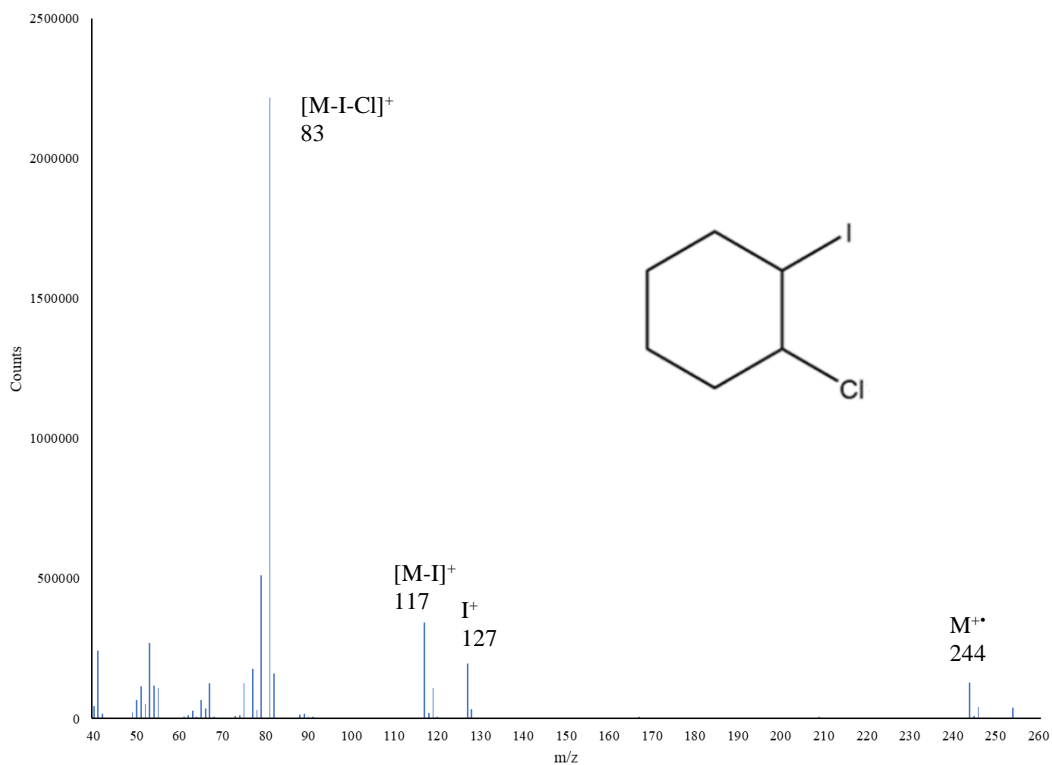
Figure 4.12. Mass spectrum of iodochlorocyclohexane.

4.3.4.2. Proposed Mechanism

Two separate mechanisms can be proposed for the visible light driven photocatalytic iodination reactions described in this section. For the iodination of cyclohexane we propose a photocatalytically activated, radical addition mechanism. This is supported by the fact that the reaction proceeded only minimally with molecular iodine, and that the yield of iodocyclohexane was increased upon addition of BiOI and visible light irradiation. In this process, iodine extraction by the photocatalyst generates an iodine radical, which then attacks the cyclohexane ring resulting in the addition of iodine.

Meanwhile, a greater degree of iodination was observed when iodine monochloride was used as the iodinating agent. Interestingly, while some production of 1-chloro-2-iodocyclohexane was observed, no production of chlorocyclohexane was observed. This is attributed to the preferential abstraction of chlorine by BiOI. This reaction is believed to not proceed with any appreciable yield due to the poor overlap of the valence band position of BiOI with the oxidation potential of iodine. Provided that other photocatalysts can be developed with a valence band tuned to that potential, the yield of this reaction will increase.

4.3.5. Photocatalytic Coupling Reactions with Cyclohexyl Halides

After investigating visible-light-driven iodination of cyclohexane, the possibility of using these iodinated compounds for coupling reactions was considered. While the direct coupling of cyclohexane molecules produced low yields, using the functionalized cyclohexyl halides instead of neat cyclohexane was proposed as an alternative substrate to increase formation of the desired coupling products. Furthermore, coupling to aryl compounds was explored because of their widespread use in chemical industry. Development of efficient routes to C-C coupling of cyclohexyl halides to aryl substrates may lead to their application in pharmaceutical and specialty chemicals industries.

4.3.5.1. Coupling Reactions with Toluene

The first approach taken to add cyclohexane to aryl compounds via coupling of cyclohexyl halides utilized toluene as the aryl substrate. This choice was made to try to mimic Heck-type reactions, where alkyl halides are added across carbon-carbon double bonds resulting in the

117

coupling of the two compounds. The reaction scheme for the coupling reaction with toluene is shown in Figure 4.13.
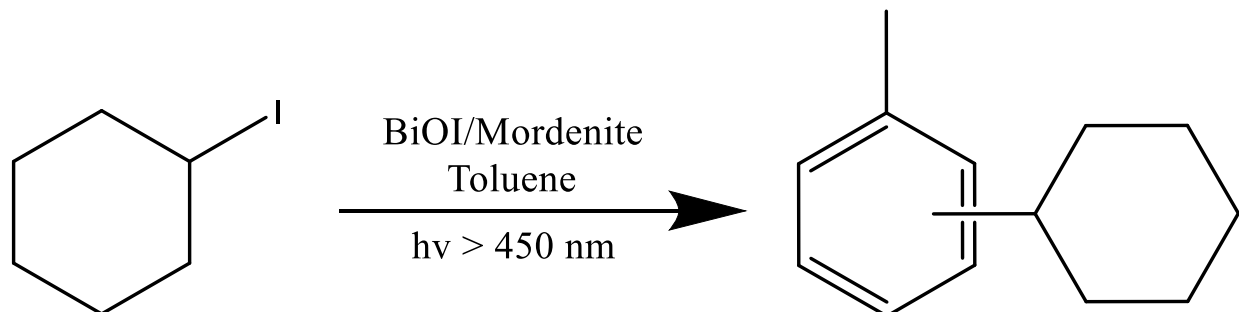
Figure 4.13. Visible light photocatalytic coupling of iodocylcohexane with toluene.

To test this photocatalytic coupling we added BiOI/Mordenite to a dilute solution of iodocyclohexane in toluene. After 16 h of visible light irradiation, the products were analyzed by GCMS. In addition to the starting material (iodocyclohexane, R_t = 6.2 min), two new peaks (R_t = 14.6 min, 14.8 min) can be observed in the TIC (shown in Figure 4.14). The mass spectrum for the peak at 14.6 min (Figure 4.15) exhibits the molecular ion for cyclohexyltoluene (m/z = 174). Performing a comparison search for both of these peaks to the NIST MS database gives a strong match for 2-cyclohexyltoluene (14.6 min) and 4-cyclohexyltoluene (14.8 min). This indicates that the desired coupling reaction can be driven by visible light photocatalysis.
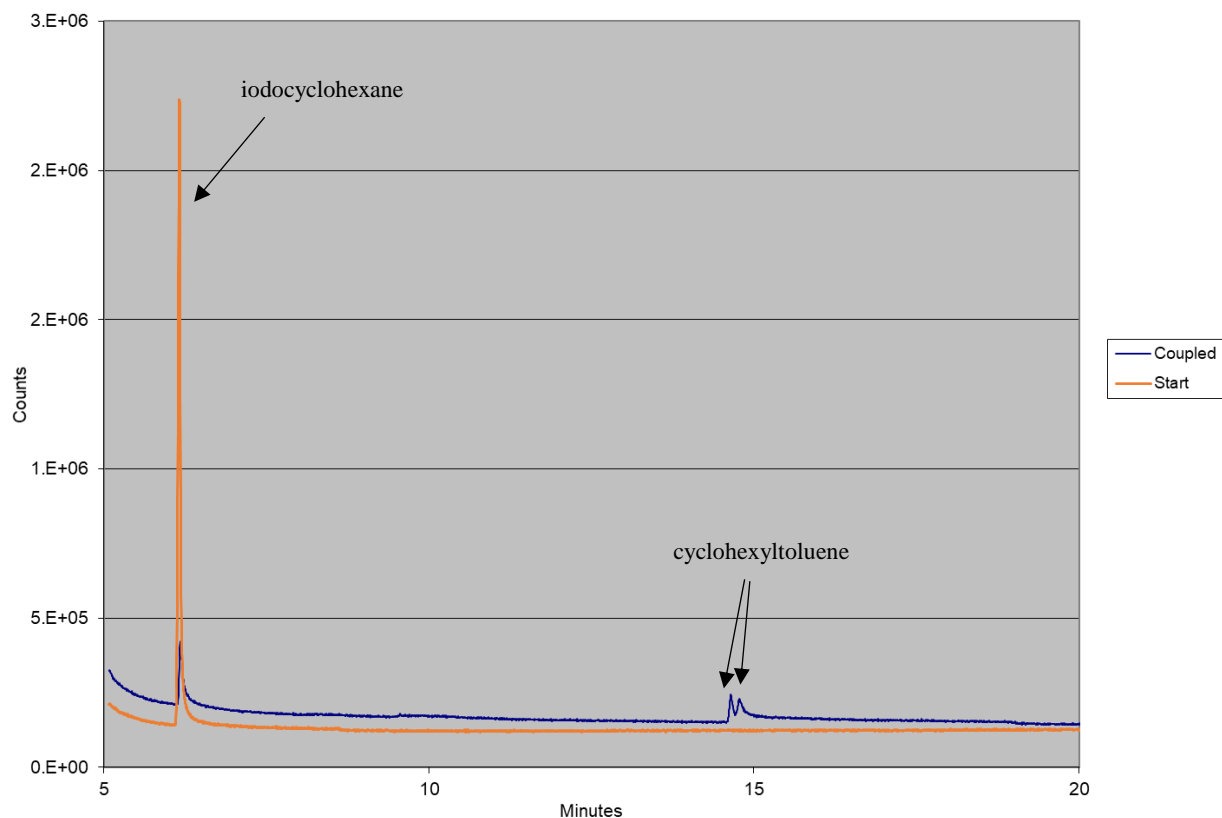
Figure 4.14. TIC for photocatalytic coupling of iodocyclohexane and toluene BiOI/Mordenite.

This reaction was then further examined with respect to the halide group. Chloro- and bromocyclohexane were tested as alternative substrates to iodocyclohexane to investigate the effect of the halide group on the yield of the coupling reaction. The results of the coupling reactions of cyclohexyl halides with toluene are summarized in Table 4.3. Iodocyclohexane produced the highest yield of coupling product, while chlorocyclohexane show the lowest yield of these trials. The origin of this observation will be discussed in further detail as part of the proposed mechanism for this reaction in section 4.3.5.4.
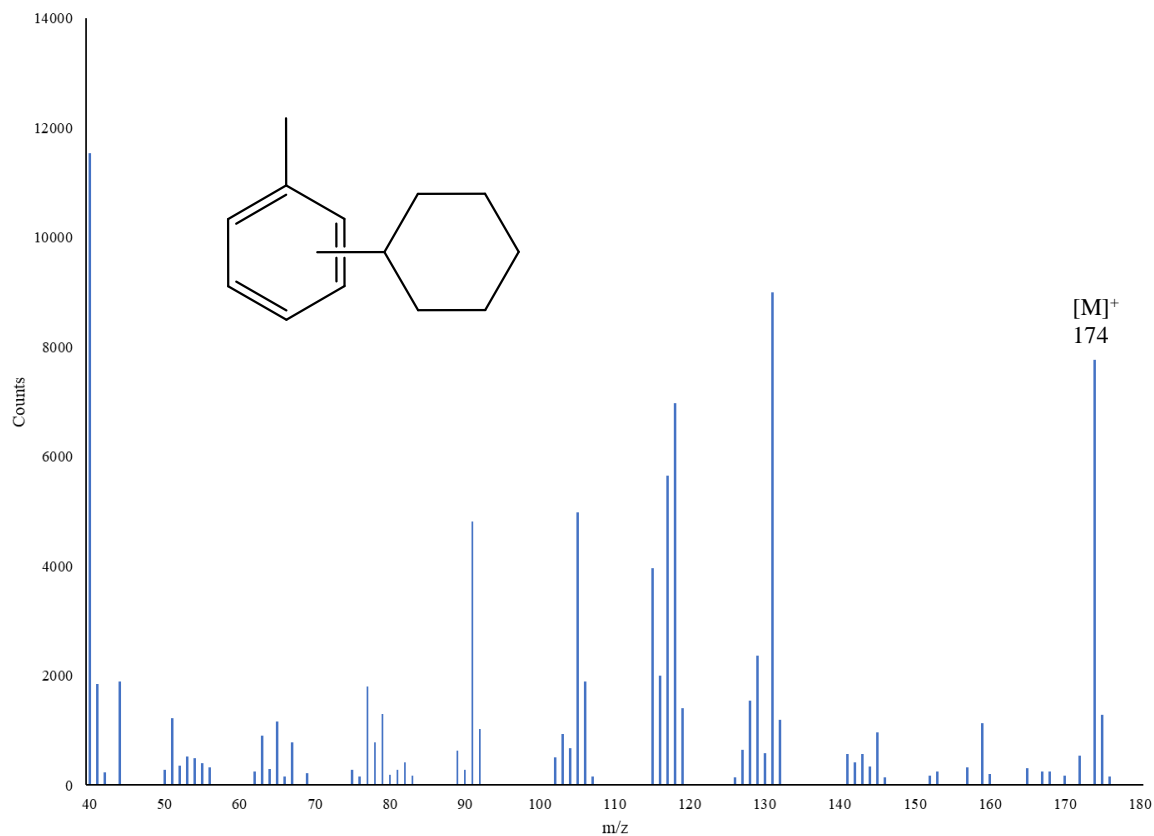
Figure 4.15. Mass spectrum of cyclohexyltoluene.

Table 4.3. Results for trials of photocatalytic coupling reaction between toluene and cyclohexyl halides with BiOI/Mordenite ($hv > 450$ nm, 16 h).

Reagent	% Conversion
Chlorocyclohexane	65%
Bromocyclohexane	90%
Iodocyclohexane	97%

4.3.5.2.   Two-step Coupling Reactions with *in situ* Generated Iodocyclohexane

To build on the idea of visible-light-driven iodination of cyclohexane (see section 4.3.2), the coupling reaction with toluene was attempted using *in situ* generated iodocyclohexane. To accomplish this, the cyclohexane iodination reaction was first conducted in a sealed contained using 0.2 mM iodine monochloride in 10 mL of cyclohexane. Following reaction, the yield of iodocyclohexane was quantified via GCMS and analysis with an internal standard. An excess amount (5 mL) of toluene was then added to the reaction mixture along with 100 mg of BiOI/mordenite, which had been shown to be the optimal reaction conditions from the previous section on coupling reaction with toluene. The TIC of GCMS analysis of the resulting solutions are shown in Figure 4.16.
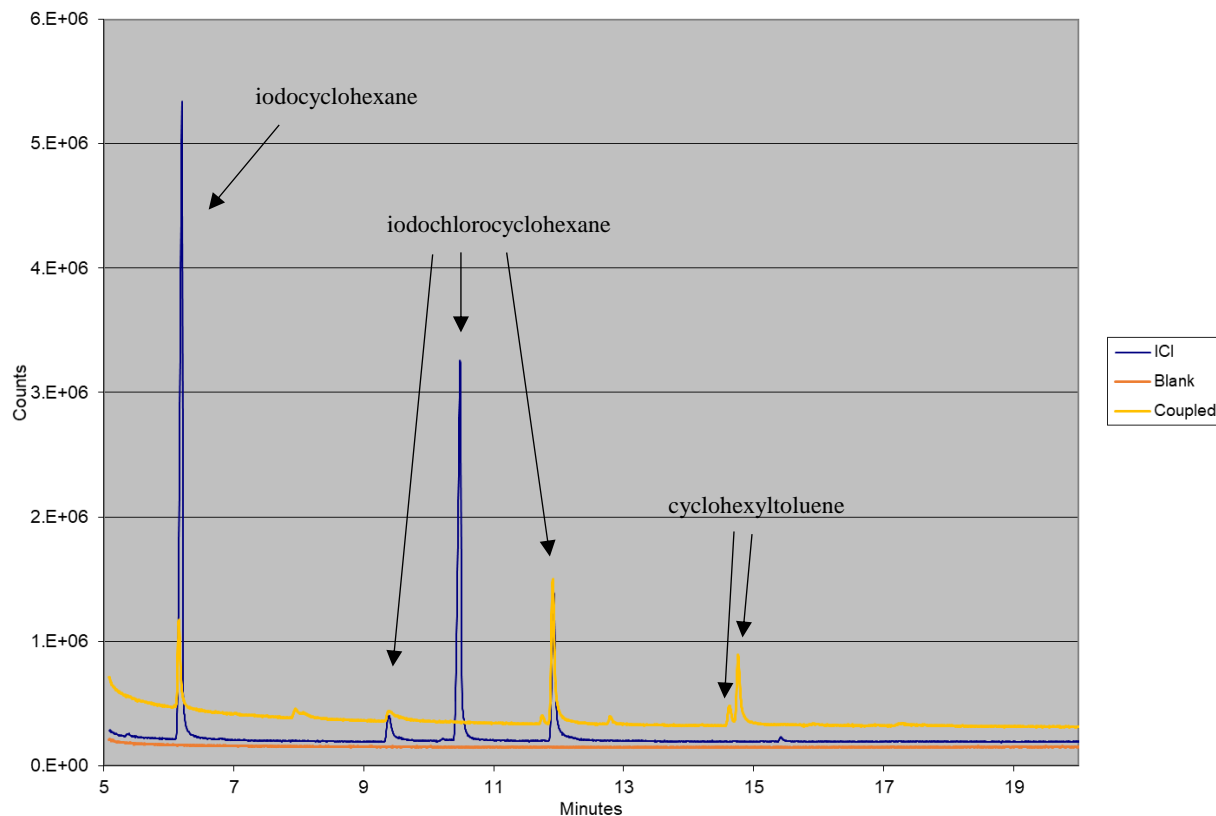
Figure 4.16. TIC for photocatalytic coupling of *in situ* generated iodocyclohexane and toluene BiOI/Mordenite.

The normal reaction products of ICl addition to cyclohexane are observed (iodocyclohexane, $R_t = 6.2$ min; iodochlorocyclohexane isomers $R_t = 9.4$ min, 10.5 min, and 11.9 min) in the initial step of the reaction. After the addition of BiOI/Mordenite and subsequent visible light irradiation, the coupling products 2-cyclohexyltoluene (14.6 min) and 4-cyclohexyltoluene (14.8 min) are observed. Interestingly, based on the TIC peak intensities, it appears that iodocyclohexane and two of the iodochlorocyclohexane isomers ($R_t = 9.4$ min, 10.5 min) are consumed during the reaction, while the remaining iodochlorocyclohexane species ($R_t = 11.9$ min) remains in the solution even after photoirradiation.

122

4.3.5.3.   Coupling Reactions with Furan

Following the series of Heck-type coupling reaction trials with cyclohexyl halides and toluene, the aryl substrate was replaced with furan. This replacement was justified by the presence of oxygen within the furan ring, which would draw electron density away from the adjacent carbons to potentially improve coupling reaction yields. This reaction was tested for chloro-, bromo-, and iodocyclohexane and however no reaction was observed for these conditions. Unlike the coupling reaction with toluene, the coupling reaction with cyclohexyl halides does not proceed when the aryl substrate is replaced with furan. Further reaction trials where the solvent was replaced with polar protic solvents did not result in the production of coupling products with furan.

4.3.5.4.   Proposed Mechanism

Given these results a reaction mechanism was proposed. The mechanism is summarized in Figure 4.17. Initially, incident visible light irradiation of energy greater than the band gap energy of BiOI promotes an electron from the valence band to the conduction band. This results in the generation of an excited electron in the conduction band and an electron hole in the valence band. The electron hole is proposed to react with iodocyclohexane, abstracting the iodine and producing a cyclohexyl radical. Toluene is also oxidized by electron holes in the valence band of BiOI. The toluene radical species produced by abstraction of hydrogen from the carbon adjacent to the methyl group exists as three resonance structures with the radical located at either the ortho- or para-positions on the benzene ring (Figure 4.17). The cyclohexyl and toluene radicals combine producing the observed cyclohexyl toluene product. The abstracted iodide and hydrogen ions combine with either a second abstracted iodide or a hydrogen ion along with two electrons from the conduction band of the catalyst producing molecular iodine, hydroiodic acid, or hydrogen gas. This is supported by the observed purple color in the reaction solution after irradiation, which is

the same color normally observed by the dissolution of iodine in cyclohexane. This is also supported by the fact that iodocyclohexane produces higher yields of coupling products than either bromocyclohexane or chlorocyclohexane. Since bromine and chlorine are more electronegative than iodine, they are less likely to form Cl^+ or Br^+ ions during the oxidation process. This mechanism explains the observation of the two separate cyclohexane addition products observed by GCMS.
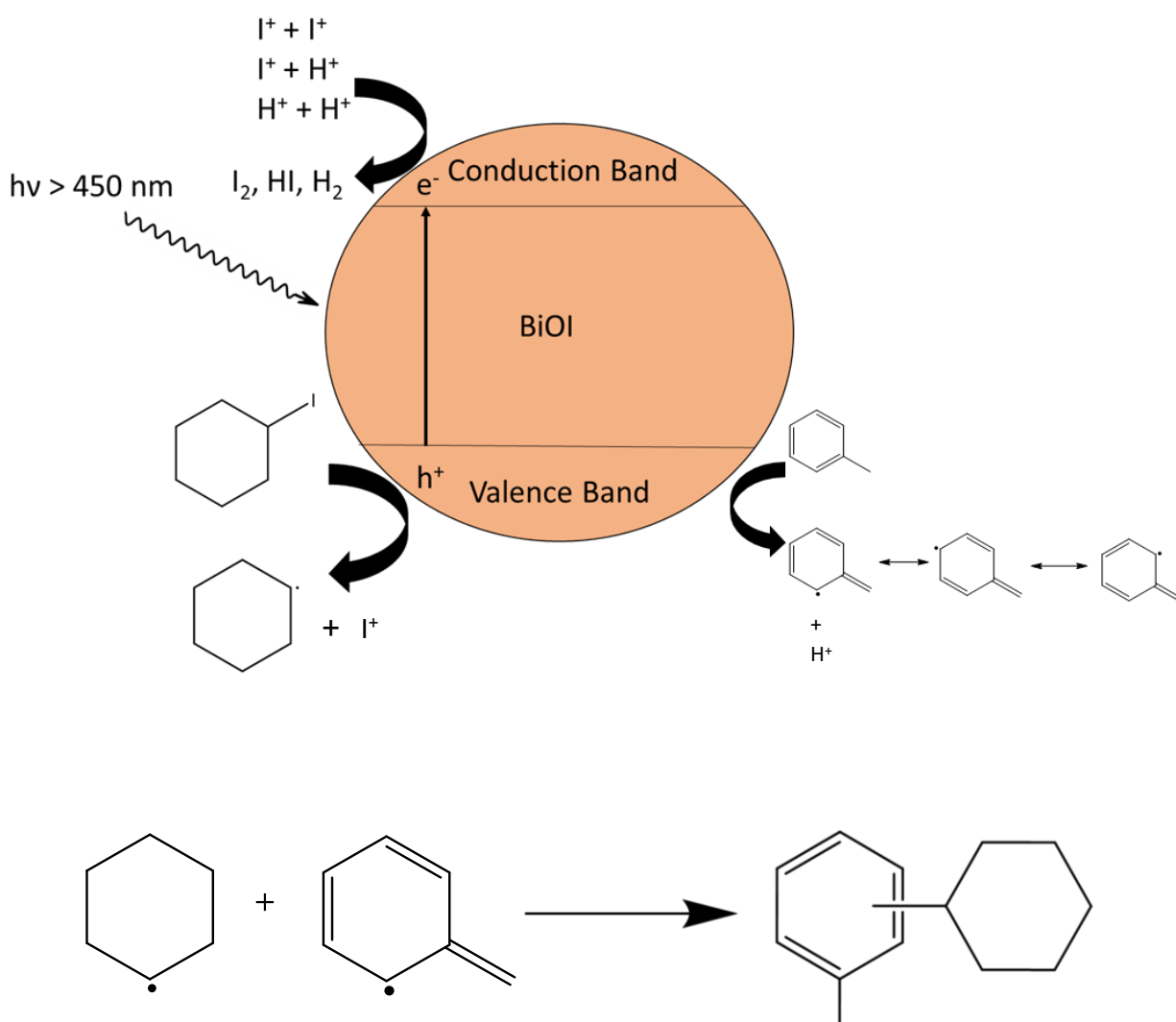
Figure 4.17. Reaction scheme for photocatalytic addition of cyclohexyl halides to toluene.

4.4. Conclusion

This chapter has explored a few applications of visible light and BiOI based photocatalytic systems to industrially relevant reactions. First, the coupling of neat cyclohexane was examined as an analog to natural gas. This reaction would allow the upgrading of dry natural gas to larger molecular weight hydrocarbons that can be used in fuels or other chemical products. The optimized reaction conditions were evaluated using visible light and synthesized BiOI, metal doped BiOI, and BiOI/Zeolite. BiOI/Mordenite was observed to produce the largest yield of bicyclohexane under visible light irradiation conditions. However, the overall yield of the dehydrodimerization reaction is still low, and further work should be conducted in order to increase the industrial relevance of this reaction.

Iodine addition was also investigated with respect to photo-initiation and photocatalysis. Cyclohexane was considered as a substrate for visible light driven photocatalytic addition of iodine. With cyclohexane, it was proposed that a radical addition mechanism was responsible for the addition of iodine. The products of the iodine addition reactions were later used in a two step process with *in situ* generation of substrates for coupling reactions.

Finally, the photocatalytic coupling of aryl compounds with cyclohexyl halides was investigated. These reactions are proposed to proceed through hole driven oxidation followed by radical coupling to the aromatic compound. Iodocyclohexane was found to be the most active cyclohexyl halide for coupling reactions. These reactions show promise for application in the chemical industry, since they all proceed under mild conditions and can be driven by freely available solar irradiation. Further investigation and optimization should be undertaken with industrial partners to realize the advantages presented by this technology.

4.5. References

1. Wood, D. A.; Nwaoha, C.; Towler, B. F. Journal of Natural Gas Science and Engineering Gas-to-liquids (GTL): A review of an industry offering several routes for monetizing natural gas. *J. Nat. Gas Sci. Eng.* **2012**, *9*, 196–208.

2. Lutz, B. New Age Gas-to-Liquid Processing. *Hydrocarb. Eng.* **2001**, *6*, 63–67.

3. Li, L.; Li, G.; Yan, C.; Mu, X.; Pan, X.; Zou, X.; Wang, X.; Chen, J. Efficient Sunlight-Driven Dehydrogenative Coupling of Methane to Ethane over a Zn(+)-Modified Zeolite. *Angew. Chemie Int. Ed.* **2011**, *50*, 8299–8303, doi:10.1002/anie.201102320.

4. Li, L.; Cai, Y.; Li, G.; Mu, X.; Wang, K.; Chen, J. Synergistic Effect on the Photoactivation of the Methane C-H Bond over Ga(3+)-Modified ETS-10. *Angew. Chemie Int. Ed.* **2012**, *51*, 4702–4706, doi:10.1002/anie.201200045.

5. Torborg, C.; Beller, M. Recent Applications of Palladium-Catalyzed Coupling Reactions in the Pharmaceutical, Agrochemical, and Fine Chemical Industries. *Adv. Synth. Catal.* **2009**, *351*, 3027–3043, doi:10.1002/adsc.200900587.

6. Jagtap, S. Heck Reaction—State of the Art. *Catalysts* **2017**, *7*, 267, doi:10.3390/catal7090267.

7. Tyagi, A.; Yamamoto, A.; Kato, T.; Yoshida, H. Bifunctional property of Pt nanoparticles deoposited on TiO2 for the photocatalytic sp3C-sp3C cross-coupling reactions between THF and alkanes. *Catal. Sci. Technol.* **2017**, *7*, 2616–2623, doi:10.1039/c7cy00535k.

8.   Tyagi, A.; Yamamoto, A.; Yoshida, T.; Yoshida, H.; Yamamoto, M. Direct cross-coupling between alkenes and tetrahydrofuran with a platinum-loaded titanium oxide photocatalyst. *Catal. Sci. Technol.* **2018**, *8*, 2546–2556, doi:10.1039/c8cy00129d.

9.   Hörner, G.; Johne, P.; Künneth, R.; Twardzik, G.; Roth, H.; Clark, T.; Kisch, H. Semiconductor Type A Photocatalysis: Role of Substrate Adsorption and the Nature of Photoreactive Surface Sites in Zinc Sulfide Catalyzed C-C Coupling Reactions. *Chem. - A Eur. J.* **1999**, *5*, 208–217.

10.   Künneth, R.; Twardzik, G.; Emig, G.; Kisch, H. Heterogeneous photocatalysis XI . Zinc sulphide catalysed dehydrodimerization of dihydropyrans and cyclohexene. *J. Photochem. Photobiol. A Chem.* **1993**, *76*, 209–215.

11.   Jiao, Z.; Zhai, Z.; Guo, X.; Guo, X. Visible-Light-Driven Photocatalytic Suzuki−Miyaura Coupling Reaction on Mott−Schottky-type Pd/SiC Catalyst. *J. Phys. Chem. C* **2015**, *119*, 3238–3243, doi:10.1021/jp512567h.

12.   Zoller, J.; Fabry, D. C.; Rueping, M. Unexpected Dual Role of Titanium Dioxide in the Visible Light Heterogeneous Catalyzed C−H Arylation of Heteroarenes. *ACS Catal.* **2015**, *5*, 3900–3904, doi:10.1021/acscatal.5b00668.

13.   Buglioni, L.; Riente, P.; Palomares, E.; Pericàs, M. A. Visible-Light-Promoted Arylation Reactions Photocatalyzed by Bismuth(III) Oxide. *European J. Org. Chem.* **2017**, 6986–6990, doi:10.1002/ejoc.201701242.

14.   Arthur, R. B.; Bonin, J. L.; Ardill, L. P.; Rourk, E. J.; Patterson, H. H.; Stemmler, E. A. Photocatalytic degradation of ibuprofen over BiOCl nanosheets with identification of intermediates. *J. Hazard. Mater.* **2018**, *358*, 1–9, doi:10.1016/j.jhazmat.2018.06.018.

15. Moyet, M. A.; Arthur, R. B.; Lueders, E. E.; Breeding, W. P.; Patterson, H. H. The role of Copper (II) ions in Cu-BiOCl for Use in the Photocatalytic Degradation of Atrazine. *J. Environ. Chem. Eng.* **2018**, *6*, 5595–5601, doi:10.1016/j.jece.2018.08.057.

16. Ahern, J. C.; Kanan, S.; Patterson, H. H. Heterogeneous Photocatalysis with Nanoclusters of D10 Metal Ions Doped in Zeolites. *Comments Inorg. Chem.* **2015**, *35*, 59–81, doi:10.1080/02603594.2014.973106.

17. Di, J.; Xia, J.; Yin, S.; Xu, H.; Xu, L.; Xu, Y.; He, M.; Li, H. One-pot solvothermal synthesis of Cu-modified BiOCl via a Cu-containing ionic liquid and its visible-light photocatalytic properties. *RSC Adv.* **2014**, *4*, 14281–14290, doi:10.1039/c3ra45670f.

18. Xia, J.; Xu, L.; Zhang, J.; Yin, S.; Li, H.; Xu, H.; Di, J. Improved visible light photocatalytic properties of Fe/BiOCl microspheres synthesized via self-doped reactable ionic liquids. *CrystEngComm* **2013**, *15*, 10132, doi:10.1039/c3ce41555d.

19. Lee, W.; Lu, C.-S.; Chuang, C.-W.; Chen, Y.-J.; Fu, J.-Y.; Siao, C.-W.; Chen, C.-C. Synthesis of bismuth oxyiodides and their composites: characterization, photocatalytic activity, and degradation mechanisms. *RSC Adv.* **2015**, *5*, 23450–23463, doi:10.1039/C4RA15072D.

REFERENCES

Achilleos, A.; Hapeshi, E.; Xekoukoulotakis, N. P.; Mantzavinos, D.; Fatta-Kassinos, D. UV-A and solar photodegradation of ibuprofen and carbamazepine catalyzed by TiO_2. *Sep. Sci. Technol.* **2010**, *45*, 1564–1570, doi:10.1080/01496395.2010.487463.

Ahern, J. C.; Fairchild, R.; Thomas, J. S.; Carr, J.; Patterson, H. H. Characterization of BiOX compounds as photocatalysts for the degradation of pharmaceuticals in water. *Appl. Catal. B Environ.* **2015**, *179*, 229–238, doi:10.1016/j.apcatb.2015.04.025.

Ahern, J. C.; Kanan, S.; Patterson, H. H. Heterogeneous Photocatalysis with Nanoclusters of D^{10} Metal Ions Doped in Zeolites. *Comments Inorg. Chem.* **2015**, *35*, 59–81, doi:10.1080/02603594.2014.973106.

Ahmad, H.; Kamarudin, S. K.; Minggu, L. J.; Kassim, M. Hydrogen from photo-catalytic water splitting process: A review. *Renew. Sustain. Energy Rev.* **2015**, *43*, 599–610.

Ai, Z.; Ho, W.; Lee, S.; Zhang, L. Efficient photocatalytic removal of NO in indoor air with hierarchical bismuth oxybromide nanoplate microspheres under visible light. *Environ. Sci. Technol.* **2009**, *43*, 4143–4150, doi:10.1021/es9004366.

Albini, A.; Fagnoni, M. 1908: Giacomo Ciamician and the Concept of Green Chemistry. *ChemSusChem* **2008**, *1*, 63–66, doi:10.1002/cssc.200700015.

Ali, I.; Kim, J. Visible-light-assisted photocatalytic activity of bismuth-TiO_2 nanotube composites for chromium reduction and dye degradation. *Chemosphere* **2018**, *207*, 285–292, doi:10.1016/j.chemosphere.2018.05.075.

Ameta, R.; Benjamin, S.; Ameta, A.; Ameta, S. C. Photocatalytic Degradation of Organic Pollutants: A Review. *Mater. Sci. Forum* **2012**, *734*, 247–272, doi:10.4028/www.scientific.net/MSF.734.247.

Bai, Y.; Ye, L.; Chen, T.; Wang, P.; Wang, L.; Shi, X.; Wong, P. K. Synthesis of hierarchical bismuth-rich $Bi_4O_5Br_xI_{2-x}$ solid solutions for enhanced photocatalytic activities of CO_2 conversion and Cr(VI) reduction under visible light. *Appl. Catal. B Environ.* **2017**, *203*, 633–640, doi:10.1016/j.apcatb.2016.10.066.

Baird, N. C. Free Radical Reactions in Aqueous Solutions: Examples from Advanced Oxidation Processes for Wastewater and from the Chemistry in Airborne Water Droplets. *J. Chem. Educ.* **1997**, *74*, 817–819.

Banerjee, S.; Dionysiou, D. D.; Pillai, S. C. Environmental Self-cleaning applications of TiO_2 by photo-induced hydrophilicity and photocatalysis. *Appl. Catal. B Environ.* **2015**, *177*, 396–428.

Bannister, F. A. The crystal structure of the bismuth oxyhalides. *J. Mineral. Soc.* **1935**, *24*, 49–58.

Belgued, M.; Amariglio, H.; Pareja, P.; Amariglio, A.; Saint-Just, J. Low Temperature Catalytic Homologation of Methane on Platinum, Ruthenium and Cobalt. *Catal. Today* **1992**, *13*, 437–445, doi:https://doi.org/10.1016/0920-5861(92)80169-N.

Benisvy, L.; Gamez, P.; Fu, T.; Kooijman, H.; Spek, A. L.; Reedijk, J. Efficient near-UV photosensitization of the Tb(III) green luminescence by use of 2-hydroxyisophthalate ligands. *Dalt. Trans.* **2008**, *3296*, 3147–3149, doi:10.1039/b805507f.

Bhatkhande, D. S.; Pangarkar, V. G.; Beenackers, A. A. Photocatalytic degradation for environmental applications - a review. *J. Chem. Technol. Biotechnol.* **2002**, *77*, 102–116, doi:10.1002/jctb.532.

Boxall, A. B. A.; Rudd, M. A.; Brooks, B. W.; Caldwell, D. J.; Choi, K.; Hickmann, S. Pharmaceuticals and personal care products in the environment: what are the big questions? Alistair B.A. Boxall, Murray A. Rudd, Bryan W. Brooks, Daniel J. Caldwell, Kyungho Choi and Silke Hickmann. *Environ. Health Perspect.* **2012**, *9*, 1221.

Braz, F. S.; Silva, M. R. A.; Silva, F. S.; Andrade, S. J.; Fonseca, A. L.; Kondo, M. M. Photocatalytic Degradation of Ibuprofen Using TiO_2 and Ecotoxicological Assessment of Degradation Intermediates against Daphnia similis. *J. Environ. Prot.* **2014**, *5*, 620–626, doi:10.4236/jep.2014.57063.

Buglioni, L.; Riente, P.; Palomares, E.; Pericàs, M. A. Visible-Light-Promoted Arylation Reactions Photocatalyzed by Bismuth(III) Oxide. *European J. Org. Chem.* **2017**, 6986–6990, doi:10.1002/ejoc.201701242.

Cao, J.; Xu, B.; Luo, B.; Lin, H.; Chen, S. Preparation, characterization and visible-light photocatalytic activity of $AgI/AgCl/TiO_2$. *Appl. Surf. Sci.* **2011**, *257*, 7083–7089, doi:10.1016/j.apsusc.2011.03.046.

Carey, J. H.; Lawrence, J.; Tosine, H. M. Photodechlorination of PCB's in the Presence of Titanium Dioxide in Aqueous Suspensions. *Bull. Environ. Contam. Toxicol.* **1976**, *16*, 697–701.

Carraway, E. R.; Hoffman, A. J.; Hoffmann, M. R. Photocatalytic Oxidation of Organic Acids Colloids Quantum-Sized Semiconductor. *Environ. Sci. Technol.* **1994**, *28*, 786–793.

Castell, J. V.; Gomez-L., M. J.; Miranda, M. A.; Morera, I. M. Photolytic Degradation of Ibuprofen. Toxicity of the Isolated Photoproducts on Fibroblasts and Erythrocytes. *Photochem. Photobiol.* **1987**, *46*, 991–996, doi:10.1111/j.1751-1097.1987.tb04882.x.

Chen, C.; Yang, S.; Guo, Y.; Sun, C.; Gu, C.; Xu, B. Photolytic destruction of endocrine disruptor atrazine in aqueous solution under UV irradiation: Products and pathways. *J. Hazard. Mater.* **2009**, *172*, 675–684, doi:10.1016/j.jhazmat.2009.07.050.

Chen, F.; Yang, Q.; Sun, J.; Yao, F.; Wang, S.; Wang, Y.; Wang, X.; Li, X.; Niu, C.; Wang, D.; Zeng, G. Enhanced Photocatalytic Degradation of Tetracycline by AgI/BiVO$_4$ Heterojunction under Visible-Light Irradiation: Mineralization Efficiency and Mechanism. *ACS Appl. Mater. Interfaces* **2016**, *8*, 32887–32900, doi:10.1021/acsami.6b12278.

Chen, F.; Yang, Q.; Yao, F.; Wang, S.; Sun, J.; An, H.; Yi, K.; Wang, Y.; Zhou, Y.; Wang, L.; Li, X.; Wang, D.; Zeng, G. Visible-light photocatalytic degradation of multiple antibiotics by AgI nanoparticle-sensitized Bi$_5$O$_7$I microspheres: Enhanced interfacial charge transfer based on Z-scheme heterojunctions. *J. Catal.* **2017**, *352*, 160–170, doi:10.1016/j.jcat.2017.04.032.

Chen, S. M.; Lu, N.; Chen, J. Y.; Yang, C. Y.; Yeh, Y. P.; Feng, T. Y.; Shih, Y. H.; Kokulnathan, T.; Chen, D. Enhanced photocatalytic degradation of atrazine by platinized titanium dioxide under 352 nm irradiation. *Water Sci. Technol.* **2017**, *75*, 1128–1137, doi:10.2166/wst.2016.593.

Cheng, H.; Huang, B.; Dai, Y. Engineering BiOX (X = Cl, Br, I) nanostructures for highly efficient photocatalytic applications. *Nanoscale* **2014**, *6*, 2009–2026, doi:10.1039/c3nr05529a.

Cheng, H.; Huang, B.; Wang, P.; Wang, Z.; Lou, Z.; Wang, J.; Qin, X.; Zhang, X.; Dai, Y. In situ ion exchange synthesis of the novel Ag/AgBr/BiOBr hybrid with highly efficient decontamination of pollutants. *Chem. Commun.* **2011**, *47*, 7054–7056, doi:10.1039/c1cc11525a.

Choi, K.; Kang, T.; Oh, S. Preparation of disk shaped ZnO particles using surfactant and their PL properties. *Mater. Lett.* **2012**, *75*, 240–243, doi:10.1016/j.matlet.2012.02.031.

Choina, J.; Kosslick, H.; Fischer, C.; Flechsig, G.-U.; Frunza, L.; Schulz, A. Photocatalytic decomposition of pharmaceutical ibuprofen pollutions in water over titania catalyst. *Appl. Catal. B Environ.* **2013**, *129*, 589–598, doi:10.1016/j.apcatb.2012.09.053.

Cui, P.; Wang, J.; Wang, Z.; Chen, J.; Xing, X.; Wang, L.; Yu, R. Bismuth oxychloride hollow microspheres with high visible light photocatalytic activity. *Nano Res.* **2016**, *9*, 593–601, doi:10.1007/s12274-015-0939-z.

Cunha-Silva, L.; Lima, S.; Ananias, D.; Silva, P.; Mafra, L.; Carlos, L. D.; Pillinger, M.; Valente, A. A.; Almeida Paz, F. A.; Rocha, J. Multi-functional rare-earth hybrid layered networks: photoluminescence and catalysis studies. *J. Mater. Chem.* **2009**, *19*, 2618, doi:10.1039/b817381h.

da Silva, J. C. C.; Teodoro, J. A. R.; Afonso, R. J. D. C. F.; Aquino, S. F.; Augusti, R. Photolysis and photocatalysis of ibuprofen in aqueous medium: characterization of by-products via liquid chromatography coupled to high-resolution mass spectrometry and assessment of their toxicities against Artemia Salina. *J. Mass Spectrom.* **2014**, *49*, 145–153, doi:10.1002/jms.3320.

Dawody, J.; Skoglundh, M.; Fridell, E. The effect of metal oxide additives (WO$_3$, MoO$_3$, V$_2$O$_5$, Ga$_2$O$_3$) on the oxidation of NO and SO$_2$ over Pt/Al$_2$O$_3$ and Pt/BaO/Al$_2$O$_3$ catalysts. *J. Mol. Catal. A Chem.* **2004**, *209*, 215–225, doi:10.1016/j.molcata.2003.08.025.

Di, J.; Xia, J.; Ji, M.; Wang, B.; Yin, S.; Zhang, Q.; Chen, Z.; Li, H. Advanced photocatalytic performance of graphene-like BN modified BiOBr flower-like materials for the removal of pollutants and mechanism insight. *Appl. Catal. B Environ.* **2016**, *183*, 254–262, doi:10.1016/j.apcatb.2015.10.036.

Di, J.; Xia, J.; Ji, M.; Yin, S.; Li, H.; Xu, H.; Zhang, Q.; Li, H. Controllable synthesis of $Bi_4O_5Br_2$ ultrathin nanosheets for photocatalytic removal of ciprofloxacin and mechanism insight. *J. Mater. Chem. A* **2015**, *3*, 15108–15118, doi:10.1039/c5ta02388b.

Di, J.; Xia, J.; Li, H.; Guo, S.; Dai, S. Bismuth oxyhalide layered materials for energy and environmental applications. *Nano Energy* **2017**, *41*, 172–192, doi:10.1016/j.nanoen.2017.09.008.

Di, J.; Xia, J.; Yin, S.; Xu, H.; Xu, L.; Xu, Y.; He, M.; Li, H. One-pot solvothermal synthesis of Cu-modified BiOCl via a Cu-containing ionic liquid and its visible-light photocatalytic properties. *RSC Adv.* **2014**, *4*, 14281–14290, doi:10.1039/c3ra45670f.

Di, J.; Xia, J.; Yin, S.; Xu, H.; Xu, L.; Xu, Y.; He, M.; Li, H. Preparation of sphere-like g-C_3N_4/BiOI photocatalysts via a reactable ionic liquid for visible-light-driven photocatalytic degradation of pollutants. *J. Mater. Chem. A* **2014**, *2*, 5340–5351, doi:10.1039/c3ta14617k.

Dong, F.; Xiong, T.; Yan, S.; Wang, H.; Sun, Y.; Zhang, Y.; Huang, H.; Wu, Z. Facets and defects cooperatively promote visible light plasmonic photocatalysis with Bi nanowires@BiOCl nanosheets. *J. Catal.* **2016**, *344*, 401–410, doi:10.1016/j.jcat.2016.10.005.

Dong, G.; Ho, W.; Zhang, L. Photocatalytic NO removal on BiOI surface: The change from nonselective oxidation to selective oxidation. *Appl. Catal. B Environ.* **2015**, *168–169*, 490–496, doi:10.1016/j.apcatb.2015.01.014.

Duan, F.; Wang, X.; Tan, T.; Chen, M. Highly exposed surface area of {001} facets dominated BiOBr nanosheets with enhanced visible light photocatalytic activity. *Phys. Chem. Chem. Phys.* **2016**, *18*, 6113–6121, doi:10.1039/C5CP06711A.

Fan, W.-Q.; Yu, X.-Q.; Song, S.-Y.; Bai, H.-Y.; Zhang, C.; Yan, D.; Liu, C.-B.; Wang, Q.; Shi, W.-D. Fabrication of TiO_2–BiOCl double-layer nanostructure arrays for photoelectrochemical water splitting. *CrystEngComm* **2014**, *16*, 820–825, doi:10.1039/C3CE42001A.

Fang, H.; Lian, J.; Wang, H.; Cai, L.; Yu, Y. Exploring bacterial community structure and function associated with atrazine biodegradation in repeatedly treated soils. *J. Hazard. Mater.* **2015**, *286*, 457–465, doi:10.1016/j.jhazmat.2015.01.006.

Feng, Y.; Liu, C.; Chen, J.; Che, H.; Xiao, L.; Gu, W.; Shi, W. Facile synthesis of BiOI/$CdWO_4$ p–n junctions: enhanced photocatalytic activities and photoelectrochemistry. *RSC Adv.* **2016**, *6*, 38290–38299, doi:10.1039/C5RA23383F.

Ferreira, V. C.; Neves, M. C.; Hillman, A. R.; Monteiro, O. C. Novel one-pot synthesis and sensitisation of new BiOCl–Bi$_2$S$_3$ nanostructures from DES medium displaying high photocatalytic activity. *RSC Adv.* **2016**, *6*, 77329–77339, doi:10.1039/C6RA14474H.

Friedmann, D.; Hakki, A.; Kim, H.; Choi, W.; Bahnemann, D. Heterogeneous photocatalytic organic synthesis: state-of-the-art and future perspectives. *Green Chem.* **2016**, *18*, 5391–5411, doi:10.1039/c6gc01582d.

Friedmann, D.; Mendive, C.; Bahnemann, D. TiO$_2$ for water treatment: Parameters affecting the kinetics and mechanisms of photocatalysis. *Appl. Catal. B Environ.* **2010**, *99*, 398–406, doi:10.1016/j.apcatb.2010.05.014.

Fujishima, A.; Honda, K. Electrochemical Photolysis of Water at a Semiconductor Electrode. *Nature* **1972**, *238*, 37, doi:10.1038/239137a0.

Gamarra, J. S.; Godoi, A. F. L.; de Vasconcelos, E. C.; de Souza, K. M. T.; Ribas de Oliveira, C. M. Environmental Risk Assessment (ERA) of diclofenac and ibuprofen: A public health perspective. *Chemosphere* **2015**, *120*, 462–469, doi:10.1016/j.chemosphere.2014.08.020.

Gammon, D. W.; Silva, M.; Aldous, C.; Sanborn, J. R.; Carr, W. C.; Pfeifer, K.; Schreider, J. P. Atrazine: Risk characterization document. *Med. Toxicol. Branch, Calif. Dep. Pestic. Regul. Calif. Environ. Prot. Agency* **2001**.

Gao, S.; Guo, C.; Lv, J.; Wang, Q.; Zhang, Y.; Hou, S.; Gao, J.; Xu, J. A novel 3D hollow magnetic Fe$_3$O$_4$/BiOI heterojunction with enhanced photocatalytic performance for bisphenol A degradation. *Chem. Eng. J.* **2017**, *307*, 1055–1065, doi:10.1016/j.cej.2016.09.032.

Gao, X.; Zhang, X.; Wang, Y.; Peng, S.; Yue, B.; Fan, C. Rapid synthesis of hierarchical BiOCl microspheres for efficient photocatalytic degradation of carbamazepine under simulated solar irradiation. *Chem. Eng. J.* **2015**, *263*, 419–426, doi:10.1016/j.cej.2014.10.110.

Granados-Oliveros, G.; Páez-Mozo, E. A.; Ortega, F. M.; Ferronato, C.; Chovelon, J. M. Degradation of atrazine using metalloporphyrins supported on TiO$_2$ under visible light irradiation. *Appl. Catal. B Environ.* **2009**, *89*, 448–454, doi:10.1016/j.apcatb.2009.01.001.

Gul, M.; Kotak, Y.; Muneer, T. Review on recent trend of solar photovoltaic technology. *Energy Explor. Exploit.* **2016**, *34*, 485–526, doi:10.1177/0144598716650552.

Haider, Z.; Zheng, J. Y.; Kang, Y. S. Surfactant free fabrication and improved charge carrier separation induced enhanced photocatalytic activity of {001} facet exposed unique octagonal BiOCl nanosheets. *Phys. Chem. Chem. Phys.* **2016**, *18*, 19595–19604, doi:10.1039/C6CP01740A.

Hao, R.; Xiao, X.; Zuo, X.; Nan, J.; Zhang, W. Efficient adsorption and visible-light photocatalytic degradation of tetracycline hydrochloride using mesoporous BiOI microspheres. *J. Hazard. Mater.* **2012**, *209–210*, 137–145, doi:10.1016/j.jhazmat.2012.01.006.

Heberer, T. Occurrence, fate, and removal of pharmaceutical residues in the aquatic environment: a review of recent research data. *Toxicol. Lett.* **2002**, *131*, 5–17, doi:10.1016/S0378-4274(02)00041-3.

Henríquez, A.; Mansilla, H. D.; Martínez, A.; Cruz, M.; Freer, J.; Contreras, D. Selective oxofunctionalization of cyclohexane over titanium dioxide – based and bismuth oxyhalide (BiOX, X = Cl, Br, I) photocatalysts by visible light irradiation. *Appl. Catal. B Environ.* **2017**, *206*, 252–262.

Hoffmann, M. R.; Martin, S. T.; Choi, W.; Bahnemann, D. W. Environmental Applications of Semiconductor Photocatalysis. *Chem. Rev.* **1995**, *95*, 69–96.

Hörner, G.; Johne, P.; Künneth, R.; Twardzik, G.; Roth, H.; Clark, T.; Kisch, H. Semiconductor Type A Photocatalysis: Role of Substrate Adsorption and the Nature of Photoreactive Surface Sites in Zinc Sulfide Catalyzed C-C Coupling Reactions. *Chem. - A Eur. J.* **1999**, *5*, 208–217.

Huang, C.; Hu, J.; Cong, S.; Zhao, Z.; Qiu, X. Hierarchical BiOCl microflowers with improved visible-light-driven photocatalytic activity by Fe(III) modification. *Appl. Catal. B Environ.* **2015**, *174–175*, 105–112, doi:10.1016/j.apcatb.2015.03.001.

Huang, R.; Southall, N.; Wang, Y.; Yasgar, A.; Shinn, P.; Jadhav, A.; Nguyen, D. T.; Austin, C. P. The NCGC pharmaceutical collection: A comprehensive resource of clinically approved drugs enabling repurposing and chemical genomics. *Sci. Transl. Med.* 2011, *3*.

IHDRC Crude Oil and Natural Gas: From Source to Final Products Available online: https://www.ihrdc.com/els/po-demo/module01/mod_001_02.htm., Accessed 3/15/2019.

Illés, E.; Takács, E.; Dombi, A.; Gajda-Schrantz, K.; Rácz, G.; Gonter, K.; Wojnárovits, L. Hydroxyl radical induced degradation of ibuprofen. *Sci. Total Environ.* **2013**, *447*, 286–292, doi:10.1016/j.scitotenv.2013.01.007.

Jablonowski, N. D.; Schäffer, A.; Burauel, P. Still present after all these years: Persistence plus potential toxicity raise questions about the use of atrazine. *Environ. Sci. Pollut. Res.* **2011**, *18*, 328–331, doi:10.1007/s11356-010-0431-y.

Jackson, H. Maine Board of Pesticides Control Pesticides and Gound Water Monitoring Program. **2006**, *28*.

Jacobs, L. E.; Fimmen, R. L.; Chin, Y.-P.; Mash, H. E.; Weavers, L. K. Fulvic acid mediated photolysis of ibuprofen in water. *Water Res.* **2011**, *45*, 4449–4458, doi:10.1016/j.watres.2011.05.041.

Jagtap, S. Heck Reaction—State of the Art. *Catalysts* **2017**, *7*, 267, doi:10.3390/catal7090267.

Jakimska, A.; Śliwka-Kaszyńska, M.; Reszczyńska, J.; Namieśnik, J.; Kot-Wasik, A. Elucidation of transformation pathway of ketoprofen, ibuprofen, and furosemide in surface water and their occurrence in the aqueous environment using UHPLC-QTOF-MS. *Anal. Bioanal. Chem.* **2014**, *406*, 3667–3680, doi:10.1007/s00216-014-7614-1.

Jia, X.; Cao, J.; Lin, H.; Zhang, M.; Guo, X.; Chen, S. Transforming type-I to type-II heterostructure photocatalyst via energy band engineering: A case study of I-BiOCl/I-BiOBr. *Appl. Catal. B Environ.* **2017**, *204*, 505–514, doi:10.1016/j.apcatb.2016.11.061.

Jiao, Z.; Zhai, Z.; Guo, X.; Guo, X. Visible-Light-Driven Photocatalytic Suzuki−Miyaura Coupling Reaction on Mott−Schottky-type Pd/SiC Catalyst. *J. Phys. Chem. C* **2015**, *119*, 3238–3243, doi:10.1021/jp512567h.

Jin, J.; Wang, Y.; He, T. Preparation of thickness-tunable BiOCl nanosheets with high photocatalytic activity for photoreduction of CO_2. *RSC Adv.* **2015**, *5*, 100244–100250, doi:10.1039/C5RA21888H.

Jones, J. G. Pollution from Fish Farms. *Water Environ. J.* **1990**, *4*, 14–18, doi:10.1111/j.1747-6593.1990.tb01552.x.

Jones, O. A.; Lester, J. N.; Voulvoulis, N. Pharmaceuticals: a threat to drinking water? *Trends Biotechnol.* **2005**, *23*, 163–167, doi:10.1016/j.tibtech.2005.02.001.

Jux, U.; Baginski, R. M.; Arnold, H.-G.; Krönke, M.; Seng, P. N. Detection of pharmaceutical contaminations of river, pond, and tap water from Cologne (Germany) and surroundings. *Int. J. Hyg. Environ. Health* **2002**, *205*, 393–398, doi:10.1078/1438-4639-00166.

Kaldas, S. J.; Cannillo, A.; Mccallum, T.; Barriault, L. Indole Functionalization via Photoredox Gold Catalysis. *Org. Lett.* **2015**, *17*, 2864–2866, doi:10.1021/acs.orglett.5b01260.

Kato, Y.; Yoshida, H.; Hattori, T. Photoinduced non-oxidative coupling of methane over silica-alumina and alumina around room temperature. *Chem. Commun.* **1998**, 2389–2390.

Katsumiti, A.; Gilliland, D.; Arostegui, I.; Cajaraville, M. P. Cytotoxicity and cellular mechanisms involved in the toxicity of CdS quantum dots in hemocytes and gill cells of the mussel Mytilus galloprovincialis. *Aquat. Toxicol.* **2014**, *153*, 39–52.

Kelly, A. W.; Nicholas, A.; Ahern, J. C.; Chan, B.; Patterson, H. H.; Pike, R. D. Alkali metal bismuth(III) chloride double salts. *J. Alloys Compd.* **2016**, *670*, 337–345, doi:10.1016/j.jallcom.2016.02.055.

Kisch, H. Semiconductor Photocatalysis for Chemoselective Radical Coupling Reactions. *Acc. Chem. Res.* **2017**, *50*, 1002–1010, doi:10.1021/acs.accounts.7b00023.

Kolpin, D. W.; Furlong, E. T.; Meyer, M. T.; Thurman, E. M.; Zaugg, S. D.; Barber, L. B.; Buxton, H. T. Pharmaceuticals, Hormones, and Other Organic Wastewater Contaminants in U.S. Streams, 1999−2000: A National Reconnaissance. *Environ. Sci. Technol.* **2002**, *36*, 1202–1211, doi:10.1021/es011055j.

Kong, T.; Wei, X.; Zhu, G.; Huang, Y. First-principles studies on facet-dependent photocatalytic properties of BiOI {001} surface. *J. Mater. Sci.* **2017**, *52*, 5686–5695, doi:10.1007/s10853-017-0803-5.

Konstantinou, I. K.; Albanis, T. A. TiO_2-assisted photocatalytic degradation of azo dyes in aqueous solution: kinetic and mechanistic investigations. *Appl. Catal. B Environ.* **2004**, *49*, 1–14, doi:10.1016/j.apcatb.2003.11.010.

Krasner, S. W.; Weinberg, H. S.; Richardson, S. D.; Pastor, S. J.; Chinn, R.; Sclimenti, M. J.; Onstad, G. D.; Thruston, A. D. Occurrence of a new generation of disinfection byproducts. *Environ. Sci. Technol.* **2006**, *40*, 7175–7185, doi:10.1021/es060353j.

Kümmerer, K. Drugs in the environment: emission of drugs, diagnostic aids and disinfectants into wastewater by hospitals in relation to other sources – a review. *Chemosphere* **2001**, *45*, 957–969, doi:10.1016/S0045-6535(01)00144-8.

Künneth, R.; Twardzik, G.; Emig, G.; Kisch, H. Heterogeneous photocatalysis XI . Zinc sulphide catalysed dehydrodimerization of dihydropyrans and cyclohexene. *J. Photochem. Photobiol. A Chem.* **1993**, *76*, 209–215.

Lee, W. W.; Lu, C. S.; Chuang, C. W.; Chen, Y. J.; Fu, J. Y.; Siao, C. W.; Chen, C. C. Synthesis of bismuth oxyiodides and their composites: characterization, photocatalytic activity, and degradation mechanisms. *RSC Adv.* **2015**, *5*, 23450–23463, doi:10.1039/C4RA15072D.

Lei, L.; Jin, H.; Zhang, Q.; Xu, J.; Gao, D.; Fu, Z. A novel enhanced visible-light-driven photocatalyst via hybridization of nanosized BiOCl and graphitic C_3N_4. *Dalt. Trans.* **2015**, *44*, 795–803, doi:10.1039/C4DT02082K.

Lei, Y.; Wang, G.; Song, S.; Fan, W.; Zhang, H. Synthesis, characterization and assembly of BiOCl nanostructure and their photocatalytic properties. *CrystEngComm* **2009**, *11*, 1857, doi:10.1039/b909013b.

Lester, Y.; Avisar, D.; Gnayem, H.; Sasson, Y.; Shavit, M.; Mamane, H. Demonstrating a New $BiOCl_{0.875}Br_{0.125}$ Photocatalyst to Degrade Pharmaceuticals Under Solar Irradiation. *Water, Air, Soil Pollut.* **2014**, *225*, 2132, doi:10.1007/s11270-014-2132-5.

Li, F. H.; Yao, K.; Lv, W. Y.; Liu, G. G.; Chen, P.; Huang, H. P.; Kang, Y. P. Photodegradation of Ibuprofen Under UV−Vis Irradiation: Mechanism and Toxicity of Photolysis Products. *Bull. Environ. Contam. Toxicol.* **2015**, *94*, 479–483, doi:10.1007/s00128-015-1494-8.

Li, G.; Jiang, B.; Xiao, S.; Lian, Z.; Zhang, D.; Yu, J. C.; Li, H. An efficient dye-sensitized BiOCl photocatalyst for air and water purification under visible light irradiation. *Environ. Sci. Process. Impacts* **2014**, *16*, 1975–1980, doi:10.1039/C4EM00196F.

Li, G.; Qin, F.; Wang, R.; Xiao, S.; Sun, H.; Chen, R. Journal of Colloid and Interface Science BiOX (X = Cl, Br, I) nanostructures: Mannitol-mediated microwave synthesis, visible light photocatalytic performance, and Cr(VI) removal capacity. *J. Colloid Interface Sci.* **2013**, *409*, 43–51, doi:10.1016/j.jcis.2013.07.068.

Li, G.; Qin, F.; Yang, H.; Lu, Z.; Sun, H.; Chen, R. Facile microwave synthesis of 3D flowerlike BiOBr nanostructures and their excellent Cr^{VI} removal capacity. *Eur. J. Inorg. Chem.* **2012**, 2508–2513, doi:10.1002/ejic.201101427.

Li, H.; Shang, J.; Ai, Z.; Zhang, L. Efficient visible light nitrogen fixation with BiOBr nanosheets of oxygen vacancies on the exposed {001} facets. *J. Am. Chem. Soc.* **2015**, *137*, 6393–6399, doi:10.1021/jacs.5b03105.

Li, H.; Shang, J.; Shi, J.; Zhao, K.; Zhang, L. Facet-dependent solar ammonia synthesis of BiOCl nanosheets via a proton-assisted electron transfer pathway. *Nanoscale* **2016**, *8*, 1986–1993, doi:10.1039/c5nr07380d.

Li, H.; Shi, J.; Zhao, K.; Zhang, L. Sustainable molecular oxygen activation with oxygen vacancies on the {001} facets of BiOCl nanosheets under solar light. *Nanoscale* **2014**, *6*, 14168–14173, doi:10.1039/C4NR04810E.

Li, H.; Zhang, L. Oxygen vacancy induced selective silver deposition on the {001} facets of BiOCl single-crystalline nanosheets for enhanced Cr(VI) and sodium pentachlorophenate removal under visible light. *Nanoscale* **2014**, *6*, 7805–7810, doi:10.1039/C4NR01315H.

Li, J.; Sun, S.; Chen, R.; Zhang, T.; Ren, B.; Dionysiou, D. D.; Wu, Z.; Liu, X.; Ye, M. Adsorption behavior and mechanism of ibuprofen onto BiOCl microspheres with exposed {001} facets. *Environ. Sci. Pollut. Res.* **2017**, *24*, 9556–9565, doi:10.1007/s11356-017-8564-x.

Li, J.; Sun, S.; Qian, C.; He, L.; Chen, K. K.; Zhang, T.; Chen, Z.; Ye, M. The role of adsorption in photocatalytic degradation of ibuprofen under visible light irradiation by BiOBr microspheres. *Chem. Eng. J.* **2016**, *297*, 139–147, doi:10.1016/j.cej.2016.03.145.

Li, J.; Zhang, L.; Li, Y.; Yu, Y. Synthesis and internal electric field dependent photoreactivity of Bi3O4Cl single-crystalline nanosheets with high {001} facet exposure percentages. *Nanoscale* **2014**, *6*, 167–171, doi:10.1039/c3nr05246j.

Li, L.; Cai, Y.; Li, G.; Mu, X.; Wang, K.; Chen, J. Synergistic Effect on the Photoactivation of the Methane C-H Bond over Ga^{3+}-Modified ETS-10. *Angew. Chemie Int. Ed.* **2012**, *51*, 4702–4706, doi:10.1002/anie.201200045.

Li, L.; Li, G.; Yan, C.; Mu, X.; Pan, X.; Zou, X.; Wang, X.; Chen, J. Efficient Sunlight-Driven Dehydrogenative Coupling of Methane to Ethane over a Zn$^+$-Modified Zeolite. *Angew. Chemie Int. Ed.* **2011**, *50*, 8299–8303, doi:10.1002/anie.201102320.

Li, Q.; Zhao, X.; Yang, J.; Jia, C.-J.; Jin, Z.; Fan, W. Exploring the effects of nanocrystal facet orientations in g-C3N4/BiOCl heterostructures on photocatalytic performance. *Nanoscale* **2015**, *7*, 18971–18983, doi:10.1039/c5nr05154a.

Li, Y.; Wang, J.; Yao, H.; Dang, L.; Li, Z. Efficient decomposition of organic compounds and reaction mechanism with BiOI photocatalyst under visible light irradiation. *J. Mol. Catal. A Chem.* **2011**, *334*, 116–122, doi:10.1016/j.molcata.2010.11.005.

Libanori, R.; Giraldi, T. R.; Longo, E.; Leite, E. R.; Ribeiro, C. Effect of TiO$_2$ surface modification in Rhodamine B photodegradation. *J. Sol-Gel Sci. Technol.* **2009**, *49*, 95–100, doi:10.1007/s10971-008-1821-1.

Lin, H.; Ding, L.; Pei, Z.; Zhou, Y.; Long, J.; Deng, W.; Wang, X. Au deposited BiOCl with different facets: On determination of the facet-induced transfer preference of charge carriers and the different plasmonic activity. *Appl. Catal. B Environ.* **2014**, *160–161*, 98–105, doi:10.1016/j.apcatb.2014.05.018.

Lin, H.; Li, X.; Cao, J.; Chen, S.; Chen, Y. Novel I$^-$-doped BiOBr composites: Modulated valence bands and largely enhanced visible light phtotocatalytic activities. *Catal. Commun.* **2014**, *49*, 87–91, doi:10.1016/j.catcom.2014.02.010.

Lin, X.; Huang, T.; Huang, F.; Wang, W.; Shi, J. Photocatalytic Activity of a Bi-Based Oxychloride Bi$_3$O$_4$Cl. *J. Phys. Chem. B* **2006**, *110*, 24629–24634, doi:10.1021/jp065373m.

Lindholm-Lehto, P. C.; Ahkola, H. S. J.; Knuutinen, J. S.; Herve, S. H. Widespread occurrence and seasonal variation of pharmaceuticals in surface waters and municipal wastewater treatment plants in central Finland. *Environ. Sci. Pollut. Res.* **2016**, *23*, 7985–7997, doi:10.1007/s11356-015-5997-y.

Liu, R.; Wu, Z.; Tian, J.; Yu, C.; Li, S.; Yang, K.; Liu, X.; Liu, M. The excellent dye-photosensitized degradation performance over hierarchical BiOCl nanostructures fabricated via a facile microwave-hydrothermal process. *New J. Chem.* **2018**, *42*, 137–149, doi:10.1039/C7NJ02990J.

Liu, Y.; Xu, J.; Wang, L.; Zhang, H.; Xu, P.; Duan, X.; Sun, H.; Wang, S. Three-Dimensional BiOI/BiOX (X = Cl or Br) Nanohybrids for Enhanced Visible-Light Photocatalytic Activity. *Nanomater.* **2017**, *7*, 64, doi:10.3390/nano7030064.

Liu, Z.; Liu, J.; Wang, H.; Cao, G.; Niu, J. Boron-doped bismuth oxybromide microspheres with enhanced surface hydroxyl groups: Synthesis, characterization and dramatic photocatalytic activity. *J. Colloid Interface Sci.* **2016**, *463*, 324–331, doi:10.1016/j.jcis.2015.10.028.

Lutz, B. New Age Gas-to-Liquid Processing. *Hydrocarb. Eng.* **2001**, *6*, 63–67.

Mao, X.; Li, X.; Wang, Y.; Fan, C.; Zhang, H. KI/H_2O_2 assisted synthesis and the changed properties of BiOCl photocatalysts. *Chem. Eng. J.* **2014**, *247*, 241–249, doi:10.1016/j.cej.2014.02.020.

Mendez-Arriaga, F.; Torres-Palma, R. A.; Petrier, C.; Esplugas, S.; Gimenez, J.; Pulgarin, C. Ultrasonic treatment of water contaminated with ibuprofen. *Water Res.* **2008**, *42*, 4243–4248, doi:10.1016/j.watres.2008.05.033.

Michael, I.; Achilleos, A.; Lambropoulou, D.; Torrens, V. O.; Pérez, S.; Petrović, M.; Barceló, D.; Fatta-Kassinos, D. Proposed transformation pathway and evolution profile of diclofenac and ibuprofen transformation products during (sono)photocatalysis. *Appl. Catal. B Environ.* **2014**, *147*, 1015–1027, doi:10.1016/j.apcatb.2013.10.035.

Miranda-García, N.; Suárez, S.; Sánchez, B.; Coronado, J. M.; Malato, S.; Maldonado, M. I. Photocatalytic degradation of emerging contaminants in municipal wastewater treatment plant effluents using immobilized TiO_2 in a solar pilot plant. *Appl. Catal. B Environ.* **2011**, *103*, 294–301, doi:10.1016/j.apcatb.2011.01.030.

Mitzi, D.B., Feild, C.A., Harrison, W. T. A., Guloy, A. M. A low-cost, high-efficiency solar cell based on dye-sensitized colloidal TiO_2 films. *Nature* **1994**, *367*, 532–8, doi:10.1038/350055a0.

Murdoch, R. W.; Hay, A. G. Genetic and chemical characterization of ibuprofen degradation by Sphingomonas Ibu-2. *Microbiology* **2013**, *159*, 621–632, doi:10.1099/mic.0.062273-0.

Offermanns, S.; Rosenthal, W. *Encyclopedic Reference of Molecular Pharmacology*; 1st ed.; Springer Verlag: Berlin, 2004

Ollis, D. F. Photocatalytic purification and remediation of contaminated air and water. *Surf. Chem. Catal.* **2000**, *3*, 405–411.

Ong, W. J.; Tan, L. L.; Chai, S. P.; Yong, S. T.; Mohamed, A. R. Facet-dependent photocatalytic properties of TiO_2-based composites for energy conversion and environmental remediation. *ChemSusChem* **2014**, *7*, 690–719, doi:10.1002/cssc.201300924.

Pan, Z.; Stemmler, E. A.; Cho, H. J.; Fan, W.; LeBlanc, L. A.; Patterson, H. H.; Amirbahman, A. Photocatalytic degradation of 17α-ethinylestradiol (EE2) in the presence of TiO_2-doped zeolite. *J. Hazard. Mater.* **2014**, *279*, 17–25, doi:10.1016/j.jhazmat.2014.06.040.

Pantelaki, I.; Voutsa, D. Formation of iodinated THMs during chlorination of water and wastewater in the presence of different iodine sources. *Sci. Total Environ.* **2018**, *613–614*, 389–397, doi:10.1016/j.scitotenv.2017.09.072.

Pathirana, H. M. K. K.; Maithreepala, R. A. Photodegradation of 3,4-dichloropropionamide in aqueous TiO_2 suspensions. *J. Photochem. Photobiol. A Chem.* **1997**, *102*, 273–277, doi:10.1016/S1010-6030(96)04455-3.

Peng, Y.; Wang, D.; Zhou, H.-Y.; Xu, A.-W. Controlled synthesis of thin BiOCl nanosheets with exposed {001} facets and enhanced photocatalytic activities. *CrystEngComm* **2015**, *17*, 3845–3851, doi:10.1039/C5CE00289C.

Pomati, F.; Netting, A. G.; Calamari, D.; Neilan, B. A. Effects of erythromycin, tetracycline and ibuprofen on the growth of Synechocystis sp. and Lemna minor. *Aquat. Toxicol.* **2004**, *67*, 387–396, doi:10.1016/j.aquatox.2004.02.001.

Qamar, M.; Yamani, Z. H. Bismuth oxychloride-mediated and laser-induced efficient reduction of Cr(VI) in aqueous suspensions. *Appl. Catal. A Gen.* **2012**, *439–440*, 187–191, doi:10.1016/j.apcata.2012.07.004.

Rajamanickam, D.; Shanthi, M. Photocatalytic degradation of an organic pollutant by zinc oxide – solar process. *Arab. J. Chem.* **2016**, *9*, 1858–1868.

Rawashdeh-Omary, M. A.; Omary, M. A.; Patterson, H. H.; May, R. V Oligomerization of $Au(CN)^{2-}$ and $Ag(CN)^{2-}$ Ions in Solution via Ground-State Aurophilic and Argentophilic Bonding. *J. Am. Chem. Soc.* **2000**, *122*, 10371–10380.

Richardson, M. L.; Bowron, J. M. The fate of pharmaceutical chemicals in the aquatic environment. *J. Pharm. Pharmacol.* **1985**, *37*, 1–12, doi:10.1111/j.2042-7158.1985.tb04922.x.

Rigos, G.; Nengas, I.; Alexis, M.; Troisi, G. M. Potential drug (oxytetracycline and oxolinic acid) pollution from Mediterranean sparid fish farms. *Aquat. Toxicol.* **2004**, *69*, 281–288, doi:10.1016/j.aquatox.2004.05.009.

Rowe, A. M.; Brundage, K. M.; Barnett, J. B. Developmental immunotoxicity of atrazine in rodents. *Basic Clin. Pharmacol. Toxicol.* **2008**, *102*, 139–145, doi:10.1111/j.1742-7843.2007.00175.x.

Ruggeri, G.; Ghigo, G.; Maurino, V.; Minero, C.; Vione, D. Photochemical transformation of ibuprofen into harmful 4-isobutylacetophenone: Pathways, kinetics, and significance for surface waters. *Water Res.* **2013**, *47*, 6109–6121, doi:10.1016/j.watres.2013.07.031.

Sánchez-Rodríguez, D.; Méndez Medrano, M. G.; Remita, H.; Escobar-Barrios, V. Photocatalytic properties of $BiOCl$-TiO_2 composites for phenol photodegradation. *J. Environ. Chem. Eng.* **2018**, *6*, 1601–1612, doi:10.1016/j.jece.2018.01.061.

Santacruz-Chávez, J. A.; Oros-Ruiz, S.; Prado, B.; Zanella, R. Photocatalytic degradation of atrazine using TiO_2 superficially modified with metallic nanoparticles. *J. Environ. Chem. Eng.* **2015**, *3*, 3055–3061, doi:10.1016/j.jece.2015.04.025.

Sarwan, B.; Pare, B.; Acharya, A. D.; Jonnalagadda, S. B. Mineralization and toxicity reduction of textile dye neutral red in aqueous phase using BiOCl photocatalysis. *J. Photochem. Photobiol. B Biol.* **2012**, *116*, 48–55, doi:10.1016/j.jphotobiol.2012.07.006.

Schwarz, P. F.; Turro, N. J.; Bossmann, S. H.; Braun, A. M.; Wahab, A. A. A. A New Method To Determine the Generation of Hydroxyl Radicals in Illuminated TiO_2 Suspensions. *J. Phys. Chem. B* **1997**, *5647*, 7127–7134.

Sfaelou, S.; Raptis, D.; Dracopoulos, V.; Lianos, P. BiOI solar cells. *RSC Adv.* **2015**, *5*, 95813–95816, doi:10.1039/C5RA19835F.

Shamsedini, N.; Dehghani, M.; Nasseri, S.; Baghapour, M. A. Photocatalytic degradation of atrazine herbicide with Illuminated Fe^{+3}-TiO_2 Nanoparticles. *J. Environ. Heal. Sci. Eng.* **2017**, *15*, 7, doi:10.1186/s40201-017-0270-6.

Shang, J.; Hao, W.; Lv, X.; Wang, T.; Wang, X.; Du, Y.; Dou, S.; Xie, T.; Wang, D.; Wang, J. Bismuth oxybromide with reasonable photocatalytic reduction activity under visible light. *ACS Catal.* **2014**, *4*, 954–961, doi:10.1021/cs401025u.

Shavisi, Y.; Sharifnia, S.; Zendehzaban, M.; Mirghavami, M. L.; Kakehazar, S. Application of solar light for degradation of ammonia in petrochemical wastewater by a floating TiO_2/LECA photocatalyst. *J. Ind. Eng. Chem.* **2014**, *20*, 2806–2813, doi:10.1016/j.jiec.2013.11.011.

Shimura, K.; Yoshida, H. Semiconductor Photocatalysts for Non-oxidative Coupling, Dry Reforming and Steam Reforming of Methane. *Catal. Surv. Asia* **2014**, *18*, 24–33, doi:10.1007/s10563-014-9165-z.

Simsek, E. B. Solvothermal synthesized boron doped TiO2 catalysts: Photocatalytic degradation of endocrine disrupting compounds and pharmaceuticals under visible light irradiation. *Appl. Catal. B Environ.* **2017**, *200*, 309–322, doi:10.1016/j.apcatb.2016.07.016.

Song, G.; Wu, X.; Xin, F.; Yin, X. $ZnFe_2O_4$ deposited on BiOCl with exposed (001) and (010) facets for photocatalytic reduction of CO_2 in cyclohexanol. *Front. Chem. Sci. Eng.* **2017**, *11*, 197–204, doi:10.1007/s11705-016-1606-y.

Song, J.; Wang, B.; Guo, X.; Wang, R.; Dong, Z. Hierarchical nanostructured 3D flowerlike BiOX particles with excellent visible-light photocatalytic activity. *J. Nanoparticle Res.* **2016**, *18*, 1–11, doi:10.1007/s11051-016-3556-1.

Song, Z.; Dong, X.; Wang, N.; Zhu, L.; Luo, Z.; Fang, J.; Xiong, C. Efficient photocatalytic defluorination of perfluorooctanoic acid over BiOCl nanosheets via a hole direct oxidation mechanism. *Chem. Eng. J.* **2017**, *317*, 925–934, doi:10.1016/j.cej.2017.02.126.

Sudrajat, H.; Sujaridworakun, P. Insights into structural properties of Cu species loaded on Bi_2O_3 hierarchical structures for highly enhanced photocatalysis. *J. Catal.* **2017**, *352*, 394–400, doi:10.1016/j.jcat.2017.05.027.

Sun, M.; Zhao, Q.; Du, C.; Liu, Z. Enhanced visible light photocatalytic activity in BiOCl/SnO$_2$: heterojunction of two wide band-gap semiconductors. *RSC Adv.* **2015**, *5*, 22740–22752, doi:10.1039/C4RA14187C.

Szabó, R. K.; Megyeri, C.; Illés, E.; Gajda-Schrantz, K.; Mazellier, P.; Dombi, A. Phototransformation of ibuprofen and ketoprofen in aqueous solutions. *Chemosphere* **2011**, *84*, 1658–1663, doi:10.1016/j.chemosphere.2011.05.012.

Tan, C.; Zhu, G.; Hojamberdiev, M.; Okada, K.; Liang, J.; Luo, X.; Liu, P.; Liu, Y. Co$_3$O$_4$ nanoparticles-loaded BiOCl nanoplates with the dominant {001} facets: efficient photodegradation of organic dyes under visible light. *Appl. Catal. B Environ.* **2014**, *152–153*, 425–436, doi:10.1016/j.apcatb.2014.01.044.

Tang, H.; Berger, H.; Schmid, P. E.; Lévy, F.; Burri, G. Photoluminescence in TiO$_2$ anatase single crystals. *Solid State Commun.* **1993**, *87*, 847–850, doi:10.1016/0038-1098(93)90427-O.

Ternes, T. A. Analytical methods for the determination of pharmaceuticals in aqueous environmental samples. *TrAC - Trends Anal. Chem.* **2001**, *20*, 419–434, doi:10.1016/S0165-9936(01)00078-4.

Tobergte, D. R.; Curtis, S. *Environmentally Benign Photocatalysts Applications of Titanium Oxide-based Materials*; Vol. 53; ISBN 9788578110796.

Torborg, C.; Beller, M. Recent Applications of Palladium-Catalyzed Coupling Reactions in the Pharmaceutical, Agrochemical, and Fine Chemical Industries. *Adv. Synth. Catal.* **2009**, *351*, 3027–3043, doi:10.1002/adsc.200900587.

Trinh, Q. T.; Banerjee, A.; Yang, Y.; Mushrif, S. H. Sub-Surface Boron-Doped Copper for Methane Activation and Coupling: First-Principles Investigation of the Structure, Activity, and Selectivity of the Catalyst. *J. Phys. Chem. C* **2017**, *121*, 1099–1112, doi:10.1021/acs.jpcc.6b09236.

Tyagi, A.; Yamamoto, A.; Kato, T.; Yoshida, H. Bifunctional property of Pt nanoparticles deoposited on TiO$_2$ for the photocatalytic sp^{3}C-sp^{3}C cross-coupling reactions between THF and alkanes. *Catal. Sci. Technol.* **2017**, *7*, 2616–2623, doi:10.1039/c7cy00535k.

Tyagi, A.; Yamamoto, A.; Yoshida, T.; Yoshida, H.; Yamamoto, M. Direct cross-coupling between alkenes and tetrahydrofuran with a platinum-loaded titanium oxide photocatalyst. *Catal. Sci. Technol.* **2018**, *8*, 2546–2556, doi:10.1039/c8cy00129d.

Vione, D.; Maddigapu, P. R.; De Laurentiis, E.; Minella, M.; Pazzi, M.; Maurino, V.; Minero, C.; Kouras, S.; Richard, C. Modelling the photochemical fate of ibuprofen in surface waters. *Water Res.* **2011**, *45*, 6725–6736, doi:10.1016/j.watres.2011.10.014.

Wang, D.; Jia, F.; Wang, H.; Chen, F.; Fang, Y.; Dong, W.; Zeng, G.; Li, X.; Yang, Q.; Yuan, X. Simultaneously efficient adsorption and photocatalytic degradation of tetracycline by Fe-based MOFs. *J. Colloid Interface Sci.* **2018**, *519*, 273–284, doi:10.1016/j.jcis.2018.02.067.

Wang, D.-H.; Gao, G.-Q.; Zhang, Y.-W.; Zhou, L.-S.; Xu, A.-W.; Chen, W. Nanosheet-constructed porous BiOCl with dominant {001} facets for superior photosensitized degradation. *Nanoscale* **2012**, *4*, 7780, doi:10.1039/c2nr32533k.

Wang, G.; Luo, X.; Huang, Y.; Kuang, A.; Yuan, H.; Chen, H. BiOX/BiOY (X, Y = F, Cl, Br, I) superlattices for visible light photocatalysis applications. *RSC Adv.* **2016**, *6*, 91508–91516, doi:10.1039/c6ra14915d.

Wang, H.; Xu, H.; Zeng, C.; Shen, Y.; Lin, Y. H.; Nan, C. W. Visible Light Photocatalytic Activity of Bismuth Ferrites Tuned by Bi/Fe Ratio. *J. Am. Ceram. Soc.* **2016**, *99*, 1133–1136, doi:10.1111/jace.14113.

Wang, Y.; Deng, K.; Zhang, L. Visible Light Photocatalysis of BiOI and Its Photocatalytic Activity Enhancement by in Situ Ionic Liquid Modification. *J. Phys. Chem. C* **2011**, *115*, 14300–14308.

Wen Lai, H.; Qingshan, Z. Electronic structures of relaxed BiOX (X=F, Cl, Br, I) photocatalysts. *Comput. Mater. Sci.* **2008**, *43*, 1101–1108, doi:10.1016/j.commatsci.2008.03.005.

Wen, X. J.; Niu, C. G.; Guo, H.; Zhang, L.; Liang, C.; Zeng, G. M. Photocatalytic degradation of levofloxacin by ternary $Ag_2CO_3/CeO_2/AgBr$ photocatalyst under visible-light irradiation: Degradation pathways, mineralization ability, and an accelerated interfacial charge transfer process study. *J. Catal.* **2018**, *358*, 211–223, doi:10.1016/j.jcat.2017.12.005.

Wood, D. A.; Nwaoha, C.; Towler, B. F. Journal of Natural Gas Science and Engineering Gas-to-liquids (GTL): A review of an industry offering several routes for monetizing natural gas. *J. Nat. Gas Sci. Eng.* **2012**, *9*, 196–208.

Wu, D.; Ye, L.; Yip, H. Y.; Wong, P. K. Organic-free synthesis of {001} facet dominated BiOBr nanosheets for selective photoreduction of CO_2 to CO. *Catal. Sci. Technol.* **2017**, *7*, 265–271, doi:10.1039/C6CY02040B.

Wu, Y.; Yuan, B.; Li, M.; Zhang, W. H.; Liu, Y.; Li, C. Well-defined BiOCl colloidal ultrathin nanosheets: Synthesis, characterization, and application in photocatalytic aerobic oxidation of secondary amines. *Chem. Sci.* **2015**, *6*, 1873–1878, doi:10.1039/c4sc03229b.

Xia, J.; Xu, L.; Zhang, J.; Yin, S.; Li, H.; Xu, H.; Di, J. Improved visible light photocatalytic properties of Fe/BiOCl microspheres synthesized via self-doped reactable ionic liquids. *CrystEngComm* **2013**, *15*, 10132, doi:10.1039/c3ce41555d.

Xia, J.; Zhang, J.; Yin, S.; Li, H.; Xu, H.; Xu, L.; Zhang, Q. Journal of Physics and Chemistry of Solids Advanced visible light photocatalytic properties of BiOCl micro/nanospheres synthesized via reactable ionic liquids. **2013**, *74*, 298–304, doi:10.1016/j.jpcs.2012.10.002.

Xie, S.; Shen, Z.; Zhang, H.; Cheng, J. Photocatalytic coupling of formaldehyde to ethylene glycol and glycolaldehyde over bismuth vanadate with controllable facets and cocatalysts. *Catal. Sci. Technol.* **2017**, *7*, 923–933, doi:10.1039/c6cy02510b.

Xiong, J.; Jiao, Z.; Lu, G.; Ren, W.; Ye, J.; Bi, Y. Facile and rapid oxidation fabrication of BiOCl hierarchical nanostructures with enhanced photocatalytic properties. *Chem. - A Eur. J.* **2013**, *19*, 9472–9475, doi:10.1002/chem.201300384.

Xiong, X.; Ding, L.; Wang, Q.; Li, Y.; Jiang, Q.; Hu, J. Synthesis and photocatalytic activity of BiOBr nanosheets with tunable exposed (010) facets. *Appl. Catal. B Environ.* **2016**, *188*, 283–291, doi:10.1016/j.apcatb.2016.02.018.

Xu, H.; Wu, Z.; Ding, M.; Gao, X. Microwave-assisted synthesis of flower-like BN/BiOCl composites for photocatalytic Cr(VI) reduction upon visible-light irradiation. *Mater. Des.* **2017**, *114*, 129–138, doi:10.1016/j.matdes.2016.10.057.

Xu, L.; He, F.; Wang, C.; Gai, S.; Gulzar, A.; Yang, D.; Zhong, C.; Yang, P. Lanthanide-doped bismuth oxobromide nanosheets for self-activated photodynamic therapy. *J. Mater. Chem. B* **2017**, *5*, 7939–7948, doi:10.1039/C7TB01983A.

Xu, Y.; Xu, S.; Wang, S.; Zhang, Y.; Li, G. Citric acid modulated electrochemical synthesis and photocatalytic behavior of BiOCl nanoplates with exposed {001} facets. *Dalt. Trans.* **2014**, *43*, 479–485, doi:10.1039/C3DT52004H.

Yang, Y.; Zhang, C.; Lai, C.; Zeng, G.; Huang, D.; Cheng, M.; Wang, J.; Chen, F.; Zhou, C.; Xiong, W. BiOX (X = Cl, Br, I) photocatalytic nanomaterials: Applications for fuels and environmental management. *Adv. Colloid Interface Sci.* **2018**, *254*, 76–93, doi:10.1016/j.cis.2018.03.004.

Yaparatne, S.; Tripp, C. P.; Amirbahman, A. Photodegradation of taste and odor compounds in water in the presence of immobilized TiO_2-SiO_2 photocatalysts. *J. Hazard. Mater.* **2018**, *346*, 208–217, doi:10.1016/j.jhazmat.2017.12.029.

Ye, L.; Chen, J.; Tian, L.; Liu, J.; Peng, T.; Deng, K.; Zan, L. BiOI thin film via chemical vapor transport: Photocatalytic activity, durability, selectivity and mechanism. *Appl. Catal. B Environ.* **2013**, *130–131*, 1–7, doi:10.1016/j.apcatb.2012.10.011.

Ye, L.; Liu, J.; Gong, C.; Tian, L.; Peng, T.; Zan, L. Two Different Roles of Metallic Ag on Ag/AgX/BiOX (X = Cl, Br) Visible Light Photocatalysts: Surface Plasmon Resonance and Z-Scheme Bridge. *ACS Catal.* **2012**, *2*, 1677–1683, doi:10.1021/cs300213m.

Ye, L.; Liu, X.; Zhao, Q.; Xie, H.; Zan, L. Dramatic visible light photocatalytic activity of MnO_x–BiOI heterogeneous photocatalysts and the selectivity of the cocatalyst. *J. Mater. Chem. A* **2013**, *1*, 8978, doi:10.1039/c3ta11441d.

Ye, L.; Su, Y.; Jin, X.; Xie, H.; Zhang, C. Recent advances in BiOX (X = Cl, Br and I) photocatalysts: synthesis, modification, facet effects and mechanisms. *Environ. Sci. Nano* **2014**, *1*, 90–112, doi:10.1039/c3en00098b.

Yin, H.; Killeen, K. The fundamental aspects and applications of Agilent HPLC-Chip. *J. Sep. Sci.* **2007**, *30*, 1427–1434, doi:10.1002/jssc.200600454.

Yu, Y.; Cao, C.; Liu, H.; Li, P.; Wei, F.; Jiang, Y.; Song, W. A Bi/BiOCl heterojunction photocatalyst with enhanced electron–hole separation and excellent visible light photodegrading activity. *J. Mater. Chem. A* **2014**, *2*, 1677–1681, doi:10.1039/C3TA14494A.

Yuliati, L.; Itoh, H.; Yoshida, H. Photocatalytic conversion of methane and carbon dioxide over gallium oxide. *Chem. Phys. Lett.* **2008**, *452*, 178–182, doi:10.1016/j.cplett.2007.12.051.

Yuliati, L.; Yoshida, H. Photocatalytic conversion of methane. *Chem. Soc. Rev.* **2008**, *37*, 1592–1602, doi:10.1039/b710575b.

Zeng, J.; Xiong, Z.; Zhang, H.; Lin, G.; Tsai, K. Nonoxidative dehydrogenation and aromatization of methane over W/HZSM-5-based catalysts. *Catal. Letters* **1998**, *53*, 119–124.

Zhang, H.; Liu, L.; Zhou, Z. Towards better photocatalysts: first-principles studies of the alloying effects on the photocatalytic activities of bismuth oxyhalides under visible light. *Phys. Chem. Chem. Phys.* **2012**, *14*, 1286–1292, doi:10.1039/C1CP23516H.

Zhang, J.; Zhang, L.; Shen, X.; Xu, P.; Liu, J. Synthesis of $BiOBr/WO_3$ p–n heterojunctions with enhanced visible light photocatalytic activity. *CrystEngComm* **2016**, *18*, 3856–3865, doi:10.1039/C6CE00824K.

Zhang, K.; Liu, C.; Huang, F.; Zheng, C.; Wang, W. Study of the electronic structure and photocatalytic activity of the BiOCl photocatalyst. *Appl. Catal. B Environ.* **2006**, *68*, 125–129, doi:10.1016/j.apcatb.2006.08.002.

Zhang, L.; Wang, W.; Sun, S.; Jiang, D.; Gao, E. Selective transport of electron and hole among {001} and {110} facets of BiOCl for pure water splitting. *Appl. Catal. B Environ.* **2015**, *162*, 470–474, doi:10.1016/j.apcatb.2014.07.024.

Zhang, X.; Ai, Z.; Jia, F.; Zhang, L. Generalized One-Pot Synthesis, Characterization, and Photocatalytic Activity of Hierarchical BiOX (X = Cl, Br, I) Nanoplate Microspheres. **2008**, 747–753.

Zhang, X.; Wang, C.-Y.; Wang, L.-W.; Huang, G.-X.; Wang, W.-K.; Yu, H.-Q. Fabrication of BiOBr$_x$I$_{1-x}$ photocatalysts with tunable visible light catalytic activity by modulating band structures. *Sci. Rep.* **2016**, *6*, 22800, doi:10.1038/srep22800.

Zhang, Y.; Park, M.; Kim, H.; Park, S. In-situ synthesis of graphene oxide/BiOCl heterostructured nanofibers for visible-light photocatalytic investigation. *J. Alloys Compd.* **2016**, *686*, 106–114, doi:10.1016/j.jallcom.2016.06.004.

Zhao, H.; Tian, F.; Wang, R.; Chen, R. A Review on Bismuth-Related Nanomaterials for Photocatalysis. *Rev. Adv. Sci. Eng.* **2014**, *3*, 3–27, doi:10.1166/rase.2014.1050.

Zhao, Y.; Zhao, B.; Liu, J.; Chen, G.; Gao, R.; Yao, S.; Li, M.; Zhang, Q.; Gu, L.; Xie, J.; Wen, X.; Wu, L.; Tung, C.; Ma, D.; Zhang, T. Oxide-Modified Nickel Photocatalysts for the Production of Hydrocarbons in Visible Light. *Angew. Chemie Int. Ed.* **2016**, *55*, 4215–4219, doi:10.1002/anie.201511334.

Zhuang, J.; Dai, W.; Tian, Q.; Li, Z.; Xie, L.; Wang, J.; Liu, P.; Shi, X.; Wang, D. Photocatalytic degradation of RhB over TiO$_2$ bilayer films: Effect of defects and their location. *Langmuir* **2010**, *26*, 9686–9694, doi:10.1021/la100302m.

Zoller, J.; Fabry, D. C.; Rueping, M. Unexpected Dual Role of Titanium Dioxide in the Visible Light Heterogeneous Catalyzed C−H Arylation of Heteroarenes. *ACS Catal.* **2015**, *5*, 3900–3904, doi:10.1021/acscatal.5b00668.
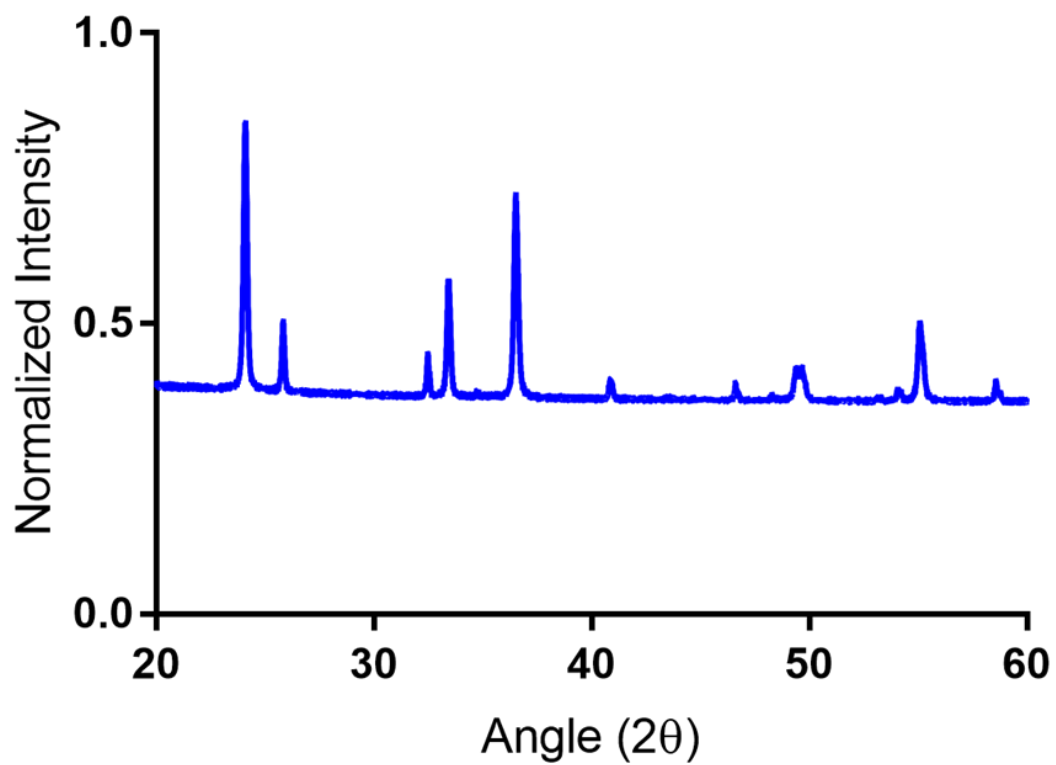
Figure A.1. X-Ray diffraction pattern obtained for BiOCl.
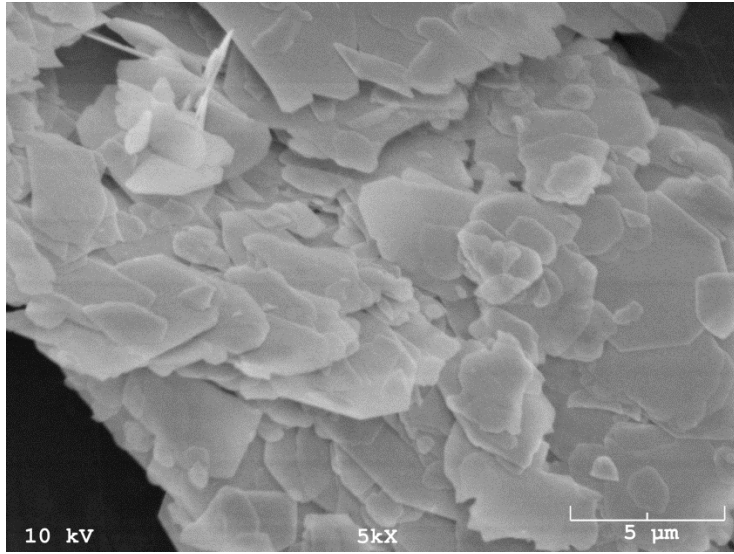
Figure A.2. SEM image of BiOCl at 5kX magnification.
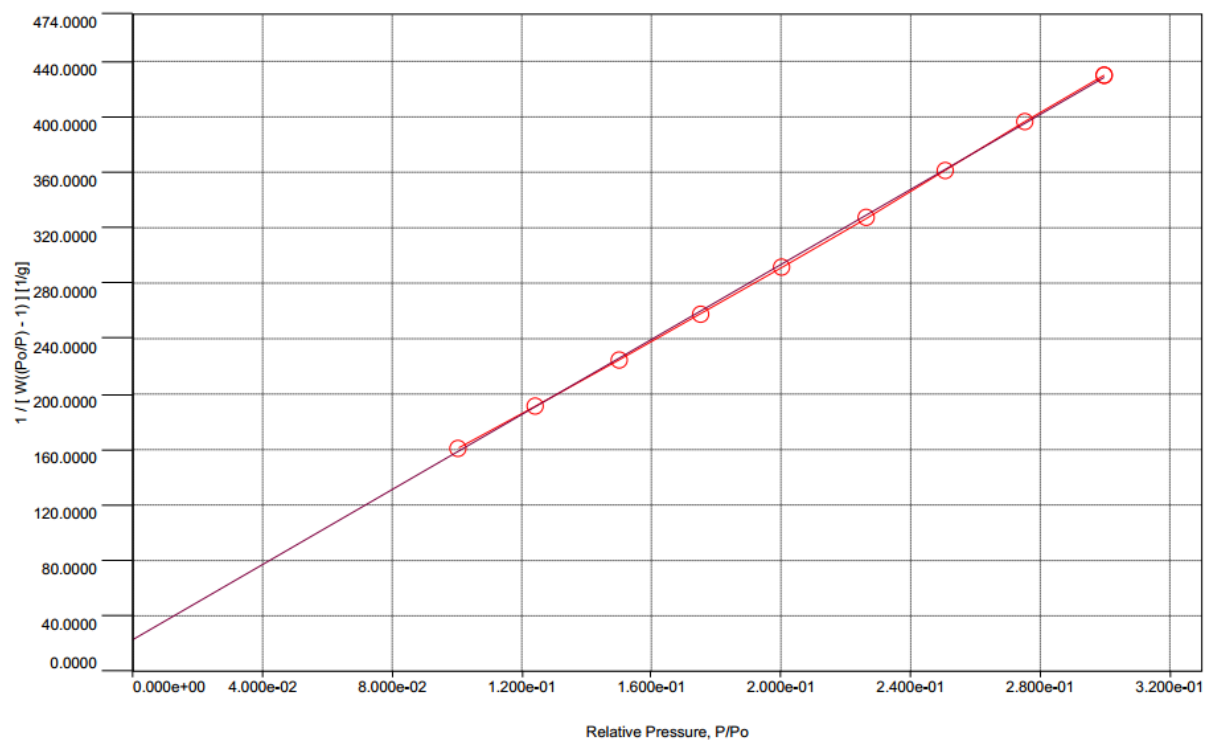
Figure A.3. BET nitrogen adsorption-desorption isotherm for BiOCl conducted at 78K.
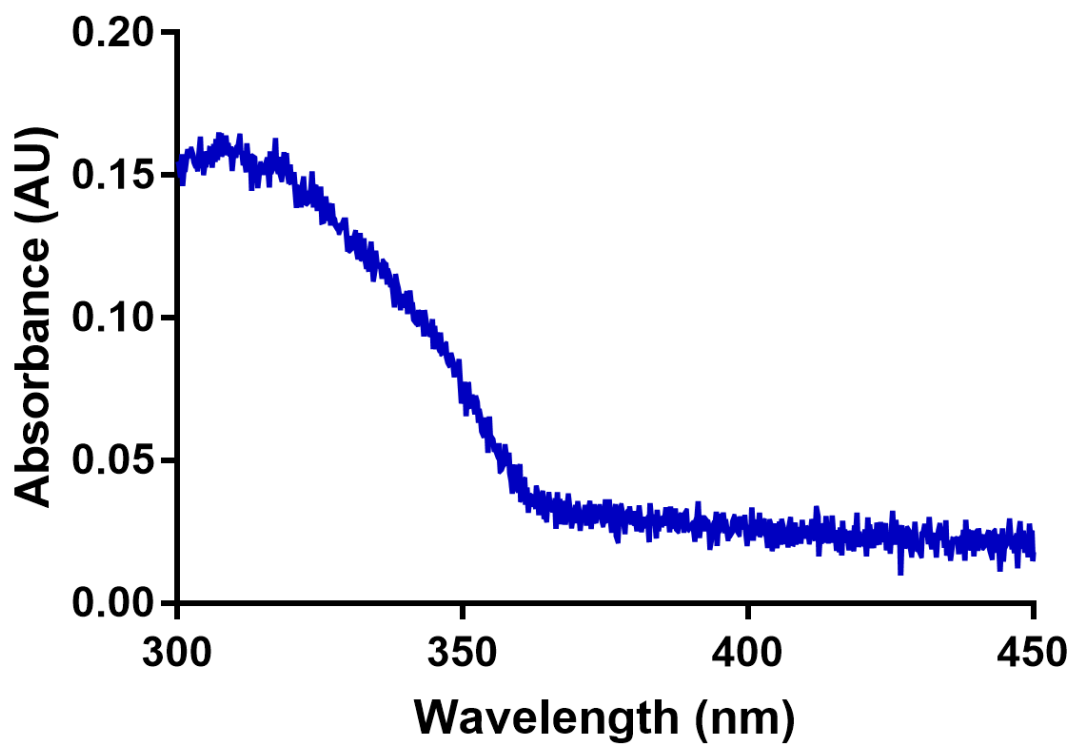
Figure A.4. UV-Vis DRS absorption spectrum for BiOCl.
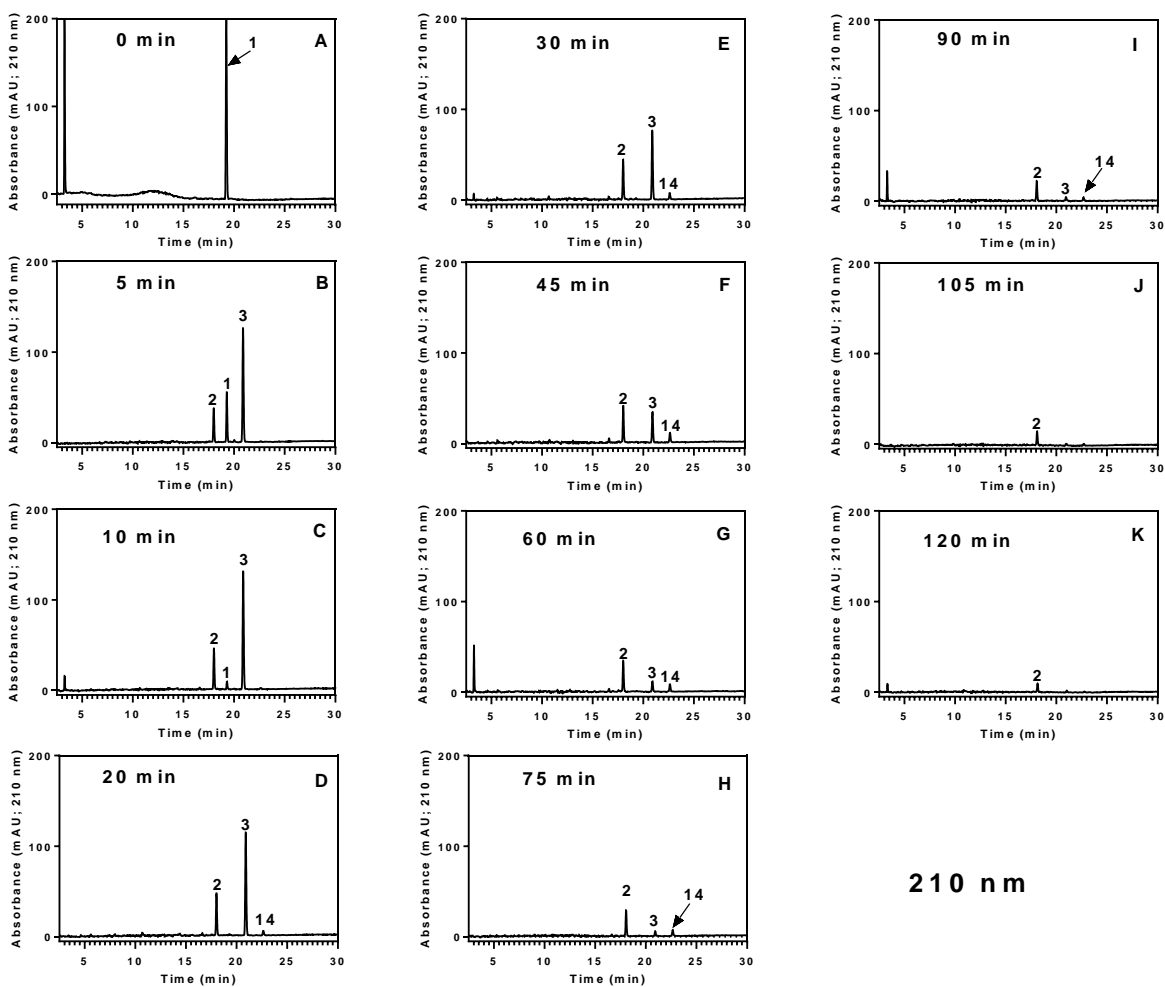
Figure A.5. HPLC-DAD chromatograms monitored at 210-nm for the analysis of the photocatalytic degradation of IBP (1) with BiOCl after photolysis times of (A) 0-min; (B) 5-min; (C) 10-min; (D) 20-min; (E) 30-min; (F) 45-min; (G) 60-min; (H) 75-min; (I) 90-min; (J) 105-min; (K) 120-min
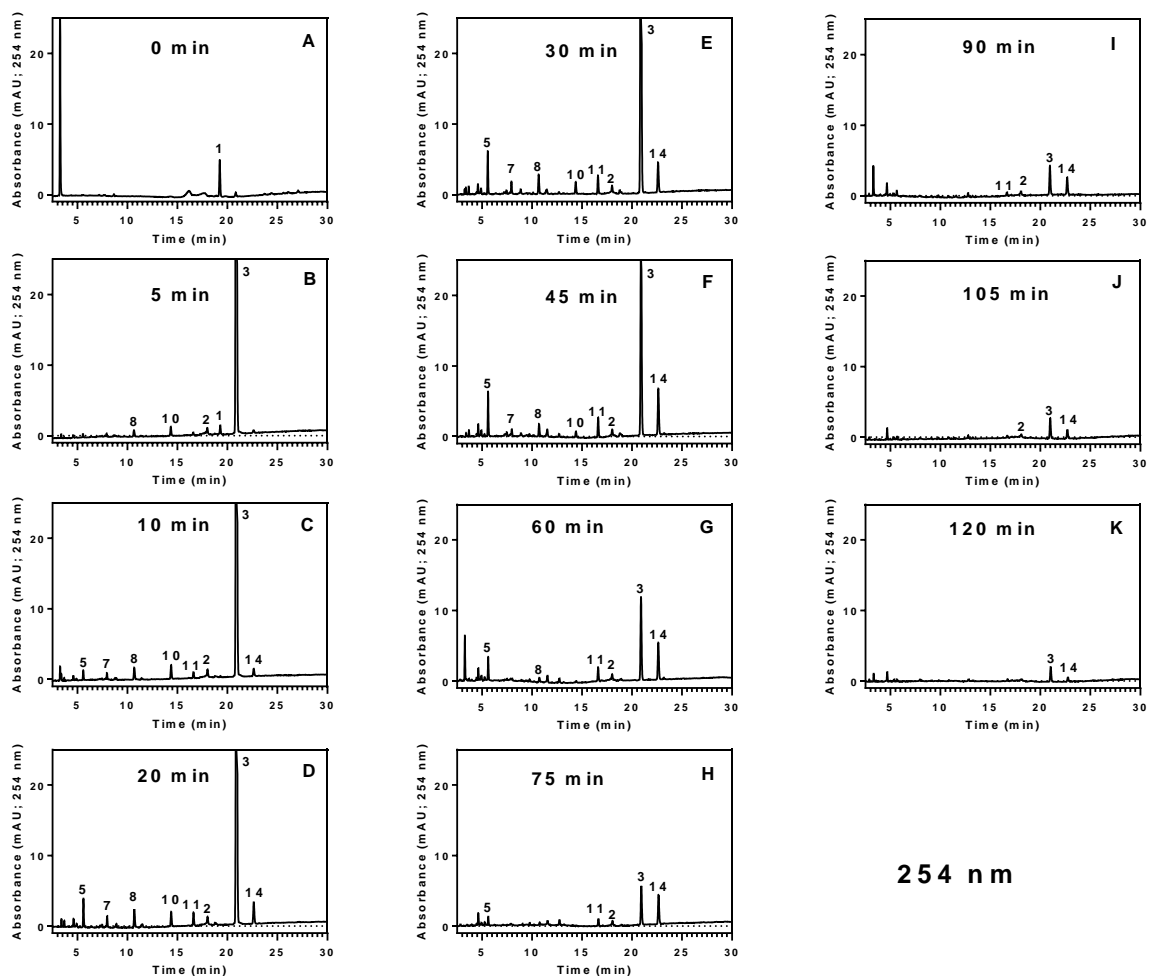
Figure A.6. HPLC-DAD chromatograms monitored at 254-nm for the analysis of the photocatalytic degradation of IBP (1) with BiOCl after photolysis times of (A) 0-min; (B) 5-min; (C) 10-min; (D) 20-min; (E) 30-min; (F) 45-min; (G) 60-min; (H) 75-min; (I) 90-min; (J) 105-min; (K) 120-min

152
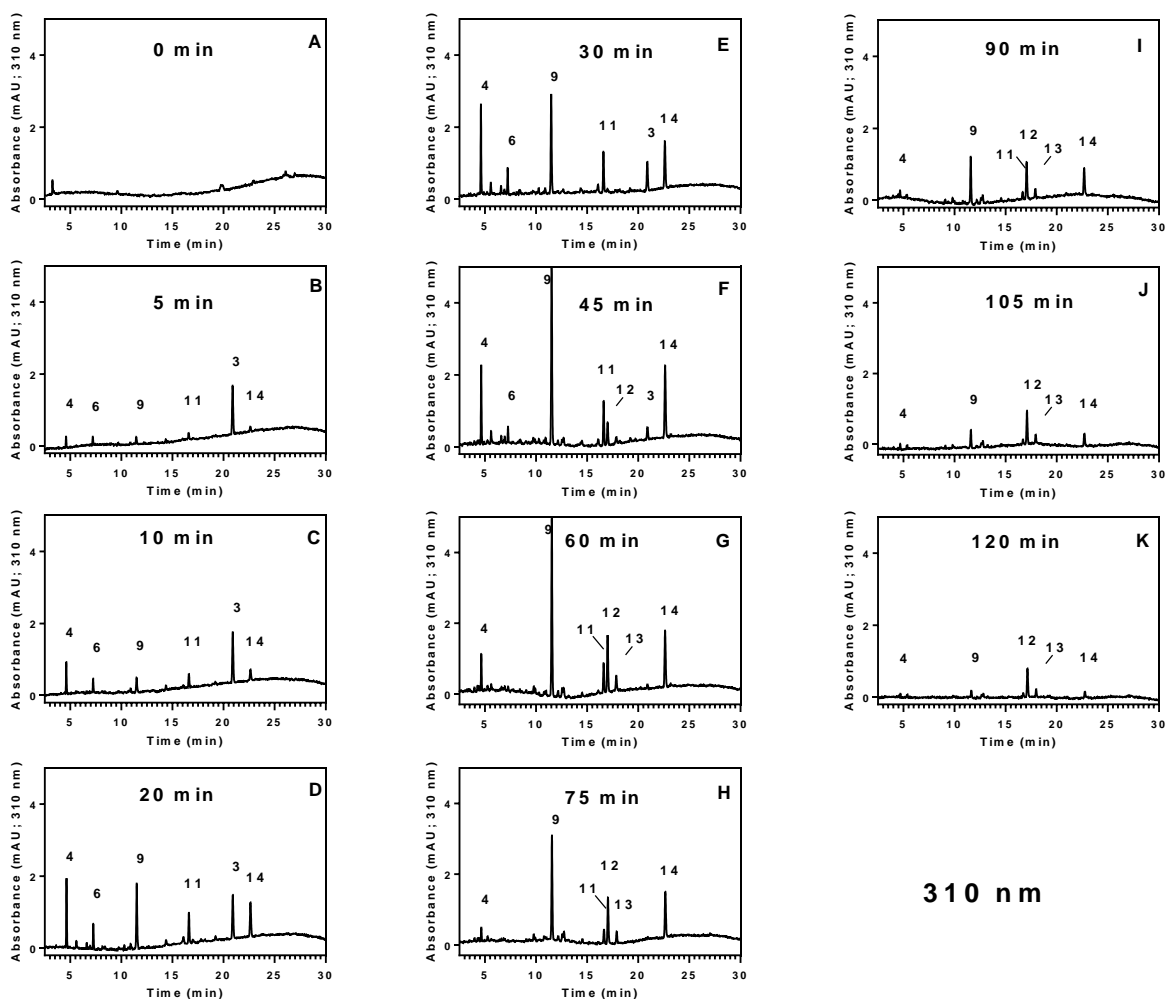
Figure A.7. HPLC-DAD chromatograms monitored at 310-nm for the analysis of the photocatalytic degradation of IBP (**1**) with BiOCl after photolysis times of (A) 0-min; (B) 5-min; (C) 10-min; (D) 20-min; (E) 30-min; (F) 45-min; (G) 60-min; (H) 75-min; (I) 90-min; (J) 105-min; (K) 120-min

153
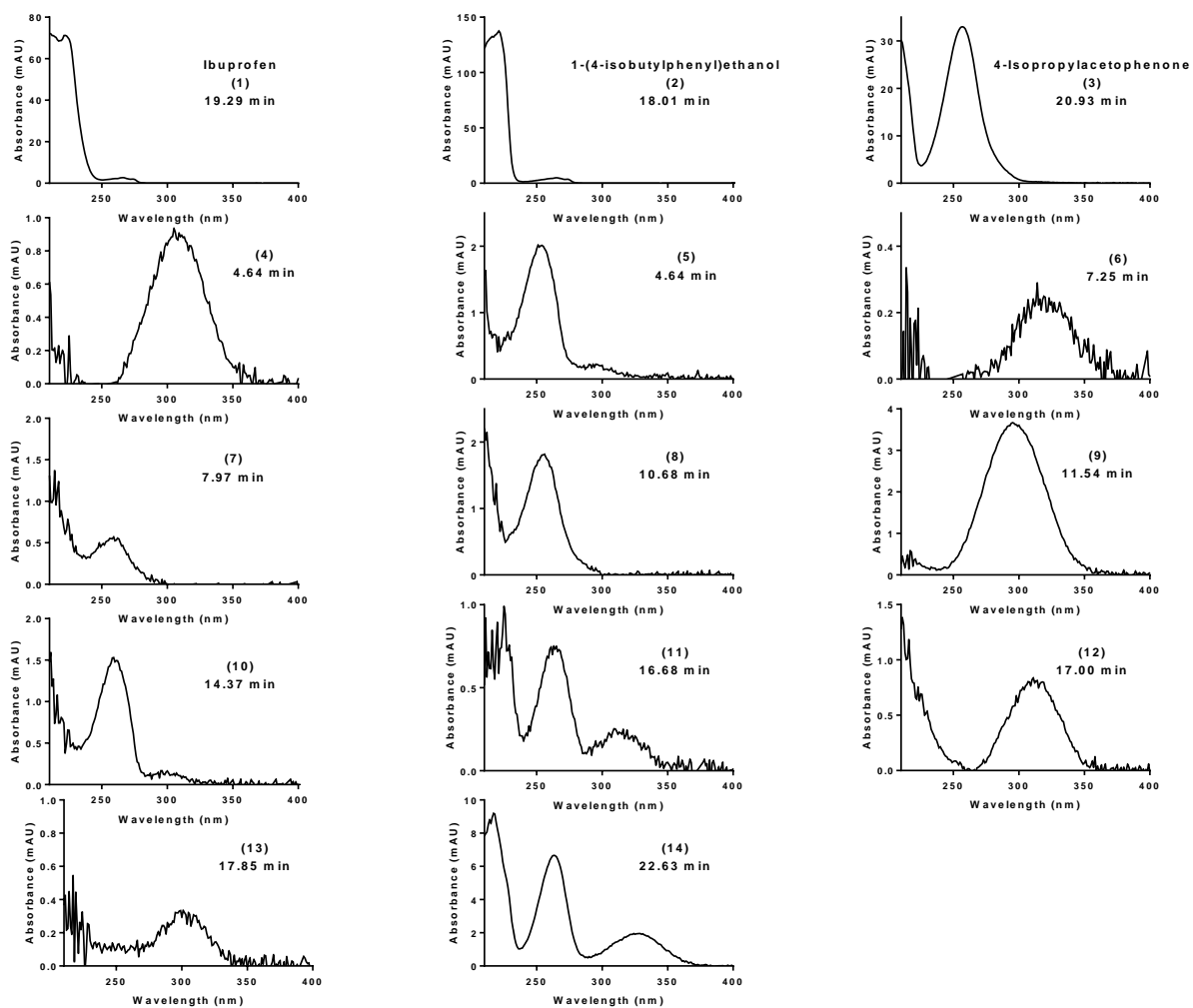
Figure A.8. (A) UV-Vis spectra extracted from HPLC-DAD chromatograms from the analysis of the photocatalytic degradation of IBP (1) with BiOCl. Spectra measured at the retention times summarized in Table 3.2.
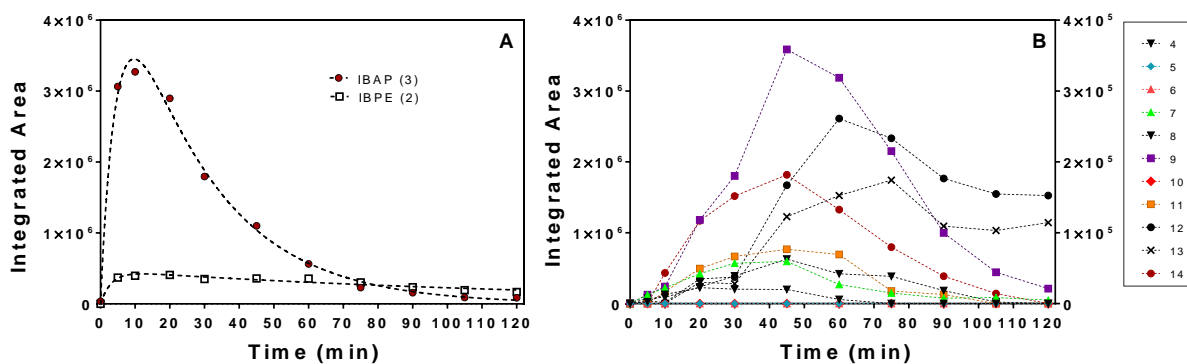
Figure A.9. Integrated peak areas from extracted ion chromatograms as a function of photolysis time for ibuprofen (1) photocatalytically degraded with BiOCl and analyzed by (+)nanoESI-LC-MS/MS. (A) Signals for IBPE (2) and IBAP (3); (B) Signals for secondary degradation products. Compounds are identified in Table 3.2.
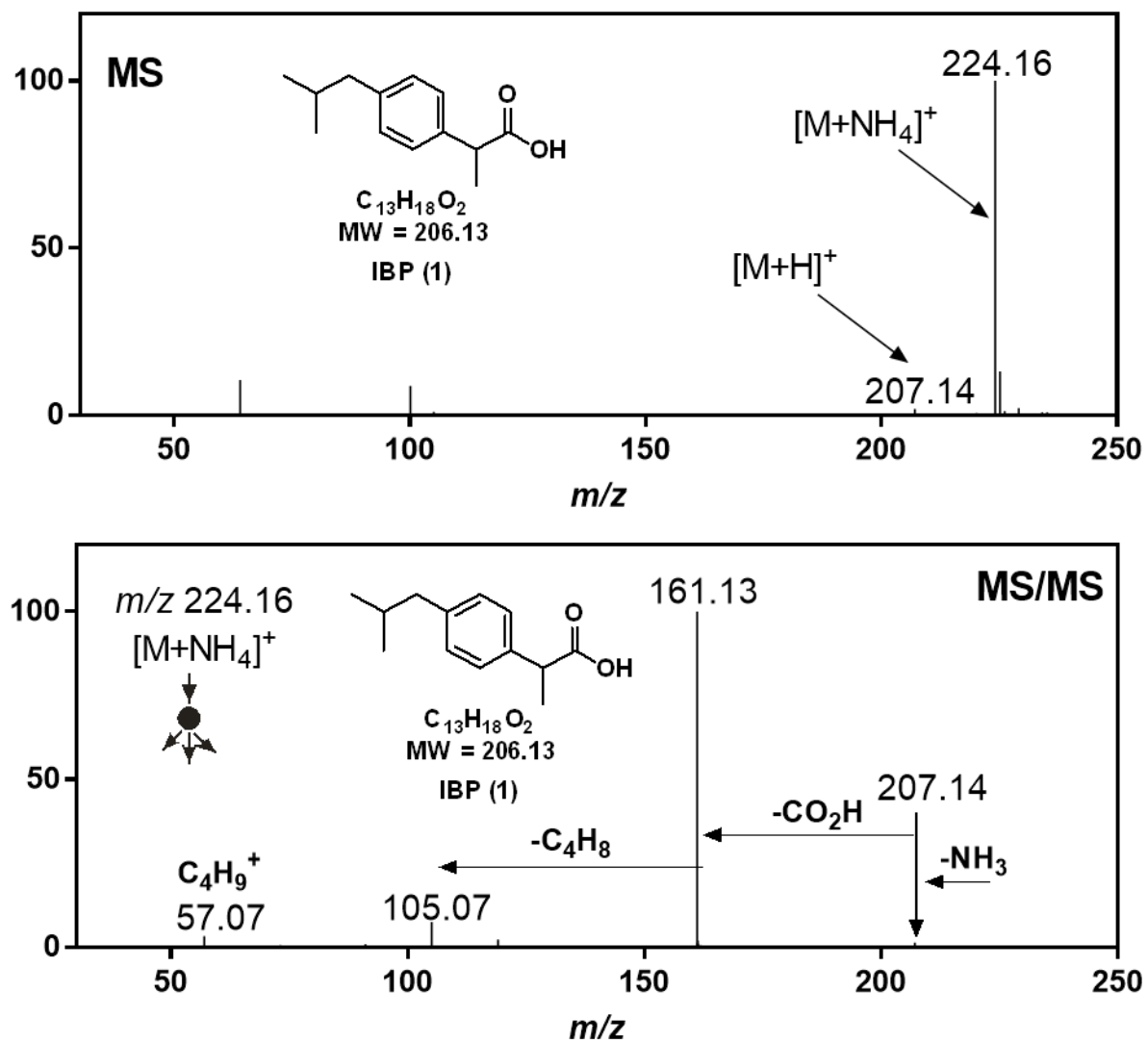
Figure A.10. MS and MS/MS spectra for IBP (**1**) from the (+)nanoESI-LC-MS/MS analysis of photodegraded IBP (**1**) with BiOCl
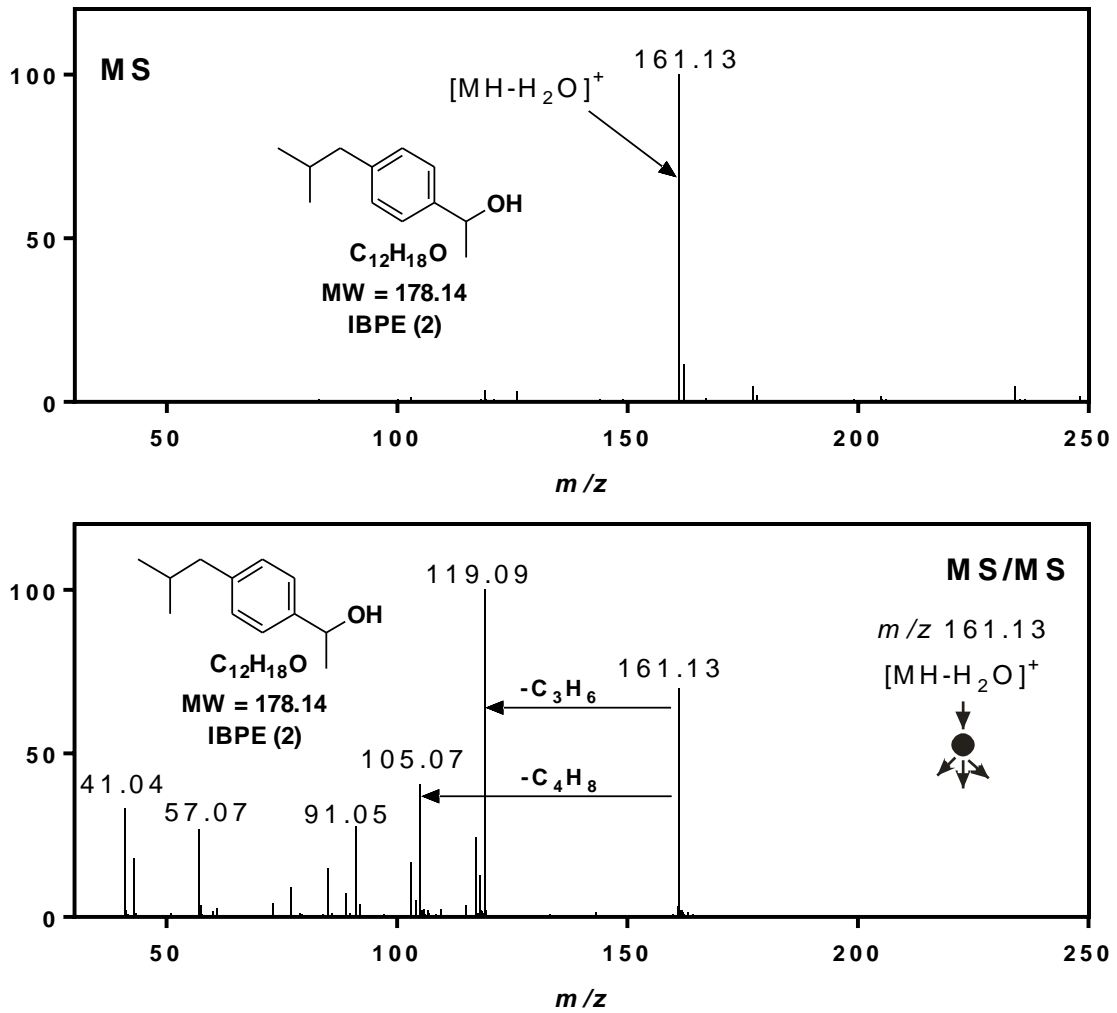
Figure A.11. MS and MS/MS spectra for IBPE (**2**) from the (+)nanoESI-LC-MS/MS analysis of photodegraded IBP (**1**) with BiOCl
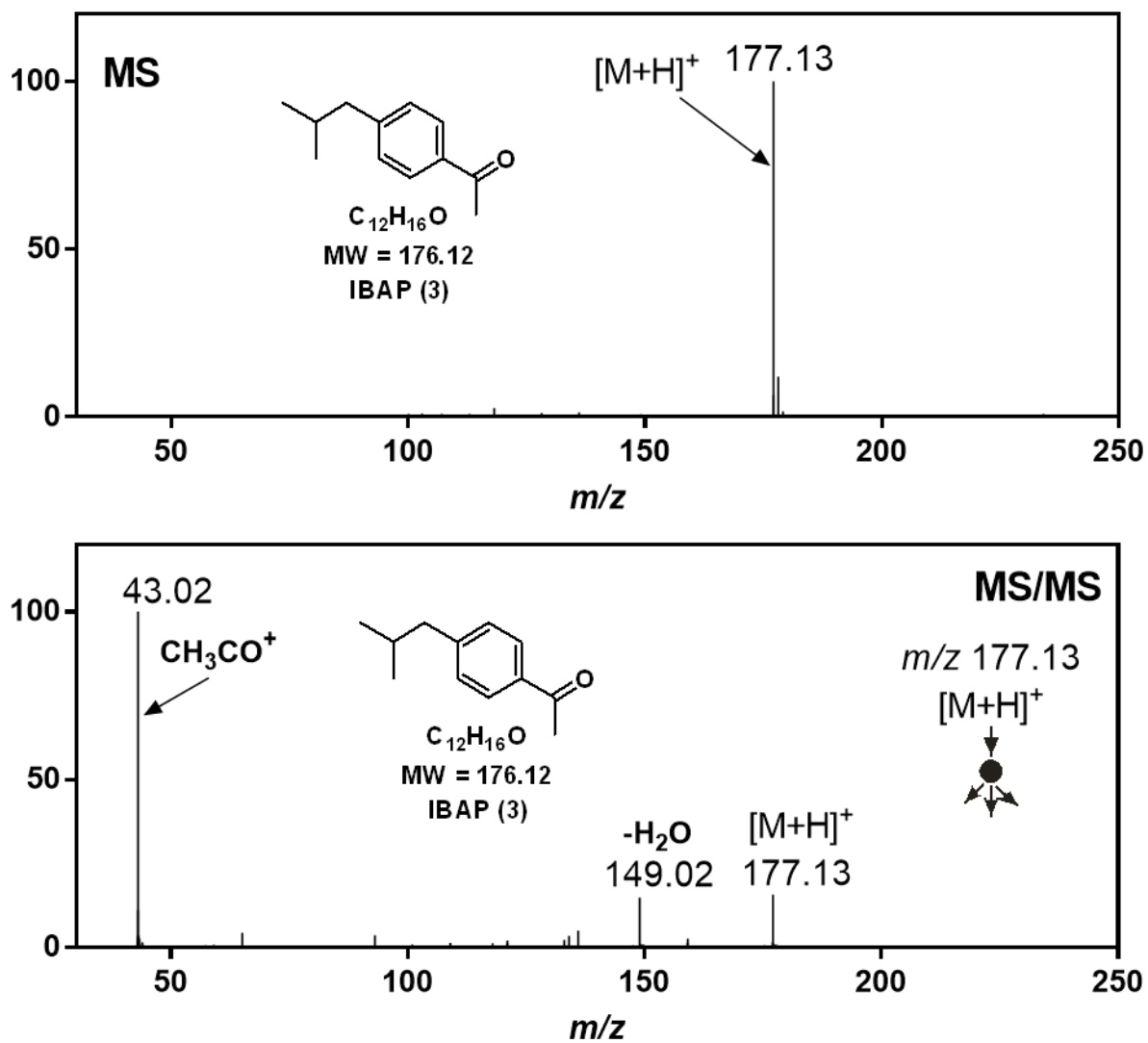
Figure A.12. MS and MS/MS spectra for IBAP (**3**) from the (+)nanoESI-LC-MS/MS analysis of photodegraded IBP (**1**) with BiOCl
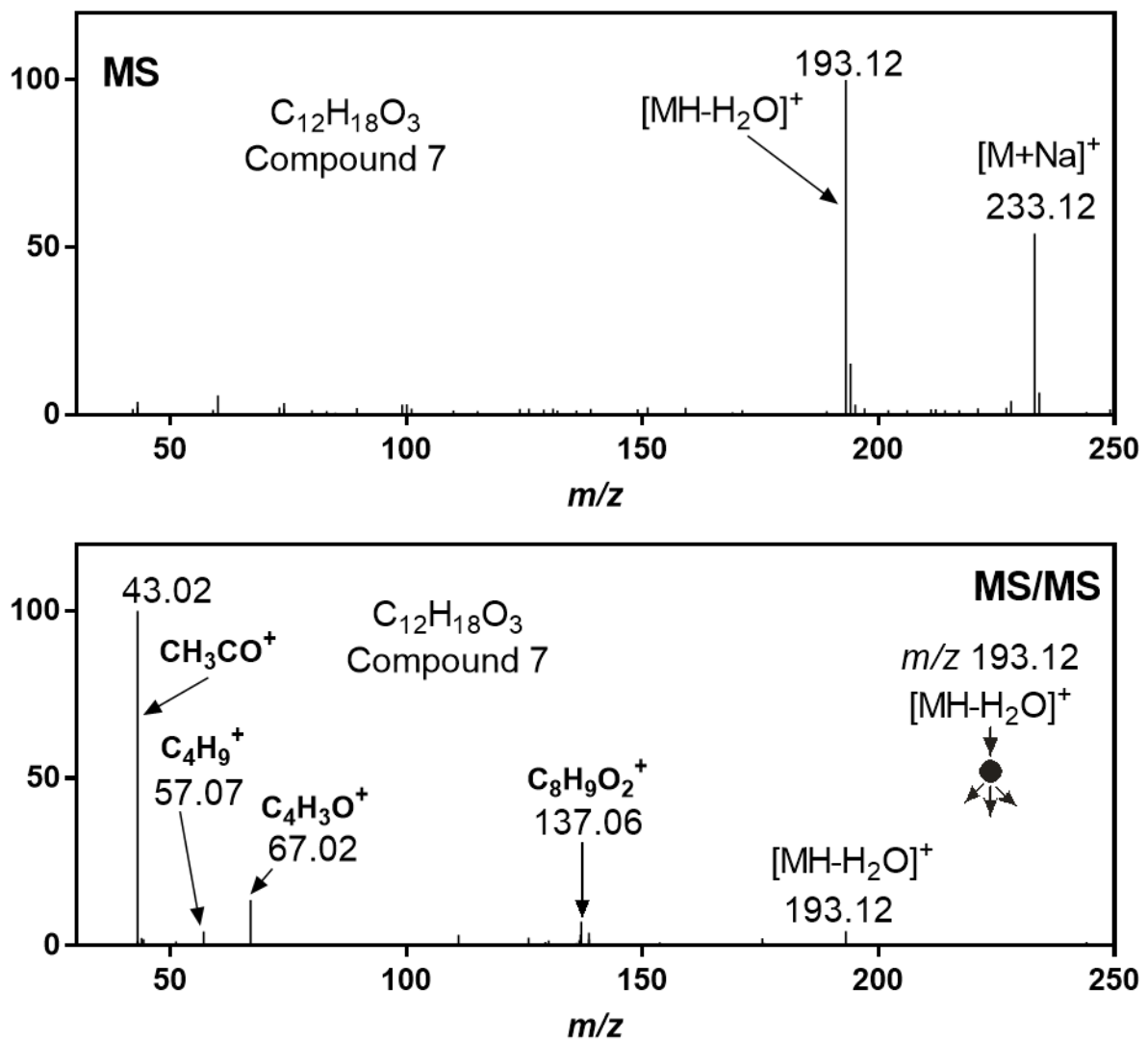
Figure A.13. MS and MS/MS spectra for Compound **7** from the (+)nanoESI-LC-MS/MS analysis of photodegraded IBP (**1**) with BiOCl
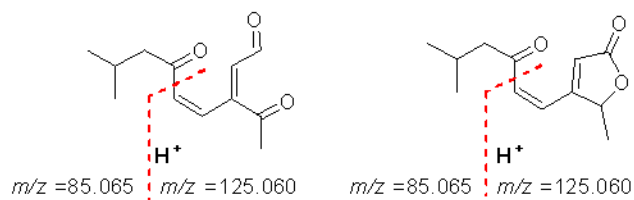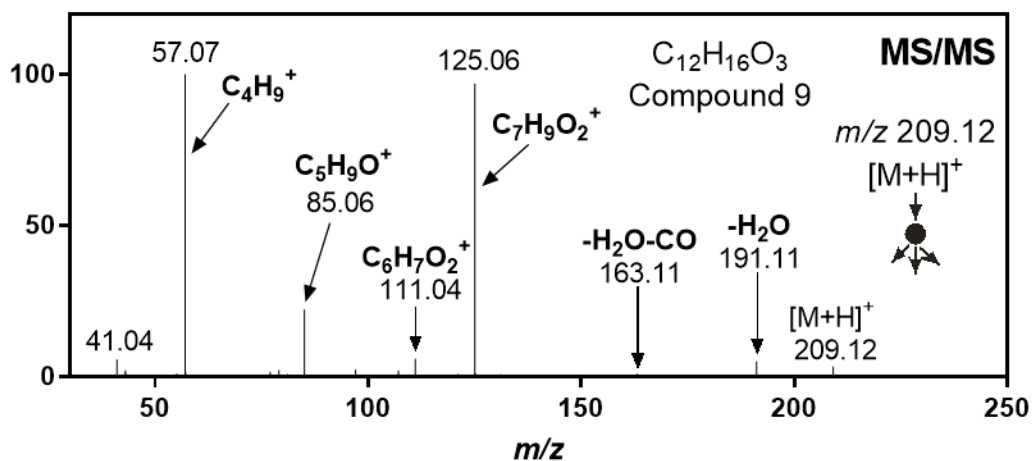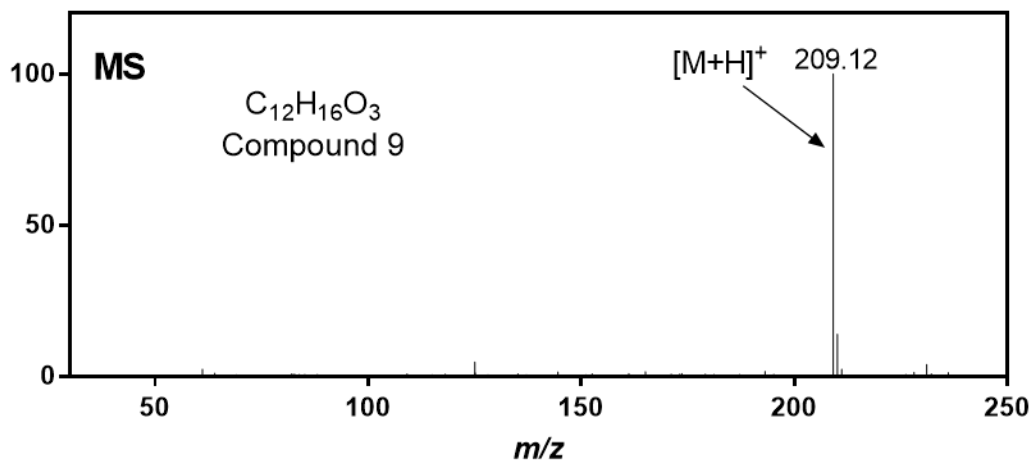
Figure A.14. MS and MS/MS spectra for Compound **9** from the (+)nanoESI-LC-MS/MS analysis of photodegraded IBP (**1**) with BiOCl
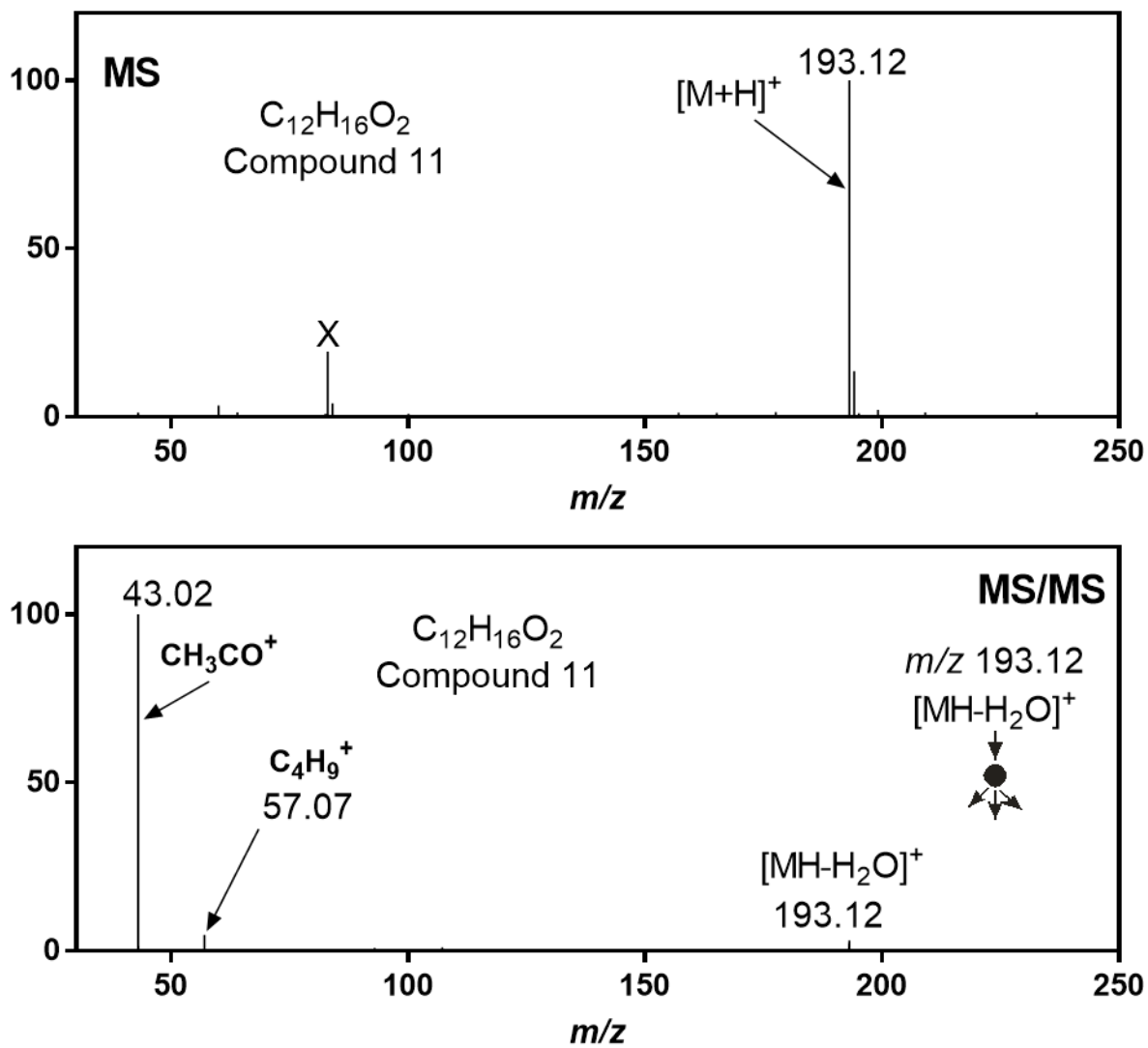
Figure A.15. MS and MS/MS spectra for Compound **11** from the (+)nanoESI-LC-MS/MS analysis of photodegraded IBP (**1**) with BiOCl

APPENDIX B: SYNTHESIS, STRUCTURE, AND LUMINESCENCE OF COPPER(I)

HALIDE COMPLEXES OF CHIRAL BIS(PHOSPHINES)

B.1 Introduction Copper(I) phosphine halide complexes are common precursors in catalysis [1] and their luminescent properties have often been investigated [2]. For both applications, varying the phosphine enables rational control of the structure and properties of the copper complex. For example, the structure of $[Cu(diphos)(X)]_n$ (X = halide) depends on the chelating bis(phosphine) diphos (Figure B.1).
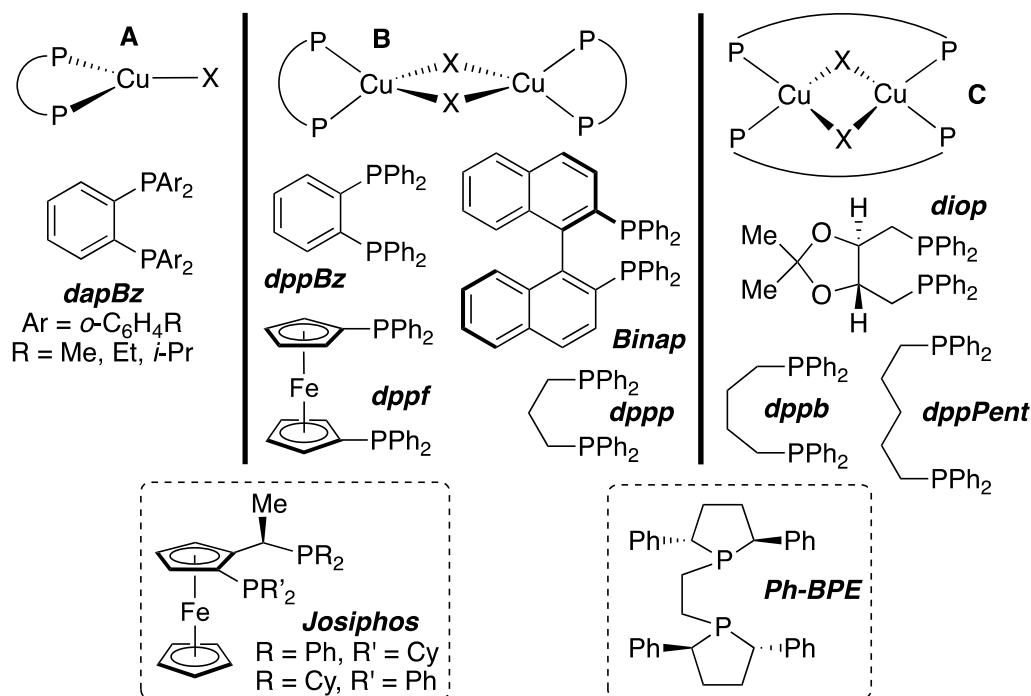
Figure B.1. Structures of $[Cu(diphos)(X)]_n$ Complexes

Three-coordinate monomers **A** are known for bulky chelates, such as Cu(dapBz)(I) [3], or for ligands with large bite angles, as in Cu(Josiphos)(Br) (R = Cy, R' = Ph, Chart 1) [4]. Four-coordinate dimers **B**, with approximately tetrahedral copper, chelating bis(phosphines), and bridging halides, are the most common, with ligands such as dppf [5], dppBz [6], Binap [7], and dppp [8]. Finally, four-coordinate dimers **C**, with both halides and bis(phosphines) bridging, are often observed with flexible ligands having larger bite angles, as in [Cu(μ-diop)(μ-X)]$_2$ (X = Cl or I) [9] or CuI complexes of dppb and dppPent [10].

The free energies of the isomers **A**-**C** are often similar (Figure B.1), so mixtures of isomers and interconversion between them can be observed. For example, both monomeric and dimeric [Cu(Josiphos)(Br)]$_n$ could be isolated in pure form; they underwent solvent-dependent interconversion [4]. Similarly, both structures **B** and **C** were observed in the same crystal for [Cu(Ph-BPE)(Cl)]$_2$ [11]. Small changes may determine the observed structure; replacing PPh$_2$ groups in dppBz with P(o-Tol)$_2$ donors resulted in a change from dimer **B** to monomer **A**, [3,6]. while extending the linker between PPh$_2$ donors by one CH$_2$ group (dppp $\rightarrow$ dppb) switched diphos from a chelate in **B** to a bridging ligand in **C** [8,10].

Luminescent properties have been reported for complexes of all three structure types, including Cu(dapBz)(I) (**A**) [3], [Cu(Binap)(I)]$_2$ (**B**) [12], and [Cu(μ-diop)(μ-Cl)]$_2$ (**C**) [9]. Changing the halide and/or the bis(phosphine) caused changes of emission color and quantum yield; the resulting structure-property relationships are potentially valuable in design and synthesis of new emitters with tailored photophysical properties [2].

With this background, we report here the synthesis, structure and luminescent properties of new copper halide complexes with the chiral bis(phospholanes) i-Pr-DuPhos and Me-FerroLANE [13], the analogous chiral bis(phosphetane) Et-FerroTANE [14], and the P(t-Bu)$_2$-substituted Josiphos

163

ligands CyPF-*t*-Bu and PPF-*t*-Bu (Scheme 1) [15]. In earlier work, Cu(*i*-Pr-DuPhos) complexes were formed *in situ* and used as precursors in asymmetric catalysis, but these starting materials were not isolated and their structures were not determined [16]. In contrast, the ferrocene-based Me-FerroLANE, Et-FerroTANE, and *t*-Bu-Josiphos derivatives, with larger bite angles, have not yet been used to prepare copper complexes or in Cu-catalyzed reactions. Besides providing structural information for catalysis, we hoped to investigate structure-property relationships in luminescence by comparing the phospholane/phosphetane/dialkylphosphino donors to the more commonly used PAr$_2$ groups shown in Figure B.1.

B.2 Results and Discussion.

Synthesis and Structure of Cu(diphos*) Halide Complexes Treatment of copper halides with (*R,R*)-*i*-Pr-DuPhos gave the dimers [Cu((*R,R*)-*i*-Pr-DuPhos)(X)]$_2$ (X = I (**1**), Br (**2**), Cl (**3**)) as light yellow solids (Figure B.2). The analogous fluoride (**4**) [17] was prepared from iodide **1** and AgF [18]. Similar reactions of CuI with (*R,R*)-Me-FerroLANE and (*S,S*)-Et-FerroTANE yielded orange [Cu((*R,R*)-Me-FerroLANE)(I)]$_2$ (**5**) and [Cu((*S,S*)-Et-FerroTANE)(I)]$_2$ (**6**). The cluster Cu$_5$I$_5$((*S,S*)-Et-FerroTANE)$_3$ (**7**), which was originally observed as a byproduct in the synthesis of **6**, was prepared rationally using a 5:3 ratio of CuI and the ligand. Finally, CuI and *t*-Bu-Josiphos ligands gave Cu((*R,S*)-CyPF-*t*-Bu)(I) (**8**) and Cu((*R,S*)-PPF-*t*-Bu)(I) (**9**) as red-orange crystals.
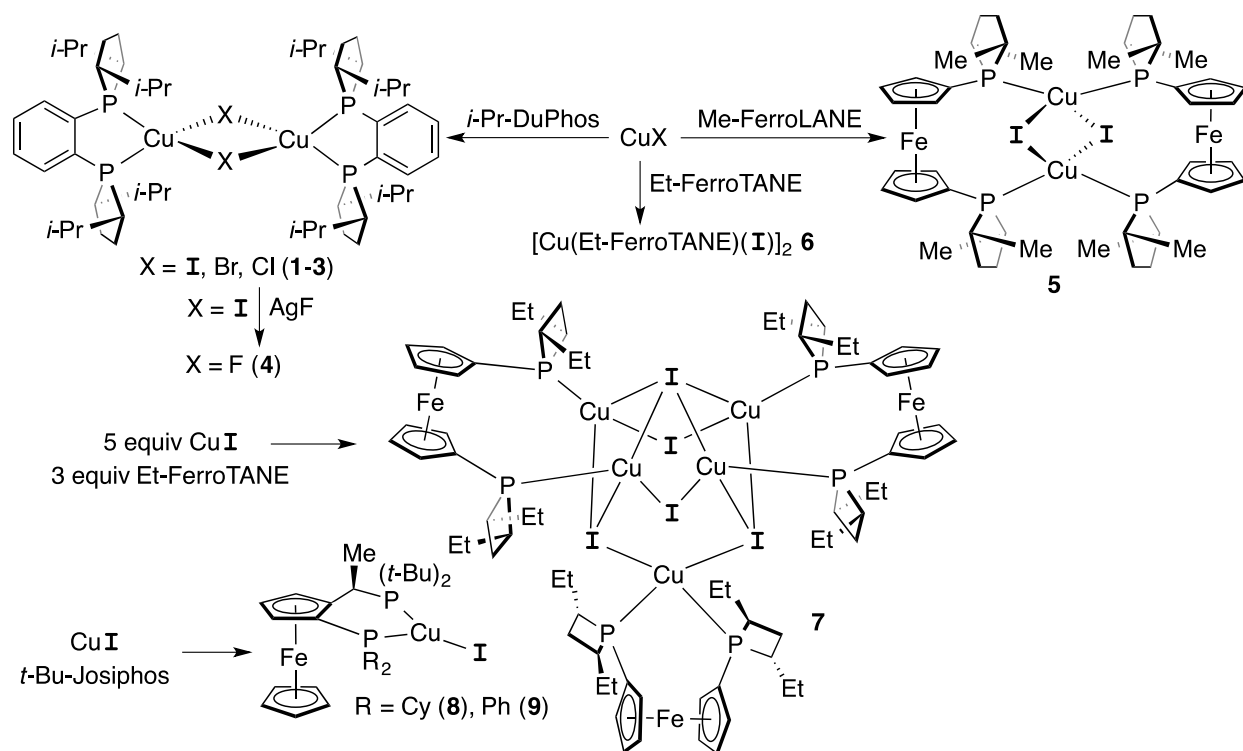
Figure B.2. Synthesis of Complexes **1**-**9**

With Me-FerroLANE and Et-FerroTANE, these syntheses also gave small amounts of phosphine oxides, presumably via oxidation by Cu(II) impurities in the CuI; similar observations were made with Me-DuPhos earlier [19]. Using commercially available higher-purity CuI avoided this problem for Me-FerroLANE complex **5**, but we were not able to obtain pure bulk samples of Et-FerroTANE complexes **6** and **7** (see the experimental section for details).

Complexes **1**-**9** were characterized spectroscopically (see below), by elemental analyses, and, for **1**-**3**, **5** and **7**-**9**, by X-ray crystallography (Figures B.3-B.6, Table B.1, and the Supporting Information).
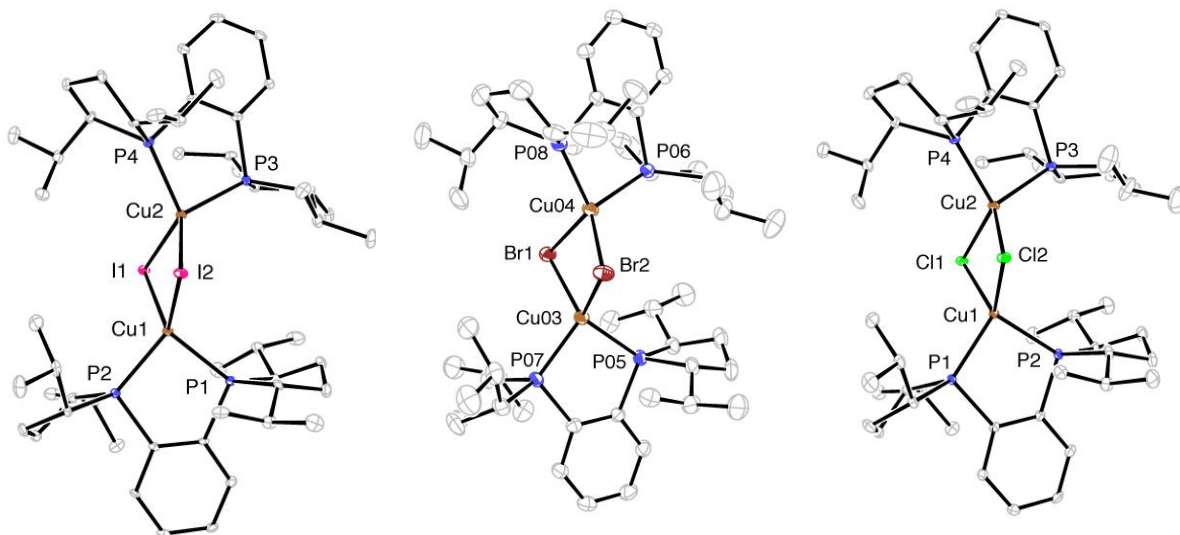
Figure B.3. ORTEP diagrams of [Cu((*R,R*)-*i*-Pr-DuPhos)(I)]₂•Et₂O (**1**•Et₂O, left), [Cu((*R,R*)-*i*-Pr-DuPhos)(Br)]₂•THF (**2**•THF, middle), and [Cu((*R,R*)-*i*-Pr-DuPhos)(Cl)]₂•THF (**3**•THF, right). The solvent molecules are not shown.
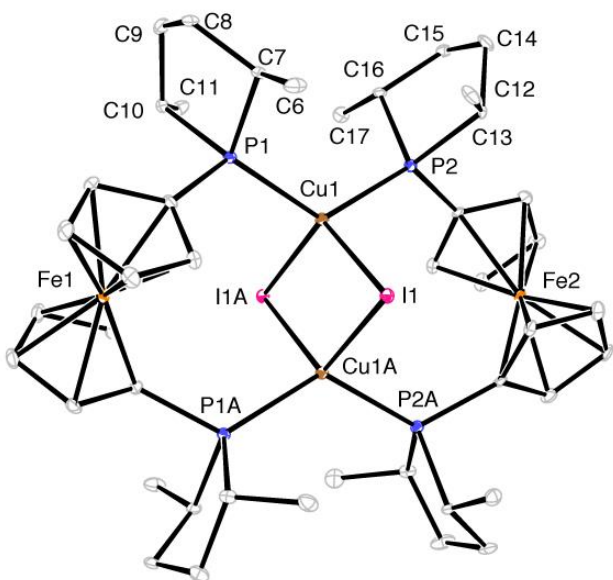
Figure B.4. ORTEP diagram of [Cu((*R,R*)-Me-FerroLANE)(I)]₂ (**5**).
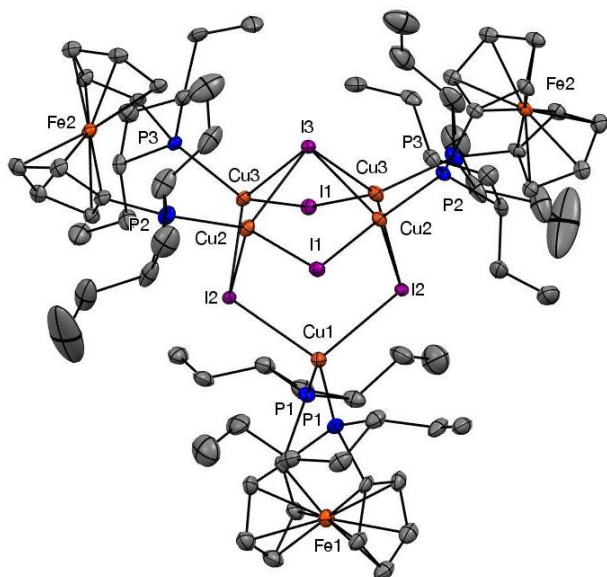
Figure B.5. ORTEP diagram of $Cu_5I_5((S,S)$-Et-FerroTANE$)_3$ (**7**), showing μ_4-I3, μ_3-I2, and μ_2-I1, as well as chelating Et-FerroTANE (P1) and bridging Et-FerroTANE (P2/P3).
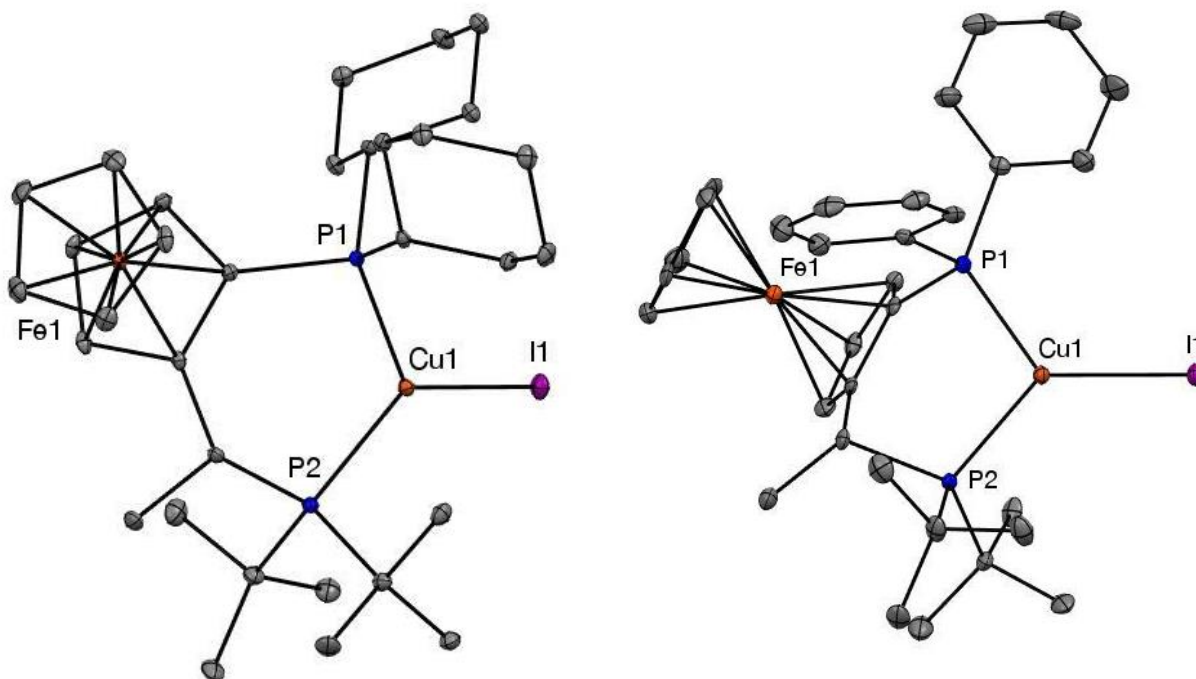
Figure B.6. ORTEP diagrams of Cu$((R,S)$-CyPF-t-Bu)(I) (**8**, left), and Cu$((R,S)$-PPF-t-Bu)(I)•CH$_2$Cl$_2$ (**9**•CH$_2$Cl$_2$, right, with the solvent molecule omitted).

The isomorphous structures of complexes **1**-**3** contained the extensively investigated $Cu_2(\mu-X)_2$ core [2], which here was puckered in a "butterfly" geometry with distorted tetrahedral coordination at copper. Unfortunately, we were not able to grow suitable crystals of fluoride complex **4** for comparison, but its structure and those of **1**-**3** were investigated computationally (see below). Table B.1 summarizes X-ray crystallographic structural data for **1**-**3** in comparison to the dppBz analogues **10**-**12**, which contain the same *o*-phenylene linker, but PPh_2 donors in place of the phospholanyl groups [6]. The Cu-X and Cu-P bond lengths were very similar, as were the P-Cu-P bite angles, but the DuPhos complexes featured larger X-Cu-X and Cu-X-Cu angles, associated with longer Cu-Cu distances.

Table B.1. Average Values of Selected Bond Lengths (Å) and Angles (deg) in [Cu(*i*-Pr-DuPhos)(X)]$_2$ Dimers **1**-**3** and the dppBz Analogues **10**-**12**

No.	X	Cu–X	Cu–P	P-Cu-P	P-Cu-X	X-Cu-X	Cu-X-Cu	Cu•••Cu	CuX$_2$/Cu'X$_2$ dihedral angle
1	I	2.6423(9)	2.255(2)	91.77(7)	116.32(6)	101.45(3)	76.28(3)	3.264	154.61
2	Br	2.4895(7)	2.2536(12)	91.51(4)	118.08(6)	95.40(5)	82.09(5)	3.208	154.50
3	Cl	2.3649(14)	2.2500(14)	91.55(5)	118.08(6)	95.40(5)	82.09(5)	3.106	154.65
10	I	2.635(9)	2.281(2)	87.5(6)	114.24(6)	109.3(3)	66.7(2)	2.898	143.7
11	Br	2.478(7)	2.259(1)	89.2(4)	114.66(4)	107.6(2)	69.8(2)	2.837	124.5
12	Cl	2.359(1)	2.254(2)	89.0(5)	116.38(6)	102.3(4)	74.8(4)	2.866	150.9

As in **1**-**3**, the structures of **5** and **7** also contained distorted tetrahedral copper, supported by bridging bis(phosphines). In **5**, the large P-Cu-P angle of 123.78(4)° was accompanied by a diamond-shaped Cu_2I_2 core including acute Cu-I-Cu angles (63.5°) and a Cu-Cu distance of

2.8694(9) Å. Similar bridging coordination in copper complexes is known for dppf [20] and its

P(t-Bu)$_2$ analogue dtbpf [21], but was not previously reported with any metal for Me-FerroLANE.

The structure of cluster **7** featured both a chelate Et-FerroTANE (bite angle = 112.5(3)°) and two

bis(phosphetanes) bridging two coppers, with an unusual Cu$_5$I$_5$ core (Figure 3) [22]. As with Me-

FerroLANE in **5**, bridging coordination of Et-FerroTANE had not been observed earlier. For the

three different types of bridging iodides in **7**, slightly longer Cu-I bonds were generally observed

with larger iodide coordination numbers (for μ_4-I(3), Cu(2)-I = 2.769(2) Å and Cu(3)-I = 2.740 Å;

for μ_3-I(2), Cu(1)-I = 2.675(2) Å, Cu(2)-I = 2.680(3) Å, and Cu(3)-I = 2.650(2) Å; for μ_2-I(1),

Cu(2)-I = 2.660(3) Å, and Cu(3)-I = 2.669(2) Å).

As described in the introduction, Cu(Josiphos)(Br) complexes with PPh$_2$ and PCy$_2$ donors

formed three-coordinate monomers or four-coordinate, bromide-bridged dimers [4]. As expected,

increasing the size of the phosphine (P(t-Bu)$_2$) and the halide (iodide) yielded monomeric crystals

of **8** and **9**. Their structures (Figure B.6) were similar to those of a related monomeric bromide

complex, with distorted trigonal planar coordination and Josiphos bite angles of 106.21(3)° and

103.62(7)°. As seen in Table B.2, changing the phosphine substituents (t-Bu/Cy/Ph) and the halide

(I/Br) had only small effects on the structures.

Table B.2. Selected Bond Lengths (Å) and Angles (deg) in Cu(*t*-Bu-Josiphos)(I) Complexes **8** and **9** and the Analogous Bromide Complex Cu(PPF-*t*-Bu)(Br)
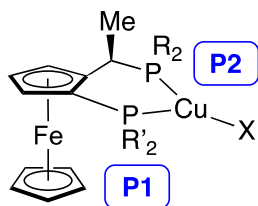
Josiphos/X	CyPF-*t*-Bu/I (8)	PPF-*t*-Bu/I (9•CH₂Cl₂)	*Rac*-PPF-Cy/Br [a]	*Enant*-PPF-Cy/Br [a]
R/R'	*t*-Bu/Cy	*t*-Bu/Ph	Cy/Ph	Cy/Ph
Cu–X	2.5187(4)	2.4970(9)	2.3130(3)	2.3232(5)
Cu–P1	2.2437(8)	2.232(2)	2.2395(6)	2.2659(7)
Cu–P2	2.2562(8)	2.2563(19)	2.2429(5)	2.2626(8)
X–Cu–P1	123.34(2)	126.16(6)	130.20(2)	130.86(2)
X–Cu–P2	130.41(2)	130.19(6)	125.88(2)	126.69(2)
P1–Cu–P2	106.21(3)	103.62(7)	102.51(2)	101.97(3)

[a] The structure of the bromide complex in reference 4b was determined separately with racemic and enantiomerically pure Josiphos ligands. All complexes in this work were prepared with enantiomerically pure ligands.

Copper complexes **1**-**9** are the first examples with these ligands. For future applications, it would be useful to determine their coordination modes spectroscopically, without recourse to X-ray crystallography. Therefore, we investigated their ^{31}P{^{1}H} NMR spectra, which all featured broad signals typical of Cu-phosphine complexes [23]. Binding *i*-Pr-DuPhos to the copper halides resulted in ^{31}P NMR coordination chemical shifts from $\square$ –11.2 (free ligand) [24] to –2.8 (F), –7.1 (Cl), –5.6 (Br), or –3.6 ppm (I; all data in CDCl₃). Shifts similar in magnitude were observed for the CuX complexes of the related *o*-phenylene-linked bis(phosphine) dppBz in **10**-**12**, from $\square$ –

13.0 (ligand) [25] to –17.2 (Cl), –19.0 (Br), and –22.1 ppm (I). Similarly, the Me-FerroLANE [31]P

NMR chemical shift moved from –1.1 (ligand) to 3.5 (CDCl$_3$) or –8.9 ppm (C$_6$D$_6$) on formation

of **5**. This surprisingly large, reversible, solvent-dependent chemical shift difference might arise

from a structural change, for example isomerization between bridging and chelate bis(phosphines),

but we have no direct evidence for this possibility. The Et-FerroTANE ^{31}P NMR signal [26]

moved from $\square$ 13.1 to two broad signals at 2.9 and –0.5 ppm (CD$_2$Cl$_2$) in **7**, which, on the basis

of their relative intensity, were assigned to chelating and bridging Et-FerroTANE, respectively.

This assignment is consistent with the ^{31}P NMR shift of [Cu(Et-FerroTANE)(I)]$_2$ (**6**, 4.7 ppm in

CD$_2$Cl$_2$), which likely contains a bridging bis(phosphine), as in **6**. For chelating *t*-Bu-Josiphos

ligands, large P(*t*-Bu)$_2$ and small PCy$_2$ or PPh$_2$ coordination chemical shifts were observed, from

$\square\square$46.6 and –15.4 to $\square\square$26.5 and –14.7 for CyPF-*t*-Bu in **8** and from $\square\square$45.9 and –26.1 to

$\square\square$32.1 and –22.3 for PPF-*t*-Bu in **9** [27]. This chelation led to large increases in J$_{PP}$, from 16 to

154 Hz and from 50 to 160 Hz for **8** and **9** respectively.

Photophysical Properties of Complexes 1-4 As shown in Figure B.7, varying the halide in

DuPhos complexes **1-4** had little effect on their UV-vis spectra in CH$_2$Cl$_2$ [28]. For **1-3**, the intense

peaks around 360 nm had extinction coefficients of ~10^4 M^{-1}, consistent with their assignment, as

in similar complexes, to (M+X)LCT charge transfer processes.
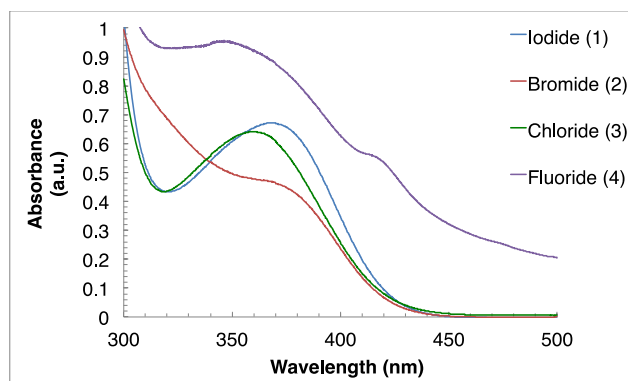
Figure B.7. UV-Vis Spectra of **1-4** in CH_2Cl_2 (10^{-4} M)

Solid samples of DuPhos complexes **1-4** emitted yellow-green light upon UV irradiation at room temperature (Figure B.8). Emission also occurred in PMMA films formed by spin-coating of CH_2Cl_2 solutions (Supporting Information) [29]. In contrast, no emission was observed in ferrocene-based **5-9**.
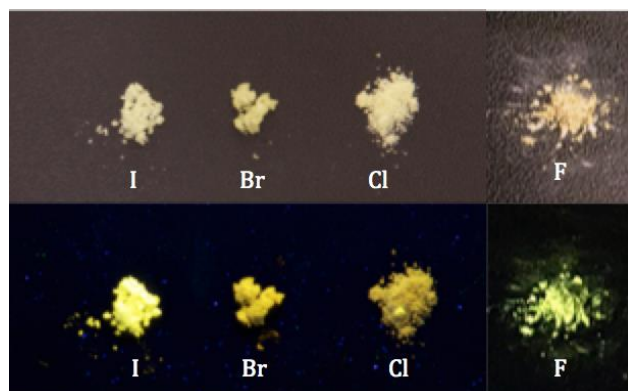
Figure B.8. Samples of **1-4** at room temperature under ambient light (above) and on UV irradiation (below).

The luminescence of **1**-**4** was further probed by low-temperature spectroscopy (Figure B.9 and Table B.3). The excitation profiles in the solid state at 77 K, with $\square_{max}$ ranging from 372 to 397 nm, were similar to the room-temperature UV-vis spectra in CH_2Cl_2 solution, except for the low-energy absorption observed in solution for fluoride **4** [28]. Quantum yields measured for solid samples at room temperature in air are included in Table B.3. Consistent with qualitative observations, iodide complex **1** had the brightest emission under these conditions.
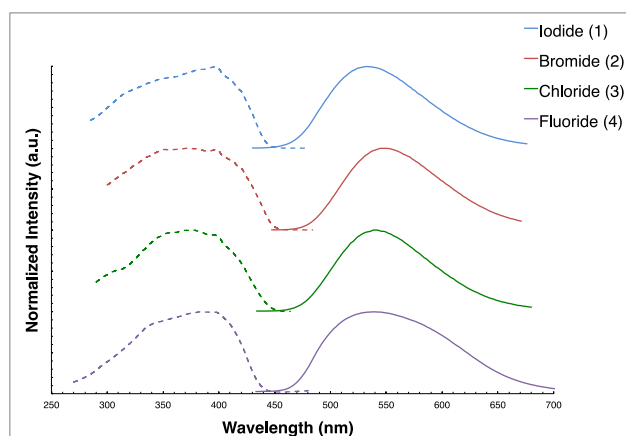
Figure B.9. Luminescence spectra of **1**-**4** at 77 K. All emission spectra were obtained using 400 nm as the excitation wavelength. All excitation spectra were obtained using the emission peak maximum.

Table B.3. Photophysical data for **1-4** (solid state, 77 K)

Compound (X)	$\lambda_{ex}(nm)^a$	$\lambda_{em}(nm)$	Apparent Stokes Shift $(cm^{-1})^b$	Quantum Yield (298 K)
1 (I)	397	532	6390	0.039(3)
2 (Br)	372	549	8670	0.017(2)
3 (Cl)	374	542	8290	<0.01
4 (F)	384	539	7490	<0.01

[a] λ_{max} from excitation spectrum [b] energy difference between absorption and emission peaks, which may not involve the same excited state

Electronic Structure of Complexes 1-4: Computational Studies To investigate the photophysical properties of DuPhos complexes **1**-**4**, we calculated the structures of their ground and excited states using DFT methods (see the experimental section and Supporting Information for details). For the ground states, the computed (gas-phase) structures were in reasonable agreement with those observed by X-ray crystallography in the solid state. The calculations slightly overestimated the Cu–X and Cu–P bond lengths, with the best agreement for functionals including a dispersion correction [30]. However, structures optimized with the B3LYP-D3 functional, which includes dispersion corrections, showed significantly larger deviations from the crystallographic metrics within the Cu_2X_2 core, especially in Cu•••Cu distances; these core metrics were better reproduced by B3LYP calculations without dispersion (Table B.4). This is an unusual deviation from current thinking, in which inclusion of dispersion is usually strongly advocated [30].

Table B.4. Comparison of gas-phase Cu-Cu distances and CuCl$_2$Cu bridge fold angles (dihedral angles between the CuCl$_2$ planes) as calculated by DFT (B3LYP-D3 and B3LYP) and determined crystallographically in the solid state.

	Cu-Cu distance (Å)			CuCl$_2$Cu Fold Angle (deg)		
	B3LYP-D3	B3LYP	X-ray	B3LYP-D3	B3LYP	X-ray
I (**1**)	3.061	3.426	3.264	143.2	157.6	154.6
Br (**2**)	2.862	3.254	3.208	145.4	164.4	154.5
Cl (**3**)	2.861	3.180	3.106	146.9	162.4	154.7
F (**4**)	2.610	2.909	-	146.2	168.9	-

A superimposition of structures of the chloride dimer **3** determined using both functionals is shown in Figure B.10. As shown in Table B.4, without dispersion corrections, the fold angle between each Cl-Cu-Cl plane is significantly larger and the Cu—Cu distance significantly longer than when dispersion corrections are included; analogous trends were observed for the I, Br and F analogues, although no crystallographic data are available for the fluoride. Thus the dispersion corrected functional underestimates the fold angle in the bridge, with a resultant large decrease in the Cu-Cu distance. We suggest that in the gas-phase calculation, in which no intermolecular interactions are included, many small intramolecular dispersion attractions between the ligand CH bonds are sufficient to cause additional folding in the bridge and reduction in the Cu-Cu distance, as shown in Figure B.10, while in the solid state these intramolecular interactions are counterbalanced by intermolecular interactions to give a more planar bridge and a longer Cu-Cu distance. This illustrates that care must be used when validating the quality of gas-phase DFT results by their agreement, or lack thereof, with crystallographic data. We will have more to say about the solution structure later.
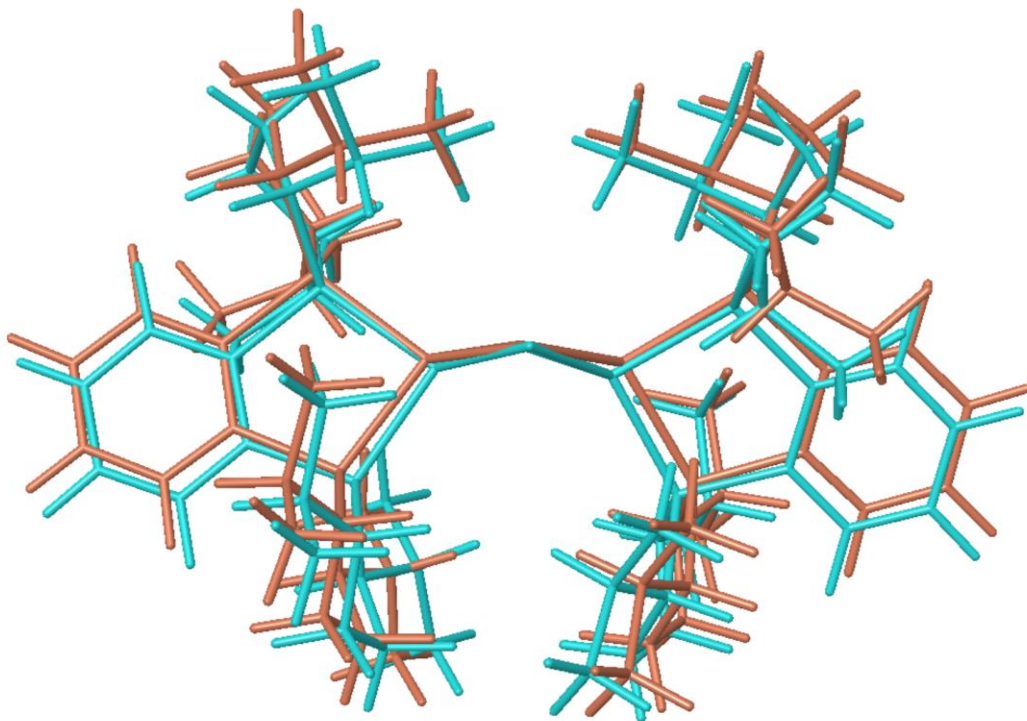
Figure B.10. DFT calculated gas-phase structures for **3** using the B3LYP-D3 (blue) and B3LYP (bronze) functionals, looking down the Cl-Cl vector.
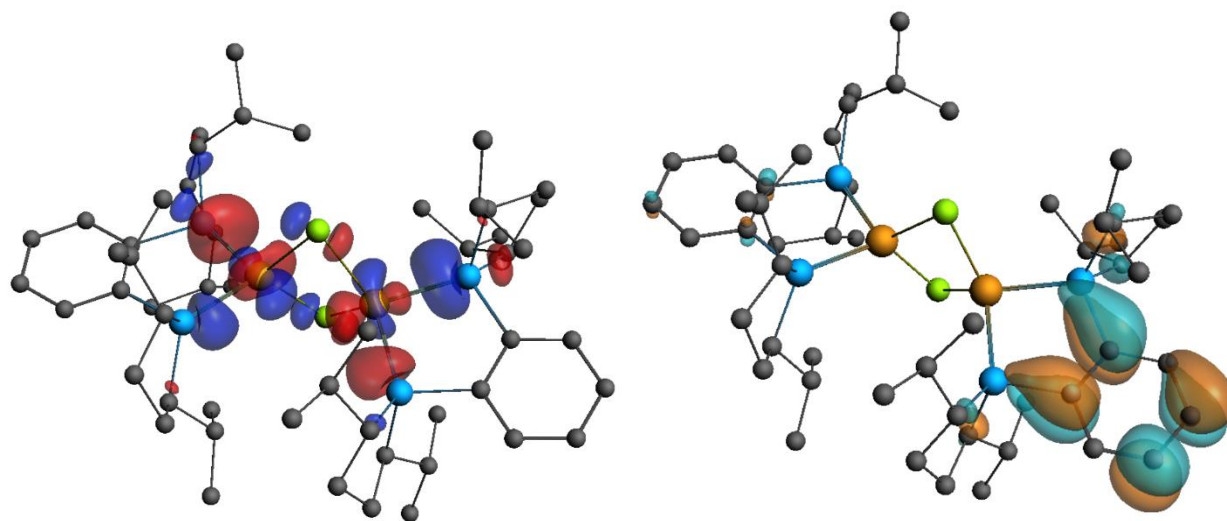
Figure B.11. Calculated (B3LYP-D3) HOMO (left) and LUMO (right) for **3**.

As shown in Figure B.11 for the chloro complex **3**, the computed HOMOs in the halide series involve interactions of Cu 3d, halide p, and the out of phase P lone pair combinations, and the LUMO is an entirely ligand based □* MO within the *i*-Pr-DuPhos *o*-phenylene group.

TD-DFT methods were used to compute the UV-vis spectra of **1**-**4** [29]. There is reasonable agreement between the computed gas-phase spectra (Figure B.12) and the experimental ones in CH₂Cl₂ solution. In particular, the calculations reproduced the similarity of the spectra and their lack of dependence on the halide. Notably, the analogous spectral calculations on the more folded B3LYP-D3 structures gave poorer agreement with experiment (see the Supporting Information) suggesting that the solution structures of these dimers may be more similar to the less folded solid state ones, in which intramolecular dispersive forces are less controlling of structure.
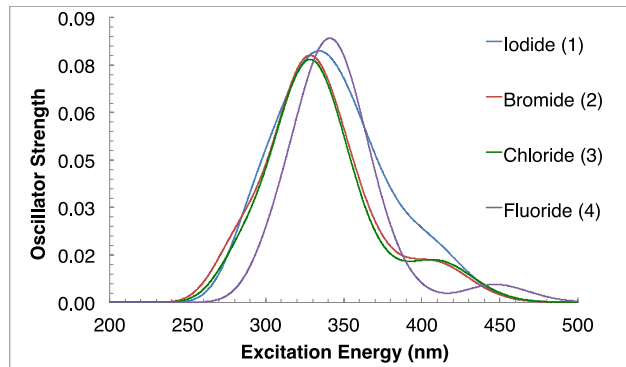
Figure B.12. Computed (B3LYP) UV-Vis Spectra of **1-4**

Optimization of the first singlet excited state was also carried out for each compound using TD-DFT methods. An overlay of the computed structures of ground and first excited states for chloride complex **3** (Figure B.13) is consistent with the expected results of a HOMO-LUMO transition and an (M+X)LCT emissive excited state. In particular, the excited state included longer Cu–X and Cu•••Cu distances, with a significantly longer C–C bond in one DuPhos aryl group, consistent with weaker bonding both in the Cu₂X₂ core and the DuPhos arene ring. The superimposition also

illustrates the significant twisting of the DuPhos ligand containing the long C-C bond relative to the ground state. Calculations without dispersion gave similar results, but with less folded Cu_2X_2 cores, as also observed for the ground states.
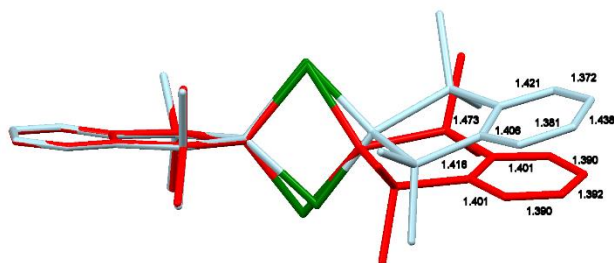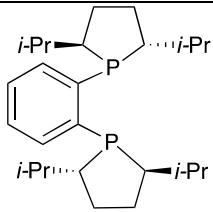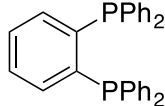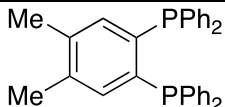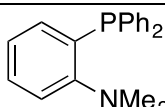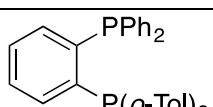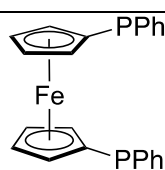
Figure B.13. Overlay of the computed (B3LYP-D3) ground state (red) and excited state (blue) structures for **3**.

Structure-Property Relationships in Photophysical Properties of 1-4 As in structurally similar Cu(I) phosphine halide complexes, we propose that excitation from a Cu_2X_2-based HOMO to a π^* acceptor phosphine LUMO (DuPhos *o*-phenylene group) [6] in **1**-**4** leads to (M+X)LCT excited states, for which the structures of the lowest-energy singlet states were optimized. By analogy to previous work [6], we assume that the emissive excited states have (M+X)LCT character, but cannot tell if they are singlets or triplets.

In related complexes, (M+X)LCT emission energy can often be tuned by changing the halide and/or the phosphine, to control the energy of the HOMO and/or LUMO [31]. Table B.5 compares low-temperature emission spectral data for **1**-**3** and analogous complexes, which all also contain P-aryl acceptor groups. Because related fluoride complexes are rare, data for **4** is not included.

Table B.5. Emission spectroscopic data (nm) for **1**-**3** and related [Cu(diphos)(X)]$_2$ Complexes[a]

number	Diphos	Cl	Br	I
1		542	549	532
2		537	524	505
3		532	517	500
4		513	498	471
5		508	503	506
6		518	520	523

[a] Data from solid-state emission spectra at 77 K, except for entry 6 (room temperature in CH$_2$Cl$_2$ solution)

In some cases (numbers 2-4), emission wavelengths showed a smooth dependence on halide, in the order Cl > Br > I. This behavior has been rationalized on the basis of the relative ligand field strengths (Cl > Br > I), which make the Cu$_2$X$_2$ HOMO highest in energy for X = Cl, leading to reduced emission energy and higher wavelength [6,31,33]. However, in some closely related structures, the halide had little effect (entries 5-6) [34,35]. Our data for **1**-**3**, likewise, did not show

a smooth trend (number 1; note that the emission maximum for fluoride **4** was at 539 nm). It has been proposed that such behavior reflects an important contribution from the phosphine donor orbitals to the HOMO [2].

A more direct test of the effects of switching from the PPh_2 donor to the phospholane group comes from comparing data for **1-3** with the dppBz analogues **10**-**12** (Table B.5, entries 1-2). The ligand field of the alkylphosphine donor phospholane should be greater than that of the arylphosphine PPh_2 group [36]. This should increase the HOMO energy, reducing emission energy and increasing wavelength, as described above for the halides. This argument is consistent with literature emission data for the phosphino-pyridine complexes in Figure B.14 containing PPh_2 and phospholane donors, a rare example of this comparison [37], and it also works in rationalizing the increased emission wavelength for **1** and **2** in comparison to their dppBz analogues **10** and **11**. The similar emission wavelengths for **3** and **12** may reflect overlaid halide effects.
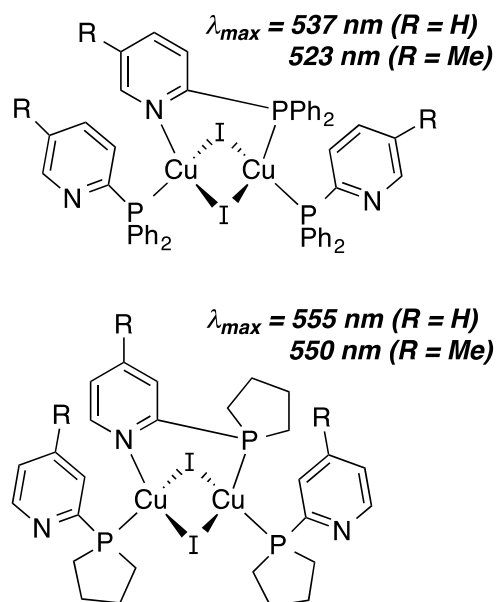
Figure B.14. Emission Wavelength Data (Solid State, Room Temperature) for Phosphine-Pyridine CuI Complexes Containing Diphenylphosphino or Phospholane Donors

B.3 Conclusions.

Structure-Property Relationships As described in the Introduction (Figure B.1), changing the bis(phosphine) controls the structure and properties of $[Cu(diphos)(X)]_n$ complexes, and we have observed similar relationships here with several chiral bis(phosphines) new to copper coordination chemistry. The synthesis and structural characterization of *i*-Pr-DuPhos complexes **1-3** established the expected chelation, which is consistent with previous hypotheses on the mechanisms of Cu(*i*-Pr-DuPhos)-catalyzed reactions [16]. The larger bite angles of the ferrocene-linked bis(phospholane) Me-FerroLANE and bis(phosphetane) Et-FerroTANE resulted in different structures, with chelating and/or bridging coordination in **5** and **7**. The combination of large bite angle, bulky phosphine substituents, and iodide ligands led to monomeric *t*-Bu-Josiphos complexes **8** and **9**, as expected in comparison to related complexes [4].

Related structure-property relationships were observed in the photophysical properties of emissive complexes **1-4**, which contain the better donor phospholanes in comparison to analogs with the more commonly used diarylphosphino groups. As shown by the comparison in Table B.5, however, varying the halide in the dimers $[Cu(diphos)(X)]_2$ may result either in smooth trends in emission energy or in discontinuities, as in our data for **1**-**4**; further structure-property studies, including additional study of rare fluoride complexes, may enable better control of these parameters. We also observed that a better match of the Cu_2X_2 core crystal structure and the solution UV-vis spectra to computed results was obtained in DFT calculations when dispersion was not included, which may be more general in such conformationally flexible systems.

B.4 Experimental Section. General Experimental Details Unless otherwise noted, all reactions and manipulations were performed in dry glassware under a nitrogen atmosphere at ambient temperature in a glove box or using standard Schlenk techniques. Pentane, CH_2Cl_2, ether,

THF, and toluene were dried over alumina columns similar to those described by Grubbs [38]. NMR spectra were recorded with 500 or 600 MHz Bruker spectrometers. ^{1}H or ^{13}C NMR chemical shifts are reported vs Me$_4$Si and were determined by reference to the residual ^{1}H or ^{13}C solvent peaks. ^{31}P NMR chemical shifts are reported vs H$_3$PO$_4$ (85%) used as an external reference. Coupling constants are reported in Hz, as absolute values. Unless indicated, peaks in NMR spectra are singlets. Quantitative Technologies Incorporated/Intertek Pharmaceutical Services (Whitehouse, NJ) or Atlantic Microlab (Norcross, GA) provided elemental analyses. Mass spectrometry was performed at the University of Illinois. Reagents were from commercial suppliers.

[Cu((*R,R*)-*i*-Pr-DuPhos)(I)]$_2$ (1) To a slurry of Cu(I) iodide (44 mg, 0.23 mmol) in 5 mL of THF was added a solution of (*R,R*)-*i*-Pr-DuPhos (96 mg, 0.23 mmol) in 2 mL of THF and the resulting yellow solution was stirred for 20 min. The solution was concentrated under vacuum to give a mixture of pale yellow powder and yellow crystalline material. The mixture was partially re-dissolved in ether (~3 mL) at room temperature, then cooled to -20 °C. Overnight, a pale yellow crystalline solid formed. The solution was decanted and the crystals were dried under vacuum (0.140 g, 99%). The solid was washed with pentane to remove a small amount of free *i*-Pr-DuPhos.

A sample recrystallized from CH$_2$Cl$_2$ contained 0.75 equiv of that solvent, according to ^{1}H NMR integration and elemental analysis. Anal. Calcd for C$_{52}$H$_{88}$Cu$_2$I$_2$P$_4$•0.75CH$_2$Cl$_2$: C, 49.43; H, 7.04. Found: C, 49.74; H, 7.08. HRMS *m/z* calcd. for C$_{52}$H$_{88}$Cu$_2$I$_2$P$_4$: 1216.2518. Found: 1216.2498. ^{31}P{^{1}H} NMR (CDCl$_3$, 25 °C): δ -3.6. ^{1}H NMR (CDCl$_3$, 25 °C): δ 7.70-7.69 (m, 4H, Ar), 7.47-7.46 (m, 4H, Ar), 2.53-2.50 (br m, 4H, CH), 2.31-2.23 (br m, 8H, CH$_2$), 2.20-2.15 (br m, 4H, CH), 2.09-2.06 (br m, 4H, CH), 1.79-1.74 (overlapping m, 4H, CH$_2$), 1.71-1.64 (br m, 4H, CH$_2$), 1.26-1.22 (br m, 4H, CH), 1.11 (d, J = 7, 12H, *i*-Pr Me), 0.94 (d, J = 7, 12H, *i*-Pr Me), 0.75 (d, J = 7,

12H, *i*-Pr Me), 0.68 (d, J = 7, 12H, *i*-Pr Me). $^{13}C\{^{1}H\}$ NMR (CDCl$_3$, 25 °C): δ 143.6 (t, J = 21, quat Ar), 134.7 (t, J = 2, CH), 129.8 (CH), 52.4 (t, J = 9, CH), 51.3 (t, J = 9, CH), 32.8 (CH$_2$), 30.7 (t, J = 8, CH), 28.7 (CH), 28.3 (CH$_2$), 24.9 (t, J = 3, *i*-Pr Me), 23.8 (t, J = 5, *i*-Pr Me), 21.5 (t, J = 3, *i*-Pr Me), 20.3 (t, J = 4, *i*-Pr Me).

[Cu((*R*,*R*)-*i*-Pr-DuPhos)(Br)]$_2$ (2) To a slurry of Cu(I) bromide (33 mg, 0.23 mmol) in 5 mL of THF was added a solution of (*R*,*R*)-*i*-Pr-DuPhos (96 mg, 0.23 mmol) in 2 mL of THF and the resulting yellow solution was stirred for 20 min. The solution was concentrated under vacuum to give a mixture of yellow powder and yellow crystalline material. The mixture was partially re-dissolved in ether (~3 mL) at room temperature, then cooled to -20 °C. Overnight, a yellow crystalline solid was formed. The solution was decanted and the crystals were dried under vacuum (0.126 g, 97%). X-ray crystallography showed that the crystals were [Cu((*R*,*R*)-*i*-Pr-DuPhos)(Br)]$_2$•THF.

Anal. Calcd for C$_{52}$H$_{88}$Cu$_2$Br$_2$P$_4$: C, 55.56; H, 7.89. Found: C, 55.56; H, 8.05. HRMS *m/z* calcd. for C$_{52}$H$_{88}$Cu$_2$Br$_2$P$_4$: 1120.2795. Found: 1120.2767. $^{31}P\{^{1}H\}$ NMR (CDCl$_3$, 25 °C): δ -5.6. ^{1}H NMR (CDCl$_3$, 25 °C): δ 7.69 (br m, 4H, Ar), 7.46 (br m, 4H, Ar), 2.51 (br m, 4H, CH), 2.25 (br m, 8H, CH$_2$), 2.13 (br m, 4H, CH), 2.03-2.02 (br m, 4H, CH), 1.79-1.74 (br m, 4H, CH$_2$), 1.70-1.63 (br m, 4H, CH$_2$), 1.2 (overlapping br m, 4H, CH), 1.1 (d, J = 7, 12H, *i*-Pr Me), 0.95 (d, J = 7, 12H, *i*-Pr Me), 0.77 (d, J = 6, 12H, *i*-Pr Me), 0.68 (d, J = 6, 12H, *i*-Pr Me). $^{13}C\{^{1}H\}$ NMR (CDCl$_3$, 25 °C): δ 143.4 (t, J = 22, quat Ar), 134.6 (Ar), 129.7 (Ar), 52.4 (t, J = 9, CH), 51.5 (t, J = 8, CH), 33.0 (CH$_2$), 30.8 (t, J = 9, CH), 28.7 (CH), 28.2 (CH$_2$), 24.9 (br t, *i*-Pr Me), 23.7 (t, J = 5, *i*-Pr Me), 21.7 (br t, *i*-Pr Me), 19.7 (t, J = 4, *i*-Pr Me).

[Cu((*R*,*R*)-*i*-Pr-DuPhos)(Cl)]$_2$ (3) To a slurry of Cu(I) chloride (23 mg, 0.23 mmol) in 5 mL of THF was added a solution of (*R*,*R*)-*i*-Pr-DuPhos (96 mg, 0.23 mmol) in 2 mL of THF and the

resulting green solution was stirred for 20 min. The solution was concentrated under vacuum to give a mixture of yellow-green powder and yellow-green crystalline material. The mixture was partially redissolved in ether (~3 mL) at room temperature, then cooled to –20 °C. Overnight, a yellow-green crystalline solid formed. The solution was decanted and the crystals were dried under vacuum (0.107 g, 89%). The solid was washed with pentane to remove a small amount of free *i*-Pr-DuPhos. X-ray crystallography showed that the crystals were [Cu((*R,R*)-*i*-Pr-DuPhos)(Cl)]$_2$•THF.

The co-crystallized solvent molecules in dimers **1**-**3** appeared to be lost easily, according to elemental analyses. For a sample which was recrystallized from THF/ether, the ^{1}H NMR spectrum showed it contained about 1.5 equiv of THF, which was apparently lost before analysis. Anal. Calcd for C$_{52}$H$_{88}$Cu$_2$Cl$_2$P$_4$: C, 60.34; H, 8.57. Found: C, 59.91; H, 8.53. Another sample, recrystallized from CH$_2$Cl$_2$, analyzed for a monosolvate. Anal. Calcd for C$_{52}$H$_{88}$Cu$_2$Cl$_2$P$_4$•CH$_2$Cl$_2$: C, 56.83; H, 8.10. Found: C, 56.52; H, 8.08. After this solid had been stored at room temperature for several days, its ^{1}H NMR spectrum showed the presence of 0.6 equiv of CH$_2$Cl$_2$. HRMS *m/z* calcd. for C$_{52}$H$_{88}$Cu$_2$Cl$_2$P$_4$: 1032.3806. Found: 1032.3789. ^{31}P{^{1}H} NMR (CDCl$_3$, 25 °C): δ -7.1. ^{1}H NMR (CDCl$_3$, 25 °C): δ 7.72-7.69 (br m, 4H, Ar), 7.48-7.47 (br m, 4H, Ar), 2.55-2.50 (br m, 4H, CH), 2.29-2.23 (br m, 8H, CH$_2$), 2.19-2.12 (br m, 4H, CH), 2.06-2.02 (br m, 4H, CH), 1.81-1.75 (apparent dq, ^{1}J$_{H-H}$ = 13, ^{2}J$_{H-H}$ = 13 4H, CH$_2$), 1.71-1.64 (apparent dq, ^{1}J$_{H-H}$ = 12, ^{2}J$_{H-H}$ = 12, 4H, CH$_2$), 1.24-1.21 (br m, 4H, CH), 1.12 (d, J = 7, 12H, *i*-Pr Me), 0.97 (d, J = 7, 12H, *i*-Pr Me), 0.80 (d, J = 7, 12H, *i*-Pr Me), 0.71 (d, J = 7, 12H, *i*-Pr Me). ^{13}C{^{1}H} NMR (CDCl$_3$, 25 °C): δ 143.4 (t, J = 22, quat Ar), 134.6 (Ar), 129.7 (Ar), 52.6 (t, J = 10, CH), 51.6 (t, J = 11, CH), 33.2 (CH$_2$), 30.9 (t, J = 9, CH), 28.9 (CH), 28.3 (CH$_2$), 25.0 (t, J = 3, *i*-Pr Me), 23.7 (t, J = 6, *i*-Pr Me), 21.8 (t, J = 7, *i*-Pr Me), 19.6 (t, J = 4, *i*-Pr Me).

[Cu((*R,R*)-*i*-Pr-DuPhos)(F)]₂ (4) A solution of [Cu((*R,R*)-*i*-Pr-DuPhos)(I)]₂ (**1**, 140 mg, 0.115 mmol) in 2 mL of THF was added to AgF (58 mg, 0.45 mmol, 2.0 equiv). The resulting slurry was protected from light and sonicated for 1.5 h in an ultrasonic cleaning bath, then filtered through Celite to remove precipitate formed during the reaction. The solvent was removed under vacuum to give a yellow-gold solid (74 mg, 64%).

The parent ion was not observed in the mass spectrum, in which the main peak was a [Cu₂(*i*-Pr-DuPhos)₂] fragment. MS *m/z* calcd. for $C_{52}H_{88}Cu_2$ (MH–2F)⁺: 963.4. Found: 963.5. ³¹P{¹H} NMR (CDCl₃, 25 °C): δ -2.8. ³¹P{¹H} NMR (THF-d₈, 25 °C): δ -6.2. ¹⁹F NMR (THF-d₈, 25 °C): δ -140.3. ¹H NMR (THF-d₈, 25 °C): δ 7.82-7.80 (m, 4H, Ar), 7.48-7.46 (m, 4H, Ar), 2.62-2.56 (br m, 4H, CH), 2.32-2.19 (br m, 16H, overlapping CH₂ and CH), 1.84 (apparent dq, J = 6, 6, 4H, CH₂), 1.79-1.70 (br m, 4H, CH₂), 1.42 (very br, 4H, CH 1.16 (d, J = 7, 12H, *i*-Pr Me), 0.96 (d, J = 8, 12H, *i*-Pr Me), 0.72 (d, J = 7, 12H, *i*-Pr Me), 0.68 (d, J = 6, 12H, *i*-Pr Me). ¹³C{¹H} NMR (THF-d₈, 25 °C): δ 144.8 (t, J = 21, quat Ar), 135.4 (t, J = 3, CH), 130.1 (CH), 52.8 (t, J = 8, CH), 51.4 (t, J = 8, CH), 32.6 (CH₂), 31.3 (t, J = 9, CH), 29.4 (CH), 29.1 (CH₂), 25.0, (br, *i*-Pr Me), 24.2 (br, *i*-Pr Me), 21.1 (*i*-Pr Me), 20.9 (br, *i*-Pr Me).

[Cu((*R,R*)-Me-FerroLANE)(I)]₂ (5) Treatment of CuI with Me-FerroLANE gave **5**; the formation of impurities in this reaction depended on the solvent and the source/purity of copper iodide, as summarized below. To a slurry of CuI (Strem, 98%; 22 mg, 0.12 mmol) in 2 mL of THF was added a solution of (*R,R*)-Me-FerroLANE (37.5 mg, 0.12 mmol) in 2 mL of THF and the resulting dark orange solution was stirred for 20 min. The solution was concentrated under vacuum to give an orange solid. The solid was redissolved in THF; slow evaporation gave a mixture of orange crystals and amorphous material (0.058 g, 86%), which contained an unidentified impurity (³¹P{¹H} NMR: □ 62.9). In a similar experiment, the orange solid was

washed with ether and pentane; X-ray quality crystals were obtained from the pale orange pentane solution. No impurities were formed in a similar preparation in toluene, which gave orange crystals after recrystallization from toluene/pentane at –20 °C. Similarly, no impurities were observed with higher-purity CuI in THF. To a slurry of "Puratronic" CuI (Alfa Aesar, 99.999%; 22 mg, 0.12 mmol) in 1 mL of THF was added a solution of (*R,R*)-Me-FerroLANE (47.5 mg, 0.12 mmol) in 2 mL of THF. The resulting bright orange solution was stirred for 20 min, then filtered through Celite. Concentration under vacuum gave analytically pure orange powder (53 mg, 42% yield).

Anal. Calcd. for $C_{44}H_{64}Cu_2I_2P_4Fe_2$: C, 43.70; H, 5.33. Found: C, 43.51; H, 5.24. HRMS *m/z* calcd. for $C_{44}H_{64}Cu_2IP_4Fe_2(M–I)^+$: 1081.0294. Found: 1081.0278. Because the ^{31}P NMR spectra were solvent-dependent, we report NMR data in different solvents. $^{31}P\{^1H\}$ NMR (CDCl$_3$, 25 °C): δ 3.5. $^{31}P\{^1H\}$ NMR (C$_6$D$_6$, 25 °C): δ –8.9. ^1H NMR (CDCl$_3$, 25 °C): δ 4.55 (4H, Cp CH), 4.34 (overlapping, 8H, Cp CH), 4.20 (4H, Cp CH), 2.75-2.72 (br m, 4H, CH), 2.43-2.41 (br m, 4H, CH), 2.27-2.23 (br m, 4H, CH$_2$), 2.02-1.98 (br m, 4H, CH$_2$), 1.62 (apparent q, J = 10, 12H, Me), 1.51-1.45 (br m, 4H, CH$_2$), 1.34-1.30 (br m, 4H, CH$_2$), 0.90 (apparent q, J = 7, Me). ^1H NMR (C$_6$D$_6$, 25 °C): δ 4.66 (4H, Cp CH), 4.17 (4H, Cp CH), 3.97 (4H, Cp CH), 3.87 (4H, Cp CH), 2.83 (4H, CH), 2.51-2.49 (br m, 4H, CH), 2.03 (4H, CH$_2$), 1.93 (4H, CH$_2$), 1.89 (apparent q, J = 8, 12H, Me), 1.51 (4H, CH$_2$), 1.25-1.21 (br m, 4H, CH$_2$), 1.19 (apparent q, J = 6, 12H, Me). All of the signals were broad. $^{13}C\{^1H\}$ NMR (CDCl$_3$, 25 °C): δ 76.4 (t, J = 12, Cp CH), 73.6 (br t, quat Cp), 73.3 (Cp CH), 71.1 (Cp CH), 70.5 (Cp CH), 36.0 (CH$_2$), 35.6 (CH$_2$), 34.9 (t, J = 9, CH), 34.0 (t, J = 9, CH), 20.9 (t, J = 9, Me), 14.9 (Me). $^{13}C\{^1H\}$ NMR (C$_6$D$_6$, 25 °C): δ 77.2 (t, J = 10, Cp CH), 75.4 (br t, quat C), 72.8 (Cp CH), 70.7 (Cp CH), 69.7 (Cp CH), 36.2 (CH$_2$), 36.0 (t, J = 8, CH), 35.3 (CH$_2$), 35.0 (t, J = 8, CH), 21.3 (t, J = 7, Me), 16.3 (Me).

Cu₂I₂((*S,S*)-Et-FerroTANE)₂ (6) As with Me-FerroLANE analogue **5**, impurities were formed in the reaction of Et-FerroTANE and CuI. Varying the solvent (THF or toluene) and/or the CuI purity (98% to 99.9999%) did not avoid this problem, and adding copper wire, to reduce putative Cu(II) impurities [39],[i] was also unsuccessful, so we were not able to get pure bulk samples of **6**. In a typical synthesis, to a slurry of CuI (Strem, 98%; 44 mg, 0.23 mmol) in 2 mL of THF was added a solution of (*S,S*)-Et-FerroTANE (102 mg, 0.23 mmol) in 1 mL of THF. The resulting orange solution was stirred for 20 min, then concentrated under vacuum to give an orange solid (134 mg, 92%). ^{31}P NMR spectra of the bulk solid (CD₂Cl₂) showed an impurity signal at 64.3 ppm (7%), which was present in all non-crystalline material. The ^{31}P NMR spectrum of a portion of the original reaction mixture (THF) showed peaks due to the impurity ($\square$ 61.2), plus additional signals at 56.7 (trace), 12.2 (Et-FerroTANE), and 3.3 ppm (**6**). Slow evaporation of this solution gave orange crystals, which X-ray crystallography showed were Cu₅I₅((*S,S*)-Et-FerroTANE)₃ (**7**).

HRMS *m/z* calcd. for $C_{48}H_{72}Cu_2IP_4Fe_2(M–I)^+$: 1137.0920. Found: 1137.0925. ^{31}P{^{1}H} NMR (CD₂Cl₂, 25 °C): δ 4.7 (**6**), 12.1 (free Et-FerroTANE, 5%), and unidentified signals at δ 64.3 (7%), 59.2 (trace), and 45.4 (trace). ^{1}H NMR (CD₂Cl₂, 25 °C): δ 4.53 (4H, Cp CH), 4.41 (8H, Cp CH), 4.36 (4H, Cp CH), 2.64 (4H, FerroTANE CH), 2.43-2.37 (br m, 12H, CH₂ and FerroTANE CH), 2.27-2.24 (br m, 4H, CH₂), 2.00-1.95 (br m, 4H, CH₂), 1.38-1.37 (br m, 4H, CH₂), 1.10 (t, J = 7, 12H, Me), 0.76 (t, J = 8, 12 H, Me). ^{13}C{^{1}H} NMR (CD₂Cl₂, 25 °C): δ 77.1 (t, J = 11, Cp), 74.5-74.4 (br m, quat C), 73.7 (Cp), 71.6 (Cp), 70.5 (Cp), 35.4 (t, J = 15, FerroTANE CH), 35.1 (t, J = 14, FerroTANE CH), 34.4 (t, J = 5, CH₂), 27.0 (t, J = 6, CH₂), 25.2 (CH₂), 14.0 (t, J = 6, Me), 12.3 (t, J = 4, Me).

Cu₅I₅((*S,S*)-Me-FerroTANE)₃ (7) To a slurry of CuI (Strem, 98%; 44 mg, 0.23 mmol, 5 equiv) in 2 mL of THF was added a solution of (*S,S*)-Et-FerroTANE (60 mg, 0.14 mmol, 3 equiv) in 1

mL of THF and the resulting solution was stirred for 20 min. The resulting orange solution was concentrated under vacuum to yield a bright orange solid (98 mg, 92%). ^{31}P NMR spectra of the bulk solid showed an impurity at 64.6 ppm (4.8%), which was present in all non-crystalline material. A portion of the solid was redissolved in THF; slow evaporation gave orange crystals of **7**, identified by X-ray crystallography. As with **6**, varying the CuI purity and the solvent (THF or toluene) did not prevent impurity formation, and we could not isolate pure bulk samples of **7**.

^{31}P{^{1}H} NMR (CDCl$_3$, 25 °C): δ 1.8 to -1.1 (br m, FerroTANE). ^{31}P{^{1}H} NMR (CD$_2$Cl$_2$, 25 °C): δ 2.9 (br, chelating FerroTANE), -0.5 (br, bridging FerroTANE). ^{1}H NMR (CD$_2$Cl$_2$, 25 °C): δ 5.11-5.03 (br m, 4H, Cp), 4.91-4.86 (br m, 4H, Cp), 4.64-4.52 (br m, 16 H, Cp), 2.78 (4H, FerroTANE CH), 2.48 (overlapping, 4H, FerroTANE CH), 2.41 (overlapping, 8H, CH$_2$ and FerroTANE CH), 2.12-1.92 (br m, 8H, CH$_2$), 1.93-1.92 (br m, 8H, CH$_2$), 1.25-1.22 (br m, 12H, CH$_2$), 1.06-1.02 (br m, 18H, Me), 0.70-0.67 (t, J = 7, 18H, Me). ^{13}C{^{1}H} NMR (CD$_2$Cl$_2$, 25 °C): δ 78.6-78.2 (br m, Cp), 72.7-72.2 (br m, Cp), 71.7 (br, Cp), 35.8 (d, J = 32, FerroTANE CH), 34.9 (d, J = 13, FerroTANE CH), 30.1 (d, J = 12, FerroTANE CH), 27.1-27.0 (br m, CH$_2$), 25.2-25.1 (br m, CH$_2$), 22.5 (Me), 13.8 (br, Me), 13.6 (br, Me), 12.5 (Me), 12.4 (d, J = 6, Me).

Cu((*R,S*)-CyPF-*t*-Bu)(I) (8) To "Puratronic" Cu(I) iodide (Alfa Aesar, 99.999%, 22 mg, 0.12 mmol) was added a solution of (*R,S*)-CyPF-*t*-Bu (67 mg, 0.12 mmol) in 2 mL of CH$_2$Cl$_2$. The resulting solution was stirred for 10 min, then concentrated under vacuum to give an orange solid which contained residual solvent (105 mg, 117%). Recrystallization from CH$_2$Cl$_2$/pentane at -20 °C gave orange crystals, which X-ray crystallography showed were Cu((*R,S*)-CyPF-*t*-Bu)(I).

Anal. Calcd. for C$_{32}$H$_{52}$FeP$_2$CuI: C, 51.59; H, 7.04. Found: C, 51.69; H, 7.01. HRMS m/z calcd. for C$_{32}$H$_{52}$FeP$_2$CuI: 744.1234. Found: 744.1235. ^{31}P{^{1}H} NMR (CH$_2$Cl$_2$, 25 °C): δ 26.5 (d, J = 154, P(*t*-Bu)$_2$), -14.7 (d, J = 154, PCy$_2$). ^{1}H NMR (CDCl$_3$, 25 °C): δ 4.50 (1H, Cp), 4.37 (2H, Cp),

4.20 (5H, Cp), 3.18 (br, 1H, C*H*Me), 2.19-2.11 (m, 4H, Cy CH and CH_2), 1.95 (t, J = 7, 3H, CH*Me*), 1.89-1.63 (m, 10H, Cy CH_2), 1.45 (d, J = 13, 9H, *t*-Bu), 1.39-1.30 (m, 6H, Cy CH_2), 1.23-1.15 (m, 2H, Cy CH_2), 1.03 (d, J = 13, 9H, *t*-Bu). $^{13}C\{^1H\}$ NMR ($CDCl_3$, 25 °C): δ 94.7 (dd, J = 14, 6, quat Cp), 74.7 (d, J = 14, quat Cp), 73.7 (Cp CH), 70.2 (d, J = 7, Cp CH), 69.7 (Cp CH), 68.0 (d, J = 4, Cp CH), 38.5 (d, J = 14, Cy CH), 37.1 (d, J = 3, *C*Me₃), 35.1 (d, J = 6, *C*Me₃), 33.8-33.7 (dd, J = 14, 7, Cy CH), 33.3 (*CH*Me), 31.2 (C*Me₃*), 31.1 (C*Me₃*), 30.9 (d, J = 10, Cy CH_2), 29.2 (d, J = 5, Cy CH_2), 28.6 (d, J = 5, Cy CH_2), 27.6 (2 Cy CH_2), 27.5 (d, J = 14, Cy CH_2), 27.2 (d, J = 12, Cy CH_2), 27.0 (d, J = 12, Cy CH_2), 26.8 (d, J = 9, Cy CH_2), 26.0 (d, J = 12, Cy CH_2), 17.5 (d, J = 4, CH*Me*).

Cu((*R,S*)-PPF-*t*-Bu)(I) (9) To "Puratronic" Cu(I) iodide (Alfa Aesar, 99.999%, 22 mg, 0.12 mmol) was added a solution of (*R,S*)-PPF-*t*-Bu (65 mg, 0.12 mmol) in 2 mL of CH_2Cl_2. The resulting solution was stirred for 10 min, then concentrated under vacuum to give an orange solid which contained residual solvent (101 mg, 103%). Recrystallization from CH_2Cl_2/pentane at -20 °C gave orange crystals, which X-ray crystallography showed were Cu((*R,S*)-PPF-*t*-Bu)(I)•CH_2Cl_2. Elemental analysis showed that another batch of crystals contained 0.5 equiv of CH_2Cl_2.

Anal. Calcd. for $C_{32}H_{40}CuFeIP_2(CH_2Cl_2)_{0.5}$: C, 50.34; H, 5.33. Found: C, 50.42; H, 5.43. HRMS m/z calcd. for $C_{32}H_{40}CuFeP_2$(M-I)$^+$: 605.1251. Found: 605.1258. $^{31}P\{^1H\}$ NMR (CH_2Cl_2, 25 °C): δ 32.1 (d, J = 160, P(*t*-Bu)₂), -22.3 (d, J = 160, PPh₂). ^1H NMR ($CDCl_3$, 25 °C): δ 8.07-8.04 (t, J = 8, 2H, Ar), 7.73 (t, J = 10, 2H, Ar), 7.49-7.46 (br m, 3H, Ar), 7.40-7.39 (br m, 3H, Ar), 4.58 (1H, Cp), 4.39 (1H, Cp), 4.08 (1H, Cp), 4.04 (5H, Cp), 3.47-3.46 (br m, 1H, C*H*Me), 1.99 (t, J = 7, 3H, CH*Me*), 1.37 (d, J = 13, 9H, *t*-Bu), 1.17 (d, J = 13, 9H, *t*-Bu). $^{13}C\{^1H\}$ NMR ($CDCl_3$, 25 °C): δ 135.4 (d, J = 26, quat Ar), 134.4 (d, J = 15, Ar CH), 134.1 (d, J = 16, Ar CH), 133.2 (dd, J = 26, 9,

quat Ar), 130.2 (Ar CH), 130.1 (Ar CH), 128.8 (d, J = 3, Ar CH), 128.7 (d, J = 2, Ar CH), 94.5 (dd, J = 20, 7, quat Cp), 75.9 (d, J = 24, quat Cp), 74.8 (d, J = 4, Cp CH), 71.0 (d, J = 8, Cp CH), 70.4 (Cp CH), 68.9 (d, J = 6, Cp CH), 37.2 (d, J = 4, CMe$_3$), 35.3 (d, J = 5, CMe$_3$), 33.0 (CHMe), 31.8 (d, J = 7, CMe_3), 31.2 (d, J = 7, CMe_3), 17.4 (d, J = 5, CHMe).

UV-vis spectroscopy UV-vis spectra were recorded on 10^{-4} M CH$_2$Cl$_2$ solutions of complexes **1-4** in a quartz cuvette at 298 K, using a Jasco V-630 spectrophotometer.

Emission spectroscopy Luminescent spectra were collected for microcrystalline samples **1-4**. Steady-state luminescence scans were run at 77 K. Liquid nitrogen was used as coolant. Spectra were taken with a Model Quantamaster-1046 photoluminescence spectrophotometer from Photon Technology International. This spectrometer uses a 75 W xenon arc lamp combined with two excitation monochromators and one emission monochromator. A photomultiplier tube at 800 V was used as the emission detector. The solid samples were mounted on a copper plate using non-emitting copper-dust high vacuum grease. All scans were run under vacuum using a Janis ST-100 optical cryostat.

Solid State Quantum Yield Measurements Solid state spectra were collected for microcrystalline samples **1-4** in air at 298 K using a Horiba PTI QM-400 spectrometer equipped with an integration sphere. Excitation wavelength for all samples was 400 nm.

Luminescence of 1-3 in PMMA thin films A 5% w/w solution of [Cu((*R,R*)-*i*-Pr-DuPhos)(I)]$_2$ (0.03 g) in 0.4 mL of dichloromethane was added to PMMA (0.03 g, atactic beads, average molecular weight = 350,000, Polysciences) and the mixture was stirred overnight. 400 μL of the pale yellow solution were pipetted onto a glass slide and spin coated at 800 RPM for 30 seconds. The resulting thin film was luminescent under UV light (see the SI for photos). The procedure

was similar for the chloride and bromide analogues **2**-**3**, which formed pale green and yellow-green solutions, respectively.

DFT Calculations For comparison, DFT calculations were carried out both at Maine and at Dartmouth, with different basis sets. At Maine, calculations were performed on complexes **1**-**3** with the *Gaussian09* program hosted by the University of Maine Advanced Computing Group. All calculations were performed with the B3LYP exchange-correlation and the LANL2DZ basis set throughout. Experimental XRD geometries of **1**-**3** were used as initial input structures for ground state optimization calculations. Optimized ground state structures were used for vertical energy calculations using the time dependent DFT (TD-DFT) method. Molecular orbitals were reproduced using *Avogadro 1.1.1*.

At Dartmouth, calculations were carried out using the hybrid B3LYP functional (both with and without the zero-damping, two-body only D3 correction of Grimme *et al.*, see text) [40] and the LACV3P** basis set, which uses Los Alamos Core potentials for Cu [41], and the 6-311G** basis for all lighter atoms [42], as implemented in the Jaguar suite of programs [43]. Computed ground state structures were confirmed as energy minima by calculating the vibrational frequencies using second derivative analytic methods, and confirming the absence of imaginary frequencies. Geometries of first singlet excited states were optimized using TD-DFT calculations as implemented in the Jaguar program. UV-VIS spectra were also calculated at the B3LYP ground state geometries using TD-DFT, with unrestricted occupations and including 48 excited states.

B.5 References

1. Recent examples: (a) Kainz, Q. M.; Matier, C. D.; Bartoszewicz, A.; Zultanski, S. L.; Peters, J. C.; Fu, G. C. Science 2016, 351, 681-684. Asymmetric copper-catalyzed C-N cross-couplings induced by visible light. (b) Jumde, R. P.; Lanza, F.; Veenstra, M. J.; Harutyunyan, S. R. Science 2016, 352, 433-437. Catalytic asymmetric addition of Grignard reagents to alkenyl-substituted aromatic N-heterocycles. (c) Iwamoto, H.; Kubota, K.; Ito, H. Chem. Commun. 2016, 52, 5916-5919. Highly selective Markovnikov hydroboration of alkyl-substituted terminal alkenes with a phosphine-copper(I) catalyst.

2. (a) Tsuge, K.; Chishina, Y.; Hashiguchi, H.; Sasaki, Y.; Kato, M.; Ishizaka, S.; Kitamura, N. Coord. Chem. Rev. 2016, 306, Part 2, 636-651. Luminescent copper(I) complexes with halogenido-bridged dimeric core. (b) Peng, R.; Li, M.; Li, D. Coord. Chem. Rev. 2010, 254, 1-18. Copper(I) halides: A versatile family in coordination chemistry and crystal engineering. (c) Ford, P. C.; Cariati, E.; Bourassa, J. Chem. Rev. 1999, 99, 3625-3648. Photoluminescence Properties of Multinuclear Copper(I) Compounds.

3. (a) Hashimoto, M.; Igawa, S.; Yashima, M.; Kawata, I.; Hoshino, M.; Osawa, M. J. Am. Chem. Soc. 2011, 133, 10348-10351. Highly Efficient Green Organic Light-Emitting Diodes Containing Luminescent Three-Coordinate Copper(I) Complexes. (b) Osawa, M.; Hoshino, M.; Hashimoto, M.; Kawata, I.; Igawa, S.; Yashima, M. Dalton Trans. 2015, 44, 8369-8378. Application of three-coordinate copper(I) complexes with halide ligands in organic light-emitting diodes that exhibit delayed fluorescence.

4. (a) Harutyunyan, S. R.; López, F.; Browne, W. R.; Correa, A.; Peña, D.; Badorrey, R.; Meetsma, A.; Minnaard, A. J.; Feringa, B. L. J. Am. Chem. Soc. 2006, 128, 9103-9118. On the Mechanism of the Copper-Catalyzed Enantioselective 1,4-Addition of Grignard Reagents to α,β-Unsaturated Carbonyl Compounds. (b) Caprioli, F.; Lutz, M.; Meetsma, A.; Minnaard, A. J.; Harutyunyan, S. R. Synlett 2013, 24, 2419-2422. Structural Characterisation of Cu Complexes of Chiral Ferrocenyl Diphosphine Ligands.

5. Trivedi, M.; Nagarajan, R.; Kumar, A.; Rath, N. P.; Valerga, P. Inorg. Chim. Acta 2011, 376, 549-556. Synthesis, characterization, crystal structures and photophysical properties of copper(I) complexes containing 1,1'-bis(diphenylphosphino)ferrocene (B-dppf) in doubly-bridged mode.

6. Tsuboyama, A.; Kuge, K.; Furugori, M.; Okada, S.; Hoshino, M.; Ueno, K. Inorg. Chem. 2007, 46, 1992-2001. Photophysical Properties of Highly Luminescent Copper(I) Halide Complexes Chelated with 1,2-Bis(diphenylphosphino)benzene.

7. (a) Volz, D.; Nieger, M.; Brase, S. Acta Cryst. E 2012, 68, m466-m467. Di-μ-iodido-bis{[(R)-(+)-2,2'-bis(diphenylphosphanyl)-1,1'-binaphthyl-□2P,P']copper(I)} 0.67-hydrate. (b) Hattori, G.; Sakata, K.; Matsuzawa, H.; Tanabe, Y.; Miyake, Y.; Nishibayashi, Y. J. Am. Chem. Soc. 2010, 132, 10592–10608. Copper-Catalyzed Enantioselective Propargylic Amination of Propargylic Esters with Amines: Copper-Allenylidene Complexes as Key Intermediates.

8. Effendy; Di Nicola, C.; Fianchini, M.; Pettinari, C.; Skelton, B. W.; Somers, N.; White, A. H. Inorg. Chim. Acta 2005, 358, 763-795. The structural definition of adducts of stoichiometry MX:dppx (1:1) M = CuI, AgI, X = simple anion, dppx=Ph2P(CH2)xPPh2, x = 3–6.

9. (a) Deng, Y. H.; Yang, Y. L.; Yang, X. J. Zeitschrift für Kristallographie - New Crystal Structures 2006, 221, 316-318. Crystal structure of diiodo-bis[(4R,5R)-trans-4,5-bis[(diphenylphosphinomethyl)- 2,2-dimethyl-1,3-dioxalane]dicopper(I), Cu2I2(C31H32O2P2)2. (b) Li, J.-X.; Du, Z.-X.; An, H.-Q.; Zhou, J.; Dong, J.-X.; Wang, S.-R.; Zhu, B.-L.; Zhang, S.-M.; Wu, S.-H.; Huang, W.-P. J. Molec. Struct. 2009, 935, 161-166. Syntheses, crystal structures and fluorescent properties of R,R-DIOP based copper (I) and cadmium (II) complexes {R,R-DIOP = (4R,5R)-trans-4,5-bis(diphenylphosphinomethyl)-2,2-dimethyl-1,3-dioxalane}.

10. Zhang, X.; Song, L.; Hong, M.; Shi, H.; Xu, K.; Lin, Q.; Zhao, Y.; Tian, Y.; Sun, J.; Shu, K.; Chai, W. Polyhedron 2014, 81, 687-694. Luminescent dinuclear copper(I) halide complexes double bridged by diphosphine ligands: Synthesis, structure characterization, properties and TD-DFT calculations.

11. Yazaki, R.; Kumagai, N.; Shibasaki, M. J. Am. Chem. Soc. 2010, 132, 5522-5531. Direct Catalytic Asymmetric Addition of Allyl Cyanide to Ketones via Soft Lewis Acid/Hard Bronsted Base/Hard Lewis Base Catalysis.

12. Kunkely, H.; Pawlowski, V.; Vogler, A. Inorg. Chem. Commun. 2008, 11, 1003-1005. Copper(I) Binap Complexes (binap = (2,2'-bis(diphenylphosphino)-1,1'-binaphthyl). Luminescence from IL and LLCT States.

13. Burk, M. J.; Gross, M. F. Tetrahedron Lett. 1994, 35, 9363-9366. New Chiral 1,1'-Bis(phospholano)ferrocene Ligands for Asymmetric Catalysis.

14. Berens, U.; Burk, M. J.; Gerlach, A.; Hems, W. Angew. Chem., Int. Ed. Engl. 2000, 39, 1981-1984. Chiral 1,1'-diphosphetanylferrocenes: New Ligands for Asymmetric Catalytic Hydrogenation of Itaconate Derivatives.

15. Blaser, H.-U.; Brieden, W.; Pugin, B.; Spindler, F.; Studer, M.; Togni, A. Top. Catal. 2002, 19, 3-16. Solvias Josiphos Ligands: from Discovery to Technical Applications.

16. (a) Wada, R.; Oisaki, K.; Kanai, M.; Shibasaki, M. J. Am. Chem. Soc. 2004, 126, 8910-8911. Catalytic Enantioselective Allylboration of Ketones. (b) Wada, R.; Shibuguchi, T.; Makino, S.; Oisaki, K.; Kanai, M.; Shibasaki, M. J. Am. Chem. Soc. 2006, 128, 7687-7691. Catalytic Enantioselective Allylation of Ketoimines. (c) Kanai, M.; Wada, R.; Shibuguchi, T.; Shibasaki, M. Pure Appl. Chem. 2008, 80, 1055–1062. Cu(I)-catalyzed asymmetric allylation of ketones and ketimines. (d) Zhong, C.; Kunii, S.; Kosaka, Y.; Sawamura, M.; Ito, H. J. Am. Chem. Soc. 2010, 132, 11440-11442. Enantioselective Synthesis of trans-Aryl- and -Heteroaryl-Substituted Cyclopropylboronates by Copper(I)-Catalyzed Reactions of Allylic Phosphates with a Diboron Derivative.

17. Heating two equiv of i-Pr-DuPhos and $CuF_2 \cdot 2H_2O$ in MeOH was proposed earlier (reference 16) to yield "Cu(i-Pr-DuPhos)(F)," but no characterization data was reported.

18. For related copper fluorides, see: (a) Gurung, S. K.; Thapa, S.; Kafle, A.; Dickie, D. A.; Giri, R. Org. Lett. 2014, 16, 1264-1267. Copper-Catalyzed Suzuki–Miyaura Coupling of Arylboronate Esters: Transmetalation with (PN)CuF and Identification of Intermediates. (b) Gulliver, D. J.; Levason, W.; Webster, M. Inorg. Chim. Acta 1981, 52, 153-159. Coordination stabilised copper(I) fluoride. Crystal and molecular structure of fluorotris(triphenylphosphine)copper(I)•ethanol (1/2), Cu(PPh3)3•2EtOH. For use of AgF to make metal fluorides, see: Martinez-Prieto, L. M.; Melero, C.; del Rio, D.; Palma, P.; Cámpora, J.; Álvarez, E. Organometallics 2012, 31, 1425-1438. Synthesis and Reactivity of Nickel and Palladium Fluoride Complexes with PCP Pincer Ligands. NMR-Based Assessment of Electron-Donating Properties of Fluoride and Other Monoanionic Ligands.

19. Côté, A.; Boezio, A. A.; Charette, A. B. Angew. Chem. Int. Ed. 2004, 43, 6525-6528. Evidence for the Structure of the Enantioactive Ligand in the Phosphine-Copper-Catalyzed Addition of Diorganozinc Reagents to Imines.

20. (a) Pilloni, G.; Graziani, R.; Longato, B.; Corain, B. Inorg. Chim. Acta 1991, 190, 165-167. Synthesis and solution state of [(μ-dppf)(Cu(dppf))2]X2 (dppf= 1,1′-bis(diphenylphosphino)ferrocene; X = ClO4−, BF4−).   (b) Díez, J.; Gamasa, M. P.; Gimeno, J.; Aguirre, A.; García-Granda, S.; Holubova, J.; Falvello, L. R. Organometallics 1999, 18, 662-669. Novel Copper(I) Complexes Containing 1,1'-Bis(diphenylphosphino)ferrocene (dppf) as a Chelate and Bridging Ligand: Synthesis of Tetrabridged Dicopper(I) Complexes [Cu2(μ-η1-C□R)2(μ-dppf)2] and X-ray Crystal Structure of [Cu2(μ-η1-C□CC6H4CH3-4)2(μ-dppf)2].

21. (a) Trivedi, M.; Singh, G.; Kumar, A.; Rath, N. P. Dalton Trans. 2013, 42, 12849-12852. A thiocyanato-bridged copper(I) cubane complex and its application in palladium-catalyzed Sonogashira coupling of aryl halides. (b) Trivedi, M.; Singh, G.; Kumar, A.; Rath, N. P. Dalton Trans. 2014, 43, 13620-13629. Syntheses, characterization, and structural studies of copper(I) complexes containing 1,1'-bis(di-tert-butylphosphino)ferrocene (dtbpf) and their application in palladium-catalyzed Sonogashira coupling of aryl halides. (c) Trivedi, M.; Singh, G.; Kumar, A.; Rath, N. P. Dalton Trans. 2015, 44, 20874-20882. 1,1'-Bis(di-tert-butylphosphino)ferrocene copper(I) complex catalyzed C-H activation and carboxylation of terminal alkynes.

22. (a) Zhang, Y.; Wu, T.; Liu, R.; Dou, T.; Bu, X.; Feng, P. Cryst. Growth Des. 2010, 10, 2047-2049. Three-Dimensional Photoluminescent Frameworks Constructed from Size-Tunable CuI Clusters. (b) Wu, T.; Li, M.; Li, D.; Huang, X.-C. Cryst. Growth Des. 2008, 8, 568-574. Anionic CunIn Cluster-Based Architectures Induced by In Situ Generated N-Alkylated Cationic Triazolium Salts. (c) Victoriano, L. I.; Garland, M. T.; Vega, A.; Lopez, C. Inorg. Chem. 1998, 37, 2060-2062. Crystal and Molecular Structures of a Neutral Pentanuclear Copper(I)−Iodide Complex. (d) Victoriano, L. I.; Garland, M. T.; Vega, A.; Lopez, C. J. Chem. Soc., Dalton Trans. 1998, 1127-1132. Syntheses, properties, crystal and molecular structure of a novel neutral pentanuclear copper(I) iodide species. Copper(I) complexes with tetraethylthiuram monosulfide.

23. Black, J. R.; Levason, W.; Spicer, M. D.; Webster, M. J. Chem. Soc., Dalton Trans. 1993, 3129-3136. Synthesis and Solution Multinuclear Magnetic Resonance Studies of Homoleptic Copper(I) Complexes of Group 15 Donor Ligands.

24. Burk, M. J.; Feaster, J. E.; Nugent, W. A.; Harlow, R. L. J. Am. Chem. Soc. 1993, 115, 10125-10138. Preparation and Use of C2-Symmetric Bis(phospholanes): Production of α-Amino Acid Derivatives via Highly Enantioselective Hydrogenation Reactions.

25. Levason, W.; Reid, G.; Webster, M. Acta Crystallographica Section C 2006, 62, o438-o440. 1,2-Bis(diphenylphosphino)benzene and two related mono-methiodides, [o-C6H4(PR2)(PR2Me)]I (R = Ph or Me).

26. Berens, U.; Burk, M. J.; Gerlach, A. (Chirotech). WO2000027855, 2000. Chiral Ligands for Asymmetric Catalysis.

27. (a) Togni, A.; Breutel, C.; Soares, M. C.; Zanetti, N.; Gerfin, T.; Gramlich, V.; Spindler, F.; Rihs, G. Inorg. Chim. Acta 1994, 222, 213-224. Synthesis and structure of new chiral ferrocenylphosphines for asymmetric catalysis. (b) Togni, A.; Breutel, C.; Schnyder, A.; Spindler, F.; Landert, H.; Tijani, A. J. Am. Chem. Soc. 1994, 116, 4062-4066. A Novel Easily Accessible Chiral Ferrocenyldiphosphine for Highly Enantioselective Hydrogenation, Allylic Alkylation, and Hydroboration Reactions. This paper reports the 31P NMR chemical shift for PPF-t-Bu as 49.9 ppm, instead of the 45.9 ppm in ref (a). (c) Spindler, F. EP0612758A1 (Ciba-Geigy), 1994. Ferrocenyldiphosphine als Liganden für Homogene Katalysatoren.

28. A reviewer pointed out that the low-energy absorption for fluoride complex 4 was anomalous in comparison to 1-3. This feature was reproducible in samples from different batches of 4, and a similar peak around 450 nm is seen in the computed spectrum (see Figure 10 below). However, we have not been able to crystallize 4 to obtain it analytically pure, so this absorption might be due to impurities. Moreover, although 1-4 appeared to be readily soluble in these dilute (10-4 M) CH2Cl2 solutions, we cannot rule out the presence of colloids and light scattering from aggregates, which might give rise to this spectral absorption. Therefore, we have not included an extinction coefficient for 4. Please see the Supporting Information (Figure S1) for more information on extinction coefficients.

29. Okano, Y.; Ohara, H.; Kobayashi, A.; Yoshida, M.; Kato, M. Inorg. Chem. 2016, 55, 5227–5236. Systematic Introduction of Aromatic Rings to Diphosphine Ligands for Emission Color Tuning of Dinuclear Copper(I) Iodide Complexes.

30. Grimme, S.; Hansen, A.; Brandenburg, J. G.; Bannwarth, C. Chem. Rev. 2016, 116, 5105-5154. Dispersion-Corrected Mean-Field Electronic Structure Methods.

31. Wallesch, M.; Volz, D.; Zink, D. M.; Schepers, U.; Nieger, M.; Baumann, T.; Bräse, S. Chem. Eur. J. 2014, 20, 6578–6590. Bright Coppertunities: Multinuclear CuI Complexes with N–P Ligands and Their Applications.

32. Hong, X.; Wang, B.; Liu, L.; Zhong, X.-X.; Li, F.-B.; Wang, L.; Wong, W.-Y.; Qin, H.-M.; Lo, Y. H. J. Luminescence 2016, 180, 64-72. Highly efficient blue–green neutral dinuclear copper(I) halide complexes containing bidentate phosphine ligands.

33. Leitl, M. J.; Küchle, F.-R.; Mayer, H. A.; Wesemann, L.; Yersin, H. J. Phys. Chem. A 2013, 117, 11823-11836. Brightly Blue and Green Emitting Cu(I) Dimers for Singlet Harvesting in OLEDs.

34. Kang, L.; Chen, J.; Teng, T.; Chen, X.-L.; Yu, R.; Lu, C.-Z. Dalton Trans. 2015, 44, 11649-11659. Experimental and theoretical studies of highly emissive dinuclear Cu(I) halide complexes with delayed fluorescence.

35. Trivedi, M.; Nagarajan, R.; Kumar, A.; Rath, N. P.; Valerga, P. Inorg. Chim. Acta 2011, 376, 549-556. Synthesis, characterization, crystal structures and photophysical properties of copper(I) complexes containing 1,1'-bis(diphenylphosphino)ferrocene (B-dppf) in doubly-bridged mode.

36. (a) Cotton, F. A.; Faut, O. D.; Goodgame, D. M. L.; Holm, R. H. J. Am. Chem. Soc. 1961, 83, 1780-1785. Magnetic Investigations of Spin-free Cobaltous Complexes. VI. Complexes Containing Phosphines and the Position of Phosphines in the Spectrochemical Series. (b) Hughes, M.; Mason, J.; Leigh, G. J.; Richards, R. L. J. Organomet. Chem. 1988, 341, 381-389. 95Mo studies of ligands relevant to dinitrogen fixation: NMR spectrochemical series based on 95Mo shielding. (c) Thomas, G. Z. Anorg. Allg. Chem. 1968, 362, 191-204. Substitutionsreaktionen an Thiocyanatokomplexen. II. Absorptionsspektren der Tetra-isothiocyanato-diphosphino-chromate(III)-Stellung sec. und tert. Phosphine in der spektrochemischen Serie. (d) Bennett, M. A.; Clark, R. J. H.; Goodwin, A. D. J. Inorg. Chem. 1967, 6, 1625-1631. Electronic and Infrared Spectral Study of Chromium(III) Derivatives of the Type [Cr(NCS)4•(ligand)2]–.

37. (a) For PPh2, see: Zink, D. M.; Bachle, M.; Baumann, T.; Nieger, M.; Kuhn, M.; Wang, C.; Klopper, W.; Monkowius, U.; Hofbeck, T.; Yersin, H.; Brase, S. Inorg. Chem. 2013, 52, 2292–2305. Synthesis, Structure, and Characterization of Dinuclear Copper(I) Halide Complexes with P^N Ligands Featuring Exciting Photoluminescence Properties. (b) For phospholane, see: Musina, E. I.; Shamsieva, A. V.; Strelnik, I. D.; Gerasimova, T. P.; Krivolapov, D. B.; Kolesnikov, I. E.; Grachova, E. V.; Tunik, S. P.; Bannwarth, C.; Grimme, S.; Katsyuba, S. A.; Karasik, A. A.; Sinyashin, O. G. Dalton Trans. 2016, 45, 2250-2260. Synthesis of novel pyridyl containing phospholanes and their polynuclear luminescent copper(I) complexes.

38. Pangborn, A. B.; Giardello, M. A.; Grubbs, R. H.; Rosen, R. K.; Timmers, F. J. Organometallics 1996, 15, 1518-1520. Safe and Convenient Procedure for Solvent Purification.

39. Johnson, D. K.; Stevenson, M. J.; Almadidy, Z. A.; Jenkins, S. E.; Wilcox, D. E.; Grossoehme, N. E. Dalton Trans. 2015, 44, 16494-16505. Stabilization of Cu(I) for binding and calorimetric measurements in aqueous solution.

40. (a) Goerigk, L.; Grimme, S. Phys. Chem. Chem. Phys. 2011, 13, 6670-6688. A thorough benchmark of density functional methods for general main group thermochemistry, kinetics, and noncovalent interactions. (b) Grimme, S.; Antony, J.; Ehrlich, S.; Krieg, H. J. Chem. Phys. 2010, 132, 154104. A consistent and accurate ab initio parametrization of density functional dispersion correction (DFT-D) for the 94 elements H-Pu.

41. (a) Dunning, T. H.; Hay, P. J., In Modern Theoretical Chemistry, Vol. 4: Applications of Electronic Structure Theory. Schaefer, H. F., III (Editor); Plenum, NY: 1977. Gaussian Basis Sets for Molecular Calculations. (b) Wadt, W. R.; Hay, P. J. J. Chem. Phys. 1985, 82, 284-298. Ab initio effective core potentials for molecular calculations. Potentials for main group elements Na to Bi. (c) Hay, P. J.; Wadt, W. R. J. Chem. Phys. 1985, 82, 299-310. Ab initio effective core potentials for molecular calculations. Potentials for K to Au including the outermost core orbitals. (d) Hay, P. J.; Wadt, W. R. J. Chem. Phys. 1985, 82, 270-283. Ab initio effective core potentials for molecular calculations. Potentials for the transition metal atoms Sc to Hg.

42. (a) Frisch, M. J.; Pople, J. A.; Binkley, J. S. J. Chem. Phys. 1984, 80, 3265-3269. Self-consistent molecular orbital methods 25. Supplementary functions for Gaussian basis sets. (b) Clark, T.; Chandrasekhar, J.; Spitznagel, G. W.; Schleyer, P. v. R. J. Comput. Chem. 1983, 4, 294-301. Efficient diffuse function-augmented basis sets for anion calculations. III. The 3-21+G basis set for first-row elements, Li–F. (c) McLean, A. D.; Chandler, G. S. J, Chem. Phys. 1980, 72, 5639-5648. Contracted Gaussian basis sets for molecular calculations. I. Second row atoms, Z=11–18. (d) Krishnan, R.; Binkley, J. S.; Seeger, R.; Pople, J. A. J. Chem. Phys. 1980, 72, 650-654. Self-consistent molecular orbital methods. XX. A basis set for correlated wave functions.

43. (a) Bochevarov, A. D.; Harder, E.; Hughes, T. F.; Greenwood, J. R.; Braden, D. A.; Philipp, D. M.; Rinaldo, D.; Halls, M. D.; Zhang, J.; Friesner, R. A. Int. J. Quantum Chem. 2013, 113, 2110-2142. Jaguar: A high-performance quantum chemistry software program with strengths in life and materials sciences. (b) Jaguar, versions 7.0-9.3, Schrödinger, LLC, New York, NY: 2007-2016.
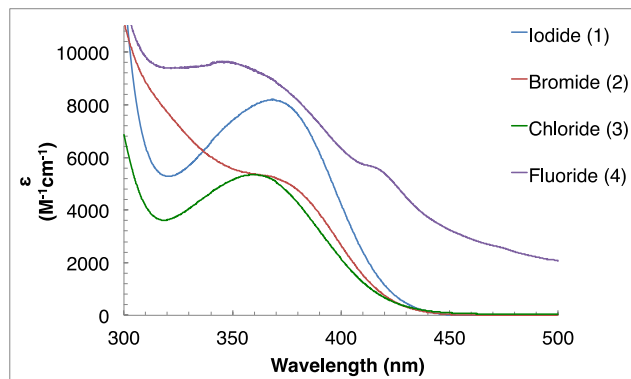
Figure C.1. UV-Vis Spectra of **1**-**4** in CH_2Cl_2 (10^{-4} M). As discussed in connection with Figure B.7 in the manuscript (see footnote 28), the extinction coefficients for **1**-**3** shown here are believed to be more reliable than that for **4**, where we cannot rule out the possibility that impurities and/or scatter from aggregates contributes to the observed absorption.
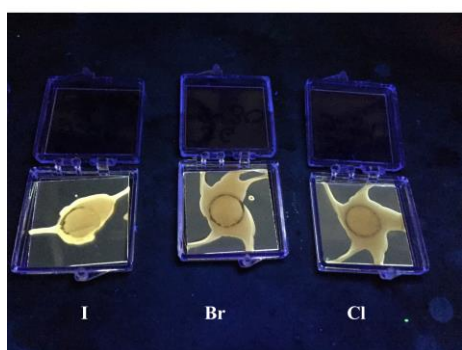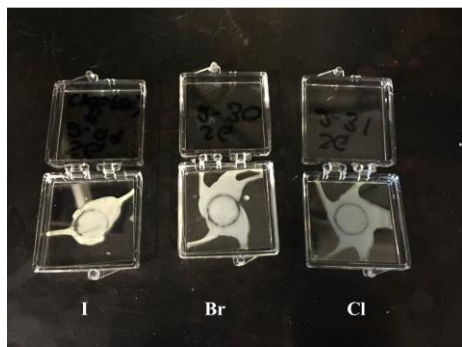
Figure C.2. PMMA films of complexes **1**-**3** under ambient light (above) and under UV light (below), showing the emission at room temperature in air.
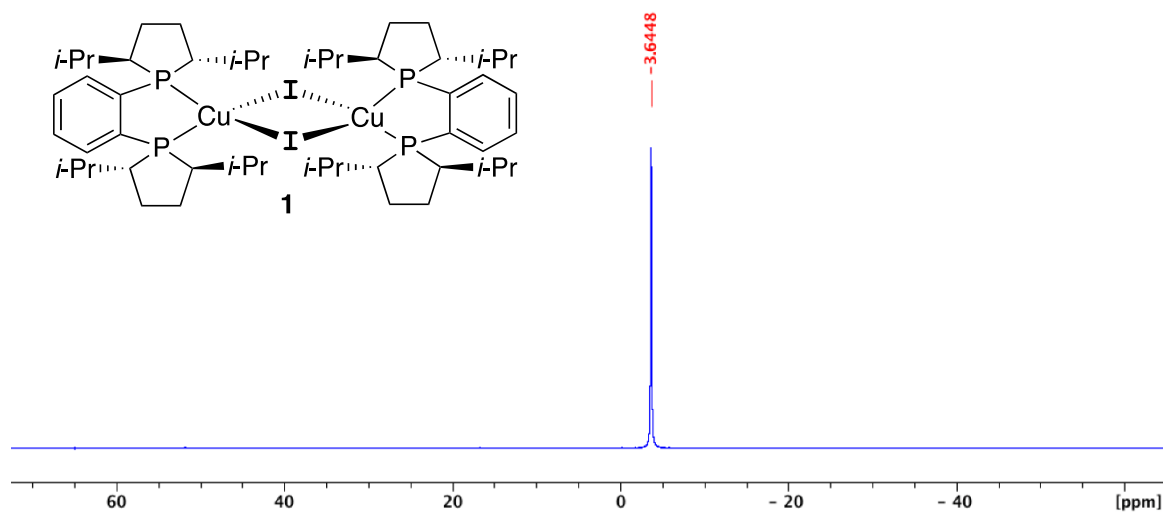
Figure C.3. ^{31}P{^{1}H} NMR (CDCl$_3$, 25 °C) Spectra of [Cu((R,R)-i-Pr-DuPhos)(I)]$_2$ (1)
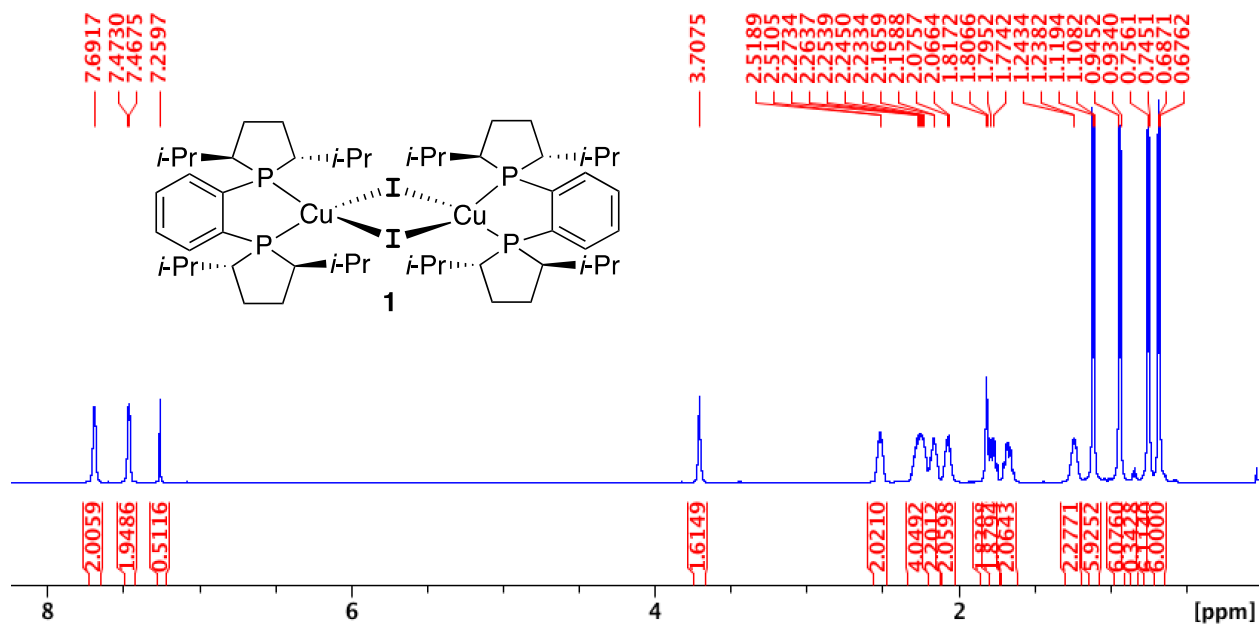
Figure C.4. ^{1}H NMR (CDCl$_3$, 25 °C) Spectra of [Cu((R,R)-i-Pr-DuPhos)(I)]$_2$ (1)
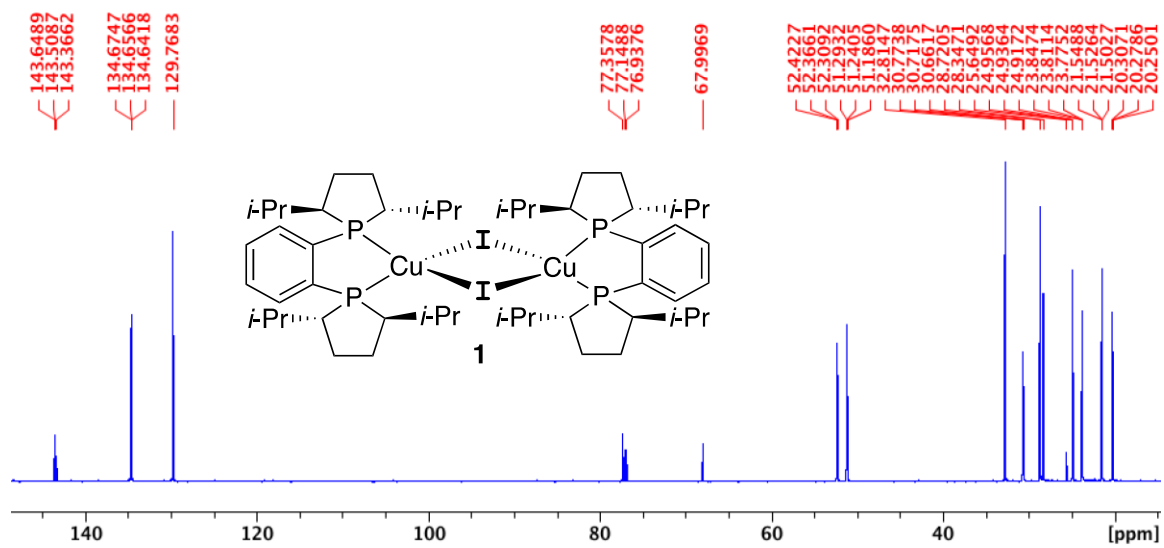
Figure C.5. $^{13}C\{^1H\}$ NMR (CDCl$_3$, 25 °C) Spectra of [Cu((R,R)-i-Pr-DuPhos)(I)]$_2$ (1)
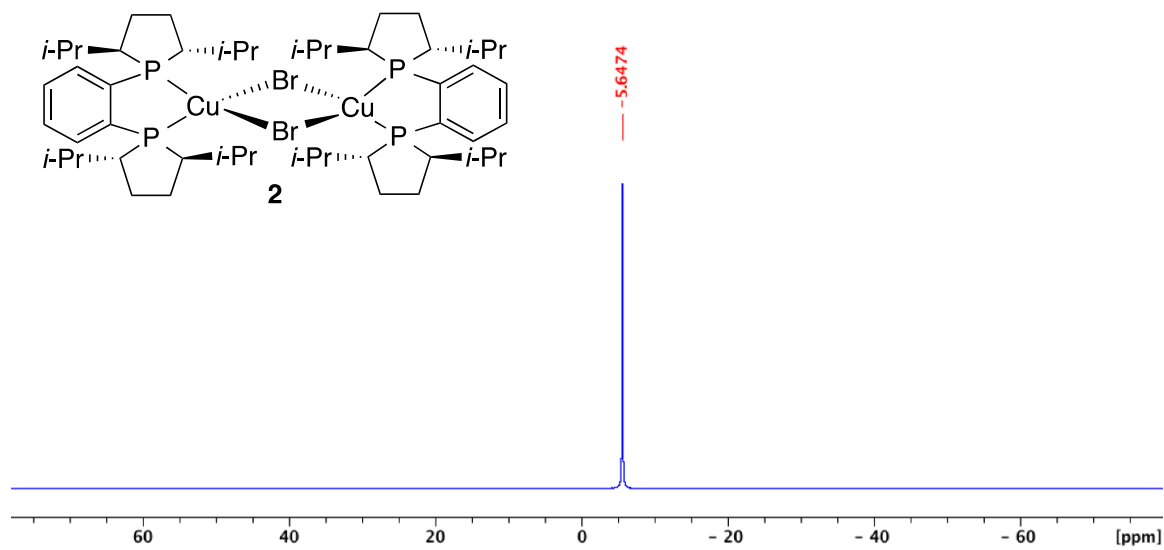
Figure C.6. $^{31}P\{^1H\}$ NMR (CDCl$_3$, 25 °C) Spectra of [Cu((R,R)-i-Pr-DuPhos)(Br)]$_2$ (2)
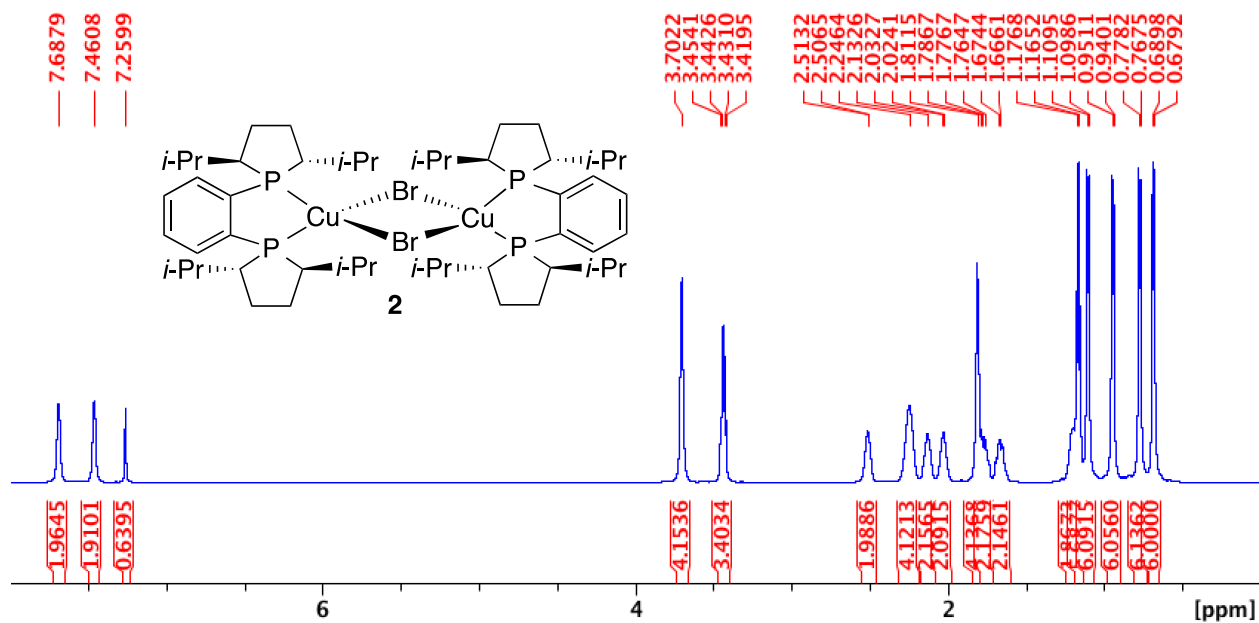
Figure C.7. ^{1}H NMR (CDCl$_3$, 25 °C) Spectra of [Cu((R,R)-i-Pr-DuPhos)(Br)]$_2$ (2)
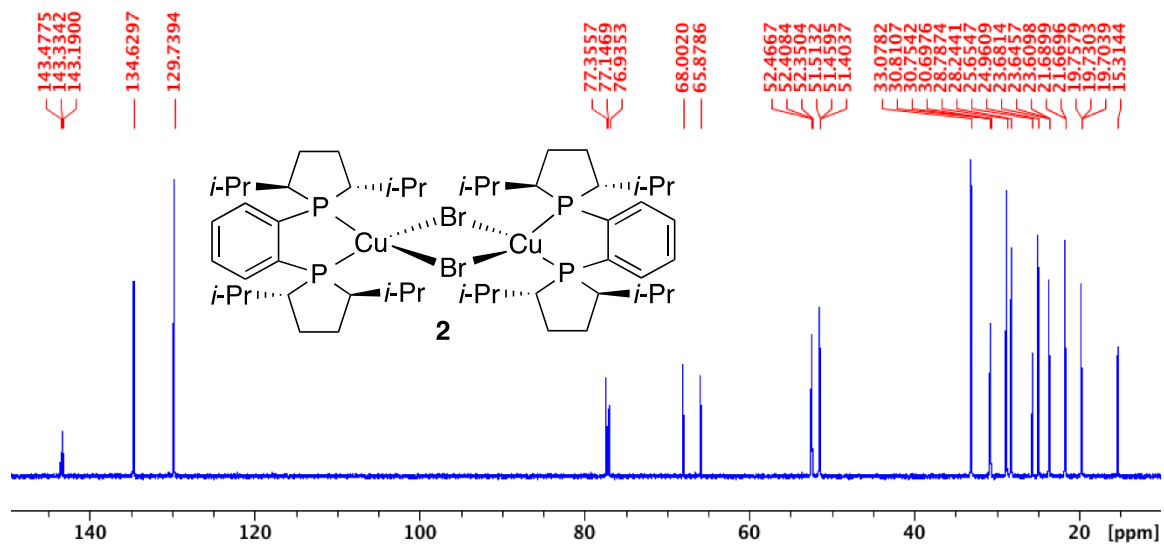
Figure C.8. ^{13}C{^{1}H} NMR (CDCl$_3$, 25 °C) Spectra of [Cu((R,R)-i-Pr-DuPhos)(Br)]$_2$ (2)
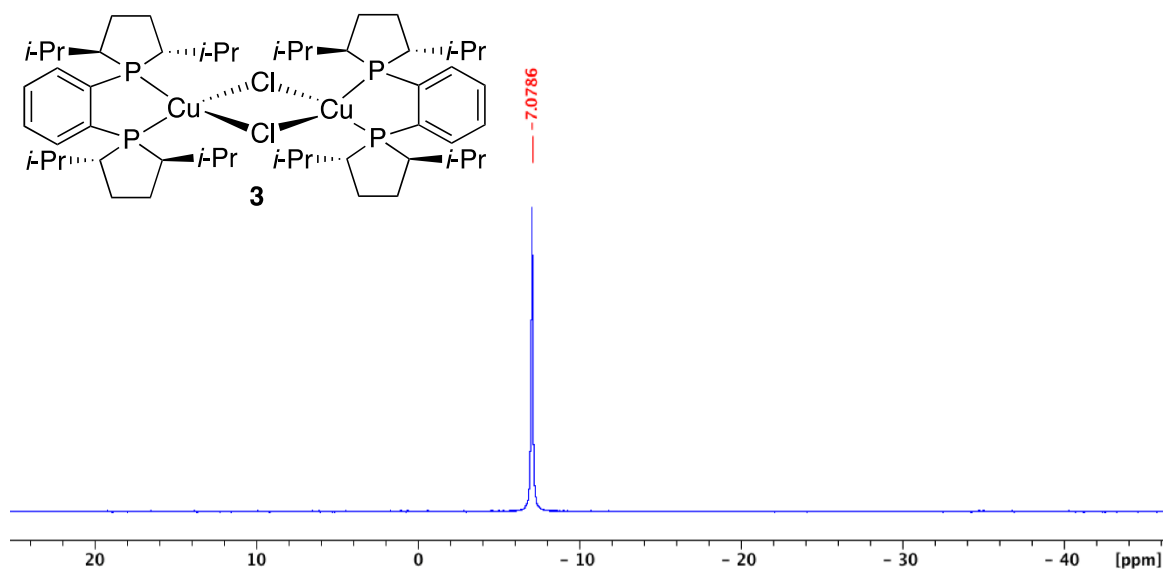
Figure C.9. $^{31}P\{^1H\}$ NMR (CDCl$_3$, 25 °C) Spectra of [Cu((R,R)-i-Pr-DuPhos)(Cl)]$_2$ (3)
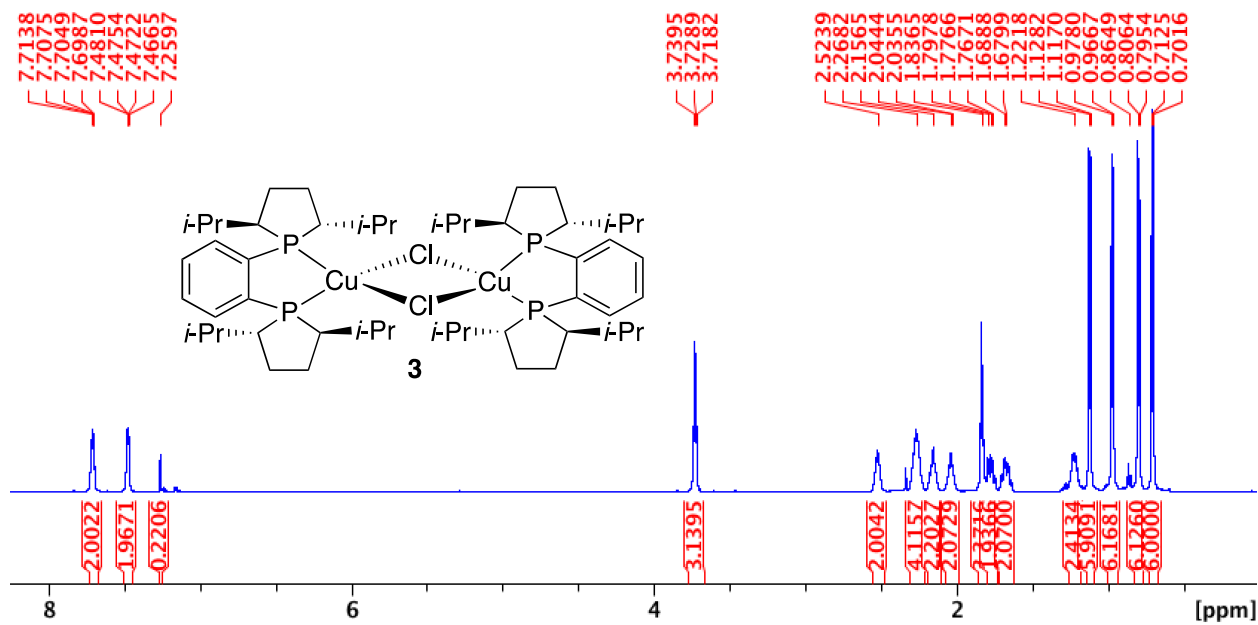
Figure C.10. ^1H NMR (CDCl$_3$, 25 °C) Spectra of [Cu((R,R)-i-Pr-DuPhos)(Cl)]$_2$ (3)
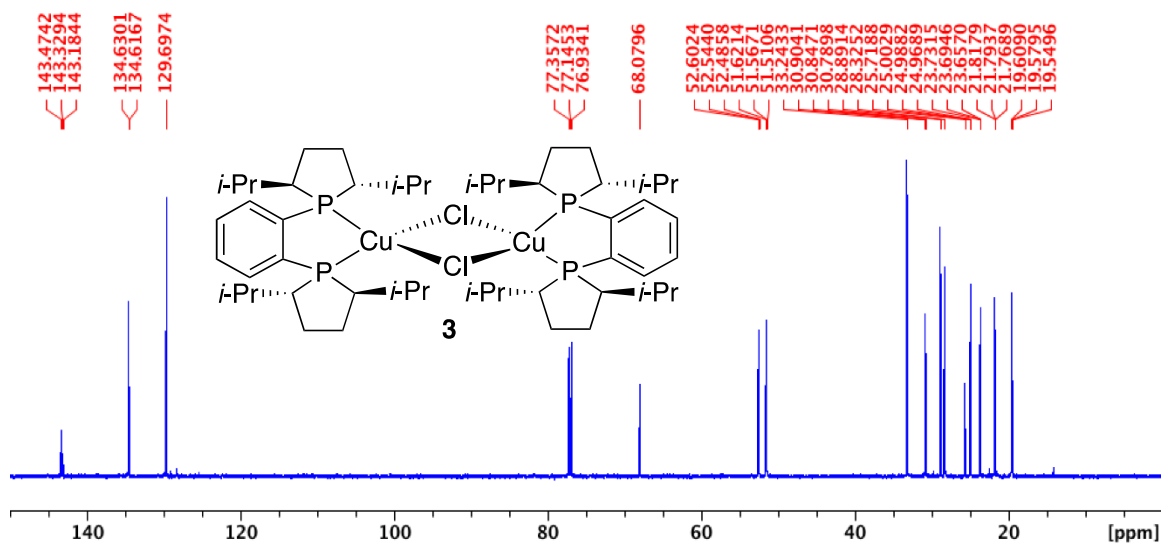
Figure C.11. $^{13}C\{^{1}H\}$ NMR (CDCl$_3$, 25 °C)Spectra of [Cu((*R,R*)-*i*-Pr-DuPhos)(Cl)]$_2$ (3)
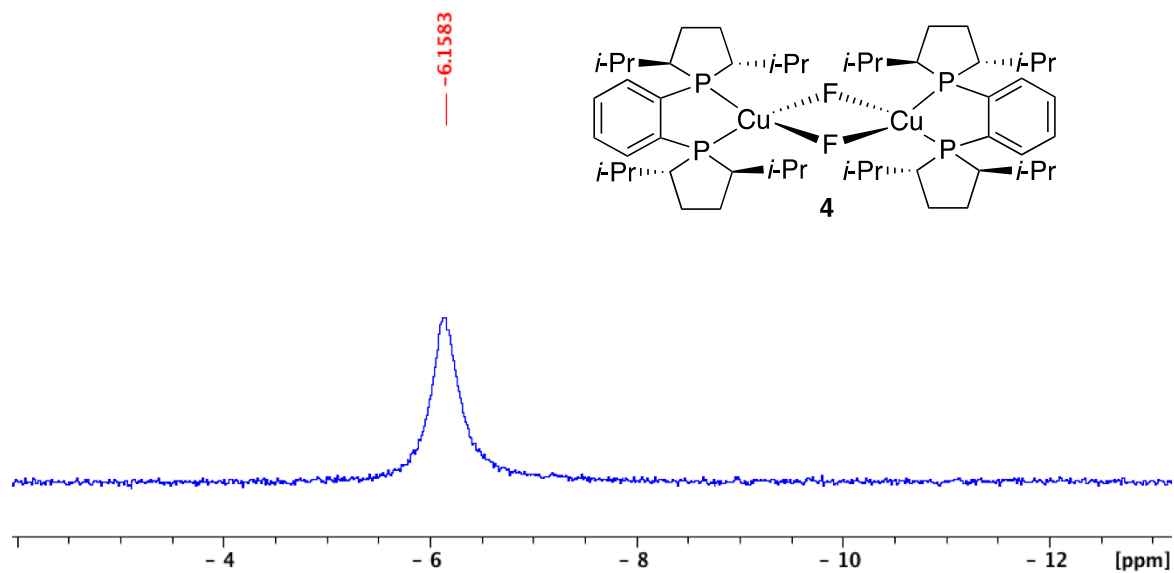
Figure C.12. $^{31}P\{^{1}H\}$ NMR (THF-d$_8$, 25 °C) Spectra of [Cu((*R,R*)-*i*-Pr-DuPhos)(F)]$_2$ (4)

209
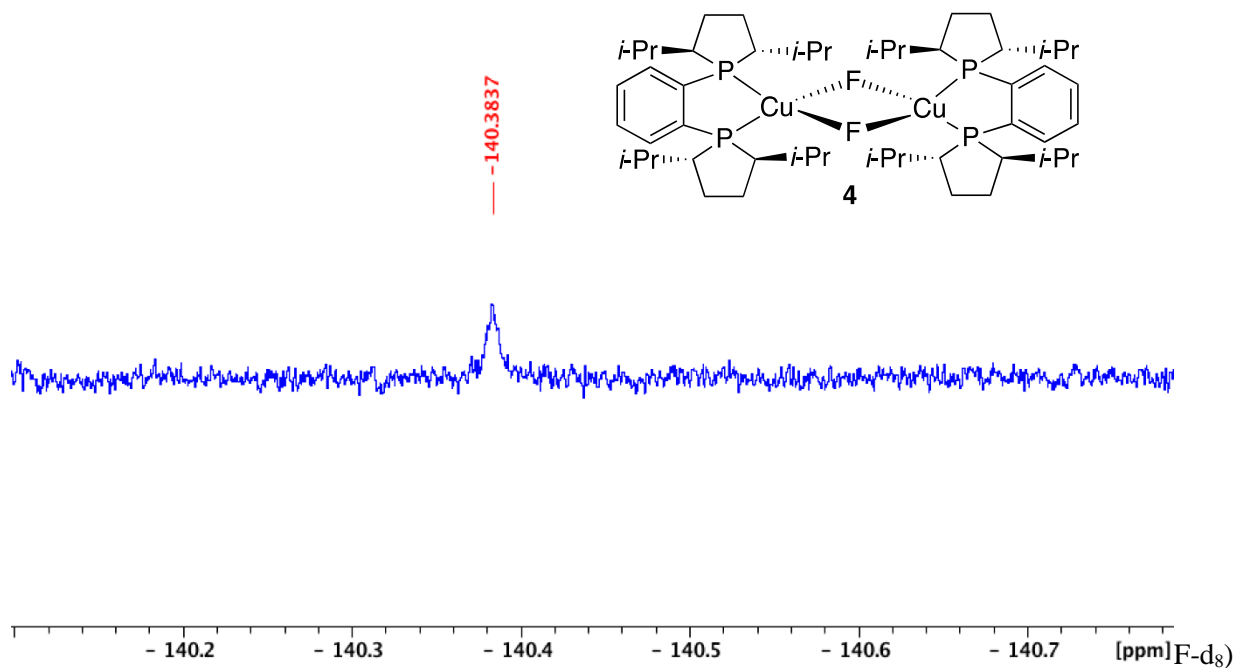
Figure C.13. ^{19}F NMR (THF-d$_8$, 25 °C) Spectra of [Cu((*R*,*R*)-*i*-Pr-DuPhos)(F)]$_2$ (4)
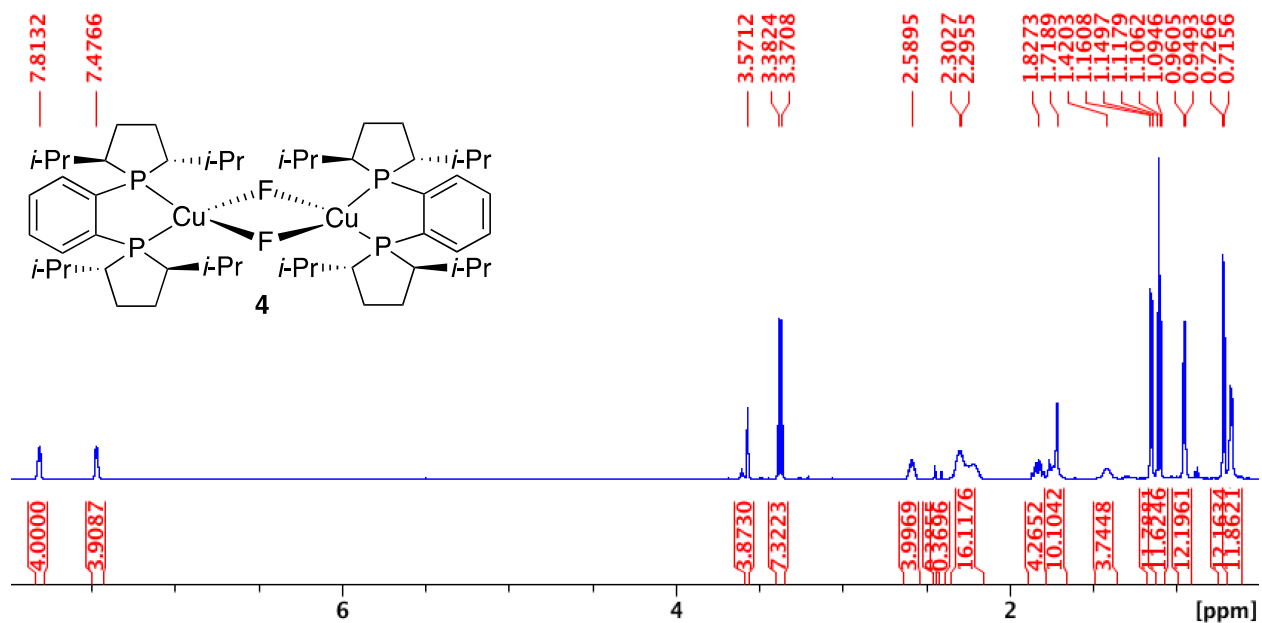
Figure C.14. ^{1}H NMR (THF-d$_8$, 25 °C) Spectra of [Cu((*R*,*R*)-*i*-Pr-DuPhos)(F)]$_2$ (4)

210
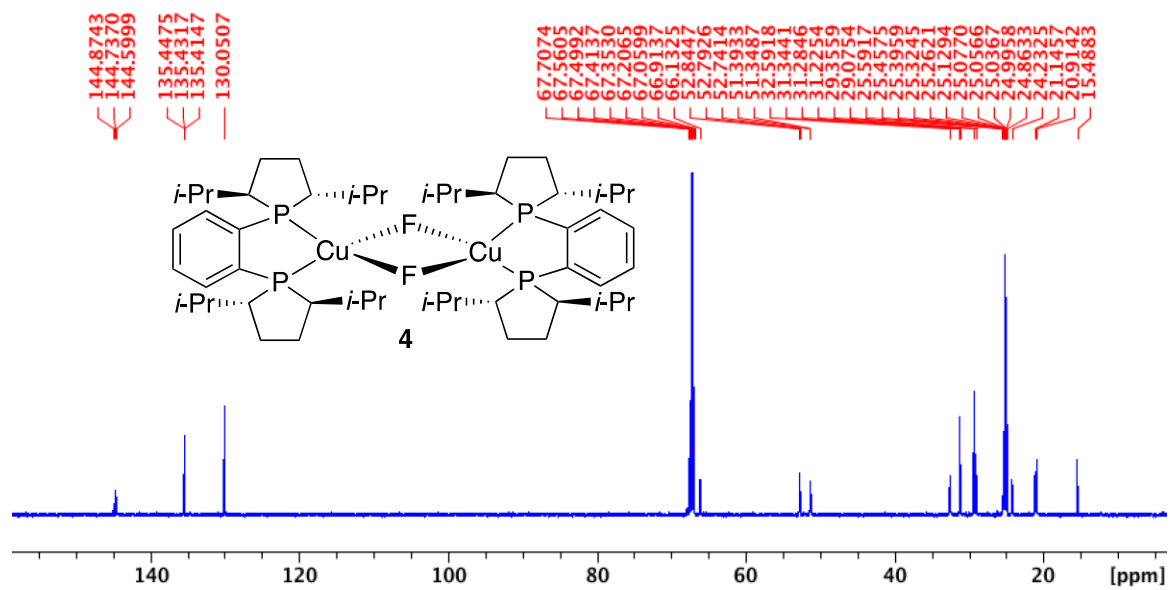
Figure C.15. $^{13}C\{^1H\}$ NMR (THF-d_8, 25 °C) Spectra of [Cu((*R,R*)-*i*-Pr-DuPhos)(F)]$_2$ (4)
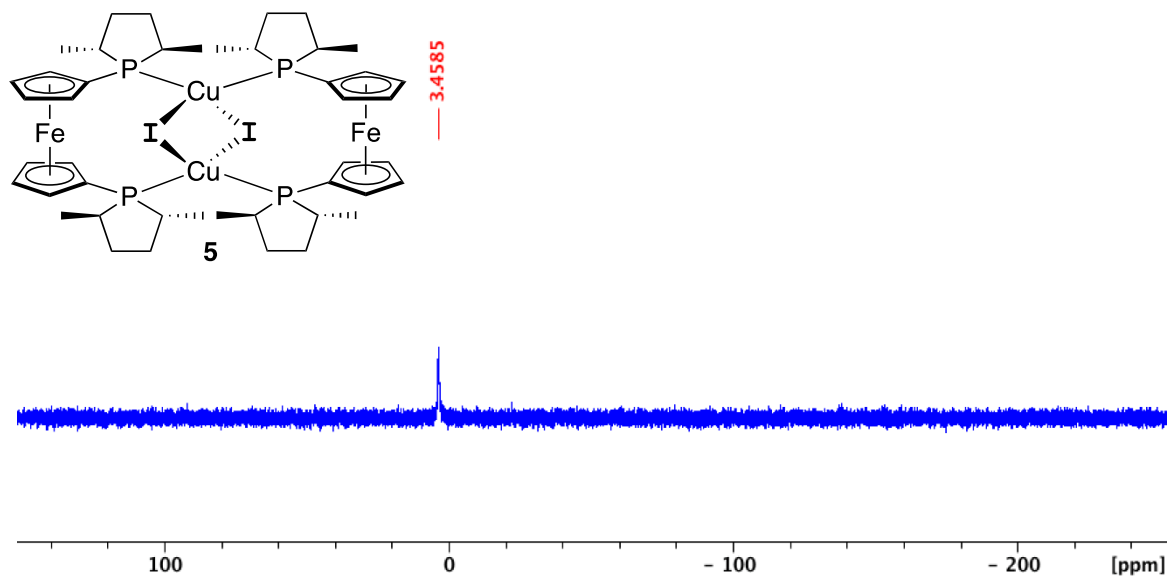
Figure C.16. $^{31}P\{^1H\}$ NMR (CDCl$_3$, 25 °C) Spectra of [Cu((*R,R*)-Me-FerroLANE)(I)]$_2$ (5)
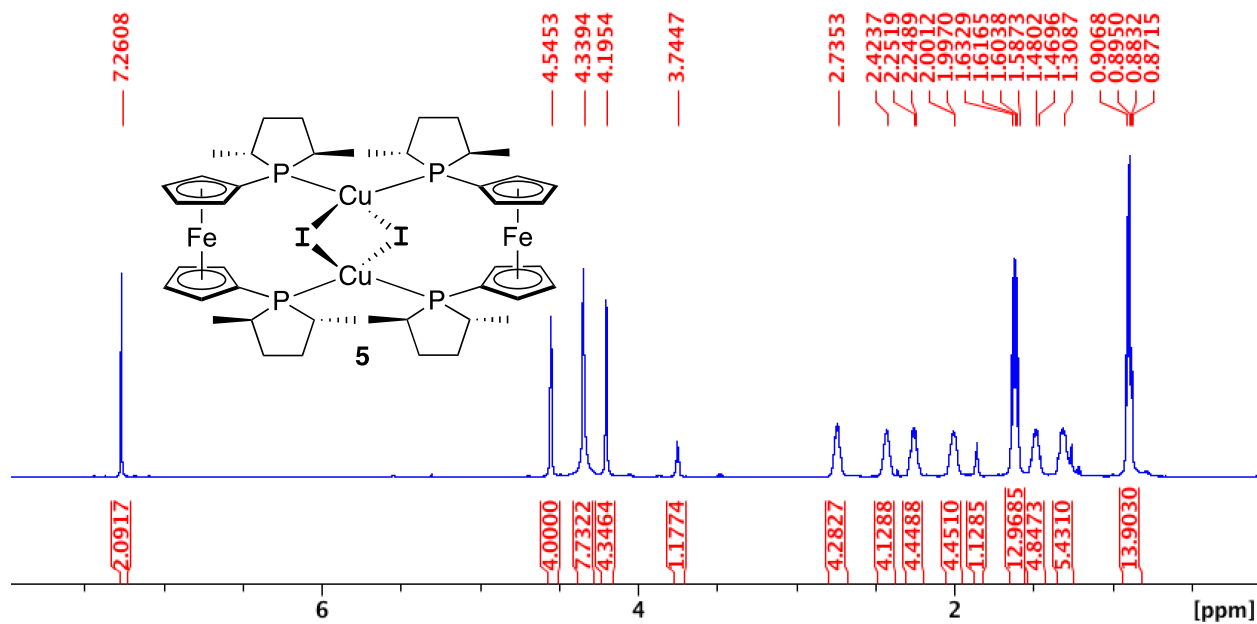
Figure C.17. ^{1}H NMR (CDCl$_3$, 25 °C) Spectra of [Cu((R,R)-Me-FerroLANE)(I)]$_2$ (5)
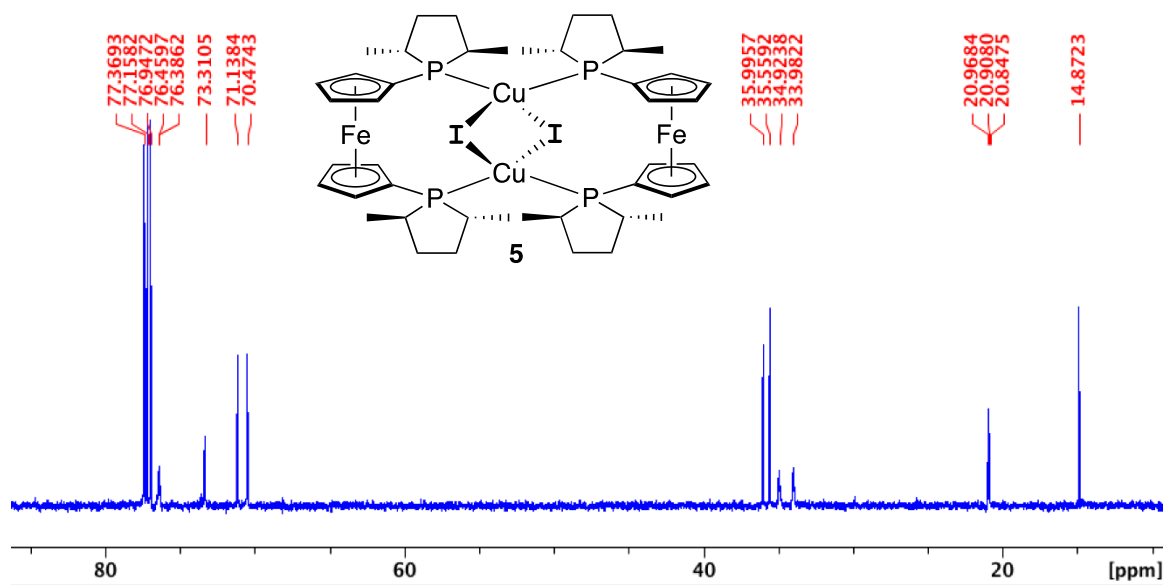
Figure C.18. ^{13}C{^{1}H} NMR (CDCl$_3$, 25 °C) Spectra of [Cu((R,R)-Me-FerroLANE)(I)]$_2$ (5)
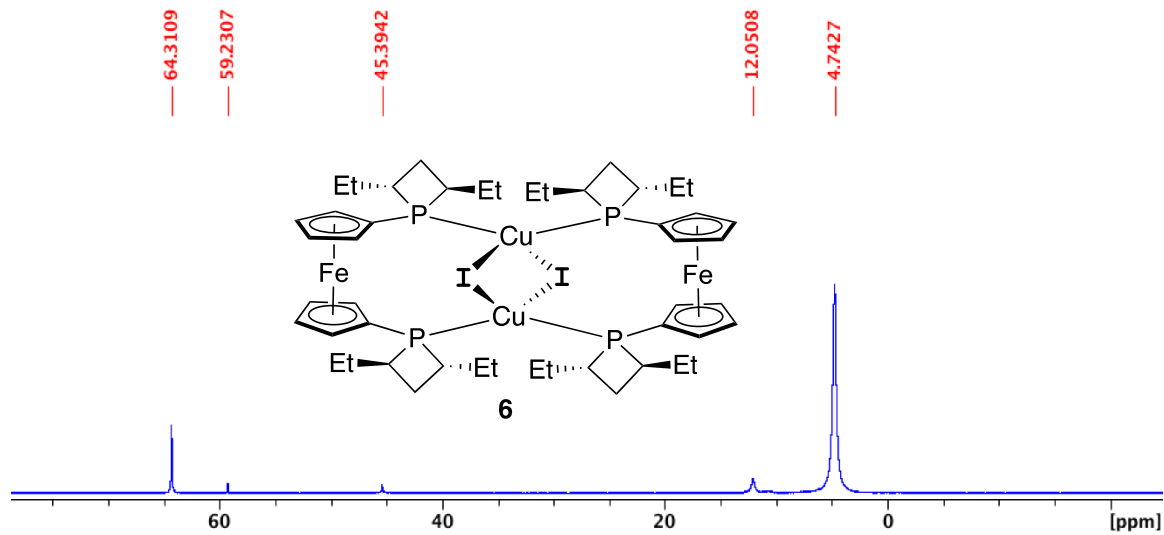
Figure C.19. $^{31}P\{^1H\}$ NMR (CD$_2$Cl$_2$, 25 °C) Spectra of Cu$_2$I$_2$((*S*,*S*)-Et-FerroTANE)$_2$ (6)
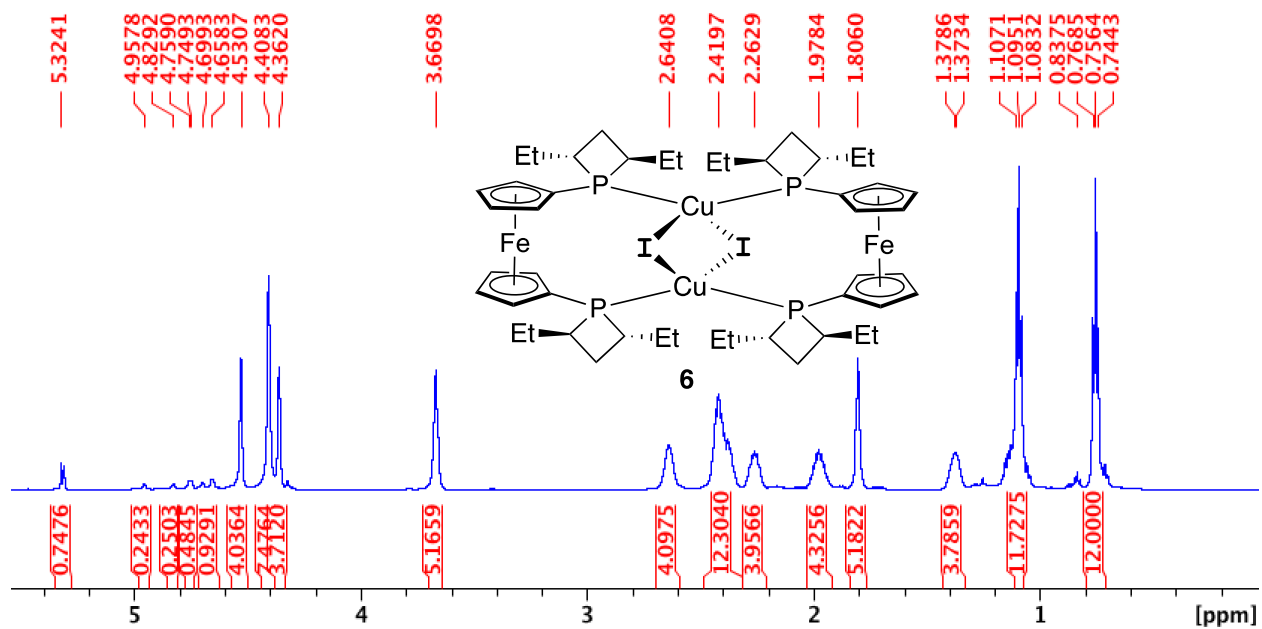
Figure C.20. ^1H NMR (CD$_2$Cl$_2$, 25 °C) Spectra of Cu$_2$I$_2$((*S*,*S*)-Et-FerroTANE)$_2$ (6)
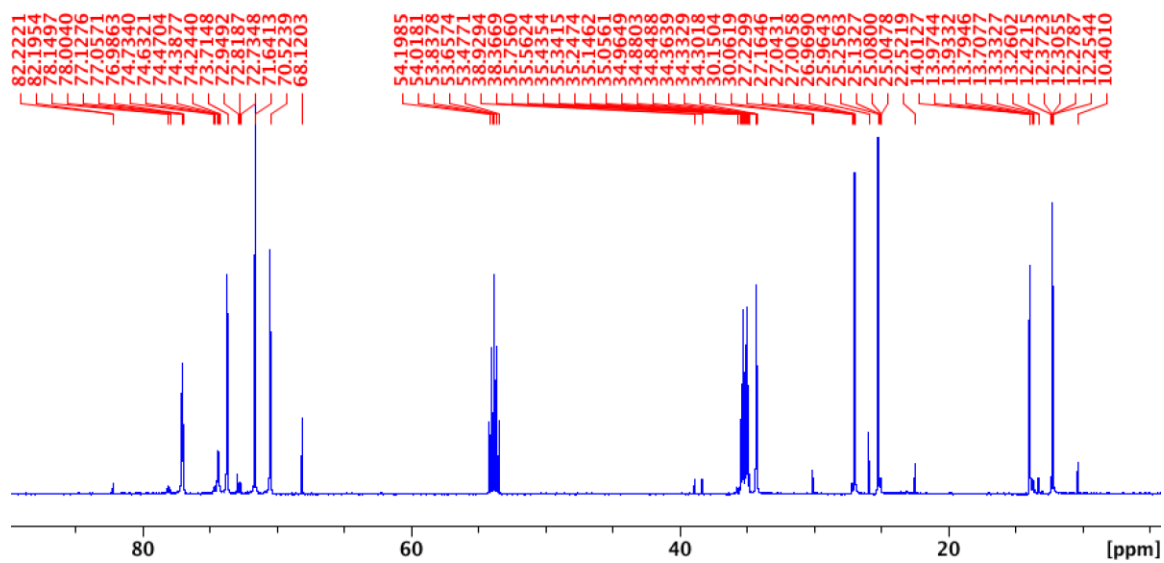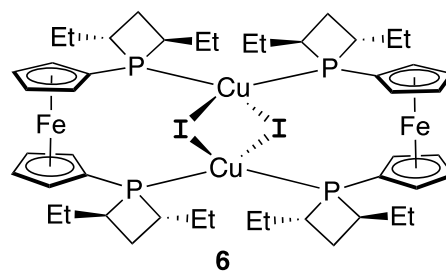
Figure C.21. $^{13}C\{^1H\}$ NMR (CD$_2$Cl$_2$, 25 °C) Spectra of Cu$_2$I$_2$((*S*,*S*)-Et-FerroTANE)$_2$ (6)
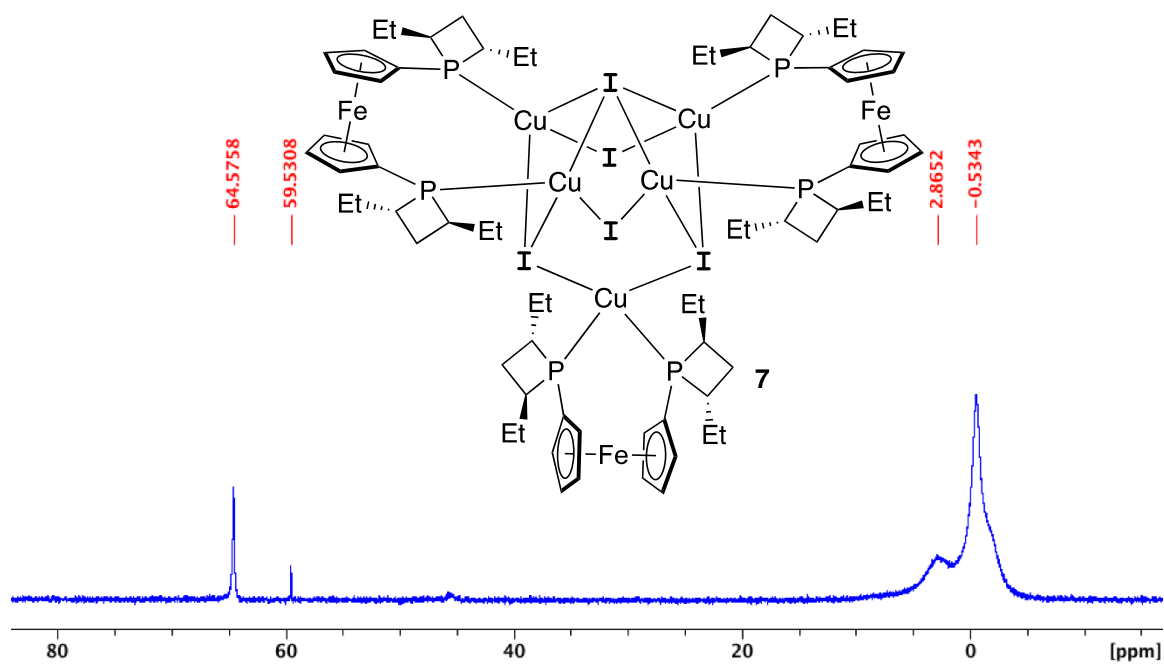
Figure C.22. $^{31}P\{^1H\}$ NMR (CD$_2$Cl$_2$, 25 °C) Spectra of Cu$_5$I$_5$((*S*,*S*)-Et-FerroTANE)$_3$ (7)
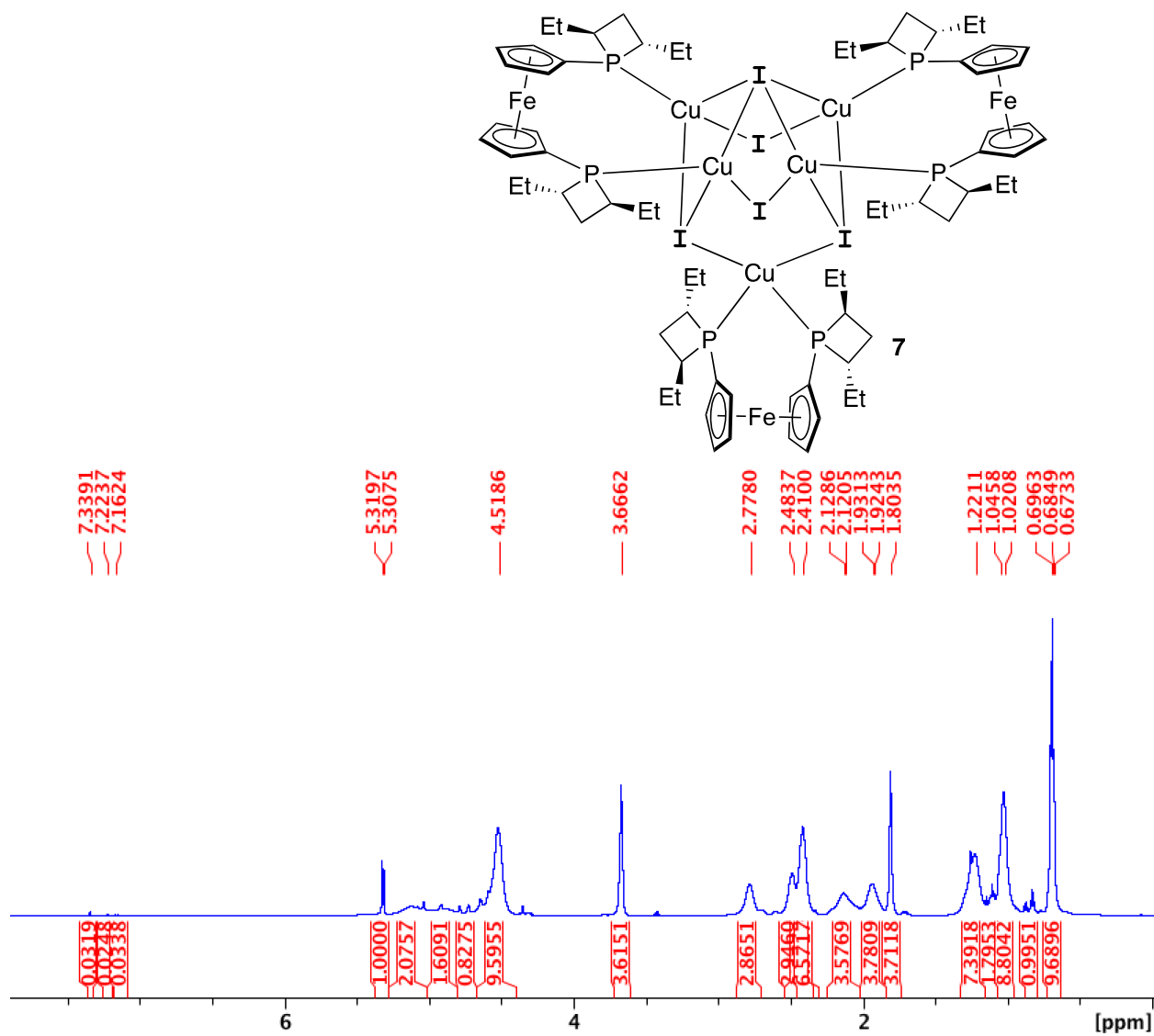
Figure C.23. ^{1}H NMR (CD$_2$Cl$_2$, 25 °C) Spectra of Cu$_5$I$_5$((*S*,*S*)-Et-FerroTANE)$_3$ (7)
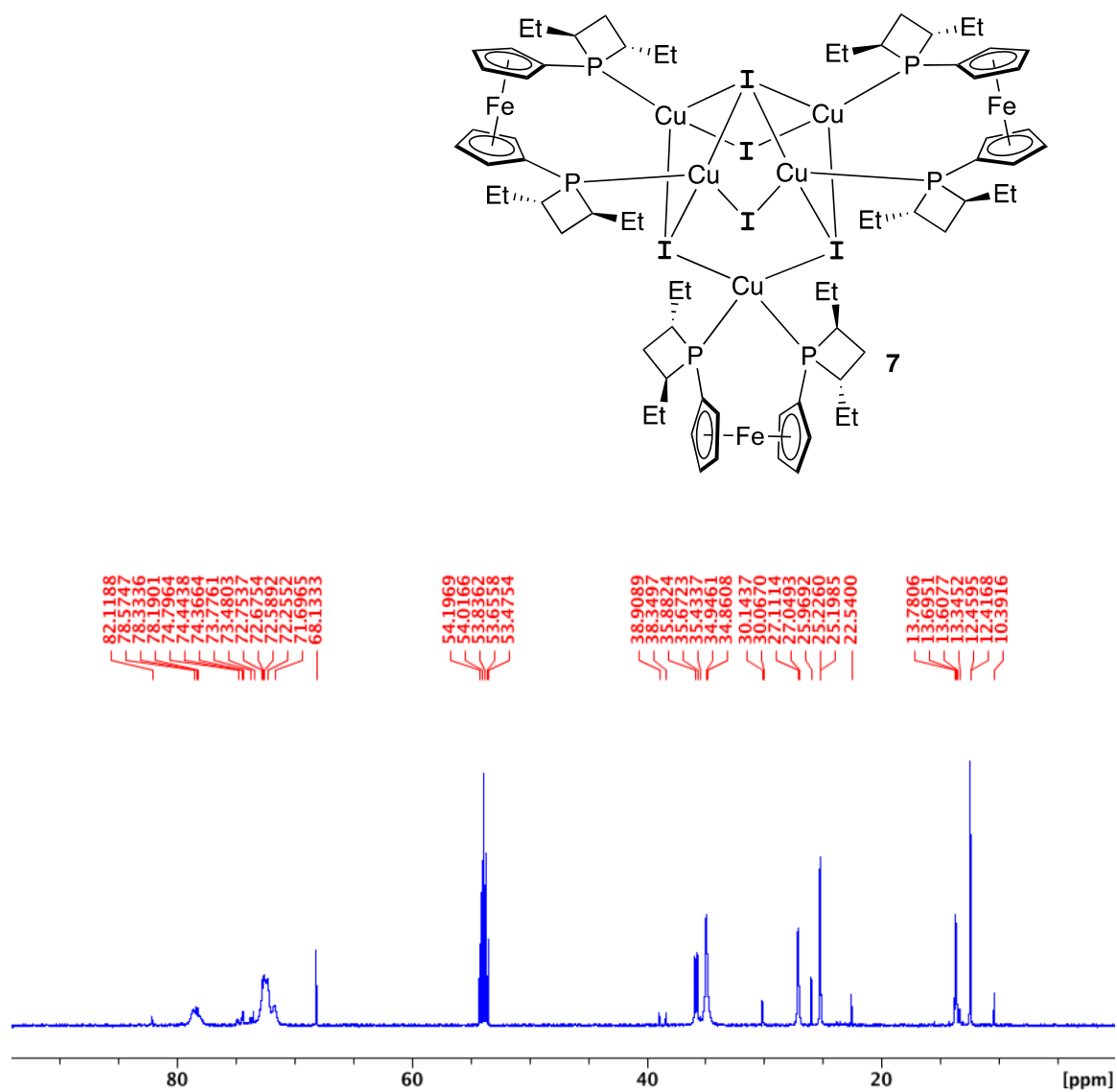
Figure C.24. $^{13}C\{^1H\}$ NMR (CD$_2$Cl$_2$, 25 °C) Spectra of Cu$_5$I$_5$((*S,S*)-Et-FerroTANE)$_3$ (7)
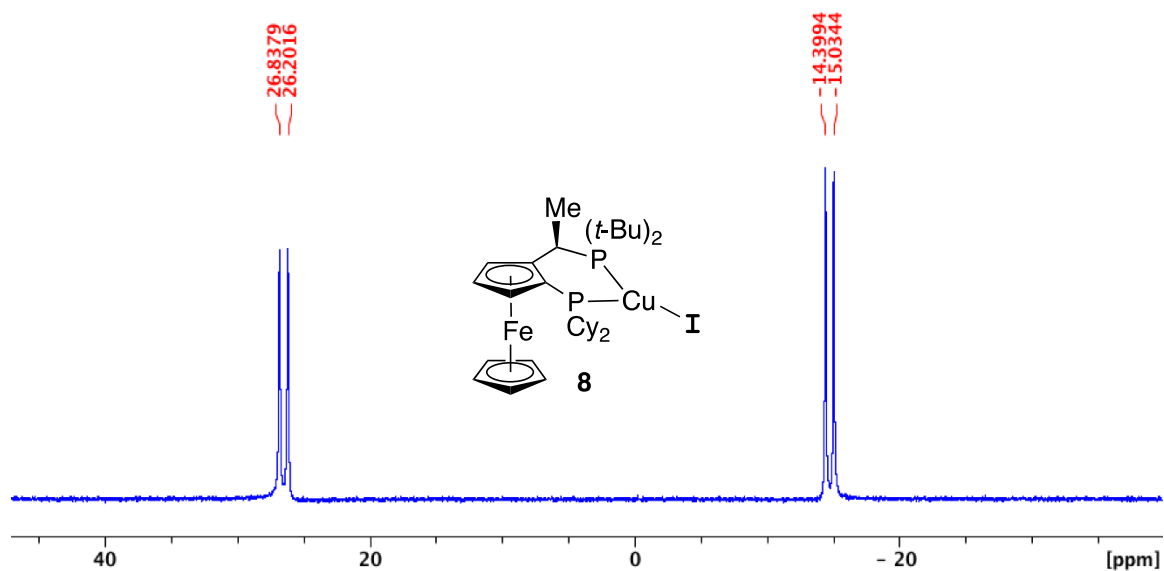
Figure C.25. $^{31}P\{^1H\}$ NMR (CH$_2$Cl$_2$, 25 °C) Spectra of Cu((R,S)-CyPF-t-Bu)(I) (8)
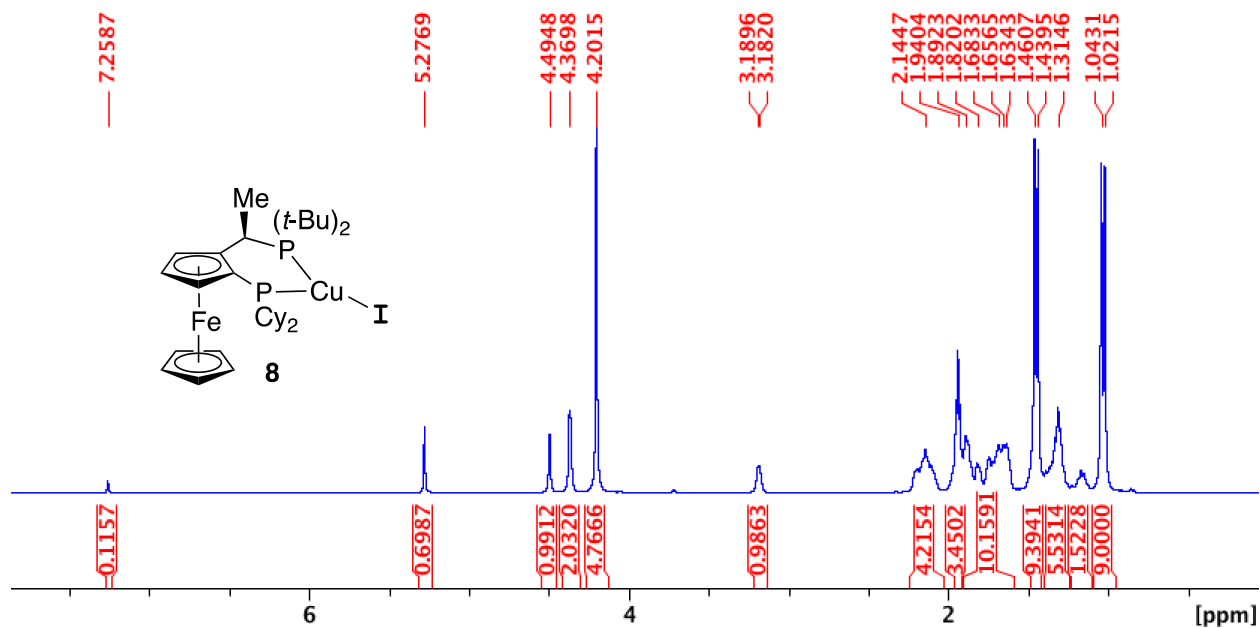
Figure C.26. ^1H NMR (CDCl$_3$, 25 °C) Spectra of Cu((R,S)-CyPF-t-Bu)(I) (8)

218
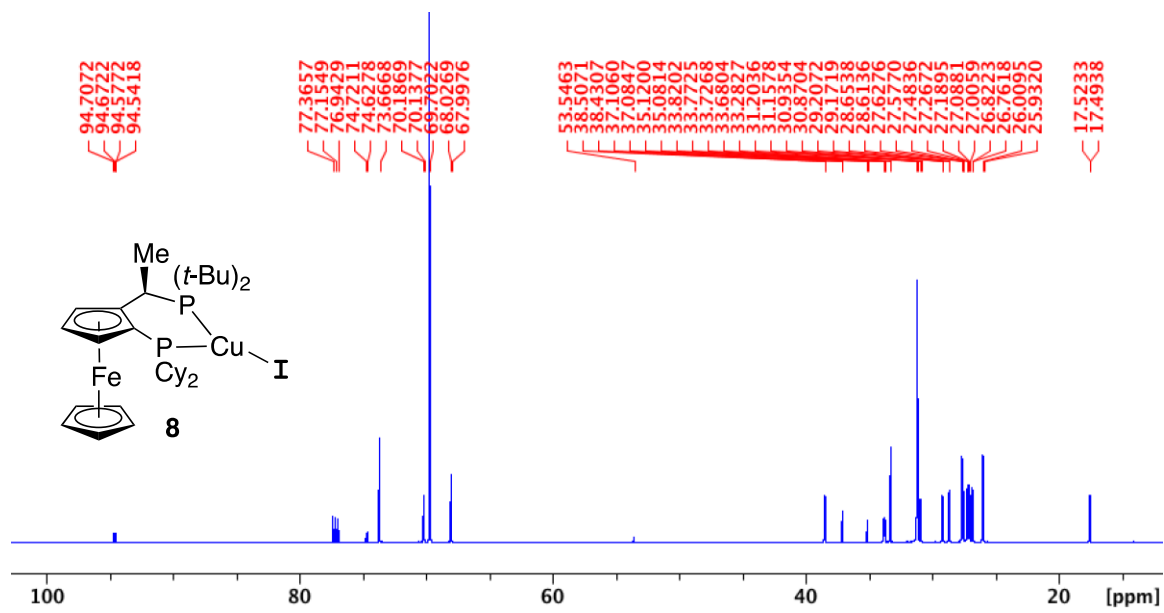
Figure C.27. $^{13}C\{^1H\}$ NMR (CDCl$_3$, 25 °C) Spectra of Cu((*R,S*)-CyPF-*t*-Bu)(I) (8)
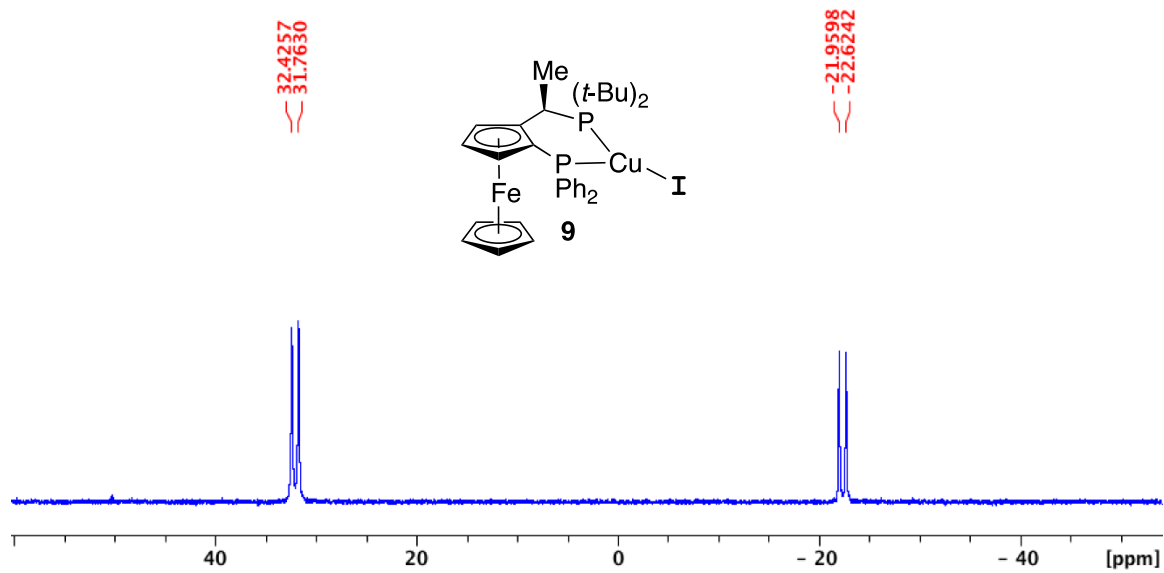
Figure C.28. $^{31}P\{^1H\}$ NMR (CH$_2$Cl$_2$, 25 °C) Spectra of Cu((*R,S*)-PPF-*t*-Bu)(I) (9)
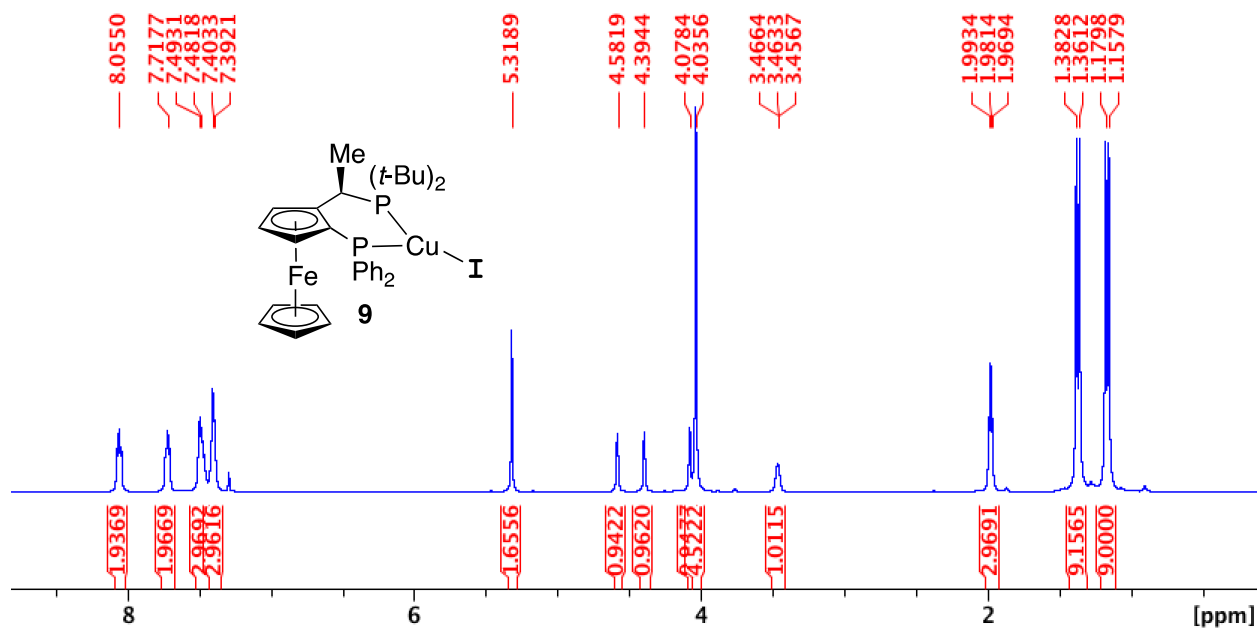
Figure C.29. ^{1}H NMR (CDCl$_3$, 25 °C) Spectra of Cu((*R,S*)-PPF-*t*-Bu)(I) (9)
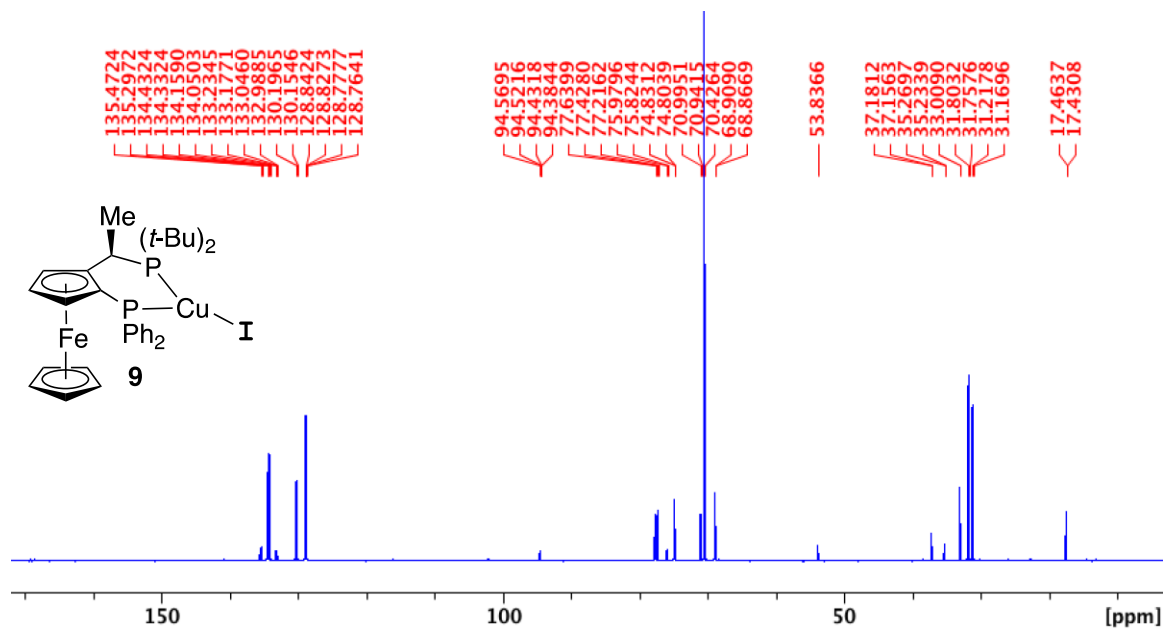
Figure C.30. ^{13}C{^{1}H} NMR (CDCl$_3$, 25 °C) Spectra of Cu((*R,S*)-PPF-*t*-Bu)(I) (9)
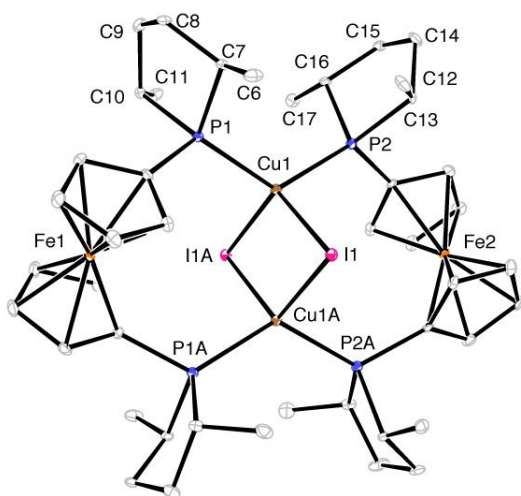
Figure C.31. ORTEP diagram of [Cu((*R,R*)-Me-FerroLANE)(I)]₂ (**5**). Selected bond lengths (Å) and angles (deg): Cu(1)-I(1) 2.7276(5), Cu(1)-I(1A) 2.7290(5), Cu(1A)-I(1) 2.7290(5), Cu(1)-Cu(1A) 2.8694(9), Cu(1)-P(1) 2.2964(11), Cu(1)-P(2) 2.2950(11), Cu(1)-I(1)-Cu(1A) 63.452(17), I(1)-Cu(1)-I(1A) 116.547(17), I(1A)-Cu(1)-Cu(1A) 58.251(16), I(1)-Cu(1)-Cu(1A) 58.297(16), P(1)-Cu(1)-I(1A) 107.32(3), P(1)-Cu(1)-I(1) 102.00(3), P(1)-Cu(1)-Cu(1A) 118.55(3), P(2)-Cu(1)-I(1) 106.58(3), P(2)-Cu(1)-I(1A) 101.55(4), P(2)-Cu(1)-Cu(1A) 117.68(3), P(2)-Cu(1)-P(1) 123.78(4). The Cu-Cu distance was 2.8694(9) Å.
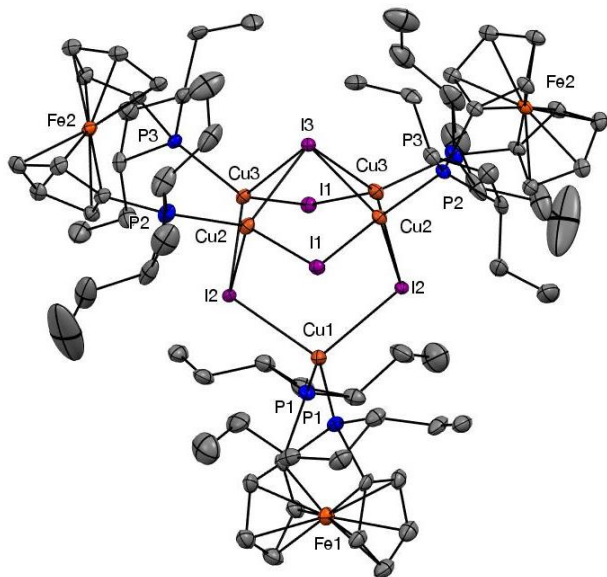
Figure C.32. ORTEP diagram of $Cu_5I_5((S,S)$-Et-FerroTANE$)_3$ (**7**). Selected bond lengths (Å) and angles (deg): I(1)-Cu(2)#1 2.660(3), I(1)-Cu(3) 2.669(2), I(2)-Cu(1) 2.675(2), I(2)-Cu(2) 2.680(2), I(2)-Cu(3) 2.650(2), I(3)-Cu(2) 2.769(2), I(3)-Cu(3) 2.740(2), Cu(1)-P(1) 2.278(5), Cu(2)-P(2) 2.243(5), Cu(3)-P(3) 2.236(5), Cu(2)#1-I(1)-Cu(3) 74.63(7), Cu(1)-I(2)-Cu(2) 108.64(7), Cu(3)-I(2)-Cu(1) 111.23(7), Cu(3)-I(2)-Cu(2) 72.52(7), Cu(2)#1-I(3)-Cu(2) 109.11(10), Cu(3)-I(3)-Cu(2)#1 71.80(7), Cu(3)-I(3)-Cu(2) 69.80(7), Cu(3)-I(3)-Cu(3)#1 110.90(10), I(2)-Cu(1)-I(2)#1 103.67(11), P(1)-Cu(1)-I(2)#1 102.85(13), P(1)-Cu(1)-I(2) 117.68(13), P(1)-Cu(1)-P(1)#1 112.5(3), I(1)#1-Cu(2)-I(2) 111.89(8), I(1)#1-Cu(2)-I(3) 102.75(8), I(2)-Cu(2)-I(3) 101.90(8), P(2)-Cu(2)-I(1)#1 107.46(15), P(2)-Cu(2)-I(2) 107.31(17), P(2)-Cu(2)-I(3) 125.35(17), I(1)-Cu(3)-I(3) 103.27(8), I(2)-Cu(3)-I(1) 108.72(8), I(2)-Cu(3)-I(3) 103.44(8), P(3)-Cu(3)-I(1) 105.65(15), P(3)-Cu(3)-I(2) 124.03(15), P(3)-Cu(3)-I(3) 109.95(15). The shortest Cu-Cu distance was 3.152 Å.
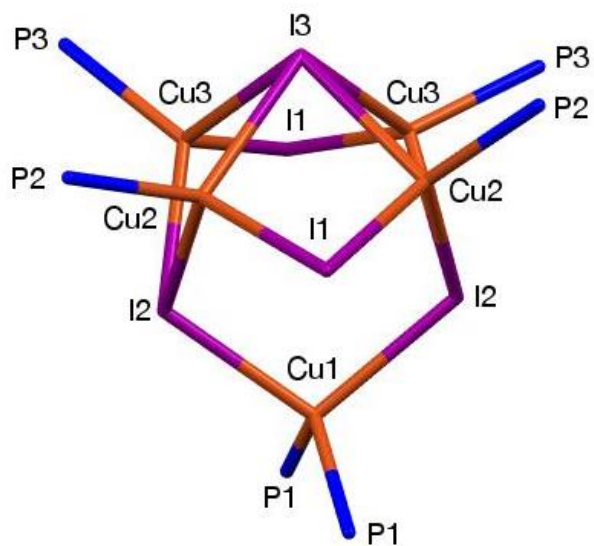
Figure C.33. The $Cu_5I_5P_6$ core of cluster **7**, showing μ_4-I3, μ_3-I2, and μ_2-I1, as well as chelating

Et-FerroTANE (P1) and bridging Et-FerroTANE (P2/P3)

Table C.1. Crystal data and structure refinement for [Cu(R,R)-i-Pr-DuPhos)(Cl)]$_2$•THF, glu467_a.

Identification code	SG1-5
Empirical formula	C56 H96 Cl2 Cu2 O P4
Formula weight	1107.18
Temperature	100 K
Wavelength	0.71073 Å
Crystal system	Monoclinic
Space group	P 21
Unit cell dimensions	a = 12.2417(8) Å $\quad$ $\square$= 90°.
	b = 15.1977(9) Å $\quad$ $\square$= 100.688(2)°.
	c = 15.9561(11) Å $\quad$ $\square$ = 90°.
Volume	2917.1(3) Å^3
Z	2
Density (calculated)	1.261 Mg/m^3
Absorption coefficient	0.966 mm^{-1}
F(000)	1184
Crystal size	0.32 x 0.27 x 0.1 mm^3
Theta range for data collection	2.317 to 27.985°.
Index ranges	-15<=h<=16, -19<=k<=19, -21<=l<=19
Reflections collected	33367
Independent reflections	13394 [R(int) = 0.0524]
Completeness to theta = 25.242°	99.9 %
Absorption correction	Semi-empirical from equivalents
Max. and min. transmission	0.2622 and 0.2192
Refinement method	Full-matrix least-squares on F^2
Data / restraints / parameters	13394 / 1 / 602
Goodness-of-fit on F^2	0.972
Final R indices [I>2sigma(I)]	R1 = 0.0480, wR2 = 0.1096
R indices (all data)	R1 = 0.0610, wR2 = 0.1169
Absolute structure parameter	0.015(6)
Extinction coefficient	n/a
Largest diff. peak and hole	1.511 and -0.342 e.Å^{-3}

Table C.2. Atomic coordinates (x 10^4) and equivalent isotropic displacement parameters (Å^2 x 10^3) for [Cu(*R,R*)-*i*-Pr-DuPhos)(Cl)]$_2$•THF, glu467_a. U(eq) is defined as one third of the trace of the orthogonalized U^{ij} tensor.

	x	y	z	U(eq)
Cu(1)	6174(1)	4373(1)	6971(1)	15(1)
Cu(2)	6185(1)	5708(1)	8447(1)	19(1)
Cl(1)	5857(1)	5899(1)	6940(1)	20(1)
P(2)	7749(1)	3754(1)	6715(1)	13(1)
Cl(2)	5921(1)	4180(1)	8406(1)	20(1)
P(1)	5151(1)	3656(1)	5860(1)	13(1)
P(3)	7761(1)	6371(1)	9091(1)	18(1)
P(4)	5172(1)	6459(1)	9246(1)	17(1)
C(36)	7299(4)	3048(3)	5771(3)	14(1)
C(33)	9043(4)	4324(4)	6532(3)	20(1)
C(52)	8882(4)	5318(4)	6462(4)	24(1)
O(1)	10285(5)	4280(4)	4594(4)	65(2)
C(51)	5965(5)	4441(4)	3987(4)	25(1)
C(30)	8503(4)	2978(3)	7533(3)	19(1)
C(41)	6156(4)	2942(3)	5446(3)	13(1)
C(39)	6582(4)	1848(3)	4447(3)	21(1)
C(14)	7712(5)	8324(4)	10900(4)	24(1)
C(37)	8063(4)	2579(3)	5391(3)	21(1)
C(32)	9948(4)	4006(4)	7271(4)	28(1)
C(21)	9942(5)	6047(4)	9126(4)	34(2)
C(43)	3410(4)	3019(4)	6641(4)	23(1)
C(15)	8070(4)	7699(3)	10372(3)	21(1)
C(27)	6828(4)	2060(4)	7667(3)	20(1)
C(45)	3933(4)	2917(4)	5835(4)	20(1)
C(46)	3105(5)	3087(4)	4994(4)	27(1)
C(16)	7316(4)	7139(3)	9867(3)	17(1)
C(28)	8042(5)	2042(4)	7551(4)	23(1)
C(2)	3457(5)	7070(4)	7933(4)	25(1)

Table C.2. Continued.

C(20)	9069(4)	5862(4)	9677(4)	23(1)
C(35)	10007(5)	5789(4)	6484(5)	38(2)
C(23)	8502(4)	7078(4)	8408(4)	24(1)
C(13)	6597(5)	8416(4)	10909(3)	22(1)
C(12)	5842(4)	7866(3)	10417(3)	20(1)
C(25)	8075(5)	8018(4)	8236(4)	27(1)
C(38)	7715(4)	2000(4)	4728(4)	22(1)
C(24)	6863(5)	8030(4)	7825(4)	25(1)
C(40)	5822(4)	2319(4)	4807(3)	19(1)
C(29)	8736(5)	1492(4)	8255(4)	35(2)
C(4)	3969(4)	7207(4)	8888(4)	22(1)
C(11)	6178(4)	7210(3)	9894(3)	18(1)
C(48)	4435(4)	4308(4)	4928(3)	17(1)
C(22)	9755(5)	6974(4)	8787(4)	34(2)
C(31)	9731(4)	3041(4)	7454(4)	26(1)
C(1)	3012(5)	6142(4)	7736(4)	31(1)
C(34)	8074(5)	5566(4)	5659(4)	31(1)
C(49)	5116(5)	4915(4)	4441(4)	26(1)
C(42)	2986(5)	3954(4)	6752(4)	31(1)
C(47)	3639(4)	3665(4)	4383(3)	22(1)
C(10)	5916(5)	5786(4)	11377(4)	32(1)
C(44)	2498(5)	2340(5)	6658(4)	38(2)
C(5)	3130(5)	7076(4)	9499(4)	32(1)
C(7)	4440(5)	5845(4)	9988(4)	24(1)
C(3)	2577(5)	7776(5)	7636(4)	37(2)
C(26)	8773(6)	8509(5)	7667(5)	43(2)
C(50)	4320(5)	5480(4)	3807(4)	33(1)
C(8)	5130(5)	5279(4)	10705(4)	31(1)
C(18)	8929(6)	4875(5)	9871(6)	53(2)
C(6)	3635(5)	6509(4)	10273(4)	28(1)
C(56)	9360(6)	4092(4)	3940(5)	42(2)
C(54)	10010(7)	5546(5)	3805(6)	57(2)

Table C.2. Continued.

C(53)	10880(6)	4960(5)	4287(6)	59(2)
C(9)	4359(6)	4694(4)	11121(5)	42(2)
C(55)	9114(6)	4893(6)	3387(5)	56(2)
C(19)	9999(8)	4428(6)	10127(7)	81(3)
C(17)	8142(7)	4768(5)	10498(6)	63(3)

_____

Table C.3. Bond lengths [Å] and angles [deg] for [Cu(*R,R*)-*i*-Pr-DuPhos)(Cl)]₂•THF, glu467_a.

Cu(1)-Cl(1)	2.3502(14)
Cu(1)-P(2)	2.2500(13)
Cu(1)-Cl(2)	2.3847(14)
Cu(1)-P(1)	2.2525(14)
Cu(2)-Cl(1)	2.3814(14)
Cu(2)-Cl(2)	2.3434(14)
Cu(2)-P(3)	2.2495(14)
Cu(2)-P(4)	2.2481(14)
P(2)-C(36)	1.848(5)
P(2)-C(33)	1.875(5)
P(2)-C(30)	1.871(5)
P(1)-C(41)	1.852(5)
P(1)-C(45)	1.861(5)
P(1)-C(48)	1.865(5)
P(3)-C(16)	1.856(5)
P(3)-C(20)	1.866(5)
P(3)-C(23)	1.880(6)
P(4)-C(4)	1.864(5)
P(4)-C(11)	1.849(6)
P(4)-C(7)	1.862(6)
C(36)-C(41)	1.409(7)
C(36)-C(37)	1.401(7)
C(33)-H(33)	1.0000
C(33)-C(52)	1.524(8)
C(33)-C(32)	1.539(7)
C(52)-H(52)	1.0000
C(52)-C(35)	1.546(8)
C(52)-C(34)	1.515(8)
O(1)-C(56)	1.419(9)
O(1)-C(53)	1.404(10)
C(51)-H(51A)	0.9800
C(51)-H(51B)	0.9800

Table C.3. Continued.

C(51)-H(51C)	0.9800
C(51)-C(49)	1.550(8)
C(30)-H(30)	1.0000
C(30)-C(28)	1.533(8)
C(30)-C(31)	1.535(7)
C(41)-C(40)	1.396(7)
C(39)-H(39)	0.9500
C(39)-C(38)	1.396(8)
C(39)-C(40)	1.381(7)
C(14)-H(14)	0.9500
C(14)-C(15)	1.393(8)
C(14)-C(13)	1.375(8)
C(37)-H(37)	0.9500
C(37)-C(38)	1.380(8)
C(32)-H(32A)	0.9900
C(32)-H(32B)	0.9900
C(32)-C(31)	1.527(8)
C(21)-H(21A)	0.9900
C(21)-H(21B)	0.9900
C(21)-C(20)	1.530(8)
C(21)-C(22)	1.511(9)
C(43)-H(43)	1.0000
C(43)-C(45)	1.547(8)
C(43)-C(42)	1.535(9)
C(43)-C(44)	1.524(8)
C(15)-H(15)	0.9500
C(15)-C(16)	1.396(7)
C(27)-H(27A)	0.9800
C(27)-H(27B)	0.9800
C(27)-H(27C)	0.9800
C(27)-C(28)	1.531(7)
C(45)-H(45)	1.0000

Table C.3. Continued.

C(45)-C(46)	1.546(7)
C(46)-H(46A)	0.9900
C(46)-H(46B)	0.9900
C(46)-C(47)	1.545(8)
C(16)-C(11)	1.405(7)
C(28)-H(28)	1.0000
C(28)-C(29)	1.526(8)
C(2)-H(2)	1.0000
C(2)-C(4)	1.551(8)
C(2)-C(1)	1.524(8)
C(2)-C(3)	1.532(8)
C(20)-H(20)	1.0000
C(20)-C(18)	1.547(9)
C(35)-H(35A)	0.9800
C(35)-H(35B)	0.9800
C(35)-H(35C)	0.9800
C(23)-H(23)	1.0000
C(23)-C(25)	1.529(8)
C(23)-C(22)	1.549(8)
C(13)-H(13)	0.9500
C(13)-C(12)	1.379(7)
C(12)-H(12)	0.9500
C(12)-C(11)	1.409(7)
C(25)-H(25)	1.0000
C(25)-C(24)	1.507(8)
C(25)-C(26)	1.550(8)
C(38)-H(38)	0.9500
C(24)-H(24A)	0.9800
C(24)-H(24B)	0.9800
C(24)-H(24C)	0.9800
C(40)-H(40)	0.9500
C(29)-H(29A)	0.9800

Table C.3. Continued.

C(29)-H(29B)	0.9800
C(29)-H(29C)	0.9800
C(4)-H(4)	1.0000
C(4)-C(5)	1.555(8)
C(48)-H(48)	1.0000
C(48)-C(49)	1.547(7)
C(48)-C(47)	1.532(7)
C(22)-H(22A)	0.9900
C(22)-H(22B)	0.9900
C(31)-H(31A)	0.9900
C(31)-H(31B)	0.9900
C(1)-H(1A)	0.9800
C(1)-H(1B)	0.9800
C(1)-H(1C)	0.9800
C(34)-H(34A)	0.9800
C(34)-H(34B)	0.9800
C(34)-H(34C)	0.9800
C(49)-H(49)	1.0000
C(49)-C(50)	1.532(8)
C(42)-H(42A)	0.9800
C(42)-H(42B)	0.9800
C(42)-H(42C)	0.9800
C(47)-H(47A)	0.9900
C(47)-H(47B)	0.9900
C(10)-H(10A)	0.9800
C(10)-H(10B)	0.9800
C(10)-H(10C)	0.9800
C(10)-C(8)	1.512(8)
C(44)-H(44A)	0.9800
C(44)-H(44B)	0.9800
C(44)-H(44C)	0.9800
C(5)-H(5A)	0.9900

Table C.3. Continued.

C(5)-H(5B)	0.9900
C(5)-C(6)	1.537(9)
C(7)-H(7)	1.0000
C(7)-C(8)	1.550(9)
C(7)-C(6)	1.538(8)
C(3)-H(3A)	0.9800
C(3)-H(3B)	0.9800
C(3)-H(3C)	0.9800
C(26)-H(26A)	0.9800
C(26)-H(26B)	0.9800
C(26)-H(26C)	0.9800
C(50)-H(50A)	0.9800
C(50)-H(50B)	0.9800
C(50)-H(50C)	0.9800
C(8)-H(8)	1.0000
C(8)-C(9)	1.534(8)
C(18)-H(18)	1.0000
C(18)-C(19)	1.464(10)
C(18)-C(17)	1.521(11)
C(6)-H(6A)	0.9900
C(6)-H(6B)	0.9900
C(56)-H(56A)	0.9900
C(56)-H(56B)	0.9900
C(56)-C(55)	1.502(10)
C(54)-H(54A)	0.9900
C(54)-H(54B)	0.9900
C(54)-C(53)	1.489(11)
C(54)-C(55)	1.536(11)
C(53)-H(53A)	0.9900
C(53)-H(53B)	0.9900
C(9)-H(9A)	0.9800
C(9)-H(9B)	0.9800

Table C.3. Continued.

C(9)-H(9C)	0.9800
C(55)-H(55A)	0.9900
C(55)-H(55B)	0.9900
C(19)-H(19A)	0.9800
C(19)-H(19B)	0.9800
C(19)-H(19C)	0.9800
C(17)-H(17A)	0.9800
C(17)-H(17B)	0.9800
C(17)-H(17C)	0.9800
Cl(1)-Cu(1)-Cl(2)	95.27(5)
P(2)-Cu(1)-Cl(1)	123.52(5)
P(2)-Cu(1)-Cl(2)	113.03(5)
P(2)-Cu(1)-P(1)	91.42(5)
P(1)-Cu(1)-Cl(1)	113.28(5)
P(1)-Cu(1)-Cl(2)	122.92(5)
Cl(2)-Cu(2)-Cl(1)	95.53(5)
P(3)-Cu(2)-Cl(1)	112.10(5)
P(3)-Cu(2)-Cl(2)	123.98(6)
P(4)-Cu(2)-Cl(1)	120.24(5)
P(4)-Cu(2)-Cl(2)	115.57(5)
P(4)-Cu(2)-P(3)	91.68(5)
Cu(1)-Cl(1)-Cu(2)	82.05(5)
C(36)-P(2)-Cu(1)	104.79(16)
C(36)-P(2)-C(33)	105.9(2)
C(36)-P(2)-C(30)	103.7(2)
C(33)-P(2)-Cu(1)	127.76(18)
C(30)-P(2)-Cu(1)	117.71(18)
C(30)-P(2)-C(33)	94.5(2)
Cu(2)-Cl(2)-Cu(1)	82.12(5)
C(41)-P(1)-Cu(1)	104.80(16)
C(41)-P(1)-C(45)	102.7(2)
C(41)-P(1)-C(48)	105.8(2)

Table C.3. Continued.

C(45)-P(1)-Cu(1)	129.47(18)
C(45)-P(1)-C(48)	92.7(2)
C(48)-P(1)-Cu(1)	118.76(17)
C(16)-P(3)-Cu(2)	104.72(17)
C(16)-P(3)-C(20)	104.9(2)
C(16)-P(3)-C(23)	105.1(2)
C(20)-P(3)-Cu(2)	128.84(18)
C(20)-P(3)-C(23)	93.8(3)
C(23)-P(3)-Cu(2)	117.14(18)
C(4)-P(4)-Cu(2)	128.53(18)
C(11)-P(4)-Cu(2)	104.54(17)
C(11)-P(4)-C(4)	101.6(2)
C(11)-P(4)-C(7)	107.7(2)
C(7)-P(4)-Cu(2)	119.12(18)
C(7)-P(4)-C(4)	93.1(3)
C(41)-C(36)-P(2)	119.4(4)
C(37)-C(36)-P(2)	121.8(4)
C(37)-C(36)-C(41)	118.7(5)
P(2)-C(33)-H(33)	108.4
C(52)-C(33)-P(2)	111.6(3)
C(52)-C(33)-H(33)	108.4
C(52)-C(33)-C(32)	115.6(5)
C(32)-C(33)-P(2)	104.2(4)
C(32)-C(33)-H(33)	108.4
C(33)-C(52)-H(52)	108.2
C(33)-C(52)-C(35)	110.8(5)
C(35)-C(52)-H(52)	108.2
C(34)-C(52)-C(33)	111.3(5)
C(34)-C(52)-H(52)	108.2
C(34)-C(52)-C(35)	110.1(5)
C(53)-O(1)-C(56)	106.7(6)
H(51A)-C(51)-H(51B)	109.5

Table C.3. Continued.

H(51A)-C(51)-H(51C)	109.5
H(51B)-C(51)-H(51C)	109.5
C(49)-C(51)-H(51A)	109.5
C(49)-C(51)-H(51B)	109.5
C(49)-C(51)-H(51C)	109.5
P(2)-C(30)-H(30)	105.8
C(28)-C(30)-P(2)	117.5(4)
C(28)-C(30)-H(30)	105.8
C(28)-C(30)-C(31)	115.4(5)
C(31)-C(30)-P(2)	105.5(4)
C(31)-C(30)-H(30)	105.8
C(36)-C(41)-P(1)	118.8(4)
C(40)-C(41)-P(1)	122.3(4)
C(40)-C(41)-C(36)	118.8(4)
C(38)-C(39)-H(39)	120.4
C(40)-C(39)-H(39)	120.4
C(40)-C(39)-C(38)	119.1(5)
C(15)-C(14)-H(14)	120.0
C(13)-C(14)-H(14)	120.0
C(13)-C(14)-C(15)	120.1(5)
C(36)-C(37)-H(37)	119.3
C(38)-C(37)-C(36)	121.3(5)
C(38)-C(37)-H(37)	119.3
C(33)-C(32)-H(32A)	109.9
C(33)-C(32)-H(32B)	109.9
H(32A)-C(32)-H(32B)	108.3
C(31)-C(32)-C(33)	108.8(5)
C(31)-C(32)-H(32A)	109.9
C(31)-C(32)-H(32B)	109.9
H(21A)-C(21)-H(21B)	108.5
C(20)-C(21)-H(21A)	110.2
C(20)-C(21)-H(21B)	110.2

Table C.3. Continued.

C(22)-C(21)-H(21A)	110.2
C(22)-C(21)-H(21B)	110.2
C(22)-C(21)-C(20)	107.6(5)
C(45)-C(43)-H(43)	107.0
C(42)-C(43)-H(43)	107.0
C(42)-C(43)-C(45)	113.0(5)
C(44)-C(43)-H(43)	107.0
C(44)-C(43)-C(45)	111.4(5)
C(44)-C(43)-C(42)	111.1(5)
C(14)-C(15)-H(15)	119.5
C(14)-C(15)-C(16)	121.0(5)
C(16)-C(15)-H(15)	119.5
H(27A)-C(27)-H(27B)	109.5
H(27A)-C(27)-H(27C)	109.5
H(27B)-C(27)-H(27C)	109.5
C(28)-C(27)-H(27A)	109.5
C(28)-C(27)-H(27B)	109.5
C(28)-C(27)-H(27C)	109.5
P(1)-C(45)-H(45)	107.7
C(43)-C(45)-P(1)	112.0(4)
C(43)-C(45)-H(45)	107.7
C(46)-C(45)-P(1)	108.2(4)
C(46)-C(45)-C(43)	113.5(4)
C(46)-C(45)-H(45)	107.7
C(45)-C(46)-H(46A)	109.5
C(45)-C(46)-H(46B)	109.5
H(46A)-C(46)-H(46B)	108.0
C(47)-C(46)-C(45)	110.9(4)
C(47)-C(46)-H(46A)	109.5
C(47)-C(46)-H(46B)	109.5
C(15)-C(16)-P(3)	121.6(4)
C(15)-C(16)-C(11)	119.2(5)

Table C.3. Continued.

C(11)-C(16)-P(3)	119.0(4)
C(30)-C(28)-H(28)	108.2
C(27)-C(28)-C(30)	110.8(4)
C(27)-C(28)-H(28)	108.2
C(29)-C(28)-C(30)	111.4(5)
C(29)-C(28)-C(27)	109.9(5)
C(29)-C(28)-H(28)	108.2
C(4)-C(2)-H(2)	107.0
C(1)-C(2)-H(2)	107.0
C(1)-C(2)-C(4)	113.0(5)
C(1)-C(2)-C(3)	112.4(5)
C(3)-C(2)-H(2)	107.0
C(3)-C(2)-C(4)	110.0(5)
P(3)-C(20)-H(20)	108.2
C(21)-C(20)-P(3)	105.2(4)
C(21)-C(20)-H(20)	108.2
C(21)-C(20)-C(18)	114.1(5)
C(18)-C(20)-P(3)	112.6(4)
C(18)-C(20)-H(20)	108.2
C(52)-C(35)-H(35A)	109.5
C(52)-C(35)-H(35B)	109.5
C(52)-C(35)-H(35C)	109.5
H(35A)-C(35)-H(35B)	109.5
H(35A)-C(35)-H(35C)	109.5
H(35B)-C(35)-H(35C)	109.5
P(3)-C(23)-H(23)	105.7
C(25)-C(23)-P(3)	116.9(4)
C(25)-C(23)-H(23)	105.7
C(25)-C(23)-C(22)	116.5(5)
C(22)-C(23)-P(3)	105.4(4)
C(22)-C(23)-H(23)	105.7
C(14)-C(13)-H(13)	120.2

Table C.3. Continued.

C(14)-C(13)-C(12)	119.6(5)
C(12)-C(13)-H(13)	120.2
C(13)-C(12)-H(12)	119.1
C(13)-C(12)-C(11)	121.9(5)
C(11)-C(12)-H(12)	119.1
C(23)-C(25)-H(25)	108.2
C(23)-C(25)-C(26)	110.4(5)
C(24)-C(25)-C(23)	111.5(5)
C(24)-C(25)-H(25)	108.2
C(24)-C(25)-C(26)	110.2(5)
C(26)-C(25)-H(25)	108.2
C(39)-C(38)-H(38)	120.0
C(37)-C(38)-C(39)	120.0(5)
C(37)-C(38)-H(38)	120.0
C(25)-C(24)-H(24A)	109.5
C(25)-C(24)-H(24B)	109.5
C(25)-C(24)-H(24C)	109.5
H(24A)-C(24)-H(24B)	109.5
H(24A)-C(24)-H(24C)	109.5
H(24B)-C(24)-H(24C)	109.5
C(41)-C(40)-H(40)	119.1
C(39)-C(40)-C(41)	121.8(5)
C(39)-C(40)-H(40)	119.1
C(28)-C(29)-H(29A)	109.5
C(28)-C(29)-H(29B)	109.5
C(28)-C(29)-H(29C)	109.5
H(29A)-C(29)-H(29B)	109.5
H(29A)-C(29)-H(29C)	109.5
H(29B)-C(29)-H(29C)	109.5
P(4)-C(4)-H(4)	107.7
C(2)-C(4)-P(4)	111.9(4)
C(2)-C(4)-H(4)	107.7

Table C.3. Continued.

C(2)-C(4)-C(5)	113.9(5)
C(5)-C(4)-P(4)	107.8(4)
C(5)-C(4)-H(4)	107.7
C(16)-C(11)-P(4)	119.8(4)
C(16)-C(11)-C(12)	118.2(5)
C(12)-C(11)-P(4)	122.0(4)
P(1)-C(48)-H(48)	104.4
C(49)-C(48)-P(1)	120.0(3)
C(49)-C(48)-H(48)	104.4
C(47)-C(48)-P(1)	105.6(4)
C(47)-C(48)-H(48)	104.4
C(47)-C(48)-C(49)	116.2(4)
C(21)-C(22)-C(23)	107.9(5)
C(21)-C(22)-H(22A)	110.1
C(21)-C(22)-H(22B)	110.1
C(23)-C(22)-H(22A)	110.1
C(23)-C(22)-H(22B)	110.1
H(22A)-C(22)-H(22B)	108.4
C(30)-C(31)-H(31A)	110.4
C(30)-C(31)-H(31B)	110.4
C(32)-C(31)-C(30)	106.5(4)
C(32)-C(31)-H(31A)	110.4
C(32)-C(31)-H(31B)	110.4
H(31A)-C(31)-H(31B)	108.6
C(2)-C(1)-H(1A)	109.5
C(2)-C(1)-H(1B)	109.5
C(2)-C(1)-H(1C)	109.5
H(1A)-C(1)-H(1B)	109.5
H(1A)-C(1)-H(1C)	109.5
H(1B)-C(1)-H(1C)	109.5
C(52)-C(34)-H(34A)	109.5
C(52)-C(34)-H(34B)	109.5

Table C.3. Continued.

C(52)-C(34)-H(34C)	109.5
H(34A)-C(34)-H(34B)	109.5
H(34A)-C(34)-H(34C)	109.5
H(34B)-C(34)-H(34C)	109.5
C(51)-C(49)-H(49)	107.1
C(48)-C(49)-C(51)	115.3(5)
C(48)-C(49)-H(49)	107.1
C(50)-C(49)-C(51)	110.6(5)
C(50)-C(49)-C(48)	109.2(5)
C(50)-C(49)-H(49)	107.1
C(43)-C(42)-H(42A)	109.5
C(43)-C(42)-H(42B)	109.5
C(43)-C(42)-H(42C)	109.5
H(42A)-C(42)-H(42B)	109.5
H(42A)-C(42)-H(42C)	109.5
H(42B)-C(42)-H(42C)	109.5
C(46)-C(47)-H(47A)	110.2
C(46)-C(47)-H(47B)	110.2
C(48)-C(47)-C(46)	107.6(4)
C(48)-C(47)-H(47A)	110.2
C(48)-C(47)-H(47B)	110.2
H(47A)-C(47)-H(47B)	108.5
H(10A)-C(10)-H(10B)	109.5
H(10A)-C(10)-H(10C)	109.5
H(10B)-C(10)-H(10C)	109.5
C(8)-C(10)-H(10A)	109.5
C(8)-C(10)-H(10B)	109.5
C(8)-C(10)-H(10C)	109.5
C(43)-C(44)-H(44A)	109.5
C(43)-C(44)-H(44B)	109.5
C(43)-C(44)-H(44C)	109.5
H(44A)-C(44)-H(44B)	109.5

Table C.3. Continued.

H(44A)-C(44)-H(44C)	109.5
H(44B)-C(44)-H(44C)	109.5
C(4)-C(5)-H(5A)	109.4
C(4)-C(5)-H(5B)	109.4
H(5A)-C(5)-H(5B)	108.0
C(6)-C(5)-C(4)	111.2(4)
C(6)-C(5)-H(5A)	109.4
C(6)-C(5)-H(5B)	109.4
P(4)-C(7)-H(7)	104.9
C(8)-C(7)-P(4)	119.1(4)
C(8)-C(7)-H(7)	104.9
C(6)-C(7)-P(4)	105.6(4)
C(6)-C(7)-H(7)	104.9
C(6)-C(7)-C(8)	115.9(5)
C(2)-C(3)-H(3A)	109.5
C(2)-C(3)-H(3B)	109.5
C(2)-C(3)-H(3C)	109.5
H(3A)-C(3)-H(3B)	109.5
H(3A)-C(3)-H(3C)	109.5
H(3B)-C(3)-H(3C)	109.5
C(25)-C(26)-H(26A)	109.5
C(25)-C(26)-H(26B)	109.5
C(25)-C(26)-H(26C)	109.5
H(26A)-C(26)-H(26B)	109.5
H(26A)-C(26)-H(26C)	109.5
H(26B)-C(26)-H(26C)	109.5
C(49)-C(50)-H(50A)	109.5
C(49)-C(50)-H(50B)	109.5
C(49)-C(50)-H(50C)	109.5
H(50A)-C(50)-H(50B)	109.5
H(50A)-C(50)-H(50C)	109.5
H(50B)-C(50)-H(50C)	109.5

Table C.3. Continued.

C(10)-C(8)-C(7)	115.4(5)
C(10)-C(8)-H(8)	106.7
C(10)-C(8)-C(9)	110.5(5)
C(7)-C(8)-H(8)	106.7
C(9)-C(8)-C(7)	110.2(5)
C(9)-C(8)-H(8)	106.7
C(20)-C(18)-H(18)	106.6
C(19)-C(18)-C(20)	112.3(6)
C(19)-C(18)-H(18)	106.6
C(19)-C(18)-C(17)	114.2(8)
C(17)-C(18)-C(20)	110.0(6)
C(17)-C(18)-H(18)	106.6
C(5)-C(6)-H(6A)	110.0
C(5)-C(6)-H(6B)	110.0
C(7)-C(6)-C(5)	108.3(5)
C(7)-C(6)-H(6A)	110.0
C(7)-C(6)-H(6B)	110.0
H(6A)-C(6)-H(6B)	108.4
O(1)-C(56)-H(56A)	110.0
O(1)-C(56)-H(56B)	110.0
O(1)-C(56)-C(55)	108.3(6)
H(56A)-C(56)-H(56B)	108.4
C(55)-C(56)-H(56A)	110.0
C(55)-C(56)-H(56B)	110.0
H(54A)-C(54)-H(54B)	109.1
C(53)-C(54)-H(54A)	111.2
C(53)-C(54)-H(54B)	111.2
C(53)-C(54)-C(55)	102.9(6)
C(55)-C(54)-H(54A)	111.2
C(55)-C(54)-H(54B)	111.2
O(1)-C(53)-C(54)	104.6(6)
O(1)-C(53)-H(53A)	110.8

Table C.3. Continued.

O(1)-C(53)-H(53B)	110.8
C(54)-C(53)-H(53A)	110.8
C(54)-C(53)-H(53B)	110.8
H(53A)-C(53)-H(53B)	108.9
C(8)-C(9)-H(9A)	109.5
C(8)-C(9)-H(9B)	109.5
C(8)-C(9)-H(9C)	109.5
H(9A)-C(9)-H(9B)	109.5
H(9A)-C(9)-H(9C)	109.5
H(9B)-C(9)-H(9C)	109.5
C(56)-C(55)-C(54)	102.6(6)
C(56)-C(55)-H(55A)	111.2
C(56)-C(55)-H(55B)	111.2
C(54)-C(55)-H(55A)	111.2
C(54)-C(55)-H(55B)	111.2
H(55A)-C(55)-H(55B)	109.2
C(18)-C(19)-H(19A)	109.5
C(18)-C(19)-H(19B)	109.5
C(18)-C(19)-H(19C)	109.5
H(19A)-C(19)-H(19B)	109.5
H(19A)-C(19)-H(19C)	109.5
H(19B)-C(19)-H(19C)	109.5
C(18)-C(17)-H(17A)	109.5
C(18)-C(17)-H(17B)	109.5
C(18)-C(17)-H(17C)	109.5
H(17A)-C(17)-H(17B)	109.5
H(17A)-C(17)-H(17C)	109.5
H(17B)-C(17)-H(17C)	109.5

_____

Symmetry transformations used to generate equivalent atoms:

APPENDIX D: LUMINESCENCE INVESTIGATION OF SAMARIUM(III)/

DICYANOAURATE(I) BASED COORDINATION NETWORKS

WITH AND WITHOUT AUROPHILIC INTERACTIONS

D.1. Introduction

The unique optical, magnetic and electronic properties of lanthanide ions have sparked intense investigation of their inherent structure.[1–5] Coordination polymers that contain lanthanide components are of great interest due to their potential application in photocatalysis, sensors, optical fiber coatings, and LEDs.[6–9] The quantum yield of the material is critical to their performance and so strategies to maximize this property have been developed. Traditionally, sensitization of lanthanide ion luminescence is achieved by π-conjugated organic chromophores that are directly coordinated to the metal centers. Donor ligands used for such applications usually have strong absorbance in the UV region and transfer their excited energy to the acceptor species.[10–14] A new class of chromophores involving transition metal complexes is emerging as suitable sensitizers of lanthanide ion acceptors.[15–17] A major advantage afforded by these chromophores is their ability to sustain a better energy match-up with most Ln^{3+} acceptor states.[18–22] Unique advantages of metal complexes over organic chromophores are that they provide a relatively high triplet quantum yield due to the rapid intersystem crossing inherent within the system (due to the heavy-atom effect), and the possibility of a facile detection of both quenching of the d-block chromophores and the sensitized emission from the lanthanide centers.[23–26] This pairing of lanthanides, which have sharp emission lines and long lifetimes, with emissive transition metals, that sensitize lanthanide emission via energy transfer, has recently generated significant interest.[27–29] The observed energy transfer between these species results from the overlap of the lower emission band of the transition metal and the excitation band of the lanthanide because of the favorable energy match-up between the two systems.[21, 30, 31]

Certain transition metals have been shown to have a greater degree of overlap with lanthanides than organic ligands do, which increases the effective quantum yield of the system.[32–37]

Au(I) in particular is known to be highly emissive as demonstrated in our previous work on gold,[38–41] and has recently been identified as a photoredox catalyst for organic reactions.[42-54] It can also be used as a building block for coordination polymers in the form of $[Au(CN)_2]^-$.[55–59] Kagomé type $Ln[Au(CN)_2]_3 \cdot 3H_2O$ systems (**LnAu₃**) have been synthesized previously and their interactions between distinct emissive units have been well studied for evidence of energy transfer via sensitization or quenching with several different lanthanides. While few other Ln/Au compounds have been studied,[60–62] these systems have also been surmised to present sensitized lanthanide emission through energy transfer from gold to the lanthanide.

We have recently reported on a new type of Ln/Au coordination polymer, $[^nBu_4N]_2[Ln(NO_3)_4Au(CN)_2]$ (**LnAu**; Ln = Nd, Eu, Gd, or Tb) where neither intra- nor interchain aurophilic interactions exist.[60] Therein we illustrated the presence of distinct chromophores observable by luminescence spectroscopy due to the lack of energy transfer in these systems. These studies compared the Kagomé type $Ln[Au(CN)_2]_3 \cdot 3H_2O$ system with our recent work on $[^nBu_4N]_2[Ln(NO_3)_4Au(CN)_2]$.[60–62] This research builds on our previous work with the goal of understanding the fundamental differences between emission properties for aurophilic and non-aurophilic coordination polymers, using the recently reported samarium(III) analogues as a focused case study.

The structures of $[^nBu_4N]_2[Sm(NO_3)_4Au(CN)_2]$ (**SmAu**) and $Sm[Au(CN)_2]_3 \cdot 3H_2O$ (**SmAu₃**) are isomorphous to other members of the **LnAu** and **LnAu₃** series and have been described previously.[61] Briefly summarizing, the **SmAu** framework contains a 1-D chain composed of repeating units of $[Sm(NO_3)_4Au(CN)_2]^{2-}$. The Sm(III) centre is 10-coordinate, composed of 8 oxygen atoms originating from 4 nitrate groups, and 2 N-cyano units originating from $[Au(CN)_2]^-$. The essentially linear dicyanoaurate unit bridges Sm(III) centers to form an overall zig-zag motif (Figure D.1). Tetrabutylammonium cations are located between the voids of the zigzag motif as well as above and below the 1-D chains.
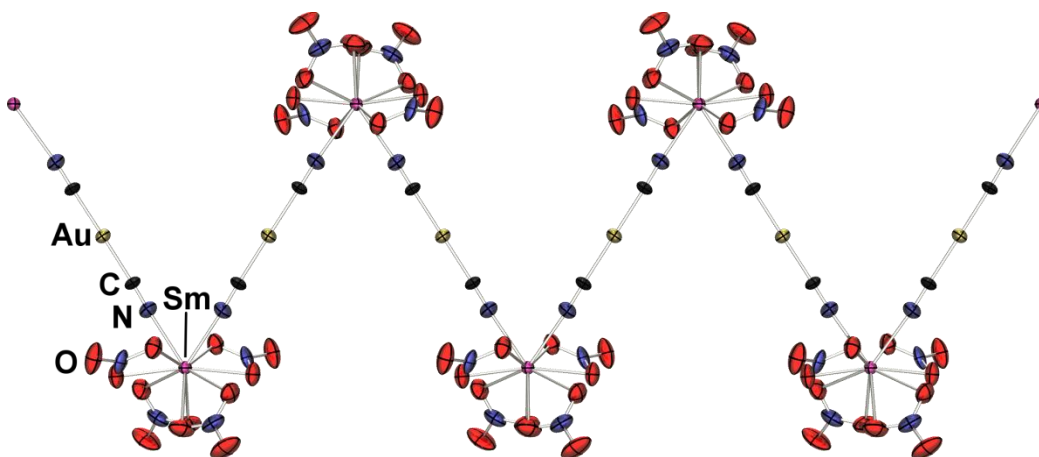
Figure D.1. One-dimensional structure of $[^nBu_4N]_2[Sm(NO_3)_4Au(CN)_2]$ (**SmAu**) (50% ellipsoids; tetrabutylammonium cations omitted for clarity)

In the **SmAu₃** framework, Sm(III) conforms to a tricapped trigonal prismatic geometry, wherein the prismatic positions are occupied by dicyanoaurate-based nitrogen atoms and the capping positions are occupied by aqua ligands. The Sm(III) centers are also bridged by linear units of $[Au(CN)_2]^-$, forming an overall 3-D network with Kagome (or alternatively trihexagonal tiling) type symmetry (Figure D.2). Additionally, a second independent network of $Sm[Au(CN)_2]_3 \cdot 3H_2O$ interpenetrates the first, supported by Au(I)-Au(I) (aurophilic) interactions.

Thus, in this contribution, we have targeted the characterization of these two systems via more detailed luminescence spectroscopy, quantum yields and lifetimes measurements. Use of the crystal structure data also enabled further investigation of the impact of the presence or absence of aurophilicity on the photophysical properties through ground state geometry optimization and calculation of the excited states using DFT simulations.
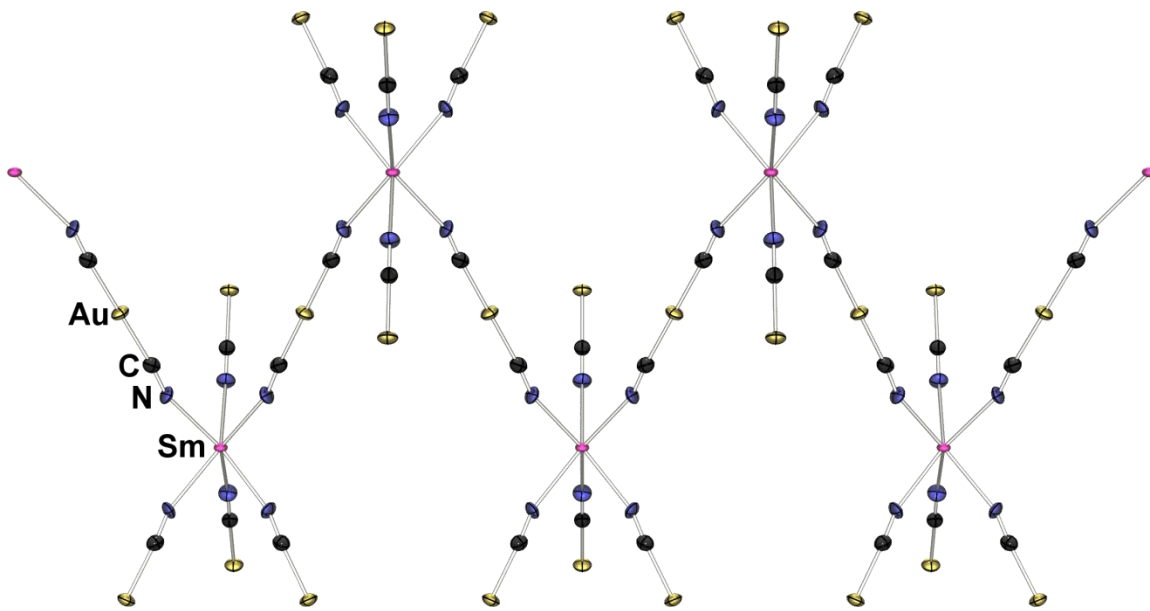
Figure D.2. One of the interpenetrated three-dimensional networks of $Sm[Au(CN)_2]_3 \cdot 3H_2O$ (**SmAu₃**) (50% ellipsoids; aqua ligands omitted for clarity)

D.2. Experimental

D.2.1. Materials

$[^nBu_4N]_2[Sm(NO_3)_4Au(CN)_2]$ (**SmAu**) and $Sm[Au(CN)_2]_3 \cdot 3H_2O$ (**SmAu₃**) were prepared according to the literature procedure.[63] All other materials were obtained from commercial sources and used as received.

D.2.2. Luminescence spectra

Steady-state luminescence scans were run between 298 K and 43 K. Spectra were taken with a Model Quantamaster-1046 photoluminescence spectrophotometer from Photon Technology International using a 75 W xenon arc lamp combined with two excitation monochromators and one emission monochromator. A photomultiplier tube at 800 V was used as the emission detector. The solid samples were mounted on a copper plate using non-emitting copper-dust high vacuum grease. All scans were run

under vacuum using a Janis ST-100 optical cryostat. Low temperature scans used liquid nitrogen for scans down to 78 K.

D.2.3. Lifetime Measurements

Luminescence lifetime measurements were collected by exciting crystals using a pulsed 360 nm LED source connected to a FG2C function generator. The emission was collected at various wavelengths using a Jobin Yvon Ramanor system, and the lifetime was read with a LeCroy 9310c Dual 400 MHz oscilloscope, collecting data every 50 ns to 2 μs per sweep, averaging 10000 sweeps per sample. Scans were run at both 298 K and 78 K using a Janis ST-100 optical cryostat. Liquid nitrogen was used as coolant.

D.2.4. Diffuse Reflectance Spectroscopy

Diffuse reflectance spectra were collected on solid samples at 298 K. The light source was a Mikropack DH-2000 deuterium and halogen light source coupled with an Ocean Optics USB4000 detector. Collected light was collected with a fiber optic cable. Spectra were referenced with PTFE. Data was processed using SpectraSuite 1.4.2_09.

D.2.5. Quantum Yield Measurements

The absolute PL quantum yield (QY) measurements on the solids were conducted using a PTI QM-40, PLQY ultrasensitive fluorimeter system containing a 6-in. integrating sphere (K-Sphere B) designed for enhanced measurement of quantum yields of solids, films, and powders. The system includes dedicated quantum yield calculation functions. Wavelength selection was conducted by software controlled excitation and emission monochromators. The QY measurements were conducted on finely ground solids uniformly spread onto the sample holder and covered with a quartz disk.

D.2.6. Computer Modeling

Calculations were performed using the Gaussian 09 Software Package (Gaussian Inc.) supported by the University of Maine Advanced Computing Group. Ground state optimizations were performed using

molecular mechanics with a Universal Force Field (UFF) parameter developed by W. A. Goddard.[64] For the **SmAu** system MM calculations were performed on a single monomer unit. However due to the metallophilic interaction in **SmAu₃**, MM ground state calculations were performed for a dimer unit. Molecular orbital calculations were performed on ground state MM structures using the hybrid density functional theory due to Becke's 3-parameter nonlocal exchange functional with the nonlocal correlation functional of Lee, Yang and Parr, B3LYP. The modified Stuttgart/Dresden effective core potential (ECP) basis set (SDD) of Fuentealba and Szentpaly was employed for all atoms. MOs were generated and visualized using the Avogadro software package 1.2.0.

D.3. Results

D.3.1. Luminescence

The luminescence spectra of non-aurophilic **SmAu** are shown in Figures D.3 and D.4 at 298 K and 78 K, respectively. The spectra of the aurophilic **SmAu₃** system are also shown in Figures D.5 and D.6 for 298 and 78 K, respectively. Distinct differences in the luminescent behavior of these two sets are observed both for the Au(I) and Sm(III) assigned emission features. The materials display dominant Au(I) peaks in the ~380 - 460 nm range for both temperatures of 298 and 78 K. In the nonaurophilic system the gold centered emission maximum is calculated by gaussian fit at 400 nm at 298 K, and a gaussian fit at 78 K indicates a slightly red-shifted maximum to 413 nm. In contrast, the aurophilic system shows an emission peak at 411 nm at 298 K and at a significantly red-shifted position of 431 nm at 78 K. At 298 K both compounds display prominent samarium assigned transitions at 559 nm, 591/600 nm, and 640/648 nm corresponding to the $^4G_{5/2} \rightarrow ^6H_{5/2}, ^4G_{5/2} \rightarrow ^6H_{7/2}$, and $^4G_{5/2} \rightarrow ^6H_{9/2}$, transitions, respectively.[65] At 78 K we observe a broad Au(I)→(CN)⁻ excitation band for both systems. Sharp reductions in excitation intensity are observed at wavelengths characteristic of trivalent rare earth ions. The sharp drop in intensity we believe is likely due to energy transfer from the $Au(CN)_2^-$ ion to the Sm(III) center. However, in the aurophilic case,

the Sm(III) excitation peaks overlap less than in the nonaurophilic case. Upon cooling to 78 K the relative emission of the Sm(III) ion (as compared with the Au(I) centered emission) increases in the nonaurophilic **SmAu** system. This is in contrast to the aurophilic case where the relative emission of Sm(III) ion *decreases* in intensity.

The increase in the Sm(III) emission intensity in the nonaurophilic **SmAu** system appears to result from an increased donor-acceptor spectral overlap between the Sm(III) excitation and Au(I) emission band indicating enhanced Au(I)→Sm(III) energy transfer efficiency. We are certain that the emission spectra of the gold band is not the result of a reabsorption due to the fast Au(I)→(CN)⁻ charge transfer in comparison to the slow Au(I)→Sm(III). As shown in Figures D.3 and D.4, a sharp drop in intensity of the Au(I) peak is observed at 402 nm at 298 K and 413 nm at 78 K. Excitation scans show a distinct sharp and narrow band at this energy, characteristic of a forbidden *f-f* absorption[66]; again, this implies that there is an overlap of a Sm(III)-excitation band and the Au(I)-emission peak, facilitating energy transfer in this case. On the other hand, because of the Au(I) emission red shift described above for the aurophilic **SmAu₃** system this overlap of the Sm(III)-excitation band and the Au(I)-emission peak does not occur in this case. The observed sharp excitation band at 405 nm in Figure D.6 for **SmAu₃** at 78 K shows that this peak no longer overlaps with samarium emission, implying a loss of Au(I)→Sm(III) to charge transfer. We have previously reported on the red shift of Au(CN)₂⁻ ions with increasing oligomer size where monomers emit at higher energies than dimers or larger oligomers.[67, 68] In this case we consider aurophilic interactions as a type of oligomerization in the crystal structure. This weak dimerization causes the red shift observed in the Au(I)→CN emission band of **SmAu₃**. Because this red shift reduces emission/excitation overlap of the Au(I) emission band with the Sm(III) excitation band, the Sm(III) emission intensity is decreased.
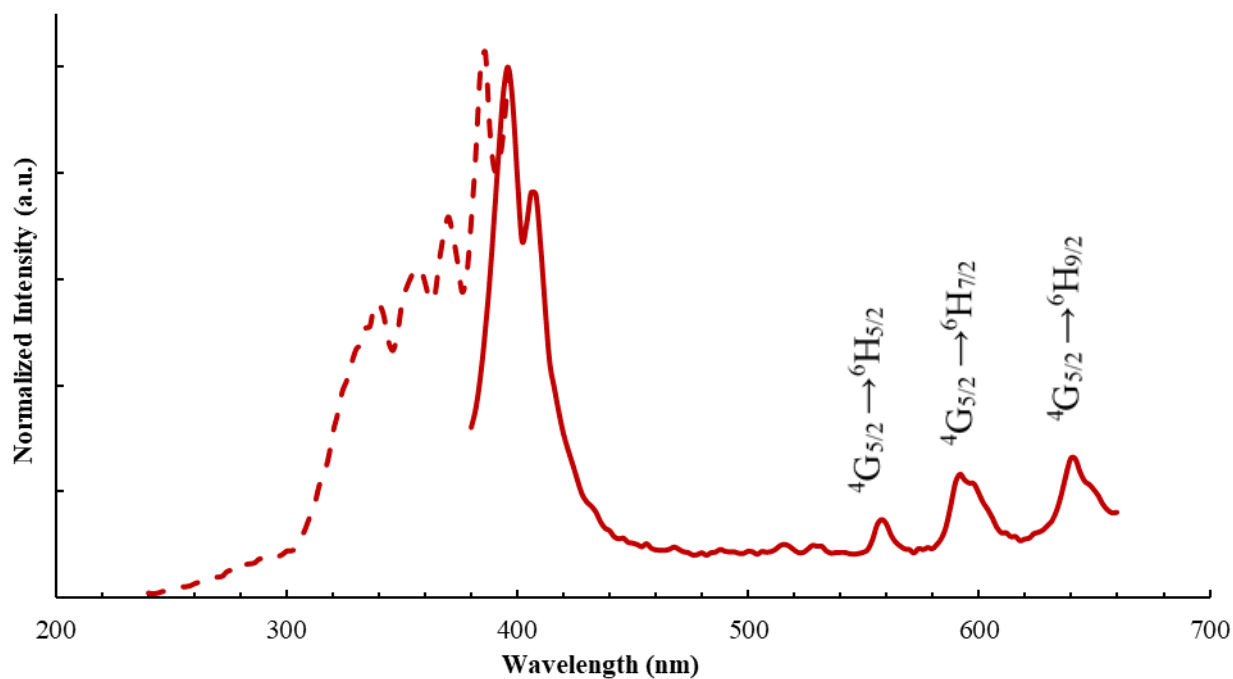
Figure D.3. Luminescence spectra of **SmAu** at 298 K. Emission obtained with an excitation at 350 nm. Excitation obtained at an emission of 415 nm
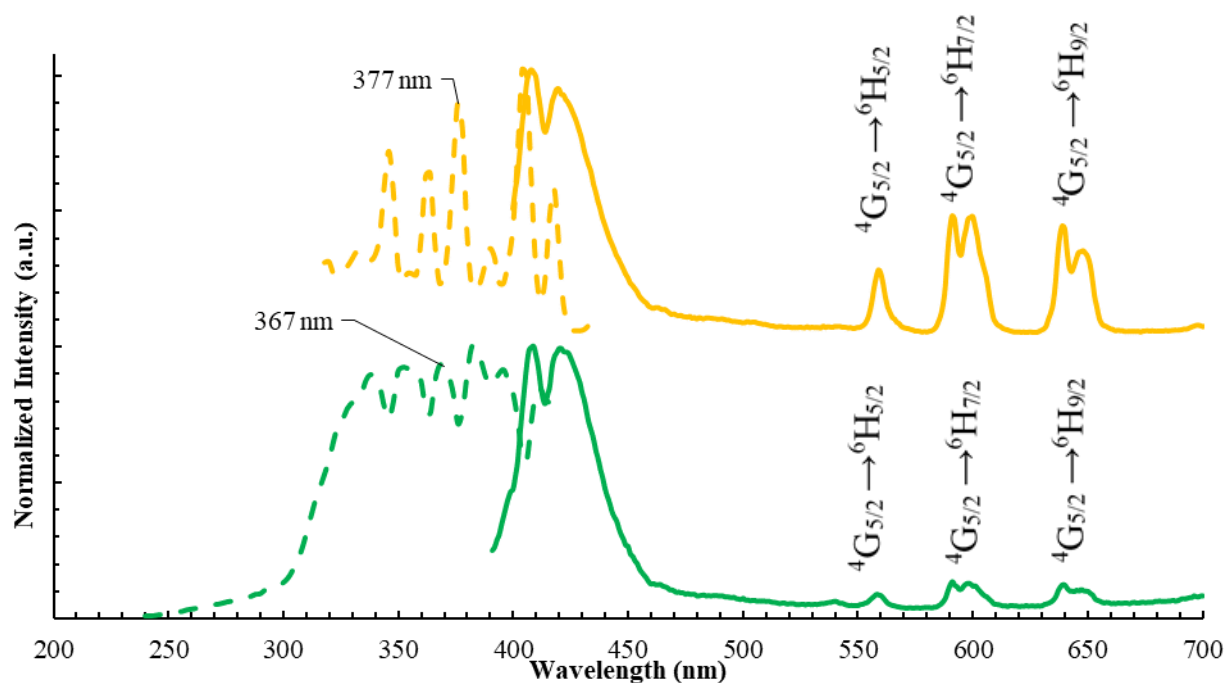
Figure D.4 Luminescence spectra of **SmAu** at 78 K. (Top) Emission obtained with an excitation at 377 nm and excitation obtained at an emission of 377 nm while (bottom) Emission obtained with an excitation at 367 nm and excitation obtained at an emission of 590 nm. Note the corresponding Sm(III) excitation and Au(I) excitation intensities, as indicated
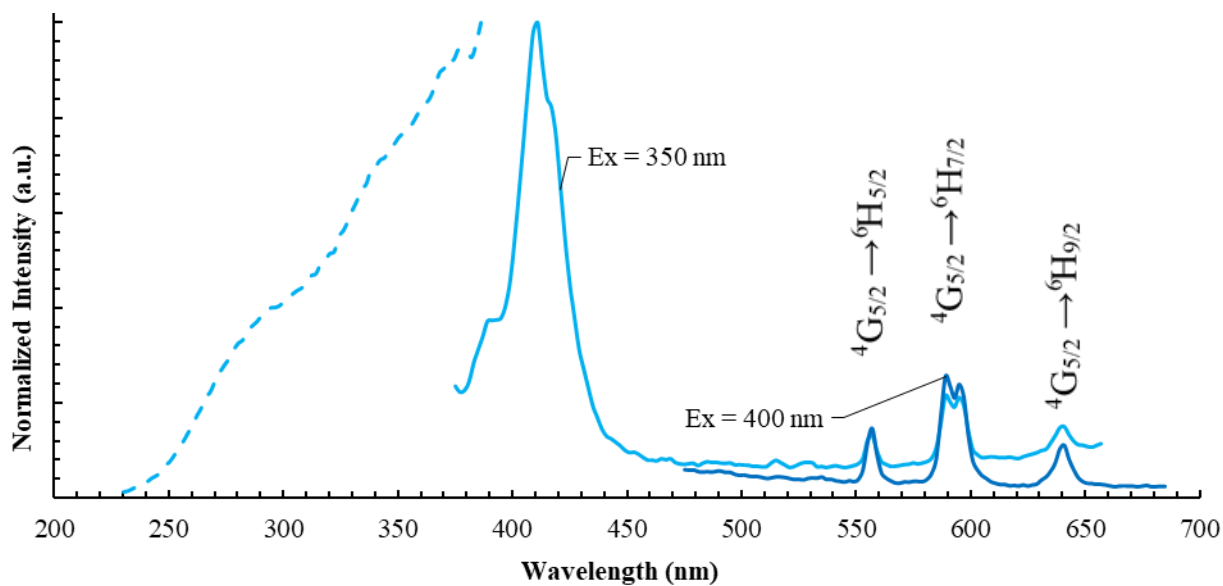
Figure D.5. Luminescence spectra of **SmAu₃** at 298 K. Emission obtained with an excitation at 350 nm and 400 nm. Excitation obtained at an emission of 410 nm
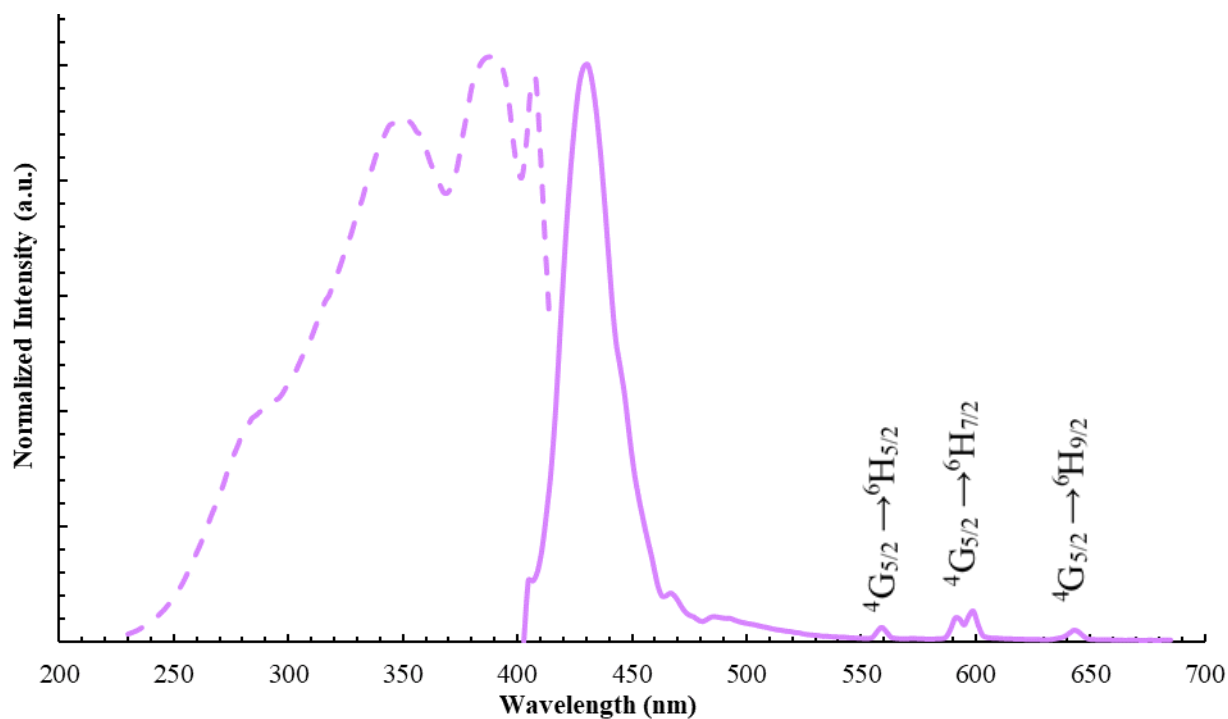
Figure D.6. Luminescence spectra of **SmAu₃** at 78 K. Emission obtained with an excitation at 388 nm. Excitation obtained at an emission of 428 nm

252

D.3.2. Diffuse Reflectance Spectroscopy

We have performed diffuse reflectance spectroscopy of both the aurophilic **SmAu₃** and the nonaurophilic **SmAu** complex at room temperature. Results are shown in Figure D.7 below. A number of sharp f–f absorptions bands are present for **SmAu** between 343 nm and 428 nm but are almost absent in the case of **SmAu₃**. In both cases we observe a broad peak at wavelengths below 428 nm which can be assigned to the dicyanoaurate-centered MLCT transition. However, in **SmAu** this band is much more narrow and less intense compared to **SmAu₃**. Unlike **SmAu₃**, in **SmAu** the $Au(CN)_2^-$ anions do not exhibit any metallophilic interactions, thus the reduction of the HOMO–LUMO gap comes from the coordination of the cyanide with the lanthanide ligands. The interaction of cyanide with a rare earth metal lowers the energy of the empty π^* orbitals of the cyanide ligand, leading to a decrease in the HOMO– LUMO gap (Au(I) d to $(CN)^- \pi^*$) and thus the absorption spectrum red-shifts. In both cases we observe weak f-f emission bands at 644 nm. These bands are stronger in the case of **SmAu** compared to **SmAu₃**. The luminescence has a decrease of the Sm(III) f-f emission in the **SmAu₃** case, presumably from back charge transfer to the aurophilic $Au(CN)_2^-$ anions. The absorption band in **SmAu₃** at 561 nm strongly supports this case where the absorption energy also corresponds to the $^4G_{5/2} \rightarrow {}^6H_{5/2}$ Sm transition.
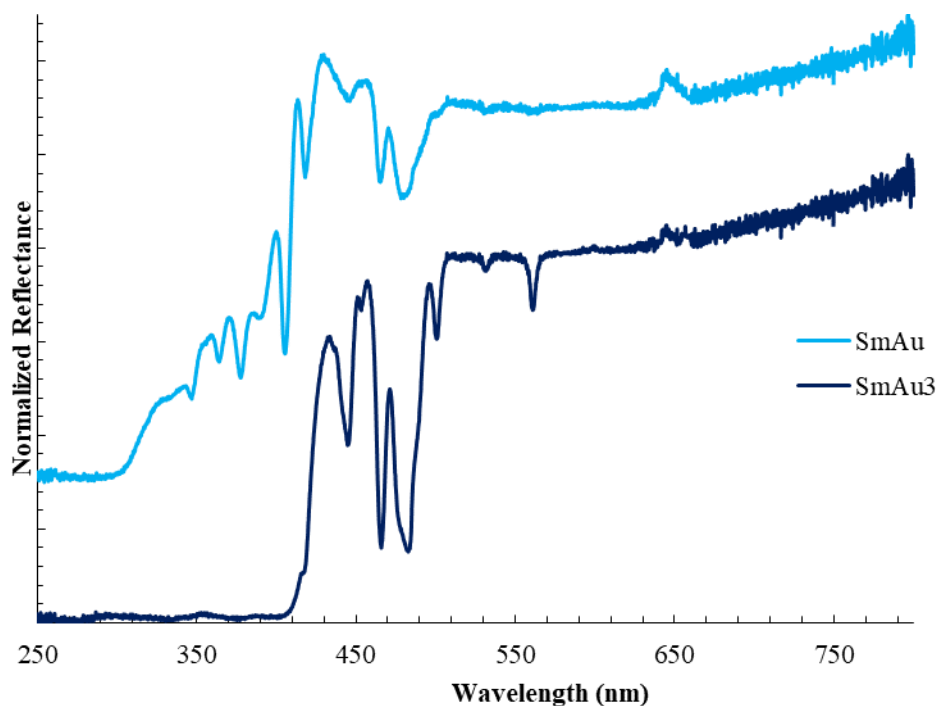
Figure D.7. Diffuse reflectance spectra of both aurophilic **SmAu₃** and nonaurophilic **SmAu** complexes

D.3.3. Quantum Yield and Lifetime Measurements

The quantum yield (QY) was measured for the bands assigned to Au(I) emission for both complexes. For nonaurophilic **SmAu** the measured QY of the Au(I) emission band was 0.13 while for **SmAu₃** the QY was 0.08. The relatively low QY of the aurophilic case is attributed to nonradiative Au(I)→Au(I) metal-metal charge transfer (MMCT) interactions between the $Au(CN)_2^-$ ions in the aurophilic **SmAu₃** which compete with luminescent Au(I)→(CN)⁻ metal-ligand charge transfer (MLCT) transitions as shown in Figure D.8. Nonaurophilic **SmAu** does not exhibit MMCT between Au(I) ions and hence shows relatively higher QY for the Au(I) emission band.
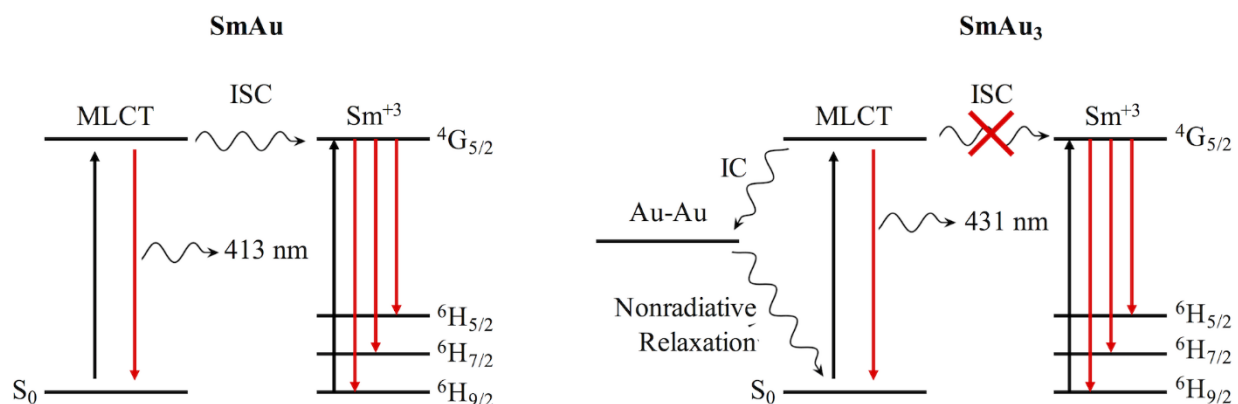
Figure D.8: Charge transfer mechanisms in the aurophilic **SmAu₃** and nonaurophilic **SmAu** cases showing a preference for MLCT→S_0 emission in the **SmAu₃** system but not in the **SmAu** system. The decreased energy between S_0 and the MLCT excited state in **SmAu₃** is not sufficient to permit and intersystem crossing to the rare earth ion. Instead an Au(I)-Au(I) charge transfer occurs. ISC = Intersystem Crossing, IC = Internal Conversion

Luminescence lifetime measurements were collected on crystal samples for both the aurophilic **SmAu₃** and the nonaurophilic **SmAu** frameworks at 298 K. Samples were excited at 365 nm with a high power LED source and emissions were observed at 600 nm for both systems. The excitation wavelength of 365 nm was chosen since both samples have excitation bands at this wavelength. Table D.1 shows that the emission lifetime is longer for the nonaurophilic framework than for the aurophilic framework. This observation can be explained by a decrease in energy transfer between the dicyanoaurate units and the lanthanide ions in the nonaurophilic frameworks.

Table D.1: Luminescence lifetimes for the Non-aurophilic [ⁿBu₄N]₂[Sm(NO₃)₄Au(CN)₂] crystals and Aurophilic Sm[Au(CN)₂]₃•3H₂O Crystals observed at 600 nm at 298 K

Framework	Emission Wavelength	Lifetime
SmAu₃	600 nm	4.34 μs ± 0.12 μs
SmAu	600 nm	4.69 μs ± 0.08 μs

The lifetime measurements are consistent with our previous findings on Tb(III) and Eu(III) metal ions coordinated to $[Au(CN)_2]^-$ anions.[60] The shorter lifetime of the aurophilic case indicate energy transfer is possible in aurophilic frameworks between Au(I)→Sm(III) metal ions as a second MMCT. In **SmAu**, Au(I)→Sm(III) are less favorable as indicated by the larger lifetime and Au(I)→Au(I) interactions are prevented by $^nBu_4N^+$ cations within the 3-D network framework while in aurophilic materials the Au-Au distances are shorter permitting MMCT. The decreased lifetime of **SmAu$_3$** would normally indicate a higher intensity of samarium emission, however, this is not observed. Since energy transfer is not occurring from Au(I)→Sm(III), we expect an increase in Au(I) emission at 411 nm. Again, the quantum yield measurements show a *decrease* in the Au(I) emission intensity. This leads us to suggest the presence of a non-radiative Au(I)→Au(I) MMCT relaxation mechanism. Since there is no oligomerization in the nonaurophilic case, this process is not present leading to an increase in the gold emission intensity. Despite the larger forbidden nature of the Au(I)→Sm(III) transfer, the increase in Au(I) emission results in an observed higher Sm(III) emission intensity.

D.3.4. Molecular Mechanics Calculations

We have performed ground state geometry molecular mechanics (MM) calculations using the UFF force field parameter for both the aurophilic **SmAu$_3$** and nonaurophilic **SmAu** materials. Results are summarized in Table D.2 and shown in Figure D.9. Ground state optimizations for **SmAu** are in agreement with experimental XRD results, which indicated a ten coordinate samarium center. The Sm-N(cyano) bond is predicted to be 2.43 Å (vs. 2.596 Å found experimentally). The $Au(CN)_2^-$ anionic ligands coordinate at a calculated N-Sm-N angle of 78.2° from the samarium(III) center compared to the experimental value of 74.4°. These calculations predict a large Au-Au distance of 6.60 Å, comparable to the experimental XRD value of 6.32 Å. This large atomic distance, which is larger than the sum of the van der Waal radii (3.32 Å), supports the nonaurophilc nature of this complex.[69] Ground state molecular mechanics optimization calculations of a **SmAu$_3$** dimer, summarized in Table D.2 and shown in Figure D.10, are in good agreement with experimental results. Metal centered Sm-O bonds of 2.349 Å are predicted compared to an

experimental value of 2.48 Å while Sm-N bond lengths of 2.62 Å are within 0.015 Å of experimental results. MM calculations accurately predict the Au-Au distance at 3.32 Å compared to the experimental value of 3.32 Å. Because of the geometric agreement between our models and the experimental results we believe our models accurately describe the **SmAu** and **SmAu₃** systems.

Table D.2: Summary of experimental and calculated ground state geometry of **SmAu** and **SmAu₃**

	SmAu		SmAu₃	
	Experimental	Calculated	Experimental	Calculated
Sm-N	2.47 Å	2.43 Å	2.60 Å	2.615 Å
Sm-O	2.44 Å	2.40 Å	2.48 Å	2.349 Å
Au-Au	6.32 Å	6.60 Å	3.32 Å	3.32 Å
N-Sm-N	74.4º	78.2º	76.0º	73.8
C-Au-C	173º	175º	180º	178º
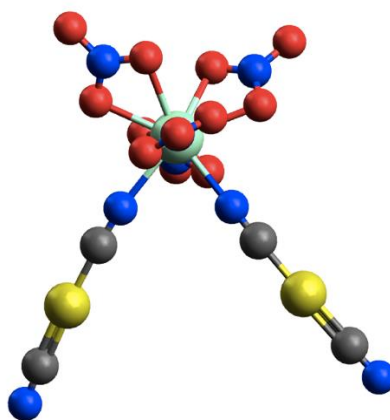
Figure D.9: Ground state geometry optimizations of **SmAu**. Cations omitted for clarity but included in geometric calculations. Yellow = gold, light blue = samarium, dark blue = nitrogen, gray = carbon, red = oxygen
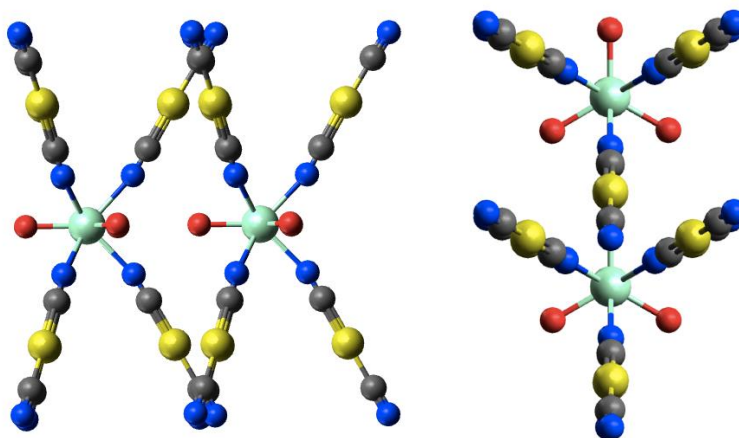
Figure D.10: Ground state geometry optimization of a two unit model of **SmAu₃**. Hydrogens omitted for clarity but included in ground state calculations. Yellow = gold, light blue = samarium, dark blue = nitrogen, gray = carbon, red = oxygen

D.3.5. Molecular Orbital Calculations

Molecular orbital calculations of **SmAu** and **SmAu₃** provide evidence for the origins of the reduced Sm emission intensity observed in the aurophilic case. We expect aurophilic interactions to result in stabilization of the Au(I) molecular orbitals.[70] Indeed, this is the case when comparing the aurophilic and nonaurophilic molecular orbitals. In the nonaurophilic case we observe Au(I) 6*s* atomic orbitals in the LUMO and a combination of the Au(I) 5*d* and CN π orbitals in the HOMO as shown in Figure D.11. Introduction of stabilizing aurophilic interactions results in lowering of the Au(I) 6*s* atomic orbitals which are now observed in MOs below the HOMO leaving the Sm(III) 4*f* atomic orbitals to compose the HOMO and LUMO. If we consider excitation and emission to occur between only the HOMO and LUMO for both cases then we can see in the aurophilic case a forbidden, low intensity, *f-f* transition occurs while for the nonaurophilic case we expect an allowed Au(CN)₂ centered MLCT. The lowering of energy for the Au(I) atomic orbitals is supported by the red shift observed in the aurophilic Au(I) emission bands previously described.
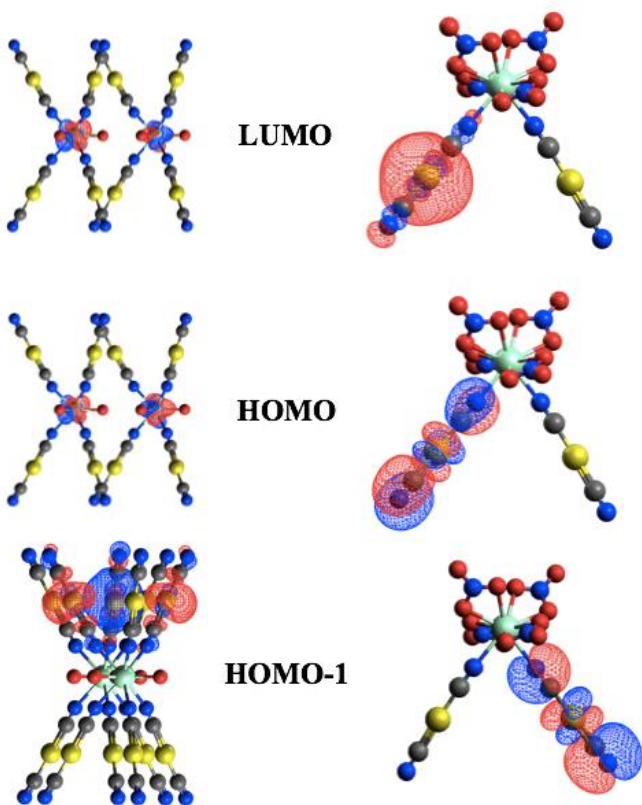
Figure D.11: Molecular orbital calculations for the aurophilic (left) **SmAu₃** and nonaurophilic (right) **SmAu** case. The HOMO-1 of **SmAu₃** contain the Au(I) 6*s* AO while in the **SmAu** these are present in the LUMO. Note that the **SmAu** HOMO and HOMO-1 are degenerate in nature

The nonaurophilic **SmAu** system is the simplest in terms of energy transfer and gives rise to the highest intensity Sm(III) emission relative to the Au(I) emission band. MO calculations reveal that excitation of **SmAu** most likely occurs as an Au(I)→CN transition followed by an intersystem crossing to the Sm(III) center $^4G_{5/2}$. In terms of 'allowedness' we consider the Au(I)→CN transition to have a larger a larger transition probability than the Au(I)→Sm(III) $^4G_{5/2}$ transition. Since we do not expect Au(I)-Au(I) MMCT quenching from Au(I) interactions in the nonaurophilic case, a higher intensity Au(I) emission band at 431 nm is observed. As previously described in Figure D.8, the lowering of energy in **SmAu₃** and addition of Au(I)→Au(I) MMCT quenching results in the independent excitation of both the Au(I)→CN and Sm(III) *f-f* transitions. The lower energy of the Au(I) 5*d* MOs decreases the probability of the intersystem crossing

pathway due to decreased emission-excitation overlap. Introduction of Au(I)-Au(I) MMCT interactions also quenches the emission of the Au(I)→CN emission band. This leaves only direct excitation of the Sm(III) ions as a possible pathway for rare earth ion emission. Direct excitation of the Sm 4f atomic orbitals is a forbidden process and results in weakened Sm(III) emission. The net result for the aurophilic case is loss of intersystem crossing for Sm(III) emission enhancement and introduction of Au(CN)$_2^-$ quenching MMCT interactions.

D.4. Conclusion

SmAu and **SmAu₃** have been synthesized and characterized to compare the photophysical properties of nonaurophilic and aurophilic samarium-gold coordination polymers. Previous single crystal XRD analysis revealed indirect interaction of Sm(III) and Au(I) for both aurophilic and nonaurophilic cases. In the nonaurophilic case a one-dimensional zigzag chain structure is observed while the aurophilic case exhibits a three-dimensional network structure. Ground state DFT calculations for these compounds are in good agreement with experimental XRD data. Spectroscopic analysis of these compounds included luminescence spectroscopy, diffuse reflectance spectroscopy, and quantum yield measurements. Comparison of the aurophilic and nonaurophilic cases demonstrate that the nonaurophilic case has higher emission intensity of both the Au(I)→CN and Sm(III) emission bands. Spectroscopically and computationally we have determined that this increased emission is due to the lack of nonradiative Au(I)-Au(I) aurophilic interactions. These interactions limit Au(I)→Sm(III) energy transfer by decreasing the emission/excitation overlap over the donor-acceptor. This is also observed in the decreased lifetime of the aurophilic case indicating a loss of Au(I)→Sm(III) energy transfer. DFT calculations show a mixed LUMO of Sm(III) and Au(CN)$_2^-$ for the nonaurophilic case, while only Sm(III) orbitals compose the LUMO for the aurophilic case. These findings are in agreement with our previous work on **LnAu** coordination polymers in which the separation of Au(I)-Au(I) chains by $^nBu_4N^+$ ligands metal ions limits the possibility of MMCT. Further study of these **LnAu** coordination frameworks will direct their use in optical applications.

D.5. References

1. Rocha J, Carlos LD, Paz FAA, Ananias D (2011) Luminescent multifunctional lanthanides-based metal-organic frameworks. Chem Soc Rev 40:926–940. doi: 10.1039/c0cs00130a

2. Marchal C, Filinchuk Y, Chen X-Y, Imbert D, Mazzanti M (2009) Lanthanide-based coordination polymers assembled by a flexible multidentate linker: design, structure, photophysical properties, and dynamic solid-state behavior. Chem Eur J 15:5273–5288. doi: 10.1002/chem.200802589

3. Eliseeva SV, Bünzli J-CG (2010) Lanthanide luminescence for functional materials and bio-sciences. Chem Soc Rev 39:189–227. doi: 10.1039/b905604c

4. Carlos LD, Ferreira RAS, Bermudez VdZ, Ribeiro SJL (2009) Lanthanide-containing light-emitting organic-inorganic hybrids: a bet on the future. Adv Mater 21:509–534. doi: 10.1002/adma.200801635

5. Auzel F (2004) Upconversion and anti-stokes processes with f and d ions in solids. Chem Rev 104:139–174. doi: 10.1021/cr020357g

6. Cunha-Silva L, Lima S, Ananias D, Silva P, Mafra L, Carlos LD, Pillinger M, Valente AA, Paz FAA, Rocha J (2009) Multi-functional rare-earth hybrid layered networks: photoluminescence and catalysis studies. J Mater Chem 19:2618-2632. doi: 10.1039/b817381h

7. Wang YF, Liu GY, Sun LD (2013) Nd^{3+}-sensitized upconversion nanophosphors: efficient *in vivo* bioimaging probes with minimized heating effect. ACS Nano 7:7200–7206. doi: 10.1021/nn402601d

8. Ong LC, Gnanasammandhan MK, Nagarajan S, Zhang Y (2010) Upconversion: road to el dorado of the fluorescence world. Luminescence 25:290–293. doi: 10.1002/bio.1229

9.   Auzel F, Pecile D, Morin D (1975) Rare earth doped vitroceramics: new, efficient, blue and green emitting materials for infrared up-conversion. J Electrochem Soc 122:101-107. doi: 10.1149/1.2134132

10.   Bekiari V, Lianos P (2003) Multicolor emission from terpyridine–lanthanide ion complexes encapsulated in nanocomposite silica/poly(ethylene glycol) sol–gel matrices. J Lumin 101:135–140. doi: 10.1016/S0022-2313(02)00405-2

11.   Benisvy L, Gamez P, Fu WT, Kooijman H, Spek AL, Meijerink A, Reedijk J (2008) Efficient near-UV photosensitization of the Tb(III) green luminescence by use of 2-hydroxyisophthalate ligands. Dalt Trans 24:3147–3149. doi: 10.1039/b805507f

12.   D'Aléo A, Xu J, Moore EG, Jocher CJ, Raymond KN (2008) Aryl-bridged 1-hydroxypyridin-2-one: sensitizer ligands for Eu(III). Inorg Chem 47:6109–6111. doi: 10.1021/ic8003189

13.   Lis S, Piskula Z, Staninski K, Tamaki S, Inoue M, Hasegawa Y (2008) Luminescence study of europium(III) tris(β-diketonato)/phosphonate complexes in chloroform. J Rare Earths 26:185–191. doi: 10.1016/S1002-0721(08)60062-9

14.   Nasso I, Bedel S, Galaup C, Picard C (2008) A water-stable and strongly luminescent terbium(III) macrocyclic complex incorporating an intracyclic pyrazolylpyridine chromophore. Eur J Inorg Chem 2064–2074. doi: 10.1002/ejic.200701209

15.   Klink SI, Keizer H, van Veggel FCJM (2000) Transition metal complexes as photosensitizers for near-infrared lanthanide luminescence. Angew Chem 39:4319–4321. doi:10.1002/1521-3773(20001201)39:23<4319::AID-ANIE4319>3.0.CO;2-X

16.   Shavaleev NM, Moorcraft LP, Pope SJA, Bell ZR, Faulkner S, Ward MD (2003) Sensitised near-infrared emission from lanthanides using a covalently-attached Pt(II) fragment as an antenna group. Chem Commun 10:1134–1135. doi: 10.1039/B301878D

17.   Shavaleev NM, Accorsi G, Virgili D, Bell ZR, Lazarides T, Calogero G, Armaroli N, Ward MD (2005) Syntheses and crystal structures of dinuclear complexes containing d-block and f-block luminophores. Sensitization of NIR luminescence from Yb(III), Nd(III), and Er(III) centers by energy transfer from Re(I)− and Pt(II)−bipyrimidine metal centers. Inorg Chem 44:61–72. doi: 10.1021/ic048875s

18.   Beltyukova S V, Tselik EI, Egorova AV (1998) Use of sensitized luminescence of lanthanides in analysis of drugs. J Pharm Biomed Anal 18:261–266. doi: 10.1016/S0731-7085(98)00158-7

19.   Panigrahi BS, Peter S, Viswanathan KS, Mathews CK (1995) Fluorescence enhancement of Tb^{3+} in Tb-aromatic acid complexes: correlation of synergistic enhancement with the structure of the ligand. Spectrochim Acta A 51:2289–2300. doi: 10.1016/0584-8539(95)01464-0

20.   Zhao G, Zhao S, Gao J, Kang J, Yang W (1997) Enhancement of fluorescence of terbium/trimesic acid/cyclodextrin system by zirconate and its application to the determination of terbium. Talanta 45:303–307. doi: 10.1016/S0039-9140(97)00133-1

21.   Lu H, Yson R, Ford J, Tracy HJ, Carrier AB, Keller A, Mullin JL, Poissan MJ, Sawan S, Patterson HH (2007) Tunable energy transfer from d^{10} heterobimetallic dicyanide(I) donor ions to terbium(III) acceptor ions in luminescent $Tb[Ag_xAu_{1-x}(CN)_2]_3$ (x = 0 -1). Chem Phys Lett 443:55–60. doi: 10.1016/j.cplett.2007.06.011

22.   Yersin H, Ammon W, Stock M, Gliemann G (1979) Non-radiative energy transfer from tunable donor states to Eu^{3+} ions. J Lumin 18-19:774–778. doi: 10.1016/0022-2313(79)90234-5

23.   Bünzli J-CG, Piguet C (2005) Taking advantage of luminescent lanthanide ions. Chem Soc Rev 34:1048–1077. doi: 10.1039/b406082m

24. Xu H-B, Shi L-X, Ma E, Zhang L-Y, Wei Q-H, Chen Z-N (2006) Diplatinum alkynyl chromophores as sensitisers for lanthanide luminescence in Pt_2Ln_2 and Pt_2Ln_4 (Ln = Eu, Nd, Yb) arrays with acetylide-functionalized bipyridine/phenanthroline. Chem Commun 4:1601–1603. doi: 10.1039/b602222g

25. Baca SG, Pope SJA, Adams H, Ward MD (2008) Cyanide-bridged Os(II)/Ln(III) coordination networks containing $[Os(phen)(CN)_4]^{2-}$ as an energy donor: structural and photophysical properties. Inorg Chem 47:3736–3747. doi: 10.1021/ic702353c

26. Shavaleev NM, Moorcraft LP, Pope SJA, Bell ZR, Faulkner S, Ward MD (2003) Sensitized near-infrared emission from complexes of Yb(III), Nd(III) and Er(III) by energy-transfer from covalently attached Pt(II)-based antenna units. Chem Eur J 9:5283–5291. doi: 10.1002/chem.200305132

27. Sakamoto M, Manseki K, Okawa H (2001) d-f heteronuclear complexes: synthesis, structures and physicochemical aspects. Coord Chem Rev 219–221:379–414. doi: 10.1016/S0010-8545(01)00341-1

28. Nonat AM, Allain C, Faulkner S, Gunnlaugsson T (2010) Mixed d-f_3 coordination complexes possessing improved near-infrared (NIR) lanthanide luminescent properties in aqueous solution. Inorg Chem 49:8449–8456. doi: 10.1021/ic1010852

29. Barta CA, Bayly SR, Read PW, Patrick BO, Thompson RC, Orvig C (2008) Molecular architectures for trimetallic d/f/d complexes: structural and magnetic properties of a $LnCu_2$ core Inorg Chem 47:2294–2302. doi: 10.1021/ic701613x

30. Zhong Y, Zeng F, Chen J, Wu S, Hou C, Tong Z (2007) Modulation of fluorescence of a terbium-complex-containing polymer by gold nanoparticles through energy transfer. J Inorg Organomet Polym Mater 17:679–685. doi: 10.1007/s10904-007-9163-y

31. Colis JCF, Staples R, Tripp C, Labrecque D, Patterson HH (2005) Metallophilic interactions in closed-shell d^{10} metal-metal dicyanide bonded luminescent systems $Eu[Ag_xAu_{1-x}(CN)_2]_3$ and their tunability for excited state energy transfer. J Phys Chem B 109:102–109. doi: 10.1021/jp046717g

32. Zang FX, Hong ZR, Li WL, Li MT, Sun XY (2004) 1.4 μm band electroluminescence from organic light-emitting diodes based on thulium complexes. Appl Phys Lett 84:2679–2681. doi: 10.1063/1.1695098

33. Zang FX, Li WL, Hong ZR, Wei HZ, Li MT, Sun XY (2004) Observation of 1.5 μm photoluminescence and electroluminescence from a holmium organic complex. Appl Phys Lett 84:5115–5117. doi: 10.1063/1.1764593

34. Poole RA, Montgomery CP, New EJ, Congreve A, Parker D, Botta M (2007) Identification of emissive lanthanide complexes suitable for cellular imaging that resist quenching by endogenous anti-oxidants. Org Biomol Chem 5:2055–2062. doi: 10.1039/b705943d

35. Okada K, Wang Y-F, Chen T-M, Kitamura M, Nakaya T, Inoue H (1999) Bright red light-emitting organic electroluminescent devices based on a novel thiophene-containing europium complex as an emitting layer. J Mater Chem 9:3023–3026. doi: 10.1039/a906215g

36. Hidvegi WvA, Gliemann G (1982) Magnetic field effects on the luminescence of quasi-one-dimensional crystals $M_x[Pt(CN)_4]_yH_2O$. J Chem Phys 76:4361-4369. doi: 10.1063/1.443570

37. Haldar KK, Patra A (2009) Fluorescence enhancement and quenching of Eu^{3+} ions by Au-ZnO core-shell and Au anoparticles. Appl Phys Lett 95:063103. doi: 10.1063/1.3204012

38. Li X, Pan Z, Baril-Robert F, Ahern JC, Patterson HH (2014) Novel luminescent heterobimetallic nanoclusters of copper(I), silver(I), and gold(I) doped in different alkali halide crystals. J Phys Chem C 118:11886-11894. doi: 10.1021/jp5026976

39. Ahern JC, Kanan S, Patterson HH (2015) Heterogeneous photocatalysis with nanoclusters of d^{10} metal ions doped in zeolites. Comments Inorg Chem 35:59–81. doi: 10.1080/02603594.2014.973106

40. Abouelwafa AS, Anson CE, Hauser A, Patterson HH, Baril-Robert F, Li X, Powell AK (2012) Photophysical properties of $\{[Au(CN)_2]^-\}_2$ dimers trapped in a supramolecular electron-acceptor organic framework. Inorg Chem 51:1294-1301. doi: 10.1021/ic201109u

41. Li X, Patterson HH (2013) A review of luminescent anionic nano system: d^{10} metallocyanide excimers and exciplexes in alkali halide hosts. Materials 6:2595–2611. doi: 10.3390/ma6072595

42. Xie J, Yu J, Rudolph M, Rominger F, Hashmi ASK (2016) Radical coupling monofluoroalkenylation of dimethylamino compounds through radical–radical cross-coupling. Angew Chem Int Ed 55:9416–9421. doi: 10.1002/anie.201602347

43. Huang L, Rudolph M, Rominger F, Hashmi ASK (2016) Photosensitizer-free visible-light-mediated gold-catalyzed 1,2-difunctionalization of alkynes. Angew Chem Int Ed 55:4808–4813. doi: 10.1002/anie.201511487

44. Xie J, Li J, Wurm T, Weingand V, Sung H-L, Rominger F, Rudolph M, Hashmi ASK (2016) A general photoinduced electron transfer-directed chemoselective perfluoroalkylation of *N,N*-dialkylhydrazones. Org Chem Front 3:841–845. doi: 10.1039/c6qo00158k

45. Kaldas SJ, Cannillo A, Mccallum T, Barriault L (2015) Indole functionalization via photoredox gold catalysis. Org Lett 17:2864–2866. doi: 10.1021/acs.orglett.5b01260

46. Um J, Yun H, Shin S (2016) Cross-coupling of Meyer-Schuster intermediates under dual gold-photoredox catalysis. Org Lett 18:484–487. doi: 10.1021/acs.orglett.5b03531

47. Xie J, Li J, Weingand V, Rudolph M, Hashmi ASK (2016) Intermolecular photocatalyzed Heck-like coupling of unactivated alkyl bromides by a dinuclear gold complex. Chem Eur J 22:12646–12650. doi: 10.1002/chem.201602939

48. Mccallum T, Slavko E, Morin M, Barriault L (2015) Light-mediated deoxygenation of alcohols with a dimeric gold catalyst. European J Org Chem 1:81–85. doi: 10.1002/ejoc.201403351

49. Xie J, Shi S, Zhang T, Mehrkens N, Rudolph M, Hashmi ASK (2015) A highly efficient gold-catalyzed photoredox α-C(sp^3)-H alkynylation of tertiary aliphatic amines with sunlight. Angew Chem Int Ed 54:6046–6050. doi: 10.1002/anie.201412399

50. McTiernan CD, Morin M, McCallum T, Scaiano JC, Barriault L (2016) Polynuclear gold (III) complexes in photoredox catalysis: understanding their reactivity through characterization and kinetic analysis. Catal Sci Technol 6:201–207. doi: 10.1039/C5CY01259G

51. Huang L, Rominger F, Rudolph M, Hashmi ASK (2016) A general access to organogold(III) complexes by oxidative addition of diazonium salts. Chem Commun 52:6435–6438. doi: 10.1039/C6CC02199A

52. Xie J, Zhang T, Chen F, Mehrkens N, Rominger F, Rudolph M, Hashmi ASK (2016) Gold-catalyzed highly selective photoredox C(sp^2)-H difluoroalkylation and perfluoroalkylation of hydrazones. Angew Chem Int Ed 55:2934–2938. doi: 10.1002/anie.201508622

53. Revol G, McCallum T, Morin M, Gagosz F, Barriault L (2013) Photoredox transformations with dimeric gold complexes. Angew Chem Int Ed 52:13342–13345. doi: 10.1002/anie.201306727

54. Ma C, Chan CT-L, To W-P, Kwok W-M, Che C-M (2015) Deciphering photoluminescence dynamics and reactivity of the luminescent metal-metal-bonded excited state of a binuclear gold(I) phosphine complex containing open coordination sites. Chem Eur J 21:13888–13893. doi: 10.1002/chem.201503045

55. Yam VW-W, Lo KK-W (1999) Luminescent polynuclear d^{10} metal complexes. Chem Soc Rev 28:323–334. doi: 10.1039/a804249g

56. Katz MJ, Sakai K, Leznoff DB (2008) The use of aurophilic and other metal-metal interactions as crystal engineering design elements to increase structural dimensionality. Chem Soc Rev 37:1884–1895. doi: 10.1039/b709061g

57. Balch AL (2007) Remarkable luminescence behaviors and structural variations of two-coordinate gold(I) complexes. Struct Bond 123:1–40. doi: 10.1007/430_2006_049

58. He X, Yam VW-W (2011) Luminescent gold(I) complexes for chemosensing. Coord Chem Rev 255:2111–2123. doi: 10.1016/j.ccr.2011.02.003

59. Katz MJ, Ramnial T, Yu H-Z, Leznoff DB (2008) Polymorphism of $Zn[Au(CN)_2]_2$ and its luminescent sensory response to NH_3 vapor. J Am Chem Soc 130:10662–10673. doi: 10.1021/ja801773p

60. Ahern JC, Roberts RJ, Follansbee P, McLaughlin J, Leznoff DB, Patterson HH (2014) Structure and emissive properties of heterobimetallic Ln−Au coordination polymers: role of Tb and Eu in non-aurophilic $[^nBu_4N]_2[Ln(NO_3)_4Au(CN)_2]$ versus aurophilic $Ln[Au(CN)_2]_3 \cdot 3H_2O/3D_2O$ chains. Inorg Chem 53:7571−7579. doi: 10.1021/ic500890r

61. Roberts RJ, Li X, Lacey TF, Pan Z, Patterson HH, Leznoff DB (2012) Heterobimetallic lanthanide–gold coordination polymers: structure and emissive properties of isomorphous $[^nBu_4N]_2[Ln(NO_3)_4Au(CN)_2]$ 1-D chains. Dalt Trans 41:6992. doi: 10.1039/c2dt30156c

62. Roberts RJ, Ahern JC, Patterson HH, Leznoff DB (2016) $Ce/Au(CN)_2^-$-based coordination polymers containing and lacking aurophilic interactions. Eur J Inorg Chem 2016:2082–2087. doi: 10.1002/ejic.201600174

63. Roberts RJ, Le D, Leznoff DB (2017) Color-tunable and white-light luminescence in lanthanide–dicyanoaurate coordination polymers. Inorg Chem 56:7948–7959. doi: 10.1021/acs.inorgchem.7b00735

64. Rappe AK, Casewit CJ, Colwell KS, Goddard WA, Skiff WM (1992) UFF, a full periodic table force field for molecular mechanics and molecular dynamics simulations. J Am Chem Soc 2:10024–10035. doi: 10.1021/ja00051a040

65. Knope KE, De Lill DT, Rowland CE (2012) Uranyl sensitization of samarium(III) luminescence in a two-dimensional coordination polymer. Inorg Chem 51:201–206. doi: 10.1021/ic201450e

66. Lo W-S, Zhang J, Wong W-T, Law G-L (2015) Highly luminescent Sm^{3+} complexes with intraligand charge-transfer sensitization and the effect of solvent polarity on their luminescent properties. Inorg Chem 54:3725–3727. doi: 10.1021/acs.inorgchem.5b00331

67. Rawashdeh-Omary MA, Omary MA, Patterson HH, May R V (2000) Oligomerization of $Au(CN)_2^-$ and $Ag(CN)_2^-$ ions in solution via ground-state aurophilic and argentophilic bonding. J Am Chem Soc 122:10371–10380. doi: 10.1021/ja001545w

68. Rawashdeh-Omary MA, Omary MA, Patterson HH, Fackler JP (2001) Excited-state interactions for $[Au(CN)_2^-]_n$ and $[Ag(CN)_2^-]_n$ oligomers in solution. Formation of luminescent gold-gold bonded excimers and exciplexes. J Am Chem Soc 123:11237–11247. doi: 10.1021/ja011176j

69. Slater JC (1964) Atomic radii in crystals. J Chem Phys 41:3199–3204. doi: 10.1063/1.1725697

70. Schmidbaur H, Schier A (2012) Aurophilic interactions as a subject of current research : an update. Chem Soc Rev 41:370–412. doi: 10.1039/c1cs15182g

APPENDIX E. RECENT ADVANCES ON TiO₂-BASED PHOTOCATALYSTS TOWARD THE DEGRADATION OF PESTICIDES AND MAJOR ORGANIC POLLUTANTS FROM WATER BODIES

E.1. Background

Rapid industrial growth worldwide has increased the urgency of issues such as climate change, looming water shortages, and environmental pollution [1,2]. In addition to the increase in pollutant volume, the growth of specialized and high-tech industries have contributed to the diversity of pollutants entering the environment [3-6]. Of particular concern is the widespread use of pesticides and their potential to enter water supplies and cause negative effects on public health. As of 2009, more than 50 countries applied in excess of 1,000 tons of pesticides in support of agricultural efforts [4].

Despite our best efforts to regulate and engineer the use of pesticides, they continue to be detected and present problems at municipal water treatment plants [5]. This demonstrates a need for alternative water treatment methods capable of fully degrading pesticides and preserving access to clean drinking water. Photocatalysis has emerged as one potential alternative to traditional water treatment methods such as UV irradiation.

The phenomenon of photocatalysis remains one of the most extensively studied subjects in inorganic photochemistry. Since the discovery of the photoelectrochemical water splitting abilities of TiO₂ in 1972, [6] it has become the most studied photocatalyst in both academic and industrial settings [7]. While TiO₂ is considered a commodity chemical and has numerous applications throughout industry, it has attracted new attention in environmental remediation efforts for areas affected by pollution. The photocatalytic properties of TiO₂ have been commercialized though formulation into materials such as self-cleaning window films and air- purifying roofing tiles [8]. Other semiconductors with similar bandgaps to TiO₂ such as ZnO and CdS have shown promising photocatalytic properties, but also show limitations involving catalyst stability and environmental toxicity [9].

Enhancement of electrochemical degradation using photocatalysis has been demonstrated in recent literature and indicates increased pollutant removal [10]. The demand for photocatalytic complexes is also observed in a myriad of industries, from solar applications including solar heat [11], solar photocatalysis [12], and batteries [12-14] to anti-corrosion [8]. Ani et al. have discussed extensively the potential for TiO_2 systems to be utilized to remove harmful compounds from petroleum wastewater [15]. Application of pristine TiO_2 photocatalysts for environmental purposes has become a popular topic of research for removal of environmental pollutants and conversion of solar energy into useful alternatives such as electricity and H_2 [15-17].

Photodegradation of organic pollutants has become a prominent research topic in recent years and viewed as a potential solution for widespread pollution. Organic pollutants such as pesticides tend to remain prevalent in soil and groundwater in areas with frequent chemical treatment. These recalcitrant molecules are known carcinogens categorized by WHO standards and can remain hazardous for years [18]. The application of TiO_2 photocatalysis to the degradation of organic pollutants was initially demonstrated by Carey et al. in 1976 [19]. Since then, the utilization of TiO_2 for photocatalytic environmental remediation purposes have been thoroughly investigated. Current methods of groundwater remediation utilize high energy UV light to degrade pollutants and sterilize aqueous solutions yet fail to achieve full mineralization of certain compounds [19-22]. Although the environmental applications of TiO_2 are promising, there are various limitations within pure TiO_2 complexes that hinder its use for environment and industrial purposes [21].

Photophysical limitations of TiO_2 complexes have made practical environmental applications of these complexes difficult, since pure TiO_2 complexes all have relatively high band gaps. This limitation permits pure TiO_2 complexes to utilize only 6% of the solar energy irradiating the planet each day. To overcome these solar harvesting limitations, research efforts have investigated potential modifications and impurities that synergistically aid TiO_2 in photocatalytic degradation.

271

E.2. Characteristics of TiO$_2$ Photocatalysts

Photocatalytic activity originates from the absorption of photons of suitable energy to overcome the band gap. Absorption of light by the complex produces an excited state electron that is promoted to the conduction band, facilitating reduction of electron acceptors such as H$_2$ and O$_2$ [21-23]. The unoccupied electron states, known as electron holes, remain in the valence band of these complexes and are capable of oxidizing substrates adsorbed to the surface as illustrated in Figure E.1 [24]. Oxidation of the surrounding environment facilitates single electron interactions that promote sequential degradation reactions. Pristine TiO$_2$ is known to have a band gap energy of 3.20 eV, which is capable of absorbing photons of wavelengths less than 350 nm, primarily in the UVA, UVB, and UVC range. Due to the fundamental principles of TiO$_2$ photochemistry and photocatalysis, TiO$_2$ and other Ti^{4+} complexes have been ideal candidates for scaffolding for potential catalytic enhancements. Aluminosilicate complexes, also known as zeolites, have been reported to be a beneficial scaffold for TiO$_2$ complexes due to their porous configuration that directs interaction between the catalyst and pollutants [23].
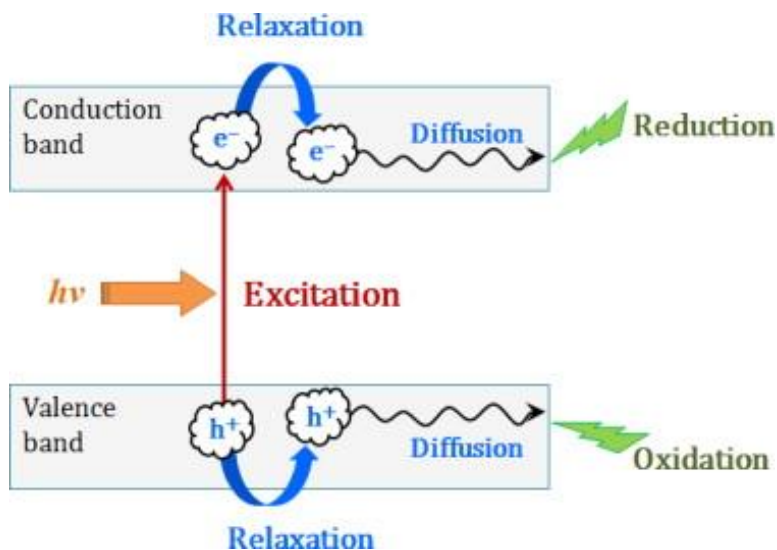
Figure E.1. Schematic illustration of the formation of photoinduced charge carriers (e$^-$/h$^+$) upon absorption of UV light[24].

The most common crystal structures of TiO_2 complexes include anatase, rutile, brookite, and monoclinic polymorphs. These polymorphs are all composed of a Ti^{4+} center with bordering oxygen atoms that act as bridging ligands, as shown in Figure E.2 [25].
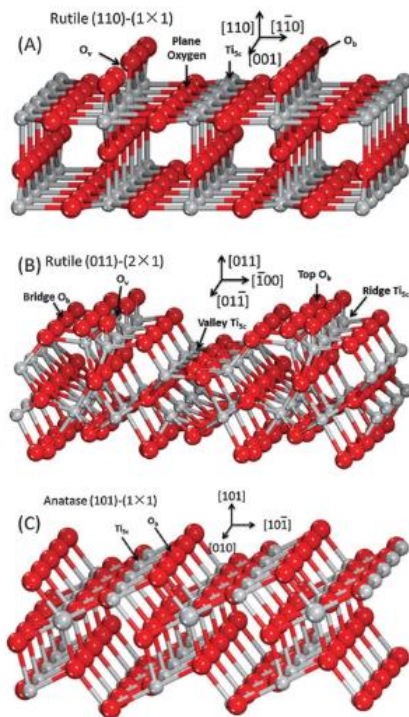
Figure E.2: Structure model of (A) rutile (110)-(1x1) (r-TiO_2(110)-(1x1)), (B) rutile (011)-(2x1) (r-TiO_2(011)-(2x1)) and (C) anatase (101)-(1x1) (a-TiO_2(101)- (1x1)). Red and grey balls stand for oxygen and titanium ions, respectively[25].

The unique structure of these TiO_2 complexes permit surface vacancies on the Ti^{4+} centers that can act as active sites for catalytic degradation [19-24]. Each of these distinct allotropes are synthesized based on the annealing temperature used during synthesis, a phenomenon reported extensively by Chen et al [26]. Anatase crystal structure is found to be a common candidate for catalyst modification for its stable configuration suitable for photodegradation studies. The anatase structure begins to revert to the rutile configurations at temperatures higher than 600 °C, indicating anatase TiO_2 is a likely candidate for environmental photocatalytic applications [27]. Catalyst size modification has been viewed as a cost-

efficient enhancement that increases surface area and photodegradation.. Both bulk and nanoscale TiO_2 systems have been investigated extensively and found to have significant differences in photochemical responses and degradation activity [27,28]. Recent studies have indicated increased pollutant adsorption due to surface area increases in TiO_2 nanosystems as opposed to bulk systems. Modification of the crystal structure facets has also become a prevalent topic of study for investigations into photoactivity enhancement of TiO_2 structures.

The valance and conduction bands that comprise the accompanying gap between them denote the changes in potential required to initiate a photoinduced charge transfer [29]. Band alignment between TiO_2 and an additional semiconductor is a significant area of study and development for catalytic enhancement. Alignment between the band structures of anatase and rutile TiO_2 have been investigated and found that alignment differences as small as 0.2 eV facilitate electron transfer between two photoactive complexes [16-21]. This difference in band alignment facilitates localized trap states of photoinduced electrons and accompanying vacancies. A schematic illustration of the role of the TiO_2 surface in removal of pollutants through the formation of photoinduced charge carriers is shown in Figure E.3 [24]. Nanostructures of TiO_2 anatase have been reported containing both (101) and (001) facets although complexes containing predominantly (101) facets are thermodynamically favored. Ong et al. have discussed the effect of mixed facet ratios within anatase TiO_2 structures and the benefits provided to photocatalytic activity [30].
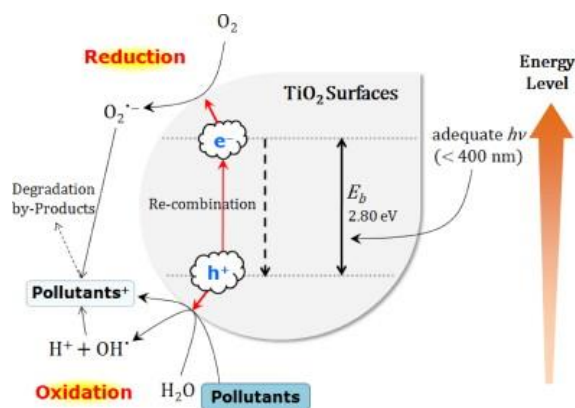
Figure E.3. Schematic illustration on removal of pollutants by the formation of photoinduced charge carriers (e^-/h^+) on a semiconductor TiO_2 particle surface[24].

To extend the photophysical capabilities of both anatase and rutile TiO_2 into the visible light range (λ = 380 nm), photoactive scaffolding such as graphitic carbon nitride (g-C_3N_4) has been viewed as an environmentally benign alternative to metallic impurities [28]. Both surface and interfacial defects have been reported to have significant roles in catalyst modification, although surface defects have been found to hinder adsorption capabilities [31]. Modification of rutile TiO_2 is an investigated aspect of enhancing photocatalytic abilities by utilizing the terminal oxygen and Ti^{4+} atoms present. These terminal atoms are the primary driving force for photo-induced electrons and accompanying vacancies to migrate from the irradiated bulk system to surface atoms for redox reactions occur. Interactions at the catalyst surface are a significant part of the photochemical processes and are required to facilitate interfacial charge transfer along the catalyst facets and the adsorbed complex.

The transfer of photoinduced electrons between adsorbed molecules such as H_2O or an organic pollutant are the driving force that permits the redox reactions necessary for photodegradation. These chemical interactions are only permitted if the photoinduced electrons are able to overcome the tendency to recombine with vacancies present in both bulk and surface atoms. Recombination of excited state electrons and vacancies is a problematic limitation of TiO_2 and overcoming this limitation is the primary goal of catalyst modification. Luminescence is one of the pathways that can directly result from electron-hole recombination and is detrimental to photochemical reactions due to conservation of excited state electrons. For this reason, the photoluminescence spectra of a series of similar photocatalysts may be compared to understand the effect of a structural change or dopant on overall photocatalytic potential [23]. Sacrificial agents such as hole trapping species have been viewed as a potential photocatalytic enhancement that reduces the recombination of photo- induced electrons and vacancies [32]. The electron trapping nature of these agents have been reported to enhance both anatase and rutile TiO_2 degradation by carrying these excited state electrons away from the catalyst surface, reducing the probability of surface recombination.

The adsorption of organic complexes such as malic acid and alkyl alcohols onto the surface of TiO_2 complexes has shown significant capabilities for transferring excited state electrons and vacancies to an

organic pollutant, facilitating degradation. Oxidation-reduction reactions within the bulk system and catalyst surface are the primary electronic pathway for degradation under ultraviolet light. This generation of accompanying electrons and vacancies can facilitate the degradation of pollutants in the surrounding environment. These active chemical species originate from the catalytic splitting of water, which hydrolyze harmful pollutants through single electron transfer reactions. For an in-depth overview of previous applications of TiO_2 for water remediation, see reviews by Friedmann et al [33], Lee et al [24], Carbajo et al [34], and Horikoshi et al. [35]. The remainder of this review will focus on the application of the TiO_2 photocatalytic degradation system to the remediation of organic pollutants from water.

E.3. Photocatalytic Reactor systems

While photocatalysis has proven to be a highly successful laboratory science, its integration into widespread water treatment applications has progressed only marginally. For this reason, a significant interest in academic and industrial research in the development of catalyst reactor systems is to implement widespread application of photocatalytic reactors in industry. The principle aspect of designing catalytic reactor systems is to maximize the interactions between the aqueous media and the catalyst to facilitate continual photodegradation. Several types of photocatalytic reactors have been developed including thin-film, packed bed, fluidized bed, swirl flow, falling film, vortex, and annular photoreactors. These reactors fall into two general philosophies of catalyst utilization where the photocatalyst is either suspended in the reaction solution or immobilized in certain fashion [36]. Here we will briefly introduce the advantages of each type and their industrial applications for environmental purposes.

E.3.1. Suspended Catalyst Reactors

The most common type of reactor employed in laboratory experiments are batch systems where the catalyst is suspended in solution. This type of reactor has been favored up to this point due to the advantage of high surface area of suspended particles which results in fast reaction rates compared to flow reactors. In such batch reactor setups, the catalyst that is introduced into a slurry must then be removed from the solution post-exposure. In these reactors, presented in Figure E.4, the required separation and recovery of the catalyst are highly unfavorable in water treatment industries, where high volume throughput is necessary [37, 38]. The use of bulk catalyst systems in heterogenous solutions has significant limitations such as catalyst recovery, durability, and loss of photophysical integrity. These limitations severely hinder environmental applications on an industrial scale by increasing operating costs as well as the potential for bioaccumulation in areas exposed to waste material. However, suspension photocatalyst reactors were found to improve the mass transfer of pollutants to the catalyst surface compared to immobilized reactors due to surface area considerations.
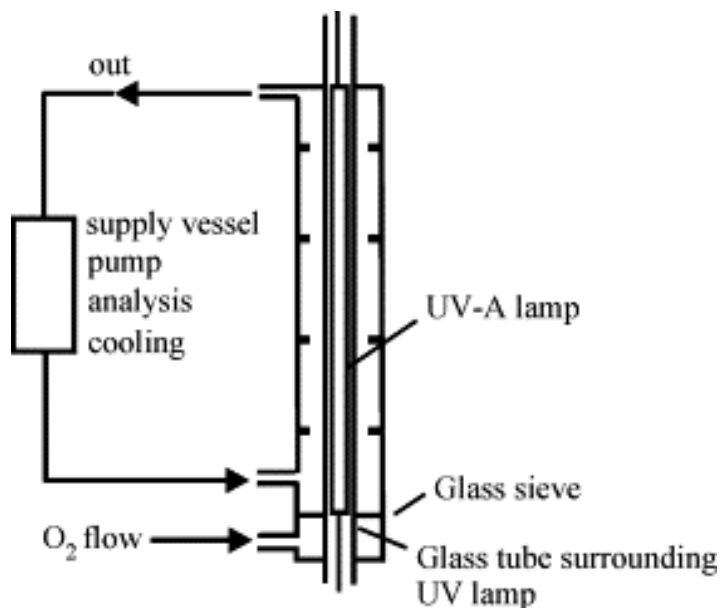
Figure E.4. Schematic of a typical photocatalytic experimental set-up, suitable for suspended or immobilized reactor conditions[37].

Slurry reactor systems using TiO_2 as a photocatalyst were used for the degradation of chloroform in water by Pruden et al. [39] . Building on this work, Kormann et al. observed an increase in chloride ion concentration during UV-TiO_2 batch reactor operations [40]. Pathirana et al. reported that the catalyst concentration is an important factor for batch photocatalyst reactor systems [41]. They found that the reaction rate continued to increase with photocatalyst concentration and reached equilibrium before beginning to decrease. This loss of reactivity was attributed to a reduction in the penetration depth of incident light caused by "shielding" via photocatalyst particles closer to the light source within the reactor. Light penetration depth is an important consideration for a suspended photocatalytic reactor and limits the maximum overall effectiveness of this type of reactor.

Another type of suspended photocatalyst reactor recently investigated is the drum reactor [42–44]. This system operates under a continuous flow with wastewater moving through three subsequent drums equipped with paddles to stir the solution as depicted in Figure E.5 [42]. This reactor design allows for the reactor residence time to be tailored to the pollutant being degraded and enables system designers to employ a large effective photocatalyst concentration without losing reactivity due to shielding. McCullagh et al. reported that the drum reactor system using 30 g/L TiO_2 was capable of removing 98% of methylene blue dye from solution after 60 minutes, demonstrating the high potential for this reactor be employed in wastewater treatment plants [42]. In later work, the same group reported that the same system is also effective at degrading hydrocarbons present in waste water, which includes pollutants such as decane, dodecane, and tetradecane [44].
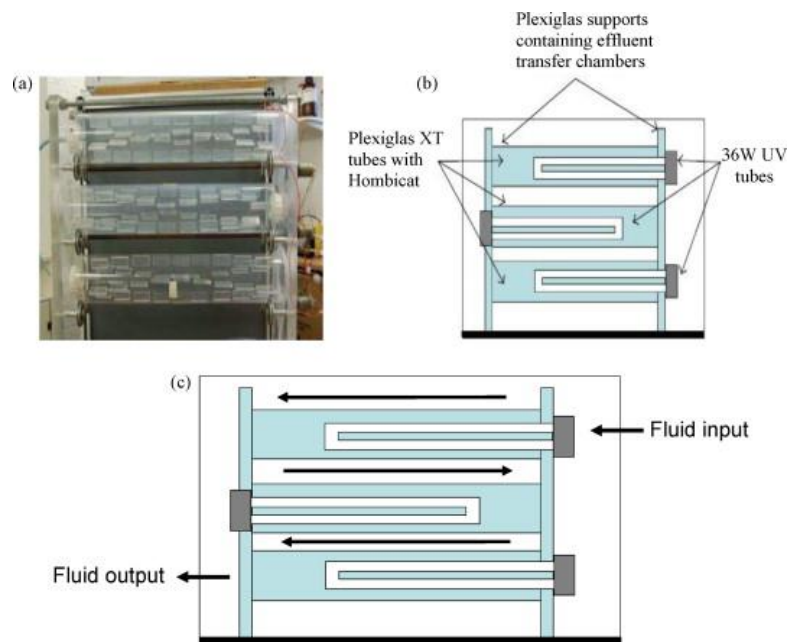
Figure E.5. Schematic of the novel drum photocatalytic reactor[42].

Fluidized bed reactors are another prominent type of suspended photocatalyst reaction system. In this type, the catalyst particles are suspended by an upward flow of fluid, thus maintaining the advantage of high surface area of a suspended photocatalytic reactor, while avoiding the need for downstream separation of catalyst. This reactor type has been confined almost exclusively to air purification for applications such as nitric oxide, methanol, and toluene vapors.

E.3.2. Immobilized Catalyst Reactors

Due to the large costs associated with separation and handling of catalyst downstream, much research has been directed at techniques for immobilizing the catalyst within the reactor system. This reduces costs since the catalyst does not need to be removed from the solution after the reaction is complete. However, this also inherently results in a loss of surface area since the catalyst must be attached to a support for

immobilization purposes. Lowering the available surface area for heterogeneous photocatalytic reactions to occur decreases the rate of the desired reaction.

Coating a surface with a thin film of TiO_2 is a common approach to preparing immobilized photocatalytic systems. Recent studies have found that immobilized anatase and rutile TiO_2 exhibit similar photocatalytic activity compared to suspension systems [45]. These thin films are synthesized in variety of ways including sol-gel processing and chemical etching into a homogenous solution that produces single or multiple layers of TiO_2 on a surface. The hydrophilic properties of TiO_2 are exploited throughout catalytic investigations and permit the adsorption of aqueous atmospheric solutions containing harmful pollutants. These intrinsic properties combined with thin film technology has led to the commercialization of catalysis chambers with interior coatings containing TiO_2 and other scaffolding compounds. Zhuang et al. synthesized a series of TiO_2 bilayers containing surface and interfacial defects and demonstrated the photocatalysis using Rhodamine B, a common pollutant used in preliminary studies. [31]

Two types of immobilized catalyst reactors were reported by Feitz et al. at the pilot scale using solar light [46]. The first was a coated mesh reactor, and the other was a packed bed system. Both systems were evaluated for their ability to remove 2 mg/L phenol from water. It was found that the packed bed reactor was able to degrade phenol seven times more efficiently than the coated mesh system. This difference was explained to be due to insufficient contact between the photocatalyst on the mesh and the phenol solution. The fixed bed system was also demonstrated to efficiently degrade dichloroacetic acid in this configuration [46].

A rotating disk reactor has been demonstrated by Dionysiou et al. for the degradation of organic pollutants in water using TiO_2 as a photocatalyst [47]. The schematic for this reactor is shown in Figure E.6, with TiO_2 photocatalyst deposited as a thin film on a disk in the center of the reactor that rotates as the reaction proceeds. This design has two major advantages where the rotation of the disk generates mixing of similar intensity to suspension reactors and the use of a thin film photocatalyst enables high rates of transport of oxygen to the photocatalyst surface. This idea was further investigated by Hamill et al. who

showed that the pollutant degradation rate of a rotating disk photocatalytic reactor is dependent on the rotation speed of the disk [48].
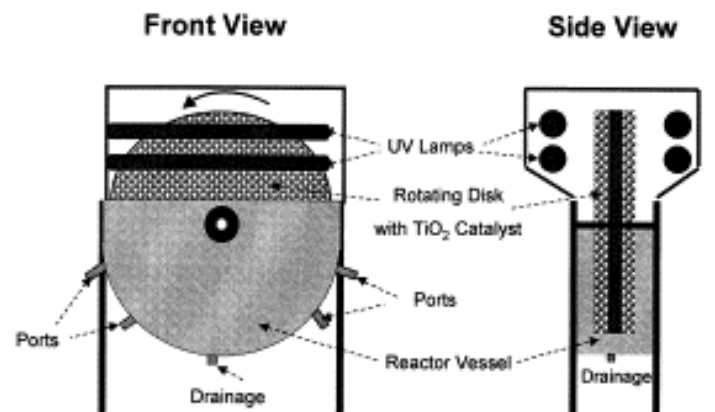
Figure E.6. Schematic of the rotating disk photocatalytic reactor[47].

Although the use of TiO$_2$ complexes has gained significant interest from environmental remediation industries, modifications that permit visible light activity are required for widespread use in environmental applications. A key factor many researchers indicate during catalytic reactor setup is the need reduce the temperature of the lamp during extended degradation periods. Efforts to reduce lamp temperature using liquid or air cooling have shown moderate success and would equate to increased operational costs in an industrial setting. Modified TiO$_2$ complexes capable of harvesting visible light are a well-studied area in recent years, yet few pilot-scale operations have been reported in the literature. The process of scaling up a photocatalytic process is complex, and many critical factors must be considered in order for the final process to be economically and technically efficient.

E.4. Photocatalytic degradation of pesticides and toxic organic pollutants using TiO$_2$ based Catalysts.

The use of pesticides leads to a tremendous increase in agricultural productivity, as they provide and secure a safe and nourishing environment for plants and other living things. Pesticides are typically used to get rid of insects, mice, and other animals. They also kill weeds, fungi, bacteria, and viruses. However, despite all the benefits they bring to our environment and everyday life, they are still deemed hazardous to the mankind. It was proven that the wastes and rinsates that come from spraying those chemicals over a large area, coupled with their frequent disposal into the environment, are causing rivers, creeks, and oceans to become contaminated. Not only they are affecting water life, but also the quality of drinking water is going down because of pesticides. Thus, seeking novel strategies and methods to treat such chemicals in a way that they do not have a negative impact on the environment into which they are disposed, has become crucial over the past years. In summary, a multitude of distinct techniques were demonstrated and employed for the efficient degradation and eradication of organic pollutants in wastewater. Several variables and parameters were controlled or varied to explore the differences in the kinetics of the reaction. Indeed, most of the methods, which employed potent catalysts, showed and exhibited successful degradation of the pesticides under various conditions as presented hereafter.

E.4.1. Photocatalytic degradation of carbamate and diuron pesticides using TiO$_2$ based Catalysts

Carbamate pesticides are commonly used for pest control from various crops [49-52]. The degradation of carbaryl was tested in the presence of TiO$_2$ aqueous suspension [49], ozone and TiO$_2$ photocatalyst [51]. UV irradiated carbaryl in the presence of suspended TiO$_2$ particles provides 99% degradation of carbaryl under optimal conditions [49]. Similarly, the addition of ozone, along with the photocatalyst, was found to speed up the mineralization of carbaryl owing to its relatively high reduction potential, which increases the degree of oxidation of carbaryl. The combination proved to have a strong impact on the decomposition rate of carbaryl in pesticide wastewaters with the strongest impact of the photocatalytic ozonation reached at pH 6 [51]. On the other hand, the effect of photocatalyst (TiO$_2$/UV), with the aid of photosensitizers such as methyl orange,

methylene blue or rose Bengal, was tested on the mineralization and toxicity degree of insecticides in wastewater [52, 61, 62]. Photosensitizer-promoted solar photocatalysis is an innovative technique for the degradation of carbaryl rinsate to CO_2 [52]. It was deduced that using TiO_2 and solar light showed 70% of the toxicity reduction efficiency of the TiO_2/UV process. However, when photosensitizers were added, in the scale of 1-2% of the initial carbaryl concentration, there was a 20% increase in the toxicity reduction efficiency of UV-TiO_2 photocatalysis. The principal mechanisms for the decomposition of carbaryl were found to be hydrolysis, hydroxylation, and quinonation [52]. This general transformation helps better understand the efficiency of photosensitizers as illustrated in the proposed photodegradation pathway presented in Figure E.7. Moreover, applying a parabolic concentrator with TiO_2/UV and $TiO_2/UV/H_2O_2$ catalysts enhanced the decomposition levels by 41% and 79%, respectively. Moreover, when the sun geometric concentration ratio increases to two, the degradation levels were enhanced to 54% and 92%, respectively [63]
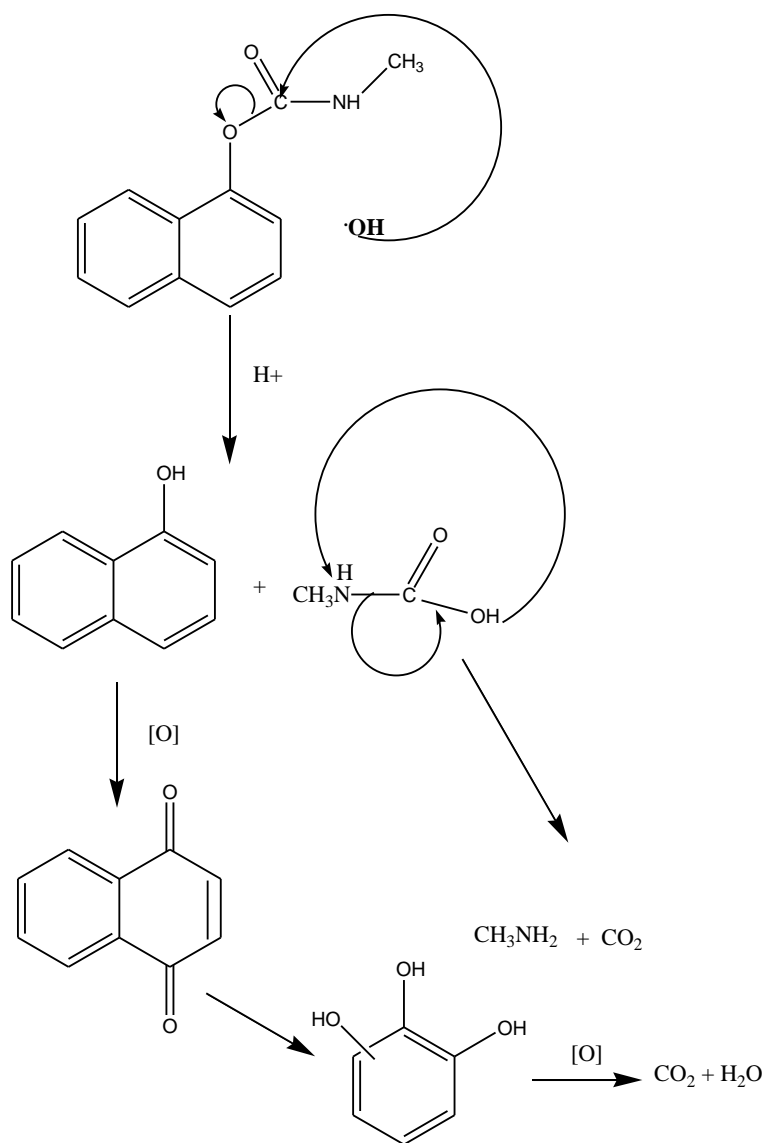
Figure E.7. Proposed photodegradation process of carbaryl.

A major development in the efficacy level of TiO_2 was observed when it was supported with a coat of granular activated carbon [64]. The degradation of carbofuran (CBF) in the presence of TiO_2-Carbon modified material followed pseudo first order with the degradation of CBF slowed down when its initial concentration is increased [64]. The modified materials showed 100% removal of CBF at optimized conditions [64]. Further, CBF degradation was studied in the presence of TiO_2 and ZnO under 254 nm and 365 nm UV light [65]. TiO_2

was found to be more efficient than ZnO catalyst where it gave a complete mineralization of CBF over a 5 h time interval with best catalytic activity was reached using 365 nm irradiation source [65]. Moreover, Re^{+3} doped nano-TiO_2 was implemented in field on tomato leaves and soil carbofuran [66]. It was determined that the degradation rate of carbofuran reached a maximum value of 54.89% when the concentration of nano TiO_2 was 0.4g/L. Overall, the decomposition rates of the pesticide in the tomato leaves and soil samples were increased by 20-30% and by 15-20%, respectively, as compared to natural degradation procedure [66]. Triadimefon and pirmicarb were photodegraded in the presence of aqueous TiO_2 suspension where the degradation process was four times faster than the photolysis of the target molecule without a catalyst [67].

As a different approach, diurons were treated by two different methods of solar photocatalysis, one with titanium oxide, and the other by photo-Fenton [68-70]. The transformation products and toxicity levels were evaluated and compared between the two methods [69]. It was found that diuron was totally disappeared in 45 min for both systems. The toxicity was reduced to a value below the threshold in a time interval that was shorter than 200 minutes, which was the time spent for 90% of mineralization to be achieved. The transformation products were identical with variation in their relative abundance [69]. Solis et al. have reported the degradation of diuron by three different approaches: single ozonation, photocatalysis, and photocatalytic ozonation [70]. Compared to the single ozonation process, the total organic carbon (TOC) removal via photocatalytic ozonation was more efficient and complete where carbon dioxide and water found as final products [70]. Overall, photocatalytic ozonation was deemed more effective in terms of mineralization levels and TOC percent removal, due to its great oxidizing capacity of organic pollutants [70]. Moreover, boron doped TiO_2 was used for the degradation of four pesticides, including diuron and compared to bare TiO_2 catalyst [71]. Boron doped TiO_2 catalyst was more effective in terms of degradation and mineralization rates in contrast to the undoped TiO_2. The synergistic effect of photocatalytic ozonation led to faster mineralization rates as compared to the individual methods of treatment. Additionally, the B-doped catalyst was stable and gave reproducible results of mineralization rates up to 75% upon three successive runs [71]. The study

indicates that the doped catalyst was more active towards the removal of the organic pollutants due to the observed increase of the pore volume and surface area of the crystal compared to the bare TiO_2 sample [71].

The degradation of chlorotoluron in the presence of aqueous suspensions of titanium oxide under diverse conditions has been reported [72]. The change in conditions involved the type of TiO_2 used, pH, catalyst concentration, substrate concentration, temperature, and the various types of electron acceptors, other than molecular oxygen. It was revealed that titanium oxide exhibited the highest efficiency rate for the decomposition of chlorotoluron. The temperature range used was 20-50°C, with no considerable change in the degradation rate of chlorotoluron occurred within that range. Expectedly, the decomposition rate was seen to increase with the concentration of the catalyst with three identified major products shown in Figure E.8.
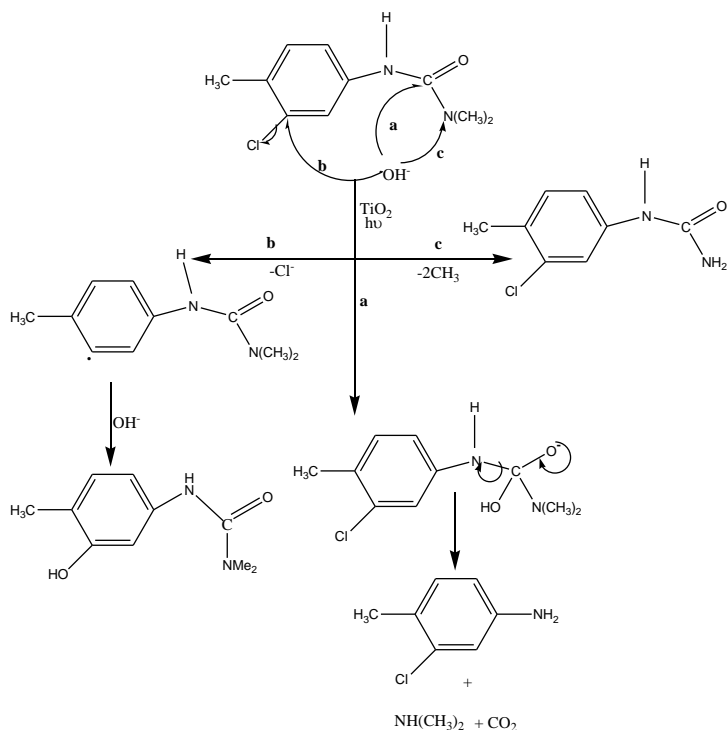
Figure E.8. A plausible mechanism for the photodegradation of chlorotoluron irradiated in the presence of TiO_2 photocatalyst.

286

Fenoll et al. have reported the decomposition of methabenzthiazuran residues in leaching water in the presence of photocatalysts and amended soils [73]. The effect of TiO_2 and ZnO was examined on the degradation rate of the organic contaminant. The use of ZnO was found to be more effective in the degradation process of the herbicide than TiO_2, although both led to significant reduction in the amount of the herbicide [73]. However, ZnO had some downsides as it was dependent on the pH of the reaction medium. The study is unique in a sense that it introduced and presented innovative approaches for the eradication of a special type of herbicides [73].

E.4.2. Photocatalytic degradation of organic dyes and pharmaceutical products.

The activity of TiO_2, ZnO, and their mixed oxide (ZnO-TiO_2), was tested and compared towards the degradation of methylene blue and naproxene, a pharmaceutical compound [74]. While the various photocatalysts gave approximately similar degradation rates in the case of the pharmaceutical compound, the efficacy of ZnO under UV irradiation exceeded that of the others in the degradation of methylene blue. Since zinc titanate is relatively more stable than ZnO in acidic environments and can integrate into its lattice elements that might alter the bandgap, it can be utilized in place of the more effective analogue ZnO as a candidate for advanced oxidation. Interestingly, the activity of both component oxides depends on the crystallographic alignment of the exposed surfaces [74].

Azo dye solutions treated with a novel hybrid technique of hydrodynamic cavitation (HC) and photocatalysis in a pilot reactor exhibited better mineralization at 5 bar as compared to individual conditions [75]. ZnO catalyst was found to be more efficient than TiO_2 with an optimum degradation rate reached at 1.0 g/L ZnO concentration. In addition, it was found that as the initial concentration of the dye increases, the decolorization and degradation rates decrease [75]. Also, azo dye (RR 180), as well as 2,4-dichlorophenoxyaceticacid (2,4-D) and antibiotic (enrofloxacin), were degraded using single ZnO catalyst and a 1:1 ratio of ZnO/TiO_2 mixture [76]. Irradiations using the UVC wavelength range of the UV light were

found to be more effective than the UVA for all the tested chemicals, however, UVA was beneficial in a sense that it utilizes solar energy, so the energy efficiency was high. The catalysts proved to be effective and successful in terms of reusability by the consecutive degradation tests, which qualifies them as reliable methods for future applications [76]. Furthermore, ultra-thin photocatalytically active TiO_2 layers with high porosity and hydrophilic properties were utilized for the degradation of methyl orange dyes. Double-side active TiO_2-modified membranes photodegraded twice the amount of photodegraded pollutant like methyl orange, when operated in the common cross-flow membrane mode under UV irradiation of both membrane surfaces [77].

E.4.3. Photocatalytic degradation of triazine pesticides using TiO_2 based Catalysts

1-Chloro-3-ethylamino-5-isopropylamino-2,4,6-triazine, better known as atrazine, is a commonly used herbicide in the agricultural industry to limit the growth of certain weeds and grasses that prove to be an interference in the cultivation of crops such as corn, sugarcane, and sorghum. Atrazine is suspected to be an endocrine disruptor that is a potent carcinogenic for humans, cause reproductive defects in fish. Furthermore, it is a very persistent chemical so it may remain in the environment even after several years have passed since its use. TiO_2 is a very effective photocatalyst for the removal of atrazine derivatives from the environment [78-84]. In specific, TiO_2 ozonation provides a significant enhancement in the degradation rate of atrazine with a gradual increase upon the increase of the amount of catalyst and the ozonation dose. When the catalyzed ozonation process was carried out for 30 min at the ozone dose of 10 mg min^{-1} and catalyst dose of 0.1 g L^{-1}, about 93% atrazine was removed from water. GC/MS analysis indicates the formation of five different products besides residual amount of atrazine as depicted in Figure E.9 [78]. The transformation products showed that the degradation of atrazine involved de-alkylation process followed by de-chlorination and de-amination steps. Toxicity tests based on the marine bacteria V. Fisheri indicated the detoxification of atrazine by catalyzed ozonation [78].
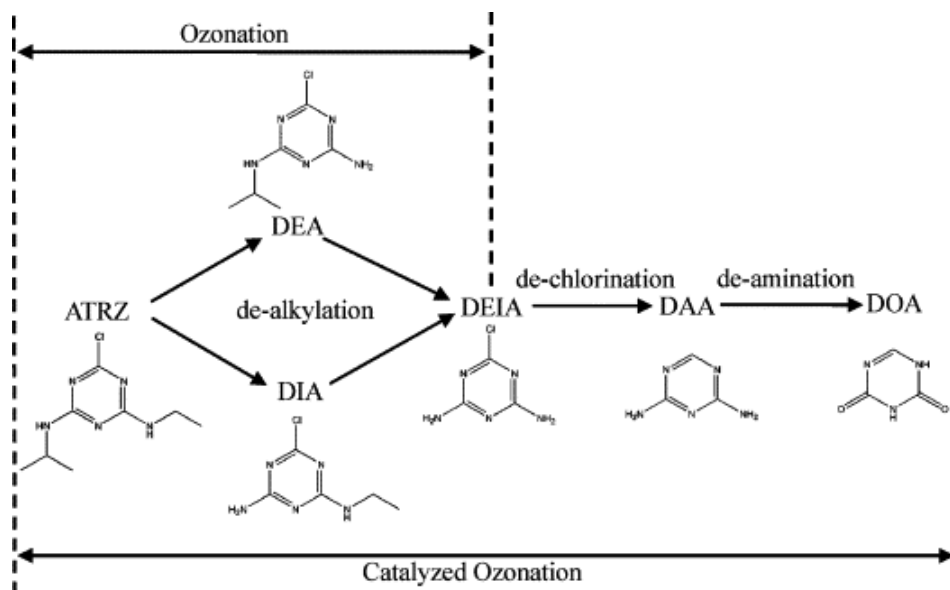
Figure E.9. Atrazine degradation and formation of transformation products by catalyzed ozonation[78].

TiO$_2$ synthesized using Boron Enrichment Waste (BEW), without the presence of any reducing agent, was found to be fast, efficient, and eco-friendly photocatalyst. The photocatalytic degradation of atrazine performed under UV-Vis irradiation depends heavily on the initial concentration of atrazine, the time of contact, and the amount of the catalyst [79]. The TiO$_2$ – BEW catalysts have good reusability when it comes to the elimination of atrazine from water [79]. In comparison, a different technique involved modifying TiO$_2$ semiconductors by adding various dyes to the surface [80]. While the surface modified catalyst was reacted with atrazine in the dark, it was noticed that the thionin and eosin Y dyes did not interact with the atrazine molecules [80]. However, it was found that in the presence of visible light, the modified TiO$_2$ semiconductor particulate system could not only degrade harmful compounds like phenols and hydrocarbons, but it could also help in the decomposition of pesticides like atrazine when similar experimental conditions are regulated [80].

N-doped TiO$_2$ particles deposited on ZnS-based phosphors microparticle (ZSP) by a sol-gel technique showed that combination of both N doped TiO$_2$ as well as the ZSP gave improved results in photocatalytic

activity for the removal of atrazine [81]. While, 45% of the atrazine were eliminated under UVA illumination, 94% of the atrazine present in the sample was successfully removed upon illumination in the presence of the catalyst [81]. Further, TiO_2 in aqueous solution as well as TiO_2 surface modified with ceramic, tetra(4-carboxyphenyl) porphyrin encapsulated various metal centers such as Fe(III), Cu(II) were used as photocatalyst towards the triazine decomposition under visible light [82, 85, 86]. While, porous TiO_2 modified ceramic shows an excellent photodegradation performance toward atrazine and thiobencarb with up to 96% of the total organic carbon removal efficiency [86], it was found that these conditions were not oxidizing enough to break down the atrazine present, and as a result, hydrogen peroxide was added as an oxidizing agent [82]. Under these conditions, the atrazine undergo degradation where Cu(II) porphyrin system caused the atrazine present to degrade by 82% after one hour of irradiation [82]. Similarly, TiO_2 deposited with metallic nanoparticles including Au, Ni, and Cu were employed for the degradation and mineralization of atrazine [83].

Au/TiO_2 was the most successful catalyst for the degradation of atrazine, followed by Cu/TiO_2 and then Ni/TiO_2. This is possible because Au is the most unreactive element as a result it is not being oxidized during the reaction. Studies have also been conducted on a graphene-TiO_2 catalyst [87]. Possible theories suggest that graphene oxide (GO) combined with titanium oxide, improve the surface area for adsorption and enhance the interfacial electron transfer between the two compounds. The composite catalyst provide a better performance than the titanium oxide alone [87]. The composite GO-TiO_2 catalyst proved to be much more efficient at photo degradation of a multitude of pesticides- atrazine, alachlor, isoproturon and diuron when compared to TiO_2-P25 system alone [87].

Another research involved the use of electrochemistry in the degradation of atrazine [88, 89]. The study uses Ti/RuTiO$_2$-DSA (dimensionally stable anode) electrode seeks to explore the differences in the results when a purely electrochemical method is compared to a photo-assisted electrochemical method [88]. Results showed that when the current density was increased, the amount of atrazine removed using the combined method was much greater than the purely electrochemical method, which could possibly be due

the formation of hydroxyl radicals because of interaction with the UV light. The photo-assisted method breaks down the heterocyclic ring of atrazine where the removal of atrazine from water and the chemical oxygen demand depend on the rate of deposition of organic material on the surface of the electrode [88]. The use of an innovative, inexpensive titanium oxide that contains both the anatase and rutile phases of titanium oxide as a photoanode in conjunction with a graphite cathode removed 99.2% of the atrazine present with faster atrazine removal observed using higher current density. The best removal took place at a pH 6 where hydroxyl radicals formed during the electrochemical process induced the dichlorination and dealkylation as depicted in Figure E.10 [89].
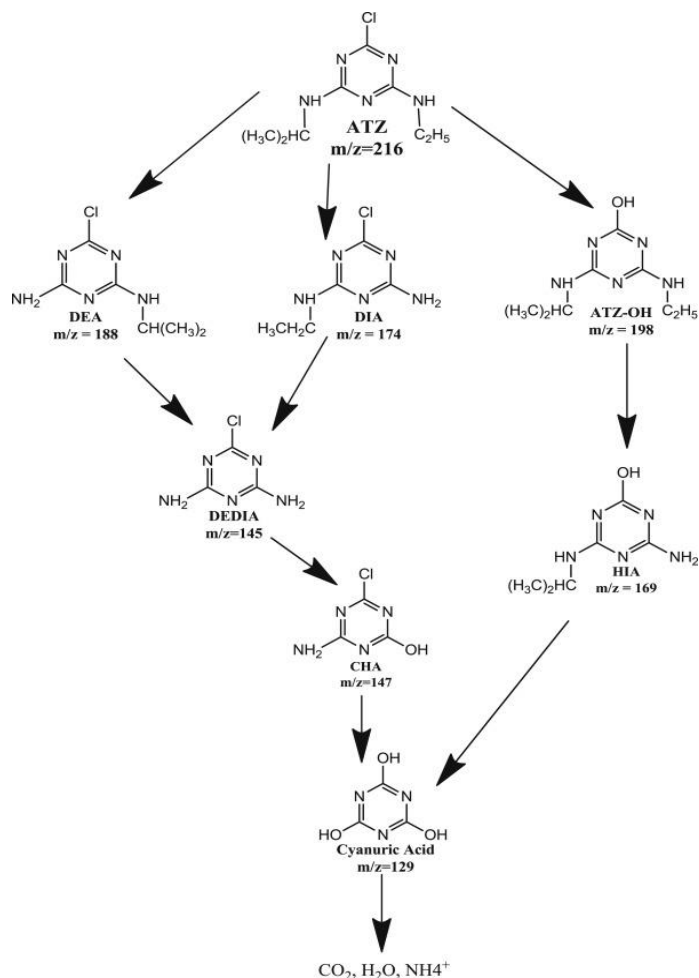
Figure E.10. Possible pathways of Atrazine degradation with electrophotocatalytic process[89].

Immobilized chitosan with TiO_2 thin film were used as photocatalyst for the removal of terbuthylazine (TBA) from water bodies [90, 91]. While the thermal degradation showed no change in TBA concentrations, both the photolytic and photocatalytic degradations have favorable results, with high removal of TBA. However, the photolytic process led to the formation of more by-products (apart from cyanuric acid), some of which were identified as toxic as TBA. In presence of the photocatalyst, the amount of cyanuric acid obtained was 37.21%, while in its absence only 16.08% was obtained, indicating that the presence of the catalyst does increase efficiency, because cyanuric acid, although cannot be degraded using photocatalysis, it can easily be removed using microbial degradation [90].

To assess the effect of different reaction conditions on the reaction chitosan immobilize TiO_2 on a glass fiber was used for photocatalytic degradation of TBA [91]. The photolytic degradation was effective with cyanuric acid was obtained as a final product. When the rate of the reaction mixture circulation was increased, the degradation was more successful as more cyanuric acid obtained [91]. Similar study include the degradation of melamine (s-triazine derivative) in presence of TiO_2 [92]. Among several oxidation techniques with a multitude of varying experimental conditions, hydroxyl radicals generated from hydrogen peroxide in presence of sulfate radicals were effective towards melamine decomposition with cyanuric acid obtained as a final product [92].

The degradation of hexazinone using mixed phase crystal nano-TiO_2 has been reported [93]. The adsorption equilibrium of hexazinone on TiO_2 was reached in 20 minutes in the dark. While hexazinone was found to be stable in the absence of the catalyst, photodegradation occurs in the presence of TiO_2. The rate of degradation differs when the amount of nano-TiO_2 is varied, but the rate was optimum at 0.1% w/w of TiO_2. The proposed degradation route fits the Langmuir – Hinshelwood model, and the final products obtained were nontoxic [93]. The adsorption of prometryn on TiO_2 also follows the Langmuir- Hinshelwood model and first order kinetics. When the reaction proceeds in the presence of the photocatalyst, only 10% reduced after 2 hours of irradiation [94]. Adding oxidants like peroxydisulfate to the reaction mixture, improved the photodegradation due to a synergistic effect with cyanuric acid was identified as a final product

[94]. Dicylanil, an insect growth regulator derived from pyrimidine, has been also investigated [95]. The rate of degradation of dicylanil was 43 times faster in the presence of the TiO$_2$ catalyst compared to the uncatalyzed reaction with complete eradication occurs in less than one hour [95].

The degradation of the herbicide metamitron (4-amino-6-phenyl-3-methyl-1,2,4-triazine-5(4H)-one) was also investigated over the TiO$_2$ catalyst [96]. When the photocatalyst was present, metamitron was fully degraded after 6 hours, whereas, one fifth of the initial herbicide persisted when the TiO$_2$ is absent [96]. Kaniou et al have studied the degradation of sulfamethazine (SMT), a sulfonamide drug using three n-type oxides the photocatalysts including: ZnO, TiO$_2$-P25, and TiO$_2$ (Anatase) [97]. After one hour of the exposure the percent decomposition was 100%, 65%, and 39% for the reactions occur with ZnO, TiO$_2$-P25, and TiO$_2$-Anatase catalysts, respectively [97].

TiO$_2$ has proved to be one of the most powerful catalysts for complete degradation of environmental pollutants [98]. Using TiO$_2$ in powder form shows the most efficient catalytic activity [98, 99]. However, when used for water decontamination, post-treatment methods are required to collect the catalyst from the reactor. One way examined is to coat the catalyst on aluminum foam using sol-gel method which, leads to a three-dimensional structure with high surface area as it ensures sufficient flow of liquid and large interface of exchange between targeted molecules and the photocatalyst [100]. While 5% of pyrimethanil went through a complete photodegradation after 19 h of exposure, 100% of the pesticide removed after 5 h upon irradiation in the presence of TiO$_2$ catalyst [100]. The catalytic activities of TiO$_2$ powder immobilized with silver modified thin films in metolachlor degradation were also investigated [98]. SEM image for the prepared immobilized catalyst films and silver-nanoparticle-doped films showed rough sponge-like surface in the immobilized films. The effective surface area were hundred times greater than the non-fractal surface due to ability of capturing pollutant molecule and photons and allowing higher light reflection [98].

The effect of zinc and titanium oxide photocatalysts on the degradation of the herbicide bentazon, under UV and visible light, along with effect of pH and electron acceptor groups on initial rate of catalysis were studied [101]. Among ZnO and TiO$_2$ from different manufacturers, TiO$_2$-P25 and ZnO exhibited the highest

293

catalytic activity attributed to their different morphology as it is one of the most critical properties for high catalytic activity. ZnO and TiO$_2$ P25 have the highest catalytic activities under UVA illumination where 97 and 81% of bentazon degraded after 90 minutes, respectively [101].

The primary kinetics of degradation of pyridaben under photocatalysis of TiO$_2$ was identified [99, 102]. The plot of the quantity of pyridaben left in the solution versus the UV irradiation time showed that the degradation follows Langmuir-Hinshelwood kinetic model [102]. The presence of TiO$_2$ particles enhances the reaction rate by 10 times compared to the uncatalyzed system, upon the exposure to wavelengths above 360 nm where a complete degradation of the pesticide has occurred [99]. Further, the illumination of pyridaben was tested in a surfactant CTAB (cetytrimethyl ammonium bromide) aqueous dispersion [103]. The results indicated enhancement in the initial rate as the concentration of the catalyst increased with strong adsorption of cationic CTAB on titania particles helped co-adsorption of pyridaben which facilitated the photocatalytic degradation. The effect of pH was minimal from pH of 3-6 but overall it increased in the range of 3-10 [103].

To enhance the photocatalytic activity, TiO$_2$ was coupled with electrochemistry and doped with non-metals like nitrogen to shift the TiO$_2$ absorption to lowest level of energy [104, 105]. Beside the nonmetal, immobilization of transition metals is effective in enhancement of TiO$_2$ photocatalysis in visible light. Iron(III) ion has the most similar radius as Ti(IV) and can be introduced to the crystal lattice to change the electronic structure and reduce the band gap. To test the modified TiO$_2$ catalyst, photocurrent of TiO$_2$/Ti and Fe-N-TiO$_2$/Ti electrodes were used to decompose thiamethoxam pesticide [104]. The effect of substrate concentration, pH, type of catalyst, catalyst dosage, and the presence of an electron acceptor such as hydrogen peroxide on the degradation of thiamethoxam were also investigated [106].

TiO$_2$ particles were used as photocatalyst for the photodegradation of the fungicide boscalid under different experimental conditions [107]. A complete degradation in presence of TiO$_2$ occurred after 90 minutes with the degradation rate increases as the pH, photonic flux, and oxygen concentration increases [107]. The presence of inorganic cations like Ca^{2+}, Na$^+$, K$^+$, Mg^{2+} and anions like CO$_3^{2-}$ tend to decrease the rate of

reaction as they adsorb on the surface of TiO_2. In a similar study, complete photodegradation of pyraclostrobin was established at pH 6.2 and 0.5 g/L of TiO_2 after 60 min of UV irradiation [108].

Hermann and Guillard have studied a laboratory photo-reactor and a pilot solar photoreactor for photodegradation of several pesticides [109]. The mass of catalyst required for an optimum light absorption was 2.5 g/L for the batch micro photo-reactor and only 0.2 g/L for the pilot photoreactor. Also, activated carbon coupled with titania enhanced the degradation rate by a factor of 2.5. This enhancement is due to spontaneous mass transfer of pollutant from activated carbon to titania because of concentration gradient between the two [109]. The photolysis and photocatalysis degradation of 6-chloronicotinic acid (6CNA) was also observed under UV radiation. While 6-CNA does not degrade easily in double deionized water, the photocatalytic degradation with immobilized TiO_2 is a fast process with pseudo first order kinetics. Although the mineralization rates estimated through TOC measurements revealed absolutely no carbon removal under photolytic degradation, 46% mineralization was reached using TiO_2 as photocatalyst after 120 minutes [110].

E.4.4. Photocatalytic degradation of Phosphorous-based pesticides using TiO_2 based Catalysts.

Photocatalytic degradation of P-based pesticides generally followed pseudo first order reactions that are expressed by Langmuir -Hinshelwood model [85, 111, 112]. The rate of degradation depends on several parameters including: pH, catalyst type and concentration, substrate concentration, and the presence of electron acceptor such as H_2O_2 [112-118]. Most studies include testing the use of TiO_2 catalysts in removing different pesticides such as malathion, dichlorvos, COD dipterex, diazinon, phorate, dimethoate, and several other organophosphorous pesticides since pesticides have been described to be harmful to the health of humans and animals [112-114, 119, 120].

The use of TiO_2 based catalysts for photolysis and degradation of malathion, isomalathion, and malaoxan has been reported [121-127]. Malathion, malaoxon, isomalathion, and radotion were studied in terms of their degradation kinetics, identification of their transformation products, their toxicity, and their degree of mineralization, during UV photolysis and TiO_2 photocatalysis. Over 75% of theoretically expected sulfur in

295

PQS and P–S groups was oxidized after 240 minutes of photolysis and photocatalysis. Several oxidation and isomerization products were identified by GC-MS [121]. The formation of malaoxon, isomalathion or trimethyl phosphate esters correlated well with the induced toxicity (inhibition of acetylcholinesterase), which was observed in photocatalysis of malathion and radotion, and in the photolysis of malaoxon and radotion [121]. N doped TiO_2 nanomaterials degraded malathion within 150 minutes when 1 g/dm^3 N-doped TiO_2 was added to 15 ppm malathion at pH = 6 under UV-light. The photocatalytic degraded products are less toxic as compared to malathion [122]. Moreover, hierarchical porous TiO_2 ceramics were obtained and proved to be good for photodegradation of various pesticides including dimethoate, lindane, dipterex, malathion, and bentazone with good reproducibility [123, 128]. Suspended and immobilized TiO_2 based catalysts were used to remove various P-based pesticides including lindane, methyl parathion, quinalphos, diazinone, and dichlorovos from water bodies [129-134].

Vela et al. have studied the photocatalyzed degradation of a mixture of six pesticides (fenitrothion, malathion, quinalphos, vinclozolin, fenarimol and dimethoate) with endocrine disrupting activity sewage wastewater effluent under natural sunlight at pilot plant scale [124]. The use of TiO_2 alongside an electron acceptor like $Na_2S_2O_8$ strongly enhances the degradation rate of the studied pesticides compared with photolytic tests. The total initial concentration of pesticides (P = 1.81 mg/L) decreased to 0.39 mg/L (22%) after 240 min of sunlight irradiation [124]. After the photoperiod, malathion was totally photodegraded in the presence of TiO_2-P25, while fenarimol was the most persistent pesticide. Although carbon-doped TiO_2 has lower band-gap energy than TiO_2-P25, the latter was more efficient in all cases than TiO_2, charge separation is consolidated which reduce the possibility of recombination [124].

2% WO_3/TiO_2 catalysts prepared by sol-gel process allowed the incorporation of very reactive WO_3 clusters over anatase TiO_2 surface [125, 126]. The synthesized TiO_2 materials exhibited a crystalline anatase phase with an average particle size of 20 nm. Results of malathion degradation using solar light indicated that 2% WO_3/TiO_2 showed better catalytic performance than sol-gel TiO_2, achieving a complete degradation after 2 hours with 63% TOC reduction after 5 hours. The previously mentioned results suggest that 2%

WO$_3$/TiO$_2$ is an active material for solar photocatalytic treatment of polluted water having pesticides [125]. The mineralization rate and the percentage of TOC removal were improved when the content of WO$_3$ was 2% due to the formation of smaller clusters and a higher surface area, which reduces the recombination process and results in better contact area between the catalyst particles and the pollutant, improving the photocatalytic reactivity and the destruction efficiency against the pesticide molecule [126].

Au–Pd co-modified TiO$_2$ nanotube film (Au–Pd–TiO$_2$) fabricated by simultaneous photo-depositing Au and Pd precursors on a self-organized TiO$_2$ nanotube film. The photocatalytic activity of the modified film revealed that the malathion elimination rate increased by 172% when the photocatalyst of the naked TiO$_2$ nanotube film was replaced by Au–Pd–TiO$_2$ [127]. This activity is attributed to the effective separation of photo-generated charge carriers and the higher synthesis rate of H$_2$O$_2$ as illustrated in Figure E.11 [127].
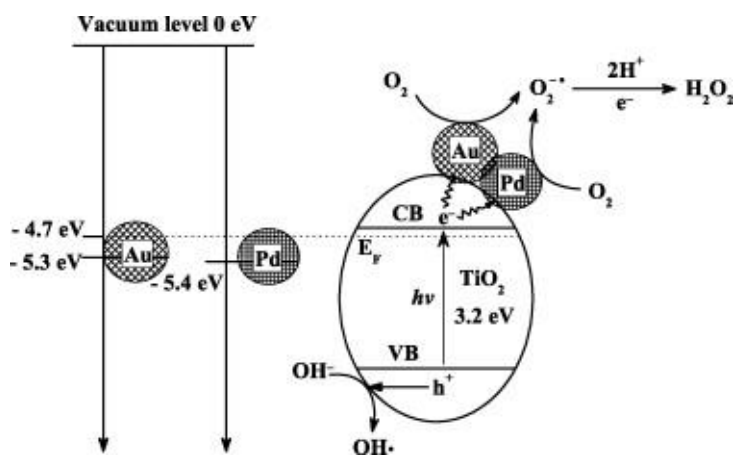
Figure E.11. Schematic diagram representing the charge-carrier transfer on Au–Pd–TiO$_2$ and its interaction with the adsorbed O$_2$[127].

Juang and Chen have reported the photocatalytic degradation rates and paths of methomyl and parathion in the presence of TiO$_2$ suspension using UV irradiation. Langmuir–Hinshelwood kinetic model was used to evaluate the apparent first-order rate constants of both pesticides at their initial stages of degradation processes. Under similar conditions, the degradation level of methomyl was faster than parathion as expected due to more complicated structures of parathion molecules [135]. In similar study, titanium dioxide proved to

be more efficient photocatalyst than ZnO since the oxidation and decomposition of the insecticide proceeded at higher reaction rates. Moreover, complete mineralization was achieved only in the presence of titanium dioxide [136]. Toxicity level was observed to be decreased during photocatalytic activity in the presence of a catalyst where eight by-products were identified during the photocatalytic activity [136]. It has been recently reported that anatase nanofibers act as good photocatalyst towards the degradation of methylparation pesticide [137]. The modified catalyst is with high surface area that enhance the adsorption of the target pesticide and thus accelerate its degradation process [137].

Several triazine derivatives and organophosphorous pesticides were investigated in aqueous TiO_2 suspensions under simulated solar light [138]. Degradation kinetics monitored through gas chromatography followed the first-order kinetics. The degradation was fast with half-lives varying from 10.2 to 38.3 minutes depending on the nature and the structure of the compounds [138]. The generated transformation products (TPs) were formed via oxidation, dealkylation, and dechlorination for s-triazines and via oxidation and photohydrolysis for organophosphates [138].

TiO_2 nanofibers containing Ag nanoparticles prepared by electrospinning were established as potential photocatalyst for the degradation of parathion. The prepared Ag/TiO_2 nanoparticles provide a higher photocatalytic performance in reaction under UV photo irradiation [139]. The enhancement was due to the narrow size distribution, high purity, uniform distribution of doped metal and ~50 nm diameter of the prepared Ag/TiO_2 nanofibers. Furthermore, the presence of metallic nanoparticles inhibits the electron-hole recombination in TiO_2 by electron capture resulting in increased hole formation to produce hydroxyl radicals, which lead to an increase in the rate parathion photodegradation reaction [139]. It was also found that the content of Ag nanoparticles on TiO_2 nanofibers performed a significant role in photocatalytic performance during the parathion degradation reaction [139].

A series of bismuth-doped titania samples were prepared and applied for the photodegradation of methyl parathion under UV-A radiation [140]. The photocatalytic degradation of methyl parathion in aqueous solutions was further promoted by the $Bi-TiO_2$ photocatalysts, compared with TiO_2 alone [140]. It has been

demonstrated that methyl parathion was degraded efficiently in aqueous Bi-TiO$_2$ suspension to the extent of 97% within 120 minutes [140].

TiO$_2$ photocatalyst was also used to degrade the most widely used organophosphorus pesticides, monocrotophos (MCP) and chlorpyrifos (CPS) using 16 W UV light source [141]. The kinetic analysis of photodegradation of monocrotophos and chlorpyrifos under different initial concentration followed the Langmuir–Hinshelwood model where, TiO$_2$ is proved to be excellent photocatalyst for degradation of monocrotophos and chlorpyrifos [141]. In addition, the degradation of pesticides chlorpyrifos, cypermethrin and chlorothalonil was examined in aqueous solution by TiO$_2$ photocatalysis under UVA (365 nm) [142]. In UV/TiO$_2$ photocatalysis, COD and TOC removal were 25.95 and 8.45% respectively whereas, UV/TiO$_2$/H$_2$O$_2$ photocatalysis revealed 53.62 and 21.54% COD and TOC removal, respectively [142]. The study is significant regarding the application of UV/TiO$_2$/H$_2$O$_2$ photocatalysis as pretreatment of chlorpyrifos, cypermethrin and chlorothalonil pesticide wastewater at pH 6, for biological treatment [142]. Batch degradation studies on Endosulphan and Chlorpyrifos were conducted in the concentration range from 5 to 25 mg/L at a pH ranging from 3.5 to 10.5 and at a catalyst loading of 0.5–2 g/L [143]. Endosulphan removal efficiency was about 80–99% and chlorpyrifos removal efficiency was about 84–94% in the presence of TiO$_2$ catalyst. The obtained high removal efficiencies (80–99%) indicate the effectiveness of this process and its potential for practical application [143].

Photocatalytic degradation of organophosphorus compounds including organophosphonic, and organophosphinic acids by TiO$_2$ immobilized silica gel in a water phase was carried out [144]. Photocatalytic degradation of organophosphorus compounds through forming various intermediates obtained via rapid absorption of acids on TiO$_2$ surface resulted in significant reduction in the concentration of these compounds even under dark condition [144]. Upon UV irradiation, total organic carbon (TOC) level increased indicating the elution of some organic intermediates into the aqueous phase [144].

While TiO$_2$ is commonly used for its high photodegradation activity, it is not easy to separate and reuse TiO$_2$ [145]. To overcome its separation, TiO$_2$ was synthesized with supports like HZSM-11 zeolite. It was

found that $TiO_2/ZSM-11$ catalysts are suitable for the degradation of the insecticide DDVP in water, resulting in degradation percentages similar to the commercial TiO_2 P25 [145]. Similarly, TiO_2 supported on H_β was tested on monocrotophos pesticides (MCP) where it was concluded that supporting TiO_2 on a zeolite makes it better for both degradation and mineralization since MCP and its intermediates were adsorbed to the supported TiO_2 [146]. Moreover, TiO_2 photocatalyst removed the toxic dichlorvos pesticides present in the air indoors; but it produced a small amount of potentially harmful by-products in the gas phase [147].

The photocatalytic degradation of organophosphorous pesticide dirchlorvos in suspended TiO_2 was also studied under solar irradiation [148]. After exposure to solar irradiation, Cl^- ions were found in large quantities whereas PO_4^{3-} was only present in small amounts due to its presence in phosphate organic compounds. Formaldehyde was also present as an unstable intermediate throughout the reaction. The presence of H_2O_2 played a role in the reaction where it increases the rate of degradation via generating $OH^\bullet$ radicals [148]. TiO_2 was found to be more effective than ZnO for the oxidation of dichlorovos that occurred at fast rate as well as the process almost reached complete mineralization [149]. The comparison of both TiO_2 and ZnO has also been seen in another study done on dimethoate pesticide, where a similar conclusion was reached in which the rate of the oxidation and decomposition of the insecticide was faster with the use of TiO_2 catalyst, hence it is the more efficient catalyst [150]. TiO_2 was able to achieve mineralization with the addition of an oxidant as well as achieve complete detoxification with the addition of peroxide [150].

Chen et al. have discussed the treatment of Dimethoate using nanosized TiO_2 powder, where the concentration of the TiO_2 catalyst increases the degradation efficiency with an optimal concentration of 0.6 g/ml [151]. With the right adjustment of the parameters, the efficiency of degradation could reach 99% in 160 minutes. Addition of oxidants and the use of ultrasonic irradiation (US) positively affects the degradation efficiency [151]. Moreover, the degradation of triazophos by sunlight in the presence of TiO_2 has a degradation rate faster than the rate caused by direct photolysis where seventeen products were produced and projected in several transformation routs [152]. A nanometer-sized titania coupled with a screen-printed carbon electrode

(SPCE) also works as a photoelectrochemical sensor that detects the organophosphorous pesticide, dichlofenthion [153].

Sonocatalytic, photocatalytic, and sonophotocatalytic degradation of diazinon were evaluated using Fe-doped TiO_2 nanoparticles which resulted in a faster degradation rate than TiO_2 alone [154]. The rate of degradation depend on the pH, catalyst dosage, and initial concentration of diazinon and concentration of Fe doping [154]. As the concentration of the catalysts and the Fe doping increased, the rate of degradation increased as well. TiO_2/Fe_2O_3 nano powder, which was present in the form of anatase and maghemite crystalline phases, respectively were used to decompose diazinon [155]. The TiO_2/Fe_2O_3 catalysts was compared with a pure TiO_2 as a catalyst in which it was concluded that TiO_2/Fe_2O_3 had high absorption in both the UV region and the visible region [155]. FeNS-TiO_2 has been found to be more effective than pure TiO_2 with diazinon pesticides in which it improved the degradation of diazinon by 53% at pH 7 [155]. Similar to other studies, the rate of degradation increases with the increase of catalyst concentration [156].

Studies were also done on different types of toxic pesticides that should be eliminated from the environment including phorate, diisopropyl fluorophosphate (DFP) and dimethylmethylphosphonate (DMMP), Chemical Oxygen Demand (COD) dipterex, as well as 2-cholor-ethylsulfide (CEES) [157-166]. Phorate degradation over TiO_2 catalyst using UV irradiation follows first order pseudo reaction with the degradation efficiency could reach 99% in 60 minutes [158]. Inorganic ions present in natural water systems like Cl^- and NO_3^- decreases the degradation rate of phorate. Using wet TiO_2 for DFP and DMMP photodegradation reduces the amount of intermediates that accumulate on the surface while still maintaining a fast degradation rate [160]. DMMP was also treated using Zr-doped TiO_2 [159]. TiO_2 doped with 6.8 wt% Zr produces the most efficient sample for the photodegradation of these pesticides [159]. Photoelectrocatalytic degradation is also used to remove pesticides such as COD dipterex using TiO_2/Ni photoelectrode [157]. Under certain experimental conditions, the rate of COD dipterex degradation reached up to 82.6% whereas the organophosphorous conversion could reach 83.5%. This study offered a new porous nickel net photocatalyst carrier, which could inhibit the recombination of electrons and holes and enhance the efficiency of

photoelectrocatalytic degradation of dipterex pesticide from wastewater, compared with the commonly used Ti metal carrier [157].

E.4.5. Photocatalytic degradation of Monochloro aromatic derivatives using TiO$_2$ based Catalysts

Several comparative studies on the photocatalytic degradation of various benzene derivatives over TiO$_2$ (Phenol, Chlorobenzene and Toluene) were established in aqueous medium [167-172]. The results demonstrate the existence of a relationship between organic compound photo degradation and the type of substituent on the aromatic ring. The degradation was faster for electron-donating substituents [167]. Photo catalysis efficiency can be increased using Pickering emulsion in degrading non-soluble organic pollutants [169]. The study showed that Pickering emulsion with TiO$_2$–Salicylic acid nanoparticles lead to improving the photocatalytic degradation of the chlorobenzene derivatives. The key point is having small drop size to increase the contact area between the contaminant photo catalysts [169]. The Photo-oxidation of 4-chloroanaline was also investigated under UV/TiO$_2$/H$_2$O$_2$ [168]. Gas chromatography and mass spectrometry screening showed that the degradation initiated by OH radicals and the intermediates formed were able to be oxidized into benzoquinone then become carboxylic acids by ring cleavage [168]. Platinum modified TiO$_2$ nanoparticles showed higher photocatalytic degradation efficiency for both phenol and 2-chhlorophenol by 87.7 and 100%, respectively [171].

Advanced oxidation processes (AOPs) are eco-friendly for destroying non-biodegradable pollutants where solar light being used for generating hydroxyl radicals [173]. TiO$_2$ photocatalytic degradation of chloropyridines in presence of UV light is being used in pharmaceutical industry and agro chemistry [173]. In the presence of TiO$_2$ as a heterogeneous photocatalyst, 3-chloropyridine and 2-chloropyridine disappearance follow a zero-order and a first-order kinetics, respectively [173]. A comparative study between homogeneous (photo-Fenton) and heterogeneous (TiO$_2$) photocatalytic degradation of 3-chloropyridine in presence of UV

and sunlight by scaling-up solar photo-Fenton process. For Fenton, photo-Fenton and direct photolysis, the results showed that Fe(II) ions facilitate mineralization of 3-chloropyridine in the presence of H_2O_2, but still it is a lot slower than in the presence of light. The time required for 100% mineralization in presence of UV light was 60 and 300 min for photo-Fenton and TiO_2 photocatalysis, respectively [173]. TiO_2 hollow microsphere calcined at 500 °C exhibited twice higher than uncalcinated sample [174]. The microstructure of the hollow microspheres lead to improvement in the efficiency of 4-chloronitrobenzene mineralization with high stability and reproducibility up to six cycles [174].

The use of nano-TiO_2 coated films as photocatalyst towards the decomposition of organochlorine pesticides having hexachlorobenzene (BHC), dicofol and cypermethrin has been reported [175]. The results showed that photocatalytic degradation efficiency is much higher than direct photolysis with all pesticides were completely degraded over the film in 45 min [175]. The potential of immobilized TiO_2-based zeolite composite photocatalyst (TiO_2-FeZ) done from commercial AEROXIDE TiO_2 P25 and iron-exchanged zeolite of ZSM5 type (FeZ), for solar assisted treatment of diclofenac (DCF) was studied [176]. TiO_2-FeZ composite was used in the photocatalytic treatment of DCF water solution. The DCF degradation adsorption happens on the catalyst surface by hydroxylation and ring cleavage [176]. Figure E.12 shows the photodegradation pathways that illustrates all products formed [176]. The biodegradability increases when there is a decrease in the aromatic DCF by-products and enhanced dechlorination of organic structures [176].
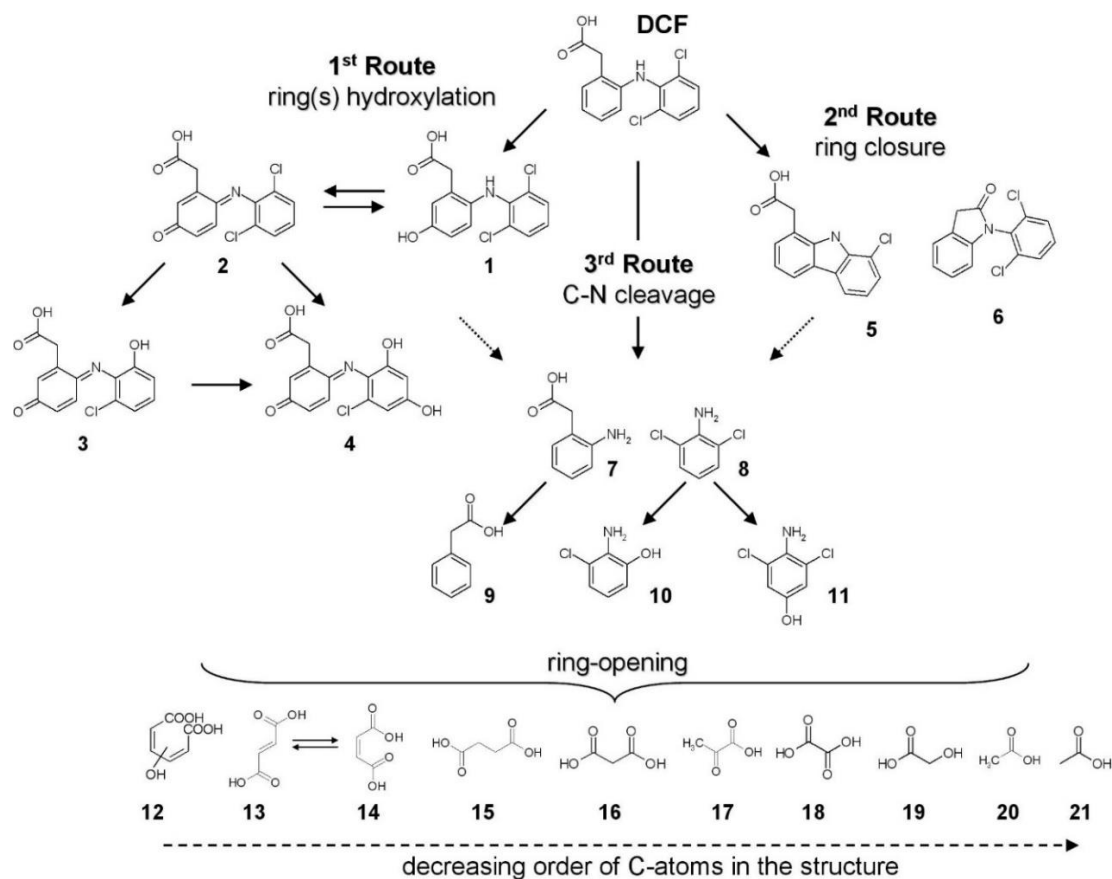
Figure E.12. Degradation pathway of diclofenac[176].

Direct photolysis and photocatalytic degradations of chlorfenapyr in TiO_2 suspensions in presence and absence of hydrogen peroxide was investigated under monochromatic UV irradiations where photo catalysis rates increased 2.5 and 3 times when TiO_2 was used at 300 and 350 nm UV, respectively [177]. Light-induced degradation of chlorfenapyr in UV was done using solution having TiO_2 as photocatalyst [178]. The degradation goes through pseudo-first-order kinetics following two pathways: First, cleaving of aliphatic ether group and forming pyrrole-□-carboxylic acid, then breaking the pyrrole group and forming 4-chloroglycine. Second, debromination of chlorfenapyr and cleaving ether group and forming pyrrole group that broke into 4-chlorophenylglycine. Glycine was degraded to form 4-chlorobenzoic acids, then break and form inorganic ions and CO_2 [178]

Photocatalytic degradation of 4-chloro-2-methylphenol (PCOC) in aqueous solutions using various TiO$_2$ catalysts have been investigated [179-185]. It has been reported that 51.4% of PCOC degraded in the presence of TiO$_2$ which can be improved by different oxidants as electron scavenger [179]. Having metal ions to UV/TiO$_2$/H$_2$O$_2$ leads to increase in photo degradation by inducing Fenton/photo-Fenton type reactions and quenching photo-ejected electrons from the TiO$_2$ surface [179]. Similarly, 4-chlorophenol (4-CP) was degraded through Fenton-like heterogeneous on TiO$_2$ and CuFe$_2$O$_4$ [184]. The results showed that the system goes through homogeneous route, using dissolved metal ions found in the solid phase catalysts. Ferric ions and hydrogen peroxide enhanced the degradation efficiency of combined chlorophenols in solar/TiO$_2$ [185]. In addition, Ag-coated Fe$_3$O$_4$@TiO$_2$ particles with a good core shell structure shows strong photocatalytic activity for the degradation of 2,4,6-trichlorophenol. The particles showed high dispersibility and stability in water so they can be reused for many cycles with convenient magnetic separability [183].

Sol–gel using titanium(IV) isopropoxide and zirconium nitrate precursors, was used for making Zr^{4+} doped nano titania [180]. TEM results showed Zr^{4+} doped TiO$_2$ is nanocrystalline, so having dopants lead to the growth of TiO$_2$ grains, increasing the surface area and decreasing the transformation of anatase to rutile. This leads to having larger photocatalytic activity for Zr^{4+} doped nano TiO$_2$ than the undoped samples. Adding metal nitrate can control the selective crystallization of anatase phase of TiO$_2$, and that provide high efficiency in the photocatalytic mineralization of 4-chlorophenol [180]. Similarly, P loaded to TiO$_2$ via sol-gel protocol leads to slowing the growth of the anatase particle and increasing its transformation to rutile. As a result, the photocatalytic activity for 4-chloro-phenol using UV irradiation on P-modified TiO$_2$ was 4.5 times higher than TiO$_2$ alone [182]. Further, sol impregnation process to fabricate Ce-TiO$_2$/CA electrode was reported [181]. Spectroscopic analyses showed that the optical absorption edge of Ce-TiO$_2$/CA is red-shifted compared with TiO$_2$/CA, and the density was 75 times higher than Ce-TiO$_2$. The conductivity of Ce-TiO$_2$/CA was shown by the spectra to be larger than Ce-TiO$_2$/FTO. As a result, Ce-TiO$_2$/CA improved the electrosorptive photodegradation of 4-chlorophenol [181].

E.4.6. Photocatalytic degradation of *Di-* and *tri-* chloro and bromo derivatives using TiO$_2$-based Catalysts

Chlorinated aromatic compounds such as dichloro [186-191], dibromo [192], and multichloro [193-201] derivatives are some of the main contaminants present in water as they are widely used as pesticides and in many chemical syntheses. They are of great health and environmental concern due to their ability to bio-accumulate, suspected carcinogenicity and potential toxicity, hence their removal is essential. Moreover, chlorophenols are currently listed in the US-EPA Clean Water Act as the primary pollutant to be removed from water. In addition to chlorinated aromatic compounds, other compounds that are potential to cause risk to humans and environment are different DDT compounds (*p,p'*-DDT, *o,p'*-DDT, *p,p'*-DDD and *p,p'*-DDE) which can also be degraded using TiO$_2$ in the form of nano tubes. Several biorecalcitrant pesticides (alachlor, atrazine, chlorfenvinfos, diuron, isoproturon, pentachlorophenol) can be degraded through oxidation processes using different form of TiO$_2$ catalysts [197, 202-207].

Advanced oxidation processes for degradation of 1,4-dichlorobenzene (1,4-DCB) and mineralization are employed under photolysis, photocatalysis on TiO$_2$, and sonolysis [186]. Photocatalysis on TiO$_2$ particles is kinetically faster for removal of 1,4-DCB than direct photolysis and sonolysis. Degradation and mineralization of 1,4-DCB using sono photo catalysis (combination of sonolysis and photocatalysis) was the fastest but required more energy than photocatalysis [186]. Fe/TiO$_2$ catalysts prove to be more effective than the pure Fe or TiO$_2$ [187]. This is due to the potential of iron to reduce toxicity of the product and enhance mineralization by trapping photo-generated electrons and holes. Hence, increasing concentration of Fe further improves the effectiveness of catalyst [187]. Moreover, mineralization of 2,4 –dichlorophenol (2,4 DCP) in water under UV irradiation was improved using immobilized Fe^0, activated carbon fiber (ACF) and TiO$_2$ as a composite membrane. 2,4 DCP degradation improved by presence of Fe^0 and TiO$_2$ at an optimum pH of 6 and optimal loading of 1 wt % Fe^0 to TiO$_2$. ACF adsorption effect was very useful for TOC removal as it adsorbs 2,4 DCP as well as intermediates [188]. The immobilized Fe^0 / TiO$_2$ /ACF catalyst proved to be reusable, stable and durable and uses adsorption, chlorination, hydroxylation and cleavage of aromatic ring

to degrade 2,4 DCP [188]. Further, 2,4 DCP degradation was tested using TiO_2/UV and laccase by simultaneous photocatalytic-enzymatic process. TiO_2/UV inactivated laccase but covalent immobilizing laccase to controlled porous glass (CPG), enhanced its stability. CPG-laccase and TiO_2/UV coupling produced better results than either individual condition, especially at high concentrations of 2,4 DCP where up to 90% removal of 2,4 DCP was attained within 2 hours [191].

Varying few parameters, such as initial DCP concentration, initial pH, photocatalyst dose of TiO_2 suspensions were tested for 2,4 DCP adsorption and degradation along with effect of three co-oxidants (hydrogen peroxide, ozone and sodium peroxodisulfate) on the photo catalytic process [190]. The DCP degradation was optimum at pH 5 and the patterns were fitted to Langmuir-Hinshelwood model. The heterogeneous photocatalysis of DCP enhanced by hydrogen peroxide, while the use of ozone did not show a significant result with sodium peroxodisulfate inhibited DCP degradation [190].

Kamble et al. have reported the solar photocatalytic oxidation of 2,4 - dichlorophenoxyacetic acid (2,4-D) using TiO_2, air and concentrated solar radiation in batch and continuous bubble column reactors. The 2,4-D adsorption on the surface of catalyst depend on the pH, the concentration, and the type of anions present. The treatment of wastewater is possible from a plant manufacturing 2,4-D using novel slurry bubble column reactor under acidic conditions [189]. In addition, doped Cs on TiO_2 was used for photocatalytic ozonated degradation of bromoxynil [192]. Results of 1% Cs/TiO_2 catalyst showed 100% degradation and mineralization of bromoxynil at basic pH in two hours as confirmed by GC-MS and a possible decomposition process is given in Figure E.13. The catalyst is fully recyclable and reusable with no loss of activity [192].
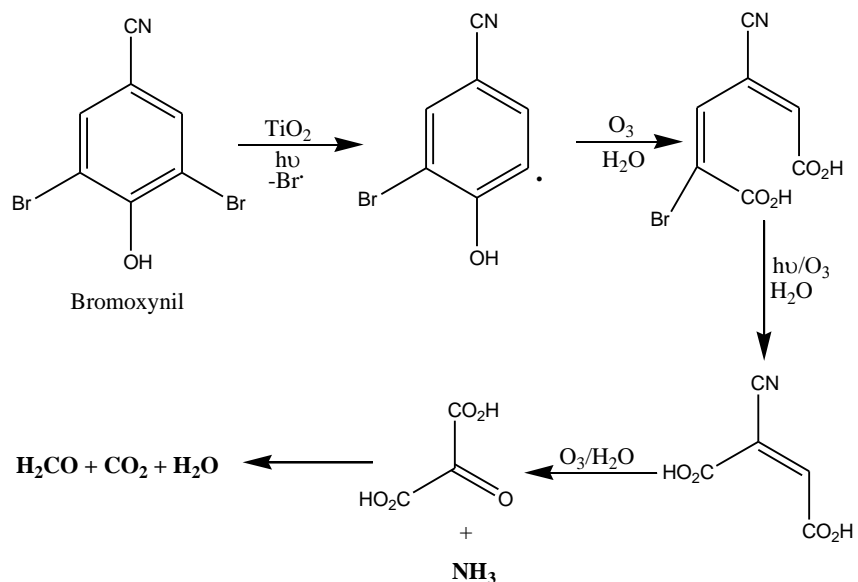
Figure E.13. Proposed reaction protocol for Bromoxynil photodegradation using TiO_2 as a photocatalyst.

Cu_2O/TiO_2/Carbon Aerogel (CA) electrode is tested for the photodegradation of 2,4,6-trichlorophenol (TCP) and removal of TOC from wastewater using visible light for its excellent electro-sorptive and highly efficient photocatalytic properties. About 96.3% removal of 2,4,6-TCP and 91.3% of TOC removal were achieved in 5.5 hours [193]. Anatase TiO_2 nano tubes loaded with Ag nano particles (Ag/TNTs) showed significant visible light absorption and about 99% pentachlorophenol (PCP) was removed after 180 minutes of visible light irradiation while pure TNTs removed only 59.4% PCP [194]. This increase of PCP removal is due to better trapping of photo generated electrons between Ag nano particles and increase in absorption of visible light by the localized surface plasmon resonance of Ag nano particles. Ag/TNTs had high catalytic activity and high stability even after being used for five cycles [194]. In addition, visible light degradation of PCP was tested using TiO_2 with B doping and Bi_2O_3 coupling (resulting a $Bi_2O_3/TiO_{2-x}B_x$). The $Bi_2O_3/TiO_{2-x}B_x$ combination gave much higher results than using each alone. This is due to each one having their own strength (B doping produce more photo generated electron-hole pairs and Bi_2O_3 inhibit the recombination of

308

photo induced charge carriers) and combination of their strengths lead to better results. This technique has proven to be effective for removal of highly toxic halogenated aromatic compounds [195].

E.4.7. Photocatalytic degradation of Chlorinated pesticides using TiO$_2$ based Catalysts

Lindane, an organochlorine pesticide, was removed using visible and solar light assisted sulfur doped TiO$_2$/peroxymonosulfate (HSO$_5^-$). Photocatalysis using visible and solar light assisted S-TiO$_2$ resulted in 31.0 and 63.4% lindane removal, respectively. Whereas, addition of 0.2 mM HSO$_5^-$ resulted in 68.2 and 99.9% lindane removal, respectively [196]. The S-TiO$_2$ film remained stable even after 4 cycles and this proved its efficiency for detoxification of water contaminated with OCPs such as lindane [196]. Moreover, novel TiO$_2$ nano tubes were used as a solid phase extraction adsorbent for p,p'-DDT [1,1,1-trichloro-2,2-bis(4-chlorophenyl)ethane], o,p'-DDT [1,1,1-trichloro-2-(o-chlorophenyl)-2-(p-chlorophenyl)ethane] and its metabolites p,p'-DDD [1,1-dichloro-2,2-bis(4-chlorophenyl)ethane], and p,p'-DDE [1,1-(2,2-dichloroethanylidene)-bis(4-chlorobenzene)] as the target analytes and then applied for analysis of real water samples [197]. The detection limits for p,p'-DDT, o,p'-DDT, p,p'-DDD and p,p'-DDE were obtained as 0.0037, 0.0053, 0.0031 and 0.0025 ng mL^{-1} under optimal conditions [197]. In analysis of environmental water samples, recoveries were obtained in the range of 81.2-115% which proved novel TiO$_2$ nano tubes having potential in decontaminating water bodies from DDT derivatives [197].

The degree of degradation of Lindane, p,p'-DDT and methoxychlor was also measured using a UV/TiO$_2$/O$_2$ system where different degradation products were identified by gas chromatography either with a mass spectrometry detector (GC-MS) or electron capture detector (GC-ECD). The two different types of photo catalysts used were powdered anatase and rutile and anatase supported on glass hollow microspheres [202]. Elimination of pesticides with anatase supported on glass hollow microspheres was obtained in the range of 68 to 90% in just 30 minutes of irradiation while only 50% removal of lindane, 85% removal of DDT and 99% removal of methoxychlor was obtained with rutile in 150 minutes of irradiation [202]. Also, due to low density of hollow microspheres, anatase supported on glass hollow microspheres was easily separated from

reaction mixture. Hence, the results showed that anatase is better catalyst than rutile and activity of 5 mg/dm^3 anatase on hollow microspheres is equivalent to that of 500 mg/dm^3 powdered anatase [202].

Photo-Fenton/ozone (PhFO) and TiO$_2$-photo catalysis/ozone (PhCO) advanced oxidation coupled systems are used for degradation of some biorecalcitrant pesticides (alachlor, atrazine, chlorfenvinfos, diuron, isoproturon, PCP) and leads to a rapid decrease in their concentrations [203]. This reaction goes through oxidation of organic molecules and using PhFO follows a first or using PhCO follows zero order kinetics. PhFO or PhCO with TiO$_2$ using UV irradiation enhances the removal of TOC in all pesticides except atrazine which experiences no TOC removal. PhFO was found to be better catalyst than PhCO for all studied pesticides except for alachlor and atrazine in which detoxification requires more than 2-3 hours. However, a reverse reaction could cause toxicity in alachlor to increase after 3 hours of treatment with PhFO [203].

E.4.8. Photocatalytic Degradation of Phenol derivatives by TiO$_2$ based Catalysts

Industrial wastewater is a major contributor to water pollution. Industrial processes such as petroleum refining, synthetic resins, coal tar, steel, coal gasification and liquefaction, pharmaceutical production, and surface runoff from coal mines release a massive amount of wastewater containing high levels of phenols and phenolic compounds [208]. These organic compounds are bio-recalcitrant and toxic and have harmful effects on organism at low concentrations [209]. Phenols and phenolic compounds pose a threat to biotic life and must be capped at a threshold concentration of **1** mg/L in inland water according to Central Pollution Control Board [208]. Degradation of these compounds occurs at slow natural rates due to their significant water solubility [209].

Conventional waste water treatment like precipitation, coagulation, chlorination, sedimentation, and combustion are inept of removing bio-recalcitrant compounds and are expensive, and therefore, new methods must be found [208, 210]. New technology has looked at the use of advanced oxidation processes (AOPs) that generate strongly oxidizing hydroxyl radicals that degrade bio-recalcitrant compounds into

biodegradable ones [211]. Heterogeneous photocatalysis using titanium oxide is one such process that has been widely researched. TiO_2 is a semiconductor with extensive environmental applications due to its ability to use solar UV light or catalytic function, low toxicity, biological and chemical inertness, availability, and low cost [208, 212]. Improvements for increased photocatalytic efficiency and recovery of titanium oxide have been extensively researched to find the optimum way to use the metal oxide catalyst in nature.

The widely used TiO_2 catalyst for phenols and phenolic-based compounds is Degussa (P-25). Saravanan et. al studied TiO_2 Anjatox as an alternative photocatalyst of phenols to the conventional photocatalyst, Degussa P-25 [208]. Degussa had a small range of catalysts loading from 1 to 4 g/L with a maximum phenol degradation of 90% at 3 g/L. This indicates the potential use of Degussa as photocatalyst for phenol degradation providing its uniform particle distribution, larger catalytic surface area, and high efficiency of phenol degradation [208]. It is observed that photocatalytic degradation of the pollutants improved by introducing solid supports that provide better adsorbent sites. Munoz et al looked at enhancing TiO_2 photo- efficiency by modifying the surface with a high surface area material such as activated carbon (AC) for its porous structure that can encapsulate organic pollutants and provide high adsorption capacity [213]. Different ratios of a home-made titania catalyst (TiEt) and AC were physically mixed to find the best performance catalysts for phenol degradation. The optimum TiEt to AC concentration ratio for phenol photodegradation was found to be 500/100 TiEt/AC [213]. Naeem et al. reported that the optimum photocatalytic degradation of phenol and 4- chlorophenol was observed when 50 mg of the solid supports, AC, SiO_2, or zeolite, were used in which activated carbon had the highest enhancement and SiO_2 had the lowest [209].

The 500/100 TiEt/AC catalytically converted 80 % of the phenol with 70% total organic carbon removal at 300 min of irradiation [213]. Intermediates formed such as hydroquinone, p- benzoquinone, resorcinol, and catechol were also adsorbed by the TiEt/AC catalysts. An ideal photo-oxidation process occurs due to activated carbon concentrating the organic pollutants on its large surface

allowing for easier access to the active sites on the titania surface [213]. TiEt/AC catalysts showed good stability and durability of photocatalytic activity in four consecutive trials, where 60% of the total organic carbon with total phenol degradation was accomplished over 36 hours of irradiation [213]. Dried rice husk solid support for TiO_2-P25 catalyst was found to have similar catalytic features to the three supports for the degradation of phenol and 4-chlorophenol. All solid supports mixed with TiO_2 enhanced the degradation of pollutants in comparison to the bare TiO_2 catalyst [209, 213].

Carbajo et. al compared the photodegradation of TiEt-450 with the conventional TiO_2- P25 on three organic pollutants: phenol, dichloroacetic acid (DCA), and pyrimethanil along with five pharmaceutical microcontaminants: ofloxacin, sulfamethoxazole, carbamazepine, flumequine, and ibuprofen [214]. Most importantly, the study followed the TiO_2 recovery using sedimentation, as this is a critical challenge that is limiting the application of the catalyst in wastewater. TiEt-450 presented a surface area of 43 m^2/g, while TiO_2 -P25 showed a slightly larger surface area of 54 m^2/g. The composition of the water matrix, deionized water or natural groundwater, influenced the phenol photodegradation for both catalysts. In deionized water, P-25 had better phenol and TOC photodegradation performance than TiEt-450 [214]. However, in natural water, conversion drastically increases for both catalysts in comparison to irradiation time in deionized water.

The presence of ions such as CO_3^{2-}/HCO_3^-, NH_4^+, SO_4^{2-}, NO_3^-, or Cl^- in natural water that are capable of scavenging photocatalyst produced hydroxyl decreases the disappearance rates of phenol and TOC with both catalysts and irradiation time. Moreover, total photo-oxidation of pharmaceuticals by both catalysts showed that ofioxacin, fiumequine, and ibuprofen required irradiation time of 5-7 minutes respectively, while sulfamethoxazole and carbamazepine need 20-30 min irradiation time. To remove all pharmaceutical microcontaminants, TiO_2-P25 required 221 minutes irradiation time while TiEt- 450 required only 28 minutes. TiEt-450 presented the best global photo-efficiency, both photo-oxidation and recovery steps, for photocatalytic removal of the previously mentioned contaminants [214].

Turki et. al compared the use of anisotropic TiO_2 nanomaterials such as nanotubes, nanowires, nanorods, and nanoparticles to the conventional TiO_2-P-25 on the photodegradation of phenol [211]. Nanotubes, nanowires, and nanorods demonstrate different adsorption ability based on their different adsorption sites. Phenol adsorption obeys a quasi-second-order reaction model that assumes that the adsorption rate is determined by the square number of vacant adsorption sites on the surface of the catalyst [211]. Among the titania nanomaterials, nanotubes calcinated at 400 °C showed the lowest phenol adsorption in both the dark and under UV by adsorbing 0.79 µmol/g and 1.25 µmol/g, respectively. The highest phenol adsorption occurred with titanate nanotube -600 adsorbing 89.34 µmol/g phenol in the dark indicating that nanomaterials poses a possible alternative to the conventional TiO_2-P25 for phenol photodegradation [211]. Since, nanosized TiO_2 can cause liver and heart damage on mice and possible affect humans if it remains in treated water, Mejia et al. studied the use of immobilized TiO_2 thick film on a compound parabolic collectors (CPC) as an alternative to TiO_2 powder. TiO_2 thick films showed a mix of anatase and rutile crystalline with nanoscopic particles. Resorcinol had a 75% removal efficiency by the film and was converted to tri-hydroxy benzenes at neutral pH [215].

E.4.9. Photocatalytic Degradation of Chlorophenols by TiO_2 based Catalysts

Dissolving transition metal ions in heterogeneous catalysts has been extensively studied for their catalyst efficiency enhancements. Transition metal doped TiO_2 catalysts provide higher concentrations of hydroxyl ions and prevent the recombination of electron-hole pairs thus enhancing the photocatalytic activity [216, 217]. Lin et al studied the degradation of chlorophenol by $CuSO_4$-doped TiO_2. Four parameters were examined, pH, temperature, initial concentration of pollutant, catalyst dosage and oxygen concentration, to see their effect on 2- chlorophenol degradation [216]. It was found that 100% of 20 ppm levels of 2-chlorophenol was degraded in the presence of the catalyst after six hours. Moreover, the dosage of catalyst was also examined where 3.0 g of the Cu-doped TiO_2 yielded an optimum result of degrading 100% of 2-chlorophenol under visible

light in six hours. While lower mass of the catalyst did not provide sufficient active sites for photocatalytic degradation, the higher masses showed agglomeration and sedimentation, which reduces the available surface area for photon absorption [216]. Furthermore, degradation of 2-chlorophenol was more favorable in acidic conditions over basic conditions, specifically at a pH of 5.5 [216].

Zhao et al studied the effect of pH, catalyst and H_2O_2 concentration on the degradation of nitrophenol [217]. The degradation of 4-nitrophenol by Fe-doped TiO_2 increased in acidic conditions similar to what is observed in 2-chlorphenol with optimum concentrations of catalyst and H_2O_2 required for degradation efficiency were 0.1g L^{-1} and 4.9 mM respectively [217]. Moreover, the effect of the pollutant structure and the electronic character of the substituents, play significant roles on the degradation efficiency by TiO_2 catalyst.

Tolosana-Moranchel et.al studied five TiO_2 catalysts: Evonik P25, Evonik P25.20, Evonik P90, Hombikat UVl00 (HBK), and Cristal ACTIV PC105 (PC105) for their degradations on phenol, 4-chlorophenol, 4-nitrophenol, and methyl p-hydroxybenzoate [212]. The efficiency of the photocatalysts followed the order: P25> P90> P25/20> PC105> HBK. This is due to the presence of mixture of anatase and rutile phases that result in improvement of electrostatic interactions between the two crystalline phases. Finally, the substituents on the phenolic compounds were studied for their influence on photodegradation, by comparing their initial degradation rates to phenol that is used as a reference. The reaction rates were observed to follow the order: phenol> 4-chlorphenol> methyl p-hydroxybenzoate> 4-nitrophenol. The reaction rate of 4-nitrophenol was reduced nearly four times in comparison to phenol [212]. It is concluded that the stronger the electron withdrawing group the lower the probability of a reaction in the unsubstituted position [212]. Ksibi et.al supports this former finding upon studying the degradation of hydroquinone, resorcinol, 4-nitrophenol, 2,4-dinitrophenol, and 2,4,6- trinitrophenol using TiO_2 catalyst [218]. 2,4-dinitrophenol presented the highest adsorption constant due to the ortho-position of the nitro group. On the other hand, 2,4,6-trinitrophenol

presented the lowest adsorption constant due to the numerous nitro groups that cause excessive hindrance of the molecule [218].

The modification of TiO_2 nanoparticles (P25) via a coating of a molecular imprinted polymer (MIP) shows increased activity and selectivity towards 2-nitrophenol (2NP) and 4-nitrophenol (4NP) [219]. The molecular imprinted polymer consists of the target molecule, 2NP or 4NP, mixed with o-phenylenediamine. The modified catalysts, 2NP-P25 and 4NP-P25 were studied for their degradation activity and selectivity in comparison to P-25 as a reference. The degradation of 2NP and 4NP occurred faster using their respective catalysts 2NP-P25 and 4NP- P25 in comparison to P25 but produced the same intermediates when using P25. However, the accumulation of the intermediates is lower in the MIP coated photocatalysts, promoting the degradation of the intermediates [219]. Herrera-Melian et al showed that P25 efficiently removes 200 ppm of 4NP, however the treated effluent must be further treated for toxicity, by constructed wetlands to achieve complete elimination and detoxification of 4NP [220]. The selectivity of MIP-coated TiO_2 is primarily affected by the difference between functional groups, molecular weights, and shape of the target molecules, 2NP and 4NP, and nontarget pollutants. Nontarget molecules that exhibit similar functional groups to the target molecule show enhanced degradation by the catalyst [219].

Perchet et.al studied the degradation of nitrophenols and nitroamines by TiO_2-P25 [210]. The TiO_2 catalysts degraded 98.1% and 94.6% of Dinoterb (2-tert-butyl-4,6-dinitrophenol) and Dinoseb (2-sec-butyl-4,6-dinitrophenol) herbicides after 8 hours irradiation period. On the other hand, the explosives, ROX and HMX, were resistant to TiO_2 photocatalytic treatment. The weak reactivity of the explosives with the catalyst could be due to their high chemical stability or to their incapacity to approach the catalyst surface under pH of 7.2 [210].

315

E.5. Concluding Remarks

As discussed in this review, in our opinion, there are several important and potentially existing catalytic systems for decontaminating of various pesticides and organic pollutants. Therefore, such systems can have a major impact on human health and safety for domestic and industrial use. Below is a summary of distinguished TiO_2 based catalyst for specific pollutant removal/degradation:

- Current literature has indicated the anatase crystal structure as the most stable configuration suitable for photodegradation studies [16-21,26,27,28].

- The most common type of reactor employed in laboratory experiments are batch systems where the catalyst of high surface area is suspended in solution [37-40].

- TiO_2/UV combination proved to have a strong impact on the decomposition rate of carbaryl in wastewaters [51]. The aid of various photosensitizers promoted solar photocatalysis for the degradation of carbaryl rinsate to CO_2 [52, 61-63].

- TiO_2-Carbon modified materials provide an active surface for the degradation of carbofuran [64].

- Boron doped TiO_2 catalyst was more effective towards diuron pesticide in terms of degradation and mineralization rates in contrast to the undoped TiO_2 where, the B-doped catalyst is stable and gave reproducible results of mineralization rates up to 75% upon several runs [71].

- Porous TiO_2 modified ceramic shows an excellent photodegradation performance toward atrazine, thiobencarb, dimethoate, lindane, methyl parathion, dipterex, malathion, quinalphos, diazinone, dichlorovos and bentazone with good reproducibility [86, 123, 128-134].

- Au–Pd co-modified TiO_2 nanotube film (Au–Pd–TiO_2) showed photocatalytic activity towards malathion, where its elimination rate increased by 172% when the photocatalyst of the naked TiO_2 nanotube film was replaced by Au–Pd–TiO_2 [127].

- Ag nanoparticles doped TiO_2 nanofibers performed a significant role in photocatalytic performance during the parathion and PCP degradation reactions [139, 194]].

- The photocatalytic activity for 4-chloro-phenol using UV irradiation on P-modified TiO$_2$ was 4.5 times higher than TiO$_2$ alone [182].

- 1% Cs/TiO$_2$ catalyst showed 100% degradation and mineralization of bromoxynil in two hours at basic conditions with fully recyclable and reusable catalyst with no loss of activity [192].

E.6. References

[1] Breffle, W.; Muralidharan, D.; Donovan, R.; Liu, F.; Mukherjee, A,; Jin, Y.; Socioeconomic evaluation of the impact of natural resource stressors on human-use services in the Great Lakes environment: A Lake Michigan case study, Resour. Policy, 2013, 38, 152–161.

[2] Pink, R.M; Water rights in China and India: A human security perspective, Asian Aff., 2016, 43, 19–35, 2016.

[3] Hassan, M.; Zhao, Y.; Xie, B.; Employing TiO2 photocatalysis to deal with landfill leachate: Current status and development, Chem. Eng. J., 2016, 285, 264–275.

[4] Liu, Y.; Liu, F.; Pan, X.; Li, J .; Protecting the environment and public health from pesticides, Environ. Sci. Technol., 2012, 46, 5658–5659.

[5] Broséus, R. et al.; Ozone oxidation of pharmaceuticals, endocrine disruptors and pesticides during drinking water treatment, Water Res., 2009, 43, 4707–4717.

[6] Fujishima, K.; Honda, A.; Fujishima, A.; Honda, K.; Electrochemical Photolysis of Water at a Semiconductor Electrode, Nature,1972, 238, 37.

[7] Zhang, X.; Wang, Y.; Liu, B.; Sang, Y.; Liu, H.; Heterostructures construction on TiO2 nanobelts: A powerful tool for building high-performance photocatalysts, Appl. Catal. B Environ., 2017, 202, 620–641.

[8] Fujishima, A.; Zhang, X.; Tryk, D.; TiO2 photocatalysis and related surface phenomena, Surf. Sci. Rep., 2008, 63, 515–582.

[9] Yu, C.; Zhou, W.; Liu, H.; Liu, Y.; Dionysiou, D.; Design and fabrication of microsphere photocatalysts for environmental purification and energy conversion, Chem. Eng. J., 2016, 287, 117–129.

[10] Garcia-Segura, S.; Brillas, E.; Applied photoelectrocatalysis on the degradation of organic pollutants in wastewaters, J. Photochem. Photobiol. C Photochem. Rev., 2017, 31, 1–35.

[11] Bouadila, S.; Skouri, S.; Kooli, S.; Lazaar, M.; Farhat, A.; Experimental investigation of a new solar air heater with packed-bed latent storage energy, Journées Int. Therm., 2013, 16, 1–5.

[12] Shavisi, Y.; Sharifnia, S.; Zendehzaban,M.; Mirghavami, M.; Kakehazar, S.; Application of solar light for degradation of ammonia in petrochemical wastewater by a floating TiO2/LECA photocatalyst, J. Ind. Eng. Chem., 2014, 20, 2806–2813.

[13] Nottrott, A.; Kleissl, J.; Washom, B.; Energy dispatch schedule optimization and cost benefit analysis for grid-connected, photovoltaic-battery storage systems," Renew. Energy, vol. 55, pp. 230–240, 2013.

[14] Lewis, N.; Toward cost-effective solar energy use, Science (80-.)., 2007, 315, 798–801.

[15] Ani, I.; Akpan, U.; Olutoye, M.; Hameed, B.; Photocatalytic degradation of pollutants in petroleum refinery wastewater by TiO2- and ZnO-based photocatalysts: Recent development, J. Clean. Prod., 2018, 205, 930–954.

[16] Mohammadpour, R.; Influence of energy band alignment in mixed crystalline TiO2 nanotube arrays: Good for photocatalysis, bad for electron transfer, J. Phys. D. Appl. Phys., 2017, 50, 505106.

[17] Kumar, S.; Rao, K.; Comparison of modification strategies towards enhanced charge carrier separation and photocatalytic degradation activity of metal oxide semiconductors (TiO2, WO3 and ZnO), Appl. Surf. Sci., 2017, 391, 124–148.

[18] Wu, B.; Ma, H.; Pan, Z.; Wang, J.; Qu, W.; Wang, B.; Drying and quality characteristics and models of carrot slices under catalytic infrared heating, Int. Agric. Eng. J., 2014, 23, 70–79.

[19] Carey, J.; Lawrence, J.; Tosine, H.; Photodechlorination of PCB's in the presence of titanium dioxide in aqueous Suspensions, Bull. Environ. Contam. Toxicol., 1976, 16, 697–701.

[20] Ye, Y.; Feng, Y.; Bruning, H.; Yntema, D.; Rijnaarts, H.; Photocatalytic degradation of metoprolol by TiO2 nanotube arrays and UV-LED: effects of catalyst properties, operational parameters, commonly present water constituents, and photo-induced reactive species, Appl. Catal. B Environ., 2017, 220, 171–181.

[21] Haoran Dong, H.; Zeng, G.; Tang, L.; Fan, C.; Zhang, C.; He, X.; He, Y.; An overview on limitations of TiO2-based particles for photocatalytic degradation of organic pollutants and the corresponding countermeasures, Water Res., 2015, 79, 128–146.

[22] Zada, A.; Qu, Y.; Ali, S.; Sun, N.; Lu, H.; Yan, R.; Zhang, X .; Jing, L.; Improved visible-light activities for degrading pollutants on TiO2/g-C3N4 nanocomposites by decorating SPR Au nanoparticles and 2,4-dichlorophenol decomposition path, J. Hazard. Mater., 2018, 342, 715–723.

[23] Pan, Z.; Stemmler, E.; JeCho, H.; Fan, W.; LeBlanc, L.; Patterson, H.; Amirbahman, A.; Photocatalytic degradation of 17α-ethinylestradiol (EE2) in the presence of TiO2-doped zeolite, J. Hazard. Mater., 2014, 279, 17–25.

[24] Lee, S.; Park, S.; TiO2 photocatalyst for water treatment applications, J. Ind. Engieneering Chem., 2013, 19, 1761–1769.

[25] Guo, Q.; Zhou, C.; Ma, Z.; Ren, Z.; Fan, H.; Yang, X.; Elementary photocatalytic chemistry on TiO2 surfaces, Chem. Soc. Rev., 2016, 45, 3701–3730.

[26] Chen, X.; Mao, S.; Titanium dioxide nanomaterials: Synthesis, properties, modifications and applications, Chem. Rev., 2007, 107, 2891–2959.

[27] Hu, X.; Tang, C.; Wen, S.; Wu, X.; Long, J.; Yang, X.; Wang, H.; Zhou, L.; Mechanisms underlying degradation pathways of microcystin-LR with doped TiO2 photocatalysis, Chem. Eng. J., 2017, 330, 355–371.

[28] Zhou, X.; Shao, C.; Li, X.; Wang, X.; Guo, X.; Liu, Y.; Three dimensional hierarchical heterostructures of g-C3N4nanosheets/TiO2 nanofibers: Controllable growth via gas-solid reaction and enhanced photocatalytic activity under visible light, J. Hazard. Mater., 2018, 344, 113–122.

[29] Lila Djouadi, L.; Khalaf, H.; Boukhatem, H.; Boutoumi, H.; Kezzime, A.; Santaballa, A.; Canle, M.; Degradation of aqueous ketoprofen by heterogeneous photocatalysis using Bi2S3/TiO2–Montmorillonite nanocomposites under simulated solar irradiation, Appl. Clay Sci., 2018, 166, 27–37.

[30] Ong, W.; Tan, L.; Chai, S.; Yong, S.; Mohamed, A.; Facet-dependent photocatalytic properties of TiO2-based composites for energy conversion and environmental remediation," Chem. Sus. Chem., 2014, 7, 690–719.

[31] Zhuang, J.; Dai, w.; Tian, Q.; Li, Z.; Xie, L.; Wang, X.; Liu, P.; Shi, X.; Wang, D.; Photocatalytic degradation of RhB over TiO2 bilayer films: Effect of defects and their location, Langmuir, 2010, 26, 9686–9694.

[32] Jiang, H.; Li, M.; Liu, J.; Li, X.; Tian, L.; Chen, P.; Alkali-free synthesis of a novel heterostructured CeO2-TiO2 nanocomposite with high performance to reduce Cr(VI) under visible light, Ceram. Int., 2018, 44, 2709–2717.

[33] Friedmann, D.; Mendive, C.; Bahnemann, D.; TiO2 for water treatment: Parameters affecting the kinetics and mechanisms of photocatalysis, Appl. Catal. B Environ., 2010, 99, 398–406.

[34] Carbajo, J.; Bahamonde, A.; Faraldos, M.; Photocatalyst performance in wastewater treatment applications: Towards the role of TiO2 properties, Mol. Catal., 2017, 434, 167–174.

[35] Horikoshi, K.; Serpone, N.; Can the photocatalyst TiO¬2 be incorporated into a wastewater treatment method? Background and prospects, Catal. Today, In Press, 2018.

[36] McCullagh, C.; Skillen, N.; Adams, M.; Robertson, P.; Photocatalytic reactors for environmental remediation: A review, J. Chem. Technol. Biotechnol., 2011, 86, 1002–1017.

[37] Dijkstra, M.; Michorius, A.; Buwalda, H.; Panneman, H.; Winkelman, J.; Beenackers, A.; Comparison of the efficiency of immobilized and suspended systems in photocatalytic degradation, Catal. Today, 2001, 66, 487–494.

[38] Manassero, A.; Satuf, M.; Alfano, O.; Photocatalytic reactors with suspended and immobilized TiO2: Comparative efficiency evaluation, Chem. Eng. J., 2017, 326, 29–36.

[39] Pruden, A.; Ollis, D.; Degradation of chloroform by photoassisted heterogeneous catalysis in dilute aqueous suspensions of titanium dioxide, Environ. Sci. Technol., 1983, 17, 628–631.

[40] Kormann, C.; Bahnemann, D.; Hoffmann, M.; Photolysis of chloroform and other organic molecules in aqueous titanium dioxide suspensions, Environ. Sci. Technol., 1991, 25, 494–500.

[41] Pathirana, H.M.; Maithreepala, R.; Photodegradation of 3,4-dichloropropionamide in aqueous TiO2 suspensions, J. Photochem. Photobiol. A Chem., 1997, 102, 273–277.

[42] McCullagh, C.; Robertson, P.; Adams, M.; Pollard, P.; Mohammed, A.; Development of a slurry continuous flow reactor for photocatalytic treatment of industrial waste water, J. Photochem. Photobiol. A Chem., 2010, 211, 42–46.

[43] Adams, M.; Campbell, I.; Robertson, P.; Novel photocatalytic reactor development for removal of hydrocarbons from water, Int. J. Photoenergy, 2008, 2008, 1–7.

[44] Salu, O.; Adams, M.; Robertson, P.; Wong, L.; McCullagh, C.; Remediation of oily wastewater from an interceptor tank using a novel photocatalytic drum reactor, Desalin. Water Treat., 2011, 26, 87–91.

[45] MiarAlipour, S.; Friedmann, D.; Scott, J.; Amal, R.; TiO2/porous adsorbents: Recent advances and novel applications, J. Hazard. Mater., 2018, 341, 404–423.

[46] Feitz, A.; Boyden, B.; Waite, T.; Evaluation of two solar pilot scale fixed-bed photocatalytic reactors, Water Res., 2000, 34, 3927–3932.

[47] Dionysiou, D.; Rotating disk photocatalytic reactor: development, characterization, and evaluation for the destruction of organic pollutants in water, Water Res., 2000, 34, 2927–2940.

[48] Hamill, N.; Weatherley, L.; Hardacre, C.; Use of a batch rotating photocatalytic contactor for the degradation of organic pollutants in wastewater, Appl. Catal. B Environ., 2001, 30, 49–60.

[49] Peris-Cardells, E.; Terol, J.; Mauri, A.; de la Guardia, M.; Pramauro, E.; Continuous flow photocatalytic degradation of carbaryl in aqueous media, Journal of Environmental Science and Health, Part B, 1993, 28, 431-445

[50] Reddy, K.; Hisanaga, T.; Tanaka , K.; Photodegradation of fungicide triadimefon and pesticide pirimicarb in aqueous TiO2 suspension, Toxicol. Environ. Chem., 1999, 68, 403-412.

[51] Rajeswari, R.; Kanmani, S.; A study on synergistic effect of photocatalytic ozonation for carbaryl degradation, Desalination, 2009, 242, 277–285.

[52] Kuo, W.; Chiang, Y.; Lai, L.; Solar photocatalysis of carbaryl rinsate promoted by dye photosensitization, Dyes and Pigments, 2008, 76, 82–87.

[53] Kanan, M.; Kanan, S.; Patterson H.; Luminescence properties of silver(I)-exchanged zeolite Y and its use as a catalyst to photodecompose carbaryl in the presence of natural organic matter, Res. Chem. Int. 2003, 29, 691-704.

[54] Kanan, S.; Kanan, M.; Patterson, H.; Silver nanoclusters doped in X and mordenite zeolites as heterogeneous catalysts for the decomposition of carbamate pesticides in solution, Res. Chem. Int., 2006, 32, 871-885.

[55] Kanan, S.; Abdo, N.; Khalil, M.; Li, X.; Abu-Yousef, I.; Barilrobert, F.; Patterson, H.; A study of the effect of microwave treatment on metal zeolites and their use as photocatalysts toward naptalam, Appl. Catal. B: Environ., 106, 350-358 (2011).

[56] Kanan, S.; Abu-Yousef, I.; Abdo, N.; Abdel Hamid, A.; Influence of AgY zeolite on the photocatalyticoxidation of pirimicarb, International Journal of Environmental Engineering, 2014, 6, 370-382.

[57] Kanan, S.; Nusri, S.; The effect of silver and silver-platinum doped into 5A zeolite on the degradation of naptalam", Advanced Materials Research, 2014, 856, 43-47.

[58] Ahern, J.; Kanan, S.; Patterson, H., "Heterogeneous Photocatalysis with Nanoclusters of D10 Metal Ions Doped in Zeolites", Comments on Inorganic Chemistry, 35, 59-81 (2015).

[59] Ahern, J.; Kanan, S.; Sara, Z.; Job, T.; Alnaizy, R.; Abu Farha, N.; Patterson, H.; Photocatalysis of fenoxycarb over silver-modified zeolites", Environ. Sci. and Poll. Res., 2015, 22, 3186-3192.

[60] Kanan, S.; Malkawi, A.; Mixed silver–zinc encapsulated zeolite-Y powders toward the photodegradation of aqueous fenoxycarb solutions, Desalination and water treatment, 2017, 100, 281.

[61] Amir, M.; Julkapli, N.; Abd Hamid, S.; Effective adsorption and photodegradation of methyl orange by TiO2-chitosan supported glass plate photocatalysis, Mater. Technol., 2017, 32, 256-264.

[62] Rabbani, M.; Bathaee, H.; Rahimi, R.; Maleki, A.; Photocatalytic degradation of p-nitrophenol and methylene blue using Zn-TCPP/Ag doped mesoporous TiO2 under UV and visible light irradiation, Desalination and Water Treatment, 2016, 57, 25848-25856.

[63] Salgado–Tra´nsito, I.; Jime´nez–Gonza´lez, A.; Ramo´n–Garcı´a, M.; Pineda–Arellano, C.; Estrada–Gasca, C.; Design of a novel CPC collector for the photodegradation of carbaryl pesticides as a function of the solar concentration ratio, Solar energy, 2015, 115, 537–551.

[64] Vishnuganth, M.; Remya, N.; Kumar, M.; Selvaraju, N.; Photocatalytic degradation of carbofuran by TiO2–coated activated carbon: Model for kinetic, electrical energy per order and economic analysis, J. Environ. manage., 2016, 181, 201–207.

[65] Mahalakshmi, M.; Arabindoo, B.; Palanichamy, M.; Murugesan, V.; Photocatalytic degradation of carbofuran using semiconductor oxides, J. Hazard. Mater., 2007, 143, 240–245.

[66] Rui, Z.; Jingguo, W.; Jianyu, C.; Lin, H.; Kangguo, M.; Photocatalytic degradation of pesticide residues with Re3+–doped nano–TiO2, J. Rare Earth, 2010, 28, 353–356.

[67] Reddy, K.; Hisanaga, T.; Tanaka , K.; Photodegradation of fungicide triadimefon and pesticide pirimicarb in aqueous TiO2 suspension, Toxicol. Environ. Chem., 1999, 68, 403-412.

[68] Patel, S.; Yadav, N.; Patel, S.; Evaluation of degradation characteristics of reactive dyes by UV/Fenton, UV/fenton/activated charcoal, and UV/fenton/TiO2 processes: A comparative study, Separation Science and Technology, 2013, 48, 1788-1800.

[69] Malato, S.; Caaceres, J.; Fernaandez–Alba, A.; Piedra, L.; Hernando, M.; Agu–Era, A.; Vial, J.; Photocatalytic treatment of diuron by solar photocatalysis: evaluation of main intermediates and toxicity, Environ. Sci. Technol., 2003, 37, 2516–2524.

[70] Solís, R.; F. Rivas, F.; Martínez–Piernas, A.; Agüera, A.; Ozonation, photocatalysis and photocatalytic ozonation of diuron. Intermediates identification, Chem. Eng. J., 2016, 292, 72–81.

[71] Qui˜nones, D.; Rey, A.; Álvarez, P.; Beltrán, F.; LiPuma, G.; Boron doped TiO2 catalysts for photocatalytic ozonation of aqueous mixtures of common pesticides: Diuron, o–phenylphenol, MCPA and terbuthylazine, Appl. Catal. B: Environ., 2015, 178, 74–81.

[72] Haque, M.; Muneer, M.; Bahnemann, D.; Semiconductor–mediated photocatalyzed degradation of a herbicide derivative, chlorotoluron, in aqueous suspensions, Environ. Sci. Technol., 2006, 40, 4765–4770.

[73] Fenoll, J.; Flores, P.; Hellın, P.; Hernandez, J.; Navarro, S.; Minimization of methabenzthiazuron residues in leaching water using amended soils and photocatalytic treatment with TiO2 and ZnO, J. Environ. Sci., 2014, 26, 757–764.

[74] Strbac, D.; Aggelopoulos, C.; Strbac, G.; Dimitropoulos, M.; Novakovi´c, M.; Iveti´c, T.; Yannopoulos, S.; Photocatalytic degradation of Naproxen andmethylene blue: comparison between ZnO, TiO2 and their mixture, Process Safety and Environmental Protection, 2018, 113, 174–183.

[75] Calıskan, Y.; Yatmaz, H.; Bektas, N.; Photocatalytic oxidation of high concentrated dye solutions enhanced by hydrodynamic cavitation in a pilot reactor, Process Safety and Environ. Prot., 2017, 111, 428–438.

[76] Topkaya, E.; Konyar, M.; Yatmaz, H.; Ozturk, K.; Pure ZnO and composite ZnO/TiO2 catalyst plates: A comparative study for the degradation of azo dye, pesticide and antibiotic in aqueous solutions, J. Coll. Int. Sci. 2014, 430, 6–11.

[77] Athanasekou, C.; Romanos, G.; Katsaros, F.; Kordatos, K.; Likodimos, V.; Falaras, P.; Very efficient composite titania membranes in hybrid ultrafiltration/photocatalysis water treatment processes, J. Memb. Sci., 2012, 392–393, 192–203.

[78] Yixin, Y.; Hongbin, C.; Pai, P.; Hongmiao, B.; Degradation and transformation of atrazine under catalyzedozonation process with TiO2 as catalyst, J. Hazard. Mater., 2014, 279, 444–451.

[79] Yola, M.; Eren, T.; Atar, N.; A novel efficient photocatalyst based on TiO2 nanoparticles involved boron enrichment waste for photocatalytic degradation of atrazine, Chem. Eng. J., 2014, 250, 288–294.

[80] Chatterjee, D.; Mahata, A.; Evidence of superoxide radical formation in the photodegradation of pesticide on the dye modified TiO2 surface using visible light, J. Photochem. Photobiol., 2004, 165, 19–23.

[81] Sacco, O.; Vaiano, V.; Han, C.; Sannino, D.; Dionysiou, D.; Photocatalytic removal of atrazine using N–doped TiO2 supported on phosphors, Appl. Catal. B: Environ., 2015, 164, 462–474.

[82] Granados–Oliveros, G.; Paez–Mozo, E.; Ortega, F.; Ferronato, C.; Chovelon, J.; Degradation of atrazine using metalloporphyrins supported on TiO2 under visible light irradiation, Appl. Catal. B: Environ., 2009, 89, 448–454.

[83] Santacruz–Chávez, J.; Oros–Ruiz, S.; Prado, B.; Zanella, R.; Photocatalytic degradation of atrazine using TiO2 superficially modified with metallic nanoparticles, J. Environ. Chem. Eng.: Part B, 2015, 3, 3055–3061.

[84] Chu, W.; Rao, Y.; Hui, W.; Removal of simazine in a UV/TiO2 heterogeneous system, J. Agric. Food Chem., 2009, 57, 6944–6949.

[85] Konstantinou, I.; Sakellarides, T.; Sakkas, V.; Albanis, T.; Photocatalytic degradation of selected s-triazine herbicides and organophosphorus insecticides over aqueous TiO2 suspensions, Environ. Sci. Technol. 2001, 35, 398-405.

[86] Aragay, G.; Pino, F.; MerkoçI, A.L.; Nanomaterials for Sensing and destroying pesticides, Chem. Rev. 2012, 112, 5317−5338.

[87] Cruz, M.; Gomez, C.; Duran–Valle, C.; Pastrana–Martínez, L.; Faria, J.; Silva, A.; Faraldos, M.; Bahamonde, A.; Bare TiO2 and graphene oxide TiO2 photocatalysts on the degradation of selected pesticides and influence of the water matrix, Appl. Surf. Sci., 2017, 416, 1013–1021.

[88] Malpass, G.; Miwa, D.; Miwa, A.; Machado, S.; Motheo, A.; Photo–Assisted Electrochemical Oxidation of Atrazine on a Commercial Ti/Ru0.3Ti0.7O2 DSA Electrode, Environ. Sci. Technol., 2007, 41, 7120–7125.

[89] Komtchou, S.; Dirany, A.; Drogui, P.; Delegan, N.; El Khakani, M.; Robert, D.; Lafrance, P.; Degradation of atrazine in aqueous solution with electrophotocatalytic process using TiO2–x photoanode, Chemosphere, 2016, 157, 79–88, 157.

[90] Cunff, J.; Tomaši, V.; Wittine, O.; Photocatalytic degradation of the herbicide terbuthylazine: Preparation, characterization and photoactivity of the immobilized thin layer of TiO2/chitosan, J. Photochem. Photobiol. A: Chem., 2015, 309, 22–29.

[91] Cunff, J.; Tomaši, V.; Gomzi, Z.; Photocatalytic degradation of terbuthylazine: Modelling of a batch recirculating device, J. Photochem. Photobiol. A: Chem., 2018, 353, 159–170.

[92] Maurino, V.; Minella, M.; Sordello, F.; Minero, C.; A proof of the direct hole transfer in photocatalysis: The case of melamine, Appl. Catal. A, Gen., 2016, 521, 57–67.

[93] Meia, M.; Dua, Z.; Xub, R.; Chena, Y.; Zhanga, H.; Qua, S.; Photocatalytic degradation of hexazinone and its determination in water via UPLC–MS/MS, J. Hazard. Mater., 2012, 221–222, 100–108.

[94] Evgenidou, E.; Bizani, E.; Christophoridis, C.; Fytianos, K.; Heterogeneous photocatalytic degradation of prometryn in aqueous solutions under UV–Vis irradiation, Chemosphere, 2007, 68, 1877–1882.

 [95] Goutailler, G.; Guillard, C.; Faure, R.; Paissea, O.; Degradation pathway of dicyclanil in water in the presence of titanium dioxide. comparison with photolysis, J. Agri. Food Chem., 2002, 50, 5115–5120.

[96] Macounová, K.; Urban, J.; Krýsová, H.; Krýsa, J.; Jirkovský, J.; Ludvík, J.; Photodegradation of metamitron (4–amino–6–phenyl–3–methyl–1,2,4–triazin–5(4H)–one) on TiO2, J. Photochem. Photobiol. A: Chem. 2001, 140, 93–98.

[97] Kaniou, S.; Pitarakis, K.; Barlagianni, I.; Poulios, I.; Photocatalytic oxidation of sulfamethazine, Chemosphere, 2005, 60, 372–380.

[98] Sakkas, V.; Arabatiz, I.; Konstantinou, I.; Dimou, A.; Albanis, T.; Falaras, P.; Metolachlor photocatalytic degradation using TiO2 photocatalysts, Appl. Catal. B: Environ. 2004, 49, 195–205.

[99] Zhu, X.; Yuan, C.; Bao, Y.; Yang, J.; Wu. Y.; Photocatalytic degradation of pesticide pyridaben on TiO2 particles, J. Mol. Catal. A: Chem., 2005, 229, 95–105.

[100] Oujji, N.; Plantara, G.; Goetz, V.; Ait ichou. I.; 3D Photocatalytic media for decontamination of water from pesticides, Mater. Res. Bull., 2018, 101, 6–11.

[101] Berberidou, C.; Kitsiou, V.; Kazala, E.; Lambropoulou, D.; Kouras, A.; Kosma, C.; Albanis, T.; Poulios, I.; Study of the decomposition and detoxification of the herbicide bentazon by heterogeneous photocatalysis: kinetics, intermediates and transformation pathways , Appl. Catal. B: Environ., 2017, 200, 150–163.

[102] Zhu, X.; Feng. X.; Yuan, C.; Cao, X.; Li, J.; Photocatalytic degradation of pesticide pyridaben in suspension of TiO2: identification of intermediates and degradation pathways, J. Mol. Catal. A: Chem., 2004, 214, 293–300.

[103] Zhu, X.; Yuan, C.; Chen. H.; Photocatalytic degradation of pesticide pyridaben. 3. in surfactant/TiO2 aqueous dispersions, Environ. Sci. Technol., 2007, 47, 263–269.

[104] Azis, M.; Nurwahidah, A.; Wibowo, D.; Nurdin. M.;   Photoelectrocatalyst of Fe co–doped N–TiO2/Ti nanotubes: Pesticide degradation of thiamethoxam under UV–visible lights, Environ. Nanotechnol, Monit. & manag, 2017, 8, 103–111.

[105] Zabar, R.; Komel, T.; Fabjan, J.; Kralj, M.; Trebse. P.; Photocatalytic degradation with immobilised TiO2 of three selected neonicotinoid insecticides: Imidacloprid, thiamethoxam and clothianidin, Chemosphere, 2012, 89, 293–301.

[106] Mir, N.; Khan, A.; Muneer, M.; Vijayalakhsmi, S.; Photocatalytic degradation of a widely used insecticide Thiamethoxam in aqueous suspension of TiO2 : Adsorption, kinetics, product analysis and toxicity assessment, Sci. total environ., 2013, 458–460, 388–398.

[107] Lagunas–Allue, L.; Martinez–Soria, M.; Sanz–Asensio, J.; Salvador, A.; Ferronato, C.;   Chovelon, J.; Photocatalytic degradation of boscalid in aqueous titanium dioxide suspension:

Identification of intermediates and degradation pathways, Appl. Catal. B: Environ. 2010, 98, 122–131.

[108] Lagunas–Allue, L.; Martinez–Soria, M.; Sanz–Asensio, J.; Salvador, A.; Ferronato, C.; Chovelon, J.; Degradation intermediates and reaction pathway of pyraclostrobin with TiO2

Photocatalysis, Appl. Catal. B: Environ. 2014, 115–116, 285–293.

 [109] Herrmann, J.; Guillard, C.; Photocatalytic degradation of pesticides in agricultural used waters, C. R. Acad. Sci. Paris, Se´rie IIc, Chimie: Chem., 2000, 3, 417–422

[110] Zabar, R.; Dolenc, D.; Jerman, T.; Franko, M.; Trebse, P.; Photolytic and photocatalytic degradation of 6–chloronicotinic acid, Chemosphere, 2011, 85, 861–868.

[111] Sud, D.; Kaur, P.; Heterogeneous photocatalytic degradation of selected organophosphate pesticides: A review, Critical Reviews in Environmental Science and Technology, 2012, 42, 2365-2407.

[112] Mak, M.; Hung, S.; Degradation of neat and commercial samples of organophosphate pesticides in illuminated TiO2 suspensions, Toxicol. Environ. Chem., 1992, 36, 155-168.

[113] Atiqur Rahman, M.; Muneer, M.; Photocatalysed degradation of two selected pesticide derivatives, dichlorvos and phosphamidon in aqueous suspensions of titanium dioxide, Desalination, 2005, 181,161–172.

[114] Sivagami, K.; Krishna, R.; Swaminathan, T.; Photo catalytic degradation of pesticides in immobilized bead photo reactor under solar irradiation, Solar Energy, 2014, 103 ,488–493.

[115] Kanan, S.; Kanan, M.; Patterson, H.; Photophysical Properties of Ag(I)-exchanged zeolite A and the photoassisted degradation of malathion, J. Phys. Chem. B, 2001, 105, 7508-7516.

[116] Kanan, S.; Samara, F.; Abu-Yousef, I.A.; Abdo, N.; Tobias, D.; Silver nanoclusters doped in zeolite to decontaminate water resources from the quinalphos pesticide, Res. Chem. Int. 2010, 36, 473-482.

[117] Kanan, S.; Abu-Yousef, I.A.; Abdo, N.; The photodecomposition of phosmet over UV irradiated silver nanoclusters doped in mordenite zeolite" Applied Catalyst B: Environ., 2007, 74, 130-136.

[118] Kanan, S.; Study of argentate, dicyanoargentate, and dicyanoaurate clusters doped in zeolites and the photoassisted degradation of NOx, malathion, carbofuran, and carbaryl. Ph.D. Thesis, The Graduate School, University of Maine, 2000.

[119] Sleiman, M.; Ferronato, C.; Chovelon, J.; Photocatalytic removal of pesticide dichlorvos from indoor Aair: A study of reaction parameters, intermediates and mineralization, Environ. Sci. Technol. 2008, 42, 3018–3024.

[120] Danoeshvar, N.; Hejazi, M.; Rangarangy, B.; Khataee, A.; Photocatalytic degradation of an rganophosphorus pesticide phosalone in aqueous suspensions of titanium dioxide, Journal of Environmental Science and Health, Part B, 2004, 39, 285-296.

[121] Kralj, M.; Cernigoj, U.; Franko, M.; Trebs, P.; Comparison of photocatalysis and photolysis of malathion, isomalathion, malaoxon, and commercial malathion—products and toxicity studies, Water Research, 2007, 41, 4504 – 4514.

[122] Kadam, A.; Dhabbe, R.; Kokate, M.; Gaikwad, Y.; Garadkar, K.; Preparation of N doped TiO2 via microwave–assisted method and its photocatalytic activity for degradation of Malathion, Spectrochimica Acta Part A: Molecular and Biomolecular Spectroscopy, 2014, 133 , 669–676.

[123] Xing, Z.; Zhou, W.; Du, F.; Zhang, L.; Li, Z.; Zhang, H.; Li, W.; Facile synthesis of hierarchical porous TiO2 ceramics with enhanced photocatalytic performance for micropolluted pesticide degradation, ACS Appl. Mater. Interfaces 2014, 6, 16653−16660.

[124] Vela, N.; Calín, M.; Yáñez–Gascóna, M.; Garrido, I.; Pérez–Lucas, G.; Fenoll, J.; Navarro, S.; Photocatalytic oxidation of six pesticides listed as endocrine disruptor chemicals from wastewater using two different TiO2 samples at pilot plant scale under sunlight irradiation, J. Photochem. Photobiol. A: Chem., 2018, 353, 271–278.

[125] Ramos–Delgado, N.; Hinojosa–Reyes, L.; Guzman–Mara, I.; Gracia–Pinilla, M.; Hernandez–Ramireza, A.; Synthesis by sol–gel of WO3/TiO2 for solar photocatalytic degradation of malathion pesticide, Catalysis Today, 2013, 209, 35– 40.

[126] Ramos–Delgado, N.; Gracia–Pinilla, M.; Maya–Treviᷡno, L.; Hinojosa–Reyes, L.; Guzman–Mar, J.; Hernández–Ramírez, A.; Solar photocatalytic activity of TiO2 modified with WO3 on the degradation of an organophosphorus pesticide, J. Hazard. Mater., 2013, 263, 36– 44.

[127] Yu, H.; Wang, X.; Sun, H.; Huo, M.; Photocatalytic degradation of malathion in aqueous solution using an Au–Pd–TiO2 nanotube film, J. Hazard. Mater., 2010, 184, 753–758.

[128] Mir, N.; Haque, M.; Khan, M.; Muneer, M.; Vijayalakshmi, S.; Photocatalytic degradation of herbicide Bentazone in aqueous suspension of TiO2: mineralization, identification of intermediates and reaction pathways, Environ. Technol., 2014, 35, 407-415.

[129] Senthilnathan, J.; Philip, L.; Removal of mixed pesticides from drinking water system by photodegradation using suspended and immobilized TiO2, J. Environ. Sci. and Health, Part B, 2009, 44, 262-270

[130] Jafari, S.; Moussavi, G.; Hossaini, H.; Degradation and mineralization of diazinon pesticide in UVC and UVC/TiO2 process, Desalination and Water Treatment, 2016, 57, 3782-3790.

[131] Nakaoka, Y.; Katsumata, H.; Kaneco, S.; Suzuki, T.; Ohta, K.; Photocatalytic degradation of diazinon in aqueous solution by platinized TiO2, Desalination and Water Treatment, 2010, 13, 427-436.

[132] Sraw, A.; Toor, A.; Wanchoo, R.; Adsorption kinetics and degradation mechanism study of water persistent insecticide quinalphos: for heterogeneous photocatalysis onto TiO2, Desalination and Water Treatment, 2016, 57, 16831-16842.

[133] Chen, H.; Shen, M.; Chen, R.; Dai, K.; Peng, T.; Photocatalytic degradation of commercial methyl parathion in aqueous suspension containing La-doped TiO2 nanoparticles, Environ. Technol., 2011, 32, 1515-1522.

[134] Sakellarides, T.; Sakkas, V.; Lambropoulou, D.; Albanis, T.; Application of solid-phase microextraction (spme) for photocatalytic studies of fenitrothion and methyl parathion in aqueous TiO2 suspensions, Internat. J. Environ. Anal. Chem., 2004, 84, 161-172.

[135] Juang, R.; Chen, C.; Comparative study on photocatalytic degradation of methomyl and parathion over UV–irradiated TiO2 particles in aqueous solutions, Journal of the Taiwan Institute of Chemical Engineers, 2014, 45, 989–995.

[136] Evgenidou, F.; Konstantinou, I.; Fytianos, K.; Poulios, I.; Albanis, T.; Photocatalytic oxidation of methyl parathion over TiO2 and ZnO suspensions, Catalysis Today, 2007, 124, 156–162.

[137] Allard, M.; Merlos, S.; Springer, B.; Cooper, J.; Zhang, G.; Boskovic, D.; Kwon, S.; Nick, K.; Perry, C.; Role of TiO2 anatase surface Mmorphology on organophosphorus interfacial chemistry, J. Phys. Chem. C, In Press, DOI: 10.1021/acs.jpcc.8b08641

[138] Konstantinuou, K.; Sakellarides, T.; Sakkas, E.V.; Albabis, T.; Photocatalytic degradation of selected s–Triazine herbicides and organophosphorus insecticides over aqueous TiO¬2 suspensions, Environ. Sci. Technol., 2001, 35, 398–405.

[139] Li, X.; Wang, F.; Qian, Q.; Liu, X.; Xiao, L.; Chen, Q.; Ag/TiO2 nanofibers heterostructure with enhanced photocatalytic activity for parathion, Mat. Let., 2012, 66, 370–373.

[140] Rengaraj, S.; Li, X.; Tanner, P.; Pan, Z.; Pang, G.; Photocatalytic degradation of methylparathion—An endocrine disruptor by Bi3+–doped TiO2, Journal of Molecular Catalysis A: Chem., 2006, 247, 36–43.

[141] Amalraj, A.; Pius, A.; Photocatalytic degradation of monocrotophos and chlorpyrifos in aqueous solution using TiO2 under UV radiation, J. Water Process Eng., 2015, 7, 94–101.

[142] Affam, A.; Chaudhuri, M.; Degradation of pesticides chlorpyrifos, cypermethrin and chlorothalonil in aqueous solution by TiO2 photocatalysis, J. Environ. Manag., 2013, 130, 160–165.

[143] Sivagami, K.; Vikraman, B.; Krishna, R.; Swaminathan, T.; Chlorpyrifos and endosulfan degradation studies in an annular slurry photo reactor, Ecotoxicol. Environ. Safety, 2016, 134, 327–331.

[144] Negishi, N.; Sano, T.; Hirakawa, T.; Koiwa, F.; Chawengkijwanich, C.; Pimpha, N.; Echavia, G.; Photocatalytic detoxification of aqueous organophosphorus by TiO2 immobilized silica gel, Appl. Catal. B: Environ., 2012, 128, 105– 118.

[145] Gomez, S.; Marchena, C.; Pizzio, L.; Pierella, L.; Preparation and characterization of TiO2/HZSM– 11 zeolite for photodegradation of dichlorvos in aqueous solution, J. Hazard. Mater. 2013, 258–259, 19– 26.

[146] Shankar, M.; Cheralathan, K.; Arabindoo, B.; Palanichamy, M.; Murugesan, V.; Enhanced photocatalytic activity for the destruction of monocrotophos pesticide by TiO2/H, J. Mol. Catal., 2004, 223, 195–200.

[147] Sleiman, M.; Ferronato, C.; Chovelon, J.; Photocatalytic removal of pesticide dichlorvos from indoor air: A study of reaction parameters, intermediates and mineralization, Environ. Sci. Technol. 2008, 42, 3018–3024.

[148] Oancea, P.; Oncescu, T.; The photocatalytic degradation of dichlorvos under solar irradiation, J. Photochem. Photobiol. A: Chem., 2008, 199, 8–13.

[149] Evgenidou, E.; Fytianos, K.; Poulios, I.; Semiconductor–sensitized photodegradation of dichlorvos in water using TiO2 and ZnO as catalysts, Appl. Catal. B: Environ., 2005, 59, 81–89.

[150] Evgenidou, E.; Fytianos, K.; Poulios. I.; Photocatalytic oxidation of dimethoate in aqueous solutions, J. Photochem. Photobiol. A: Chem. 2005, 175, 29–38.

[151] Chen, J.; Wang, D.; Zhu, M.; Gao. Z.; Photocatalytic degradation of dimethoate using nanosized TiO2 powder, Desalination, 2007, 207, 87–94.

[152] Aungpradit, T.; Sutthivaiyakit, P.; Martens, D.; Sutthivaiyakit, S.; Kettrup, A.; Photocatalytic degradation of triazophos in aqueous titanium dioxide suspension: Identification of intermediates and degradation pathways, J. Hazard. Mater., 2007, 146, 204–213.

[153] Li, H.; Li, J.; Yang, Z.; Xu, Q.; Hu, X.; A novel photoelectrochemical sensor for the organophosphorus pesticide dichlofenthion based on nanometer–sized titania coupled with a screen–printed electrode, Anal. Chem. 2011, 83, 5290–5295.

[154] Tabasideh, S.; Maleki, A.; Shahmoradi, B.; Ghahremani, E.; Mckay.G.; Sonophotocatalytic degradation of diazinon in aqueous solution using iron doped TiO2 nanoparticles, Sep. Pur. Technol. 2017, 189, 186–192.

[155] Mirmasoomi, S.; Ghazi, M.; Galedari, M.; Photocatalytic degradation of diazinon under visible light using TiO2/Fe¬2O3 nanocomposite synthesized by ultrasonic–assisted impregnation method, Sep. Purif. Technol., 2017, 175, 418–427.

[156] Hossaini, H.; Mousssavi, G.; Farrokhi, M.; The investigation of the LED–activated FeFNS–TiO2 nanocatalyst for photocatalytic degradation and mineralization of organophosphate pesticides in water, Water Res., 2014, 59, 130–144.

[157] Fang, T.; Yang, C.; Liao, L.; Photoelectrocatalytic degradation of high COD dipterex pesticide by using TiO2/Ni photo electrode, J. Environ. Sci., 2012, 24, 1149–1156.

[158] Wu, R.; Chen, C.; Lu, C.; Hsu, P.; Chen. M.; Phorate degradation by TiO2 photocatalysis: parameter and reaction pathway investigations, Desalination, 2010, 250, 869–875.

[159] Mattsson, A.; Lejon, C.; Stengl, V.; Bakardjieva, S.; Oplustil, F.; Andersson, P.; Osterlund, L.; Photodegradation of DMMP and CEES on zirconium doped titania nanoparticles, Appl. Catal. B: Environ., 2009, 92, 401–410.

[160] Kiselev, A.; Mattson, A.; Andersson, M.; Palmqvist, A.; Osterlund. L.; Adsorption and photocatalytic degradation of diisopropyl fluorophosphates and dimethyl methylphosphonate over dry and wet rutile TiO2, J. Photochem. Photobiol. A: Chem. 2006, 184, 125–134.

[161] Moss, J.; Szczepankiewicz, S.; Park, E.; Hoffmann, M.; Adsorption and Photodegradation of Dimethyl Methylphosphonate Vapor at TiO2 Surfaces, J. Phys. Chem. B 2005, 109, 19779-19785.

[162] Rusu, C.; Yates, Jr., J.; Photooxidation of Dimethyl Methylphosphonate on TiO2 Powder, J. Phys. Chem. B 2000, 104, 12299-12305

[163] Waghe, A.; Kanan, S.M.; Abu-Yousef, I.A.; Jensen, B.; Tripp, C.P.; Infrared study of UV irradiated tungsten trioxide powders containing adsorbed dimethyl methyl phosphonate and trimethyl phosphate, Res. Chem. Int., 2006, 32, 613-623.

[164] Kanan, S.; Tripp, C.P.; Prefiltering strategies for metal oxide based sensors: The use of chemical displacers to selectively dislodge adsorbed organophosphonates from silica surfaces, Langmuir, 2002, 18, 722-728.

[165] El-Sayed, Y.; Abu-Farha, N.; Kanan, S.; Synthesis and characterization of porous WO3– SnO2 nanomaterials: An infrared study of adsorbed pyridine and dimethyl methylphosphonate, Vibrational Spectroscopy, 2014, 75, 78-85.

[166] Kanan, S.M.; Tripp ,C.P.; Synthesis, FTIR studies and sensor properties of WO3 powders, Current Opinion in Solid State & Materials Science, 2007, 11, 19–27.

[167] Bougheloum, C.; Messalhi, A.; Photocatalytic degradation of benzene derivatives on TiO2 catalyst, Physics Procedia, 2009, 2, 1055–1058.

[168] Nitoi, I.; Oancea, P.; Cristea, I.; Constsntin, L.; Nechifor, G.; Kinetics and mechanism of chlorinated aniline degradation by TiO2 photocatalysis, J. of Photochem. Photobiol A: Chem., 2015, 298, 17–23.

[169] Nsib, M.; Maayoufi, A.; Moussa, N.; Tarhouni, N.; Massouri, A.; Houas, A.; Chevalier, Y.; TiO2 modified by salicylic acid as a photocatalyst for the degradation of monochlorobenzene via Pickering emulsion way, J. Photochem. Photobiol. A: Chem., 2013, 251, 10–17.

[170] Chang, S.; Chung, W.; Yu, S.; Lee, S.; Photocatalytic degradation of 4-chlorophenol using a Ag/TiO2/Fe3O4 composite under UV-A irradiation, Desalination and Water Treatment, 2015, 54, 3646-3653.

[171] Barakat, M.; Al-Hutailah, R.; Qayyum, E.; Rashid, J.; Kuhn, J.; Pt nanoparticles/TiO2 for photocatalytic degradation of phenols in wastewater, Environ. Technol., 2014, 53, 137-144.

[172] Elghniji, K.; Salem, S.; Mosbah, M.; Elaloui, E.; Moussaoui, Y.; Detoxification of 4-chlorophenol in TiO2 sunlight system: effect of raw and treated solution on seed germination and plants growth of various sensitive vegetables, Toxicol. Environ. Chem., 2014, 96, 869-879.

[173] Ortega–Liébana, M.; Sánchez–López, E.; Hidalgo–Carrillo, J.; Marinas, A.; Marinas, J.; Urbano, F.; A comparative study of photocatalytic degradation of 3–chloropyridine under UV and solar light by homogeneous (photo–Fenton) and heterogeneous (TiO2) photocatalysis, Appl. Catal. B: Environ., 2012, 127, 316–322.

[174] Ye, M.; Chen, Z.; Wang, W.; Shen, J.; Ma, J.; Hydrothermal synthesis of TiO2 hollow microspheres for the photocatalytic degradation of 4–chloronitrobenzene. J. Hazard. Mater., 2010, 184, 612–619.

[175] Yu, B.; Zeng, J.; Gong, L.; Zhang, M.; Zhang, L.; Chen, X.; Investigation of the photocatalytic degradation of organochlorine pesticides on a nano–TiO2 coated film, Talanta, 2007, 72, 1667–1674.

[176] Salaeh, S.; Perisic, D.; Biosic, M.; Kusic, H.; Babic, S.; Stangar, U.; Dionysiou, D.; Bozic, A.; Diclofenac removal by simulated solar assisted photocatalysis using TiO2–based zeolite catalyst; mechanisms, pathways and environmental aspects, Chem. Eng. J., 2016, 304, 289–302.

[177] Cao, Y.; Chen, J.; Huang, L.; Wang, Y.; Hou, Y.; Lu, Y.; Photocatalytic degradation of chlorfenapyr in aqueous suspension of TiO2, J. Mol. Catal. A: Chem., 2005, 233, 61–66.

[178] Cao, Y.; Yi, L.; Huang, L.; Hou, Y.; Lu, Y.; Mechanism and pathways of chlorfenapyr photocatalytic degradation in aqueous suspension of TiO2, Environ. Sci. Technol., 2006, 40, 3373–3377.

[179] Irmak, S.; Kusvuran, E.; Erbatur, O.; Degradation of 4–chloro–2–methylphenol in aqueous solution by UV irradiation in the presence of titanium dioxide, Appl. Catal. B: Environ., 2004, 54, 85–91.

[180] Venkatachalam, N.; Palanichamy, M.; Arabindoo, B.; Murugesan, V.; Enhanced photocatalytic degradation of 4–chlorophenol by Zr4+ doped nano TiO2, J. Mol. Catal. A: Chem., 2007, 266, 158–165.

[181] Wang, Y.; Pan, Z.; Qin, D.; Bai, S.; Peng, Q.; Preparation of Ce–TiO2 /carbon aerogel electrode and its performance in degradation of 4–chlorophenol, J. Rare Earths, 2018, 36, 374–378.

[182] Elghniji, K., Hentati, O., Mlaik, N., Mahfoudh, A. and Ksibi, M. (2012). Photocatalytic degradation of 4–chlorophenol under P–modified TiO2/UV system: Kinetics, intermediates, phytotoxicity and acute toxicity. Journal of Environmental Sciences, 24(3), pp.479–487.

[183] Choi, K.; Park, S.; Park, B.; Jung, J.; Recyclable Ag–coated Fe3O4@TiO2 for efficient photocatalytic oxidation of chlorophenol. Surf. Coat. Technol., 2017, 320, 240–245.

[184] Kuan, C.; Chang, S.; Schroeder, S.; Fenton–like oxidation of 4–chlorophenol: homogeneous or heterogeneous?, Indust. Eng. Chem. Res., 2015, 54, 8122–8129.

[185] Abeish, A.; Ang, M.; Znad, H.; Enhanced solar–photocatalytic degradation of combined chlorophenols using ferric ions and hydrogen peroxide, Indust. Eng. Chem. Res., 2014, 53, 10583–10589.

[186] Selli, E.; Bianchi, C.; Pirola, C.; Cappelletti, G.; Ragaini, V.; Efficiency of 1,4 dichlorobenzene degradation in water under photolysis, photocatalysis on TiO¬2 and sonolysis, J. Hazard. Mat., 2008, 153, 1136–1141.

[187] Liu, L.; Chen, F.; Yang, F.; Chen, Y.; Crittenden, J.; Chem. Eng. J., 2012, 181–182, 189–195.

[188] Liu, L.; Chen, F.; Yang, F.; Stable photocatalytic activity of immobilized Fe0/TiO2/ACF on composite membrane in degradation of 2,4–dichlorophenol, Sep. Pur. Technol., 2009, 70, 173–178.

[189] Kamble, S.; Deosarkar, S.; Sawant, S.; Moulijn, J.; Pangarkar, V.; Photocatalytic degradation of 2,4–dichlorophenoxyacetic acid using concentrated solar radiation: batch and continuous operation, Indust. Eng. Chem. Res., 2004, 43, 8178–8187.

[190] Melian, E.; Diaz, O.; Rodrigues, J.; Arana, J.; Pena, J.; Adsorption and photocatalytic degradation of 2,4–dichlorophenol in TiO2 suspensions. Effect of hydrogen peroxide, sodium peroxodisulphate and ozone, Appl. Catal. A: Gen., 2013, 455, 227–233.

[191] Jia, J.; Zhang, S.; Wang, P.; Wang, H.; Degradation of high concentration 2,4 dichlorophenol by simultaneous photocatalytic–enzymatic process using TiO2/UV and laccase, J. Hazard. Mater. 2012, 205–206, 150–155.

[192] Maddila, S.; Lavanya, P.; Jonnalagadda. S.B.; Degradation, mineralization of bromoxynil pesticide by heterogeneous photocatalytic ozonation, J. Indust. Eng. Chem., 2015, 24, 333–341.

[193] Wang, Y.; Zhang, Y.; Zhao, G.; Tian, H.; Shi, H.; Zhou, T.; Cu2O/TiO2/carbon aerogel electrode and its efficient electrosorption–assisted visible light photocatalytic degradation of 2,4,6–trichloropheno, Appl. Mater. Interf. 2012, 4, 3965–3972.

[194] Yu, L.; Yang, X.; Ye, Y.; Peng, X.; Wang, D.; Silver nanoparticles decorated anatase TiO2 nanotubes for removal of pentachlorophenol from water, J. Coll. Interf. Sci. 2015, 453, 100–106.

[195] Su, K.; Ai, Z.; Zhang, L.; Efficient visible light–driven photocatalytic degradation of pentachlorophenol with Bi2O3/TiO2−xBx, J. Phys. Chem., 2012, 116, 17118–17123.

[196] Khan, S.; Han, C.; Khan, H.; Boccelli, D.; Nadagouda, M.; Dionysiou, D.; Efficient degradation of lindane by visible and simulated solar light–assisted S–TiO2/peroxymonosulfate process: Kinetics and mechanistic investigations, J. Mol. Catal. A: Chem., 2017, 428, 9–16.

[197] Zhou, Q.; Ding, Y.; Xiao, J.; Liu, G.; Guo, X.; Investigation of the feasibility of TiO2 nanotubes for the enrichment of DDT and its metabolites at trace levels in environmental water samples, J. Chromat. A. 2007, 1147, 10–16.

[198] Maddila, S.; Rana, S.; Pagadala, R.; Maddila, S.; Vasam, C.; Jonnalagadda, S.; Ozone-driven photocatalyzed degradation and mineralization of pesticide, Triclopyr by Au/TiO2, J. Environ. Sci. and Health, Part B, 2015, 50, 571-583.

[199] Kanan, S.; Samara, F.; Dioxins and furans: A review from chemical and environmental perspectives, Trends in Environmental Analytical Chemistry, 2018, 17, 1-13.

[200] Samara, F.; Al Shamsi, M.; Kanaan, F.; Kanan, S.; "Photocatalytic UV degradation of 2, 3, 7, 8-tetrachlorodibenzofuran in the presence of silver zeolite, Res. Chem Intermed., 2017, https://doi.org/10.1007/s11164-017-2913-8.

[201] Samara, F.; Jermani, E.; Kanan, S.; Photocatalytic UV-degradation of 2,3,7,8-tetrachlorodibenzo-p-dioxin (TCDD) in the presence of silver doped zeolite", Arabian Journal of Chemistry, In Press, http://dx.doi.org/10.1016/j.arabjc.2014.12.009

[202] Zaleska, A.; Hupka, J.; Wiergowski, M.; Biziuk, M.; Photocatalytic degradation of lindane, p,p`–DDT and methoxychlor in an aqueous environment, J. Photochem. Photobiol. A: Chem., 2000, 135, 213–220.

[203] Farre, M.; Franch, M.; Malato, S.; Ayllon, J.; Peral, J.; Domenech, X.; Degradation of some biorecalcitrant pesticides by homogeneous and heterogeneous photocatalytic ozonation, Chemosphere, 2005, 58, 1127–1133.

[204] Ananpattarachai, J.; Kajitvichyanukul, P.; Photocatalytic degradation of p,p′-DDT under UV and visible light using interstitial N-doped TiO2, Journal of Environmental Science and Health, Part B, 2015, 50, 247-260.

[205] Lin, Y.; Tseng, S.; Huang, W.; Wu, W.; Enhanced photocatalysis of pentachlorophenol by metal-modified Titanium (IV) Oxide, J. Environ. Sci. and Health, Part B, 2006, 41, 1143-1158.

[206] San, N.; HatipoǦlu, A.; ÇInar, Z.; Effect of molecular properties on the photocatalytic degradation rates of dichlorophenols and dichloroanilines in aqueous TiO2 suspensions, Toxicol. Environ. Chem., 2004, 86, 147-162.

[207] Schneider, J.; Matsuoka, M.; Takeuchi, M.; Zhang, J.; Horiuchi, Y.; Anpo, M. Bahnemann, D.; Understanding TiO2 Photocatalysis: Mechanisms and Materials, Chemical Reviews, 2014, 114, 9919-9986.

[208] Saravanan, P.; Pakshirajan, K.; Saha, P.; Degradation of phenol by TiO2–based heterogeneous photocatalysts in presence of sunlight, J. Hydro–Environ. Res., 2009, 3, 45–50.

[209] Naeem, K.; Ouyang, F.; Influence of supports on photocatalytic degradation of phenol and 4–chlorophenol in aqueous suspensions of titanium dioxide, J. Environ. Sci. 2013, 25, 399– 404.

[210] Perchet, G.; Merlina, G.; Revel, J.; Hafidi, M.; Richard, C.; Pinelli, C.; Evaluation of a TiO2 photocatalysis treatment on nitrophenols and nitramines contaminated plant wastewaters by solid–phase extraction coupled with ESI HPLC–MS, J. Hazard. Mater., 2009, 166, 284–290.

[211] Turki, A.; Guillard, C.; Dappozze, F.; Ksibi, Z.; Berhault, G.; Kochkar, H.; Phenol photocatalytic degradation over anisotropic TiO2 nanomaterials: Kinetic study, adsorption isotherms and formal mechanisms, Appl. Catal. B: Environ., 2015, 163, 404–414.

[212] Tolosana–Moranchel, A.; Anderson, J.; Casas, J.; Faraldos, M.; Bahamonde, A.; Defining the role of substituents on adsorption and photocatalytic degradation of phenolic compounds, J. Environ. Chem. Eng. 2017, 5, 4612–4620.

[213] Garcia–Munoz, P.; Carbajo, J.; Faraldos, M.; Bahamonde, A.; Photocatalytic degradation of phenol and isoproturon: effect of adding an activated carbon to titania catalyst, J. Photochem. Photobiol. A: Chem. 2014, 287, 8–18.

[214] Carbajo, S.; Jimenez, M.; Miralles, S.; Malato, S.; Faraldos, M.; Bahamonde, A.; Study of application of titania catalysts on solar photocatalysis: Influence of type of pollutants and water matrices, Chem. Eng. J., 2016, 291, 64–73.

[215] Morales–Mejia, J.; Almanza, R.; Gutierrez, F.; Solar photocatalytic oxidation of hydroxy phenols in a CPC reactor with thick TiO2 films, Energy Procedia. 2014, 57, 597–606.

[216] Lin, J.; Sopajaree, K.; Jitjanesuwan, T.; Lu, M.; Application of visible light on copper- doped titanium dioxide catalyzing degradation of chlorophenols, Sep. Purif. Technol. 2018, 191, 233–243.

[217] Zhao, B.; Meleb, G.; Pio, P.; Li, J.; Palmisano, L.; Vasapollo, G.; Degradation of 4–nitrophenol (4–NP) using Fe–TiO2 as a heterogeneous photo–Fenton catalyst, J. Hazard. Mater., 2010, 176, 569–574.

[218] Ksibi, M.; Zemzemi, A.; Boukchina, R.; Photocatalytic degradability of substituted phenols over UV irradiated TiO2, J. Photochem. Photobiol. A: Chem., 2003, 159, 61–70.

[219] Shen, X.; Zhu, L.; Liu, G.; Yu, H.; Tang, H.; Enhanced photocatalytic degradation and selective removal of nitrophenols by using surface molecular imprinted titania, Environ. Sci. Technol. 2008, 42, 1687–1692.

[220] Herrera–Melian, J.; Martin–Rodriguez, A.; Ortega–Mendez, A.; Arana, J.; Dona–Rodriguez, J.; Perez–Pena, J.; Degradation and detoxification of 4–nitrophenol by advanced oxidation technologies and bench–scale constructed wetlands, J. Environ. Manag., 2012, 105, 53–60.

APPENDIX F. SYNTHESIS, STRUCTURE, AND PHOTOPHYSICAL PROPERTIES OF A 3D NETWORK WITH GOLD DICYANIDE DONORS COORDINATED TO AZA[5]HELICENE VIOLOGEN ACCEPTORS

F.1 Introduction

Viologens are redox active, strong electron accepting diquaternary salts of 4,4'-bipyridine with the ability to form ion-pair charge transfer complexes (IPCT) with donors such as dicyanoaurate. Charge transfer properties of IPCT can be applied in photochromic and electrochromic devices.[1–4] The photoreduction properties of viologens have been known for several years with applications as herbicides, photocleaving agents, and electronic devices. However, the photophysical and photochemical properties of viologens are mostly unexplored.[5] Phenyl-viologens such as 1,1'-bis-(2,4-dinitrophenyl)-4,4'-bipyridinium (DNP^{2+}) have shown desirable optical and electronic properties due to extended π conjugation.[6,7] The π-π stacking interactions of phenyl viologens are being explored in chemistry and biology due to its effect on the photophysical properties of 3D networks.[8] In conjunction, dicyanoaurate (I) complexes are also of interest as they form one of the most stable two-coordinate complexes, with reports of high stability constants as well as potential applications in semiconductor materials and photonic devices.[9,10] Dicyanoaurate(I) has also unique geometric and charge-transfer properties as the d^{10} Au(I) metal center favors aurophilic interactions and aggregation of $[Au(CN)_2^-]^{n-}$, which allow tuning of the optical properties.[7,11]

Due to their strong electron accepting potential, viologens are luminescence quenchers of triplet metal-to-ligand charge transfer (MLCT) luminescence in complexes containing Au(I). In our previous studies, we observed low energy phosphorescence from a 3D network consisting of DNP^{2+} coupled with dicyanoaurate(I) dimers (**Figure F.1**).[7] These results were surprising given that DNP^{2+} is non-luminescent in its free state. The observed luminescence in this complex revealed unique photophysical properties that were attributed to an IPCT transition arising from the heavy atom effect due to gold-viologen orbital overlap.[7,12] It would be interesting to study the photochemical interaction of other methylated phenyl viologens which possess extended π conjugation and are luminescent in the free state with dicyanoaurate(I). 5,10-dimethyl-5,10-diaza[5]helicene bistetrafluoroborate viologen was synthesized a few years ago and the synthetic route has recently been optimized.[5,12] In addition, it is one of the few viologens known which has chirality due to the helical aromatic heterocycle.[5,13] It was shown that this compound has energy holding abilities and is a good electron transfer contender due to its V_e being greater than V_h (electronic coupling for electron and hole respectively).[14] The conductivity spectra and refractive index of this viologen highlighted its ability of high intra/inter molecular charge transfer within the crystal and ability to yield significant outputs with low input.

In our current study, we extend our previous work on methyl viologen (MV^{+2}) systems by synthesizing 5,10-dimethyl-5,10-diaza[5]helicene (heli[5]viologen (7^{2+}) and coupling it with two molecules of $[Au(CN)_2]^-$ to form complex **8** as shown in **Figure F.1**. We report the synthesis and characterization of the N,N-dimethylaza[5]helicene dicyanoaurate (Au heli-viologen) complex using nuclear magnetic resonance (NMR). The crystal structure of Au heli-viologen was determined by single crystal X-ray diffraction. We studied the optical properties of this complex using temperature variable photoluminescence, diffuse reflectance spectroscopy (DRS), and Stern-Volmer analysis. Density Functional Theory (DFT) calculations were performed to assist with interpretation of the experimental data.
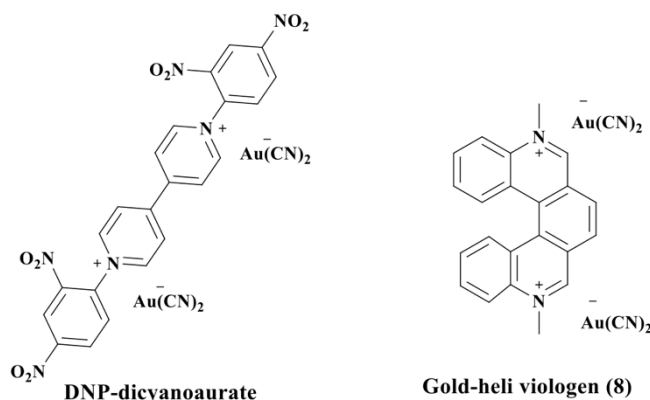

DNP-dicyanoaurate   **Gold-heli viologen (8)**

Figure F.1. Previously studied DNP^{2+} viologen complex with dicyanoaurate and complex **8**, Au heli-viologen (5,10-diazadimethyl[5]helicene viologen complexed with dicyanoaurate)

F.2 Experimental

Synthetic procedures.

General procedure. All reagents were purchased from Sigma-Aldrich and Fisher Scientific and used directly without further purification. All products were purified with silica-gel flash chromatography or preparative HPLC. HPLC was performed on a Gilson analytical to semi-preparative system using Kinetex 5 µm EVO C18 100Å 4.6 x 150 mm for analytical and Kinetex 5 µm EVO C18 100Å 21.1 x 150 mm for preparative purpose. Products were characterized by ^{1}H and ^{13}C NMR and mass spectrometry. NMR characterization results and *J* values were compared with published results. ^{1}H and ^{13}C NMR spectra were recorded on Agilent/Varian 400 MHz and 101 MHz NMR spectrometer respectively. Mass spectra were recorded using a Synapt G2 Q-TOF ESI mass spectrometer. Mass spectra for all reported compounds can be found in Appendix G.

       Synthesis of bis-1,2-tributylstannyl ethylene (2). Tributylstannyl acetylene (328 mg, 1 mmol) & tributylstannyl hydride (291 mg, 1 mmol) were added to a vial with AIBN (3.3 mg, 0.02 mmol). The mixture was heated and stirred at 100 ºC for 6 hrs. Water was added to the reaction mixture and the product was extracted with four aliquots

of methylene chloride and dried over Na_2SO_4. The solvent was evaporated under reduced pressure yielding **2**. This product was used in the following step without further purification. Yield: 549 mg (90%). **¹H NMR (400 MHz, CDCl₃)** δ 6.89 (s, 2H), 1.46-1.64 (m, 12H), 1.25-1.44 (m, 12H), 0.80-0.98 (m, 30H) ppm.

Synthesis of (E)-1,2-di(quinoline-3-yl)ethene (4).

Stille Coupling. 3-Bromoquinoline (**1**) (131 mg, 0.63 mmol) and compound **2** (194 mg, 0.32 mmol) were added to a vial purged with N_2. Tris(dibenzylideneacetone)dipalladium (Pd(0) catalyst, 5 mol%) & 2-dicyclohexylphosphino-2',4',6'-triisopropylbiphenyl (Xphos, 0.2 eq.) were added to the reaction vial, followed by addition of dry toluene (4 mL) under N_2. The reaction mixture was heated at 110 °C for 2 days. The solvent was evaporated under reduced pressure and the crude product was purified with flash chromatography using 70%:30% ethyl acetate:hexane mixture with 1% triethylamine to get (E)-1,2-Di(quinoline-3-yl)ethene. Yield: 51 mg (57%).

Hiyama-Heck Coupling. A mixture of triethoxyvinylsilane (**3**) (0.43 g, 2.25 mmol) and sodium hydroxide (0.5 M, 18 mL) was added to a 40 mL pressure vial, followed by addition of 3-bromoquinoline (**1**) (0.75 g, 3.60 mmol) & palladium acetate (0.5 mol%). The reaction vial was sealed with a heat resistant teflon resistant screw cap and the mixture was stirred at 140 °C for 6 hrs. After cooling, the green precipitate was filtered and washed with 10:1 ethyl acetate:chloroform. The solvent was evaporated under vacuum. Yield: 0.46 g (91%). **¹H NMR (400 MHz, CDCl₃)** δ 9.19 (d, 2H, *J*=2.1 Hz), 8.25 (d, 2H, *J*=2.1 Hz), 8.11 (d, 2H, *J*=8.4 Hz), 7.86 (d, 2H, *J*=8.0 Hz), 7.72 (ddd, 2H, *J*=8.3,7.0,0.9 Hz), 7.58 (ddd, 2H, *J*=8.1, 6.7, 0.9 Hz), 7.47 (s, 2H) ppm. **¹³C NMR (101 MHz, DMSO-d⁶)** δ 175.40, 151.16,149.62,145.85, 137.60, 130.34, 130.07, 128.96, 127.61, 116.79 ppm. **HRMS (TOF MS ES+)** m/z calculated for $C_{20}H_{15}N_2$ ([M-H]⁺) 283.1235, found 283.1231

Synthesis of 5,10-diaza[5]helicene (5).
Compound **4** (0.6 g, 2.1 mmol) was dissolved in ethyl acetate (500 mL) in a round bottom flask. A condenser was attached to the top and the setup was mounted inside an RPR-100 photoreactor on a stir-plate. The mixture was stirred and irradiated at 350 nm for 7 hrs. The crude product was purified with silica-gel chromatography using 70%:30% ethyl acetate:hexane. Yield: 0.43 g (73%). **¹H NMR (400 MHz, CDCl₃)** δ 9.46 (s, 2H), 8.65 (dd, 2H, *J*=8.4, 1.2 Hz), 8.29 (dd, 2H, *J*=8.3, 1.3 Hz), 8.14 (s, 2H), 7.76 (ddd, 2H, *J*=8.3, 7.0, 1.3 Hz), 7.44 (ddd, 2H, *J*=8.4, 7.0, 1.3 Hz) ppm. **¹³C NMR (101 MHz, CDCl₃)** δ 152.53, 145.88, 129.71, 129.48, 129.43, 128.17, 127.32, 127.26, 125.61, 124.38 ppm. **HRMS (TOF MS ES+)** m/z calculated for $C_{20}H_{13}N_2$ ([M-H]⁺) 281.1079, found 281.1070. Benzo-[b]-1,8-diaza[4]-helicene (**6**) was recovered as a side-product. Yield: 0.11 g (19%) (ESI)

Synthesis of dimethylaza[5]helicene (7) (bis-tetrafluoroborate-7a or dichloride salt-7b).
To trimethyl oxonium tetrafluoroborate (Meerwein's salt, 0.356 g, 2.39 mmol) in a 40 mL scintillation vial was added anhydrous methylene chloride (100 mL) under N_2. 5,10-diaza[5]helicene (**5**) (0.223 g, 0.80 mmol) in anhydrous methylene chloride (20 mL) was then added to the vial under N_2. The vial was stirred under N_2 for 24 hrs. Methylene chloride was removed under

vacuum. The dried yellow solid was triturated with warm 90% ethanol. The crude (**7a**) was further purified with preparative HPLC using 5% to 15% acetonitrile in 10 minutes. Yield: 233 mg (60%). DOWEX 1×8 200-400 mesh ion-exchange resin (*Acros*) (11.25 g) was loaded onto a column and washed with methanol followed by equilibration with 50% aqueous ethanol. Compound **7a** (225 mg, 0.46 mmol) dissolved in acetonitrile (0.5 mL) was loaded into the column. The column was washed with 50% aqueous ethanol. The fractions were concentrated and reloaded on the column and collected two more times. Combined fractions were concentrated under reduced pressure to yield the product (**7b**). Yield: 167 mg (95%).

7a- **^{1}H NMR (400 MHz, CD$_3$CN)** δ 10.04 (d, 2H, *J*=2.2 Hz), 8.72 (d, 2H, *J*=8.5 Hz), 8.67 (d, 2H, *J*=1.5 Hz), 8.57 (d, 2H, *J*=8.5 Hz), 8.24 (ddd, 2H, *J*=8.7, 7.4, 1.3 Hz), 7.88 (ddd, 2H, *J*=8.3, 7.3, 1.0 Hz), 4.82 (s, 6H) ppm. **^{13}C NMR (101 MHz, CD$_3$CN)** δ 154.82, 136.93, 135.12, 133.74, 131.78, 131.06, 129.86, 129.32, 127.33, 120.34, 47.60 ppm. **HRMS (TOF MS ES+)** m/z calculated for C$_{20}$H$_{15}$N$_2$ ([M]$^{+2}$) 155.0735, found 155.0731

7b- **^{1}H NMR (400 MHz, CD$_3$OD)** δ 10.54 (d, 2H, *J*=2.2 Hz), 8.86 (d, 2H, *J*=8.4 Hz), 8.82 (d, 2H, *J*=1.2 Hz), 8.75 (d, 2H, *J*=8.7 Hz), 8.28 (ddd, 2H, *J*=8.6, 7.3, 1.3 Hz), 7.92 (ddd, 2H, *J*=8.2, 7.3, 1.0 Hz), 4.99 (s, 6H) ppm. **^{13}C NMR (101 MHz, CD$_3$OD)** δ 155.89, 137.21, 135.33, 133.99, 132.12, 130.97, 130.46, 129.73, 127.63, 120.59, 47.12 ppm. **HRMS (TOF MS ES+)** m/z calculated for C$_{20}$H$_{15}$N$_2$ ([M]$^{+2}$) 155.0735, found 155.0735

Synthesis of Au heli-viologen (8). To a solution of N,N-Dimethylaza[5]helicene dichloride (**7b**) (40 mg, 0.104 mmol) in water (30 mL), potassium dicyanoaurate (60 mg, 0.21 mmol) in water was added while stirring. The precipitate was filtered after 10-12 hours and solvent was slowly evaporated to complete the precipitation of N,N-Dimethylaza[5]helicene dicyanoaurate (**8**). Yellow solid was dried under reduced pressure and used for crystallization. Yield- 49 mg (58%).

Crystallization. Au heli-viologen (Complex **8**) (10 mg) was dissolved in ethanol (0.2 mL) in a 2 mL scintillation vial. This vial was covered with porous aluminum foil and placed in a 20 mL scintillation vial containing cyclohexane (2 mL). This closed system was kept inside the fume hood for 8 to 9 days. Small crystals formed through slow vapor diffusion. Results were reproduced with methanol as a solvent and n-hexane as anti-solvent.[15]

^{1}H NMR (400 MHz, CD$_3$OD) δ 10.49 (d, 2H, *J*=2.2 Hz), 8.89 (d, 2H, *J*=8.8 Hz), 8.80 (d, 2H, *J*=2.1 Hz), 8.75 (d, 2H, *J*=9.0 Hz), 8.29 (ddd, 2H, *J*=8.6, 7.5, 1.1 Hz), 7.95 (ddd, 2H, *J*=8.6, 7.5, 1.1 Hz), 4.97 (s, 6H) ppm. **^{13}C NMR (101 MHz, D$_2$O)** δ 153.67, 135.70, 134.10, 133.08, 130.69, 129.96, 129.93, 128.96, 128.51, 126.43, 119.03 ppm.

Crystallography. A small yellow block-like crystal of Au heli-viologen (**8**) having dimensions 0.057 x 0.063 x 0.092 mm^3 was secured to a Mitegen cryomount using Paratone oil. Single crystal reflection data were collected on a Rigaku Oxford Diffraction (ROD) Synergy-S X-ray diffractometer equipped with a HyPix-6000HE hybrid photon counting (HPC) detector. The data were collected at 100 K using Mo K$_{\alpha1}$ radiation from a data collection strategy calculated using CrysAlis^{Pro} which was also responsible for unit cell determination, initial indexing, data collection, frame integration, Lorentz-polarization corrections and final cell

parameter calculations.[16] A numerical absorption correction via face indexing was performed using the SCALE3 ABSPACK algorithm integrated into CrysAlis[Pro].[17] The crystal structure was solved via intrinsic phasing using ShelXT and refined using *olex2.refine* within the Olex2 graphical user interface.[18–20] The structural model's space group was unambiguously verified by PLATON.[21] Structural refinement of the reflection data for **8** resulted in the identification of electron density peaks associated with a highly disordered interstitial CH_2Cl_2 molecule that could not be satisfactorily modeled. This minor impurity may have been trapped during screening of solvents for crystallozation. The data were treated using the SQUEEZE routine in PLATON, then refined on F^2 to acceptable levels.[22] The final structural refinement included anisotropic temperature factors on all non-hydrogen atoms and hydrogen atoms were attached via the riding model at calculated positions using appropriate HFIX commands. The crystallographic and refinement data for Au heli-viologen is listed in **Table F.1**. Crystallographic data for this paper has been deposited with the Cambridge Crystallographic Data Centre with the CCDC number 1558366. This data can be obtained free of charge from the Cambridge Crystallographic Data Centre via www.ccdc.cam.ac.uk/data_request/cif.

Spectroscopy studies. Steady-state photoluminescence scans were collected between 298 K and 10 K. Spectra were taken with a Model Quantamaster-1046 photoluminescence spectrophotometer from Photon Technology International using a 75 W xenon arc lamp combined with two excitation monochromators and one emission monochromator. A photomultiplier tube at 800 V was used as the emission detector. The solid samples were mounted on a copper plate using non-emitting copper-dust high vacuum grease. All scans were collected under vacuum with a Janis ST-100 optical cryostat. Infrared spectra were collected on solid samples at 298 K using a Perkin Elmer FT-IR Spectrum Two equipped with a Universal Attenuated Total Reflectance (UATR) accessory and a LiTaO3 MIR detector. Diffuse reflectance spectra were collected on solid samples at 298 K. The light source was a Mikropack DH-2000 deuterium and halogen light source coupled with an Ocean Optics USB4000 detector. Scattered light was collected with a fiber optic cable. Spectra was referenced with polytetrafluoroethylene. Data was processed using SpectraSuite 1.4.2_09.

Stern-Volmer quenching experiments. For quenching experiments, **7^{2+}** was used as the quencher. After determining proper quencher concentration ranges, the quenching experiment performed using the $[Au(CN)_2]^-$ sample solutions. A stock solution of 5 x 10^{-4} M $K[Au(CN)_2]$ was first prepared, and then 1 mL of stock solution was distributed among all quenching vials. The quencher solution was then added to the quenching vials in increments of 50 uL. The contents of each vial were then transferred to cuvettes and the emission spectrum of each sample was measured separately. Emission scans were conducted on a Jobin Yvon Systems Fluorolog 3 Spectrofluorometer. The excitation monochromator was referenced to a secondary detector, and the emission monochromator was calibrated to a water Raman peak to ensure the accuracy of scans.

Molecular modelling. All geometry parameters were determined using Gaussian '16 software (Gaussian Inc.) with the University of Maine Advanced Computing Group.[23] All ground state and excited state calculations were performed using density functional theory (DFT) and time-dependent density functional theory (TD-DFT) calculations using the M06 meta-hybrid functional[24,25] with

the CEP-31G(d) basis set employed for all atoms.[26,27] XRD structures were used as initial structural input. From the structural data we have developed a neutral model that is composed of two 7^{2+} units bridged by a dimer $[Au(CN)_2]_2^{-2}$ and capped with terminal $[Au(CN)_2]^-$ monomer units. This model contains all subunits present within the crystal structure. Isodensity representations of molecular orbitals were generated using GaussView 5.0 software (Gaussian Inc.). MOs were generated and visualized using the Avogadro 1.2.0 software program.[28]

F.3 Results and discussion

Synthesis. In order to access the Au heli-viologen (**8**), two different salts of 7^{2+} were made as shown in **Figure F.2**. Initially, a stepwise synthetic route was used to access compound **4** via a Wittig reaction in four steps from quinoline-3-carbaldehyde.[13] A palladium catalyzed route was eventually preferred over the stepwise route to increase efficiency and yield. Stille coupling with 3-bromoquinoline and **2** using Pd(0) catalyst and Xphos ligand produced relatively low yield (57%) of the desired compound **4**. Pd(II) catalyzed Hiyama-Heck cross-coupling was explored with triethoxyvinylsilane to get better scalability and higher yield (91%).[5]

5,10-diaza[5]helicene (**5**) was made by photocyclization of **4** in a photoreactor (350 nm), which was equipped with a magnetic stir plate, and cooling fan to minimize the heating. Methylation of **5** with trimethyloxonium tetrafluoroborate under nitrogen produced the BF$_4$ salt of heli[5]viologen (**7a**) which was purified with preparative HPLC. Due to the limited solubility of **7a** in aqueous solvents, the tetrafluoroborate counterion was exchanged for chloride counterions using DOWEX ion-exchange resin. The chloride heli-viologen (**7b**) showed high solubility in aqueous solvents and was further reacted with potassium dicyanoaurate to produce gold-coupled viologen, **8** in powder form. The powder was dried and used for luminescence experiments and crystallization via vapor diffusion method. The crystallization conditions via a vapor diffusion method for Au heli-viologen (**8**) were optimized and methanol:n-hexane and ethanol:cyclohexane were used as solvent:anti-solvent to get single crystals for X-ray diffraction analysis.[15]
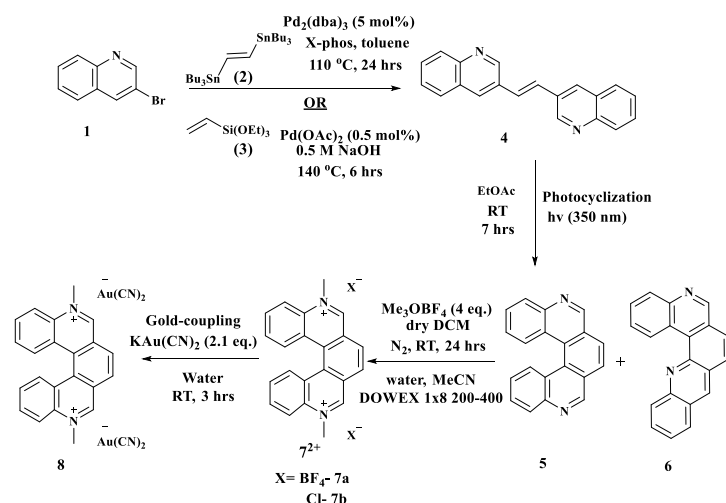
Figure F.2. Overall synthetic scheme.

Single Crystal X-Ray Diffraction. The solid state structure of Au heli-viologen crystallized in the centrosymmetric monoclinic space group *C2/c* and contained one viologen dication and two [Au(CN)$_2$]$^-$ anions on general positions as the elements of the asymmetric unit (**Figure F.3**). When looking into the *bc*-plane of the unit cell, one of the [Au(CN)$_2$]$^-$ anions lies perpendicular to this plane (and parallel to the *a*-axis) at a distance of 3.3773(6) Å between the Au(I) atom of the dicyanoaurate anion and the centroid of the aromatic ring sitting at the turn of the right-handed helical viologen. Typically, dicyanoaurate anions are linear with N-Au-N angles approaching 180°; however within the structure of Au heli-viologen, the [Au(CN)$_2$]$^-$ anion lying above the turn of the helicate deviates from linearity, showing an N-Au-N angle of 174.0(3)°.[29] Such a deviation from linearity can be rationalized upon the application of symmetry to the asymmetric unit. After applying crystallographic symmetry, this dicyanoaurate anion dimerizes with itself and supports the formation of a bond between the monovalent gold atoms at a distance of 3.3098(11) Å, a value on par with those published in a previous report.[30] As a direct consequence of the binding of the neighboring, symmetry-equivalent [Au(CN)$_2$]$^-$ anions to one another, their dimerization imparts some structural rigidity as evidenced by the smaller size of the thermal parameters of the dimer's constituent gold, carbon and nitrogen atoms.
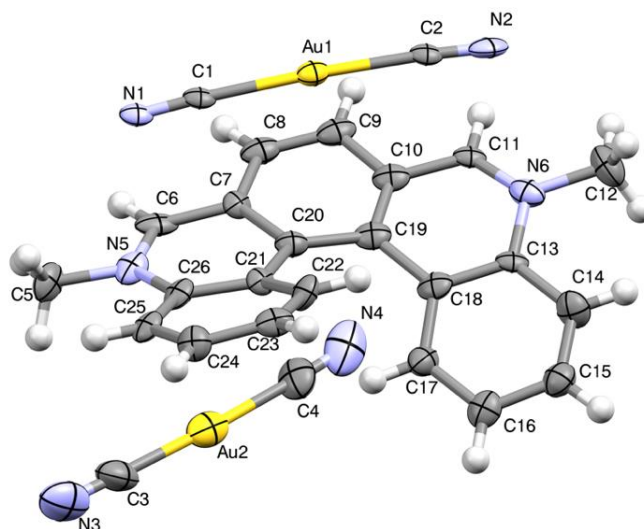
345

Figure F.3. Asymmetric unit elements of Au heli-viologen containing a viologen dication and two [Au(CN)$_2$]$^-$ anions. Ellipsoids shown at 50% probability.

Projections of the asymmetric unit along the *b*-axis demonstrated strong one-dimensional overlap between the dimerized [Au(CN)$_2$]$^-$ anions and the nearly-planar region of the viologen dications parallel to that axis. Such an orientation of these moieties relative to one another within the solid state structure may provide evidence for the onset of interesting spectroscopic properties. Despite the potential for the dicyanoaurate anion located above the turn of the helical viologen in concert with its propensity to dimerize upon the application of crystallographic symmetry to generate interesting spectroscopic features, the second [Au(CN)$_2$]$^-$ anion in the asymmetric unit does not dimerize upon the application of crystallographic symmetry. Unlike the anion in the asymmetric unit which does dimerize, the second anion has much more linear geometry as evidenced by its N-Au-N angle of 176.5(5)°. Thermal parameters for the second dicyanoaurate anion also demonstrate more thermal motion as evidenced by the larger anisotropic displacement ellipsoids for its constituent gold, carbon and nitrogen atoms. Between the anion and the helical viologen, the closest contact occurred between the centroid of the phenyl at the turn in the helix and N4 from the terminal nitrile at a distance of 3.351(19) Å. This distance suggests the onset of a potential dipole-dipole interaction given the positioning of the electron-rich nitrile relative to the electron-deficient phenyl ring of the dication.[31] Also, given the less intimate molecular orbital overlap between this latter dicyanoaurate and the planar surface of the viologen, suggests that unlike the former [Au(CN)$_2$]$^-$, the latter is more spectroscopically innocent.

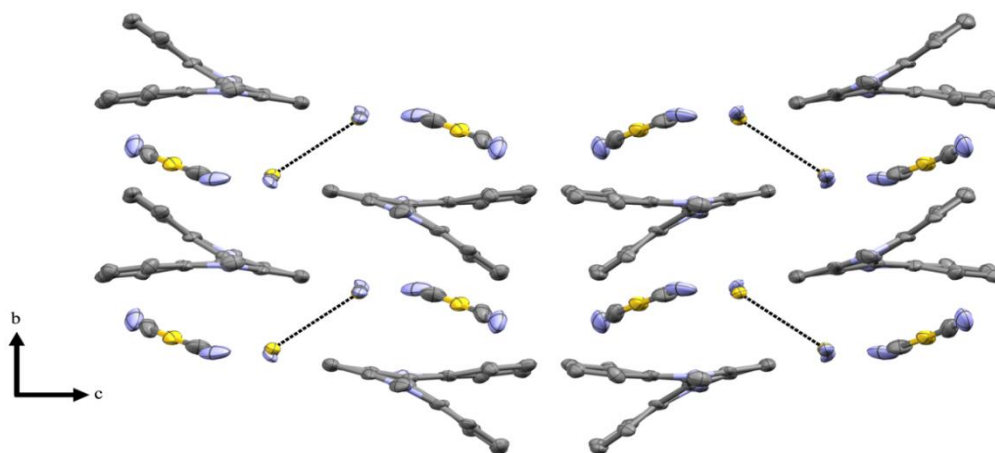**Figure F.4**. View along the *a*-axis of Au heli-viologen crystal. The dotted lines show dimer interactions among adjacent

[Au(CN)$_2$]$^-$ anions.

Compound	Au heli-viologen
CCDC Code	1558366
Formula	C26H18Au2N6
Formula weight	808.41
Temp.	100(2)
Space group	C2/c
a, Å	13.7875(4)
b, Å	12.4750(3)
c, Å	28.7102(8)
α, deg	90.00
β, deg	91.977(3)
γ, deg	90.00
volume, Å^3	4935.2(2)
Z	8
Density (calculated), mg/m^3	2.176
μ, mm^{-1}	11.903
Scan	ω scan
θ range for data collection, deg	6.68-50.06
Reflections measured	4339
Independent observed reflns.	4338
Independent reflns. [I>2σ]	4082
Data/restraints/parameters	4338/38/273
R_{int}	0.0244
Final R Indices [I>2σ]	R$_1$ = 0.0593, wR$_2$ = 0.1471
R Indices (all data)	R$_1$ = 0.0620, wR$_2$ = 0.1481
Goodness-of-fit on F^2	1.009

[a] R = R_I = $\sum|F_o|-|F_c||/\sum|F_o|$ for observed data only. R$_w$ = wR_2 = $\{\sum [w(F_o{}^2 - F_c{}^2)^2]/ \sum [w(F_o{}^2)^2]\}^{1/2}$ for all data.

Table F.1. Crystal refinement data of Au heli-viologen. Select bond lengths and angles available in Table G.1 and G.2.[a]

347

Analysis of the bond distances within the different $[Au(CN)_2]^-$ anions as a function of their being free or dimerized in the solid state also revealed subtle differences (**Figure F.4**). Within the dicyanoaurate anion that dimerizes, the bond distances between the nitriles and the Au(I) were measured at distances of 2.007(16) and 2.011(15) Å while those in the free anion were measured at 1.98(2) and 1.94(2) Å respectively. The nitrile distances from the different anions also revealed differences as those from the dimerized anion were measured at 1.09(2) and 1.132(19) Å while their analogues from the free $[Au(CN)_2]^-$ revealed distances of 1.12(3) and 1.17(3) Å between the constituent carbon and nitrogen atoms. Such a difference can be hypothesized on the basis of dimerization between the neighboring dicaynoaurate anions upon the application of symmetry. Electron density is donated from the nitrile into the corresponding Au-C bond, resulting in a shortening of the former and a lengthening of the latter. This build-up of electron density on the monovalent Au atom, in concert with the nearby positioning of a symmetry-related anion, supports bond formation between the gold atoms. Relevant bond distances within the free dicyanoaurate anion are similar to those reported in the literature as no intramolecular donation of electron density to support Au-Au bond formation occurs.[29]

Infrared Spectroscopy. Au heli-viologen (**8**) is a coordination polymer, where a dominant vibrational feature is the cyanide stretch. We show the IR vibrational spectra of this region in **Figure G.13**. The $v_s(C\equiv N)$ of the gold(I) dicyanide anions are observed at 2,140 cm^{-1}, 2,152 cm^{-1}, 2,160 cm^{-1}, and 2,165 cm^{-1}, indicating that the CN ligands are slightly inequivalent throughout the crystal motif. This split is in agreement with the structural data which shows the presence of monomer $[Au(CN)_2]^-$ and dimer $[Au(CN)_2]_2^{-2}$ units. For oligomer units of metal cyanides, the $v_s(C\equiv N)$ vibrational mode moves to lower energies as the oligomer size increases due to the increased electron density of the CN π^* LUMO.[32] In keeping with this, we have assigned the bands at 2,140 cm^{-1} and 2,152 cm^{-1} to the $v_s(C\equiv N)$ vibration modes of the dimers and the 2,160 cm^{-1} and 2,165 cm^{-1} bands to the vibrational modes of the monomer subunits.

Photophysical Studies. To investigate the absorption of Au heli-viologen, we have performed diffuse reflectance measurements of solid microcrystalline samples of both Au heli-viologen (**8**) and 7^{2+} at 298 K (**Figure F.5**). Solid samples of gold coordinated 7^{2+} are yellow in color and absorb strongly in the UV. As seen in the spectra, the absorption falls off sharply around 475 nm with an optical absorption edge of 2.39 eV. This edge is slightly more variable for the gold free 7^{2+} which slowly tappers off through the visible range and is identical to previous reports of MV^{2+} which are assigned to a $\pi \to \pi^*$ state.[5] Introduction of $[Au(CN)_2]^-$ results in few changes in the DRS spectra in comparison to 7^{2+}. The appearance of higher energy bands at 268 nm not observed in the gold free 7^{2+} are assigned to a metal to ligand charge transfer (MLCT) localized to the $[Au(CN)_2]^-/[Au(CN)_2]_2^{-2}$ subunits consistent with reports elsewhere.[33] The majority of the band remains a $\pi \to \pi^*$ state of the 7^{2+}.
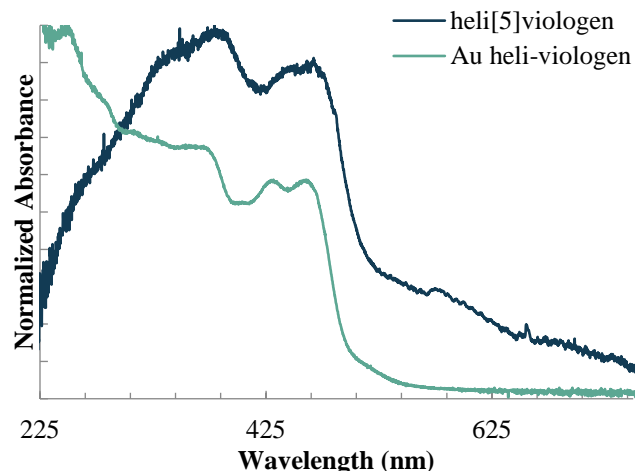
Figure F.5. Solid state DRS absorption spectrum of solid samples of Au heli-viologen and MV^{2+} at 298 K converted via Kubelka-Monk.

As an aromatic cation, 7^{2+} is well equipped to accept electrons from the electron rich gold(I) dicyanide anions as reported for other viologen like molecules.[7] To probe this we have performed temperature variable photoluminescence measurements of microcrystalline samples of Au heli-viologen between 298 K and 10 K. The spectra are shown in **Figure F.6** and are overlaid to demonstrate the change in peak shape and relative intensity with respect to temperature. We observe that the excitation spectrum of Au heli-viologen (**8**) consists of two bands: one high energy band at 375 nm, and one low energy band at 470 nm. A shift in the relative intensity towards the high energy band is observed upon temperature change. No significant shift in the position of either excitation band is observed at lower temperatures. At room temperature, compound **8** in microcrystalline form shows one broad triplet emission band at 580 nm ($\tau_{298\ K}$ = 1.01 μs, $\tau_{78\ K}$ = 1.12 μs). At lower temperatures the relative emission intensity increases and a second, lower-energy band appears at 608 nm. This band first appears at 129 K, and does not shift during cooling. Time-dependent measurements show much shorter lifetime of this band ($\tau_{78\ K}$ = 130 ns) in comparison to that of the band at 580 nm. Based on previous reports of 7^{2+} the data reported here, the 580 nm band is assigned to a triplet $\pi\rightarrow\pi^*$ localized to 7^{2+}. The emission band observed at 608 nm is a new feature was not observed in previous reports of 7^{2+}. The both the lifetime and wavelength of this band are too long for cation $S_1\rightarrow S_0$ emission. Instead these values better fit expected values for $[Au(CN)_2]^{-2}$ emission. We have observed similar behavior in $Au(CN)_2^-/DNP^{+2}$ structures where low temperature emission is dominated by $[Au(CN)_2]^{-2}$ bands but quenched at 298 K.[7] The absence of $[Au(CN)_2]^{-2}$ emission above 129 K indicates quenching by 7^{2+} at high temperatures. In this case we belive an $[Au(CN)_2]^{-2}$ excited state electron from initial $S_1\rightarrow S_0$ absorption is transferred to the lowest S_1 of the 7^{2+} (**Figure F.7**).
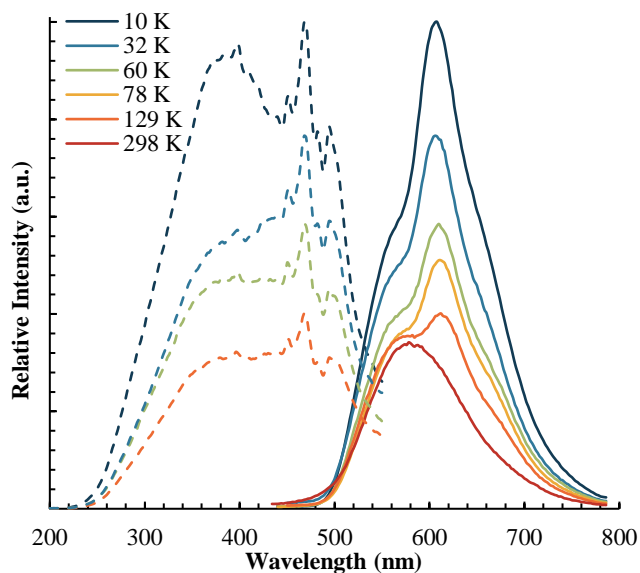
Figure F.6. Luminescence spectra of Au heli-viologen between 10 K and 298 K. Excitation (dashed) and emission (solid).
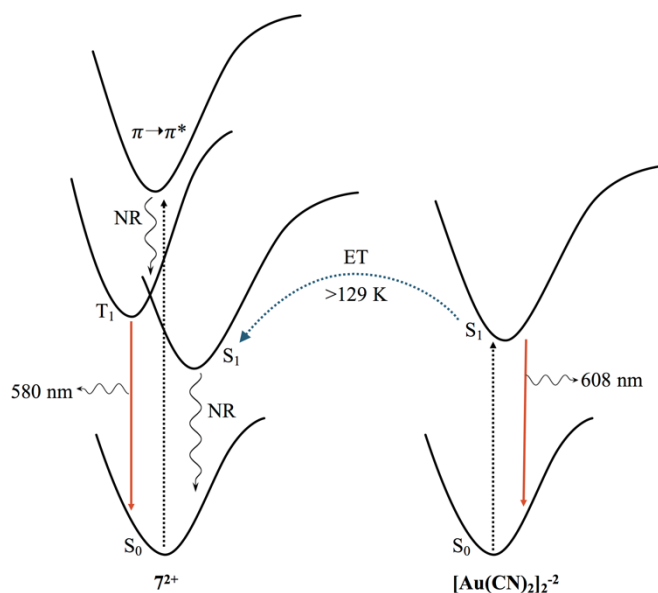

Figure F.7. Energy diagram of emission pathways for Au heli-viologen. At higher temperatures the 7^{2+} emission by $T_1{\rightarrow}S_0$ is favored along with quenching of $[Au(CN)_2]^{-2}$ via the excited S_1 to $\mathbf{7^{2+}}$ S_1. At low temperatures (<129 K) electron transfer is absent resulting in $[Au(CN)_2]^{-2}$ $S_1{\rightarrow}S_0$ emission. S_0, ground state; S_1, first excited state; T_1, first triplet state; NR, nonradiative decay; ET, electron transfer.

Electron Transfer Analysis. An analysis of this system was performed via Stern-Volmer and a Rehm-Weller to support the proposed electron transfer. First, a Stern-Volmer analysis was performed in order to examine the nature of $\mathbf{7^{2+}}$ quenching of $[Au(CN)_2]^-$, specifically to determine if the observed quenching is due to electron transfer or resonance.[34] First, the ground state absorption spectra of the components were compared to the combined mixture. **Figure F.8** shows that the absorption spectrum of

350

a mixture of 7^{2+} and potassium dicyanoaurate is the simple sum of the two component absorption spectra. The lack of an additional absorption band in the mixed spectrum indicates that no ground state electronic interaction occurs between the two species. From this observation, we conclude that no static quenching occurs in this system.
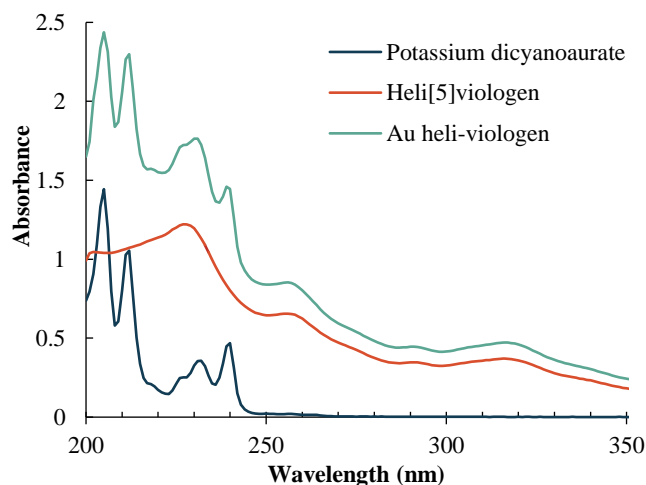

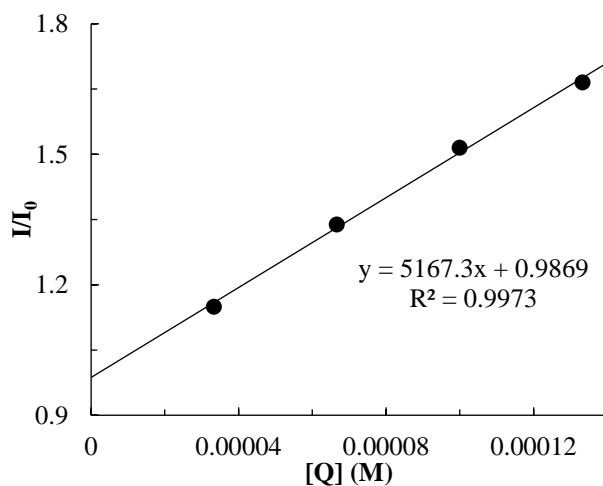**Figure F.8**. Absorption spectra of potassium dicyanoaurate, heli[5]viologen, and Au heli-viologen in methanol (5 x 10^{-4} M).

Figure F.9. Stern-Volmer plot for aqueous Au heli-viologen.

While our previous experiment indicates no ground-state quenching, we further investigated the possibility of quenching in the excited-state. The effect of 7^{2+} as a dynamic quencher of $[Au(CN)_2]^-$ photoluminescence was investigated by measuring the photoluminescence of a series of 7^{2+}/dicyanoaurate solutions. Luminescence intensity associated with $[Au(CN)_2]^-$ was observed to decrease as the concentration of 7^{2+} was increased. Since we observe photoluminescence quenching upon addition of 7^{2+}, this data can be fit to the Stern-Volmer equation to further analyze the photophysical kinetics of the system. **Figure F.9** shows the Stern-Volmer plot constructed for this experiment. From this plot a K_{SV} value can be determined (**K_{SV} = 5170 M^{-1}).** The data show that quenching is observed for this system. This indicates that there is a significant interaction between gold dicyanoaurate species

and 7^{2+} during the photophysical excitation and relaxation process. This observation provides further support for our assignment of the emission band observed at 608 nm as a $[Au(CN)_2]^-\rightarrow 7^{2+}$ electron transfer.

The Rehm-Weller Equation[35] can be used to support the proposed electron transfer by determining whether the process is thermodynamically favorable.

$$\Delta G_{ET} = (E_{ox} - E_{red}) - E_s - e_o^2/\varepsilon_a$$

In the Rehm-Weller Equation shown above, ΔG_{ET} is the free energy change associated with the electron transfer process, E_{red} and E_{ox} are the reduction potential of the viologen 7^{2+} acceptor and oxidation potential of the $[Au(CN)_2]_2^{2-}$ donor respectively, E_s represents the energy of the singlet state energy at 78 K (average of the lowest energy excitation band and highest energy emission band), and e_o^2/ε_a is taken as the attraction that the ion pair experiences.[12,36] We have calculated the E_{ox} (1.74 eV) via DFT by taking the difference in energy between an optimized structure of $[Au(CN)_2]_2^{2-}$ and $[Au(CN)_2]_2^-$. For the Au heli-viologen, ΔG_{ET} is therefore calculated as: ((1.74 + 0.22) - 2.32 - 0.15) = -0.51 eV, indicating the electron transfer is spontaneous. This calculated free energy change supports an electron transfer process as a feasible explanation for the observed quenching system.

Computational Modelling. DFT calculations were performed to interpret the photophysical changes and emission spectra of Au heli-viologen upon excitation. A neutral model of gold(I) dicyanide coordinated to 7^{2+}, shown in **Figure F.10**, was developed containing both $[Au(CN)_2]^-$ and $[Au(CN)_2]_2^{-2}$ subunits. Calculated ground state geometry parameters, Table S3 (ESI), are in good agreement with experimental values with short Au···Au distances supportive of aurophilic interactions. Calculations at the $[Au(CN)_2]_2^{-2}$ center accurately predict a short Au···Au distance of 3.435 Å compared to an experimental value of 3.310 Å. The close contact distance between the CN^- anion and the N^+ cation of the phenyl (3.155 Å) is slightly shorter than the experimental value of 3.216 Å. We attribute this shortened distance to the lack of surrounding $[Au(CN)_2]^-$ ions normally present. The loss of surrounding anions causes our model to overly rely on the central electron rich $[Au(CN)_2]_2^{-2}$ dimer to balance the cationic viologen ion.

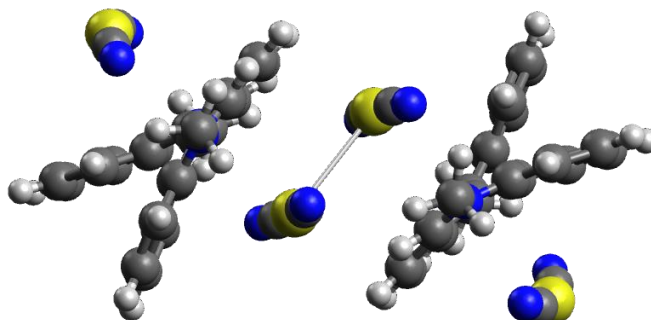**Figure F.10.** DFT M06/CEP-31G(d) calculated ground state of $[Au(CN)_2]^-/[Au(CN)_2]_2^{-2}$ coordinated 7^{2+}. Close Au···Au distance (3.435 Å) shown.

TD-DFT calculated UV-vis spectra, **Figure G.14**, show agreement of our model with the experimental UV-Vis results with both having strong absorption bands at energies higher than 500 nm. An excited state at 399 nm is predicted with a strong oscillator strength of 0.0132. This excited state energy aligns with our experimental luminescence excitation value of 400 nm. The highest contributing molecular orbital transition calculations performed for this excited state are shown in **Figure F.11 (**complete list of contributions summarized and illustrated in **Table G.5** and **Figure G.15**). TD-DFT calculations predict that two general types of electron transitions occur upon excitation at 399 nm. The first centers on the electron donating MOs (HOMO-9, and HOMO-11) which are primarily composed of the 7^{+2} π^* with minor contribution from the neighboring $[Au(CN)_2]^-$ anion. The electron accepting MO (LUMO) is composed of the 7^{2+} π^* and clearly represents a $\pi \rightarrow \pi^*$ transition. In the second case, the electron donating MO (HOMO) is exclusively composed of the dimerized $[Au(CN)_2]_2^{-2}$ subunit with no contribution from the neighboring 7^{+2} cations. This molecular orbital calculated transition is clearly an electronic transfer and demonstrates the emissive quenching of $[Au(CN)_2]^-$ by the viologen in the solid state observed in the experimental photophysical data.
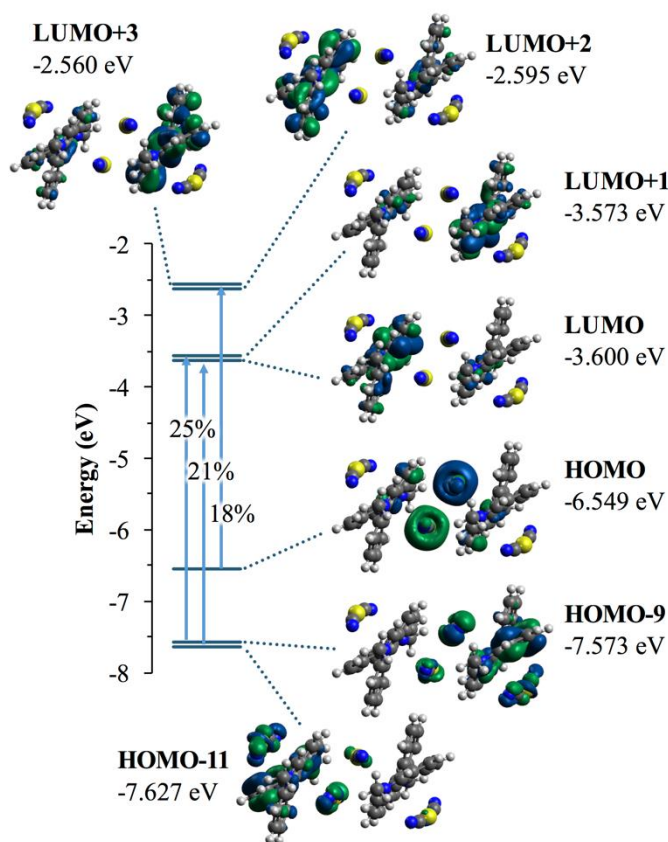

Figure F.11. TD-DFT M06/CEP-31G(d) energy diagram calculated for Au heli-viologen at 399 nm excitation for top 3 transitions. Transition percent contributions are noted.

F.4 Conclusions

Here we report for the first time the synthesis of a 3D network Au heli-viologen. The structure, characterized by single crystal X-ray diffraction, was found to consist of $[Au(CN)_2]^-$ dimers and monomers trapped within $\mathbf{7^{2+}}$ units. Photophysical studies show that at 298 K this complex emits at 580 nm via a triplet $\pi\rightarrow\pi^*$ transition localized to the $\mathbf{7^{2+}}$. Cooling to low temperatures results in a new emission band at 608 nm. Lifetime measurements and DFT calculations indicate that this new singlet band is the appearance of $[Au(CN)_2]_2^{-2}$ emission. The lack of this emission at temperatures higher than 129 K indicates that quenching occur from $\mathbf{7^{2+}}$. Stern-Volmer and Rehm-Weller analysis of this transition supports our assignment by revealing that quenching of $[Au(CN)_2]_2^{-2}$ by $\mathbf{7^{2+}}$ involves the transfer of an electron between ion pairs. Study of further 3D networks involving better electron donors (such as dicyanoargentate coupled to MV^{2+}) will provide insight into the electron-transfer phenomenon investigated here.

F.5 Notes and references

1   T. Nagamura, S. Muta and K. Shiratori, *Chem. Phys. Lett.*, 1995, **238**, 353–358.

2   T. Nagamura and K. Sakai, *J. Chem. Soc. Faraday Trans. 1 Phys. Chem. Condens. Phases*, 1988, **84**, 3529–3537.

3   T. Nagamura, *Pure Appl. Chem.*, 1996, **68**, 1449–1454.

4   D. Cummins, G. Boschloo, M. Ryan, D. Corr, S. N. Rao and D. Fitzmaurice, *J. Phys. Chem. B*, 2000, **104**, 11449–11459.

5   X. Zhang, E. L. Clennan, N. Arulsamy, R. Weber and J. Weber, *J. Org. Chem.*, 2016, **81**, 5474–5486.

6   A. S. Abouelwafa, V. Mereacre, T. S. Balaban, C. E. Anson and A. K. Powell, *CrystEngComm*, 2010, **12**, 94–99.

7   A. S. Abouelwafa, C. E. Anson, A. Hauser, H. H. Patterson, F. Baril-Robert, X. Li and A. K. Powell, *Inorg. Chem.*, 2012, **51**, 1294–1301.

8   D. L. Nelson and M. M. Cox, *Lehninger Principles of Biochemistry*, Macmillan, 5th edn., 2010.

9   A. G. Sharpe, *Acadmic Press London*.

10   D. Chasseau, P. Guionneau, M. Rahal, G. Bravic, J. Gaultier, L. Ducasse, M. Kurmoo and P. Day, *Synth. Met.*, 1995, **70**, 945–946.

11   D. B. Leznoff, B.-Y. Xue, R. J. Batchelor, F. W. B. Einstein and B. O. Patrick, *Inorg. Chem.*, 2001, **40**, 6026–6034.

12   X. Zhang, E. L. Clennan and N. Arulsamy, *Org. Lett.*, 2014, **16**, 4610–4613.

13   C. Bazzini, S. Brovelli, T. Caronna, C. Gambarotti, M. Giannone, P. Macchi, F. Meinardi, A. Mele, W. Panzeri, F. Recupero, A. Sironi and R. Tubino, *European J. Org. Chem.*, 2005, 1247–1257.

14   A. Irfan, M. Assiri and A. G. Al-Sehemi, *Org. Electron. physics, Mater. Appl.*, 2018, **57**, 211–220.

15   B. Spingler, S. Schnidrig, T. Todorova and F. Wild, *CrystEngComm*, 2012, **14**, 751–757.

16   R. O. Diffraction, 2017.

17   Rigaku Oxford Diffraction, 2017.

18   G. M. Sheldrick, *Acta Crystallogr. Sect. A Found. Adv.*, 2015, **71**, 3–8.

19   L. J. Bourhis, O. V. Dolomanov, R. J. Gildea, J. A. K. Howard and H. Puschmann, *Acta Crystallogr. Sect. A Found. Adv.*, 2015, **71**, 59–75.

20   O. V. Dolomanov, L. J. Bourhis, R. J. Gildea, J. A. K. Howard and H. Puschmann, *J. Appl. Crystallogr.*, 2009, **42**, 339–341.

21   A. L. Spek, *Acta Crystallogr. Sect. D Biol. Crystallogr.*, 2009, **65**, 148–155.

22   A. L. Spek, *Acta Crystallogr. Sect. C Struct. Chem.*, 2015, **71**, 9–18.

23   Frisch, M. J.; Trucks, G. W.; Schlegel, H. B.; Scuseria, G. E.; Robb, M. A.; Cheeseman, J. R.; Scalmani, G.; Barone, V.; Mennucci, B.; Petersson, G. A.; Nakatsuji, H.; Caricato, M.; Li, X.; Hratchian, H. P.; Izmaylov, A. F.; Bloino, J.; Zheng, G.; Sonnenberg, J. L.; Hada, M.; Ehara, M.; Toyota, K.; Fukuda, R.; Hasegawa, J.; Ishida, M.; Nakajima, T.; Honda, Y.; Kitao, O.; Nakai, H.; Vreven, T.; Montgomery, J. A.; Peralta, Jr., J. E.; Ogliaro, F.; Bearpark, M.; Heyd, J. J.; Brothers, E.; Kudin, K. N.; Staroverov, V. N.; Kobayashi, R.; Normand, J.; Raghavachari, K.; Rendell, A.; Burant, J. C.; Iyengar, S. S.; Tomasi, J.; Cossi, M.; Rega, N.; Millam, J. M.; Klene, M.; Knox, J. E.; Cross, J. B.; Bakken, V.; Adamo, C.; Jaramillo, J.; Gomperts, R.; Stratmann, R. E.; Yazyev, O.; Austin, A. J.; Cammi, R.; Pomelli, C.; Ochterski, J. W.; Martin, R. L.; Morokuma, K.; Zakrzewski, V. G.; Voth, G. A.; Salvador, P.; Dannenberg, J. J.; Dapprich, S.; Daniels, A. D.; Farkas, O.; Foresman, J. B.; Ortiz, J. V.; Cioslowski, J.; Fox, D. J. Gaussian 16, Revision B.01, Gaussian, Inc., Wallingford CT, **2016**.

24   Y. Zhao and D. G. Truhlar, *Theor. Chem. Acc.*, 2008, **120**, 215–241.

25   Y. Zhao and D. G. Truhlar, *Acc. Chem. Res.*, 2008, **41**, 157–167.

26   W. J. Stevens, M. Krauss, H. Basch and P. G. Jasien, *Can. J. Chem.*, 1992, **70**, 612–630.

27   T. R. Cundari and W. J. Stevens, *J. Chem. Phys.*, 1993, **98**, 5555–5565.

28   M. D. Hanwell, D. E. Curtis, D. C. Lonie, T. Vandermeersch, E. Zurek and G. R. Hutchison, *J. Cheminform.*, 2012, **4**, 17.

29   M. Stender, M. M. Olmstead, A. L. Balch, D. Rios and S. Attar, *Dalton Trans.*, 2003, 4282.

30   R. Galassi, M. M. Ghimire, B. M. Otten, S. Ricci, R. N. McDougald, R. M. Almotawa, D. Alhmoud, J. F. Ivy, A.-M. M. Rawashdeh, V. N. Nesterov, E. W. Reinheimer, L. M. Daniels, A. Burini and M. A. Omary, *Proc. Natl. Acad. Sci.*, 2017, 201700890.

31   D. Yang, Y. Jiao, L. Yang, Y. Chen, S. Mizoi, Y. Huang, X. Pu, Z. Lu, H. Sasabe and J. Kido, *J. Mater. Chem. A*, 2015, **3**, 17704–17712.

32   A. D. Nicholas, D. A. Welch, X. Li and H. H. Patterson, *Inorganica Chim. Acta*, 2018, **471**, 40–49.

33   X. Li and H. Patterson, *Materials (Basel).*, 2013, **6**, 2595–2611.

34   E. L. Clennan, X. Zhang and T. Petek, *Phosphorus. Sulfur. Silicon Relat. Elem.*, 2017, **192**, 222–226.

35   D. Rehm and A. Weller, *Isr. J. Chem.*, 1970, **8**, 259–271.

36   D. Parker, *Coord. Chem. Rev.*, 2000, **205**, 109–130.

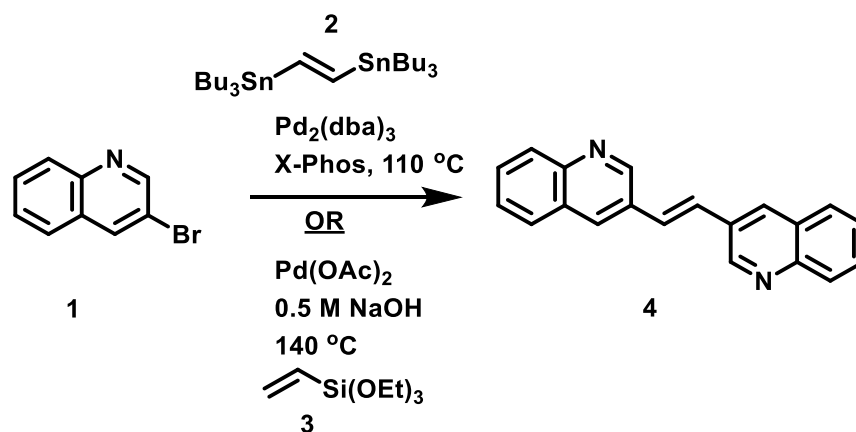**Synthetic and Crystallization Details.**

Figure G.1. Scheme for the Stille Coupling reaction.

Stille Coupling.

Bis-1,2-tributylstannyl ethane (**2**): Tributylstannyl acetylene (328 mg, 1 mmol) & tributylstannyl hydride (291 mg, 1 mmol) were added to a vial with AIBN (3.3 mg, 0.02 mmol). The mixture was heated and stirred at 100 °C for 6 hrs. Water was added to the reaction mixture and the product was extracted with four aliquots of methylene chloride and dried over Na_2SO_4. The solvent was evaporated under reduced pressure. Yield: 549 mg (90%). **^{1}H NMR (400 MHz, CDCl$_3$)** δ 6.89 (s, 2H), 1.46-1.64 (m, 12H), 1.25-1.44 (m, 12H), 0.80-0.98 (m, 30H) ppm. Characterization data closely matches with the reference (Hou, J.; Tan, Z.; He, Y.; Yang, C.; Li, Y. *Macromolecules* **2006**, *39* (14), 4657–4662)

3-Bromoquinoline (131 mg, 0.63 mmol) and Bis-1,2 tributylstannyl ethene (194 mg, 0.32 mmol) were added to a vial purged with N_2. Tris(dibenzylideneacetone)dipalladium (0) catalyst (0.1 eq.) & 2-dicyclohexylphosphino-2',4',6'-triisopropylbiphenyl (Xphos) (0.2 eq.) were added to the reaction vial, followed by addition of dry toluene (4 mL) under N_2. The reaction mixture was heated to 110 °C for 2

days. The solvent was evaporated under reduced pressure and crude was purified with flash chromatography using 70%:30% ethyle acetate:hexane mixture with 1% triethylamine to get (E)-1,2-Di(quinoline-3-yl)ethane (**4**). Yield: 51mg (57%).

Hiyama-Heck Coupling.

A mixture of triethoxyvinylsilane (0.43 g, 2.25 mmol) and sodium hydroxide (0.5 M, 18 mL) was added to a 40 mL pressure vial, followed by addition of 3-bromoquinoline (0.75 g, 3.60 mmol) & palladium acetate (0.5 mol%). The reaction vial was sealed with teflon, heat resistant screw cap, and the mixture was stirred at 140 ºC for 6 hrs. After cooling, the green precipitate was filtered and washed with 10:1 ethyl acetate:chloroform. The product (**4**) was dried under vacuum. Yield: 0.46 g (91%). **¹H NMR (400 MHz, CDCl₃)** δ 9.19 (d, 2H, *J*=2.1 Hz), 8.25 (d, 2H, *J*=2.1 Hz), 8.11 (d, 2H, *J*=8.4 Hz), 7.86 (d, 2H, *J*=8.0 Hz), 7.72 (ddd, 2H, *J*=8.3,7.0,0.9 Hz), 7.58 (ddd, 2H, *J*=8.1,6.7,0.9 Hz), 7.47 (s, 2H) ppm. **¹³C NMR (101 MHz, DMSO-d⁶)** δ 175.40, 151.16,149.62,145.85, 137.60, 130.34, 130.07, 128.96, 127.61, 116.79 ppm. **HRMS (TOF MS ES+)** m/z calculated for C₂₀H₁₅N₂ [M-H]⁺ 283.1235, found 283.1231
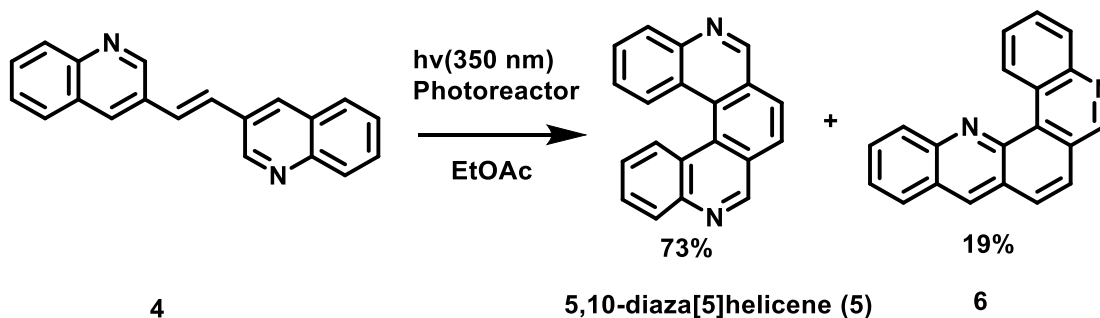
Figure G.2. Scheme for the Hiyama-Heck coupling reaction.

(E)-1,2-Di(quinoline-3-yl) ethane (**4**) (0.6 g, 2.1 mmol) was dissolved in ethyl acetate (500 mL) in a round bottom flask. A cold(water-trapped) condenser was attached to the top and the setup was mounted inside a photoreactor on a stir-plate. The mixture was stirred and irradiated at 350 nm for 7 hrs. The solvent was evaporated and the product (**5**) was purified with silica-gel chromatography using 70%:30% ethyl acetate:hexane. Yield: 0.43 g (73%) **¹H NMR (400 MHz, CDCl₃)** δ 9.46 (s, 2H), 8.65 (dd, 2H,

J=8.4,1.2 Hz), 8.29 (dd, 2H, *J*=8.3,1.3 Hz), 8.14 (s, 2H), 7.76 (ddd, 2H, *J*=8.3,7.0,1.3 Hz), 7.44 (ddd, 2H,

J=8.4,7.0,1.3 Hz) ppm. **^{13}C NMR (101 MHz, CDCl$_3$)** δ 152.53, 145.88, 129.71, 129.48, 129.43, 128.17,

127.32, 127.26, 125.61, 124.38 ppm. **HRMS (TOF MS ES+)** m/z calculated for C$_{20}$H$_{13}$N$_2$ [M-H]$^+$

281.1079, found 281.1070. Side-product- Benzo-[b]-1,8-diaza[4]-helicene (**6**) Yield: 0.11 g (19%) **^{1}H**

NMR (400 MHz, CDCl$_3$) δ 11.37 (d, 1H, *J*=Hz), 9.37 (s, 1H), 8.75 (s,1H), 8.49 (d, 2H, *J*=8.7 Hz), 8.30

(d,2H, *J*=8.1 Hz), 8.09-7.98 (m, 2H), 7.93-7.83 (m, 4H), 7.67 (dd, 1H, *J*= 7.96, 6.92 Hz) ppm.
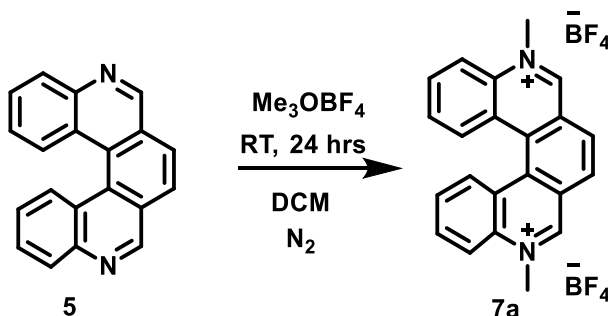
Figure G.3. Scheme for the methylation of compound (5).

To trimethyloxonium tetrafluoroborate/ Meerwein's salt (0.356 g, 2.39 mmol) in a 40 mL scintillation

vial was added anhydrous methylene chloride (100 mL) under N$_2$. Solution of 5,10-diaza[5]helicene (**5**)

(0.223 g, 0.80 mmol) in anhydrous methylene chloride (20 mL) was added to the vial under N$_2$. The

reaction mixture was stirred under nitrogen for 24 hrs. Methylene chloride was removed under vacuum.

The crude product was triturated with warm 90% ethanol. The product (**7a**) was further purified with

preparative HPLC using 5% to 15% acetonitrile in 10 minutes. Yield: 233 mg (60%) **^{1}H NMR (400**

MHz, CD$_3$CN) δ 10.04 (d,2H,*J*=2.2 Hz), 8.72 (d,2H,*J*=8.5 Hz), 8.67 (d, 2H, *J*=1.5 Hz), 8.57 (d, 2H,

J=8.5 Hz), 8.24 (ddd, 2H, *J*=8.7,7.4,1.3 Hz), 7.88 (ddd, 2H, *J*=8.3,7.3,1.0 Hz), 4.82 (s, 6H) ppm. **^{13}C**

NMR (101 MHz, CD$_3$CN) δ 154.82, 136.93, 135.12, 133.74, 131.78, 131.06, 129.86, 129.32, 127.33,

120.34, 47.60 ppm. **HRMS (TOF MS ES+)** m/z calculated for C$_{20}$H$_{15}$N$_2$ [M]$^{+2}$ 155.0735, found 155.0731
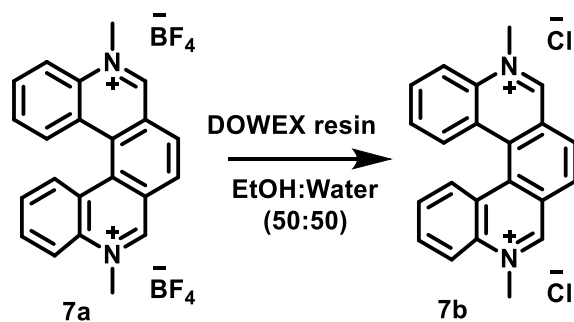
Figure G.4. Scheme for the tetrafluoroborate/chloride exchange reaction.

DOWEX® 1×8 200-400 mesh ion-exchange resin (*Acros©)* (11.25 g) was loaded into a column and washed with methanol followed by equilibration with 50% aqueous ethanol. N,N-Dimethylaza[5]helicene (Tetrafluoroborate) (225 mg, 0.46 mmol) dissolved in acetonitrile (0.5 mL) was loaded on the column. The column was washed with 50% aqueous ethanol. The collected product was concentrated and reloaded on the column and collected two more times. The filtrate was concentrated under reduced pressure to yield the product (**7b**). Yield: 167 mg (95%). **¹H NMR (400 MHz, CD₃OD)** δ 10.54 (d, 2H, *J*=2.2 Hz), 8.86 (d, 2H, *J*=8.4 Hz), 8.82 (d, 2H, *J*=1.2 Hz), 8.75 (d, 2H, *J*=8.7 Hz), 8.28 (ddd, 2H, *J*=8.6,7.3,1.3 Hz), 7.92 (ddd, 2H, *J*=8.2,7.3,1.0 Hz), 4.99 (s, 6H) ppm. **¹³C NMR (101 MHz, CD₃OD)** δ 155.89, 137.21, 135.33, 133.99, 132.12, 130.97, 130.46, 129.73, 127.63, 120.59, 47.12 ppm. **HRMS (TOF MS ES+)** m/z calculated for $C_{20}H_{15}N_2$ $[M]^{+2}$ 155.0735, found 155.0735
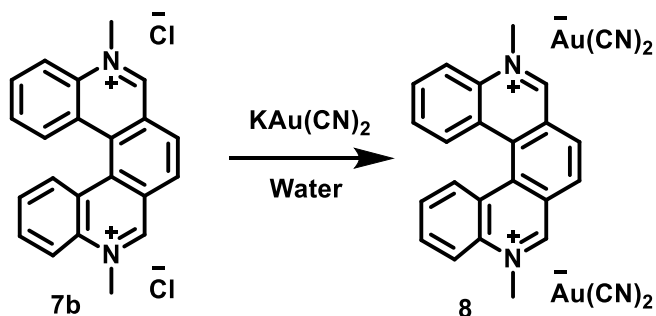
Figure G.5. Scheme for the synthesis of Au heli-viologen from compound (7b).

To a solution of N,N-Dimethylaza[5]helicene dichloride (**7b**) (40 mg, 0.104 mmol) in dI water (30 mL), potassium dicyanoaurate (60 mg, 0.21 mmol) in dI water was added while stirring. Within a hour precipitate started forming. The precipitate was filtered and solvent was slowly evaporated to complete the precipitation of N,N-Dimethylaza[5]helicene dicyanoaurate. The powdery product (**8**) was dried under reduced pressure and used for crystallization. Yield: 49 mg (58%). **^{1}H NMR (400 MHz, CD$_3$OD)** δ 10.49 (d,2H,J=2.2 Hz), 8.89 (d,2H,J=8.8 Hz), 8.80 (d,2H,J=2.1 Hz), 8.75 (d,2H,J=9.0 Hz), 8.29 (ddd,2H,J=8.6,7.5,1.1 Hz), 7.95 (ddd,2H,J=8.6,7.5,1.1 Hz), 4.97 (s,6H) ppm. **^{13}C NMR (101 MHz, D$_2$O)** δ 153.67, 135.70, 134.10, 133.08, 130.69, 129.96, 129.93, 128.96, 128.51, 126.43, 119.03 ppm.

Crystallization.

N,N-Dimethylaza[5]helicene dicyanoaurate (10 mg) was dissolved in ethanol (0.2 mL) in a 2 mL scintillation vial. This vial was covered with porous aluminum foil and placed in a 20 mL scintillation vial containing cyclohexane (2 mL). The vial was capped, and the system was kept inside the fume hood for 8 to 9 days. Small crystals yielded through slow vapor diffusion. The results were reproduced with methanol as a solvent and n-hexane as antisolvent.
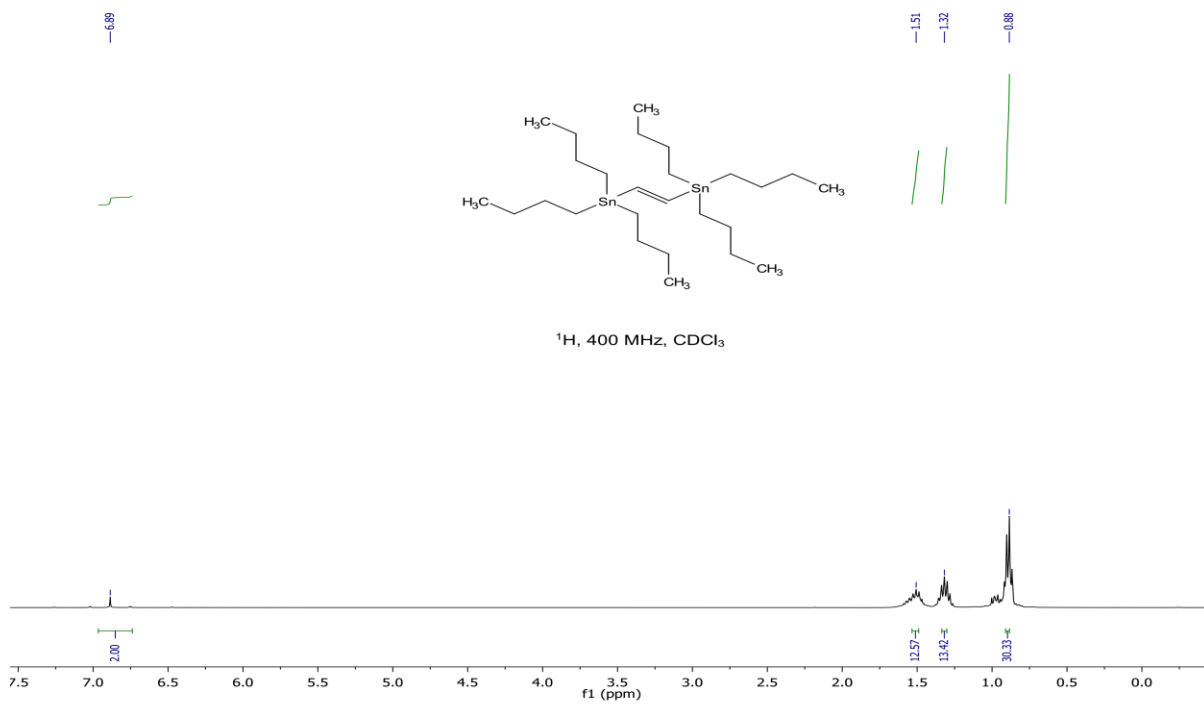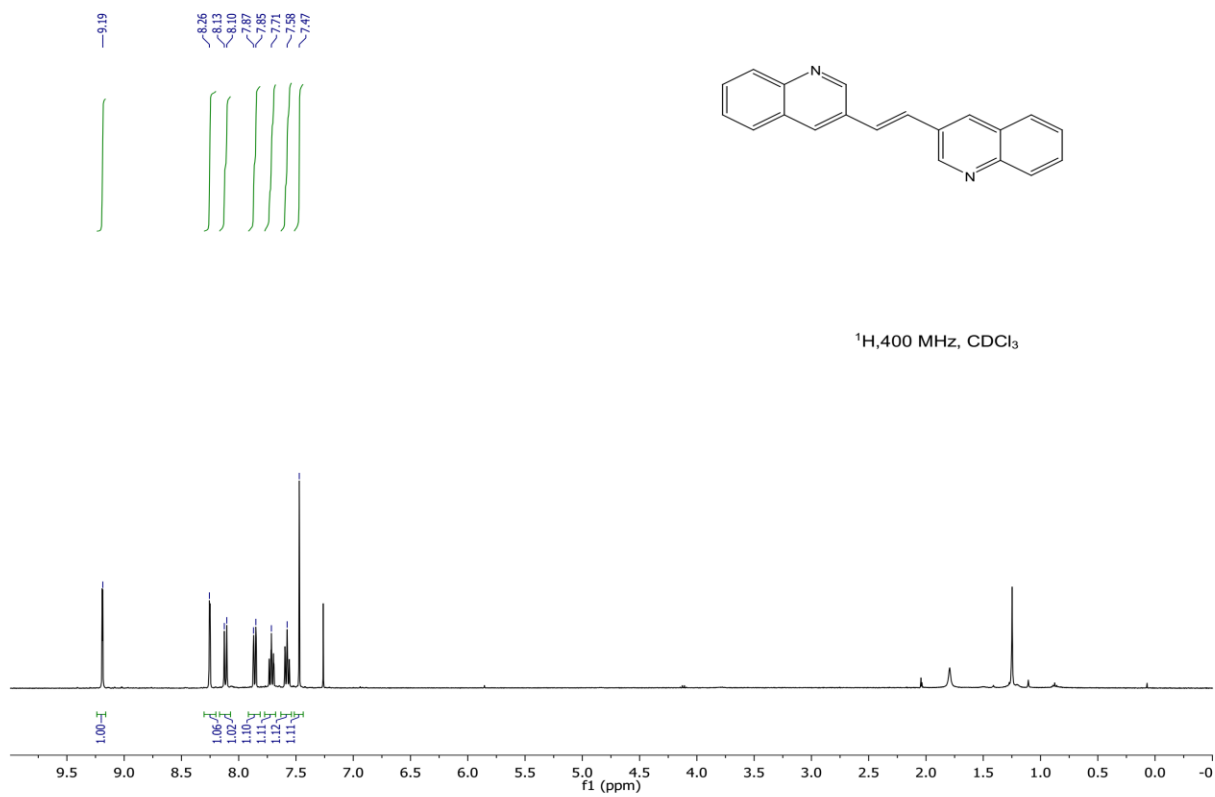
Figure G.6. ¹H MNR spectrum of **2**.

¹H,400 MHz, CDCl₃
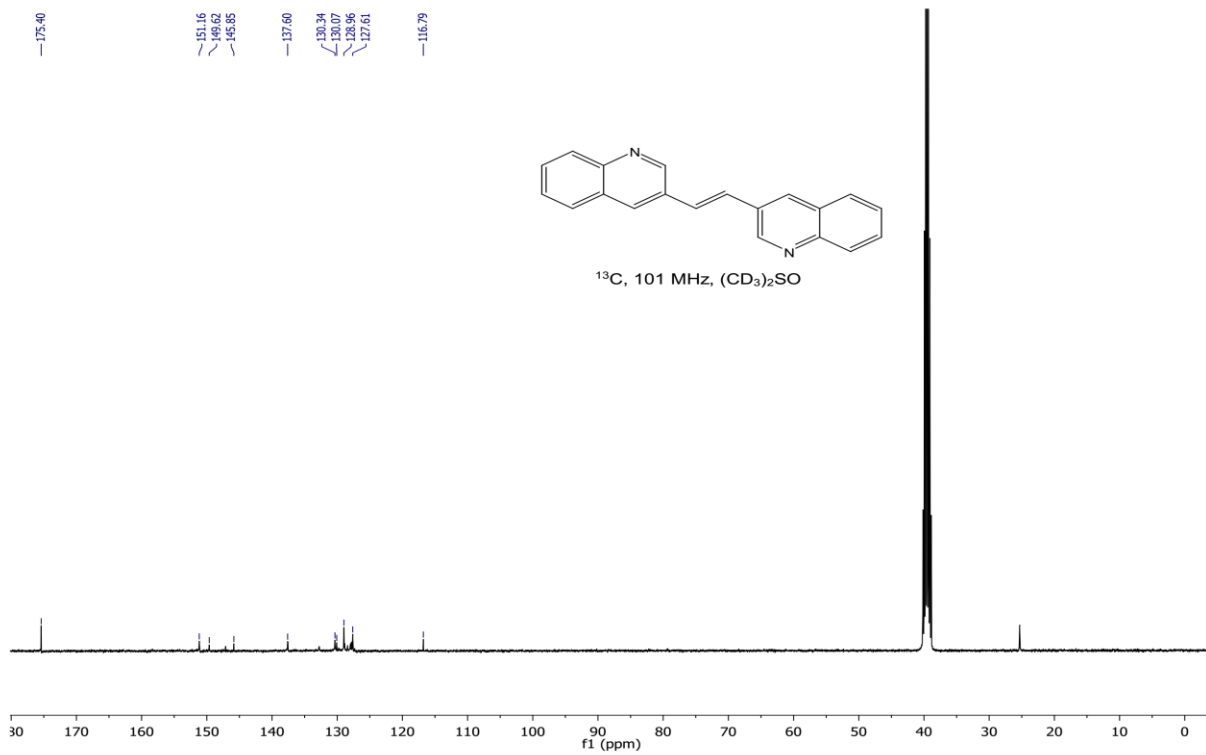
Figure G.7. ¹H MNR spectrum of **4**.

Figure G.8. [13]C MNR spectrum of **4**.

Figure G.9. ¹H MNR spectrum of **5**.

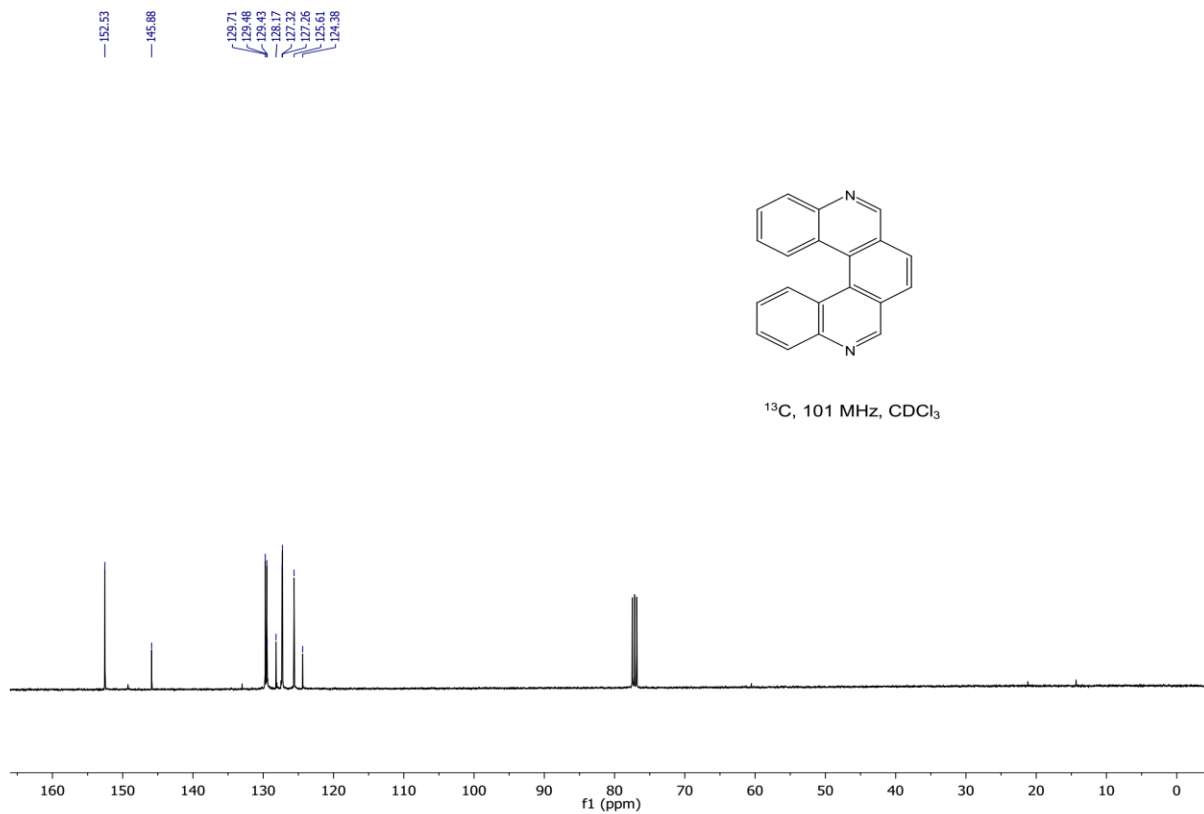¹³C, 101 MHz, CDCl₃
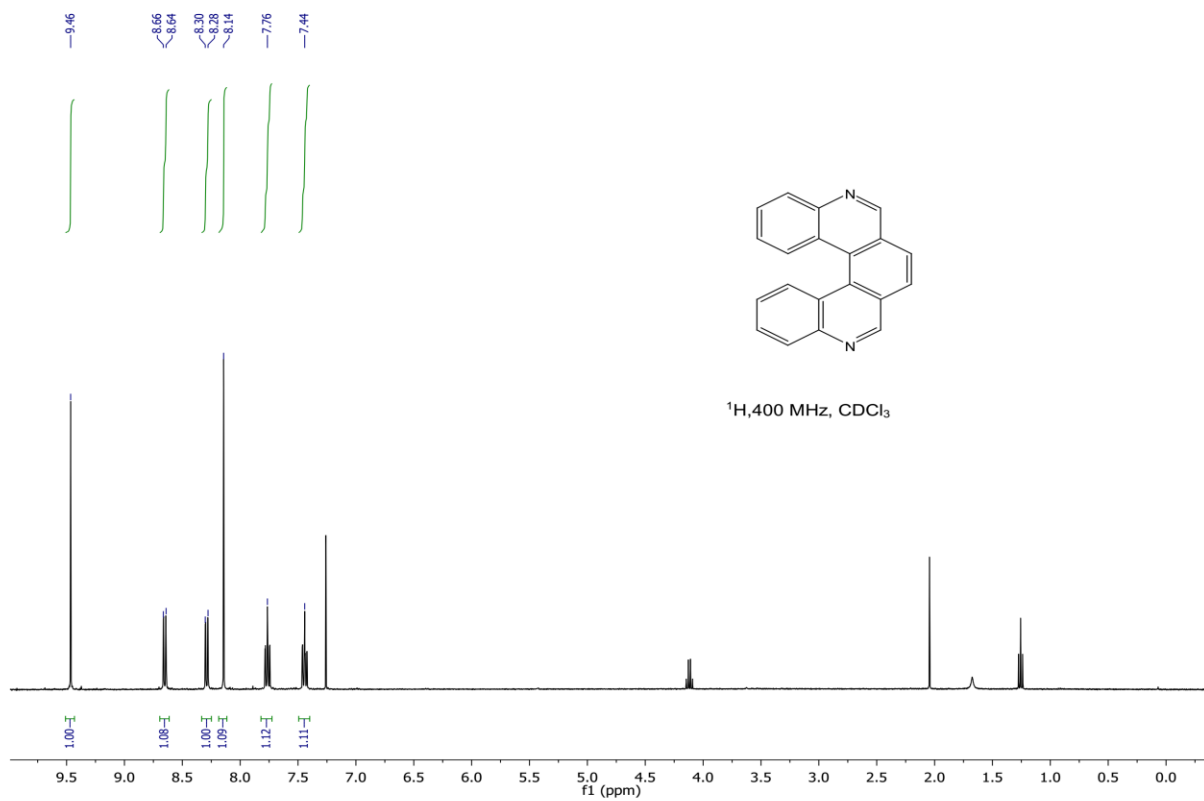
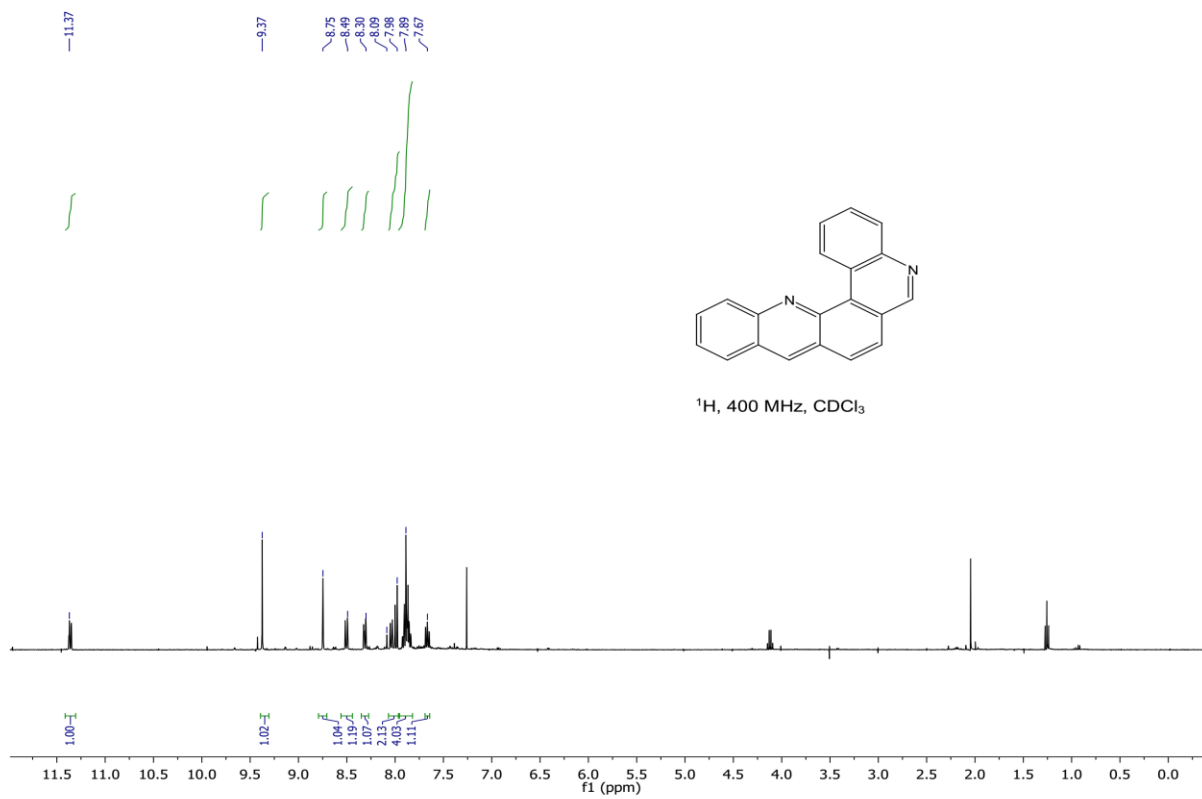**Figure G.10.** ¹³C MNR spectrum of **5**.

Figure G.11. ¹H MNR spectrum of **6**.
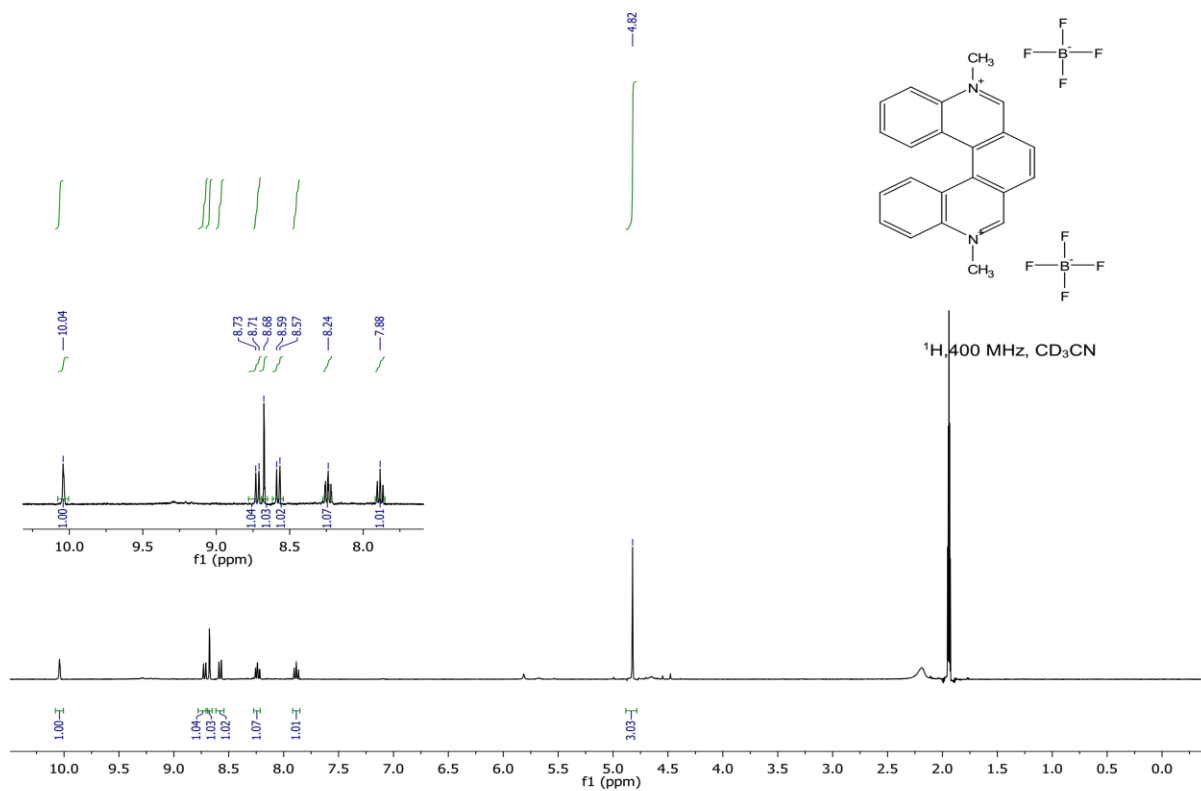
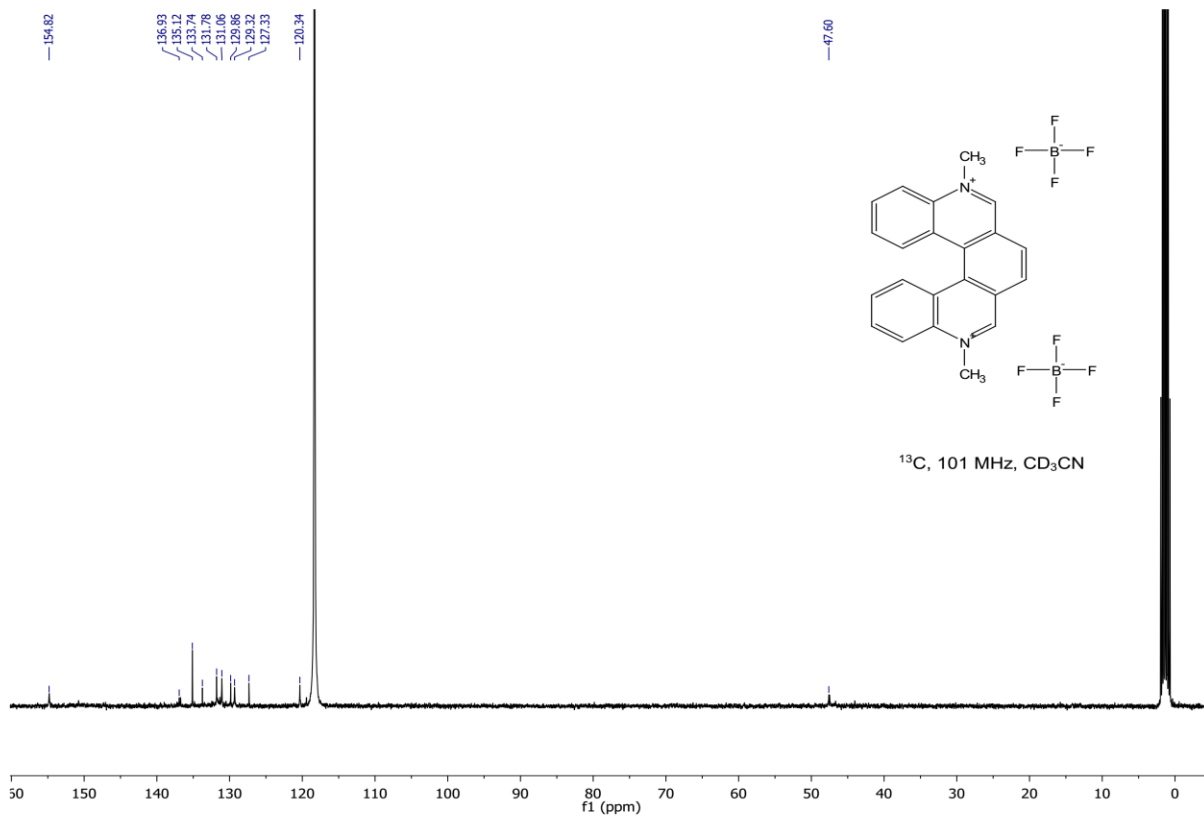**Figure G.12.** ^{1}H MNR spectrum of **7a**.

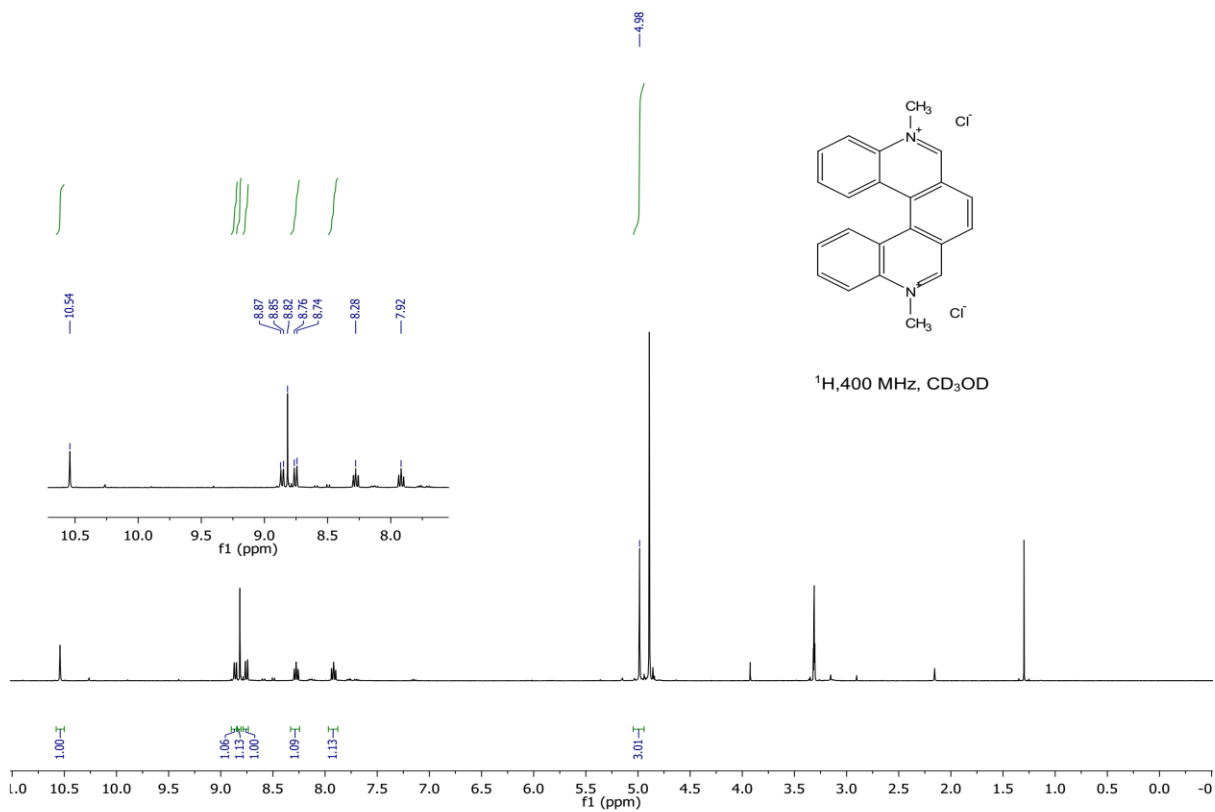**Figure G.13.** ^{13}C MNR spectrum of **7a**.

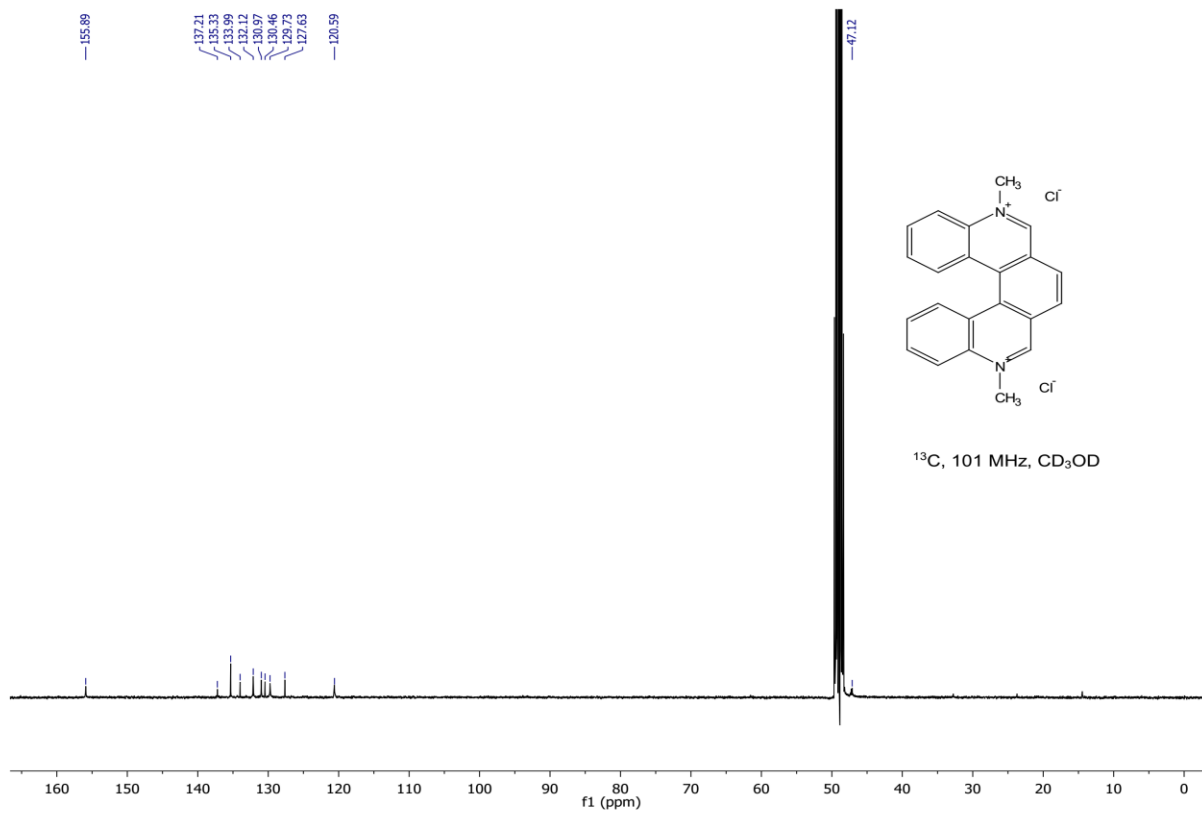**Figure G.14.** ^{1}H MNR spectrum of **7b**.

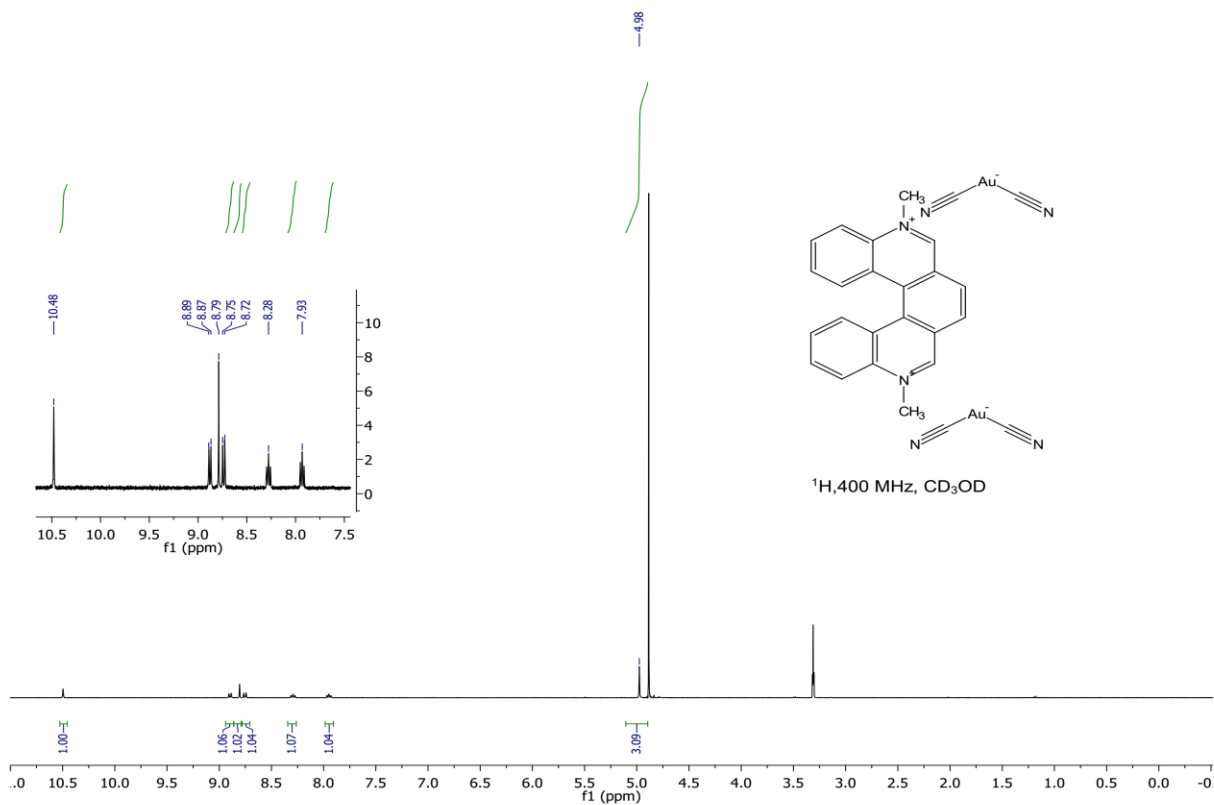**Figure G.15.** [13]C MNR spectrum of **7b**.

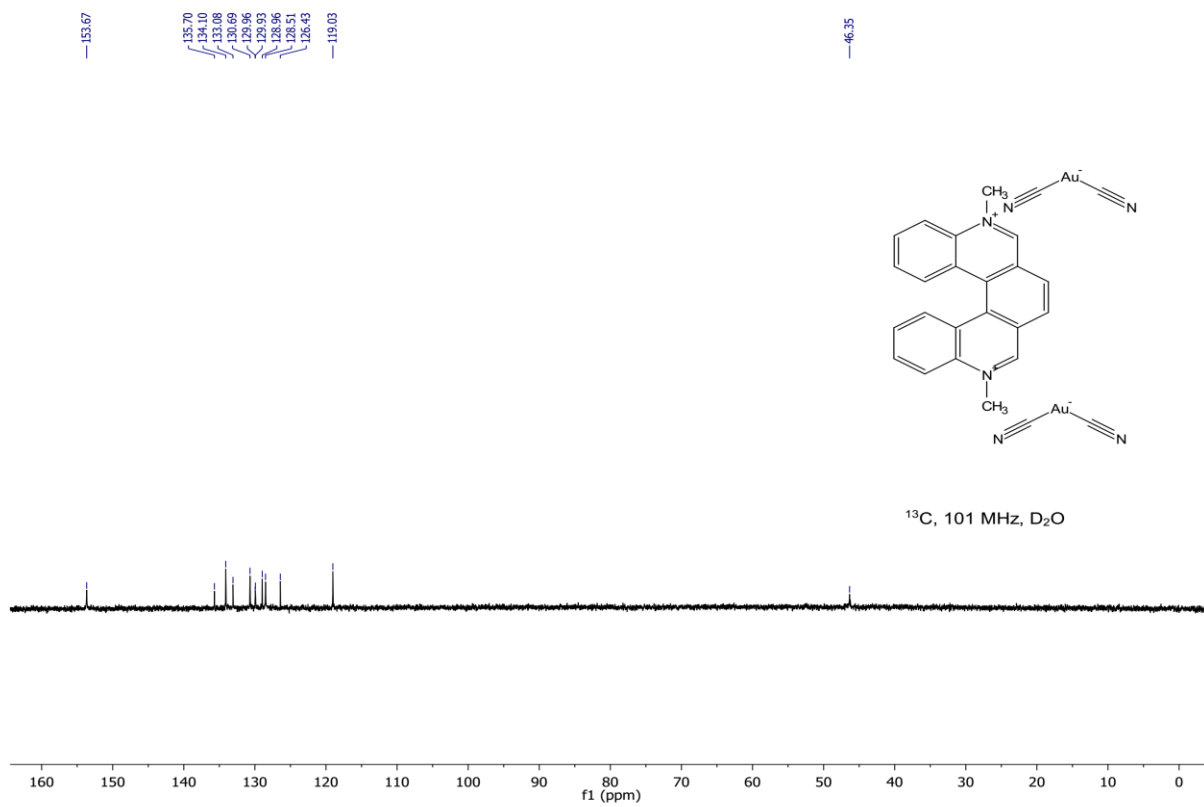**Figure G.16.** ¹H MNR spectrum of **8**.
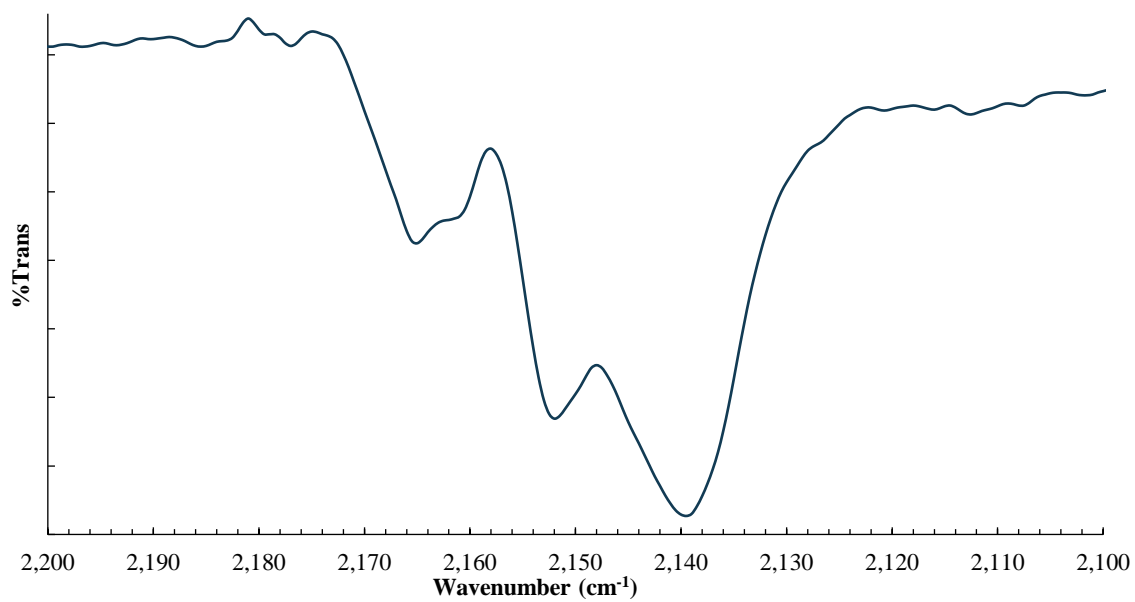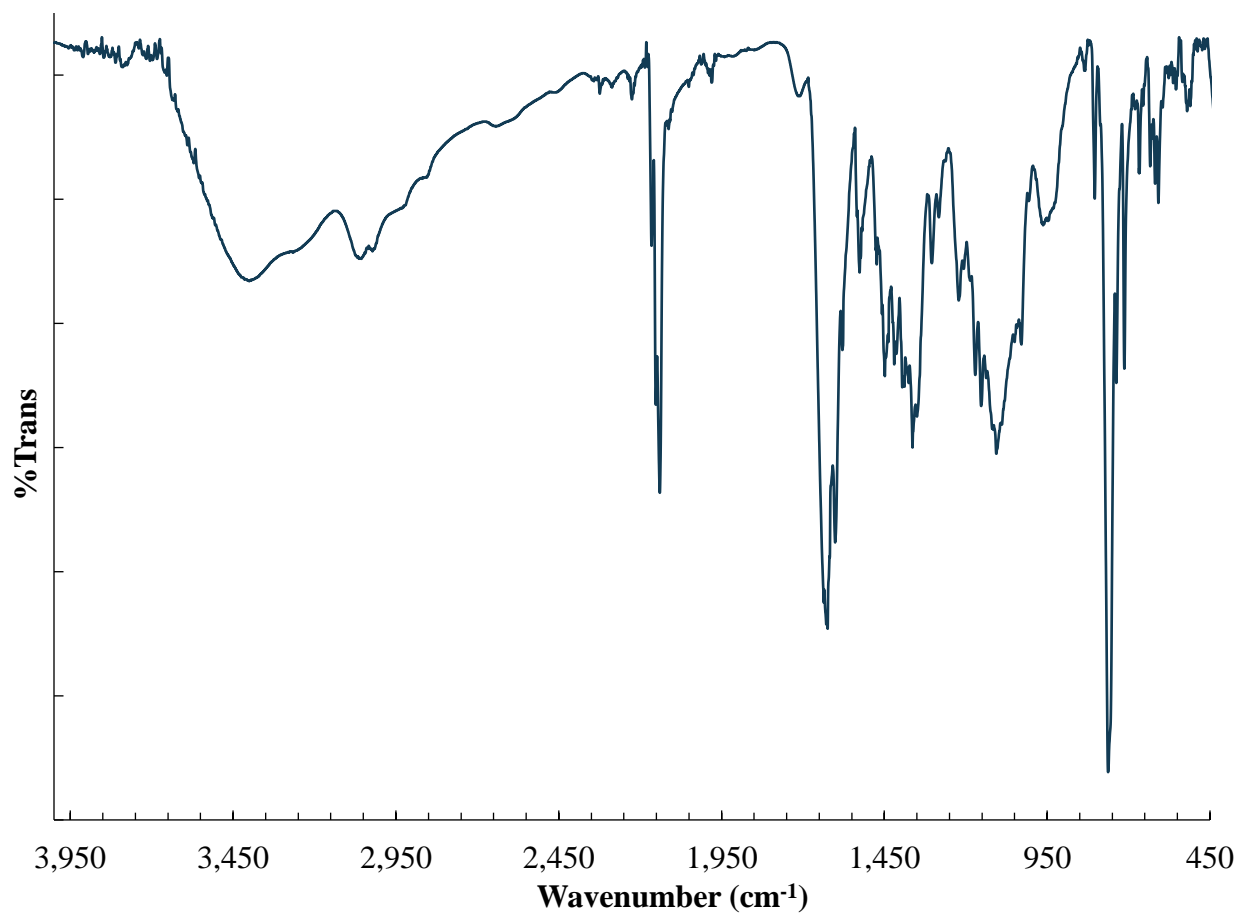
Figure G.17. ^{13}C MNR spectrum of **8**.

Figure G.18. IR spectrum of microcrystalline Au heli-viologen (**8**) at 298 K.

Table G.1. Select bond lengths of Au heli-viologen.

Au(1)-C(1)	2.0107(1)	C(9)-C(10)	1.4369(1)
Au(1)-C(2)	2.0068(1)	C(10)-C(11)	1.4131(1)
Au(2)-C(4)	1.9837(1)	C(10)-C(19)	1.3644(1)
Au(2)-C(3)	1.9433(1)	C(13)-C(18)	1.4101(1)
N(1)-C(1)	1.1318(1)	C(13)-C(14)	1.4156(1)
N(2)-C(2)	1.0913(1)	C(14)-C(15)	1.3473(1)
N(3)-C(3)	1.1708(1)	C(15)-C(16)	1.3870(1)
N(4)-C(4)	1.1198(1)	C(16)-C(17)	1.3998(1)
N(5)-C(5)	1.4637(1)	C(17)-C(18)	1.3923(1)
N(5)-C(6)	1.2860(1)	C(18)-C(19)	1.4561(1)
N(5)-C(26)	1.4028(1)	C(19)-C(20)	1.4407(1)
N(6)-C(11)	1.3096(1)	C(20)-C(21)	1.4663(1)
N(6)-C(12)	1.4724(1)	C(21)-C(26)	1.4320(1)
N(6)-C(13)	1.4031(1)	C(21)-C(22)	1.4159(1)
C(6)-C(7)	1.4320(1)	C(22)-C(23)	1.3267(1)
C(7)-C(8)	1.4136(1)	C(23)-C(24)	1.4234(1)
C(7)-C(20)	1.4379(1)	C(24)- (C25)	1.3774(1)
C(8)-C(9)	1.3398(1)	C(25)-C(26)	1.3754(1)

Table G.2. Select bond angles of Au heli-viologen.

C(1)-Au(1)-C(2)	176.62(1)	N(6)-C(13)-C(14)	120.77(1)
C(3)-Au(2)-C(4)	177.67(1)	C(13)-C(14)-C(15)	120.78(1)
Au(1)-C(1)-N(1)	177.15(1)	C(14)-C(15)-C(16)	121.68(1)
Au(1)-C(2)-N(2)	175.42(1)	C(15)-C(16)-C(17)	117.87(1)
Au(2)-C(3)-N(3)	175.29(1)	C(16)-C(17)-C(18)	122.24(1)
Au(2)-C(4)-N(4)	176.96(1)	C(13)-C(18)-C(17)	117.82(1)
C(11)-N(6)-C(13)	119.08(1)	C(13)-C(18)-C(19)	118.40(1)
C(12)-N(6)-C(13)	119.16(1)	C(17)-C(18)-C(19)	118.40(1)
C(11)-N(6)-C(12)	121.62(1)	C(10)-C(19)-C(20)	116.99(1)
C(5)-N(5)-C(26)	118.65(1)	C(10)-C(19)-C(18)	116.94(1)
C(6)-N(5)-C(26)	122.98(1)	C(18)-C(19)-C(20)	125.97(1)
C(5)-N(5)-C(6)	117.87(1)	C(7)-C(20)-C(21)	116.80(1)
N(5)-C(6)-C(7)	123.13(1)	C(19)-C(20)-C(21)	126.22(1)
C(6)-C(7)-C(8)	120.84(1)	C(7)-C(20)-C(19)	116.64(1)
C(8)-C(7)-C(20)	121.99(1)	C(20)-C(21)-C(26)	119.32(1)
C(6)-C(7)-C(20)	117.14(1)	C(22)-C(21)-C(26)	116.97(1)
C(7)-C(8)-C(9)	119.55(1)	C(20)-C(21)-C(22)	122.64(1)
C(8)-C(9)-C(10)	118.18(1)	C(21)-C(22)-C(23)	121.43(1)
C(9)-C(10)-C(19)	124.38(1)	C(22)-C(23)-C(24)	120.64(1)
C(11)-C(10)-C(19)	120.09(1)	C(23)-C(24)-C(25)	119.77(1)
C(9)-C(10)-C(11)	115.47(1)	C(24)-C(25)-C(26)	119.63(1)
N(6)-C(11)-C(10)	122.91(1)	N(5)-C(26)-C(21)	117.72(1)
N(6)-C(13)-C(18)	120.16(1)	C(21)-C(26)-C(25)	120.78(1)
C(14)-C(13)-C(18)	118.99(1)	N(5)-C(26)-C(25)	121.41(1)

Table G.3. DFT B3LYP/LANL2DZ select ground state parameters of Au heli-viologen with comparison to experimental values.

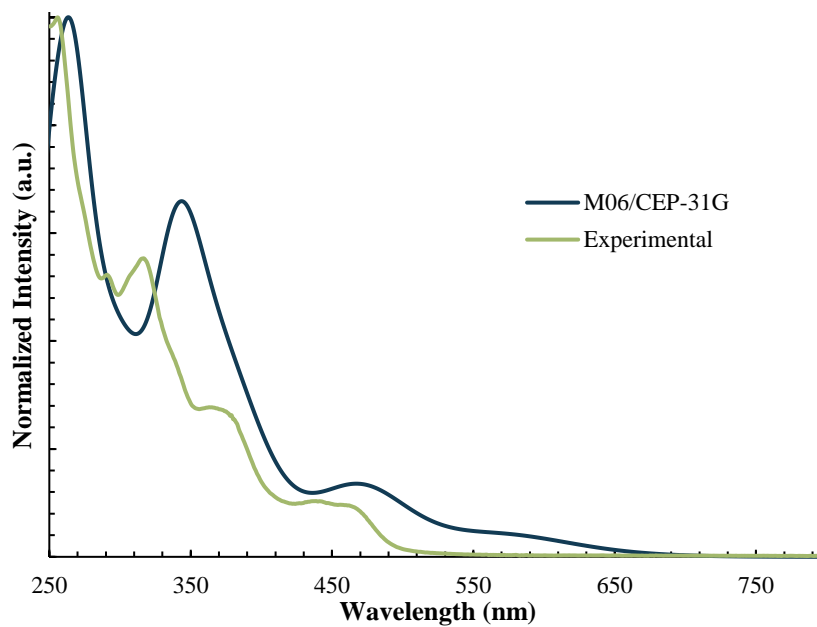| | Distance (Å) / Angle (º) | |
	Experimental*	Calculated*
Au···Au	3.310	3.327
$N_{Au(CN)_2}$···$N_{aza[5]helicene}$	3.216	3.088
Au-C	2.010	2.029
C-Au-C	176.6	166.8
N-C-Au	177.1	169.6

*Average distances

Figure G.19. TD-DFT M06/CEP-31G calculated UV-vis of Au heli-viologen compared to experimental UV-Vis.

Table G.4. TD-DFT calculated excited states of of Au heli-viologen with corresponding energy and f-oscillation.

Excited State Number	Excited State Energy	Excited State f-oscillation
7	428 nm	0.0078
8	425 nm	0.0067
9	423 nm	0.0014
10	421 nm	0.0000
11	421 nm	0.0069
12	420 nm	0.0027
13	406 nm	0.0004
14	404 nm	0.0009
15	401 nm	0.0028
16	399 nm	0.0132
17	392 nm	0.0011
18	390 nm	0.0083

Table G.5. Calculated MO transitions of Au heli-viologen for excited state at 399 nm with percent contribution.

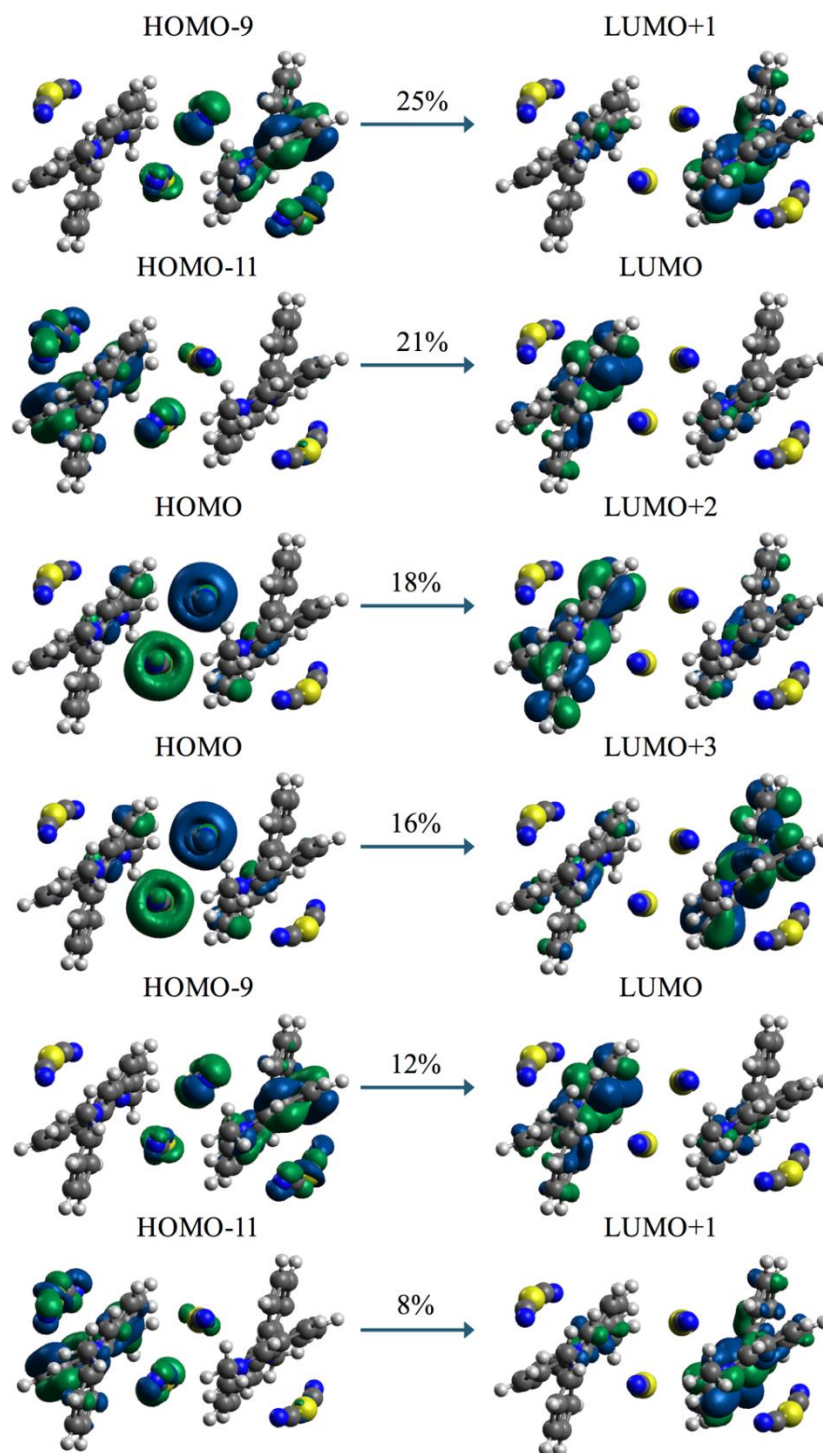| Orbital Transition	% Contribution
HOMO-9→LUMO+1	25%
HOMO-11→LUMO	21%
HOMO→LUMO+2	18%
HOMO→LUMO+3	16%
HOMO-9→LUMO	12%
HOMO-11→LUMO+1	8%

Figure G.20. Isodensity representations of MO transitions of excited state at 399 nm for Au heli-viologen with percent contribution.

BIOGRAPHY OF THE AUTHOR

Robert Brent Arthur was born in Durham, North Carolina on July 9, 1990. After graduating from Wando High School in Mount Pleasant, South Carolina, Robert entered Clemson University in Clemson, South Carolina to pursue a Bachelor's degree in Chemistry. After one year at Clemson University, Robert transferred to the College of Charleston in Charleston, South Carolina, where he graduated with a Bachelor's degree in Chemistry. Robert then worked for two years for the MeadWestvaco Corporation in North Charleston, South Carolina in the role of Associate Chemist. Robert entered the graduate program of the Department of Chemistry at the University of Maine in the fall of 2015. Robert has been a Teaching Assistant for the General Chemistry program of the department from 2015 to 2019 and is the recipient of the Outstanding General Chemistry Teaching Assistant Award from the Department of Chemistry. Robert is a candidate for the Doctor of Philosophy degree in Chemistry from the University of Maine in May 2019.